ASME
SETTING THE STANDARD



**Transactions of the ASME, Journal of Turbomachinery** (ISSN 0889-504X) is published quarterly (Jan., Apr., July, Oct.) by The American Society of Mechanical Engineers, Three Park Avenue, New York, NY 10016. Periodicals postage paid at New York, NY and additional mailing offices.
POSTMASTER: Send address changes to Transactions of the ASME, Journal of Turbomachinery, c/o THE AMERICAN SOCIETY OF MECHANICAL ENGINEERS, 22 Law Drive, Box 2300, Fairfield, NJ 07007-2300.
**CHANGES OF ADDRESS** must be received at Society headquarters seven weeks before they are to be effective. Please send old label and new address.
**STATEMENT from By-Laws.** The Society shall not be responsible for statements or opinions advanced in papers or ... printed in its publications (B7.1, Par. 3).


# Journal of Turbomachinery

**Published Quarterly by ASME**

**VOLUME 128 • NUMBER 4 • OCTOBER 2006**

## TECHNICAL PAPERS



(**Contents continued on inside back cover**)

This journal is printed on acid-free paper, which exceeds the ANSI Z39.48-1992 specification for permanence of paper and library materials. ♾™
♻ 85% recycled content, including 10% post-consumer fibers.

Journal of Turbomachinery Volume 128, Number 4 OCTOBER 2006



## TECHNOLOGY REVIEW



The ASME Journal of Turbomachinery is abstracted and indexed in the following:

*Aluminum Industry Abstracts, Aquatic Science and Fisheries Abstracts, Ceramics Abstracts, Chemical Abstracts, Civil Engineering Abstracts, Compendex (The electronic equivalent of Engineering Index), Corrosion Abstracts, Current Contents, Ei EncompassLit, Electronics & Communications Abstracts, Energy Information Abstracts, Engineered Materials Abstracts, Engineering Index, Environmental Science and Pollution Management, Excerpta Medica, Fluidex, Fuel and Energy Abstracts, INSPEC, Index to Scientific Reviews, Materials Science Citation Index, Mechanical & Transportation Engineering Abstracts, Mechanical Engineering Abstracts, METADEX (The electronic equivalent of Metals Abstracts and Alloys Index), Metals Abstracts, Oceanic Abstracts, Pollution Abstracts, Referativnyi Zhurnal, Shock & Vibration Digest, Steels Alert*

# Modeling and Experimental Investigation of Micro-hydrostatic Gas Thrust Bearings for Micro-turbomachines

**C. J. Teo**

**Z. S. Spakovszky**

Gas Turbine Laboratory,
Department of Aeronautics and Astronautics,
Massachusetts Institute of Technology,
Cambridge, MA 02139

*One major challenge for the successful operation of high-power-density micro-devices lies in the stable operation of the bearings supporting the high-speed rotating turbomachinery. Previous modeling efforts by Piekos (2000, "Numerical Simulation of Gas-Lubricated Journal Bearings for Microfabricated Machines," Ph.D. thesis, Department of Aeronautics and Astronautics, MIT), Liu et al. (2005, "Hydrostatic Gas Journal Bearings for Micro-Turbo Machinery," ASME J. Vib. Acoust., **127**, pp. 157–164), and Spakovszky and Liu (2005, "Scaling Laws for Ultra-Short Hydrostatic Gas Journal Bearings," ASME J. Vib. Acoust. **127**, pp. 254–261) have focused on the operation and stability of journal bearings. Thrust bearings play a vital role in providing axial support and stiffness, and there is a need to improve the understanding of their dynamic behavior. In this work, a rigorous theory is presented to analyze the effects of compressibility in micro-flows (characterized by low Reynolds numbers and high Mach numbers) through hydrostatic thrust bearings for application to micro-turbomachines. The analytical model, which combines a one-dimensional compressible flow model with finite-element analysis, serves as a useful tool for establishing operating protocols and assessing the stability characteristics of hydrostatic thrust bearings. The model is capable of predicting key steady-state performance indicators, such as bearing mass flow, axial stiffness, and natural frequency as a function of the hydrostatic supply pressure and thrust-bearing geometry. The model has been applied to investigate the static stability of hydrostatic thrust bearings in micro-turbine generators, where the electrostatic attraction between the stator and rotor gives rise to a negative axial stiffness contribution and may lead to device failure. Thrust-bearing operating protocols have been established for a micro-turbopump, where the bearings also serve as an annular seal preventing the leakage of pressurized liquid from the pump to the gaseous flow in the turbine. The dual role of the annular pad poses challenges in the operation of both the device and the thrust bearing. The operating protocols provide essential information on the required thrust-bearing supply pressures and axial gaps required to prevent the leakage of water into the thrust bearings. Good agreement is observed between the model predictions and experimental results. A dynamic stability analysis has been conducted, which indicates the occurrence of instabilities due to flow choking effects in both forward and aft thrust bearings. A simple criterion for the onset of axial rotor oscillations has been established and subsequently verified in a micro-turbocharger experiment. The predicted frequencies of the unstable axial oscillations compare well with the experimental measurements.*
[DOI: 10.1115/1.2219760]

## Background and Motivation

All high speed rotating devices require thrust bearings to provide axial support and stiffness. Examples of such devices for power—micro-electro-mechanical systems (MEMS) applications in the Massachusetts Institute of Technology (MIT) Microengine project are shown in Fig. 1 and include micro-turbochargers [1], micro-turbopumps [2], and micro-turbine-generators [3]. The thrust bearings of these micro-devices are hydrostatic, as they possess several significant advantages over their hydrodynamic counterparts. For example, hydrodynamic thrust bearings are incapable of developing a sufficiently high stiffness at low rotational speeds, since the magnitude of the stiffness arises from the relative motion between the stationary and rotating bearing surfaces. In contrast, hydrostatic thrust bearings depend on a controllable external pressure supply to generate stiffness, which depends only weakly on the rotational speed of the rotor. Furthermore, hydrodynamic thrust bearings in general require smaller clearances than their hydrostatic counterparts. This poses two major challenges in power-MEMS applications: (1) The drag penalty associated with hydrodynamic thrust bearings outweighs that of hydrostatic thrust bearings, and (2) the requirement for smaller running gaps in hydrodynamic thrust bearings renders them more susceptible to failure due to geometric nonuniformities. Hydrodynamic thrust bearings are also known to possess poor stability characteristics at high speeds, as discussed by Constantinescu and Galetuse [4,5]. In view of the above-mentioned shortcomings of hydrodynamic thrust bearings, inherent restrictor-orifice hydrostatic thrust bearings were selected to provide axial support and stiffness in the MIT MEMS-based micro-devices.

There are a number of challenges associated with the development of micro-hydrostatic thrust bearings. The geometric dimensions of the micro-hydrostatic thrust bearings employed in the

Contributed by the International Gas Turbine Institute (IGTI) of ASME for publication in the JOURNAL OF TURBOMACHINERY. Manuscript received October 1, 2004; final manuscript received February 1, 2005. IGTI Review Chair: K. C. Hall. Paper presented at the ASME Turbo Expo 2005: Land, Sea and Air, Reno, NV, June 6–9, 2005, Paper No. GT2005-68222.

  

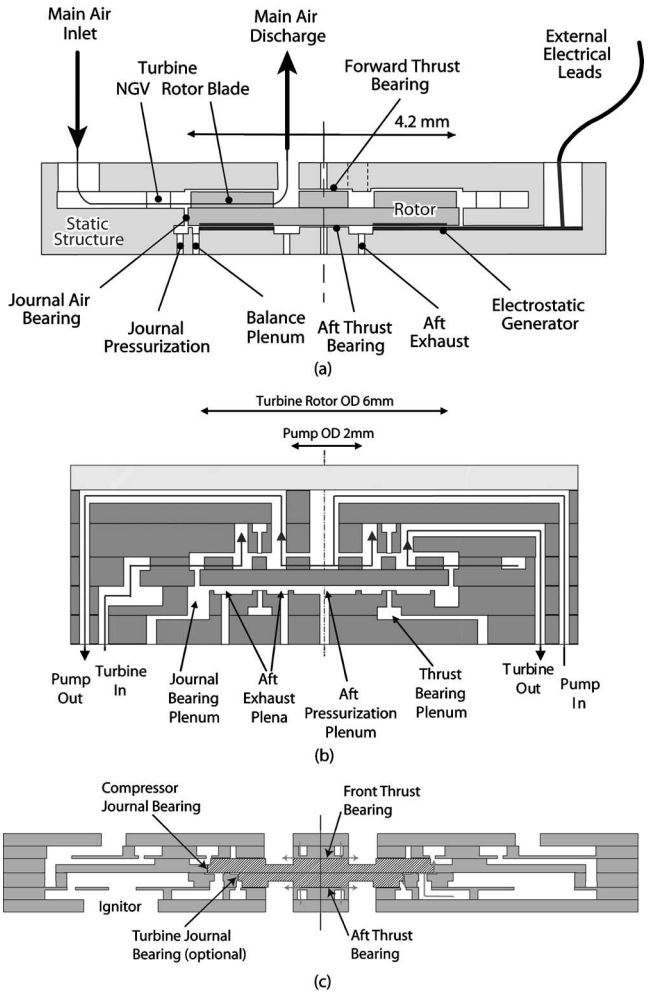


**Fig. 1 Cross-sectional view of silicon-based MIT micro-devices; (*a*) micro-turbine-generator, (*b*) micro-turbopump, (*c*) micro-turbocharger**

MIT micro-devices are typically one to two orders of magnitude smaller than conventional hydrostatic thrust bearings (the thrust-bearing gap of the MIT micro-devices is of order 3 $\mu$m). The critical dimensions of micro-thrust bearings have to be controlled to higher levels of precision to ensure an equivalent level of reliability in operation as compared to their macro-scale counterparts. The low Reynolds numbers and high pressure ratios encountered in the micro-thrust-bearings give rise to increased interactions between viscous and compressible flow effects, necessitating the development of new models to accurately predict the bearing performance and stability. In many of the micro-devices there exists a strong coupling between the thrust bearings and the other integral components of the micro-system which poses a major challenge to the stable operation of the bearings.

**Nature of the Issues.** Figure 1 shows three MIT micro-devices supported axially by means of hydrostatic forward and aft thrust bearings. Figure 1(*a*) depicts a micro-electrostatic turbine generator, which is fabricated on the aft side of a 4.2-mm-diameter silicon rotor, and driven by a radial-inflow turbine etched on the forward side. In this device, the electrostatic attraction between the rotor and stator can result in a negative (destabilizing) axial stiffness[1] experienced by the spinning rotor. Operating protocols are thus necessary to ensure stable operation of the thrust bearings in the presence of electrostatic pull-in forces.

The cross-sectional view of a micro-turbopump is displayed in Fig. 1(*b*). The 6-mm-diameter turbopump rotor consists of a radial-outflow centrifugal pump driven by a radial-inflow turbine, both of which are situated on the forward side of the rotor. The pump, with the primary function to discharge liquid fuel to the combustion chamber of a micro-rocket, is separated from the turbine by the forward annular hydrostatic thrust bearing. Both the turbine and thrust bearings are operated using an inert gas to reduce the viscous drag which can impose a large penalty on the overall performance of the turbomachinery. This implies that the forward thrust bearing serves the dual role of a bearing providing axial support and stiffness and a seal to prevent the leakage of the liquid from the pump into the gas turbine. Such a configuration poses rotordynamic challenges which are manifested by the design requirements of a rotor speed of 750,000 rpm yielding pressures of 32 atm at pump outlet and 9 atm at turbine exit. It is thus important to assess the performance and dynamic behavior of the annular thrust-bearing system. Furthermore, operating protocols are required to ascertain the appropriate thrust-bearing supply pressure and control the rotor axial position depending on pump outlet pressure.

Figure 1(*c*) illustrates the cross-sectional view of a micro-turbocharger. Experiments on the micro-turbochargers were initially performed with low thrust-bearing supply pressures, to keep the flow through both forward and aft thrust bearings unchoked. In an attempt to increase the axial stiffness of the thrust bearings to avoid resonance issues near the natural frequency, the supply pressure to both thrust bearings was increased, operating with choked flow through the orifices of both thrust bearings. This had a detrimental effect on thrust-bearing dynamic behavior and stability, which will be discussed in detail in this paper.

The close coupling between the thrust bearings and the rest of the micro-device system is the major motivation behind the development of accurate and reliable analytical models. These models help establish operating protocols to ensure the stable operation of the bearings under a variety of operating conditions. The developed analytical model is also capable of estimating the steady-state performance characteristics of micro-hydrostatic thrust bearings. The quantities of interest are axial stiffness, natural frequency, and mass flow rates for different thrust-bearing hydrostatic supply pressures. In addition, the analytical model can be used to analyze the static and dynamic stability of these micro-thrust bearings. For static stability considerations, it is necessary to ensure that coupling effects due to interference of other micro-device components do not introduce negative stiffness which exceed the thrust bearings' stiffness. In terms of dynamic stability, the developed models capture the essential mechanisms underlying the dynamic instability phenomena and help establish design guidelines and criteria to avoid their occurrence.

**Objectives and Scope of the Paper.** The objectives and goals of this paper are to (1) develop an analytical model with the above mentioned capabilities, (2) assess the accuracy of the model by comparing steady-state experimental data to analytical predictions, (3) illustrate the applicability of the model based operating protocols to the experimental testing of micro-devices, (4) experimentally investigate the thrust-bearing operating conditions under which dynamic instability occurs, and (5) compare experimental results to a priori analytical predictions to evaluate their validity and usefulness.

The paper is organized as follows. The essential components of the newly developed analytical hydrostatic thrust-bearing model are first described in detail. The model is subsequently used to predict the steady-state performance characteristics of the MIT micro-devices and to establish operating protocols. The importance of static stability considerations is demonstrated in two micro-devices, the micro-electrostatic turbine-generator and the micro-turbopump. Next, experimental results obtained from these two devices are presented to demonstrate the feasibility of the

[1]A decreasing axial gap increases the electrostatic attraction force such that the stiffness is negative.

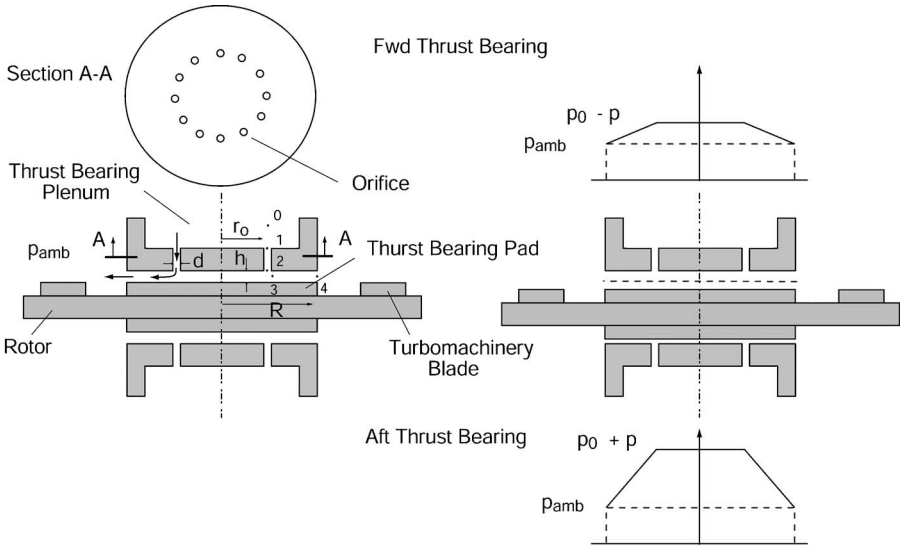


**Fig. 2 Geometric configuration of inherent-restrictor orifice hydrostatic thrust bearings (not to scale)**

operating protocols. The models are then utilized to investigate the dynamic stability of the thrust bearings, and operating conditions under which axial oscillations occur are predicted. Finally, experiments are carried out in a micro-turbocharger to investigate thrust-bearing dynamic stability. The experimental results are compared to a priori model predictions and the ability to capture the underlying mechanisms is assessed. Finally, the results and conclusions of this research are summarized.

## Analytical Model for Hydrostatic Thrust Bearings

The newly developed hydrostatic gas-thrust-bearing model consists of two parts, a steady-state fluid dynamic model to predict hydrostatic thrust-bearing performance and an unsteady flow model to capture the dynamic behavior and stability of the thrust-bearing-rotor system.

**Steady-State Thrust-Bearing Performance Model.** Figure 2 shows the configuration and dimensional variables of the inherently compensated-orifice hydrostatic thrust bearings. The bearings rely on an external source of pressurized gas supplied through a series of orifice restrictors (typically of 10 $\mu$m diameter and 100 $\mu$m length), which together with the thrust-bearing gap (nominally 2 $\mu$m to 3 $\mu$m deep), generate the axial stiffness. The key advantage of hydrostatic thrust bearings is their ability to provide an almost constant stiffness independent of the rotational speed of the rotor. The steady-state operating characteristics of the thrust bearings are modeled using a fluid resistance model, whose key components are outlined in Fig. 2. The station numbers are also labeled in the figure, and the mechanism for the generation of axial stiffness is illustrated schematically. The rotor is supported axially by means of a forward and an aft thrust bearing. When the rotor is given a slight perturbation in the axial direction and comes into closer proximity with the aft thrust-bearing pad, the hydraulic resistance in the outflow region of the aft thrust-bearing pad increases, thus necessitating a larger pressure difference between the outlet of the orifices and the thrust-bearing exhaust (vented to atmosphere). The increase in static pressure over the aft thrust-bearing pad culminates in a larger restoring axial force acting on the rotor. The opposite occurs on the forward thrust bearing, and the consequence is a net upward axial force acting on the rotor disk to restore the equilibrium axial position of the rotor.

The inlet loss from station 0 to station 1 is manifested as a drop in stagnation pressure of the fluid at the entrance of each orifice. This loss can be described as

$$\frac{\Delta P_t}{P_t - P} = 0.5 \tag{1}$$

where the loss coefficient of 0.5 was obtained from handbooks of hydraulic resistance [6], and has been verified by computational fluid dynamics (CFD) calculations performed by Gong [7].

The flow through each of the circular orifices (from station 1 to station 2) is modeled as a compressible, isothermal, fully developed viscous flow. In view of the high thermal conductivity of silicon, the isothermal assumption is reasonable. The relevant equations governing such a flow are given in Shapiro [8] and can be summarized by the following expression for the corrected mass flow:

$$\frac{\dot{m}\sqrt{\Re T_{t2}}}{AP_{t2}\sqrt{\gamma}} = \Phi\left(\mathrm{Re}_d, \frac{P_{s2}}{P_{t1}}, \frac{L}{d}\right) = \Psi(M_2) \tag{2}$$

The corrected mass flow at the exit of each orifice depends on the Reynolds number $\mathrm{Re}_d \equiv \rho V d/\mu = \dot{m}d/A\mu = 4\dot{m}/\pi d\mu$, the ratio of the static pressure at the exit of the orifice $P_{s2}$ to the total pressure at the inlet $P_{t1}$, and the aspect ratio of the orifice $L/d$, where $L$ and $d$ are the length and diameter of the orifice, respectively. It should be noted that although the Reynolds number of the flow is sufficiently low so as to render the flow laminar, the effects of friction and the associated decrease in stagnation pressure tends to increase the Mach number of the flow to appreciable values, thus necessitating the effects of compressibility to be taken into account. However, in contrast to the familiar Fanno flow involving adiabatic flow through ducts, where choking occurs at a local Mach number of unity, the isothermal flow through ducts chokes at a local Mach number of $1/\sqrt{\gamma}$ [8]. Furthermore, since the flow is laminar ($\mathrm{Re}_d = \mathrm{O}(10^2)$), viscous effects, which are quantified by the friction coefficient $C_f$, can be related analytically to the Reynolds number $\mathrm{Re}_d$ via $C_f = 16/\mathrm{Re}_d$. Also, since $C_f M^2 (L/d)$ is of order one, compressibility effects have to be taken into account even though the flow is dominated by viscous effects. The viscous losses through the orifices are normally neglected in the modeling of macro-scale hydrostatic thrust bearings employing orifice restrictors, as exemplified by the work of Eshghy [9]. However, since the Reynolds numbers of the flows through the orifices of hydrostatic micro-gas-thrust bearings considered in this work are typically one order of magnitude smaller, the viscous losses are

not negligible and have to be correctly accounted for.

The turning losses at the exit of the orifices (from stations 2 to 3) are modeled using the following empirical correlation by Vohr [10]:

$$\frac{\Delta P_t}{P_t - P} = 0.31\left(\frac{\mathrm{Re}_h}{2000}\right) - 0.122\left(\frac{\mathrm{Re}_h}{2000}\right)^2 + 0.282\left(\frac{\mathrm{Re}_h}{2000}\right)^3 \quad (3)$$

where $\mathrm{Re}_h = 2\dot{m}/\pi d\mu$.

After leaving the orifices, the fluid flows outward through the radial region between the stator and rotor, before finally being discharged into the surrounding atmosphere. This occurs from stations 3 to 4. In the radial outflow region, the static pressure distribution, which varies both radially and circumferentially, is computed numerically using a finite-element method. The flow in this region is assumed to be isothermal and the mass flow $\dot{m}$ is driven by the difference in the squares of the static pressure $\Delta P^2$ between the exit of the orifices and the thrust bearing exhaust. This can be expressed nondimensionally as

$$\frac{\Delta P^2}{\left(\frac{\mu \Re T \dot{m}}{h^3}\right)} = \phi\left(N, \frac{r}{R}\right) \quad (4)$$

where $h$ is the thrust bearing clearance. The ratio $\Delta P^2/(\mu \Re T \dot{m}/h^3)$ can be interpreted as a dimensionless hydraulic resistance between the exit of the orifices and the thrust bearing exhaust, and the magnitude of this resistance depends on the layout and geometrical configuration of the orifices, which in turn depends on the number of orifices $N$ and the normalized radial location of the orifices $r/R$. Assuming the value of $h$ to be constant, the static pressure $P$ in the outflow region can be obtained by solving the Laplace equation for $P^2$

$$\nabla^2 P^2 = 0 \quad (5)$$

Having identified and modeled the individual resistances leading from the thrust-bearing supply plenum[2] to the thrust-bearing exhaust, the objective is to iteratively solve for the mass flow rate $\dot{m}$ given a thrust-bearing supply pressure and fixed thrust-bearing geometrical configuration. The static pressure distribution in the outflow region between the stator and rotor can then be integrated to yield the axial force acting on the rotor. Figure 3 shows the finite-element solution of the static pressure distribution on the thrust-bearing pad of a micro-turbocharger, previously displayed in Fig. 1(*c*). The analytical model is capable of predicting key steady-state performance parameters as a function of the hydrostatic supply pressure and thrust-bearing geometry, such as bearing mass flow, axial stiffness, and natural frequency. In addition to thrust bearings with circular pads the model can also be employed to analyze the performance of thrust bearings with annular pads. Both thrust-bearing configurations have found applications in the micro-devices presented in Fig. 1.

In order to verify the validity of the hydraulic resistance model, experimental results obtained from a micro-turbocharger shown in Fig. 1(*c*) were compared to results predicted from the model. Figure 4 displays static flow test results obtained experimentally by varying the supply pressure to the aft thrust bearing and monitoring the variations in mass flow through the forward thrust bearing. In the latter the supply pressure is kept constant. The modeling results presented in Fig. 4 match the experimental data well, both in trend and magnitude. This indicates that the resistances in the thrust-bearing system are well modeled.

Analytical predictions for axial natural frequency of the micro-turbocharger thrust bearings are plotted against thrust-bearing supply pressure in Fig. 5. The results show a monotonic increase in axial stiffness and thus natural frequency with supply pressure.

[2]The pressure supply to the thrust-bearing supply plenum is held at a constant value, whereas the thrust-bearing exhaust is nominally at atmospheric pressure.

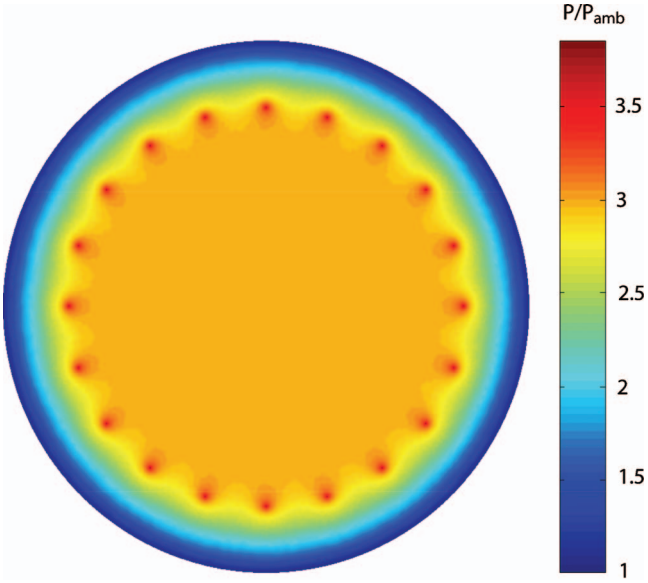


**Fig. 3 Finite element solution of the normalized static pressure distribution on the thrust-bearing pad of a micro-turbocharger (not to scale)**

The figure also indicates that a supply pressure in both forward and aft bearings of at least 95 psi is required to ensure that the bearings operate subcritically up to the rotor design speed of 1.2 million rpm. This is an important consideration and avoids potential resonance effects arising from transcritical operation. The required thrust-bearing mass flow rates for various thrust-bearing supply pressures are also shown in Fig. 5. The thrust-bearing mass flow rates are typically 2% of the turbomachinery mass flow at design speed.

**Dynamic Thrust-Bearing System Model.** Although steady-state operating characteristics are important, one issue in the design of fluid film bearings is stability. Prior to describing the details of the dynamic stability model, it is useful to highlight the essential difference between static and dynamic stability. Static instability refers to a pure divergence from the system's initial equilibrium state and can be analyzed solely from the static or steady-state characteristics of the system at the perturbed state. On

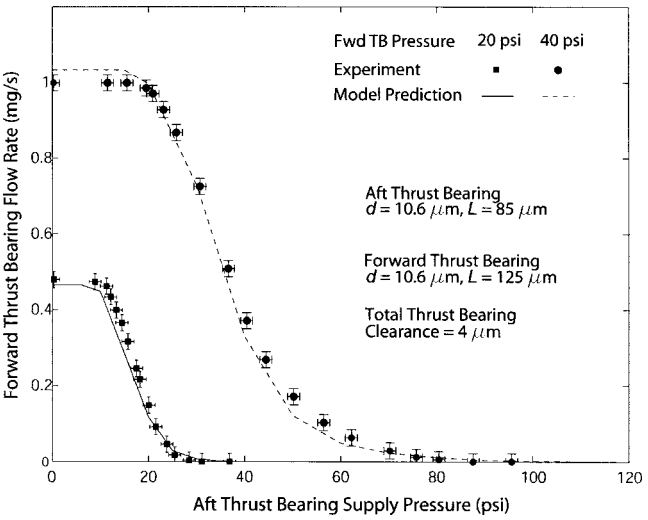


**Fig. 4 Experimental measurement and model predictions of forward thrust-bearing mass flow rate as a function of aft thrust-bearing pressure setting**

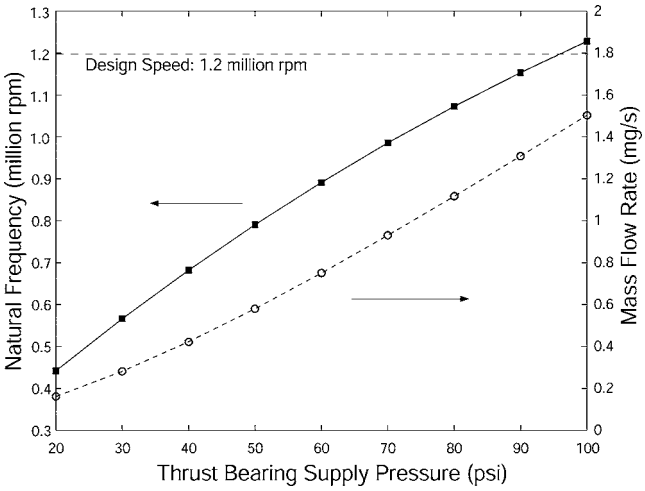


**Fig. 5 Variations of thrust-bearing natural frequency and mass flow rate with supply pressure for a micro-turbocharger**

the other hand, dynamic instability corresponds to oscillations of exponentially growing amplitude which usually have to be treated using a dynamic analysis that accounts for the temporal evolution of perturbations in the system. As an example, for a classical mass-spring-damper system with mass $m$, spring constant $k$, and damping coefficient $c$, static instability occurs for negative values of $k$ whereas dynamic instability corresponds to negative values of $c$.

The dynamic stability of hydrostatic thrust bearings has previously been studied by Licht et al. [11] and Roudebush [12] for circular thrust bearings with a circular central recess, by Allen et al. [13] and Stowell [14] for annular thrust bearings, and by Chen and Ho [15] for capillary compensated multipocket thrust bearings. All of the work focused on instabilities arising from undesirable "air-hammering" effects. The dynamic stability of one thrust bearing operating in isolation is first analyzed to elucidate the essential physics, before extending the approach to study the dynamic stability of both the forward and aft thrust bearings operating in tandem, as is the case in the MIT micro-devices. The state variables chosen for this analysis are the static pressure at the exit of the orifices $p$ and the thrust bearing gap $h$. Referring to Fig. 6, small perturbations in mass flow into and out of the thrust bearing gap arise due to small perturbations $p'$ and $h'$ about the

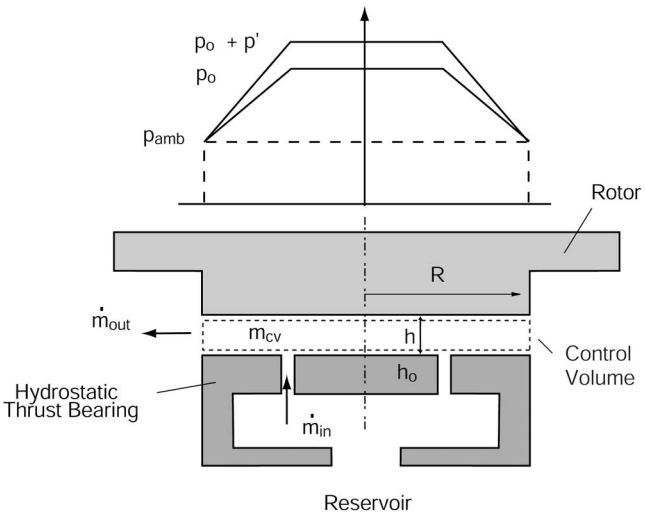


**Fig. 6 Dynamic stability model for hydrostatic thrust bearing**

equilibrium states $p_0$ and $h_0$. The time rate of change of fluid mass in the bearing gap is given by the difference in the perturbed mass flow rates into and out of the thrust bearing gap

$$\frac{dm'}{dt} = \dot{m}'_{\text{in}} - \dot{m}'_{\text{out}} = -(C_1 + C_2)p' - C_3 h' \tag{6}$$

where the coefficients are $C_1=(d\dot{m}_{\text{in}}/dp)_0$, $C_2=(\partial\dot{m}_{\text{out}}/\partial p)_0$, and $C_3=(\partial\dot{m}_{\text{out}}/\partial h)_0$, respectively. It is useful to note that $\dot{m}'_{\text{in}}$ only depends on $p'$ and does not depend on $h'$. This is due to the fact that the mass flow into the thrust-bearing gap has to match the mass flow out of the orifices. The perturbed mass flow out of the orifices, given by Eq. (2), is solely a function of the static pressure perturbations at the exit of the orifices since the thrust-bearing supply pressure $P_{\text{supply}}$, the geometry of the orifices, and the fluid medium are assumed constant.

Under steady-state conditions the mass of gas $m_{CV}$ between the bearing surfaces is

$$m_{CV} = \int_0^{2\pi}\int_0^R \rho h_0 r dr d\theta = \frac{h_0}{\Re T}\int_0^{2\pi}\int_0^R p r dr d\theta \tag{7}$$

which can be evaluated once the pressure at every location along the thrust-bearing pad is known. Corresponding to perturbations $p'$ and $h'$, the perturbed time rate of change of the fluid mass between the bearing surfaces becomes

$$\frac{dm_{CV'}}{dt} = \left(\frac{\partial m_{CV}}{\partial p}\right)_0 \dot{p}' + \left(\frac{\partial m_{CV}}{\partial h}\right)_0 \dot{h}' = C_4\dot{p}' + C_5\dot{h}' \tag{8}$$

From conservation of mass considerations, one can write using Eq. (6)

$$\frac{dm_{CV'}}{dt} = \dot{m}'_{\text{in}} - \dot{m}'_{\text{out}} \tag{9}$$

Hence, one obtains

$$C_4\dot{p}' + C_5\dot{h}' + (C_1 + C_2)p' + C_3 h' = 0 \tag{10}$$

The perturbations $h'$ and $p'$ are also coupled by Newton's second law governing the axial motion of the rotor. This yields

$$m_R\ddot{h}' = \left(\frac{\partial F_p}{\partial p}\right)_0 p' = \frac{\Re T}{h_0}C_4 p' = C_6 p' \tag{11}$$

where $m_R$ is the mass of the rotor.

Coupling Eqs. (10) and (11), the final ordinary differential equation (ODE) which governs the perturbed axial motion of the rotor takes the form

$$\dddot{h}' + \left(\frac{C_1 + C_2}{C_4}\right)\ddot{h}' + \frac{C_5 C_6}{M_R C_4}\dot{h}' + \frac{C_3 C_6}{M_R C_4}h' = 0 \tag{12}$$

which is a third-order differential equation in $h'$. The stability of the system is described by the above equation and is readily analyzed by applying the Routh-Hurwitz stability criterion. This yields the following criterion for dynamic stability:

$$\frac{C_1 + C_2}{C_3} > \frac{C_4}{C_5} \tag{13}$$

The values of the coefficients $C_1, C_2, C_3, C_4$, and $C_5$ can be obtained using the steady-state thrust-bearing model introduced earlier. Equation (13) reveals that one of the main factors which drives the system toward instability is a low value of coefficient $C_1$, which in fact becomes zero when the flow through the orifices of the thrust bearing chokes. When this occurs the mass flow out of the orifices becomes independent of the back pressure, thus $C_1=(d\dot{m}_{\text{in}}/dp)_0=0$. It is also of interest to note that for an incompressible fluid with constant density $C_4$ becomes zero and Eq. (12) reduces to a second-order ODE in $h'$, which can then be expressed in a more familiar fashion as

$$m_R\ddot{h}' + c\dot{h}' + kh' = 0 \tag{14}$$

This is the equation of motion for a linear mass-spring-damper system, with spring constant $k$ given by $C_3C_6(C_1+C_2)$ and damping constant $c$ given by $C_5C_6(C_1+C_2)$. As discussed previously, static instability ensues when $k$ becomes negative. However, static stability is necessary but not sufficient, and in practice dynamic stability is often violated first. In the presence of dynamic effects, the phase difference between the unsteady perturbations in $p'$ and $h'$ may be such that in one cycle or period of the perturbations, the net disturbance energy input into the system is positive. This causes the amplitude of $h'$ to experience exponential growth and results in dynamic instability.

The above analysis was carried out for a single thrust bearing configuration first.[3] Since the rotors of the MIT micro-devices are axially supported by a forward and an aft thrust bearing, it is necessary to extend the preceding analysis and to couple the disturbance of the rotor axial location to the dynamics of the dual thrust-bearing system (see Fig. 1). This eventually leads to a coupled system of equations

$$M_R\dddot{h}' + \left(\frac{C_{1a}+C_{2a}}{C_{4a}}\right)M_R\ddot{h}' + \left(\frac{C_{5a}C_{6a}}{C_{4a}} + \frac{C_{5f}C_{6f}}{C_{4f}}\right)\dot{h}' + \left(\frac{C_{2a}C_{6a}}{C_{4a}} + \frac{C_{2f}C_{6f}}{C_{4f}}\right)h' + C_{4f}\left(\frac{C_{1a}+C_{2a}}{C_{4a}} - \frac{C_{1f}+C_{2f}}{C_{4f}}\right)p_f' = 0 \tag{15}$$

and

$$C_{5f}\dot{h}' + C_{2f}h' - C_{4f}p_f' - (C_{1f}+C_{2f})p_f' = 0 \tag{16}$$

The subscripts "$f$" and "$a$" in the above equations denote the forward and aft thrust bearings, respectively. In contrast to Eq. (12) the order of the characteristic polynomial or the number of poles for the system is now increased from three to four. The system is dynamically stable if, and only if, all the roots of the characteristic equation have negative real parts, indicating exponential decay of the oscillations.

**Limitations of the Analytical Model.** Although the analytical model adequately accounts for the effects of compressibility and the radial and circumferential variation of the static pressure in the thrust-bearing pad, the model is limited to hydrostatic thrust bearings with orifices located axisymmetrically at the same radial location. The simple restrictor model is not applicable to thrust bearing configurations where several sets of orifices are arranged at different radial locations. Furthermore, the model assumes a constant thrust bearing gap, neglecting any tilting of the rotor. The model also does not address the effects of geometric nonuniformities in the orifices. These limitations are further addressed and the model is extended to account for the mentioned effects in a companion paper [16].

## Model Applications and Experimental Investigation

The complications associated with the operation of the three micro-devices depicted in Fig. 1 have previously been highlighted. In the following, the models are employed to study the static stability of the thrust-bearing system in these micro-devices and to establish necessary operating protocols guaranteeing stable operation. Using the operating protocols experiments are subsequently performed to investigate their applicability.

**Static Stability and Operating Protocol for a Micro-electrostatic Turbine Generator.** The issue of thrust-bearing static instability arises in the micro-electrostatic turbine generator depicted in Fig. 1(*a*). In this micro-device, the electrostatic attraction between the rotor and stator is captured by the characteristic force $F_p$ between two parallel plate capacitors.

[3]Most of the research reported in the literature focuses on the dynamic stability of a single thrust bearing operating in isolation.

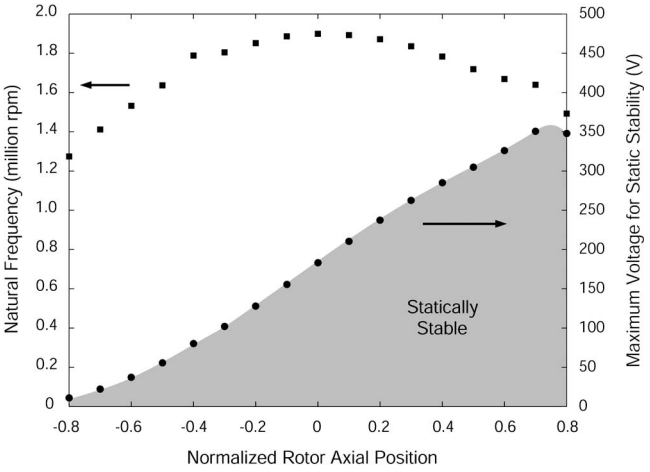


**Fig. 7 Thrust-bearing natural frequency versus rotor axial position for micro-electrostatic turbine generator**

$$F_P = -\frac{\epsilon_0 v^2 A}{4g^2} \tag{17}$$

where $\varepsilon_0$ is the permittivity of free space, $v$ is the voltage difference between the stator and rotor, $A$ is the effective area of the electrodes on the stator and rotor, and $g$ is the generator running gap. This pull-in force $F_p$ results in a negative (destabilizing) axial stiffness $k_p$ experienced by the spinning rotor

$$k_p = -\frac{\partial F_p}{\partial g} = -\frac{\epsilon_0 v^2 A}{2g^3} \tag{18}$$

The magnitude of the destabilizing stiffness increases with increasing voltage difference $v$ and decreasing generator gap $g$.

For static stability, the net axial stiffness must be positive such that

$$|k_B| > |k_P| \tag{19}$$

where $k_B$ is the thrust-bearing axial stiffness. Using Eq. (18), the criterion for the maximum allowable voltage between the stator and rotor becomes

$$v < \sqrt{\frac{2g^3 k_B}{\epsilon_0 A}} \tag{20}$$

In Fig. 7, the natural frequency of the thrust bearings is plotted as a function of rotor axial position with a supply pressure of 70 psi and 50 psi applied to the forward and aft thrust bearings, respectively. The total thrust-bearing gap is 3 $\mu$m and a nondimensional axial rotor position of zero implies that the rotor is axially centered between the forward and aft static structures. A positive axial rotor position indicates the rotor operating in closer proximity to the static structure on the forward side, with the rotor coming into physical contact with the static structure at a nondimensional rotor axial position of unity. Knowledge of the axial stiffness for various rotor axial positions allows the maximum allowable voltage between the stator and rotor to be evaluated from Eq. (20). The results are displayed in Fig. 7 which shows that the maximum allowable voltage between the stator and rotor decreases drastically for a rotor operating in closer proximity to the static structure on the aft side. This is due to a larger destabilizing stiffness which increases strongly with a decreasing generator gap, in accordance with Eq. (20). The maximum allowable voltage increases as the rotor operates in closer proximity to the forward static structure and shows a peak at a rotor axial position of approximately 0.7. This dip in maximum allowable voltage is due to the softening of the thrust bearings for large positive rotor axial positions. The stiffness of each of the thrust bearings is

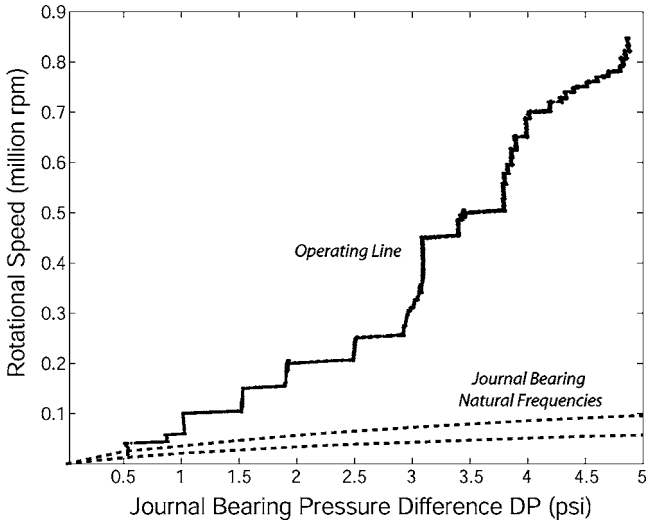


**Fig. 8 Experimental demonstration of operating schedule for a micro-electrostatic turbine generator which achieved a maximum speed of 850,000 rpm (93% design speed)**

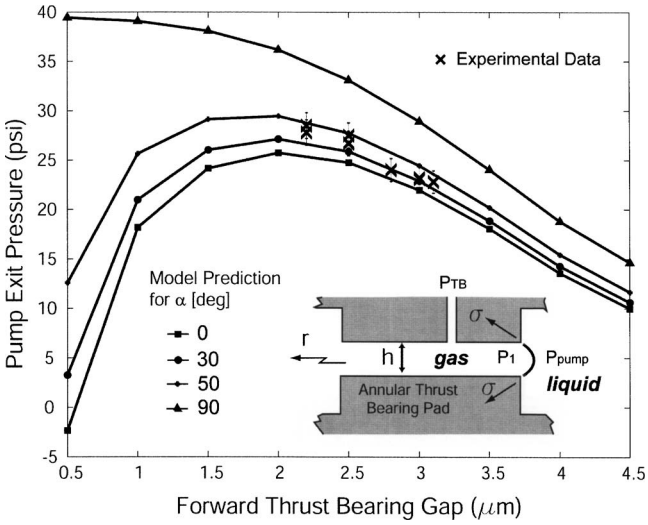


**Fig. 9 Comparison of experimental results and analytical predictions for operating protocol on micro-turbopump. Inset shows hydrostatic analysis performed on liquid-gas interface at the intersection between the turbopump outlet and the forward thrust bearing**

maximum when the flow resistance due to the orifice (from stations 1 to 2 in Fig. 2) is approximately equal to the resistance due to the radial outflow region from the exit of the orifices to the edge of the thrust bearing pad (from stations 3 to 4 in Fig. 2). For large positive eccentricities, which correspond to small forward thrust bearing gaps, the flow resistance due to the radial outflow region dominates the resistance due to the orifice. This results in a reduction in stiffness due to the forward thrust bearings and hence a reduction in the overall stiffness of the system. It can be further inferred from Fig. 7 that the maximum allowable voltage is approximately 350 V, corresponding to a rotor axial position of 0.7. However, it might not be desirable to operate the rotor and bearings at such high rotor axial positions. However, if only a maximum voltage of 300 V is required, it might be feasible to operate the thrust bearings at rotor axial positions close to 0.5.

Figure 7 serves as an important plot for the successful operation of the micro-electrostatic turbine generator, as it provides information pertaining to the maximum allowable generator voltage which can be applied between the rotor and stator without resulting in static instability. It also indicates that, based on static stability considerations, the rotor should be operated closer to the forward static structure at rotor axial positions not exceeding 0.7 in order to maximize the allowable voltage between electrodes on the stator and the rotor. By careful implementation of the operating protocols, the rotors of these devices have been experimentally spun up to 850,000 rpm which corresponds to 93% design speed, as shown in Fig. 8. Voltages of up to 120 V have been applied between the electrodes without any observable electrostatic pull-in effects.

**Stability of Annular Thrust Bearings With Liquid-Gas Interface in Micro-Turbopumps.** The analytical model also serves as a tool for establishing operating protocols in the micro-turbopump, shown in Fig. 1(*b*). Referring to Fig. 9, a simple hydrostatic analysis is performed on the liquid-gas interface at the intersection between the pump outlet and the forward thrust bearing. The analysis reveals that the static pressure $P_1$ along the inner rim of the annular forward thrust-bearing pad has to exceed the pump outlet pressure $P_{\text{pump}}$ in order to support the surface tension forces due to the liquid-gas interface. For such small micron-sized thrust-bearing clearances $h$, the surface tension forces are of great significance. The force balance at the liquid-gas interface yields

$$P_1 = P_{\text{pump}} + \frac{2\sigma \cos \alpha}{h} \tag{21}$$

where $\sigma$ is the surface tension and $\alpha$ is the contact angle of the wetting interface ($\alpha < 90$ deg). Equation (21) imposes a constraint on the allowable combinations of $P_1$, $P_{\text{pump}}$, and $h$ necessary for static equilibrium of the liquid-gas interface. Since the value of $P_{\text{pump}}$ increases with the square of the rotational speed the value of $P_1$ has to increase accordingly for a fixed forward thrust-bearing gap $h$. If $P_1$ is raised above its allowable value, gas bubbles can enter the pump, resulting in a two-phase flow at the pump outlet. The gas bubbles tend to conglomerate into larger slugs of gas pockets which impede the liquid flow and reduce the mass flow through the pump. Conversely, if $P_1$ is allowed to fall below $P_{\text{pump}}$, liquid leaks into the annular thrust-bearing pad and results in a significant increase in viscous drag and destabilizing hydrodynamic torques. However, all this is further complicated by the fact that $P_1$ and $h$ are not independent, but rather, $P_1$ depends on both the thrust bearing supply pressure $P_{\text{supply}}$ and clearance $h$. The delicate nature of the equilibrium expressed in Eq. (21) indicates the necessity for establishing an operating protocol for the appropriate combination of values of $P_{\text{supply}}$ and $h$ at different values of $P_{\text{pump}}$. The values of $P_1$ for given values of $P_{\text{supply}}$ and $h$ can be computed numerically by solving Eq. (5) with imposed Dirichlet type boundary conditions, $P = P_{\text{ambient}}$, along the outer rim of the forward thrust-bearing pad and Neumann type boundary conditions, $\partial P / \partial n = 0$ (corresponding to zero normal flow) along the inner rim of the forward thrust-bearing pad. Having obtained $P_1, P_{\text{pump}}$ can then be solved using Eq. (21).

Figure 10 depicts analytical predictions for the possible combinations of $P_{\text{supply}}$ and $h$ required for different values of $P_{\text{pump}}$, assuming a contact angle of $\alpha = 50$ deg. For a fixed thrust-bearing supply pressure $P_{\text{supply}}$ the allowable pump outlet pressure $P_{\text{pump}}$ first increases with increasing values of $h$ before reaching a maximum at $h = h_{\text{crit}}$ (marked by the dotted line) and subsequently decreases for larger values of $h$. The occurrence of this maximum is due to the interplay between $P_1$, which decreases with increasing values of $h$, and surface tension forces which increase significantly (as $1/h^3$) with decreasing values of $h$. For small values of $h$, the surface tension forces increase much more rapidly than $P_1$ as $h$ is reduced, thus giving rise to a reduction in the allowable value of $P_{\text{pump}}$. Starting with the rotor in an axially centered lo-

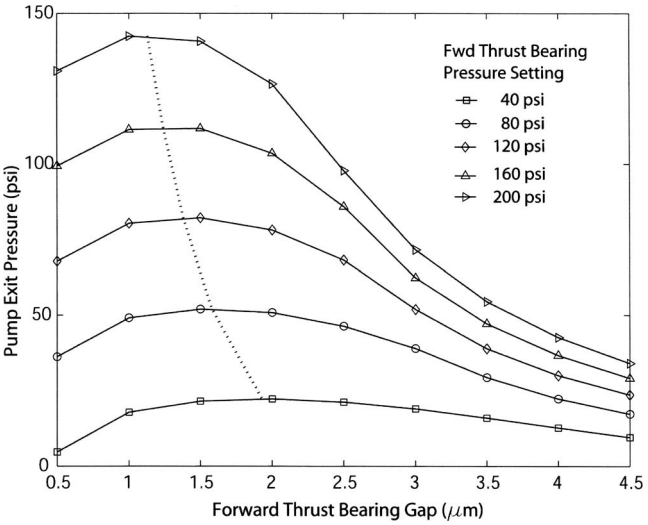


**Fig. 10 Required forward thrust-bearing pressure settings for different pump-outlet pressures and different forward thrust-bearing clearances**

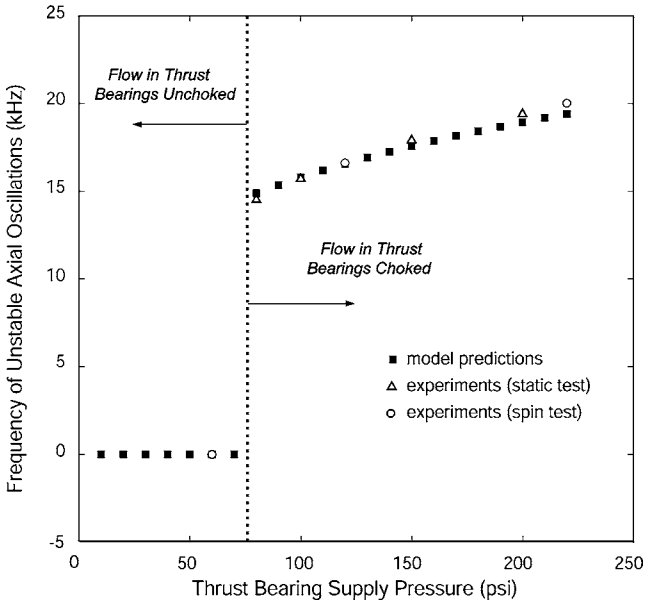


**Fig. 11 Comparison of experimental measurements and analytical predictions of the frequency of unstable axial oscillations for different thrust-bearing supply pressures. The uncertainties in pressure and frequency measurements are ±1.25 psi and ±2 Hz, respectively.**

cation and with $P_{supply}$ fixed, $P_{pump}$ increases quadratically with the rotor speed, thus requiring a smaller forward thrust bearing gap $h$ to maintain the static equilibrium of the liquid-gas interface. However, when $h$ is reduced below $h_{crit}$, the allowable $P_{pump}$ begins to decline. Hence, from an operational perspective, it is necessary to operate the rotor at thrust-bearing clearances greater than $h_{crit}$ for a given value of $P_{supply}$.

During actual experimental runs on the micro-turbopumps, the thrust-bearing clearance $h$ can be measured to a high degree of accuracy by monitoring the pressure drops and flow rates across the radial seals on the aft side of the static structure as shown in Fig. 1(*b*). Experiments were performed to evaluate the validity of the operating protocols which have been generated using the analytical model. The value of $P_{supply}$ was held constant at 50 psi and the value of $h$ was gradually reduced until bubbles started to form in the turbopump. Values of thrust-bearing clearance $h$ which correspond to the onset of appearance of bubbles in the pump are plotted in Fig. 9 as crosses for various values of $P_{pump}$. Also shown on the same figure are analytical predictions for different values of contact angle $\alpha$. The experimental data are seen to fall between the analytical predictions corresponding to contact angles $\alpha$ between 30 deg and 50 deg, which compare favorably to values of $\alpha \approx 30$ deg cited in the literature for air-water interface on silicon (see, for example, [17]). The established operating protocols proved to be a useful guide when operating the rotor at various speeds.

In view of the above complications associated with achieving the correct combination of $h, P_{pump}$, and $P_{supply}$, one design guideline is to avoid using the thrust bearing for sealing purposes.

Although static stability is necessary, it is not sufficient for determining the overall stability of a system. To assess the overall stability of a system, dynamic stability considerations have to be made as well. This is discussed next.

## Dynamic Stability of Hydrostatic Thrust Bearings

An a priori dynamic stability analysis was carried out on the thrust-bearing system of a micro-turbocharger using the analytical model described previously. The analysis predicted that the thrust bearings were dynamically stable (the roots of the characteristic equation were either real or had negative real parts) when the supply pressure to both thrust bearings was kept below 60 psi and the rotor was axially centered. Under such circumstances the orifices of both thrust bearings were essentially unchoked. However, when the rotor was axially centered and the supply pressure to both thrust bearings was increased beyond 60 psi, the analytical model predicted the onset of dynamic instability.

To further understand the nature of the dynamic instability, the roots of the characteristic equation were investigated for different rotor axial positions and a thrust-bearing supply pressure of 120 psi. For every rotor axial position investigated, two of the roots are real and negative, while the remaining two roots are complex. For rotor axial positions between −0.3 and 0.3 (i.e., when the rotor is operated almost axially centered), the two complex roots have positive real parts, thus indicating that the system is dynamically unstable. For these rotor axial positions, it is observed that the flow through the orifices of both thrust bearings is choked. However, for larger positive and negative rotor axial positions, the two complex roots have negative real parts, indicating that the system is dynamically stable. Under such circumstances, although the flow through the orifices of one of the thrust bearings is choked, the flow through the orifices of the other thrust bearing remains unchoked. Even though a thrust bearing operating in isolation might be dynamically unstable due to flow choking, the overall system remains stable. The other unchoked thrust bearing is capable of stabilizing the entire bearing system. This highlights the importance of analyzing the entire dual thrust-bearing system as a whole, and it is misleading to draw conclusions based on the dynamic stability of each individual thrust bearing operating in isolation.

To test the above model prediction, experiments were subsequently performed on the micro-turbocharger. Both the rotational speed and axial position of the rotor can be measured using an ultra-high frequency response fiber-optic sensor overlooking a series of speed bumps etched on the surface of the rotor. When the supply pressure to both thrust bearings was increased beyond 60 psi, the fiber-optic sensor precipitously detected a high frequency axial oscillation of the rotor, which was in fact also within the audible frequency range of the human ear. The frequency of these axial oscillations for various thrust-bearing supply pressures was quantified by passing the real-time voltage signal through a spectrum analyzer, and the measured frequency of oscillations is presented in Fig. 11. Also shown in the same figure are analytical predictions which only occur for thrust-bearing supply pressures

in excess of 60 psi when the flow through the orifices of both thrust bearings is choked. Good agreement is observed between the a priori analytical predictions and the experimental measurements, thus validating the ability of the simple model to accurately predict the frequency of the instability. The analytical model seems to capture the essential mechanism responsible for driving the system toward dynamic instability and establishes a simple criterion for thrust-bearing dynamic stability: If the flow through both forward and aft thrust bearings is choked, the system is dynamically unstable.

## Summary and Conclusions

An analytical model to predict the steady-state performance of inherent-restrictor orifice hydrostatic thrust bearings for application to micro-turbomachines has been developed. Although the Reynolds number of the flow through the bearings is low, the Mach numbers are relatively high. The effects of both compressibility and viscosity have been incorporated into the resistance model, which is capable of predicting variations in axial stiffness, natural frequency, and mass flow rates as functions of the thrust-bearing supply pressure. In terms of applicability, the model can be employed to analyze the performance of thrust bearings with both circular and annular pads. Both thrust-bearing configurations have been employed on the MIT micro-devices. An analytical model for analyzing thrust-bearing dynamic stability was introduced and extended to dual thrust-bearing systems for application to the MIT micro-devices. The model illustrates the role of choked flow in the orifices as one of the drivers of dynamic instability manifested in axial oscillations.

The analytical model was further utilized to develop operating protocols for micro-devices such as the micro-electrostatic turbine generator and the micro-turbopump, where the coupling effects of the accompanying components within the micro-system introduce undesirable negative stiffness, subjecting the bearings to static instability. The validity and usefulness of these operating protocols have been verified during experimental testing of these micro-devices. In the micro-electrostatic turbine generator, implementation of the operating protocols has allowed the rotors of these devices to be operated up to 93% of their design speed (850,000 rpm). No observable electrostatic pull-in effects were observed for voltages of up to 120 V applied between the electrodes. On the micro-turbopump, experiments performed at low pump outlet pressures have shown the validity of the operating protocols in successfully preventing the leakage of liquid from the pump outlet into the thrust bearing pads.

In addition to static stability, the thrust-bearing dynamic stability of a micro-turbocharger was also addressed using the analytical model. A priori predictions were made pertaining to the thrust-bearing supply pressures required for dynamic instability. The predicted axial dynamic instability was subsequently verified and demonstrated in experiments performed on a micro-turbocharger. The frequency of unstable oscillations was found to show good agreement with the model predictions, verifying the ability of the analytical model to capture the key mechanisms responsible for dynamic instability. The combined experimental and modeling efforts further demonstrate that a criterion for the onset of dynamic instability is the occurrence of flow choking through the orifices of both the forward and aft thrust bearings.

## Acknowledgment

The authors would like to thank Dr. F. F. Ehrich, Dr. S. A. Jacobson and L. X. Liu for the very useful discussions and helpful comments, and Dr. H. Q. Li for his invaluable help and insight on micro-fabrication issues. This research was sponsored by DARPA and the U.S. Army Research Laboratory under the Collaborative Technology Alliance Program.

## Nomenclature

$\alpha$ = contact angle of liquid-gas interface
$C_f$ = friction coefficient
$C$ = coefficients for dynamic stability analysis
$d$ = orifice diameter
$\varepsilon_0$ = permittivity of free space
$F_p$ = generator pull-in force
$\gamma$ = ratio of specific heats
$g$ = generator gap
$h$ = thrust-bearing gap or clearance
$k$ = axial stiffness
$L$ = orifice length
$\dot{m}$ = mass flow
$m_R$ = mass of rotor
$M$ = Mach number
$\mu$ = dynamic viscosity
$P_{\text{supply}}$ = thrust-bearing supply pressure
$P_{\text{pump}}$ = pressure at pump outlet
$P_s, P_t$ = static pressure, stagnation pressure
$r$ = radial coordinate
$R$ = radius of thrust-bearing pad
Re = Reynolds number
$\Re$ = specific gas constant
$\rho$ = fluid density
$\sigma$ = surface tension
$T, T_t$ = static temperature, total temperature
$V$ = fluid velocity
$v$ = voltage difference between stator and rotor
$\Psi, \Phi, \phi$ = functions

## References

[1] Savoulides, N., 2004, "Development of a MEMS Turbocharger and Gas Turbine Engine," Ph.D. thesis, Department of Aeronautics and Astronautics, MIT.
[2] Diez, S., 2003, "Preliminary Performance Characteristics of a Microfabricated Turbopump," M.Sc. thesis, Department of Aeronautics and Astronautics, MIT.
[3] Steyn, J. L., Kendig, S. H., Khanna, R., Lyszczarz, T. M., Umans, S. D., Yoon, J. U., Livermore, C., and Lang, J. H., 2005, "Generating Electric Power With a MEMS ElectroQuasiStatic Induction Turbine-Generator," *Proc. of the IEEE MEMS Conference*, January 30–February 3, Miami Beach, FL.
[4] Constantinescu, V. N., and Galetuse, S., 1987, "On the Dynamic Stability of the Spiral-Groove Gas-Lubricated Thrust Bearing," ASME J. Tribol., **109**, pp. 183–188.
[5] Constantinescu, V. N., and Galetuse, S., 1990, "Stability Criterion for Spiral Grooved Thrust Gas Bearings," ASME J. Tribol., **112**, pp. 734–737.
[6] Idelchik, I. E., 1994, *Handbook of Hydraulic Resistance*, 3rd ed., CRC Press, Boca Raton, FL.
[7] Gong, Y., 2004, private communications, MIT Gas Turbine Laboratory.
[8] Shapiro, A. H., 1953, *The Dynamics and Thermodynamics of Compressible Fluid Flow*, Vol. I, Ronald Press, New York.
[9] Eshghy, S., 1975, "Optimum Design of Multiple-Hole Inherently Compensated Air Bearings," J. Lubr. Technol., **97**, pp. 221–227.
[10] Vohr, J. H., 1966, "An Experimental Study of Flow Phenomenon in the Feeding Region of an Externally Pressurized Gas Bearing," *Proc. ASME Lubrication Symposium*, New Orleans, LA, June.
[11] Licht, L., Fuller, D. D., and Sternlicht, B., 1958, "Self Excited Vibrations of an Air-Lubricated Thrust Bearing," Trans. ASME, **80**(2), pp. 411–414.
[12] Roudebush, W. H., 1957, "An Analysis of the Effect of Several Parameters on the Stability of an Air-Lubricated Hydrostatic Thrust Bearing," NACA Technical Note 4095.
[13] Allen, D. S., Stokes, P. J., and Whitley, S., 1961, "The Performance of Externally Pressurized Bearings Using Simple Orifice Restrictors," ASLE Trans., **4**, pp. 181–196.
[14] Stowell, T. B., 1971, "Pneumatic Hammer in a Gas Lubricated Externally Pressurized Annular Thrust Bearing," ASME J. Appl. Mech., **93**, pp. 498–503.
[15] Chen, N. N. S., and Ho, K. W., 1981, "Performance Study of a Hydrostatic Air Thrust Bearing," Wear, **70**, pp. 207–217.
[16] Teo, C. J., and Spakovszky, Z. S., 2006, "Analysis of Tilting Effects and Geometric Nonuniformities in Micro-hydrostatic Gas Thrust Bearings," ASME J. Turbomach., **128**, pp. 606–615.
[17] Senturia, S., 2001, *Microsystem Design*, Kluwer Academic, Dordrecht, The Netherlands.

# Analysis of Tilting Effects and Geometric Nonuniformities in Micro-hydrostatic Gas Thrust Bearings

**C. J. Teo**

**Z. S. Spakovszky**

Gas Turbine Laboratory,
Department of Aeronautics and Astronautics,
Massachusetts Institute of Technology,
Cambridge, MA 02139

*The Massachusetts Institute of Technology (MIT) microengine rotors are supported by hydrostatic gas journal and hydrostatic gas thrust bearings. Due to the low length-to-diameter ratio of the devices, the thrust bearings play an important role in providing sufficient tilting stiffness to resist any tilting motion about the spinning axis of the rotor. The performance of the thrust bearings can be influenced by geometric nonuniformities such as thrust-bearing clearances and orifice diameters, and profiles which arise in the process of micro-fabrication. To enable stable high speed operation of the micro-devices, it is important to quantify these effects. Furthermore, a thrust-bearing analysis tool needs to be developed that is able to explore different thrust-bearing arrangements and configurations. In this work, an analytical model is established for analyzing the effects of rotor tilt and geometric nonuniformities in micro-hydrostatic gas thrust bearings for application to micro-turbomachinery. A previously developed model (Teo and Spakovszky, 2006, "Modeling and Experimental Investigation of Micro-hydrostatic Gas Thrust Bearings for Micro-turbomachines," ASME J. Turbomach., **128**, pp. 597–605) is generalized and extended for application to thrust bearings with orifices arranged in nonaxisymmetric configurations. As a consequence of rotor tilt or geometric nonuniformities, the flow through individual orifices of the thrust bearing becomes nonuniform. The orifice flows are in turn coupled to the hydrostatic pressure field in the thrust-bearing pad, and a Green's function approach is adopted to solve the coupled system. The hydrodynamic thrust-bearing forces induced by the pumping action of the rotor rotation are determined by solving the Reynolds equation. The model is able to predict thrust-bearing tilting stiffness and variations in the thrust-bearing mass flow rates as a function of rotor tilting angle for a variety of orifice arrangements. The model can be applied to analyze the effects of nonuniformities in orifice diameter and the presence of clogged orifices on tilting and the concomitant reduction in tilting stiffness. In addition, the effects of orifice taper are analyzed using an influence-coefficient method for one-dimensional compressible, viscous flows. Results obtained for various taper ratios are presented and discussed. The model serves as a useful tool for specifying design tolerances during the fabrication of micro-hydrostatic gas thrust bearings and is used in the experiments to estimate the tilting angle of the rotor during operation.* [DOI: 10.1115/1.2219761]

## Introduction and Motivation

In a previous paper by Teo and Spakovszky [1], the authors presented an analytical model for predicting the steady-state performance characteristics of inherent-restrictor orifice hydrostatic thrust bearings for application to micro-turbomachines. The model is capable of predicting thrust bearing performance and the static and dynamic stability of the thrust bearing system. In addition the model helped establish thrust bearing operating protocols used in the experimental testing of the Massachusetts Institute of Technology (MIT) micro-devices. An overview of the MIT micro-engine project is given in Epstein [2]. The key advantage of the original analytical model, which utilizes a fluid resistance approach, is its simplicity. However, the model is limited to axisymmetric configurations with the thrust-bearing orifices placed along the same radial location. The thrust-bearing clearances and the geometric dimensions of the orifices were assumed uniform. In this work, an approach employing Green's functions is presented, which allows one to extend the applicability of the original model.

One of the primary motivations for generalizing the model is to quantify the tilting stiffness of the thrust bearings. Unlike conventional axial-flow turbomachines, where engine architecture is based on long slender shafts supporting the rotating structure, the rotors of the MIT micro-devices consist of thin disks with very low thickness-to-diameter ratios (L/D) and thrust bearings located near the center of the disk. Hence, the rotors are more prone to unwanted tilting and the journal bearing system is unable to exert an appreciable torque to resist the tilting. The onus of providing a tilting stiffness thus lies in the thrust bearings, and it is therefore crucial to quantify its magnitude. The tilting stiffness characteristics of hydrostatic thrust bearings have previously been studied by Al-Bender and Brussel [3] for circular centrally fed thrust bearings, by Yabe and Watanabe [4] and Yabe and Yamamoto [5] for annular pad thrust bearings, and by Nakamura and Yoshimoto [6,7] for rectangular double-pad thrust bearings.

In addition, thrust bearing performance may be compromised due to the presence of geometric nonuniformities such as orifice diameters and profiles. The lack of precise control of geometric uniformity constitutes one of the major challenges encountered during micro-fabrication. Occasionally, one has to contend with

Contributed by the International Gas Turbine Institute (IGTI) of ASME for publication in the JOURNAL OF TURBOMACHINERY. Manuscript received October 1, 2004; final manuscript received February 1, 2005. Review Chair: K. C. Hall. Paper presented at the ASME Turbo Expo 2005: Land, Sea and Air, Reno, NV, June 6–9, 2005, Paper No. GT2005-68223.

  

the presence of more severe defects, such as the failure of a number of orifices to etch through completely. Another anomaly which has been observed pertains to the profile of the orifices, where the diameters of the orifices are found to vary considerably along their lengths, thus resulting in tapered rather than uniform orifice profiles. The focus of this paper is then to quantify the magnitudes of the torques and static tilting angles arising from the presence of these undesirable geometric nonuniformities and defects.

**Objectives and Scope of the Paper.** One of the primary goals of this paper is to generalize and extend the capabilities of the hydrostatic thrust-bearing model presented in Teo and Spakovszky [1], and to analyze nonaxisymmetric thrust-bearing configurations. More specifically the paper addresses the following objectives: (1) quantification of the thrust-bearing tilting stiffness, in addition to evaluating torques and rotor tilting angles due to geometric nonuniformities in thrust-bearing clearance or orifice diameter; (2) assessment of the performance of thrust bearings with novel arrangement of thrust-bearing orifices; (3) quantification of the performance of annular thrust bearings which are coupled to the turbomachinery; and (4) analysis of the pitch and yaw dynamics of a thrust-bearing-rotor system with nonzero dynamic imbalance using a two degrees-of-freedom rotordynamic model.

**Layout of Paper.** The layout of the paper is as follows. First, the Green's function formulation for generalizing the original analytical model presented in Teo and Spakovszky [1] is explained in detail. The modeling approach for hydrostatic and hydrodynamic tilting stiffness are also presented. The extended model is subsequently employed to predict the thrust-bearing tilting stiffness in the MIT micro-devices. Variations in mass flows through the thrust bearings as a function of the rotor tilting angle are quantified and utilized to indicate the tilting angle of the rotor. Next, a specific example is presented to elucidate how the generalized model can be applied to other thrust-bearing configurations with novel arrangements of orifices. In addition, the model is used to predict and to analyze the performance of annular thrust bearings with variable exhaust pressures which depend on the rotational speed of the rotor. The ability to analyze the resultant torques and static tilting angles due to geometric nonuniformities (i.e., clogged orifices) is demonstrated. An influence-coefficient based approach to model the compressible, viscous internal flows through tapered orifices is then presented to illustrate the effects of tapered orifices on thrust bearing performance. The paper then analyzes the rotordynamics in terms of a pitching and yawing response of a two degrees-of-freedom thrust-bearing-rotor system subjected to dynamic imbalance. Finally, a linear perturbation analysis in pursuit of an eigenvalue problem is performed to study the dynamic stability of the system subjected to small perturbations about its steady-state tilting angle.

## Thrust Bearing Configurations

In the design of micro-hydrostatic thrust bearings, desirable attributes which have to be taken into consideration include large axial and tilting stiffness, low mass flow and power consumption, as well as static and dynamic stability. Furthermore, the microfabrication processes associated with the manufacture of microthrust bearings have to be sufficiently robust to yield acceptably low levels of geometric nonuniformities. In particular, the thrust-bearing clearances and the geometric dimensions have to meet stringent tolerance requirements.

Figure 1 illustrates three possible thrust-bearing configurations. Figure 1(*a*) shows the baseline thrust-bearing configuration with a circular thrust-bearing pad, together with 20 orifices uniformly distributed around the circumference. Figure 1(*b*) shows a novel circular pad thrust-bearing configuration, with 37 orifices distributed on different radial locations so as to form a hexagonal array. For ease of reference, this configuration will be referred to as a hexagonal thrust-bearing hereafter. Figure 1(*c*) shows an annular thrust bearing, with a single row of 20 orifices arranged uniformly at the mean radius.

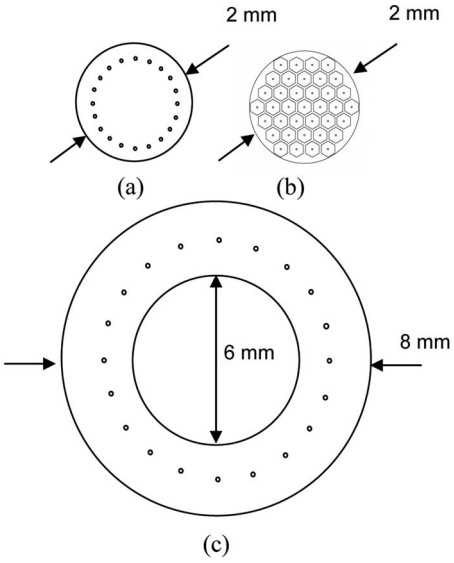


**Fig. 1 Schematic illustration of three different configurations of hydrostatic thrust bearings: (*a*) baseline configuration, (*b*) hexagonal configuration, and (*c*) annular configuration**

One useful simplification in the modeling of the baseline configuration is to assume that the flow through each orifice contributes equally to the overall stiffness of the system, thus permitting all the orifices to be modeled as springs with equal stiffness. Since the hexagonal thrust bearing has almost double the number of orifices compared to the baseline configuration, one may conjecture the hexagonal thrust bearing to possess superior axial and tilting stiffness, in contrast to the baseline configuration. An annular thrust bearing with the same radial extent as the baseline configuration is also expected to have larger axial and tilting stiffness, since both the effective area of the thrust-bearing pad and the radial location of the orifices are larger.

In order to assess the performance of the various thrust-bearing configurations shown in Fig. 1, it is necessary to extend the capabilities of the analytical model presented in Teo and Spakovszky [1]. In particular, to evaluate the thrust-bearing tilting stiffness, the refined model needs to be able to handle scenarios with nonuniform thrust-bearing clearances. Moreover, the extended analytical model should have the attribute of simultaneously coupling the flow field through all the individual orifices and the bearing gap in an efficient manner. For instance, the flow field through each individual orifice of the hexagonal thrust bearing is strongly coupled to the flow field of other orifices, even in the absence of tilting effects. Depending on the micro-turbomachinery application, the inner and outer radii of the thrust-bearing pad may be subjected to different static pressure boundary conditions, and the model should have the capability to deal with a variety of diverse boundary conditions.

## Modeling Approach

**Rotordynamic Model for Yaw and Pitch Dynamics.** This section presents the approach used to analyze the tilting response of the rotor-thrust-bearing system in terms of yaw and pitch dynamics. Referring to Fig. 2, in the absence of rotation, the vertical axis through the geometric center and *fixed to the rotor* is OB. This is termed the static axis. The axis *fixed to the static structure*, which coincides with the static axis OB in this configuration is OZ. The dynamic imbalance $\chi$ is the angular misalignment between the static axis OB and the principal axis OA (the principal axis cor-

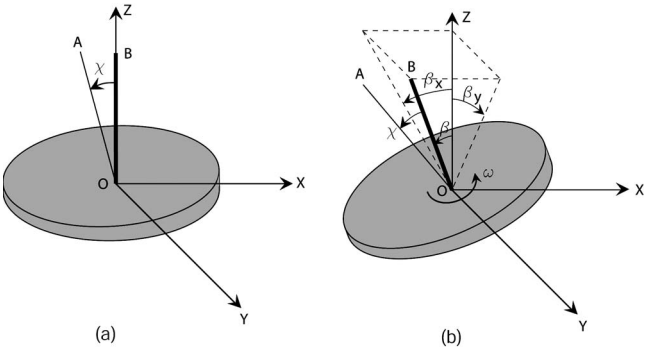


**Fig. 2 Schematic for two degrees-of-freedom rotordynamic model for pitch and yaw dynamics. (*a*) Rotor at rest. (*b*) Rotor spinning at speed $\omega$.**

responding to the polar moment of inertia of the rotor). When the rotor is set into motion, the static axis OB, which is fixed to the rotor, exhibits a coning motion about OZ at a small inclination angle $\beta$. Denoting the projections of $\beta$ onto the $x$-$z$ and $y$-$z$ planes by $\beta_x$ and $\beta_y$, respectively, the linearized equations of motion governing $\beta_x$ and $\beta_y$ are given by

$$I\ddot{\beta}_x + I_p\omega\dot{\beta}_y + k_{xx}\beta_x + k_{xy}\beta_y + c\dot{\beta}_x = (I - I_p)\chi\omega^2 \cos \omega t \quad (1)$$

$$I\ddot{\beta}_y - I_p\omega\dot{\beta}_x + k_{yy}\beta_y - k_{xy}\beta_x + c\dot{\beta}_y = (I - I_p)\chi\omega^2 \sin \omega t \quad (2)$$

The notation for the Euler angles $\beta_x$, $\beta_y$, and $\phi$ (where $\omega = \dot{\phi}$) follows the same convention as that used in Childs [8], where $\beta_x$ is the yaw angle and $\beta_y$ is the pitch angle ($\beta_x, \beta_y \ll 1$). Here, $k_{xx}$ and $k_{yy}$ are the thrust-bearing direct-coupled hydrostatic tilting stiffness, $c$ is the thrust-bearing angular damping, and $k_{xy}$ is the cross-coupled stiffness due to hydrodynamic effects. The cross-coupled stiffness $k_{xy}$ couples angular displacements $\beta_x$ and $\beta_y$ and vice versa. Note that the direct-coupled stiffness $k_{xx} = k_{yy} = K^{\text{hs}}$ and damping coefficient $c$ can be calculated as a function of $\beta$. In addition to $k_{xy} = K^{\text{hd}}$, which couples $\beta_x$ and $\beta_y$, an additional source of coupling arises due to the gyroscopic terms $I_p\omega\dot{\beta}_y$ and $I_p\omega\dot{\beta}_x$ in Eqs. (1) and (2). The nonhomogeneous driving terms on the right-hand side of each equation depend on the diametral and polar moments of inertia, denoted by $I$ and $I_p$, respectively, as well as the dynamic imbalance $\chi$. In the limit of infinite rotational speeds, the inclination angle $\beta$ of the conical motion approaches the dynamic imbalance $\chi$. Physically, the polar principal axis OA aligns itself with the inertial axis OZ as a consequence of gyroscopic stiffening which becomes increasingly dominant at high speeds. If $\beta$ becomes excessively large, physical contact between the rotor and static structure is liable to occur.

It is now possible to subject the rotor to small perturbations in inclination angles to analyze the linear dynamic stability of the system. This involves linearizing Eqs. (1) and (2) and solving them as an eigenvalue problem. The resultant fourth-order characteristic polynomial then yields

$$(Is^2 + k + cs)^2 + (I_p\omega s + k_{xy})^2 = 0 \quad (3)$$

The real part of each of the eigenvalues carries information pertaining to the stability of the inclination motions to small perturbations about the equilibrium condition.

**Fluid Dynamic Model.** The direct-coupled and cross-coupled tilting stiffness and damping coefficients need to be determined in order to calculate the dynamic behavior. This is achieved using a fluid dynamic model for the hydrostatic force, hydrodynamic force, and damping force. For the micro-hydrostatic gas thrust bearings analyzed in this work, the time taken for the hydrostatic fluid to flow through the thrust-bearing gap is small compared to

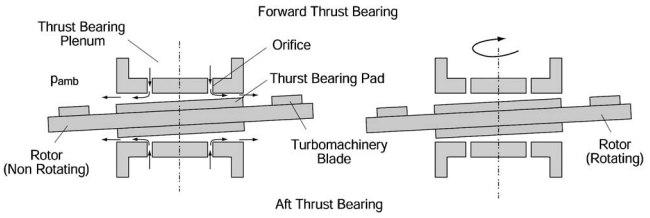


**Fig. 3 Decoupled models for hydrostatic moments (left) and hydrodynamic moments (right)**

the period for one complete revolution of the rotor. Even at the maximum design speed, the reduced frequency $\hat{\omega} = \omega L/U$ is of order 0.1, where $\omega$ is the rotational frequency of the rotor and $L/U$ is the mean flow through time for the hydrostatic fluid. In view of the very low reduced frequencies, it is possible to assume that the flow induced by the motion of the rotor (shown on the right of Fig. 3) can be separated from the flow arising due to the externally applied hydrostatic pressure drop across the thrust bearing (depicted on the left of Fig. 3).

The following describes in detail the modeling approach for each of the three primary force components acting on the rotor, namely, the hydrostatic force, the hydrodynamic force, and the damping force.

**Hydrostatic Force Model: Generalized Analytical Model Employing Green's Function.** In evaluating the forces and moments acting on the rotor due to the externally supplied hydrostatic pressure, the rotor is assumed to be stationary, as depicted on the left of Fig. 3. In cylindrical coordinates, the continuity equation along the thrust-bearing pad can be expressed as

$$\nabla \cdot (\rho\vec{q}) = \frac{\partial}{\partial r}(\rho q_r) + \frac{1}{r}\frac{\partial}{\partial\theta}(\rho q_\theta) = \sum_{i=1}^{N} Q_i\delta(\vec{r}_i) \quad (4)$$

where $\vec{q} = q_r\vec{e}_r + q_\theta\vec{e}_\theta$ is the volumetric flow rate per unit length normal to the local direction of flow. The right-hand side accounts for hydrostatic mass injection of $Q_i$ at discrete locations $\vec{r}_i$ along the thrust bearing gap.

Assuming the flow to be locally of Poiseuille type, the pressure field $P$ in the thrust bearing gap is related to the volumetric flow rate $\vec{q}$ via

$$\vec{q} = -\left(\frac{h^3}{12\mu}\right)\nabla P \quad (5)$$

where $\mu$ is the dynamic viscosity of the fluid. Substituting Eq. (5) in Eq. (4) thus yields

$$\nabla \cdot \left(\frac{\rho h^3}{12\mu}\nabla P\right) = -\sum_{i=1}^{N} Q_i\delta(\vec{r}_i) \quad (6)$$

Assuming an ideal gas and the flow to be isothermal, Eq. (6) becomes

$$\nabla \cdot (h^3 \nabla P^2) = -24\mu\Re T\sum_{i=1}^{N} Q_i\delta(\vec{r}_i) \quad (7)$$

In Teo and Spakovszky [1] the thrust bearing gap $h$ was assumed to be uniform. Here, this assumption is relaxed and the general situation where $h = h(r, \theta)$ is analyzed. Noting that (away from the orifices)

$$\nabla \cdot [h^3 \nabla (P^2 - P_{\text{amb}}^2)] = 0 \quad (8)$$

and letting

$$-p = (P^2 - P_{\text{amb}}^2)/24\mu\Re T \quad (9)$$

the governing equation for the pressure field becomes

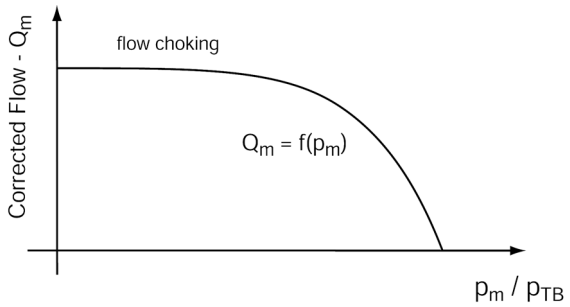


**Fig. 4 Mass flow rate versus pressure drop across thrust-bearing orifice**

$$\nabla \cdot (h^3 \nabla p) = \sum_{i=1}^{N} Q_i \delta(\vec{r}_i) \tag{10}$$

Equation (10) is a linear equation for $p$. To solve this equation, the method of Green's function is employed, where the Green's function is obtained by solving for the impulse response along the thrust bearing pad

$$\nabla \cdot [h^3 \nabla G(\vec{r},\vec{r}')] = \delta(\vec{r}) \tag{11}$$

A finite-element method with the appropriate boundary conditions is used to compute the Green's function $G(\vec{r},\vec{r}')$ numerically.

Physically, the Green's function $G(\vec{r},\vec{r}')$ yields the pressure at the position $\vec{r}'$ within the thrust bearing pad for a unit mass flow through an orifice of diameter $d$ placed at $\vec{r}$. Hence, at the exit of the $m$th orifice (located at $\vec{r}_m$), the pressure $G(\vec{r}_n,\vec{r}_m)$ due to unit mass flow through orifice $n$ (located at $\vec{r}_n$) is given by

$$\nabla \cdot [h^3 \nabla G(\vec{r}_n,\vec{r}_m)] = \delta(\vec{r}_n) \tag{12}$$

By superposition, the resultant pressure at the exit of the $m$-th orifice due to the combined flows through all the $N$ orifices is given by

$$p_m = \sum_{n=1}^{N} G(\vec{r}_n,\vec{r}_m) Q_n \quad m = 1, \ldots, N \tag{13}$$

where $Q_n$ is the mass flow rate through the $n$-th orifice. Note that Eq. (13) is a set of $N$ equations for $2N$ unknowns $p_m$ and $Q_m$, where $m = 1, \ldots, N$. In order to close the system, another set of $N$ equations is required. These are obtained from the pressure-drop-flow-rate relationship across each of the $N$ orifices

$$Q_m = f(p_m), \quad m = 1, \ldots, N \tag{14}$$

A typical functional form for Eq. (14) is illustrated in Fig. 4. Since the flow through the orifice chokes for sufficiently low values of $p_m$ and sufficiently high values of thrust bearing supply pressure $P_{TB}$, $\partial Q_m / \partial (p_m / P_{TB})$ approaches zero at low values of $p_m$. Note that Eq. (14) is nonlinear and one ends up with a set of coupled nonlinear algebraic equations, for which the values of $p_m$ and $Q_m$ are to be determined.

One common approach to solve such nonlinear algebraic equations is to employ the multidimensional Newton's method with the vector of unknowns denoted by

$$\vec{w} = [p_1, \ldots, p_N, Q_1, \ldots, Q_N]^T \tag{15}$$

The system of Eqs. (13) and (14) can then be expressed as

$$F(\vec{w}) = \begin{bmatrix} Q_1 - f(p_1) \\ \vdots \\ Q_N - f(p_N) \\ -p_1 + \sum_{n=1}^{N} G(\vec{r}_n,\vec{r}_1) Q_n \\ \vdots \\ -p_N + \sum_{n=1}^{N} G(\vec{r}_n,\vec{r}_N) Q_n \end{bmatrix} = \begin{bmatrix} 0 \\ \vdots \\ 0 \\ 0 \\ \vdots \\ 0 \end{bmatrix} \tag{16}$$

The multidimensional Newton's method is given by

$$J_F(\vec{w})(\vec{w}^* - \vec{w}) = -F(\vec{w}) \tag{17}$$

where the Jacobian $J_F(\vec{w})$ is

$$J_F(\vec{w}) = \begin{bmatrix} A_{N\times N} & I_{N\times N} \\ -I_{N\times N} & B_{N\times N} \end{bmatrix} \tag{18}$$

where the $I_{N\times N}$ is the $N$ by $N$ identity matrix,

$$A_{N\times N} = \begin{bmatrix} -f'(p_1) & 0 & \cdots & 0 \\ 0 & \ddots & \ddots & \vdots \\ \vdots & \ddots & \ddots & 0 \\ 0 & \cdots & 0 & -f'(p_N) \end{bmatrix} \tag{19}$$

and

$$B_{N\times N} = \begin{bmatrix} G(\vec{r}_1,\vec{r}_1) & \cdots & G(\vec{r}_N,\vec{r}_1) \\ \vdots & \ddots & \vdots \\ G(\vec{r}_1,\vec{r}_N) & \cdots & G(\vec{r}_N,\vec{r}_N) \end{bmatrix} \tag{20}$$

Once the values of the $2N$ unknowns are found, the static pressure at any location $\vec{r}$ along the thrust bearing pad can be simply determined using

$$p(\vec{r}) = \sum_{n=1}^{N} G(\vec{r}_n,\vec{r}) Q_n \tag{21}$$

Note that the above equation is simply a discrete version of Green's formula. Knowledge of the pressure field $p(\vec{r})$ facilitates the evaluation of the hydrostatic forces $F^{hs}$ and moments $M^{hs}$ acting on the rotor. The resulting hydrostatic tilting stiffness $K^{hs} = \partial M^{hs} / \partial \beta$ can then be evaluated for varying rotor tilting angles $\beta$.

The Green's function approach for analyzing the tilting effects of hydrostatic thrust bearings has previously been employed by Yabe and Watanabe [4] and Yabe and Yamamoto [5] for annular thrust-bearing pads. The authors employed an analytical expression for the Green's function specifically for application to annular pad thrust bearings. However, for the approach described above and adopted in this work, the Green's function is obtained numerically. This approach is more general, as it permits a wide variety of thrust bearings with unconventionally shaped pads to be analyzed. In particular, analytical expressions for the Green's function are only available for simple geometrical configurations.

**Hydrodynamic Force Model.** As a consequence of rotor tilt, the spinning motion of the rotor drags the flow along a circumferentially varying clearance, thus giving rise to hydrodynamic pressures. This can be modeled using the Reynolds equation. For incompressible flow in cylindrical coordinates, the Reynolds equation becomes

$$\nabla \cdot (h^3 \nabla P) = 6\mu\omega \frac{\partial h}{\partial \theta} \tag{22}$$

The forces $F^{hd}$ and moments $M^{hd}$ due to the hydrodynamics can thus be evaluated for varying rotor tilting angles $\beta$ and rotational speeds $\omega$. The hydrodynamic torque $M^{hd}$ acts in a direction which is orthogonal to the rotor tilt, and thus contributes a cross-coupled

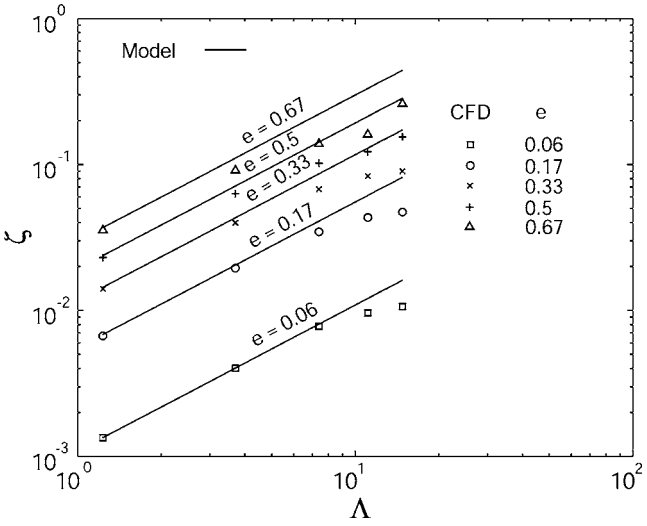


**Fig. 5 Cross-coupled hydrodynamic torque comparison between incompressible analytical model and CFD calculations**

torque and hence hydrodynamic tilting stiffness $K^{hd}=\partial M^{hd}/\partial\beta$.

In order to assess compressibility effects on the modeling results, fully compressible CFD calculations were performed. In Fig. 5, the nondimensional hydrodynamic moment $\zeta=M^{hd}/(P_aR^3)$ is plotted as a function of the bearing number $\Lambda=(6\mu\omega R^2)/(P_ah^2)$ for varying normalized tip deflections $e$ (and hence rotor tilting angles). The incompressible model results compare well to the compressible CFD results and consistently yield higher values of $M^{hd}$ at high bearing numbers. Hence, the use of an incompressible assumption leads to a marginal overprediction of the cross-coupled hydrodynamic torques and stiffness. This in turn gives rise to more conservative modeling results, since larger magnitudes of cross-coupled hydrodynamic torques increase the system's tendency toward instability.

In addition to the above-mentioned cross-coupled component, fluid compressibility results in hydrodynamic moments with a direct-coupled component. This direct-coupled hydrodynamic torque acts in a direction which opposes the rotor tilt, and hence contributes to a direct-coupled hydrodynamic tilting stiffness. However, at the rotational speeds and tilting angles of interest, the direct-coupled hydrodynamic torques are negligible compared to the direct-coupled hydrostatic torques.[1]

In summary, the incompressible model enables the calculation of the resulting hydrodynamic torques which only contribute to a cross-coupled hydrodynamic tilting stiffness. As a consequence, the direct-coupled tilting stiffness arises solely due to hydrostatics.

**Damping Force Model.** The damping force and associated torque is determined from the pressure distribution established when the flow is squeezed through the gap and the thrust-bearing orifices due to the tilting motion of the rotor. This pressure field in the gap can be obtained by solving the Reynolds equation of the form

$$\nabla\cdot(h^3\nabla P)=12\mu\frac{\partial h}{\partial t} \tag{23}$$

together with the appropriate homogeneous boundary conditions $P=0$ at the outlet of the thrust-bearing pad and at the entrance of the thrust-bearing orifices. However, the tilting motion of the rotor induces different mass flow rates through the individual orifices, thus necessitating the Green's function formulation to evaluate the varying mass flows and pressures at the exit of the individual orifices. The damping forces and torques are dependent on the rotor tilting angle, the tilting rate, and the bearing geometry. The damping coefficient for the tilting motion $c$ can thus be determined by evaluating the pressure forces and concomitant tilting torques arising from a rotor tilt rate of $\dot{\beta}$.

**Fluid Dynamic Effects of Tapered Orifices.** One source of geometric nonuniformity which may arise during the microfabrication process is the tapering of the thrust-bearing orifices. In order to model the compressible, viscous flow through an orifice with variable cross-sectional area $A$, a one-dimensional compressible flow with friction, heat addition, and area change is employed [9,10]. Assuming the flow through the orifices to be isothermal, the fractional change in static temperature can be expressed as

$$\frac{dT}{T}=\frac{(\gamma-1)M^2}{1-M^2}\frac{dA}{A}+\frac{(1-\gamma M^2)\left(1+\frac{\gamma-1}{2}M^2\right)}{1-M^2}\frac{dT_0}{T_0}-\frac{\gamma(\gamma-1)M^4}{2(1-M^2)}4f\frac{dr}{D_h}=0 \tag{24}$$

where $f$ is the local friction factor and $D_h$ is the local hydraulic diameter. The fractional change in the square of the Mach number $dM^2/M^2$ is given by

$$\frac{dM^2}{M^2}=-2\frac{\left(1+\frac{\gamma-1}{2}M^2\right)}{1-M^2}\frac{dA}{A}+\frac{(1+\gamma M^2)\left(1+\frac{\gamma-1}{2}M^2\right)}{1-M^2}\frac{dT_0}{T_0}+\frac{\gamma M^2\left(1+\frac{\gamma-1}{2}M^2\right)}{(1-M^2)}4f\frac{dr}{D_h} \tag{25}$$

and the fractional change in the static pressure $dP/P$ can be expressed as

$$\frac{dP}{P}=\frac{\gamma M^2}{1-M^2}\frac{dA}{A}+\frac{\gamma M^2\left(1+\frac{\gamma-1}{2}M^2\right)}{1-M^2}\frac{dT_0}{T_0}-\frac{\gamma M^2[1+(y-1)M^2]}{2(1-M^2)}4f\frac{dr}{D_h} \tag{26}$$

In the above Eqs. (25) and (26), the coefficients corresponding to fractional changes in area, stagnation temperature, and wall frictional effects only depend on the local Mach number and are known as the influence coefficients. Using Eq. (24) to eliminate $dT_0/T_0$ in Eqs. (25) and (26) yields

$$\frac{dM^2}{M^2}=-\left[\frac{2\left(1+\frac{\gamma-1}{2}M^2\right)}{1-M^2}+\frac{(\gamma-1)M^2(1+\gamma M^2)}{(1-M^2)(1-\gamma M^2)}\right]2\frac{dD}{D}+\left[\frac{\gamma(\gamma-1)M^2(1+\gamma M^2)}{2(1-M^2)(1-\gamma M^2)}+\frac{\gamma M^2\left(1+\frac{\gamma-1}{2}M^2\right)}{1-M^2}\right]\frac{16\mu\pi dx}{\dot{m}} \tag{27}$$

and

$$\frac{dP}{P}=\left[\frac{\gamma M^2}{1-M^2}+\frac{\gamma(\gamma-1)M^4}{(1-M^2)(1-\gamma M^2)}\right]2\frac{dD}{D}+\left[-\frac{\gamma^2(\gamma-1)M^6}{2(1-M^2)(1-\gamma M^2)}-\frac{\gamma M^2[1+(\gamma-1)M^2]}{2(1-M^2)}\right]\frac{16\mu\pi dx}{\dot{m}} \tag{28}$$

Using Eqs. (27) and (28), the fractional change in the square of

[1]For a 1 mm radius thrust bearing with a nominal clearance of 3 $\mu$m rotating at a design speed of $1.2\times10^6$ rpm, a (large) rotor tip deflection of 1.5 $\mu$m gives rise to a direct-coupled hydrodynamic torque which is approximately 20% of the direct-coupled hydrostatic torque at a nominal supply pressure of 4 atm.

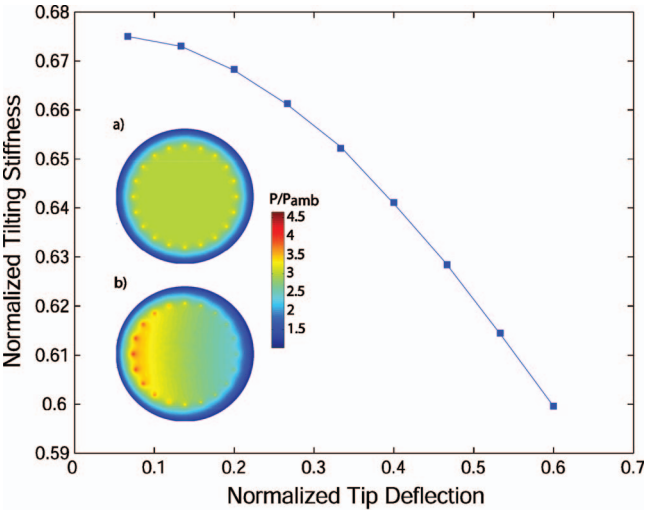


**Fig. 6 Variation of thrust-bearing tilting stiffness with normalized tip deflection; baseline configuration**

the Mach number $dM^2/M^2$ and the fractional change in the static pressure $dP/P$ can be evaluated numerically along the entire length of the orifice. The resulting model is used to assess the effects of geometric nonuniformities on thrust-bearing dynamic behavior.

## Generalized Model Applications

**Prediction of Thrust-Bearing Direct-Coupled Tilting Stiffness for Baseline Configuration.** The first application of the new model formulation is the evaluation of the direct-coupled tilting stiffness in hydrostatic thrust bearings. This is illustrated for the baseline thrust-bearing configuration shown in Fig. 1(*a*), which is the configuration adopted in the MIT micro-turbocharger [12]. In addition to providing the necessary axial stiffness, the thrust bearings have the additional onus of restoring the rotor to its equilibrium configuration when it is subjected to tilting perturbations about its spinning axis. The model is applied to the baseline thrust-bearing configuration and the computed static pressure distribution on the thrust-bearing pad is shown in Fig. 6. The radius of the thrust-bearing pad is 1 mm, the supply pressure to the thrust-bearing orifices is held constant at 60 psi (corresponding to a static pressure ratio $P_{\text{supply}}/P_{\text{ambient}}=5$), and the nominal thrust bearing gap is 3 $\mu$m. Figure 6(*a*) illustrates the baseline situation of an untilted rotor, where the static pressure distribution is seen to be axisymmetric. Computation results obtained for a rotor tip deflection of 2 $\mu$m are displayed in Fig. 6(*b*) and the static pressure on the thrust bearing pad becomes nonaxisymmetric with a larger static pressure building up in regions of smaller axial gaps. The concomitant nonaxisymmetric pressure distribution gives rise to a restoring torque which tends to oppose the tilting of the rotor. The monotonic increase in magnitude of the restoring torque with tilting angle thus results in a tilting stiffness, whose magnitude is nondimensionalized and plotted in Fig. 6 for a range of dimensionless rotor tip deflections.[2] The dimensionless direct-coupled tilting stiffness is defined as $k^+=k/(\sqrt{A}P_{\text{supply}}r^2)$, where $k$ is the direct-coupled tilting stiffness, $A$ is the thrust bearing surface area, and $r$ is the radial location of the orifices. The rotor tip deflections are normalized using the maximum allowable tip deflection. Knowledge of the tilting stiffness allows one to predict the rotordynamic behavior pertaining to the pitching and yawing of the rotor, which is discussed in a later section.

[2]Since the thrust-bearing gap is 3 $\mu$m, the corresponding maximum tip deflection of the rotor is also 3 $\mu$m.

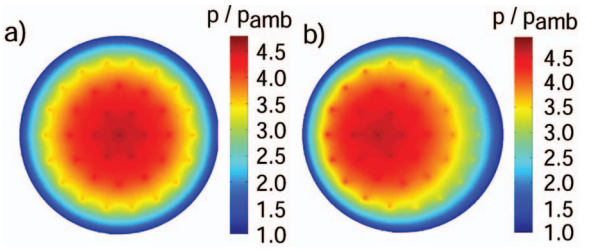


**Fig. 7 Normalized static pressure distribution on thrust-bearing pad for hexagonal thrust-bearing configuration: (*a*) untilted, (*b*) tilted**

**Performance Analysis of Hydrostatic Thrust Bearings with Unconventional Orifice Arrangements.** Next, the potential improvements in direct-coupled tilting stiffness of unconventional and novel thrust-bearing configurations are assessed. The new model is employed to perform a feasibility study of the hexagonal thrust bearing shown previously in Fig. 1(*b*). Using the Green's function formulation, the modeling results for the static pressure distribution along the thrust-bearing pad are shown in Figs. 7(*a*) and 7(*b*) for cases in which the rotor is untilted and tilted with a tip deflection of 2 $\mu$m, respectively. The supply pressure to the thrust bearings was kept constant at 60 psi for all calculations presented in this section, in order to compare the results to the original baseline configuration shown in Fig. 6(*a*). For the untilted case shown in Fig. 7(*a*), the static pressure distribution is nearly axisymmetric. When the rotor tip deflection is 2 $\mu$m, the high pressure "pocket" shifts outward toward regions where the thrust-bearing gaps are smaller, and provides a restoring torque and direct-coupled tilting stiffness in response to angular perturbations on the rotor. The results are summarized and the two configurations are compared to one another in Table 1. The table also includes results for the annular thrust bearing which is discussed next.

Table 1 presents two sets of results for the hexagonal thrust-bearing configuration. The total thrust-bearing clearance of 5.5 $\mu$m, which optimizes the axial stiffness for the baseline case, is found to be suboptimal for the hexagonal case. A total clearance of 7 $\mu$m maximizes the axial stiffness for the case with a hexagonal arrangement of orifices. It is apparent from the table that the hexagonal thrust bearing has a marginally lower axial and direct-coupled tilting stiffness, as compared to the original baseline case. However, the mass flow requirement for the hexagonal thrust bearing is perceptibly higher. The hexagonal thrust bearing is thus seen to be inferior to the baseline configuration in terms of steady-state performance, even though the hexagonal thrust bearing has 37 orifices, whereas the original configuration has only 20 orifices.

As discussed previously, one useful simplification in the modeling of the baseline configuration is to assume that the flow through each orifice contributes equally to the overall direct-coupled tilting stiffness of the system, thus permitting all the ori-

**Table 1 Comparison of key operating characteristics of baseline thrust-bearing configuration with hexagonal and annular configurations**

| Type | Axial stiffness (N/m) | Mass flow (g/s) | Tilting stiffness (N m/rad) |
|---|---|---|---|
| Total clearance=5.5 $\mu$m | | | |
| Original/Baseline | $2.2\times10^5$ | $1.00\times10^{-3}$ | 0.089 |
| Hexagonal | $1.7\times10^5$ | $1.19\times10^{-3}$ | 0.087 |
| Annular | $8.3\times10^5$ | $1.15\times10^{-3}$ | 5.0 |
| Total clearance=7 $\mu$m (optimized for axial stiffness) | | | |
| Hexagonal | $1.9\times10^5$ | $1.73\times10^{-3}$ | 0.075 |

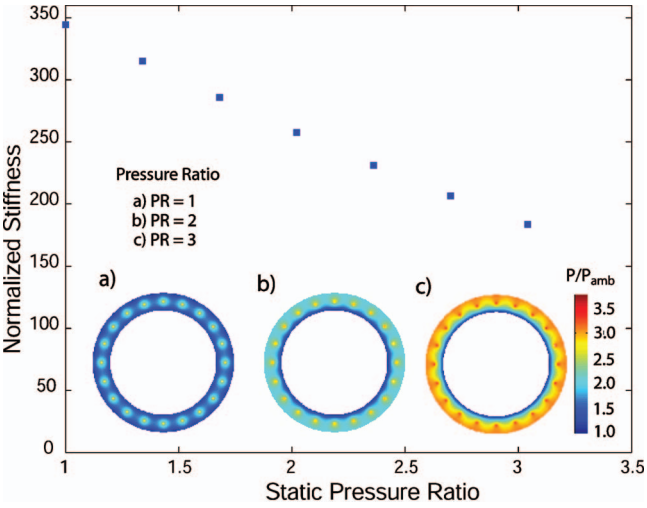


**Fig. 8 Variation of annular thrust-bearing axial stiffness with compressor rotor outlet static pressure**

fices to be modeled as springs with equal spring constants. When the number of orifices is increased and located at different radial locations, one might hypothesize that the overall stiffness of the system will increase, since there is an increase in the total number of springs. However, as seen from the above results, these orifices do not contribute equally to the overall axial stiffness of the system due to the interaction between the pressures and flows for orifices placed at different radial locations. Even after optimizing the axial gap for maximum stiffness, the hexagonal thrust bearing is still inferior in performance, since the gap is optimized for the *overall* thrust-bearing system, and not with respect to individual orifices.

In summary, the Green's function approach serves as an effective modeling tool to analyze novel thrust-bearing orifice configurations. Apart from modeling thrust-bearing configurations with novel arrangements of orifices, the Green's function approach can be easily extended to thrust-bearing pads which are not circular. As an example, the tilting characteristics of the rectangular thrust bearings considered by Kwan and Post [11] can be easily analyzed using this approach.

**Prediction of Annular Thrust-Bearing Performance Subjected to Varying Outlet Static Pressures.** One further application of the Green's function formulation is to assess the design of annular hydrostatic thrust bearings. One major proposal for improving the performance of the radial-outflow compressor of the MIT micro-turbocharger is to shroud the compressor [13] in order to improve the turbomachinery component efficiency. It might then be feasible to incorporate an annular thrust bearing on the shroud in replacement of the thrust bearing at the center of the rotor. However, as the rotational speed increases, the pressure rise across the compressor rotor increases quadratically with the rotational speed. This implies that the static pressure along the outer rim of the annular thrust bearing no longer remains constant, while the static pressure along the inner rim is approximately at ambient pressure. It is thus of interest to investigate the effects of an increase in pressure ratio across the compressor rotor on the axial stiffness of the annular thrust bearing. This can be readily assessed using the Green's function formulation. Figures 8(*a*)–8(*c*) show the static pressure distribution over the thrust-bearing pad of an annular thrust bearing for normalized static pressure ratios across the annular pad of 1, 2, and 3, respectively. The supply pressure to the thrust bearing was held fixed at 60 psig. The inner and outer rims of the thrust-bearing pads are located at radial locations of 3 mm and 4 mm, respectively. The dimensionless axial stiffness of the annular thrust bearing is plotted against the static pressure ratio across the annular pad in Fig. 8. The results show a monotonic decrease in axial stiffness with increasing pressure ratio. The dimensionless axial stiffness is defined by $K^+ = K/(\sqrt{A}P_{\text{supply}})$, where $K$ is the axial stiffness, $A$ is the area of the thrust-bearing pad, and $P_{\text{supply}}$ is the thrust-bearing supply pressure. For a static pressure ratio of roughly 3, the thrust bearing loses approximately 50 % of the axial stiffness compared to a stationary rotor. Since the turbomachinery and the bearings are closely coupled, such considerations are important to the design of annular thrust bearings for micro-turbomachinery applications.

Next, the axial stiffness of the annular thrust bearing is compared with the baseline configuration. Although the area of the annular thrust bearing is seven times higher than the baseline configuration, the axial stiffness is only three times greater and subsequently decreases for increasing static pressure ratios. A larger thrust-bearing area thus does not translate into a corresponding linear increase in axial stiffness. Referring to Fig. 6(*a*), for the baseline configuration, the circular array of orifices serves as a fence to maintain a high pressure near the center of the pad. This contributes significantly to the axial stiffness, since variations in the thrust-bearing gap give rise to variations in static pressure in this region. This in turn contributes to the restoring force acting on the rotor. In contrast, for the annular thrust bearing, a high pressure region is only maintained in the close vicinity of the orifices, with the static pressure dropping rapidly to ambient conditions along both the inner and outer edges of the circular pad. From a stiffness per unit thrust-bearing area perspective, the baseline configuration is thus more efficient in utilizing the available area to generate axial stiffness.

In summary, annular thrust bearings are in general superior to the baseline thrust-bearing configuration in terms of direct-coupled tilting stiffness. However, annular thrust bearings do not as efficiently utilize the available area to generate axial stiffness. Furthermore, coupling effects between the turbomachinery and annular thrust bearings may result in a deteriorated thrust-bearing performance.

**Experimental Prediction of Rotor Tilting Angle.** A series of experiments were performed on a micro-turbocharger. Although the pressures to both the forward and aft thrust bearings were held constant during the course of the experiments, the mass flows through *both* thrust bearings were found to decrease monotonically with increasing rotor speeds. A purely axial displacement of the rotor would result in a mass flow increase in one of the thrust bearings and a simultaneous decrease in the other (provided the flows through the orifices are unchoked). Therefore, it was conjectured that this simultaneous reduction in mass flows through both thrust bearings must arise as a consequence of rotor tilt.

The Green's function formulation has been used to test the above hypothesis and the model has been employed to compute the mass flows through each of the individual orifices as a function of the rotor tilting angle. The total mass flow through the thrust bearings was measured during the course of experiments. The total thrust-bearing mass flow rate at each tilting angle was readily evaluated by summing up the flows through the individual orifices. According to the model, the mass flow through the thrust bearing decreases monotonically with increasing rotor tilting angles or tip deflections. The mass flow predictions match the experimental data well, corroborating the above hypothesis.

In summary, using the measured decrease in thrust-bearing mass flow, the model is capable of predicting the rotor tilting angle. Since it is nearly impossible to physically and accurately measure the rotor tilting angle using conventional instrumentation in the MIT micro-devices, the analytical predictions are thus invaluable for providing a quantitative estimate.

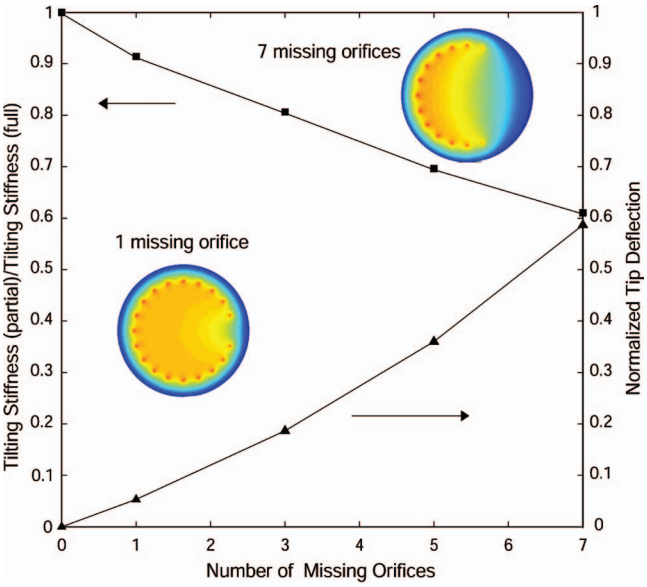


**Fig. 9 Variation in tip deflection and tilting stiffness with number of missing orifices**

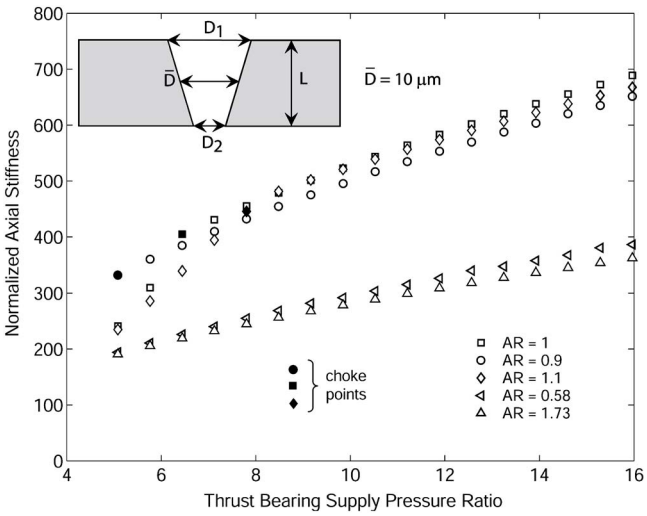


**Fig. 10 Effects of tapered orifices on thrust-bearing normalized stiffness**

## Effects of Geometric Nonuniformities in Thrust-Bearing Orifices

**Torques and Static Tilting Angles Arising from Clogged Orifices.** One of the main problems arising from micro-fabrication is the precise control of the thrust-bearing clearances and the orifice dimensions. In this regard, the Green's function formulation serves as a useful design tool to quantify the effects of geometric nonuniformities arising from micro-fabrication. For example, the effects of a nonuniform clearance $h(r,\theta)$ on the thrust-bearing direct-coupled tilting stiffness can be easily assessed, as elucidated by the calculations shown in Fig. 6.

Variations in thrust-bearing orifice diameters constitute a commonly observed geometric nonuniformity. One scenario characterizing such a geometric nonuniformity is the presence of clogged orifices, or more precisely, orifices which fail to be etched through as a consequence of photolithographic problems or breakdown of the photoresist. Figure 9 presents the static pressure distribution on the thrust-bearing pad for two cases: one clogged orifice and seven clogged orifices in a row. The total number of orifices is 20 and the supply pressure to the thrust bearing is set to 60 psi. Two main consequences are seen to arise due to the presence of clogged orifices. First, the deviation from an axisymmetric pressure distribution results in a net out-of-plane torque acting on an untilted rotor, which is in turn counterbalanced by the thrust-bearing tilting stiffness. The rotor will thus experience a net static tilting angle and a corresponding rotor tip deflection, which is plotted nondimensionally in Fig. 9 as a function of the number of clogged orifices. As expected, the rotor tip deflection increases monotonically with the number of clogged orifices. An excessively large tip deflection may give rise to large out-of-plane hydrodynamic torques which may in turn lead to instability.

A second consequence of unetched orifices is the reduction in magnitude of the direct-coupled tilting stiffness, as also shown in Fig. 9. This arises from the fact that fewer orifices contribute to the net tilting stiffness. Although in this discussion the approach has been to adopt the most severe scenario to illustrate the ability of the model to provide adequate predictions, the model is capable of handling other more specific and less severe cases of geometric nonuniformities such as variations in lengths and diameters of the thrust-bearing orifices.

**Effects of Tapered Orifices.** Another geometric nonuniformity which tends to arise during the micro-fabrication process is the tapering of the thrust-bearing orifices. The viscous, compressible flow through an orifice with variable cross-sectional area can be readily handled using the influence-coefficient approach described previously. The discussion here is confined to linearly tapered orifices, although the method is well suited for orifices of any general geometrical profile. The profile of such a linearly tapered orifice is given by

$$D(x) = \frac{2\bar{D}}{\sqrt{AR}+1} + 2\left(\frac{\bar{D}}{L}\right)\left(\frac{\sqrt{AR}-1}{\sqrt{AR}+1}\right)x \tag{29}$$

where $\bar{D}=(D_1+D_2)/2$ is the mean diameter of the orifice, and $AR=\sqrt{D_2/D_1}$ is the area ratio of the outlet to the inlet of the orifice. An area ratio greater than unity ($D_2>D_1$) denotes a negatively tapered orifice, whereas a value of less than unity ($D_1>D_2$) represents a positively tapered orifice. Figure 10 depicts the dimensionless thrust-bearing axial stiffness as a function of supply pressure for orifices of length $L=100$ $\mu$m, an average orifice diameter $\bar{D}=10$ $\mu$m, and different area ratios AR. For the baseline case where the orifices are untapered (i.e., AR=1), the flow through the orifices of both the forward and aft thrust bearings choke at a supply pressure ratio ($P/P_{amb}$) of approximately 6.4, where $P_{amb}=14.7$ psi.

When the orifices have a slight positive taper AR$\approx$0.9, the natural frequency and hence stiffness are greater than the baseline case with untapered orifices for supply pressure ratios ranging between 5.1 and 6.4. Note that the presence of the positively tapered orifices causes the orifices to choke at a lower thrust-bearing supply pressure ratio of 5.1. Although the static axial stiffness may be higher than the baseline case, the thrust bearings become dynamically unstable at lower thrust-bearing pressures as a result of the choked flow through the orifices. A negative taper of AR$\approx$1.1 shows an opposite trend. Compared to the baseline case, the natural frequency and stiffness are decreased for supply pressure ratios ranging between 5.8 and 7.1. Due to negative taper, the flow through the orifices has less tendency to choke and the orifices remain unchoked up to a thrust-bearing supply pressure ratio of 7.8. As a consequence, slightly negative tapered orifices have the advantage of delaying the occurrence of flow choking and therefore the onset of dynamic instability (see Teo and Spakovszky [1] for details).

In the above scenarios, the taper ratios analyzed were relatively small. For a larger positive taper ratio of AR$\approx$1.73, the natural

frequency and stiffness are found to be significantly lower compared to the baseline case. A similar trend is observed for orifices with a large negative taper ratio of AR $\approx$ 0.58. Although the mean diameter $\bar{D}$ of the orifices is 10 $\mu$m, the overall hydraulic resistance is significantly larger due to the stronger contribution from orifice sections with lower diameters. The flow resistance due to the 5.5 $\mu$m gap in the "radial" outflow region of the thrust-bearing land is thus too small to match the resistance posed by the orifices. This results in low values of stiffness. Moreover, due to the flow choking near regions where the diameters are excessively small, dynamic instabilities can be triggered more easily.

In summary, the influence-coefficient method for compressible, viscous orifice flows can be incorporated into the original model to assess the effects of nonuniform orifice profiles on hydrostatic thrust-bearing performance. The model can be used as a design tool to specify tolerance requirements related to the allowable taper ratio for a given level of thrust-bearing performance, as well as to predict the thrust-bearing performance based on actual geometric measurements pertaining to the profile of the orifices. For thrust bearings with orifice area ratios ranging between 0.9 and 1.1, the axial stiffness with tapered orifices are not expected to deviate significantly from the untapered case. Positively tapered orifices may, however, lead to flow choking which induce dynamic instabilities at lower thrust-bearing supply pressures. Orifice area ratios which deviate significantly from unity result in a considerable reduction in thrust-bearing axial stiffness.

## Pitch and Yaw Dynamics of a Rotor With Dynamic Imbalance

In this section, the pitch and yaw dynamics of a rotor-thrust-bearing system is analyzed using Eqs. (1) and (2). For an isotropic system with $k_{xx}=k_{yy}=K^{hs}$, the yaw and pitch angles $\beta_x$ and $\beta_y$ are equal and the tilting angle of the rotor is simply quantified by a single parameter $\beta$. The Green's function formulation can be applied to evaluate the variation of $K^{hs}$ and $c$ as a function of $\beta$. The values of $K^{hd}$ are determined using the Reynolds equation. Two primary ways of reducing the values of $\beta$ at high speeds are (1) to increase the direct-coupled thrust bearing tilting stiffness $K^{hs}$ and (2) to maintain low levels of dynamic imbalance $\chi$ by reducing the rotor etch nonuniformity and the bond misalignment between the compressor and turbine disks. Figure 11(*a*) illustrates the variation of the inclination angle $\beta$ with rotational speed for a micro-turbocharger rotor with three different values of dynamic imbalance $\chi$ subjected to the same thrust bearing pressures and therefore direct-coupled tilting stiffness. At a fixed rotational speed, the inclination angle $\beta$ is greater for rotors with larger dynamic imbalance $\chi$. Assuming the maximum allowable tip deflection is 3 $\mu$m,[3] the rotor with a dynamic imbalance of $\chi=1.5$, which corresponds to an asymptotic tip deflection of 4.5 $\mu$m, is suggested to fail at a quarter of the design speed. Without considering the effects of dynamic stability, the maximum allowable tilting angle is limited by the total thrust-bearing clearance or the minimum clearances imposed by the presence of labyrinth seals. The above analysis thus implies that, in order to reduce the likelihood of physical contact between the rotor and static structure as the rotor accelerates, it is necessary to ensure that the rotor possesses a sufficiently low normalized dynamic imbalance $\chi$ of order 0.5.

The effect of thrust-bearing direct-coupled tilting stiffness is shown in Fig. 11(*b*) for rotors with a normalized dynamic imbalance of $\chi=1$, which corresponds to 3 $\mu$m tip deflection. An increase in thrust-bearing supply pressure and therefore direct-coupled tilting stiffness results in smaller inclination angles $\beta$ for the same rotational speed. The implication of this is that an increase in thrust-bearing direct-coupled tilting stiffness has the beneficial effect of reducing the rotor tilting angle and hence the likelihood of physical contact between the rotor and the static structure.

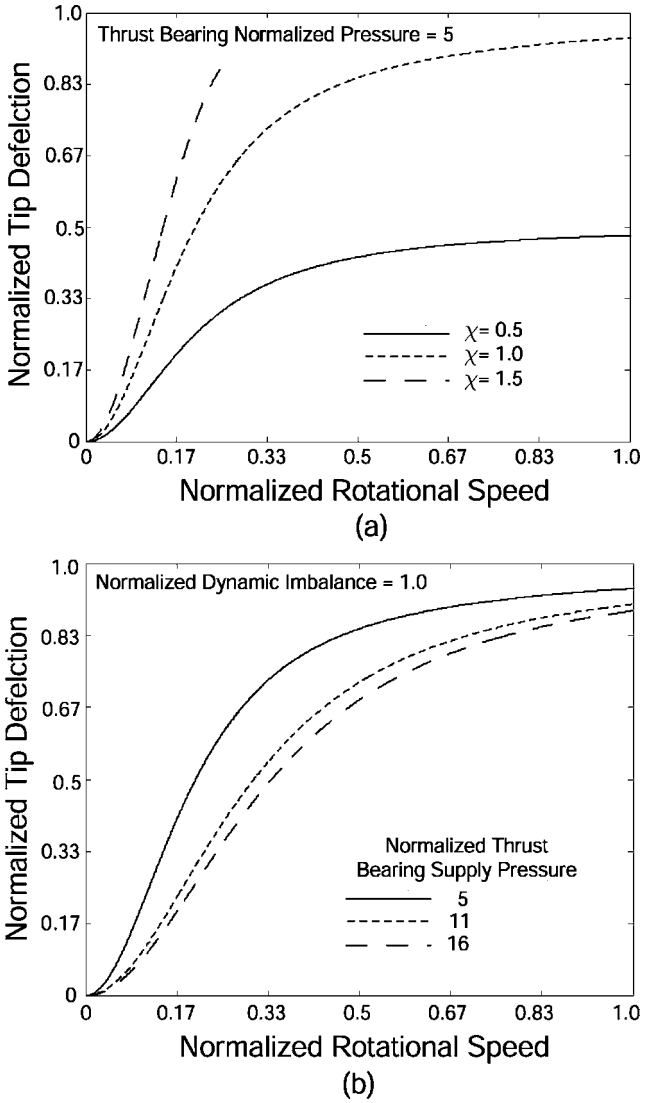


**Fig. 11** (*a*) **Variation of tip deflection with rotational speed for different dynamic imbalance levels $\chi$.** (*b*) **Variation of tip deflection with rotational speed for a rotor with normalized dynamic imbalance of 1.0 for different thrust-bearing supply pressures.**

The above analysis implies that if it is possible to quantify the dynamic imbalance of the rotor during the micro-fabrication process, the two degrees-of-freedom model for the yaw and pitch dynamics is capable of predicting the steady-state inclination behavior of the rotor at different operating speeds and thrust-bearing conditions.

It is essential to analyze the dynamic stability of the rotor-thrust-bearing system subjected to small perturbations in rotor inclination angles. The eigenvalue problem for dynamic stability has previously been obtained in Eq. (3). If any of the eigenvalues has a positive real part, the system is deemed to be dynamically unstable. For the specific case of the micro-turbocharger rotor with a large dynamic imbalance of $\chi=1.0$ and supported by the baseline thrust bearings with supply pressures of 60 psi, the eigenvalues are found to be complex conjugate pairs. The real parts of each complex conjugate pair are determined for the entire range of operating speeds. All real parts are found to be negative, implying linear stability of the inclination or coning motion. Although the

[3]This corresponds to a normalized dynamic imbalance $\chi=1.0$.

real part of the eigenvalues are all negative, some of them have magnitudes very close to zero (corresponding to neutral stability). Coupling effects from other components of the system, such as the gas journal bearings located at the outer periphery of the rotor [14], can render them positive and hence unstable. This is currently being investigated.

## Summary and Conclusions

A Green's function approach has been employed to extend and generalize the simple analytical model presented in Teo and Spakovszky [1] for inherent-restrictor orifice hydrostatic thrust bearings for application to micro-turbomachinery. The hydrodynamic thrust-bearing forces induced by the pumping action of the rotor rotation are determined by solving the Reynolds equation. The extended model serves as an effective tool to assess the thrust-bearing tilting stiffness and the effects of geometric nonuniformities occurring in the micro-fabrication process. Other attributes and capabilities of the enhanced model include the prediction of the steady-state performance of thrust bearings with unconventional orifice arrangement, the investigation of coupling effects with the turbomachinery components in annular thrust bearings, and the quantification of the rotor tilting angles using experimentally measured thrust-bearing mass flow rates. The Green's function formulation is also capable of assessing the torques and rotor tilting angles arising from geometric nonuniformities in orifice length and diameter. A wide range of micro-fabrication defects and anomalies such as the presence of unetched or missing orifices can be readily assessed. Effects of orifice taper can be dealt with by incorporating an influence-coefficient approach for compressible, viscous internal flows through orifices with varying cross-sectional area.

The yaw and pitch dynamics of a rotor-thrust-bearing system with dynamic imbalance has been analyzed using a two degrees-of-freedom rotordynamic model. The model is capable of evaluating the static rotor tilting angles and dynamic stability for different operating speeds and thrust-bearing conditions.

For the various thrust-bearing configurations investigated, the baseline configuration was found to be superior to the hexagonal configuration in terms of axial and tilting stiffness and mass flow consumption. Annular thrust bearings have the primary advantage of higher tilting stiffness, but they do not make as efficient use of the bearing land as the baseline configurations. Coupling effects between annular thrust bearings and the turbomachinery also have an adverse effect on the static performance of the bearings. The generalized model is useful in evaluating the impact of micro-fabrication tolerances and manufacturing uncertainties on thrust-bearing performance. The maximum allowable geometric nonuniformity in terms of thrust-bearing clearance and orifice diameter and taper can be specified to achieve the required thrust-bearing performance. The maximum allowable dynamic imbalance for stable high speed operation has also been quantified.

## Acknowledgment

The authors would like to thank Dr. F. F. Ehrich, Dr. S. A. Jacobson, and L. X. Liu for the very useful discussions and helpful comments, and Dr. H. Q. Li for his invaluable help and insight on microfabrication issues. This research was sponsored by DARPA and the U.S. Army Research Laboratory under the Collaborative Technology Alliance Program.

## Nomenclature

$A$ = area
AR = area ratio
$\beta_x, \beta_y$ = Euler angles
$c$ = angular damping
$\chi$ = dynamic imbalance
$D$ = orifice diameter
$D_h$ = hydraulic diameter
$e$ = normalized tip deflection
$f$ = friction coefficient
$G$ = Green's function
$\gamma$ = ratio of specific heats
$h$ = thrust-bearing gap or clearance
$I$ = diametral moment of inertia
$I_p$ = polar moment of inertia
$k$ = angular stiffness
$K$ = axial stiffness
$K^{\mathrm{hd}}$ = cross-coupled hydrodynamic tilting stiffness
$K^{\mathrm{hs}}$ = direct-coupled hydrostatic tilting stiffness
$L$ = orifice length
$\Lambda$ = bearing number
$\dot{m}$ = mass flow
$M$ = Mach number
$\mu$ = dynamic viscosity
$\omega$ = rotational speed
$P, P_t$ = static pressure, stagnation pressure
$P_{\mathrm{supply}}$ = thrust-bearing supply pressure
$r$ = radial location of orifices
$R$ = radius of thrust-bearing pad
Re = Reynolds number
$\Re$ = specific gas constant
$\rho$ = fluid density
$s$ = Laplace variable
$T, T_0$ = static temperature, total temperature
$\zeta$ = nondimensional hydrodynamic moment

## References

[1] Teo, C. J., and Spakovszky, Z. S., 2006, "Modeling and Experimental Investigation of Micro-hydrostatic Gas Thrust Bearings for Micro-turbomachines," ASME J. Turbomach., **128**, pp. 597–605.
[2] Epstein, A., 2004, "Millimeterscale, Micro-Electromechanical Systems Gas Turbine Engines," ASME J. Eng. Gas Turbines Power, **126**, pp. 205–226.
[3] Al-Bender, F., and Brussel, H. V., 1992, "Tilt Characteristics of Circular Centrally Fed Aerostatic Bearings," Tribol. Int., **25**, pp. 189–197.
[4] Yabe, H., and Watanabe, N., 1988, "A Study on the Running Accuracy of an Externally Pressurized Gas Thrust Bearing (Load Capacity Fluctuation Due to Machining Errors of the Bearing)," JSME Int. J., Ser. III, Series III, **31**, pp. 114–120.
[5] Yabe, H., and Yamamoto, M., 1989, "A Study on the Running Accuracy of an Externally Pressurized Gas Thrust Bearing (Bearing Stiffness and Damping Coefficient)," JSME Int. J., Ser. III, Series III, **32**, pp. 618–624.
[6] Nakamura, T., and Yoshimoto, S., 1996, "Static Tilt Characteristics of Aerostatic Rectangular Double-Pad Thrust Bearings With Compound Restrictors," Tribol. Int., **29**, pp. 145–152.
[7] Nakamura, T., and Yoshimoto, S., 1997, "Static Tilt Characteristics of Aerostatic Rectangular Double-Pad Thrust Bearings With Double Row Admissions," Tribol. Int., **30**, pp. 605–611.
[8] Childs, D., 1993, *Turbomachinery Rotordynamics - Phenomena, Modeling and Analysis*, John Wiley and Sons, N.Y.
[9] Shapiro, A. H., 1953, *The Dynamics and Thermodynamics of Compressible Fluid Flow*, Ronald Press, New York, Vol. I.
[10] Greitzer, E. M., Tan, C. S., and Graf, M. B., 2004, *Internal Flow: Concepts and Applications*, Cambridge University Press, Cambridge, England.
[11] Kwan, Y. P., and Post, J. B., 2000, "A Tolerancing Procedure for Inherently Compensated, Rectangular Aerostatic Thrust Bearings," Tribol. Int., **33**, pp. 581–585.
[12] Savoulides, N., 2004, Development of a MEMS Turbocharger and Gas Turbine Engine, Ph.D. thesis, Department of Aeronautics and Astronautics, MIT.
[13] Sirakov, B., 2004, "Characterization and Design of Non-Adiabatic Micro-Compressor Impeller and Preliminary Design of Self-Sustained Micro Engine System," Ph.D. thesis, Department of Aeronautics and Astronautics, MIT.
[14] Liu, L. X., 2005, "Theory for Hydrostatic Gas Journal Bearings for Micro-Electro-Mechanical Systems," Ph.D. thesis, Department of Mechanical Engineering, MIT.

# An Investigation of Wake-Shock Interactions in a Transonic Compressor With Digital Particle Image Velocimetry and Time-Accurate Computational Fluid Dynamics

**Steven E. Gorrell**
**David Car**
**Steven L. Puterbaugh**

Air Force Research Laboratory,
AFRL/PRTF,
Bldg. 18,
Wright-Patterson AFB,
OH 45433

**Jordi Estevadeordal**
Innovative Scientific Solutions, Inc.,
2766 Indian Ripple Road,
Dayton, OH 45440

**Theodore H. Okiishi**
College of Engineering,
104 Marston Hall,
Iowa State University,
Ames, IA 50011

*The effects of varying axial gap on the unsteady flow field between the stator and rotor of a transonic compressor stage are important because they can result in significant changes in stage mass flow rate, pressure rise, and efficiency. Some of these effects are analyzed with measurements using digital particle image velocimetry (DPIV) and with time-accurate simulations using the 3D unsteady Navier-Stokes computational fluid dynamics solver TURBO. Generally there is excellent agreement between the measurements and simulations, instilling confidence in both. Strong vortices of the wake can break up the rotor bow shock and contribute to loss. At close spacing vortices are shed from the trailing edge of the upstream stationary blade row in response to the unsteady, discontinuous pressure field generated by the downstream rotor bow shock. Shed vortices increase in size and strength and generate more loss as spacing decreases, a consequence of the effective increase in rotor bow shock strength at the stationary blade row trailing edge. A relationship for the change in shed vorticity as a function of rotor bow shock strength is presented that predicts the difference between close and far spacing TURBO simulations.* [DOI: 10.1115/1.2220049]

## Introduction

The interactions between the bow shock of a rotor and an upstream stationary blade row are known to impact the aerodynamic performance of transonic fans and compressors [1,2]. In the design of transonic fans and compressors attention must be paid to this impact. The forward and inlet region of a rotor blade row produces the majority of pressure rise and determines the maximum mass flow that the blade passage can pass [3]. The shock orientation is determined by blade geometry as well as inlet Mach number, flow direction, and back pressure. Conventional wisdom suggests that bow shocks that propagate upstream of a transonic blade row are weak and are not strong contributors to the performance of that blade row taken by itself. However, measured and numerical data show that the rotor bow shock contributes to losses via blade row interactions when the axial distance between blade rows is sufficiently small.

Time-accurate computational fluid dynamics (CFD) codes are being developed that make it possible to analyze the unsteady interactions between blade rows and evaluate their effects on aeromechanic and aerodynamic performance. However, very limited data has been published that can be used to validate these unsteady codes. Recent experiments have demonstrated that DPIV [4–10] is able to capture the unsteady fluid dynamics associated with blade row interactions.

The purpose of this paper is to combine time-accurate CFD with DPIV to visualize and investigate the details of interactions between a rotor bow shock and the blade and wake of an upstream stationary row. This comparison of measured and computed data will also serve to validate the ability of TURBO to capture the details of the unsteady flows in a compressor stage. By validating TURBO the groundwork is laid for a detailed examination of the role vortex shedding and wake-shock interactions play in determining aerodynamic performance.

Design systems in use today do not explicitly account for the impact of unsteady flows on the performance of a fan/compressor stage. Due to the trend toward increased relative Mach numbers and decreased axial spacing, it is important to understand how wake-shock interactions affect the performance of a transonic compressor. This is one of the technical challenges that must be overcome in order to develop highly loaded fans and compressors without sacrificing efficiency.

Wake-shock interaction has been the subject of only a few experimental and numerical investigations. Ottavy et al. [11,12] made laser two-focus anemometer measurements between an IGV and a transonic rotor. Upstream of the shock wave the IGV wake depth was reduced and the wake was overturned as a result of an expansion zone in the flow due to the curvature of the rotor blade suction surface. Downstream of the shock wave the IGV wake deficit increased and the wake was underturned.

A very interesting 2D numerical study of a stator-rotor configuration was presented by Zachcial and Nurnberger [13]. Their simulations showed that at a transonic operating condition the rotor bow shock caused vortex pairs to be shed from the upstream stator. A subsonic simulation showed the rotor potential field caused the stator wake to deflect. Thus, depending on the strength of the bow wave, different wake properties and shed vortices resulted. The authors also changed the stator to rotor axial gap between 35% and 47% of stator chord length and showed how the wake structure entering the rotor affected the rotor loss coefficient. How the wake migrated through the rotor impacted the rotor

Contributed by the International Gas Turbine Institute (IGTI) of ASME for publication in the JOURNAL OF TURBOMACHINERY. Manuscript received October 1, 2004; final manuscript received February 1, 2005. IGTI Review Chair: K. C. Hall. Paper presented at the ASME Turbo Expo 2005: Land, Sea and Air, Reno, NV, June 6–9, 2005, Paper No. GT2005-69107.

  

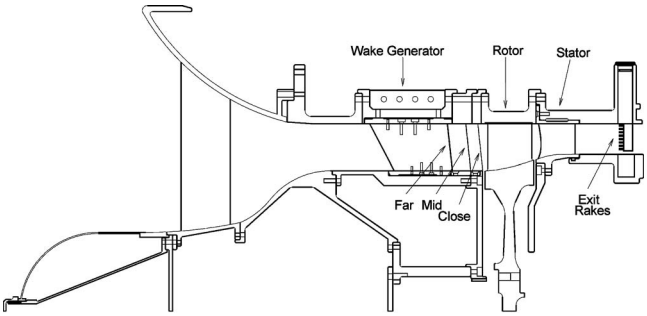


**Fig. 1 Stage matching investigation rig layout**

loss coefficient and the transport depended on the orientation of the wake as it entered the rotor. The manner in which the wake impinged on the rotor blade and the differing paths the pairs of counter-rotating vortices traveled through the rotor were suggested as the reason for changes in rotor loss generation.

Sanders and Fleeter [6] have made both PIV and blade surface static pressure measurements in the IGV passage upstream of a transonic rotor. The shock interaction with the IGV trailing edge caused the trailing edge stagnation point to move periodically from the pressure to suction surfaces of the IGV. This interaction accounted for peak-to-peak fluctuations in static pressure as large as 60% of the inlet total pressure.

An experimental analysis of wake-shock interactions in a transonic turbine cascade by Carscallen et al. [14] showed a relationship between Mach number and vortex shedding. Excellent measurements were obtained showing how vortex size, shedding frequency, and loss generation were related and varied with changes in Mach number.

This paper will describe the experimental and numerical methods used to obtain the data followed by a comparison of DPIV and time-accurate CFD results. Analysis of the effect axial spacing has on rotor bow shock interaction with an upstream wake generator and its wakes will then be presented.

## Experimental Method

The DPIV measurements were acquired on the U. S. Air Force's Stage Matching Investigation (SMI) rig. It is a high-speed, highly loaded compressor consisting of three blade rows: a wake generator, rotor, and stator as shown in Fig. 1. The rig was designed so that the wake generator to rotor axial spacing and the wake generator blade count could be varied. The axial spacings were denoted as "close," "mid," and "far." The wake generator blade count could be set to 12, 24, or 40, or the rig could be run without any wake generators (identified as the "clean inlet" configuration).

Details of the SMI rig are found in [1,15]. The purpose of the wake generators was to create total pressure loss typically found in modern-technology, highly loaded, low-aspect-ratio fan and compressor front stages. A two-dimensional representation was desired in order to isolate the effect of different wake parameters on the downstream stage performance. The wake generators are uncambered symmetric airfoils that do not turn the flow. They have a small leading edge and a blunt trailing edge. This shape creates a large base drag and no swirl. Solidity is held constant from hub to tip by varying the chord, the intent being to hold spanwise loss and wake width constant.

Calibration of the wake generators [15,16] showed this was the case except near the endwalls. The wake measurements provided the expected wake behavior at the different wake generator-rotor spacings. Wake depth was deepest at close spacing and became shallower at mid and far spacing. The wake width was nearly constant from hub to case. This confirmed the intent of the wake generator design to produce a two-dimensional wake profile. The calculated velocity profiles showed that the wake depth was similar at the hub and case but deeper near mid span. Wake analysis by Chriss et al. [16] showed that the SMI wake generator wakes demonstrated trends similar to that found in the literature.

Due to the blunt trailing edge of the wake generator, its wakes may be wider than what would be produced from a normally cambered stator airfoil. Regardless of the wake thickness, the loss produced was very near the design intent and well within the range typically found in highly loaded stators. Further, a recent cascade experiment by Langford et al. [17] confirms that large vortices can be induced at the trailing edge of a modern stator by the passing of a shock wave.

**SMI Performance.** As reported by Gorrell et al. [1], the SMI rig test documented that the axial spacing between an upstream stator and downstream transonic rotor had a significant effect on stage performance. Mass flow rate, pressure ratio, and efficiency all decreased as the axial spacing between the wake generator and transonic rotor was reduced.

Analysis of the experimental data showed that in addition to expected profile and mixing losses associated with the upstream blade row, loss was generated when the blade rows were close together. This additional loss production occurs as a result of interaction between the upstream wake generator and downstream transonic rotor. The extra loss was most significant between 20% and 70% span and coincides circumferentially in the vicinity of the wake generator wakes.

Time-accurate simulations [2] of the SMI experiment revealed some important aspects of the production of this additional loss. At close spacing the rotor bow shock was chopped by the wake generator trailing edge and formed a pressure wave on the upper surface of the wake generator that propagated upstream until it weakened. The bow shock was oblique as it interacted with the wake generator trailing edge, but the resulting pressure wave that formed was turned more normal to the wake generator blade surface. The resulting moving shock produced an entropy rise. The magnitude of loss production was affected by the strength of the bow shock and how much it turned as it interacted with the trailing edge of the wake generator. At far spacing the rotor bow shock degenerated into a bow wave before it interacted with the stator trailing edge and no significant pressure wave formed on the stator upper surface. For this condition, no additional loss was produced.

To remove any effects the downstream stator may have had on performance with changes in blade-row axial spacing, the SMI rig was modified to run without the stator. A radial rake was designed and fabricated to measure the total pressure and temperature downstream of the rotor. This wake was then traversed circumferentially in increments of 2.5% wake generator pitch.

The performance characteristic for the SMI two blade row configuration is shown in Fig. 2. A consequence of removing the stator was a severe increase in backpressure in the facility flowpath downstream of the test article that limited the maximum mass flow rate attainable. For this reason the data shown in the wake generator/rotor-only configuration was only obtained for operating conditions ranging from just below peak efficiency to near-stall. While the speed line operation was limited, the observations made at the available conditions were felt to be representative of the complete flow range.

DPIV data were acquired at close spacing, mass flow rate of 14.0 kg/s (point A) and at far spacing, mass flow rate of 14.6 kg/s (point B). TURBO simulations were run at these mass flow rates and an additional far spacing simulation was run at 14.0 kg/s (point C) to directly compare CFD results at the same mass flow rate.

## DPIV System

The DPIV system used to obtain the measurements presented in this paper has been described in detail by Estevadeordal et al. [8]. Two frequency-doubled Nd:YAG lasers were employed for instantaneous marking of the seed particles in the flow field. Com-

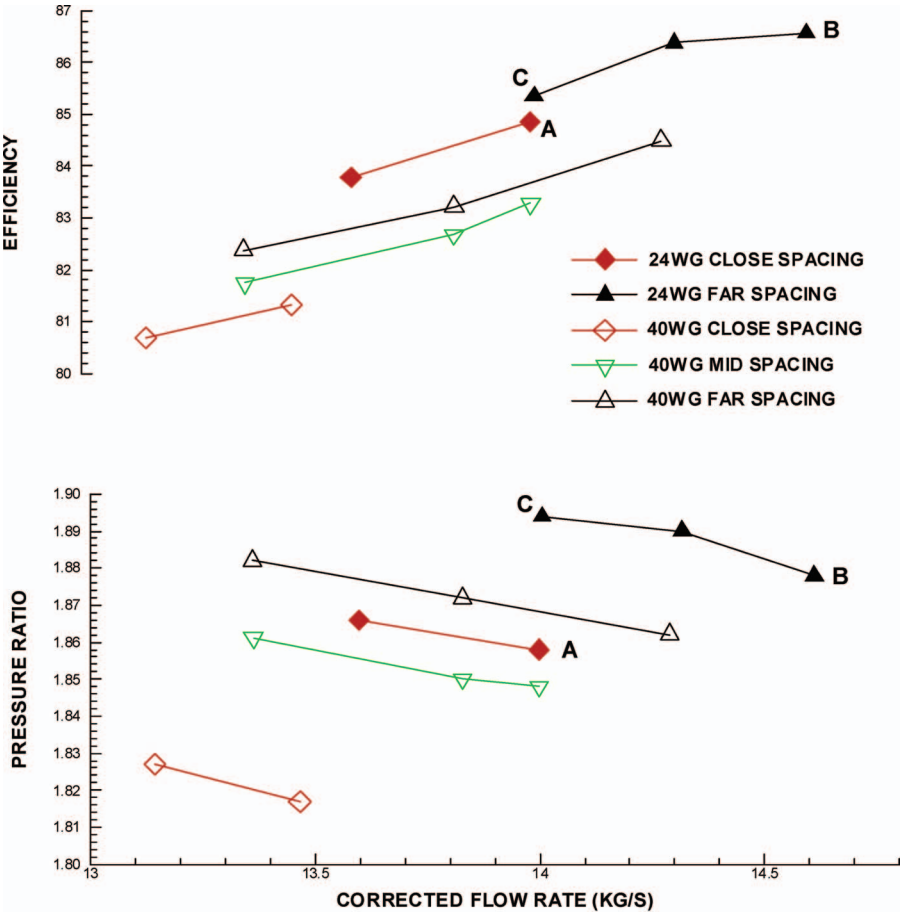


**Fig. 2 Wake generator/rotor only performance, 100% Nc**

bined by a polarizing cube or a beam combiner, the beams were directed through sheet-forming optics and illuminated the test section with a 2D plane of thickness ~1 mm. The scattering from the seed particles was recorded on a cross-correlation CCD camera with $1008 \times 1018$ pixels (Redlake ES1.0). The camera maximum repetition rate was 15 double exposures per second and was set to 10 Hz for synchronization with the laser repetition rate. The time delay between the lasers was typically 2 $\mu$s. A 105-mm Nikon lens was used.

The laser-sheet delivery system consisted of a probe inserted in an enlarged wake generator, light-sheet-forming optics, prisms, and probe holders for mounting the optics and for protecting them from contaminated seed materials. To minimize perturbations to the flow the modified wake generator was located two wake generator pitches below the wake generator centered at the receiving window. Figure 3 shows an illustration of the DPIV measurement area.

The shape of the laser sheet (thickness, width, focal distance) could be changed through various combinations of the spherical-lens focal length, the cylindrical-lens diameter, and the distance between them inside the modified wake generator as well as through external optics (a spherical lens) located in the laser path. The spanwise location of the laser sheet was changed by rotating the probe (Fig. 4). As shown in this figure, the laser sheet is inclined and not at a constant radius.

The camera was aligned and focused on the laser sheet prior to each run. It was mounted on a tripod to minimize the effect of rig vibrations. After every experiment the laser-sheet and camera locations were verified for possible misplacements. In the present experiments the only change required was slight refocusing, with negligible magnification effects.

The viewing window had the same curvature as the rotor case (radius is 241.3 mm), was made of chemically strengthened glass, and had a thickness of 2 mm. The effect of window curvature and thickness was investigated [9] and found to have a negligible effect for the present setup. Local seeding introduced upstream of the rig bellmouth was employed and the seed material used was sub-micron-size smoke particles generated from a glycerin and water mixture.

The rotor one-per-revolution signal was used for triggering the

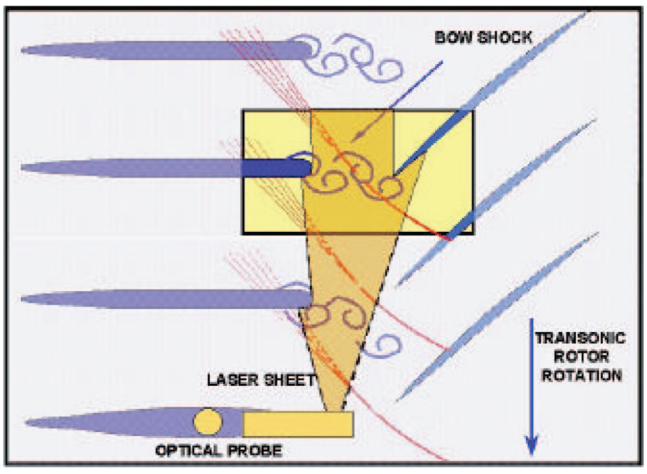


**Fig. 3 Illustration of DPIV measurement area**

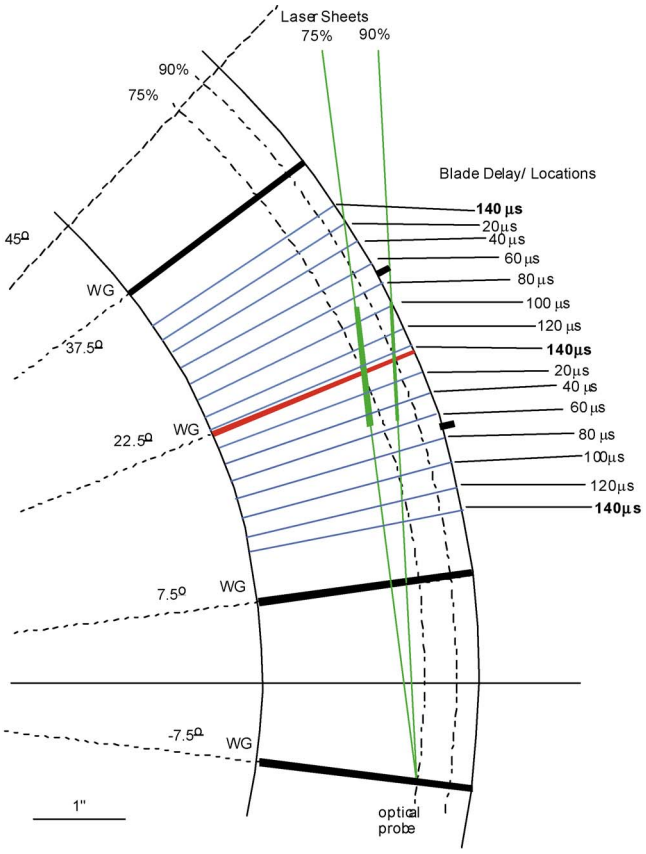


**Fig. 4 Laser-sheet spanwise locations for 24-WG configuration with respect to the blade clockings (delays/locations)**

synchronization system. A digital pulse generator (Stanford DG535) and a camera frame-grabber (National Instruments PCI-1424) were used.

Once the DPIV images were captured and digitized, the velocity field was obtained using cross-correlation techniques over interrogation domains of the images using software developed internally. The dimensions of each interrogation domain were dependent on particle density, estimated local velocity gradients, particle-image size, and desired spatial resolution. The peak of the correlation map corresponded to the average velocity displacement within the interrogation spot. An intensity-weighted peak-searching routine was used to determine the location of the peak with subpixel accuracy. To improve the signal-to-noise ratio in the correlation maps, a correlation-correction scheme [18] was applied wherein each map was multiplied by its immediate four neighborhoods. Zero padding was also employed for added accuracy. The software provides a choice of various correlation engines and correlation peak locators and incorporates several improvements to standard (single-pass) PIV techniques such as recursive estimation of the velocity field through a multipass algorithm for increased resolution. Two passes with interrogation cells overlapping 75% were performed. The overlapping includes new particles in every subregion which yields more vectors. Average routines allowed for removal of outliers beyond any number of standard deviations. Because of the strong phase-locked flow features, the median offered a valid, robust, and smooth statistical representation of the average velocity field [7]. Typically, the velocity field was calculated by combining 50 image pairs for each rotor blade clocking.

Many factors are involved in the calculation of DPIV uncertainty such as laser, CCD, seeding, imaging, algorithms, oscilloscope, etc. The highest uncertainty was found to be associated with the velocity calculation which involves $\Delta x$ (the displacement in pixels of each interrogation region), $\Delta t$ (the time interval between the two exposures), and the magnification of the digital image relative to the object (pix/m). The displacement in pixels obtained by peak-locator algorithms provided subpixel accuracy ($<0.1$ pixels) after correction for various biases [18]. The $\Delta t$ was adjusted to yield typical displacements in the main stream $>10$ pixels, and the uncertainty was thus $<1\%$. Values in the wake region, however, may have higher uncertainties due to the lower $\Delta x$. The maximum uncertainty in $\Delta t$ was calculated from the time interval between the two laser pulses with the aid of an oscilloscope (uncertainty 2%). It was found that this uncertainty increased with lower laser power and with lower $\Delta t$. A conservative number for the present experiments, which employed a $\Delta t$ of about 2 $\mu$s and powers around 10 mJ, was found to be 1%. The magnification was measured using images of grids located in the laser-sheet plane to better than 1%. Combining these conservative measurements of uncertainty yields a maximum error of $<2\%$ for the free-stream velocity and $\sim 10\%$ in the wake near the wake generator trailing edge.

## Numerical Method

The numerical simulations were performed using the parallel code TURBO [19–22] developed by Dr. Jenping Chen at Mississippi State University with support from NASA, industry, and DoD. TURBO solves the unsteady RANS equations in the rotating frame of reference. The solution algorithm is an implicit finite volume solver that incorporates Newton subiterations and a Block-Jacobi Gauss-Seidel relaxation scheme at each time step. Turbulence modeling is accomplished with the NASA/CMOTT $k$-$\epsilon$ model specifically developed for turbomachinery flows [23]. Axial communication between blade rows is through a sliding interface that does not distort the grid.

Interprocessor communication is accomplished through the use of the Message Passage Interface (MPI) Library. Memory is distributed so that each processor has exclusive access to its own partition of memory, which typically resides in the processor. The TURBO code has demonstrated excellent parallel efficiency on several high performance computing machines. During the past year, the authors have run TURBO using between 52 and 212 processors, each case yielding a parallel efficiency near 95%.

**SMI Simulation.** The grids used for the simulations were created in the average passage grid (APG) generator of Beach [24]. The grids are elliptically smoothed H meshes. Phase lag boundary conditions were used allowing one blade passage of each blade row to be modeled. The rotor grid size was $189\times71\times81$ nodes in the axial, radial, and tangential directions, respectively, and extends to the exit rake instrumentation plane used in the experiment. The clearance region was modeled with eight nodes and used a periodic boundary condition across the blade tip. The close spacing wake generator grid size was $138\times71\times61$ nodes and the far spacing wake generator grid size was $230\times71\times61$ nodes. Additional details of the grid are described by Turner et al. [25].

Consistent boundary conditions at the inlet and exit were used for both far and close simulations. At the inlet the total pressure, total temperature, and radial and tangential flow angles were defined. An inlet turbulence intensity of 2% was specified. Radial equilibrium was specified at the exit and a hub static pressure was varied to obtain the desired mass flow rate.

Much was learned by Gorrell et al. [2] regarding the grid resolution required to model unsteady flow features and capture details such as shock propagation and wake shedding and transport. The original grid reported in [2] was sufficient for use by AP-NASA in the analysis and design role. However, it became apparent that a TURBO simulation with that grid did not accurately model the wake shedding and transport. At the time of the 2002 simulations the available computing resources and time to obtain a converged solution were limiting factors. The development of a parallel version of TURBO combined with high performance

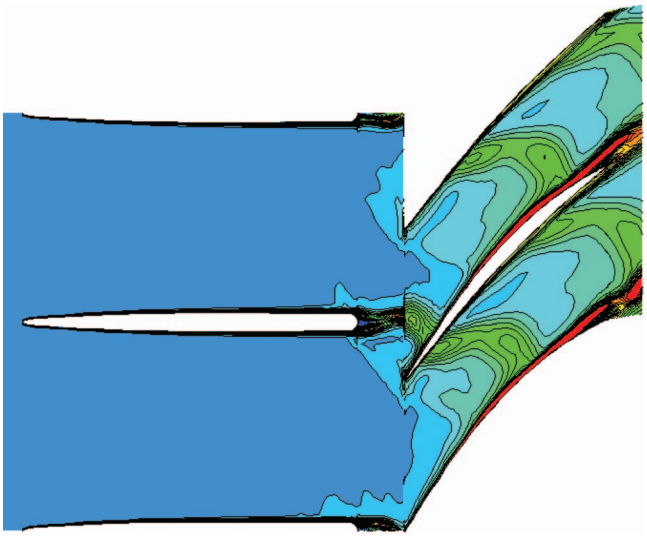

**Fig. 5 Entropy flux contours at close spacing, 75% span from 2002 simulation [2] (466,293 nodes)**

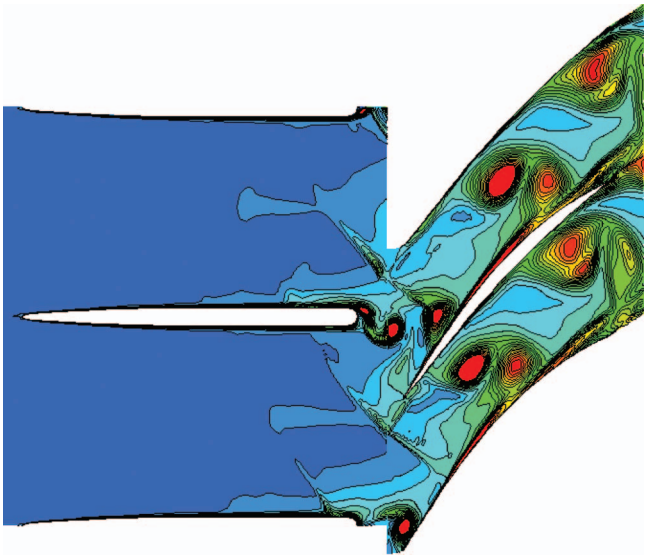

**Fig. 6 Entropy flux contours at close spacing, 75% span from present simulation (1,684,617 nodes)**

computers (HPCs) made more detailed simulations possible. A comparison showing the difference between the 2002 and present simulations is shown in Figs. 5 and 6. While the 2002 grid sufficiently captured the inviscid shock features, the denser grid used for the present simulations captured much more of the important details of vortex shedding and transport through the rotor.

## Results

Comparisons of the TURBO simulations and DPIV measurements are provided for the close and far spacing configurations. DPIV data were acquired for seven different rotor blade positions but only those pertinent to validation or description of wake-shock interactions are compared with CFD in this paper. There are two aspects of time-accurate CFD validation. This paper focuses on the unsteady flow features captured by a time-accurate code. Presumably, by capturing more details of the unsteady flow, the time

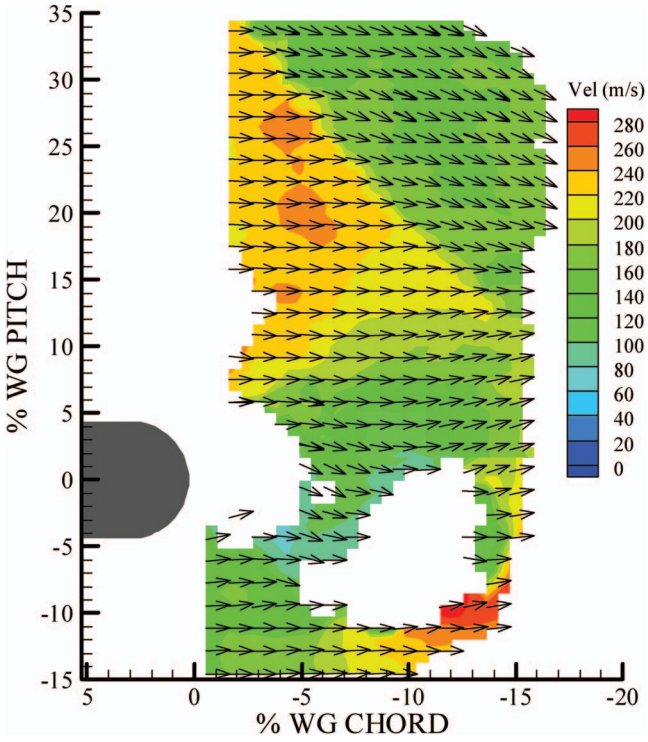


**Fig. 7 DPIV close spacing velocity magnitude contours for operating point A of Fig. 2, rotor at 34% above wake generator pitch**

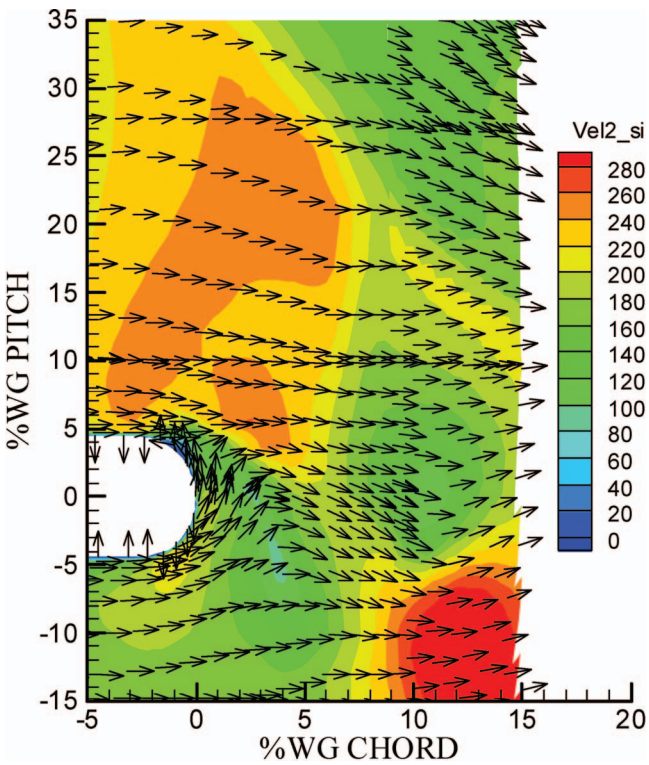


**Fig. 8 TURBO close spacing velocity magnitude contours for operating point A of Fig. 2, rotor at 34% above wake generator pitch**

average of the unsteady simulation is more accurate. A detailed time-average comparison of these simulations with steady-state exit profiles measured behind the rotor is given by Turner et al. [25].

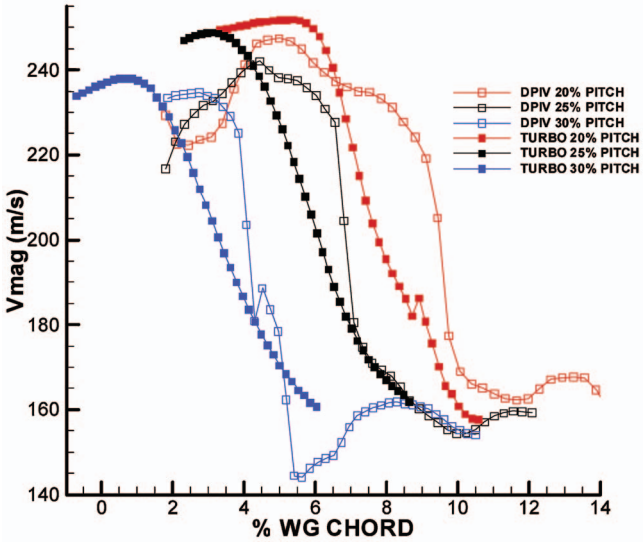


**Fig. 9 TURBO/DPIV velocity magnitude comparison across shock, close spacing**

From the time-average results the axial Mach number through the wake generators at 75% span was determined to be 0.57 and the Reynold's number based on wake generator trailing edge diameter was $5.78 \times 10^4$.

**Close Spacing Comparison.** Figures 7 and 8 present the DPIV and TURBO data at an instant in time corresponding to a rotor leading edge position 34% above wake generator pitch and a mass flow rate of 14.0 kg/s (operating pont A of Fig. 2). The three-dimensional TURBO results were interpolated onto a two-dimensional grid matching the orientation of the DPIV plane (see Fig. 4). Since the DPIV system measured the axial component and a radial and tangential combination component of velocity, the numerical velocity magnitude for comparison was mapped onto the DPIV plane.

During acquisition of the DPIV data at close spacing it was observed that the wake shedding was synchronized to the passing of the rotor bow shock [7]. This caused the shock and vortices to always be in the same relative position ("phase-locked"), resulting in little variation between individual realizations of an ensemble and the ensemble average. It was shown that in such cases the median offers a more robust statistic for outlier (bad or missing vectors) removal than the mean. However, problems arise in cases when there are insufficient data in certain areas of the images. Various DPIV noise sources encountered during close spacing data acquisition were the lack of seeding in the center of the vortex due to the difficulty in mixing seed particles inside the vortex center, glare from the hub reflections, and oil deposits from seed condensation on the receiving window. These problems result in a lack of vectors and reduce the capability of capturing a complete flow field representation. Consequently the median actually provides a more smeared representation of the flow than a phase-locked single realization. Therefore a composite was created (Fig. 7) by combining vector areas from the best instantaneous data sets to capture more accurately the velocity field to be compared with the TURBO simulation. Unfortunately, the vortex region could not be recovered from any realization at this operating condition and therefore is omitted.

Both the experimental and numerical data showed that the bow shock is broken up by the wake. The angle and velocity gradient defining the rotor bow shock are very similar above 20% wake generator pitch. Figure 9 plots the velocity magnitude measured by DPIV and predicted by TURBO at three different pitch locations. The minimum and maximum velocities agree within 1.5% to 3%.

The vortices that define the wake are visible through flow visualization images obtained by increasing the amount of seed in the flow and calculated entropy flux defined as $\rho u \Delta s / C_p$. Unfortunately, due to lack of vortex data, the DPIV could not be used for comparison at this operating condition. Figures 10 and 11 shows the vortex size and wake shape are very similar between the flow visualization and TURBO simulation. The large vortex is centered at the same location (11% wake generator chord, −6% wake gen-

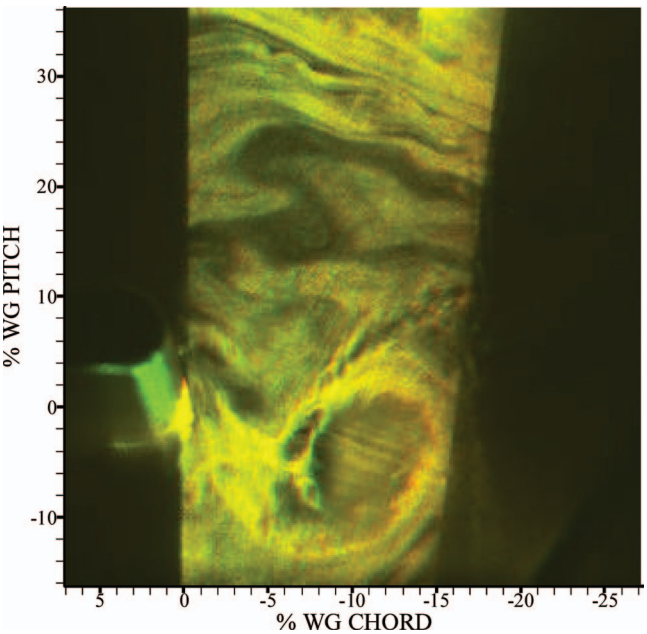


**Fig. 10 Close spacing flow visualization for operating point A of Fig. 2, rotor at 34% above wake generator pitch**

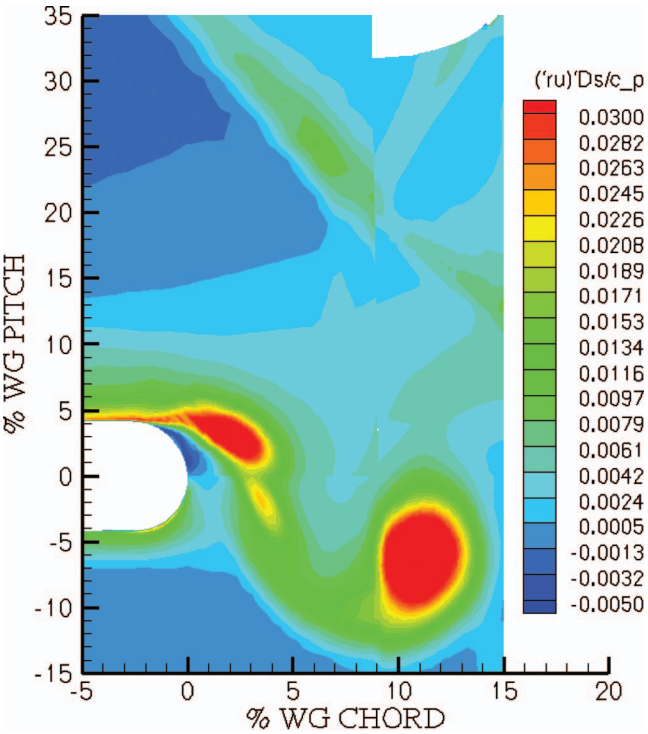


**Fig. 11 TURBO close spacing entropy flux contours for operating point A of Fig. 2, rotor at 34% above wake generator pitch**

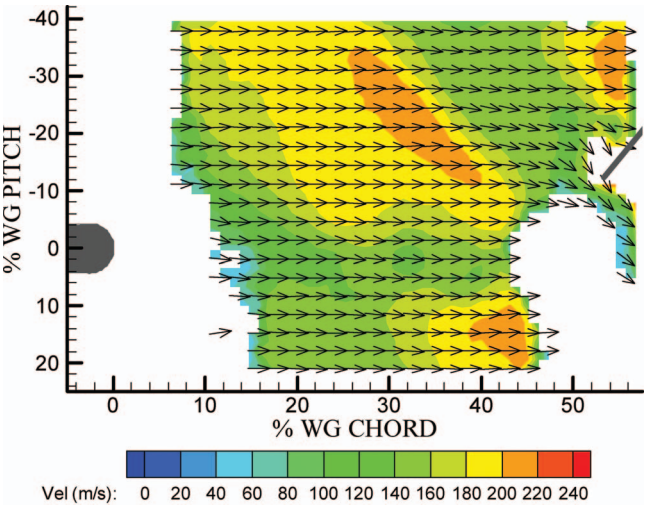


**Fig. 12 DPIV far spacing velocity magnitude contours for operating point B of Fig. 2, rotor at 13% above wake generator pitch**

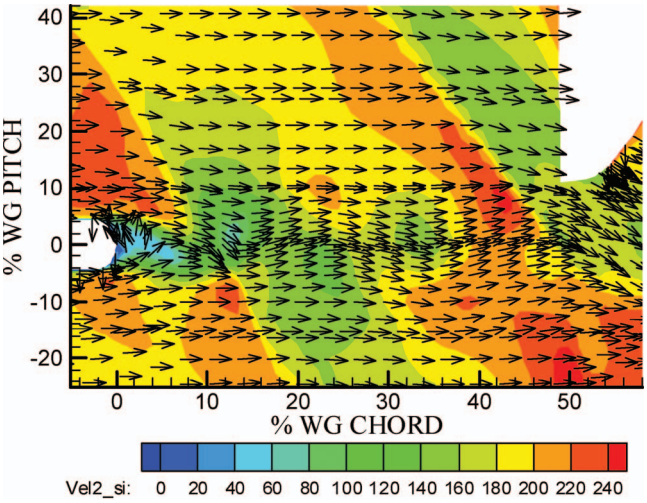


**Fig. 13 TURBO far spacing velocity magnitude contours for operating point B of Fig. 2, rotor at 13% above wake generator pitch**

erator pitch) and is of similar size. Variations in seed distribution as observed in Fig. 10 were attributed to the upstream location of the seeding port and the repeatability of the seeding system.

**Far Spacing Comparison.** Figures 12 and 13 compare DPIV and TURBO for the far spacing configuration at a mass flow rate of 14.6 kg/s (operating point B of Fig. 2) and a rotor leading edge position at 13% above wake generator pitch. The shock near the rotor shown in the DPIV plot of Fig. 12 appears more smeared than the CFD. This was attributed [7] to the fact that at far spacing the wake shedding was not as synchronized to the passing of the rotor bow shock as was observed at close spacing. Thus the location of the wake and shock captured by individual realizations could vary slightly. It was not the individual DPIV images that were smeared but the average of 50 of those images. With the greater distance between the wake generator trailing edge and rotor leading edge there are two rotor bow shocks in the flow field. The comparison of velocity change across the shock shown in Fig. 14 is made at the shock nearest the rotor between 15% and 35% above wake generator pitch. The shock angle and velocity magnitude compare well. The TURBO velocity magnitude is greater upstream of the shock than DPIV but still matches to

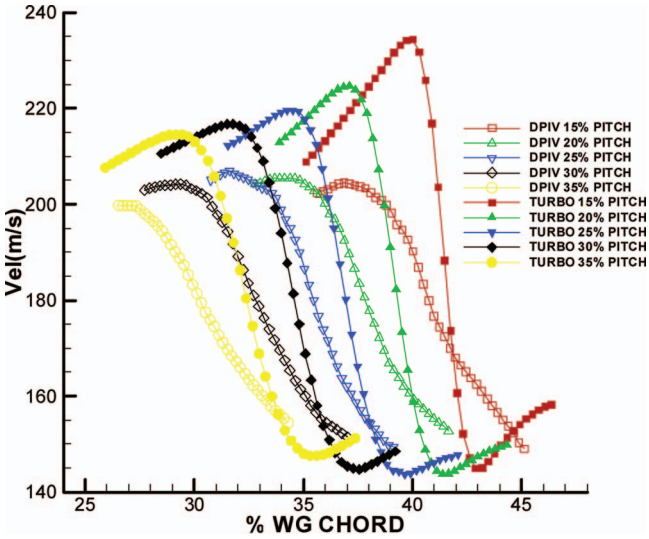


**Fig. 14 TURBO/DPIV velocity magnitude comparison across shock, far spacing**

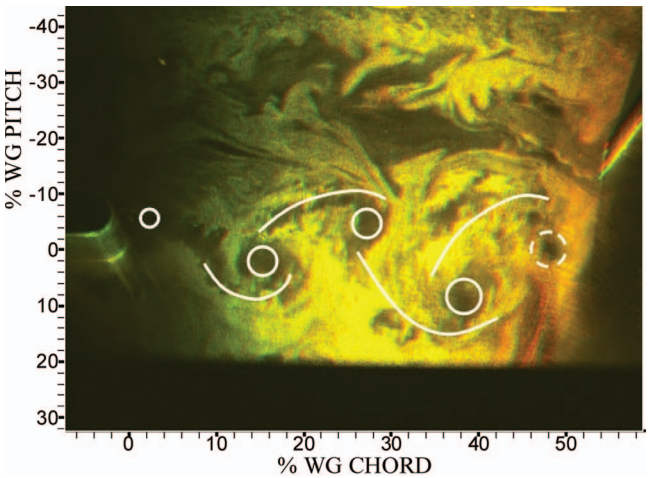


**Fig. 15 Far spacing flow visualization for operating point B of Fig. 2, rotor at 13% above wake generator pitch**

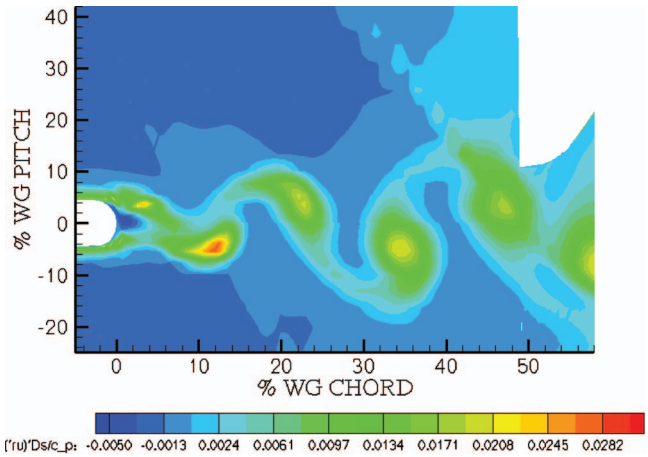


**Fig. 16 TURBO far spacing entropy flux contours for operating point B of Fig. 2, rotor at 13% above wake generator pitch**

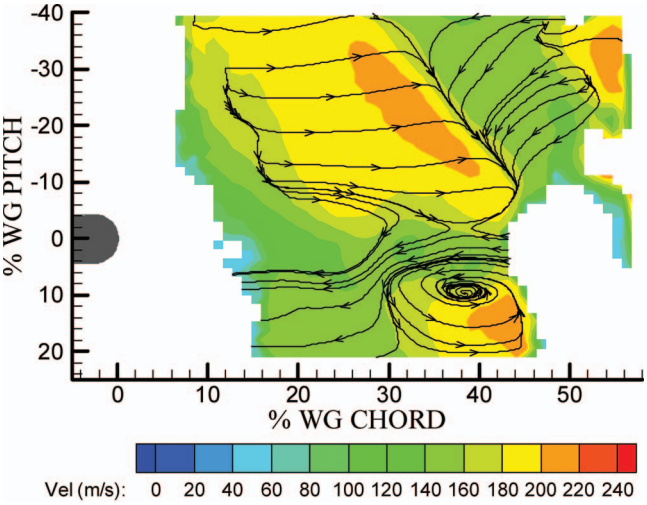


**Fig. 17 DPIV far spacing with convection velocity subtracted for operating point B of Fig. 2, rotor at 13% above wake generator pitch**

within 6% to 13%. The TURBO velocity magnitude (Fig. 13) shows the upstream shock is broken up by the stronger wake near the wake generator trailing edge but the mixed out wake does not affect the downstream shock as drastically. The shape of the downstream shock does change due to the interaction. At this operating condition DPIV measurements were obtained in the wake and the low velocity regions correlate well to the TURBO simulation. It is difficult to ascertain whether the shock in Fig. 12 is broken up by the wake or if there is insufficient DPIV resolution.

The vortex size and shape at far spacing are presented in Figs. 15 and 16. The wake is defined by two vortex pairs between the wake generator and rotor. In the flow visualization image the vortex centers have been drawn with circles and the braids that connect the vortices have been drawn with lines. Due to the interaction with the bow shock the last vortex is difficult to discern and is estimated with a dashed circle. There is good qualitative agreement between the flow visualization and TURBO entropy flux. The size and shape of the shed vortices are similar.

## Discussion of Results

The DPIV and time-accurate TURBO capture very similar details of the unsteady wake-shock interaction. The unsteady details compared in this paper and the time-average data comparison of Turner et al. [25] establish confidence in the ability to investigate shock-vortex interactions in this transonic compressor. Very fine three-dimensional meshes are required to capture the details of the unsteady flow field in the TURBO simulation. A three-dimensional grid is required to calculate the vorticity vector and, as demonstrated by Turner et al. [25], there is an inward radial migration of the vortices shed from the tip of the wake generator that must be resolved to correctly predict the radial efficiency profile at the exit of the rotor. High performance parallel computers are therefore necessary to obtain solutions in a reasonable time frame. In reality, most insight is gained by analyzing both the experimental measurements and CFD simulation. Each has their strengths and weaknesses. Combined together, a thorough investigation is possible.

The vortices that define the wake can have significant influence on wake-shock interactions. The unsteady motions related to the shock and vortices can be investigated using quantities derived from the DPIV velocity field. Figure 17 shows how subtracting a constant axial component (convective) of velocity can be used to represent the motion from a frame of reference moving at that velocity [26]. The second (downstream) vortex and saddle point can be readily identified by this method. Although sufficient data were not available to do this at close spacing for the configuration presented in this paper, other measurements made on the SMI rig with the downstream stator present have been successful (see Ref. [10]) at isolating the shed vortex at close spacing with DPIV.

A comparison of TURBO simulations at the same mass flow rate as shown in Figs. 18 and 19 provides insight into the loss creation process resulting from the blade row interactions under study. These figures are both at 14.0 kg/s corresponding to operating points A and C of Fig. 2, 75% span, with the rotor in the same position. The comparison reveals a significant increase in entropy generation within the shed vortices at the close spacing configuration versus far. It is postulated that this increase in loss is due to the increase in local, short-term loading at the trailing edge of the upstream blade row that results from the action of the stronger shock present in the close configuration. Since entropy and vorticity can be related through Crocco's theorem, it is desirable to relate the increase in vorticity resulting from the interaction to quantities that would be known or easily calculable at

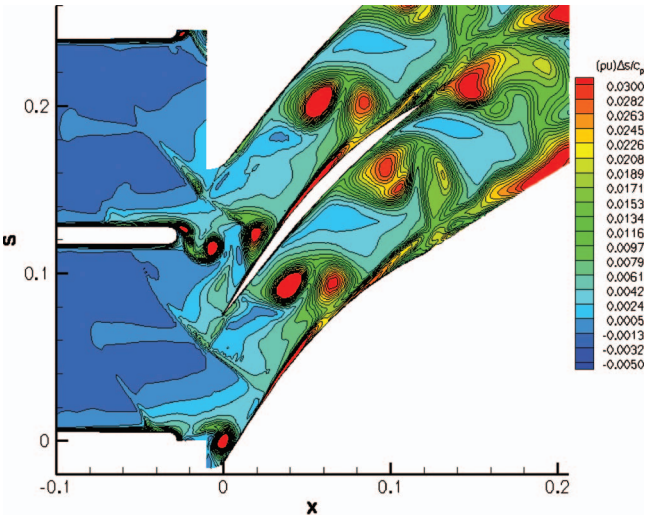


**Fig. 18 TURBO close spacing entropy flux contours for operating point A of Fig. 2, constant 75% span**

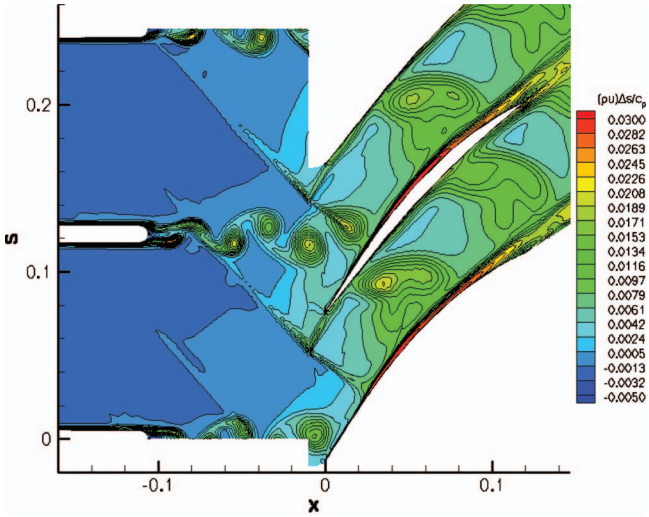


**Fig. 19 TURBO far spacing entropy flux contours for operating point C of Fig. 2, constant 75% span**

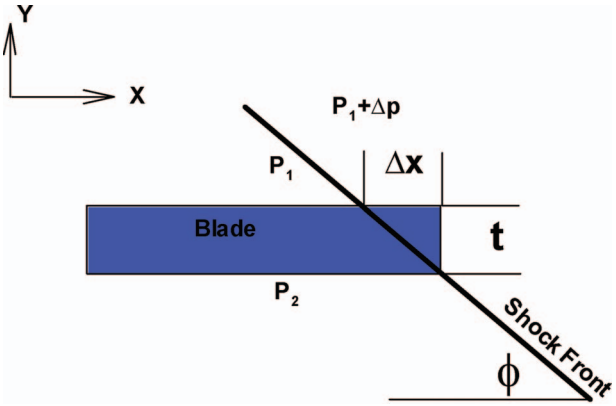


**Fig. 20 Sketch defining relationship between interaction and vortex generation**

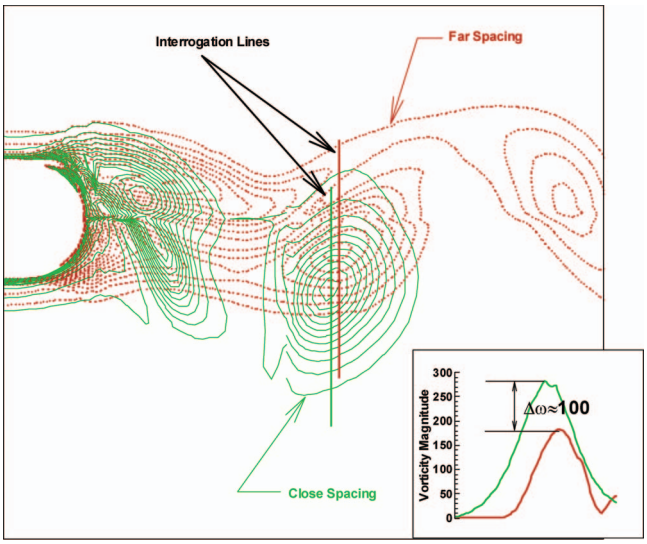


**Fig. 21 TURBO comparison of close and far spacing shed vortices for operating points A and C of Fig. 2, 70% span**

design time. This is an important first step to developing a method of calculating interaction loss for design-type applications.

**Vorticity Generation.** Based on the DPIV measurements and TURBO simulations, a simple relation for the vorticity generation due to the rotor bow shock interaction with the wake generator trailing edge is presented. A simple sketch of the geometry under consideration is shown in Fig. 20. The trailing edge region is approximated as a blunt trailing edge with finite thickness, $t$. As the rotor shock impinges upon the trailing edge at an angle $\phi$, the blade loading changes thereby altering the net circulation of the blade cross section. This change in circulation likely explains the observation of Sanders and Fleeter [6] that a shock interacting with an IGV caused the trailing edge stagnation point to move periodically between the pressure and suction surfaces. If it is assumed that the trailing edge is sufficiently small such that the change in shock strength, $\Delta p$, over its axial projection, $\Delta x$, across the trailing edge can be neglected, then the change in tangential blade loading (which is the component of force perpendicular to the incoming flow in this instance) is:

$$\Delta F_y \approx \Delta p \Delta x = \Delta p \frac{t}{\tan \phi} \tag{1}$$

If the change in circulation of the blade cross section is equivalent to the change in bound vorticity within the area encompassing the blade section, and the change in vorticity occurs locally within an area on the order of the trailing edge thickness, then the change in circulation is approximately:

$$\Delta\Gamma = \int \int_{dA} \Delta \boldsymbol{\omega} \cdot d\boldsymbol{A} \qquad \Delta\Gamma \approx \Delta\omega \frac{\pi t^2}{4}$$
$$\Delta A \approx \pi t^2/4 \tag{2}$$

where $\Delta\omega$ is the change in vorticity. From circulation theory, the blade loading perpendicular to the incoming free stream is a product of the magnitude of circulation with the free stream velocity and density. Therefore, the change in blade loading for a steady incoming free stream is proportional to the change in circulation:

$$\Delta F_y = \rho_\infty V_\infty \Delta\Gamma \Rightarrow \Delta\Gamma = \frac{\Delta F_y}{\rho_\infty V_\infty} \tag{3}$$

Substituting the previous relationships for the change in blade loading and circulation into Eq. (3) yields an equation for the change in vorticity:

$$\Delta\omega = \Delta p \frac{4}{\pi \tan(\phi) \rho_\infty V_x S} \frac{S}{t} = \frac{4}{\pi} \frac{\Delta p}{\dot{m}} \frac{1}{\lambda} \tag{4}$$

where $S$ is the wake generator pitch and $\lambda$ is the trailing edge blockage, i.e., the ratio of trailing edge thickness to pitch. Equation (4) can also be rewritten as:

$$\Delta\omega = \left(\frac{4}{\pi \tan(\phi)}\right)\left(\frac{\Delta p}{\bar{p}}\right)\left(\frac{\bar{p}}{\dot{m}}\right)\left(\frac{1}{\lambda}\right) \tag{5}$$

where $\bar{p}$ is the average pressure across the incoming shock.

Interestingly, a model which has received much attention recently is that of Morfey and Fischer [27] relating the shock strength, $\Delta p/\bar{p}$, as a function of rotor Mach number, axial flow Mach number, and ratio of axial distance to rotor pitch. This may be used here to calculate the shock strength at a given location upstream of the rotor.

Note that the shock strength is only a function of the rotor geometry, which supports the observation of Chriss et al. [16] that the additional loss associated with the interaction was more dependent on the rotor than the number of wake generators present. This was determined by calibrating both a 24 and 40 wake generator configuration in isolation to determine the total pressure loss at various distances downstream of the wake generator bladerow. The loss was then used to correct the three-blade-row performance of the SMI rig at the rotor face to determine the effect of axial spacing on the flow capacity of an embedded compressor stage (two blade rows). Correcting for the wake generator profile and mixing loss did not fully account for the change in flow capacity of the stage. This additional loss was theorized to be caused by the interaction of the rotor with the upstream wake generator. Interestingly, the change in flow capacity when accounting for the loss of the wake generators was nearly identical for the 24 and 40 wake generator configurations at both mid and far spacing and was nearly identical for the close spacing when accounting for measurement error. This suggests that the additional loss generation was mainly associated with the rotor.

A comparison was made between the shed vortex of the close and far spacing simulations to determine whether this correlation captures the effect of the impulsive loading due to the shock. The close and far spacing CFD simulations were both performed at the same inlet flow rate of 14 kg/s. Figure 21 shows an overlay of vorticity magnitude contours for the close and far spacing solutions at approximately 70% span with solid and dotted contour lines for the close and far spacing solutions, respectively. A time

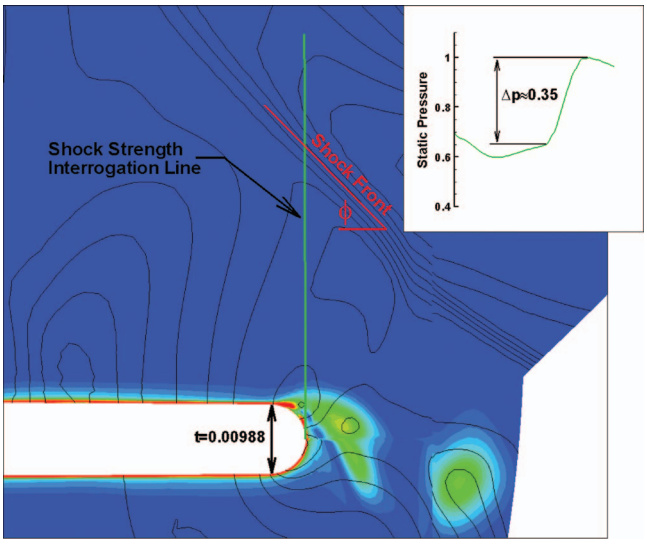


**Fig. 22 TURBO close spacing vorticity magnitude contours and static pressure rise across bow shock for operating point A of Fig. 2**

step was chosen for the far spacing solution that put the vortex shed from the lower surface of the wake generator approximately the same percent chord downstream as the close spacing configuration such that any diffusion of vorticity into the freestream would be comparable for the two cases. It was assumed that the interaction of the far spacing solution was negligible and is representative of the baseline performance (natural shedding) of the wake generator. The vortex core was interrogated for the two solutions and the vorticity magnitude is plotted in the inset of Fig. 21. The change in nondimensional peak vorticity magnitude between the two solutions is approximately 100. The close solution was then interrogated to determine the shock strength, shock angle, wake generator inlet axial momentum, and trailing edge thickness and is shown in Fig. 22 with the inset showing the static pressure rise across the shock. The values were determined to be:

$$\Delta p = 0.35; \quad t = 0.00988; \quad \phi = 45 \text{ deg}; \quad \rho_\infty V_\infty = 0.511$$

Substituting these values into Eq. (5) derived for the change in vorticity due to the interaction yields a nondimensional value of approximately 88. This is within 12% of the value calculated from the simple interrogation of the close and far spacing solutions. This simple correlation may be used to capture a significant portion of the perturbation vorticity generated from this interaction. It is clear from comparisons of the close and far spacing simulations that a significant difference in entropy exists in the vortex cores. A linearization of Crocco's theorem can be used with the perturbation vorticity correlation presented here to determine the perturbation entropy generated from this interaction and from there the impact on performance may be assessed. Also, at this point a heuristic argument can be made that after the initial impulsive loading of the wake generator due to the traveling shock, the rapid dissipation of the shock as it travels upstream results in the unloading of the wake generator. This unloading should result in the shedding of vorticity of the same magnitude, but opposite sign, as that shed due to the impulsive loading. The earlier simulations of Gorrell et al. [2] along with the high fidelity ones presented here show the shock propagation and dissipation and vortex shedding. One would have to account for this secondary shedding when deriving the impact this event may have on the overall stage performance.

## Conclusions

Both DPIV data and time-accurate CFD simulations have been studied to understand wake-shock interactions in a transonic compressor. DPIV data are very useful in validating the ability of time-accurate CFD to model complex unsteady flow fields associated with transonic blade row interactions. From a validation standpoint there is excellent agreement between the results of the TURBO code and DPIV. This is due to the fine three-dimensional meshes used in the simulation. Such grids are necessary to capture the important details of shock propagation and vortex shedding. Used together, the measured and numerical data provide the insight needed to understand the flow physics of wake-shock interactions.

As the axial spacing between the upstream wake generator and downstream rotor decreased, the vortices shed from the wake generator increased in size and produced additional loss. This is the result of a stronger rotor bow shock driving the vortex shedding of the upstream blade row at close spacing.

A simple relation for the change in vorticity as a function of stator geometry and rotor bow shock strength correlated well with the change in shed vorticity magnitude between the far and close spacing configurations. Combining this correlation with a linearization of Crocco's theorem and the shock decay model of Morfey and Fisher [27] may prove to be a suitable basis for derivation of a loss model for this interaction.

With the validation of TURBO as a tool to investigate blade row interactions, further research can now be carried out to develop an interaction model useful in streamline curvature design systems. This will allow design engineers to account for this loss mechanism, which may prove particularly important in transonic multistage matching.

## Acknowledgment

The authors would like to recognize the CARL and ISSI staff who assisted with the SMI test program and data acquisition. Dr. Jenping Chen, Dr. Michael Remotigue, and Professor Mark Turner are acknowledged for their assistance with the numerical simulations. The simulations were run using computers at the Aeronautical Systems Center, Major Shared Resource Center (ASC MSRC) at Wright-Patterson AFB. The authors thank the Propulsion Directorate management for supporting the research and allowing the presentation and publication of this paper.

## References

[1] Gorrell, S. E., Okiishi, T. H., and Copenhaver, W. W., 2003, "Stator-Rotor Interactions in a Transonic Compressor, Part 1: Effect of Blade-Row Spacing on Performance," ASME J. Turbomach., **125**, pp. 328–335.
[2] Gorrell, S. E., Okiishi, T. H., and Copenhaver, W. W., 2003, "Stator-Rotor Interactions in a Transonic Compressor, Part 2: Description of a Loss Producing Mechanism," ASME J. Turbomach., **125**, pp. 336–345.
[3] Cumpsty, N. A., 1989, *Compressor Aerodynamics*, Longman Scientific and Technical, New York.
[4] Wernet, M. P., 2000, "Development of Digital Particle Imaging Velocimetry for use in Turbomachinery," Exp. Fluids, **28**, pp. 97–115.
[5] Balzani, N., Scarano, F., Reithmuller, M. L., and Breugelmans, F. A. E., 2000, "Experimental Investigation of the Blade-to-Blade Flow in a Compressor Rotor by Digital Particle Image Velocimetry," ASME J. Turbomach., **122**, pp. 743–750.
[6] Sanders, A., and Fleeter, S., 2000, "Experimental Investigation of Rotor-Inlet Guide Vane Interactions in Transonic Axial-Flow Compressor," J. Propul. Power, **16**, pp. 421–430.
[7] Estevadeordal, J., Gogineni, S., Goss, L., Copenhaver, W., and Gorrell, S., 2001, "DPIV Study of Wake-Rotor Synchronization in a Transonic Compressor," AIAA Paper No. 01-3095.
[8] Estevadeordal, J., Gogineni, S., Goss, L., Copenhaver, W., and Gorrell, S., 2002, "Study of Wake-Blade Interactions in a Transonic Compressor Using Flow Visualization and DPIV," ASME J. Fluids Eng., **124**, pp. 166–175.
[9] Copenhaver, W., Estevadeordal, J., Gogineni, S., Gorrell, S., and Goss, L., 2002, "DPIV Study of Near-Stall Wake-Rotor Interactions in a Transonic Compressor," Exp. Fluids, **33**, pp. 899–908.
[10] Estevadeordal, J., Gorrell, S., and Copenhaver, W., 2004, "DPIV Study of Wake-Rotor Interactions in a Transonic Compressor Under Various Operating Conditions," 11th International Symposium on Flow Visualization, August, Notre Dame, IN.

[11] Ottavy, X., Trebinjac, I., and Voullarmet, A., 2001, "Analysis of the Interrow Flow Field Within a Transonic Axial Compressor: Part 1—Experimental Investigation," ASME J. Turbomach., **123**, pp. 49–56.
[12] Ottavy, X., Trebinjac, I., and Voullarmet, A., 2001, "Analysis of the Interrow Flow Field Within a Transonic Axial Compressor: Part 2—Unsteady Flow Analysis," ASME J. Turbomach., **123**, pp. 57–63.
[13] Zachcial, A., and Nurnberger, D., 2003, "A Numerical Study on the Influence of Vane-Blade Spacing on a Compressor Stage at Sub- and Transonic Operating Conditions," ASME Paper No. GT2003-38020.
[14] Carscallen, W. E., Fleige, H. U., and Gostelow, J. P., 1996, "Transonic Turbine Vane Wake Flows," ASME Paper No. 96-GT-419.
[15] Gorrell, S. E., Copenhaver, W. W., and Chriss, R. M., 2001, "Upstream Wake Influences on the Measured Performance of a Transonic Compressor Stage," J. Propul. Power, **17**, pp. 43–48.
[16] Chriss, R. M., Copenhaver, W. W., and Gorrell, S. E., 1999, "The Effects of Blade-Row Spacing on the Flow Capacity of a Transonic Rotor," ASME Paper No. 99-GT-209.
[17] Langford, M., Guillot, S., Ng, W., Breeze-Stringfellow, A., Solomon, W., and Estevadeordal, J., 2005, "Experimental Investigation of the Effects of a Moving Shock Wave on Compressor Stator Flow," ASME Paper No. GT2005-68722.
[18] Raffel, M., Willert, C. E., and Kompenhans, J., 1998, *Particle Image Velocimetry*, Springer, New York.
[19] Chen, J. P., and Briley, W. R., 2001, "A Parallel Flow Solver for Unsteady Multiple Blade Row Turbomachinery Simulations," ASME Paper No. 2001-GT-348.
[20] Chen, J. P., Celestina, M. L., and Adamczyk, J. J., 1998, "Comparison of Time-Accurate Calculations for the Unsteady Interaction in Turbomachinery Stage," AIAA Paper No. 98-3292.
[21] Chen, J. P., and Barter, J. W., 1994, "A New Procedure for Simulating Unsteady Flows Through Turbomachinery Blade Passages," ASME Paper No. 94-GT-151.
[22] Barter, J. W., Vitt, P. H., and Chen, J. P., 2000, "Interaction Effects in a Transonic Turbine Stage," ASME Paper No. 2000-GT-0376.
[23] Zhu, J., and Shih, T. H., 2000, "CMOTT Turbulence Module for NPARC," Contract Report NASA CR 204143, NASA Glenn Research Center, Lewis Field, OH.
[24] Beach, T., 2003, personal communication, AP Solutions.
[25] Turner, M. G., Gorrell, S. E., and Car, D., 2005, "Radial Migration of Shed Vortices in a Transonic Rotor Following a Wake Generator: A Comparison Between Time Accurate and Average Passage Approach," ASME Paper No. GT2005-68776.
[26] Adrian, R. J., Christensen, K. T., and Liu, Z.-C., 2000, "Analysis and Interpretation of Instantaneous Turbulent Velocity Fields," Exp. Fluids, **29**, pp. 275–290.
[27] Morfey, C. L., and Fisher, M. J., 1970, "Shock-Wave Radiation from a Supersonic Ducted Rotor," Aeronaut. J., **74**, pp. 579–585.

# Numerical Optimization of a Vaned Shroud Design for Increased Operability Margin in Modern Centrifugal Compressors

**M. T. Barton**
**M. L. Mansour**
**J. S. Liu**
**D. L. Palmer**

Honeywell Aerospace,
111 S. 34th Street,
Phoenix, AZ 85034

*This paper describes the computational fluid dynamics (CFD) approach coupled with an automated grid generation technique utilized for the numerical optimization of a modern centrifugal compressor with an inducer vaned shroud for increased operability margin. The grid generation process was automated to permit rapid optimization of the impeller and vaned shroud geometry. A three-dimensional, viscous, steady flow, mixing-plane approach was utilized to numerically analyze the impeller and vaned shroud in a coupled fashion to capture the interaction effects. The numerical technique verifies the ability of the vane shroud to extend compressor surge margin at the part-speed operating condition, while maintaining acceptable high-speed performance. CFD analyses confirm that the aerodynamics of the vaned shroud match expectation, and are consistent with the mass-averaged compressor speedline characteristics generated from the CFD results.*
[DOI: 10.1115/1.2187526]

## Introduction

Helicopter turboshaft engines must operate over a wide speed range from maximum rated power (MRP) down to a cruise power setting, but the compressor must be sized to deliver the required high-speed flow. When a centrifugal compressor with fixed geometry is operated at reduced speed and power conditions, the impeller blade leading edge operates at high incidence angles. This dramatically reduces compressor efficiency and surge margin at part-power conditions.

In 1994, Honeywell obtained a patent (U.S. 5,277,541) for a device designed to achieve the function of a variable flow capacity impeller. The purpose of this device, called a vaned shroud, is to enhance impeller performance, allowing the impeller to accommodate increased flow requirements at high speed, while achieving good efficiency and surge margin at the SFC-critical part-power operating condition.

Recent advances in CFD capabilities to analyze the vaned shroud and impeller now make the concept more attractive, since CFD can be used to optimize the design with less need for multiple, costly rig tests. For an innovative concept such as the vaned shroud, CFD analyses offers the most practical method of developing the concept into a test article.

Currently, Honeywell is developing a two-stage centrifugal compressor for the U.S. Army Small Heavy Fuel Engine (SHFE) program. This compressor incorporates a vaned shroud on the first stage compressor. The aero/mechanical design of the vaned shroud has been completed using the described numerical approach, and initial demonstration tests in a fully instrumented compressor rig are planned for the first quarter of 2005.

## Description of Impeller and Vaned Shroud

Figure 1 is a schematic of the centrifugal compressor with vaned shroud. The impeller is a state-of-the-art design, featuring splitter blades for good efficiency and flow capacity; high inducer loading for reduced clearance sensitivity, and large backsweep angle for good efficiency and operating range. The vaned shroud airfoils are attached to the stationary shroud in the leading edge (inducer) region, as shown in Fig. 2. Referring to Fig. 3, the vaned shroud system features an impeller with reduced inducer blade height (relative to the blade height that would be needed to deliver a certain flow rate without a vaned shroud), and a vaned passage around the outer circumference of the inducer. This vaned passage provides a secondary air inlet to the impeller. The vanes in the passage are tangentially slanted in the direction of impeller rotation, to preferentially augment airflow into the impeller at high speed, while at part-speed discouraging airflow out of the impeller through the secondary inlet.

The vaned shroud design is entirely passive, having no moving parts, control valves, etc. The potential benefits of the vaned shroud design relative to a conventional centrifugal compressor design are:

- Significant increase in part-speed surge margin
- Simple, passive device with no moving parts
- Can be easily retrofitted to existing designs
- Eliminates the need for surge bleed and/or variable geometry
- Enhanced design point efficiency, because the design point is less compromised for part speed range
- Lower recirculation losses as compared to a ported shroud.

## Selection of CFD Analysis Method

Improvements in computer processor speeds and CFD methods today allow for the routine use of steady flow, single and multiblade row, 3D viscous CFD codes [1], for the analysis and optimization of turbomachinery blade rows. This permits viscous and three-dimensional effects to be simulated realistically and provides more design options to optimize the blade row for best performance. The ability to analyze isolated blade rows has led to many innovations in compressor performance improvement, ranging from development of a swept fan rotor [2] to the development of controlled-diffusion stators [3]. Indeed, much of the progress

Contributed by the International Gas Turbine Institute (IGTI) of ASME for publication in the JOURNAL OF TURBOMACHINERY. Manuscript received October 1, 2003; final manuscript received March 1, 2004. IGTI Review Chair: A. J. Strazisar. Paper presented at the International Gas Turbine and Aeroengine Congress Exhibition, Vienna, Austria, June 13–17, 2004, Paper No. GT2004-54287.

  

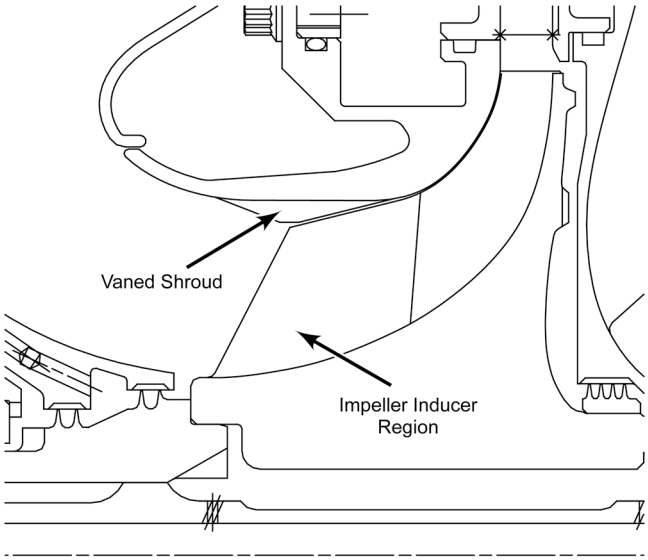


**Fig. 1 Centrifugal compressor application of vaned shroud**

made in compressor aerodynamics in the last two decades can be attributed to the application of CFD technology in the detailed blade design phase.

Design of turbomachinery components using single blade row CFD tools, however, has faced considerable challenges regarding closely coupled blade rows, where strong blade row interactions exist. Because unsteady flow, multi-blade-row CFD analyses are prohibitive and limited by the available computing resources, the use of steady flow, multi-blade-row (multistage) CFD techniques are currently filling the void and providing a better level of fidelity than single blade row models. Consequently, the use of steady flow multistage CFD simulation tools in the aerodynamic design of multistage turbomachines is considered to be another major breakthrough. In the steady flow aerodynamic modeling of multistage turbomachines, CFD developers have basically taken two different approaches. The simplest of the two is the mixing-plane approach, introduced in the Advanced Ducted Propfan Analysis Code (ADPAC) program in the early 1980s [4–8]. In this approach a mixing plane is specified half distance between the modeled blade rows. On this plane the momentum and energy fluxes are averaged tangentially to provide a spanwise profile of momentum, pressure, energy and through flow mass that is common to the two blade rows. As the CFD solution converges these profiles on the common plane converge to a spanwise distribution that reflects the upstream and the downstream influence of the two

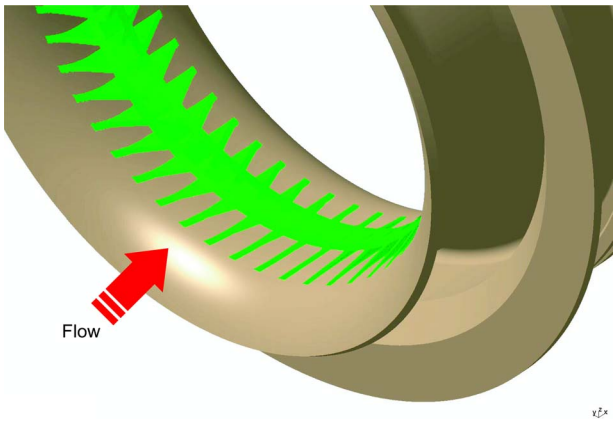


**Fig. 2 Isometric view of vaned shroud**

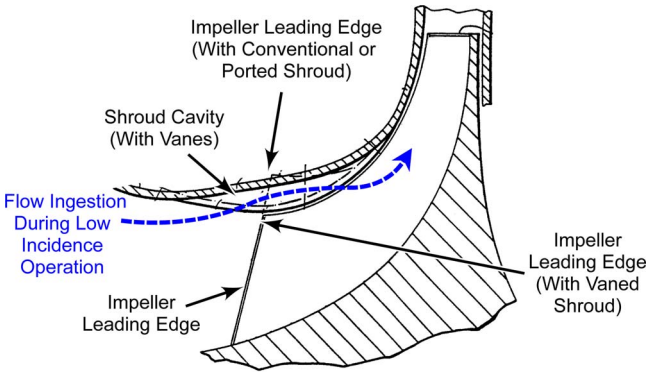


**Fig. 3 Patented vaned shroud improves surge margin with a clean, simple installation**

blade rows on each other, which influences the spanwise distribution and migration of the flow in the two adjacent blade rows based on how they interact together. The second approach which is a step higher in fidelity and more rigorous in its mathematical model was developed by Adamczyk in 1985, hereby referred to as the Average-Passage Flow Model [9–11]. As described in a more recent lecture [12], this approach allows the most significant features of blade row interaction due to unsteadiness to be captured by this steady and fully viscous flow model. The average-passage technique goes a step further than the mixing plane approach, accounting for the effects of wakes and propagation of potential flow field effects, in a global steady flow fashion using distribution of body forces or average-passage stresses.

Due to the lack of an average-passage steady flow multi-blade-row CFD tool that can simulate aerodynamic flow in centrifugal impellers with splitters (partial blades), the ADPAC mixing-plane approach was used as the multi-blade-row design and analysis tool for the present study.

## Grid Generation Program and Process

The objective of this design is the optimization of the vaned shroud and impeller geometry to achieve maximum stall margin and maximum operating performance, pressure ratio and efficiency. Grid generation of such geometry is very time consuming when performed manually. Manual attempts using the GRIDGEN and the FLUENT/GAMBIT programs resulted in three to four weeks to complete the grid generation task. Such a time-consuming grid generation approach can drastically handicap the aerodynamic designer and limit the ability to optimize the geometry for maximum performance within the available design schedule. To make this aerodynamic design optimization achievable, the GRIDGEN program was selected for grid generation due to its ability to run in an automated fashion. In addition to the GRIDGEN programs' flexibility in generating multi-block structured grids, it also features the option of using a pre-written script file (called a "GLYPH" file) that drives the grid generator in a push-button automated fashion. This approach allowed a total of 48 different design iterations of the vaned shroud and impeller combination to be completed in the span of six months, thus providing tremendous productivity savings during the detailed design phase. The multi-block structured grid that was generated for this multi-blade-row configuration is shown in Fig. 4. The grid is comprised of 15 blocks. Six of the grid blocks belong to the vane geometry and passage, while the remaining blocks belong to the impeller, with the mixing-plane located between the vane shroud and the impeller, as shown in Fig. 4. Figure 5 provides a more detailed view of the grid and the tip clearance modeling scheme. The impeller main and splitter blades are modeled with square edged tip sections with separate H-type grid blocks used to discretize the flow region between the blade tip and the stationary casing.

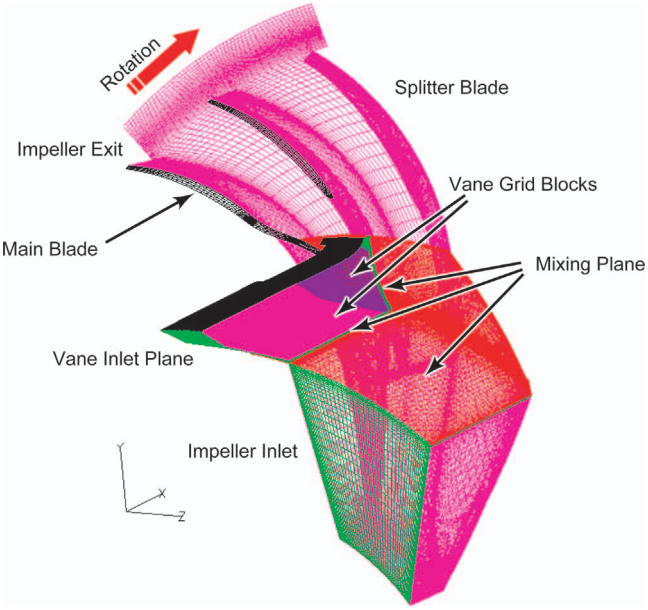


**Fig. 4 Computational fluid dynamics (CFD) model**

## Computational Fluid Dynamic Modeling and Simulation

ADPAC was used to perform the steady flow mixing-plane CFD analyses of the centrifugal impeller and vaned shroud combination. ADPAC is a finite volume, multi-grid code that uses time marching techniques for a time-dependent solution of the 3D Reynolds-averaged Navier-Stokes equations. ADPAC offers an explicit five stage Runge-Kutta time marching technique, with implicit residual smoothing applied after each time step. Convective fluxes of the discretized equations are handled using a second order centered scheme, stabilized with artificial scalar dissipation.

ADPAC employs a multi-block structured mesh discretization, which provides extreme flexibility for analyzing complex geometry. Turbulent flows are simulated using one of two turbulence closure models, the Baldwin-Lomax algebraic turbulence model [13] and the two-equation K-R turbulence model [14]. The Baldwin-Lomax model was used for the present study, for its robustness and computational efficiency.

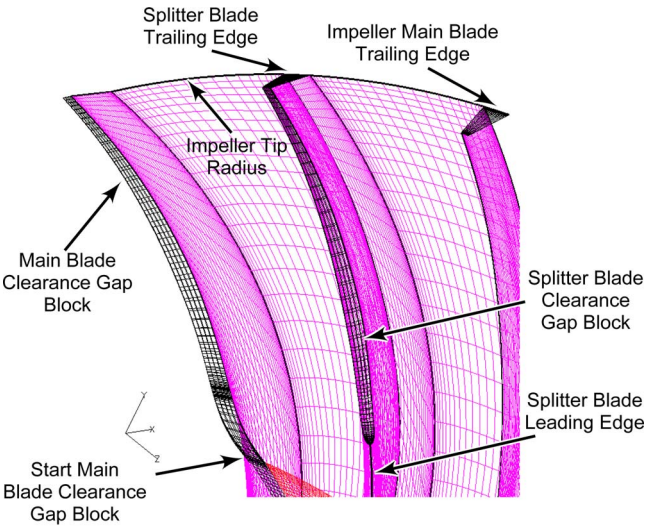


**Fig. 5 Grid detail showing clearance modeling technique**

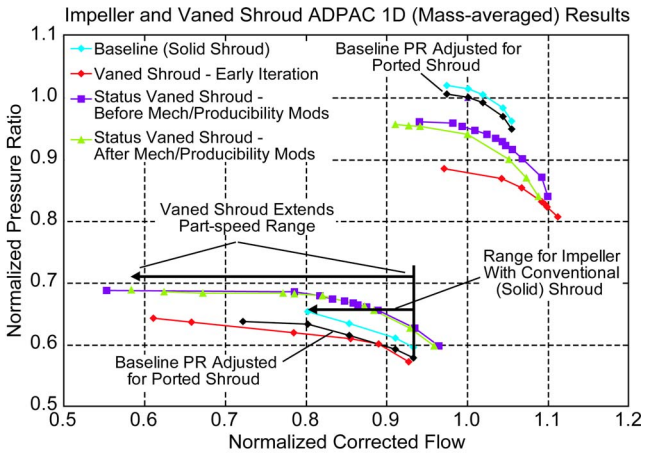


**Fig. 6 Pressure ratio versus flow map from ADPAC**

ADPAC also offers parallel processing capability, which uses the message passing interface (MPI) protocol to communicate information between different computational platforms [15]. Parallel processing and multi-blocking features make ADPAC a state-of-the-art CFD code with excellent computational speed.

The computational domains that were used in the 3D viscous steady flow mixing plane simulations are also shown in Fig. 4.

## Design Optimization Results and Discussion

A total of 48 design iterations of the impeller and vaned shroud combination were evaluated using the ADPAC program. For each design iteration, full speed-line characteristics were generated at 85% and 100% corrected speed. These characteristics were plotted by calculating impeller inlet and exit mass-averaged one dimensional (1D) flowfield parameters from the ADPAC analyses. The speed-line characteristics were used to evaluate performance (flow, pressure ratio, efficiency and surge margin), and to guide the iteration process. For each speed-line, the impeller and vaned shroud inlet total conditions were held constant while the impeller exit static pressure was successively increased to move the operating point up the speed-line from choke to stall. Stall side operating points are defined for the present study as the lowest-flow points at which a numerical solution could be obtained with inlet mass flow rate exhibiting a constant value versus iteration count. Numerical stall is considered to be reached when the calculated inlet mass flow rate continues to drop slowly with iteration count, without converging to a constant value.

Parameters that were varied during the vaned shroud optimization process included vane count, lean angle, thickness, thickness distribution, radial and meridional extent, and camber angle. Initial iterations focused on changes to the vaned shroud only, but later optimization efforts included modifications to the impeller geometry to further optimize performance. Impeller blade height at the vaned shroud trailing edge was also varied to optimize the inducer diffusion rate, and the impeller exit (exducer) blade angle was reduced slightly to recapture some pressure loss at 100% speed.

Figures 6 and 7 summarize the 1D performance predictions from ADPAC analyses of the baseline impeller (with a conventional solid shroud), for an early iteration of the vaned shroud impeller, and for the final design vaned shroud impeller. This final vaned shroud design was also modified to achieve acceptable mechanical vibratory margins, and to meet producibility requirements. The modifications included the addition of a full-circumference stiffening ring (see Fig. 2), an increase in the thickness of the vaned shroud airfoils, and the inclusion of fillets.

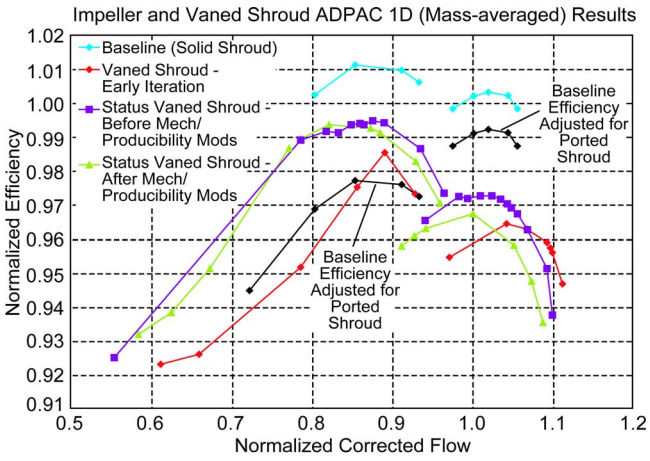


**Fig. 7 Efficiency versus flow map from ADPAC**

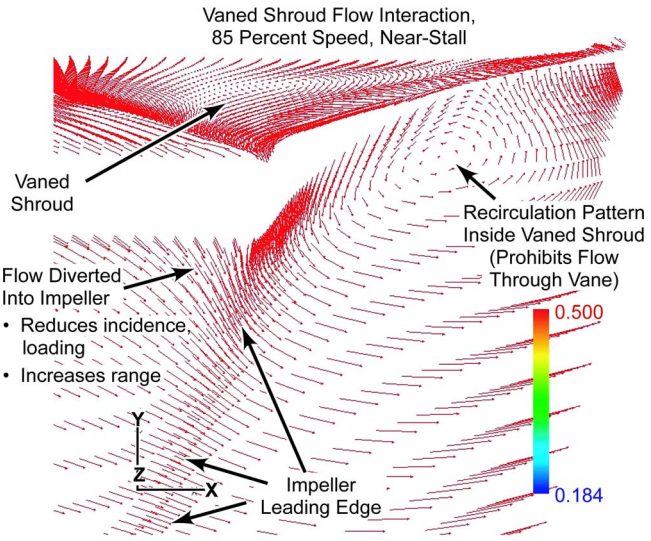


**Fig. 8 CFD analyses confirms internal flow physics of vaned shroud**

These modifications resulted in a small performance penalty at high speed, but had no adverse performance impact at the SFC-critical part-speed condition (see Figs. 6 and 7).

Figures 6 and 7 also show the performance for the baseline impeller modified for the effects of a ported shroud. (The ported shroud [16] is a passive inducer vent that allows communication of the inducer flow with the inlet duct. When operating at part-speed, some flow from the inducer exhausts through the vent, relieving inducer stall and providing improved part-speed surge margin. The ported shroud is currently in production on the T800 turboshaft engine, used in the Army's Commanche helicopter.) These corrections are based on back-to-back rig test data from a similar compressor, tested with a solid shroud, and then tested with a ported shroud. A ported shroud can deliver much of the surge margin increase of a vaned shroud, but this benefit is delivered at the expense of increased recirculation losses. For these reasons, the vaned shroud ADPAC results are most reasonably compared to baseline impeller characteristics that are corrected to reflect ported shroud losses.

Figure 6 shows the pressure ratio versus flow speed-line characteristics from ADPAC. Note the large increase in surge margin at 85% speed for the vaned shroud designs, compared to the baseline impeller. It is also important to note that the vaned shroud designs deliver the design-intent flow at 100% speed, ensuring that engine takeoff horsepower requirements will be met.

Of the 40-plus design iterations performed for this study, the part-speed surge margin predicted by CFD for the vaned shroud never varied by more than a few percent. This indicates that the design is relatively insensitive to hardware variations with respect to its prime function (part-speed range extension at low loss.) This robustness will be an important benefit for the vaned shroud in a regular production environment, where some part-to-part variation is unavoidable, and where the ability to specify less stringent tolerances will result in lower fabrication costs.

Figure 7 shows the efficiency versus flow speed-line characteristics from ADPAC. The final vaned shroud impeller design has almost a two point efficiency improvement over the ported shroud design at the SFC-critical part-speed operating condition, while delivering a very substantial increase in part-speed operating range. The decreased efficiency predicted for the vaned shroud at 100% speed is not considered to be problematic for the turboshaft engine application, where 100% speed represents a maximum power (takeoff) condition. (CFD studies have also revealed additional options to further improve the high-speed efficiency of the vaned shroud impeller. Over the course of this initial optimization, high-speed efficiency was increased by more than one point. Planned rig testing of the vaned shroud impeller will yield data that will provide additional insight into the performance and behavior of the design, and will further aid efforts in improving high-speed efficiency.)

Figures 6 and 7 show that there is a significant improvement in performance for the vaned shroud impeller between the earlier design iteration and the final design. This improvement shows the utility of the CFD analyses and optimization techniques developed for this study. In particular, the automated grid generation feature reduced the time needed to prepare each new iteration for analysis, allowing the design team to perform more iterations, vary more factors, and more thoroughly optimize the design.

Figure 8 shows the detailed flowfield conditions at the vaned shroud and impeller interface at a very high throttle condition (85% corrected speed, extreme stall side, flow ~65% of design flow), as calculated from the ADPAC CFD model. The flow vectors show that the mixing plane is very effective in capturing and communicating the reversed flow between the impeller inducer tip and the vanes. At this highly throttled stall-side operating point, the vane shroud is working as intended. An internal recirculation

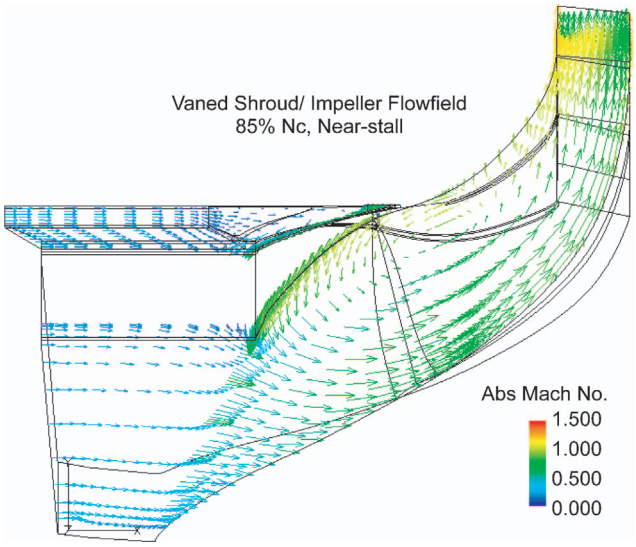


**Fig. 9 Vaned shroud/impeller flowfield from ADPAC CFD analyses at 85% Nc near-stall showing flow diverted toward impeller hub**

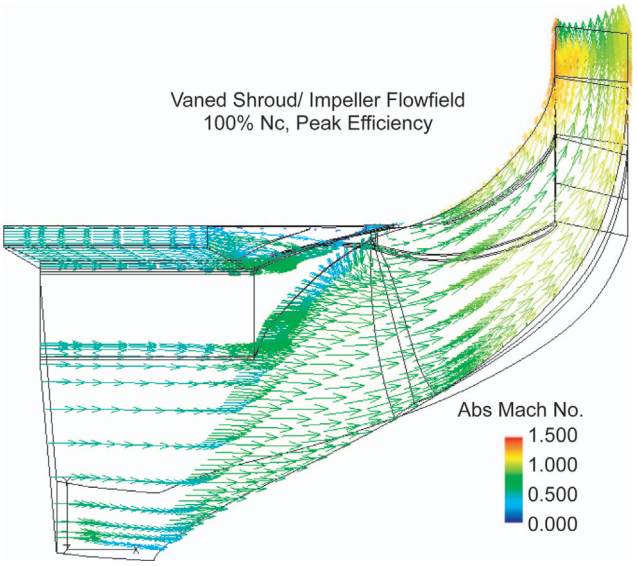


**Fig. 10 Vaned shroud/impeller flowfield from ADPAC CFD analyses at 100% Nc peak efficiency showing flow admitted through the vanes**

cell inhibits flow through the vane, redirecting flow toward the hub, and thus improving incidence and unloading the impeller inducer. This is the mechanism for the substantial range extension offered by the vaned shroud.

Figure 9 is a larger scale view of the impeller/vaned shroud flowfield at the 85% corrected speed, near-stall throttle condition. Figure 10 is a similar view at 100% corrected speed, peak efficiency. At the high speed, low incidence operating condition shown in Fig. 10, the vane shroud is working as intended, by admitting flow through the vanes. This mechanism is critical to attaining design-intent flow capacity (and therefore horsepower or thrust) at the high speed (takeoff) operating condition.

These CFD flow visualization results confirm the internal physics of the vaned shroud, providing the microscopic insight into the function of the device. These microscopic results are also consistent with the macroscopic behavior of the impeller.

## Conclusions

The three-dimensional (3D) viscous steady flow mixing-plane approach was utilized to model an impeller and vaned shroud combination and capture the interaction effects. The success of this innovative design demonstrates the utility of the CFD analysis and optimization techniques developed for this study. In particular, the automated grid generation feature reduced the time required to prepare each new iteration for analysis, allowing the design team to perform more iterations, vary more factors, and more thoroughly optimize the design. For new and innovative concepts such as the vaned shroud, CFD analyses provides the most practical method for developing the concept in an efficient, timely and cost effective manner.

The numerical technique verifies the ability of the vane shroud to extend centrifugal compressor surge margin at the part-speed operating condition, while maintaining acceptable high-speed performance. CFD analyses confirm that the aerodynamics of the vaned shroud and impeller combination match expectation, and are consistent with the mass-averaged compressor speed-line characteristics generated from the CFD results.

## Acknowledgment

The authors wish to thank D. Durschmidt, J. Gunaraj, T. Marshall, M. Matwey, N. Nolcheff, and J. Slovisky of Honeywell Aerospace for their assistance in this design effort. The authors also thank the management of Honeywell Aerospace, and Kevin Kerner of the United States Army AATD for supporting this study and for permitting the publication of this paper.

## Nomenclature

ADPAC = advanced ducted propfan analysis code
CFD = computational fluid dynamics
DAWES = three-dimensional, viscous, steady flow computational fluid dynamics code
FLUENT = CFD code marketed by FLUENT, Inc.
GAMBIT = grid generator program for FLUENT
GLYPH = file containing commands in scripting language that drive a GRIDGEN session
GRIDGEN = general purpose grid generation program marketed by Pointwise, Inc.
MRP = maximum rated power
SFC = specific fuel consumption
SHFE = small heavy fuel engine (a U.S. Army turboshaft engine demonstrator program)
1D = one dimensional
3D = three dimensional

## References

[1] Dawes, W., 1988, "Development of a 3D Navier-Stokes Solver for All Types of Turbomachinery," ASME Paper 88-GT-70.
[2] Wadia, A., 1997, "Inner Workings of Aerodynamic Sweep," ASME Paper 97-GT-401.
[3] Hobbs, D. E., and Weingold, H. D., 1984, "Development of Controlled Diffusion Airfoils for Multistage Stage Compressor Applications," ASME J. Eng. Gas Turbines Power, **106**, pp. 271–278.
[4] Hall, E. J., and Delaney, R. A., 1990, "Investigation of Advanced Counterrotation Blade Configuration Concepts for High Speed Turboprop Systems: Task I-Ducted Propfan Analysis," NASA Contract Rep. NASA CR, **185217**, NAS3-25270.
[5] Hall, E. J., and Delaney, R. A., 1992, "Investigation of Advanced Counterrotation Blade Configuration Concepts for High Speed Turboprop Systems: Task II-Unsteady Ducted Propfan Analysis-Final Report," NASA Contract Rep. NASA CR **187106**, NAS3-25270.
[6] Hall, E. J., and Delaney, R. A., 1992, "Investigation of Advanced Counterrotation Blade Configuration Concepts for High Speed Turboprop Systems: Task V-Counterrotation Ducted Propfan Analysis-Final Report," NASA Contract Rep. NASA CR **187126**, NAS3-25270.
[7] Hall, E. J., and Delaney, R. A., 1994, "Investigation of Advanced Counterrotation Blade Configuration Concepts for High Speed Turboprop Systems: Task VIII-Cooling Flow/Heat Transfer Analysis, Final Report" NASA Contract Rep. NASA CR, **195359**, NAS3-25270.
[8] Hall, E. J., and Delaney, R. A., 1995, "Investigation of Advanced Counterrotation Blade Configuration Concepts for High Speed Turboprop Systems: Task VII-Endwall Treatment Inlet Flow Distortion Analysis Final Report" NASA Contract Rep. NASA CR, **195468**, NAS3-25270. Hall, E. J., and Delaney, R. A., 1995, "Investigation of Advanced Counter-rotation Blade Configuration Concepts for High Speed Turboprop Systems: Task VII-ADPAC User's Manual," NASA Contract Rep. NASA CR, **195472**, NAS3-25270.
[9] Adamczyk, J. J., 1985, "Model Equation for Simulating Flows in Multistage Turbomachinery," ASME Paper 85-GT-226.
[10] Adamczyk, J. J., Mulac, R. A., and Celestina, M. L. 1986, "A Model for Closing the Inviscid Form of the Average-Passage Equation System," ASME Paper 86-GT-227.
[11] Adamczyk, J. J., Celestina, M. L., Beach, T. A., and Barbet, M., 1990, "Simulation of Three Dimensional Viscous Flows Within a Multistage Turbine," J. Turbomach., **112**(3), pp. 370–376.
[12] Adamczyk, J. J., 1999, "Aerodynamic Analysis of Multistage Turbomachinery Flows in Support of Aerodynamic Design," 1999 Freeman Scholar Lecture.
[13] Baldwin, B. S., and Lomax, H. M., 1978, "Thin Layer Approximation and Algebraic Model for Separated Turbulent Flows," AIAA Pap. 78-257.
[14] Goldberg, U. C., 1994, "Towards a Pointwise Turbulence Model for Wall-Bounded and Free Shear Flows," Boundary Layer and Free Shear Flows, ASME FED - **184**, pp. 113–118.
[15] "MPI: A Message-Passing Interface Standard," Message Passing Interface Forum, May 5, 1994, University of Tennessee, Knoxville, Report No. CS-94-230.
[16] Palmer, D. L., and Waterman, W. F., 1994, "Design and Development of a Two-Stage Centrifugal Compressor," ASME Paper 94-GT-202.

# The Influence of Variable Gas Properties on Turbomachinery Computational Fluid Dynamics

**John D. Northall**
Rolls-Royce plc,
P.O. Box 3,
Moor Lane,
Derby DE24 8BJ, UK
e-mail: john.northall@rolls-royce.com

*This paper describes the inclusion of variable gas properties within a Reynolds average Navier-Stokes solver for turbomachinery and its application to multistage turbines. Most current turbomachinery computational fluid dynamics (CFD) models the gas as perfect with constant specific heats. However, the specific heat at constant pressure $C_P$ can vary significantly. This is most marked in the turbine where large variations of temperature are combined with variations in the fuel air ratio. In the current model $C_P$ is computed as a function of the local temperature and fuel air ratio using polynomial curve fits to represent the real gas behavior. The importance of variable gas properties is assessed by analyzing a multistage turbine typical of the core stages of a modern aeroengine. This calculation includes large temperature variations due to radial profiles at inlet, the addition of cooling air, and work extraction through the machine. The calculation also includes local variations in fuel air ratio resulting from the inlet profile and the dilution of the mixture by the addition of coolant air. A range of gas models is evaluated. The addition of variable gas properties is shown to have no significant effect on the convergence of the algorithm, and the extra computational costs are modest. The models are compared with emphasis on the parameters of importance in turbine design, such as capacity, work, and efficiency. Overall the effect on turbine performance prediction of including variable gas properties in three-dimensional CFD is found to be small.* [DOI: 10.1115/1.2221324]

## Introduction

Reynolds averaged Navier-Stokes (RANS) computational fluid dynamics (CFD) programs are now a well established part of the turbomachinery design process. Such programs were first used to analyze three-dimensional (3D) flow phenomena such as secondary flow in individual blade rows using inlet and exit boundary conditions taken from through-flow analyses. In the 1980s the 3D steady solution of individual blade rows was coupled together to form multistage calculations [1] using mixing planes between the blade rows. This overcomes the dependency of the single row solution on assumptions for the inlet and exit boundary conditions and enables designers to assess issues such as stage matching. In recent years the advent of optimization wrap around systems [2] has moved 3D CFD earlier into the design process.

It is a common practice within 3D CFD programs to model the working fluid as a perfect gas. Here this is taken to mean [3] that the gas law is

$$p = R\rho T \tag{1}$$

and the internal energy per unit mass is a function only of temperature

$$de = C_V(T)dT \tag{2}$$

(Some other authors refer to a gas with such properties as an ideal gas.) It follows that the enthalpy is related to the temperature via the specific heat at constant pressure $C_P$, also a function of temperature only, where

$$dh = C_P dT \quad \text{and} \quad R = C_P - C_V \tag{3}$$

In most turbomachinery 3D CFD programs $R$, $C_V$, and $C_P$ are taken as constants. However, while constant $R$ is a good approximation for air and standard kerosene, $C_P$ varies with both temperature and gas composition [4]. Figure 1 indicates the behavior of $C_P$ for a mixture air and kerosene over a range relevant for turbomachinery. Note that the effect of higher temperature and greater concentration of fuel combustion products both act to increase $C_P$, thus in a combustion chamber, exit flow temperature and fuel air ratio (FAR) profiles act together to enhance the variation of $C_P$.

The use of constant gas properties is unlikely to introduce a significant error in a single blade row, but when computing the flow in a multistage machine the variations in gas properties can become significant. This applies to both compressors and turbines; but the turbine is expected to be affected more because of the presence of fuel products and the large temperature differences between the mainstream gas and the cooling air. As an example, consider the flow through the high pressure (HP) and intermediate pressure (IP) turbines of a modern jet engine. A typical radially averaged static temperature falls from 1880 K at HP inlet to 1200 K at IP exit, while the fuel air ratio (FAR) falls from 0.0281 to 0.0244 (due to the dilution of the mainstream gas with cooling air). As can be seen from Fig. 1 this gives a variation in $C_P$ from 1310 J/Kg/K to 1225 J/kg/K, or about 7%. A key turbine parameter is the capacity. The choking mass flow is given by [5]

$$\dot{m} = \frac{AP_0}{\sqrt{C_P T_0}} \frac{\gamma}{\sqrt{\gamma - 1}} \left( \frac{\gamma + 1}{2} \right)^{-(\gamma+1)/2(\gamma-1)} \tag{4}$$

In this example the variation in $C_P$ is equivalent to a variation in $\gamma$ from 1.281 to 1.306 giving an equivalent increase of 0.7% in the mass flow. This difference is significant in the design process so that choosing an appropriate constant $C_P$ is important. However, using the appropriate value for one blade row will introduce an error if used in the next blade row. Such effects will increase as

Contributed by the International Gas Turbine Institute (IGTI) of ASME for publication in the JOURNAL OF TURBOMACHINERY. Manuscript received October 1, 2004; final manuscript received February 1, 2005. IGTI Review Chair: K. C. Hall. Paper presented at the ASME Turbo Expo 2005: Land, Sea and Air, Reno, NV, June 6–9, 2005, Paper No. GT2005-68478.

  

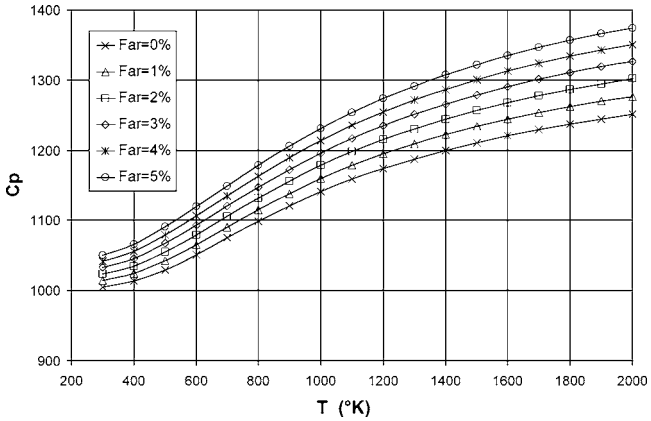


**Fig. 1 Variation of $C_P$ with temperature and fuel air ratio**

more stages are included. For these reasons many through-flow programs do model the variation of gas properties. Furthermore, in reality there are strong radial variations in the temperature and fuel concentration exiting the combustion chamber, and local nonuniformities are exacerbated by the introduction of cooling air adjacent to the blade surfaces and annulus walls.

The necessity of including real gas effects into turbomachinery CFD has been recognized for many years in the case of steam turbines where an account has to be taken of phase changes. Similar considerations apply to compressors acting on refrigerant gases. The inclusion of real gas properties into a RANS code using interpolation from gas tables for both these applications was reported in [6]. Recently Yao and Amos [7] considered the effect of temperature and fuel air ratio in multistage turbines using polynomial curve fits to the gas data. The present work takes a similar approach; but goes further by including cooling air, allowing the fuel fraction to be transported through the machine and considering alternative models.

The objective of the work reported here was to add variable gas properties to a 3D multistage code, motivated by its application to the calculation of multistage aerodynamics, particularly of turbines. A range of modifications to the constant $C_P$ code are considered and their effects compared by evaluating their impact on engineering parameters.

## The CFD Solver

The 3D Navier-Stokes solver used in this study is the Moore elliptic flow program (MEFP) [8,9]. MEFP is a structured grid solver which uses an iterative scheme similar to Patankar's SIMPLER scheme [10]. The unique feature of MEFP is the use of upwinded control volumes to simultaneously achieve stability and accuracy. This is a well-established method for the analysis [11,12] and design [2] of turbomachinery flows. The version used here forms one of the solvers available in a much larger computational fluid dynamics system. This offers a range of modeling features including a film cooling model [13] (based on the stripping model of Crawford et al. [14]), a mixing plane model, and the capacity to model annulus wall cooling flows and shroud leakage. It is these features that make the program suitable for the present study. The turbulence model used in the examples below is the Moores' mixing length model [12], and all the cases here were run fully turbulent.

## The Gas Models Studied

Four models of the gas properties through a multistage turbomachine are considered here.

(1) Constant $C_P$ throughout all blade rows.
(2) Constant $C_P$ that differs from blade row to blade row.
(3) $C_P$ is a function of local temperature and FAR, where FAR is a prescribed function with a 1D variation in the through-flow direction.
(4) $C_P$ is a function of local temperature and FAR, where FAR is computed by the convection of fuel through the machine.

The models are ordered in increasing physical fidelity but at increasing computational cost. Model 1 is the previously existing capability, and model 4 is the closest to the real physics.

**Model 2: Constant $C_P$ Differing From Blade Row to Blade Row.** Model 2 is a computationally cheap generalization of the base constant $C_P$ model, which has the further attraction of being quick to implement in a 3D CFD program. When using this model the calculations within each blade row proceed as for model 1, except when considering interactions between blade rows. During mixing plane multistage calculations the mixing plane needs attention, whereas during output processing the calculation of stage efficiency also needs to take account of different $C_P$ values within the stage.

The mixing plane model computes the flux of absolute total enthalpy in one blade row which it passes to the adjacent row to compute new boundary conditions, thereby ensuring that absolute total enthalpy is conserved. In model 2 the enthalpy is computed using the simple relationship $h=C_PT$ within each blade row. It is argued that the gas temperature $T$ should not change as a result of the change in $C_P$. It is, therefore, necessary to compensate for the change of $C_P$ when transferring the total enthalpy flux. This results in a shift in level of $H$ given by

$$H_{\text{shift}} = (C_P|_2 - C_P|_1)T|_1 \tag{5}$$

where conditions in the averaged blade row are denoted by the subscript 1 and conditions in the blade row to be updated are denoted by subscript 2. The enthalpy flux passed to blade row 2 is then given by

$$H|_2 = H|_1 + H_{\text{shift}} \tag{6}$$

When calculating the turbine stage efficiency we have to compare conditions at inlet to the vane and exit from the rotor, where $C_P$ may differ from the vane to the rotor. The efficiency definition becomes

$$\eta_{\text{stage}} = \frac{(\text{work})}{(\text{ideal\_work})} = \frac{\tilde{H}_{\text{in}} - H_{\text{shift}} - \tilde{H}_{\text{ex}}}{\tilde{H}_{\text{in}} - H_{\text{shift}} - H_{\text{ex,ideal}}} \tag{7}$$

based on vane inlet and rotor exit conditions. Here the ideal exit total enthalpy is the mass average of the ideal total enthalpies obtained by expanding each inflow gas stream $k$ to the mass average total pressure over the mainstream exit. Thus

$$H_{\text{ex,ideal}} = \frac{1}{\dot{m}_{\text{ex}}} \sum_k \{\dot{m}_k H_{k,\text{ideal}}\} \tag{8}$$

the summation being over all the inflows to the stage, including film cooling and annulus wall leakage flows. For inflows into the vane domain the ideal exit total enthalpy is computed by a two step process to account for the jump across the mixing plane. Consider the mainstream inflow (other inflows to the vane are treated in the same way), this will have an ideal total enthalpy at the vane exit given by

$$H_{v,\text{ex,ideal}} = \tilde{H}_{\text{in}} \left( \frac{\tilde{P}_{v,\text{ex}}}{\tilde{P}_{\text{in}}} \right)^{(\gamma_v - 1)/\gamma_v} \tag{9}$$

This is taken across the mixing plane as

$$H_{r,\text{in,ideal}} = H_{v,\text{ex,ideal}} + H_{\text{shift}}$$

then expanded to the stage exit using the rotor values of $C_P$ and $\gamma$, i.e.,

$$H_{\text{ex,ideal}} = H_{r,\text{in,ideal}} \left( \frac{\tilde{P}_{\text{ex}}}{\tilde{P}_{r,\text{in}}} \right)^{(\gamma_r - 1)/\gamma_r} \tag{10}$$

Substituting for $H_{r,\text{in,ideal}}$ and assuming, for an ideal process, that $\tilde{P}_{r,\text{in}} = \tilde{P}_{v,\text{ex}}$ gives

$$H_{\text{ex,ideal}} = \left[ H_{\text{in}} \left( \frac{\tilde{P}_{v,\text{ex}}}{\tilde{P}_{\text{in}}} \right)^{(\gamma_v - 1)/\gamma_v} + H_{\text{shift}} \right] \left( \frac{\tilde{P}_{\text{ex}}}{\tilde{P}_{v,\text{ex}}} \right)^{(\gamma_r - 1)/\gamma_r} \tag{11}$$

For inlets in the rotor domain no such correction is required.

**Model 3: $C_P(T,\text{FAR})$ With FAR Prescribed.** The relationship between temperature and enthalpy is modeled as polynomial curve fits to data for a stoichiometric mixture of standard dry air with standard kerosene [15]. That is $h = h(T,\text{FAR})$, thus $C_P$ also becomes a function of $T$ and FAR. The consequence of this is that it is no longer valid to relate enthalpy to temperature using $h = C_P T$ as a simple integral of $dh = C_P dT$, instead the full formula

$$h = h_{\text{ref}} + \int_{T_{\text{ref}}}^{T} C_P(T,\text{FAR}) dT$$

must be used. A similar complication arises in integrating the entropy $s$ defined by

$$Tds = dh - \frac{dp}{\rho} \quad \text{or} \quad ds = \frac{C_P dT}{T} - \frac{R dp}{p}$$

leading to

$$s_2 - s_1 = \int_{T_1}^{T_2} \frac{C_P(T,\text{FAR}) dT}{T} - R \ln(p_2/p_1).$$

For example, given the velocity, static pressure, and temperature at a point the calculation of total pressure is done as follows. Find the enthalpy $h$ from the static temperature and fuel air ratio using the curve fit. Compute the total enthalpy using $H = h + 1/2u^2$, whence the total temperature by iteratively inverting the curve fit. Then the isentropic change from static to total conditions requires an integration, as in the above relation for entropy, giving

$$\ln(P_0/p) = \frac{1}{R} \int_{T}^{T_0} \frac{C_P(T,\text{FAR}) dT}{T}$$

whence

$$P_0 = p \cdot \exp\left\{ \frac{1}{R} \int_{T}^{T_0} \frac{C_P(T,\text{FAR}) dT}{T} \right\}.$$

In practice a subroutine library [15] is employed to perform the common thermodynamic calculations based on the curve fits.

The continuity and momentum equations are unchanged by the addition of variable gas properties while the energy equation requires only minor adjustment. In the MEFP algorithm the energy equation is solved for the stagnation temperature (rotary in a rotating blade row), to accommodate variable gas properties this is changed to total enthalpy (or rothalpy). For simplicity, constant values of laminar and turbulent Prandtl number have been retained so that the thermal conductivity will vary with temperature and fuel ratio in the same way as $C_P$. This could easily be generalized if appropriate, for example, if the objective is to calculate heat transfer.

It follows that the bulk of the effort in converting a CFD program to handle variable gas properties is in modifying the thermodynamic calculations.

**Model 4: $C_P(T,\text{FAR})$ With Fuel Convection.** This requires an extra transport equation to be solved for the fuel fraction

$$\nabla \cdot (\rho F \underline{u}) - \nabla \cdot (\mu_F \nabla F) = 0 \tag{12}$$

For simplicity it is assumed that the diffusion can be approximated by taking $\mu_F$ to be the sum of the laminar and turbulent viscosities as used for momentum. This is solved every outer iteration and used to update the fuel air ratio and hence the gas properties for the next iteration.

The inclusion of the fuel fraction equation interacts with three of the other modeling features used in the examples below.

(1) The fuel air ratio must be added to the parameters whose radial profiles are passed across the mixing plane. Note that there is a natural averaging appropriate to fuel air ratio which sums the fuel and air mass flows through each circumferential element, then the average fuel air ratio is computed as the ratio of the mass flow sums.
(2) The shroud leakage model also calculates the average FAR where the flow is extracted from the mainstream and uses this to update the fuel fraction on the corresponding inflow boundary. Again this is based on the total mass of fuel extracted so that if the reinjected mass flow is greater than that extracted (to model the addition of coolant in the leakage path) then the total mass of fuel is conserved.
(3) The terms added to the fuel fraction equation by the stripping model of film cooling are assumed to correspond to pure air.

Fuel fraction is specified on all inlets, in particular there will be a strong radial profile at the mainstream inlet when combustion chamber exit conditions are used. The combustion chamber CFD commonly relates fuel fraction directly to total enthalpy as

$$H(r) = [1 - F(r)]H_4 + F(r)(LCV + H_f) \tag{13}$$

where $H_4$ is the constant combustion chamber inlet total enthalpy and $H_f$ is the total enthalpy of the fuel before it is burnt. In the calculations below this relationship has been used to obtain an inlet profile of fuel fraction based on the inlet total temperature profile and by assuming that $H_f$ is negligibly small.

## Results

A version of the variable gas properties subroutine library which replicates the constant gas properties thermodynamics was used to provide initial code verification. Three turbomachinery examples of increasing complexity were then run.

**Single Blade Row.** An HP NGV (nozzle guide vane) from a turbine rig was used as a single blade row test. This means that the fuel air ratio is zero and the total temperature is constant at inlet, so that the effect of variable gas properties is expected to be very small. Nevertheless it provides a good check on the coding, and gives an accurate value for the run time penalty for using variable gas properties (without the complication of any significant change in the flow field and consequent changes in the convergence path). The NGV was run for 200 iterations on an $85 \times 37 \times 36$ grid (axial, circumferential, radial) (113,220 nodes). Convergence plots for the variable gas properties case (model 3, model 4 is the same since FAR is everywhere zero) were virtually indistinguishable from the constant $C_P$ case. The constant $C_P$ case ran in 62 min (on a single 2.8 GHz Linux PC) while the variable gas properties run took 65 min, or less than 5% longer.

The constant $C_P$ value used was appropriate to the inlet. The two solutions are very close in terms of exit profiles and loss. For example, Fig. 2 shows the spanwise variation of mass average total pressure loss coefficient, defined by

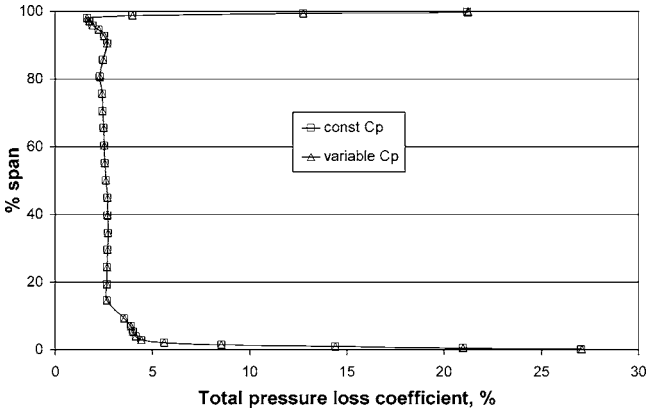


**Fig. 2 Mass average exit total pressure loss coefficient versus span**

$$\{P_0\_\text{loss}\_\text{coefft}\} \equiv \frac{(P_{0,\text{in}} - \tilde{P}_{0,\text{ex}})}{P_{0,\text{in}}}$$

But there is a slight difference in the total mass flow, the variable gas properties case passes 0.1% more mass flow than the constant $C_P$ solution. This difference is in line with that expected from Eq. (4) resulting from the reduction in $C_P$ at the throat.

**Single Stage HP Turbine.** The single stage HP turbine analyzed here is an amalgamation of rig and engine features. The geometry has a long exit duct finishing in a parallel section and there is no coolant air, typical of a rig. However, the inlet conditions have a strong radial temperature profile typical of the conditions at exit from the combustion chamber in an engine. This enables the importance of including variable gas properties for cases with a strong temperature profile to be assessed separately from the effects of cooling air. The rotor is shrouded but the shroud leakage is not modeled in this calculation.

The calculation grid sizes for the results presented here were $165 \times 59 \times 64$ and $205 \times 49 \times 67$ for the vane and rotor, respectively, or 1.3 million nodes in all. Calculations on coarser grids of around 100,000 nodes per row were considered inadequate after the following consistency check. The work done on the rotor can be calculated either by comparing the total enthalpy at the inlet and exit from the blade row, or by integrating the forces on the rotating surfaces to obtain the torque. Comparing the results of these two work sums is a good test of numerical accuracy because it tests the accuracy to which mass, momentum and energy are solved. The coarser grid led to differences in the work equivalent to 1% in efficiency. The finer grid reduced these errors by a full order of magnitude to 0.1%, showing that they are truncation errors. As will be seen below the differences between the gas models are sufficiently small for this level of accuracy to be necessary.

At inlet the total pressure, total temperature, and flow angles are prescribed. The total pressure and angles are constant radially; but the total temperature has a variation of 850 K from midpassage peak to a low at the wall. At exit the static pressure is specified on the casing and simple radial equilibrium used to give the radial variation (a valid assumption since the exit is in a parallel duct). A low exit pressure condition was chosen so that the turbine is operating close to choking. All four of the gas models described above were run on this example. The single constant value of $C_P$ was chosen as an estimate of the value at the vane throat position, since this will give the best estimate of the mass flow. Similarly, when a different constant $C_P$ was used for the rotor, an estimate of the rotor throat value was used. In model 3 the specified FAR is constant everywhere, since no coolant is present. In model 4 an inlet radial profile of FAR is derived from the temperature profile using Eq. (13).

The calculations were run on a cluster of Linux PCs with the simple parallel processing strategy of running each blade row on a separate processor. Mixing plane fluxes are then communicated between the blade rows using a parallel virtual machine (pvm) [16], to couple the blade rows into a stage calculation. All calculations were run for the same number of iterations.

The gas models are compared in terms of turbine performance parameters in Table 1. In the table the turbine inlet capacity is defined as

$$\{\text{Inlet}\_\text{capacity}\} = \dot{m}\sqrt{\tilde{T}_0}/\tilde{P}_0 \tag{14}$$

evaluated at stage inlet using mass averages. The work is computed from the power as

$$\{\text{Specific}\_\text{work}\} \equiv \text{Power}/(\dot{m}\tilde{T}_0)|_{\text{in}} \tag{15}$$

The efficiency is also based on power

$$\eta_{\text{stage}} = \frac{(\text{Power})}{[\dot{m}_{\text{in}}(\tilde{H}_{0,\text{in}} - \tilde{H}_{0,\text{ex,ideal}})]} \tag{16}$$

Clearly the changes are small. The negligible change in capacity is a direct consequence of selecting the constant $C_P$ for the vane to be the throat value. As an indication of the numerical errors the maximum to minimum fractional mass flow difference across the axial grid surfaces through the turbine is at most 0.0002. Therefore the capacity differences between models 1, 2, and 3 are not numerically significant; but model 4 is slightly different. There is a consistent trend for the work and efficiency to reduce as the gas model becomes more physically realistic. The biggest change results from introducing convection of the fuel fraction (models 3 to 4) which reduces the efficiency by 0.15% out of a total change of only 0.26% from having $C_P$ constant everywhere. Looking at the radial profile of $C_P$ at the inlet in Fig. 3 it is apparent that including the radial variation of FAR (model 4) does significantly increase the variation over that due to the temperature profile alone (model 3).

In terms of exit conditions from the stage, there is again little variation between the solutions. Figure 4 shows the radial profile of the whirl angle about half an axial chord downstream of the rotor trailing edge, the solutions are virtually indistinguishable. Note that there is considerable secondary flow in the rotor due to the strong inlet radial temperature profile.

The extra run time for the more sophisticated models of the gas is less than 5% for all models, even in the model where an extra transport equation is being solved. A surprise here is the noticeable increase in time to run model 2, which involves minimal changes to model 1. Each calculation will take a slightly different convergence path, it appears that the path for model 2 happens to

**Table 1 Single stage turbine performance versus gas model**

| Gas model | 1 | 2 | 3 | 4 |
|---|---|---|---|---|
| (Turbine inlet capacity)/(model 4 capacity) | 0.9993 | 0.9994 | 0.9993 | 1 |
| (Specific work)/(model 4 specific work) | 1.0019 | 1.0018 | 1.0015 | 1 |
| (Stage efficiency (%)) - (model 4 efficiency) | 0.26 | 0.22 | 0.15 | 0 |
| Percent increase in run time versus model 1 | | +2.75% | +1.6% | +4.9% |

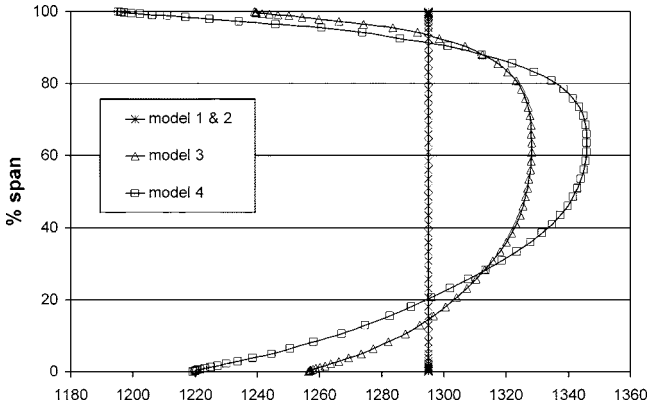


**Fig. 3 Inlet $C_P$ versus span**

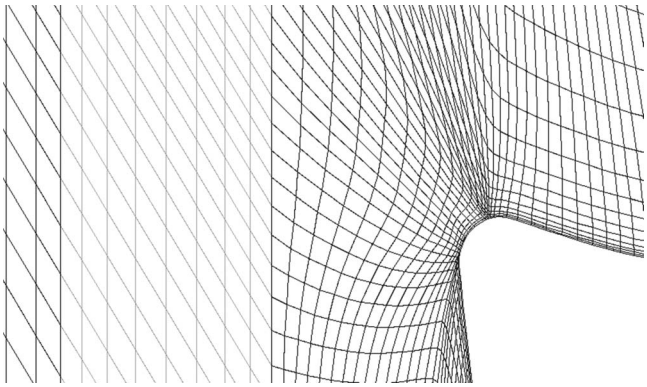

**Fig. 6 IP rotor leading edge on outer annulus wall**

trigger more iterations of some inner loops. As such this 2.75% is representative of the sort of scatter in run time due to any minor change, for example in boundary conditions.

**HP/IP Turbine With Cooling Air.** The final test case is a single stage HP turbine plus a single stage IP turbine run at engine conditions. This includes all film cooling and leakage flows as well as the combustion chamber radial temperature profile at inlet. An overview of the turbine is shown as Fig. 5. Film cooling is introduced through the blade surfaces of the HP vane and blade using the stripping model [13]. A series of strips of cells on the annulus walls are tagged as secondary inlets to model coolant injection through the endwalls. On these inlets meridional flow angle, swirl velocity, total temperature, and mass flow are specified with the mass flow achieved by the iterative scheme adjusting a spatially constant inlet total pressure. Further inlets are used to model cooling air exhausting into the mainstream through slots in the trailing edges of the HP and IP vanes. For both rotors the shroud leakage is modeled by coupling an inlet on the annulus wall downstream of the rotor to an exit ahead of it. On this exit a constant level of static pressure is iteratively adjusted to achieve a specified mass flow. Inflow is permitted to occur locally on this exit with inlet conditions derived from the mass average of the out flowing fluid, i.e., based on a plenum model. Approximately 25% of the mainstream inlet mass flow is added as cooling air in total, of which about 15% is added in the HP NGV row and most of the rest in the region of the HP rotor. All the walls are set to be adiabatic.

A fine grid has again been used, which has $165\times59\times63$, $189\times49\times66$, $175\times61\times56$, and $189\times47\times69$ points in the four rows giving over 2.4 million nodes in total (the background grid shown in Fig. 5 is coarser). Figure 6 shows a closeup of the IP rotor leading edge on the casing with the shroud leakage extraction slot exit grid drawn in grey.

In this case the constant $C_P$ values for model 2 have been set to the mass average of the inlet $C_P$ values for each row from model 3, see Fig. 7. Model 1 uses the HP vane value throughout and the distribution for model 3 is close to that for model 4.

It is interesting to compare the evolution of the mass average total temperature though the machine for the constant $C_P$ model (model 1) and the full variable gas model (model 4), as shown in Fig. 8. In the HP NGV the temperature drops as a result of the addition of cooling air. Since this is cold relative to the mainstream it has a lower $C_P$ in the variable gas properties models,

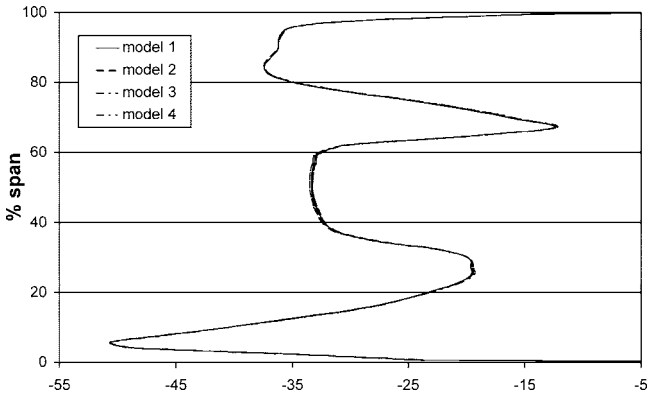


**Fig. 4 Mass average exit whirl angle (deg) versus span**

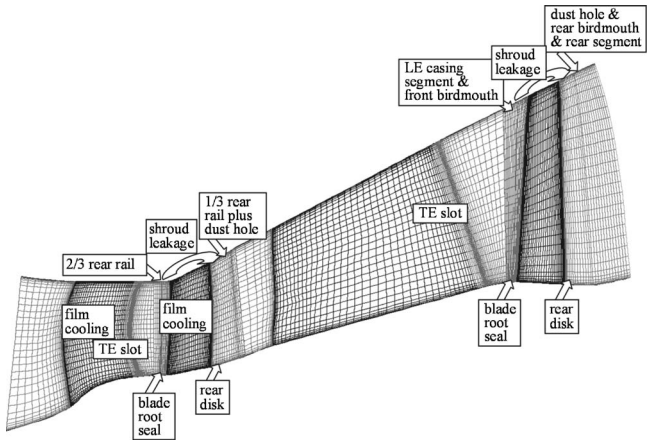


**Fig. 5 HP/IP turbine secondary air flows**

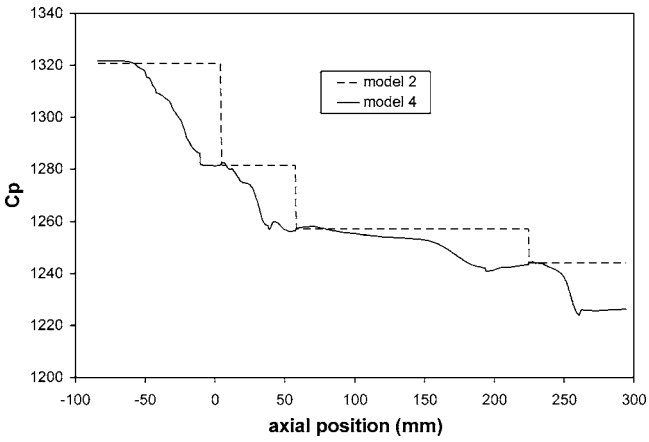


**Fig. 7 $C_P$ axial variation**

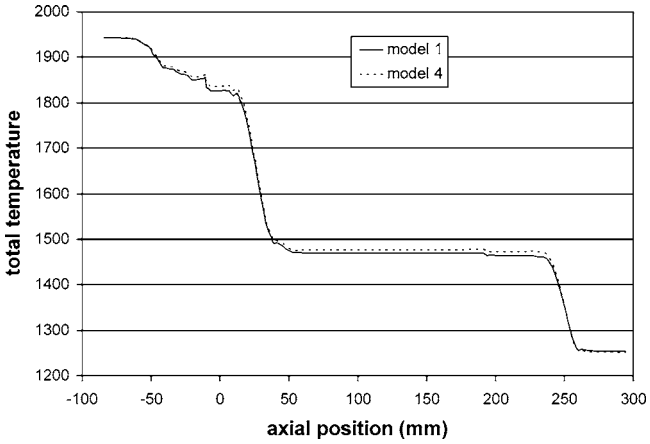


**Fig. 8 Mass average total temperature versus axial distance for models 1 and 4**

hence its enthalpy is lower than in the constant $C_P$ case. So when the cooling air is mixed with the mainstream it produces less cooling in model 4 than in model 1, the exit temperature is about 10 K higher. In the HP rotor the work extracted is about the same in the two cases, thus the total enthalpy drop is about the same. Since $C_P$ is lower in model 4 the total temperature drop is larger, this effect is greater than the opposing effect of the cooling air added in the rotor. At the HP rotor exit the temperature in model 4 is only about 5 K higher than model 1. In the IP vane a relatively small amount of coolant air is added, leading to only a 3 K increase in the temperature difference between the models at vane exit. In the IP rotor the constant work effect dominates the cooling air effect resulting in the curves crossing over. At IP rotor exit the temperature of model 4 is 2 K lower than that of model 1. However, as a result of the variable gas properties having opposing effects on the temperature changes due to the cooling air and the work extraction, the two models predict similar temperatures throughout.

Consider the overall turbine performance parameters. In the presence of secondary inlets and exits the specific work is defined by Eq. (15) where the inlet becomes the mainstream inlet. The stage efficiency is defined as

$$\eta_{\text{stage}} \equiv \frac{\left\{ \sum_{i=\text{inlets}} (\dot{m}H_0)_i - \sum_{i=\text{exits}} (\dot{m}H_0)_i \right\}}{\left\{ \sum_{i=\text{inlets}} (\dot{m}H_0)_i - \sum_{i=\text{sec\_exits}} (\dot{m}H_0)_i - (\dot{m}H_{0\_\text{ideal}})\big|_{\text{main\_exit}} \right\}} \tag{17}$$

where the ideal exit total enthalpy is computed as the mass average of the ideal total enthalpies of each of the inlets expanded isentropically to the mainstream exit condition. The ideal expansion of each gas stream to the mainstream exit conditions is based on the gas properties of that stream. The film cooling air is treated as another inlet; but, in the case of the rotor, using feed gas conditions at the blade root. The control volume adopted for the work sum is envisaged to cut through the blade platform, then the work done on the coolant as it travels through the blade internal passages can be ignored in the work sum. The results are given in Table 2.

Considering the HP first, the capacity is marginally higher for model 4, as it was in the single stage case, but only by at most 0.2%. The most significant difference is in the stage efficiency which is over 1.5% higher for models 3 and 4 where $C_P$ is a function of the local conditions. Since the work does not show this change the difference must be due to a change in the ideal work extraction. Investigation shows that this is due to the large differences in the value of $C_P$ used to calculate the ideal exit total enthalpy for the cooling flows, since models 1 and 2 will use a value appropriate to the mainstream whereas models 3 and 4 will use the coolant temperature and zero FAR to compute a much lower value. Thus it is more an artefact of the efficiency definition used than representing significant differences in the flow field.

In the IP stage, model 1 shows about 1/2% lower capacity than the other models. The mass flow is fixed by the HP vane and only differs slightly between the models; the difference in IP capacity is a result of the differences in total pressure and temperature at IP inlet. The work is high by a similar margin on model 1, again the dominant factor causing this is the change in IP inlet total temperature. The IP efficiencies differ by much less than those in the HP. The effect of the value of $C_P$ applied to the cooling air is much weaker than in the HP because the amount of coolant added is almost an order of magnitude less. However, this effect will be stronger in model 1 than model 2 because model 1 is applying a value of $C_P$ to the coolant which is appropriate to the HP mainstream rather than the IP mainstream. The effect of the coolant $C_P$ when added to the gradual reduction in efficiency with the more physical models which was seen in the single stage example is likely to explain the small differences in the IP efficiency.

Examination of the profiles of circumferentially averaged flow at exit from the machine shows no significant differences between the four gas models. The shift in exit total temperature shown in Fig. 8 appears as a fairly uniform shift across the span.

Comparing the program run times model 4 takes 8.6% longer than 1, with models 2 and 3 being intermediate. The convergence histories are similar for all models.

## Conclusions

Overall the effect on turbine performance prediction of including variable gas properties in 3D CFD is small.

The largest difference found is a 1.5% change in stage efficiency in the presence of cooling air. This is due to the different values of $C_P$ used in calculating the ideal exit enthalpy of the cooling air.

In the present algorithm the extra cost of solving a fuel fraction equation and calculating $C_P$ from local temperature and fuel air ratio is less than 10%. This model is, therefore, preferred to either of the intermediate variable $C_P$ models.

**Table 2 HP turbine performance versus gas model**

| Gas model | 1 | 2 | 3 | 4 |
|---|---|---|---|---|
| **HP** | | | | |
| (Turbine inlet capacity)/(model 4 capacity) | 0.9984 | 0.9989 | 0.9980 | 1 |
| (Specific work)/(model 4 specific work) | 0.9983 | 1.0015 | 1.0002 | 1 |
| (Stage efficiency (%)) - (model 4 efficiency) | −1.6 | −1.7 | 0.09 | 0 |
| **IP** | | | | |
| (Turbine inlet capacity)/(model 4 capacity) | 0.9950 | 0.9994 | 0.9999 | 1 |
| (Specific work)/(model 4 specific work) | 1.006 | 1.000 | 1.001 | 1 |
| (Stage efficiency (%)) - (model 4 efficiency) | 0.07 | 0.08 | 0.13 | 0 |

## Acknowledgment

The author would like to thank Rolls-Royce plc for permission to publish this paper, and Professor N A Cumpsty for his encouragement to write it.

## Nomenclature

$A$ = area
$C_V$ = specific heat at constant volume
$C_P$ = specific heat at constant pressure
$e$ = internal energy per unit mass
$F$ = fuel fraction
FAR = fuel air ratio
$H$ = total enthalpy
LCV = lower calorific value (of the fuel)
$\dot{m}$ = mass flow rate
$p$ = static pressure
$P_0$ = total pressure
$R$ = the gas constant
$s$ = entropy
$T$ = static temperature
$T_0$ = total temperature
$u$ = velocity
$\gamma = C_P/C_V$ = ratio of specific heats
$\rho$ = density
$\eta$ = efficiency
$\mu$ = viscosity

### Superscripts

$\tilde{\varphi}$ = denotes the mass average of any parameter $\varphi$

### Subscripts

in = inlet conditions
ex = exit conditions
$r$ = rotor conditions
$v$ = vane conditions

## References

[1] Denton, J. D., 1990, "The Calculation of Three Dimensional Viscous Flow Through Multistage Turbomachines," ASME Paper No. 90-GT-19.
[2] Shahpar, S., 2001, "Three-Dimensional Design and Optimisation of Turbomachinery Blades Using the Navier-Stokes Equations," ISABE-2001-1053.
[3] Batchelor, G. K., 1967, *An Introduction to Fluid Dynamics*, CUP, Cambridge, UK, pp. 37–43.
[4] U. S. Standard Reference Data System, 1971, JANAF Thermochemical Tables, 2nd ed., NSRDS-NBS 37, U.S. Department of Commerce.
[5] Cumpsty, N., 2003, *Jet Propulsion*, 2nd ed., CUP, Cambridge, UK, p. 65.
[6] Boncinelli, P., Rubechini, F., Arnone, A., Cecconi, M., and Cortese, C., 2004, "Real Gas Effects in Turbomachinery Flows: A Computational Fluid Dynamics Model for Fast Computations," ASME Paper No. 2003-GT-38101.
[7] Yao, Y., and Amos, I., 2004, "Numerical Study of Axial Turbine Flow with Variable Gas Property," ASME Paper No. GT2004-53748.
[8] Moore, J. G., 1989, "Pressure Correction Calculation Procedures for 3D Viscous Flow," *Numerical Methods for Flows in Turbomachinery* (VKI Lecture Series No. 1989-06), von Karmen Institute for Fluid Dynamics, Rhode-Saint-Genese, Belgium.
[9] Moore, J. G., 1989, "Calculation of 3D Flow Without Numerical Mixing," *Numerical Methods for Flows in Turbomachinery* (VKI Lecture Series No. 1989-06), von Karmen Institute for Fluid Dynamics, Rhode-Saint-Genese, Belgium.
[10] Patankar, S. V., 1980, *Numerical Heat Transfer and Fluid Flow*, Hemisphere, Washington, DC, pp. 131–134.
[11] Northall, J. D., Moore, J. G., and Moore, J., 1987, "Three-Dimensional Viscous Flow Calculations for Loss Prediction in Turbine Blade Rows," Paper No. C267, I. Mech. E. Conf. On Turbomachinery — Efficiency Prediction and Improvement.
[12] Robinson, C. J., Northall, J. D., and McFarlane, C. W. R., 1989, "Measurement and Calculation of the Three-Dimensional Flow in Axial Compressor Stators, With and Without End-Bends," ASME Paper No. 89-GT-6.
[13] Chew, J. W., Taylor, J. W., and Bonsell, J. J., 1996, "CFD Developments for Turbine Heat Transfer," Paper No. C449/035, I. Mech. E. Conf.
[14] Crawford, M. E., Kays, W. M., and Moffat, R. J., 1980, "Full-coverage Film Cooling, Part 2: Heat Transfer Data and Numerical Simulation," ASME Paper No. 80-GT-44.
[15] Cobell, P. A., 1996, "Computer Programmers Guide For The BS09/BS29 - RRAP Compatible Thermodynamic Subroutines — Issue 7," CUG BS09, Rolls-Royce plc Internal Report, Derby, UK.
[16] Geist, A., Beguelin, A., Dongarra, J., Jiang, W., Manchek, R., and Sunderam, V., 1994, *PVM: Parallel Virtual Machine A User's Guide and Tutorial for Networked Parallel Computing*, MIT Press, Cambridge, MA.

C. Prakash
C. P. Lee
D. G. Cherry
R. Doughty
A. R. Wadia

General Electric Aviation,
30 Merchant Sreet,
Princeton Hill P20,
Cincinnati, OH 45246

# Analysis of Some Improved Blade Tip Concepts

*Over tip leakage in high-pressure turbines contributes to aerodynamic losses and migration of hot gasses towards the tip resulting in increased thermal distress. Consequently, turbine designers continue to search for improved blade tip concepts that offer the promise of reducing tip leakage. The present paper deals with the computational fluid dynamics analyses of some such tip configurations. The geometries, patented by GE, are variants of a conventional squealer tip and include (i) a pressure side tip shelf with vertical squealer tip wall and (ii) a pressure side tip shelf with an inclined squealer tip wall. It is found that the inclined shelf results in separation of flow leaking over the tip, resulting in reduced leakage and improved efficiency. The inclined shelf also shows a reduced efficiency derivative with clearance.* [DOI: 10.1115/1.2220050]

## 1 Introduction

In order to separate the moving blade from the stationary casing in a high-pressure turbine, a finite clearance between the two is necessary. Such a clearance, however, provides a path for the gasses to leak from the pressure side to the suction side, which manifests as loss and reduced turbine efficiency. Further, depending on the overall flow field and the temperature profile at the turbine inlet, the gasses migrating over the tip can be hot, resulting in excessive thermal distress in the tip region. In response to these considerations, turbine designers continue to search for improved blade concepts that offer the promise of reducing tip leakage and thus enhancing blade performance and durability.

Figure 1 shows a so-called squealer tip configuration, which is used in many of GE's HPT blade designs. This consists of a recessed squealer cavity at the top, bounded by squealer tip walls of finite thickness. The blade ends at the floor of the cavity. The squealer walls form additional blade surface and function to reduce the effective clearance for the leakage path. The squealer tip walls also serve as "sacrificial material" that distances the casing from the bulk of the blade, reducing the possibility of contact between the two in case of a rub. Instead, when the rub occurs, it is the squealer tip wall that is lost. The wall is refurbished during the engine repair cycle.

Due to its practical importance, the subject of blade tip aerodynamics and heat transfer has been a focus of several analytical and experimental investigations. A recent review of these studies has been provided by Bunker [1] and by Glezer et al. [2]. Acharya et al. [3] have recently investigated different leakage reduction strategies including pressure-side squealer, suction-side squealer, mean chamber line squealer, and pressure plus suction side squealers located either along the edges of the blade or moved inwards.

The present study investigates two new blade tip concepts, which are variants of the conventional squealer tip. The first, shown in Fig. 2, will be referred to as the straight shelf. The key feature of this GE patented [4] configuration is the presence of a shelf on the pressure side near the base of the squealer tip cavity. The walls of the squealer tip adjacent to the shelf are straight. As over the rest of the pressure surface, film cooling is applied over the shelf. As the leakage fluid flows over the pressure surface, the shelf acts as a backward facing step, resulting in a separated vortex flow over it. The cooling applied at the shelf is caught in this rolling vortex and serves to better cool the pressure surface near the tip. Without the shelf, the film does not cover the surface as well and cooling is less effective.

The second configuration investigated is also a GE patented concept [5] and is shown in Fig. 3. It is referred to as an inclined shelf because the squealer wall over the shelf is inclined towards the pressure side. As the leakage fluid flows over the pressure surface, the incline forces it to turn by a larger angle—compared to a straight shelf—resulting in separation (vena-contracta effect) that serves to reduce leakage.

Experienced designers will observe that the above tip concepts are inspired by similar ideas that are utilized in the design of labyrinth seals.

As already mentioned, the present study deals with a numerical investigation of the blade tip concepts shown in Figs. 1–3. The goal is to compare the aero benefits in terms of leakage and efficiency.

## Numerical Analysis

The proposed blade tip concepts were investigated via a three-dimensional, steady, viscous flow computational fluid dynamics (CFD) analysis following GE's well-established practices for single blade row simulations. Starting with a UG solids model, the commercial grid generation package ICEM-HEXA was used to generate the grid. Typical grid sizes range around 700,000 cells. The disposition of the grid conformed to established GEAE practices for wall function grids. Typically ~10 cells were employed in the radial direction in the tip region at lower clearance and ~20 at the higher clearance. Within the squealer cavity (and between the shelf and blade tip), ~20 cells were employed in the radial direction. In order to make the predicted differences (deltas) between the different geometries more reliable, a best effort was made to limit the differences in the grid to the near tip region, leaving the grid away from the tip as close as possible for all three configurations. The CFD analysis employed the commercial code STARCD. The computations are turbulent and the *k*-epsilon model is employed. The boundary conditions at the flow path inlet

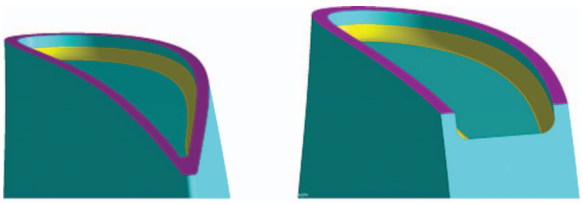

**Fig. 1 A Conventional squealer tip**

Contributed by the International Gas Turbine Institute (IGTI) of ASME for publication in the JOURNAL OF TURBOMACHINERY. Manuscript received October 1, 2004; final manuscript received February 1, 2005. IGTI Review Chair: K. C. Hall. Paper presented at the ASME Turbo Expo 2005: Land, Sea and Air, Reno, NV, June 6–9, 2005, Paper No. GT2005-68333.

  

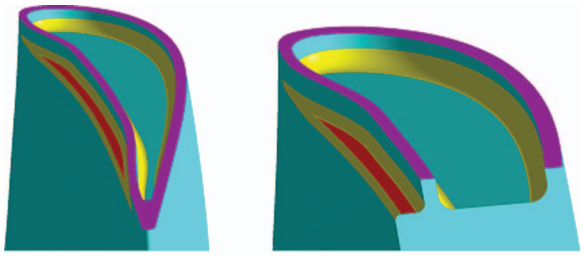

Fig. 2 Straight shelf

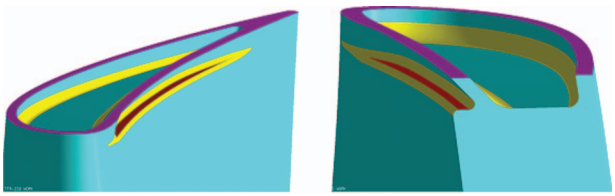

Fig. 3 Inclined-shelf

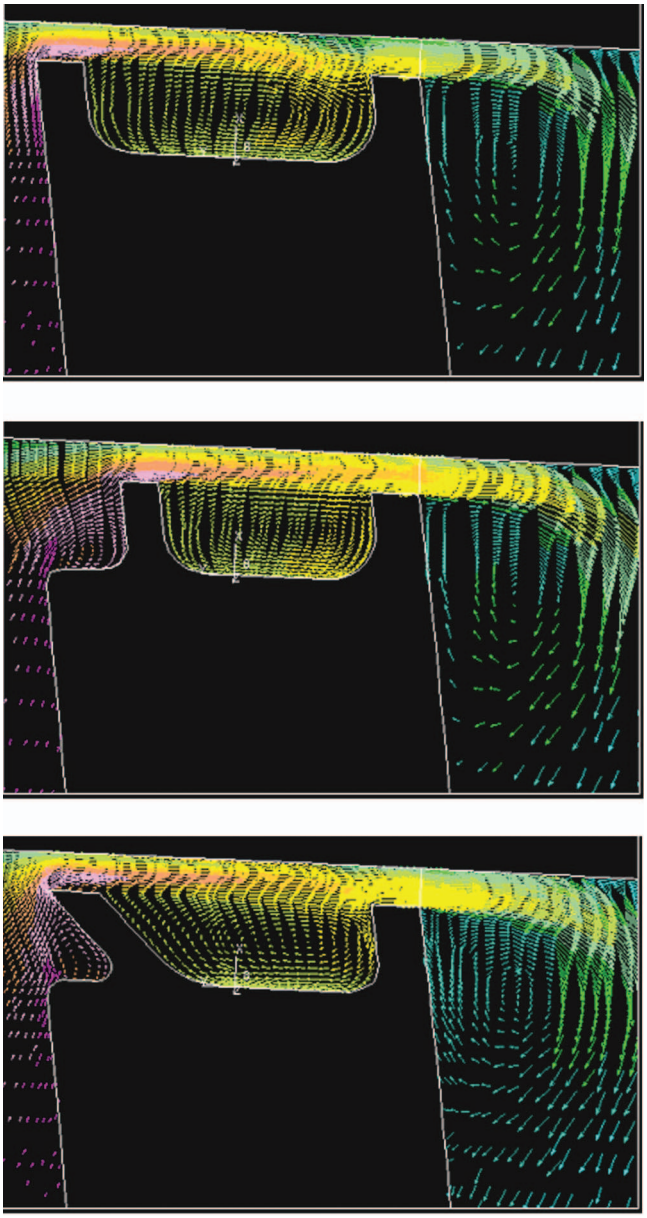

Fig. 4 (*a*) Flow over conventional tip. (*b*) Flow over straight shelf. (*c*) Flow over inclined shelf.

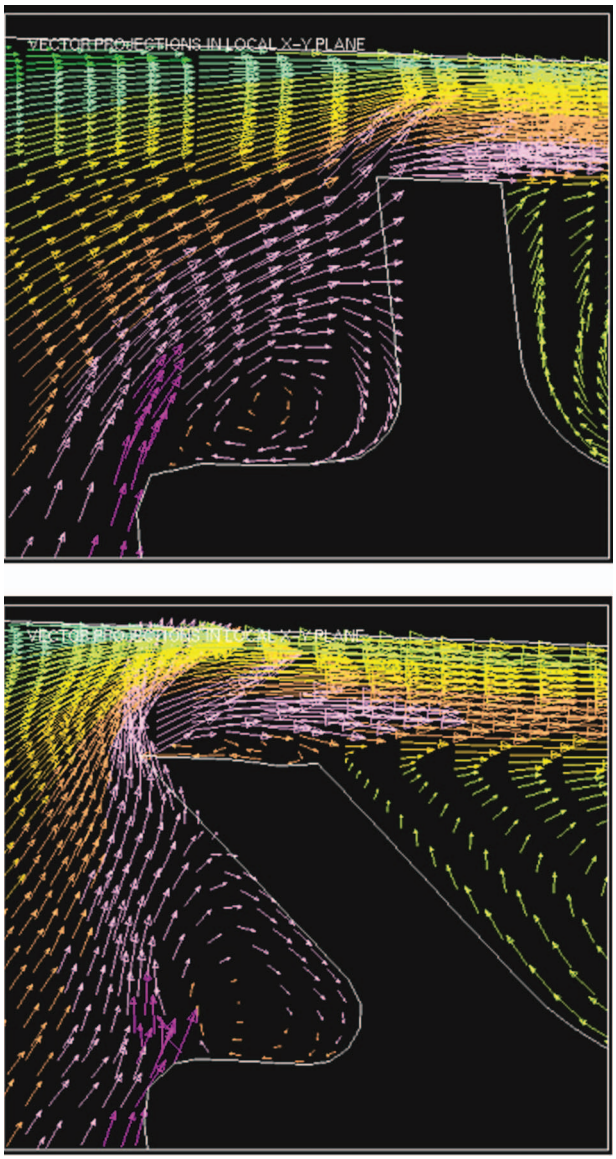


Fig. 5 (*a*) Flow over straight shelf. (*b*) Flow over the inclined shelf.

consist of radial profiles of total pressure, total temperature, flow angles, and turbulent intensity and length scale. At the exit to the flow path, radial profile of static pressure is prescribed.

## Results and Discussion

Figure 4 shows representative plots of flow as it leaks over the blade tip. The vectors are projections on a plane that is near normal to the main flow direction (~ mean chamber line). Typical features of the flow, as expected, are evidenced. As can be seen, the flow field is quite complex and consists of a large recirculation zone in the squealer cavity. The vortex formed over the suction surface may be noted where the mixing between the leakage and the main flow contributes to losses that reduce the turbine efficiency.

The more interesting features of the flow, which help explain the behavior of a straight and inclined shelves, are more clearly evident from Fig. 5, which shows magnified plots in the near shelf region. As can be seen from Fig. 5(*a*), the leakage flow sees the shelf as a backward facing step and forms a vortex over it. Any film cooling applied in this region gets rolled up in this vortex and covers the surface better as compared to a no-shelf configuration.

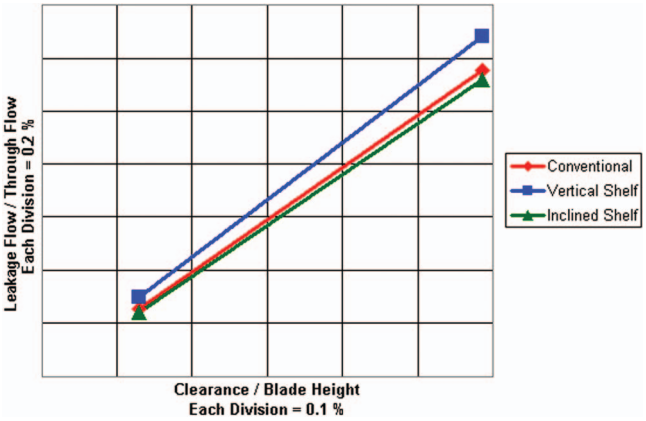


**Fig. 6 Variation of leakage flow**

The inclined shelf, Fig. 5(*b*), retains this feature of the shelf. However, due to the large turn that the leaking fluid must make, the separation over the tip is more pronounced with the inclined shelf compared to the straight shelf. This separation (vena-contracta effect) serves to block the path of the leakage flow and thus reduce leakage and enhance efficiency.

The leakage flow over the tip is computed as the total mass flux across a curved surface strip formed by extending the suction surface of the blade from the top of the squealer tip to the casing. Figure 6 shows the variation of leakage flow with clearance. The leakage flow is normalized with the total flow through the passage and the clearance is normalized with the blade height. As expected, leakage increases with tip clearance. Going from the conventional tip (no shelf) to a vertical shelf, the leakage is found to increase. This can be explained by noting that the shelf is created by pushing (denting) the pressure surface in, which results in reducing the distance over which the pressure difference between the pressure and suction side has to act to drive the leakage flow. However, going on to the inclined shelf, the leakage is reduced. This is a consequence of the more pronounced flow separation over the inclined squealer tip wall (Fig. 5(*b*)) as the flow is forced to turn over the inclined angle. This separation bubble (vena-contracta effect) serves as a blockage in the path of the flow and the leakage is reduced.

The variation of efficiency with clearance is shown in Fig. 7. Efficiency is computed as the ratio of the actual work extracted in the blade row compared to ideal work. The variation of efficiency in Fig. 7 ties in well with the leakage plot in Fig. 6, namely, that as leakage increases, the efficiency decreases. Compared to a conventional tip (no shelf), the vertical shelf loses ~0.05% in efficiency while the inclined shelf is better by ~0.1% to 0.2%.

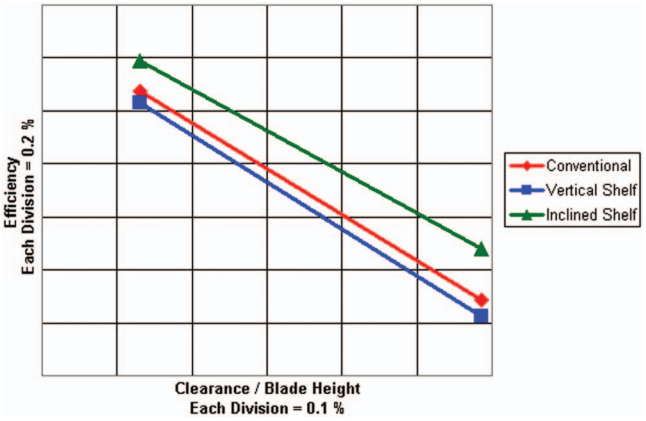


**Fig. 7 Variation of blade row efficiency**

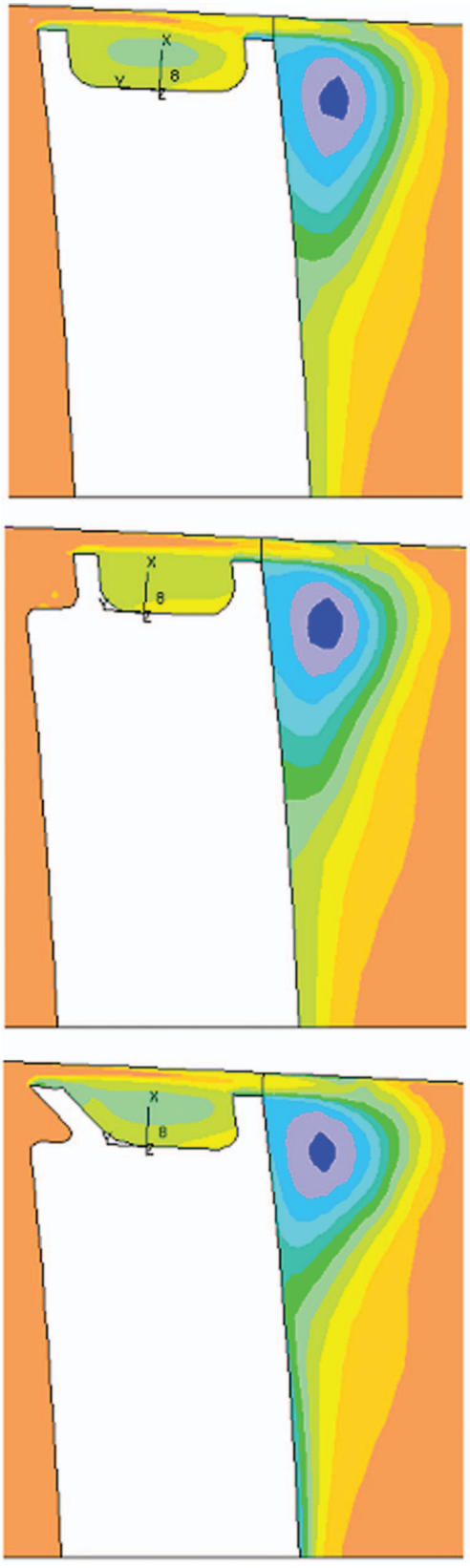


**Fig. 8 (*a*) Total relative pressure. Conventional squealer tip. (*b*) Total relative pressure. Vertical shelf. (*c*) Total relative pressure. Inclined shelf.**

The variation of efficiency with clearance is also an important quantity of practical interest. For the conventional tip, the vertical

shelf, and the inclined shelf, the efficiency derivative with clearance is estimated to be ~1.72, 1.77, and 1.56, respectively, all of which agree well with the range (1.5–2.0) used in various correlations. In addition to the higher efficiency, the reduced derivative is another benefit of the inclined shelf.

Figure 8 shows another set of plots which restate the findings discussed afore. Shown in these plots is the variation of total relative pressure in a plane that cuts across the flow path. The term relative refers to a frame that rotates with the blade. Blue color shows regions of low total pressure, a consequence of mixing and loss. As is evident, the extent of the blue region is biggest for the vertical shelf and smallest for the inclined shelf. This agrees with the former having the lowest and the latter the highest efficiency.

While the above discussion has focused primarily on leakage and efficiency, it must be recalled that efficiency depends on many other factors besides leakage (e.g., profile losses, secondary losses, etc.) that are impacted by the different flow fields associated with different geometries. This is evidenced by the present results that show a more notable difference in the efficiency between different geometries even though the differences in the leakage are small.

Since the geometries compared in this study are not too dissimilar, the inverse relationship between leakage and efficiency is generally found to hold (i.e., higher leakage implies lower efficiency). It must be pointed out, however, that this inverse relationship may not be a general rule that can be applied between any two different geometries. As an example, it is conceivable that one geometry may lead to higher leakage of unturned fluid near the front of the blade while the other may result in more leakage near the rear end of the blade after the flow has turned and done the useful work. In such a case, it is possible for the second geometry to have both higher efficiency and higher leakage than the first. Further, as already stated, different flow behavior associated with different geometries may lead to differences in other loss mechanisms that affect efficiency.

## Summary

This paper reports the results of a numerical study aimed at comparing aero performance of three blade tip configurations. These include a conventional squealer tip, a tip with a shelf on the pressure side with vertical squealer tip walls (called the vertical shelf), and a tip with a pressure side shelf and inclined squealer wall (called the inclined shelf). Both the shelf concepts are GE patented [4,5] and relatively recent. The shelf acts as a backward-facing step in the path of leakage fluid and creates a vortex flow. CFD simulations, not discussed in the present paper, indicate that film cooling applied on the shelf is entrapped in this vortex and covers the surface better. However, the vertical shelf results in higher leakage and reduced efficiency. When, however, the shelf is applied in conjunction with an inclined squealer wall, the flow undergoes separation over the tip, resulting in leakage reduction and efficiency gain. The inclined shelf configuration thus provides both a heat transfer and an aero performance advantage. The computations were done at both cruise and takeoff conditions and the conclusions discussed were found to hold for both the conditions. In addition, computations have recently been done for a different engine and the inclined shelf again appears superior to a standard vertical shelf. It must be acknowledged that the present simulations assume a sharp edge at the tip of the blade. In a real circumstance the edge may be rounded due to manufacturing and rub/wear. Such blended edges affect the nature of the separated flow over the tip and may reduce the aero (not as much the heat transfer) benefits of the inclined shelf compared to the vertical shelf.

## Acknowledgment

The authors thank GE Aircraft Engines for granting permission to publish this work. Thanks are due to Steve Brassfield of GEAE for help with drafting. Useful discussions with John Starkweather, Chief Engineer, GEAE, are also acknowledged.

## References

[1] Bunker, R. S., 2004, "Axial Turbine Blade Tips: Function, Design, and Durability," AIAA J. Propul. Power, **22**(2), pp. 271–285.
[2] Glezer, B., Harvey, N., Camci, C., Bunker, R., and Ameri, A., 2004, "Turbine Blade Tip Design and Tip Clearance Treatment," Von Karman Institute for Fluid Dynamics Lecture Series VKI-LS 2004-02, ISSN0377-8312, Brussels, Jan. 19–23.
[3] Acharya, S., Yang, H., Prakash, C., and Bunker, R., 2003, "Numerical Study of Flow and Heat Transfer on a Blade Tip with Different Leakage Reduction Strategies," ASME Paper No. 2003-GT-38617.
[4] Butts, D., Nourse, J. G., and Simmons, R. C., 1993, "Tip Cooled Blade," U.S. Patent No. 5,261,789.
[5] Cherry, D. G., Lee, C. P., Prakash, C., Wadia, A. R., Keith, B. D., and Brassfield, S. R., 2004, "Turbine Blade Having Angled Squealer Tip," U.S. Patent No. 6,672,829.

# Aerodesign and Testing of an Aeromechanically Highly Loaded LP Turbine

**F. J. Malzacher**

**J. Gier**

**F. Lippl**

MTU Aero Engines,
80995 München, Germany

*Future turbo systems for aircraft engines need very compact geometry, low weight, and high efficiency components. The geared turbofan enables the engine designer to decouple the speed of the fan and the LP turbine to combine a low speed fan with a high speed LP turbine. The low pressure turbine is a key component for this concept. The technological challenge is very much driven by the very high low-spool speed. Resulting as well from high inlet temperatures, the LP turbine needs cooling of the first stage. A new MTU LPT concept for such a high speed turbine has been developed and tested in a turbine rig. The concept consists of a two-stage turbine for extremely high speed and high stage pressure ratio (ER 2.3). This leads to extra high mechanical loading and an exotic combination of high Mach numbers (transonic) and very low Reynolds numbers. In this paper some design features are described. Some elements of the airfoil design were also tested in additional cascade tests. The two-stage turbine was tested at the Altitude Test Facility of the ILA, Stuttgart. The test setup is described including details of the instrumentation. Test data shows a good turbine performance. Measurements are also compared to 3D CFD, which is used to analyze local effects.* [DOI: 10.1115/1.2172646]

## Introduction

The main selling argument for future business and regional Jets is a significant technical and economical advantage of airframe and propulsion systems compared to the existing technology. The development of today's jet engines is driven by the customer's request for low direct operation costs. This leads to new concepts which deal, on the one hand, with higher bypass ratios, and on the other hand, with the geared configuration, decoupling the fan, and LP shaft speed.

MTU Aero Engines is cooperating with Pratt & Whitney Canada (P&W C), Pratt & Whitney America (P&W A), and Fiat Avio on the definition, development, and testing of geared turbofan systems. In this cooperation, MTU delivers the high speed LPT. The propulsion system considered here is dedicated to empower the lower and medium thrust class (10–20 klb) for the next generation of business jets and regional aircraft.

The target of such a new engine is to reduce the direct operating costs by 10% including minimized acoustic emissions and improved environmental friendliness. The name for this system is PW800.

MTU Aero Engines achieved the LPT competence through more than ten engine programs since 1980. For geared systems, MTU succeeded in the early 1990s with the three-stage LPT for the advanced ducted propfan [1,2], where very high efficiency levels were realized.

For the verification of of the new technologies needed, the work was split into two work-packages. The first is the development and manufacturing of the LP turbine technology rig for a demonstrator engine called Advanced Technology Fan Integrator [3]. This includes the testing of component characteristics with sea level and flight tests. This package is realized in cooperation with P&W C. The first successful low spool engine Demonstrator was run in March 2001 at a PWC Test Facility after a very short development time of nine months.

The second work-package consists of a detailed aero-investigation by establishing an additional highly instrumented coldflow rig. The engine test cannot be instrumented as detailed as it is necessary to get all the relevant information concerning the quality of the aerodynamic design, especially the efficiency split on the component level. Therefore, this coldflow rig is the second leg for substantiation of the LP turbine technology readiness. The Cold Flow Test Rig tests were performed in April 2002 at the Altitude Test Facility of the University of Stuttgart.

This program also includes the development of new technologies such as advanced rotor concept, assembly-disassembly procedure, extreme minishroud design, and lightweight single crystal for the cooled LP1 blade.

**The Concept.** High efficiencies need different conditions for each component. High bypass ratios necessitate larger fan diameters, raising the circumferential velocitiy at the fan tip. However, this is aerodynamically limited by strong shock systems occuring at high velocities, leading to a limited turning speed of the LP shaft. The LP turbine, on the other hand, needs a high speed for optimal blade turning and Mach number levels. The conventional turbofan couples these two components on one spool, which leads to a compromised design for both. The geared turbofan concept decouples these two components, hence fan and LPT can work in their individual optimum speed range. In addition, this provides the chance to reduce stage count and airfoil count in the LPT without losing too much efficiency. Based on conceptual studies, it could be derived that this configuration has the highest potential for the next engine generation.

**The Challenge.** Several interesting technical solutions have to be found to make this system work. The most challenging are the very high Mach numbers due to the very high stage pressure ratio, the high gasloads on the static structures, the high stress levels in the rotating parts, and on top, the high temperature level, which implies the necessity of cooling for the first stage.

The focus in this paper is the aerodynamic design. The most interesting new aerodynamic feature is the combination of HPT-like Mach numbers and very low Reynolds numbers under the challenging mechanical boundary conditions.

The main topics to be investigated in this program were:

- the feasibility of the specified efficiency level at the aerodesign point

Contributed by the Turbomachinery Division of ASME for publication in the JOURNAL OF TURBOMACHINERY. Manuscript received November 10, 2003; final manuscript received December 19, 2003. Review conducted by D. Wisler.

  

Table 1 Turbine characteristics

| | |
|---|---|
| No. of stages | 2 |
| Pressure ratio | >5.7 |
| $\Delta H/u^2$ | 1.4 |
| $c_{ax}/u$ | 0.55 |
| Re number blade 2 | 60,000 |
| $Ma_{exit}$ blade 2 | 1 |
| Speed [RPM] | 10000 |
| Inlet flow rate [kg/s $\sqrt{}$(K/bar)] | 145 |
| $A^*n^2$ [inch$^2$ rpm$^2$] | 6.9 |

- the turbine map, the component's behavior at partload, and offdesign conditions
- the lapse rate (impact of Reynolds number on efficiency and flow rate)
- the impact of the combined effect of Mach and Reynolds numbers
- the detailed measurement including the interturbine duct, profile pressure distributions on the vanes, stage worksplit, and the stage reactions
- the derivation of potential for further improvements for the real product
- the influence of high airfoil area-taper on the radial work-distribution in the turbine

This includes the validation of aerodesign tools for this application class.

## Boundary Conditions and Main Design Parameters

The main design parameters at rig aero design point (ADP) are given in Table 1.

**Aerodynamic Boundary Conditions.** The comparison of pressure ratio vs. stage count of this test turbine compared to other LP turbines is given in Fig. 1. Conventional turbines need up to seven stages for the pressure ratio of ≈5.5. The first technological step was done by an Engine 3 E turbine for the advanced ducted propfan with P&WA. This MTU LP turbine had three stages for this pressure ratio. The turbine presented here is also designed for a geared turbofan but handles the same pressure ratio with two stages. In spite of the massive difference in aerodynamic loading (pressure-ratio wise), it is also possible to achieve high efficiency

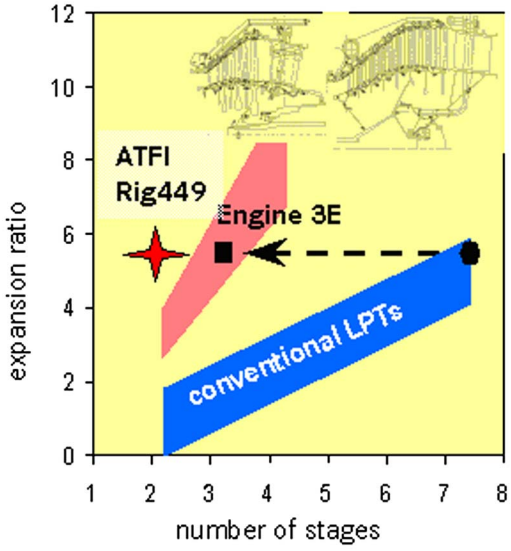


Fig. 1 LP turbine aero loading pressure ratio versus stage count

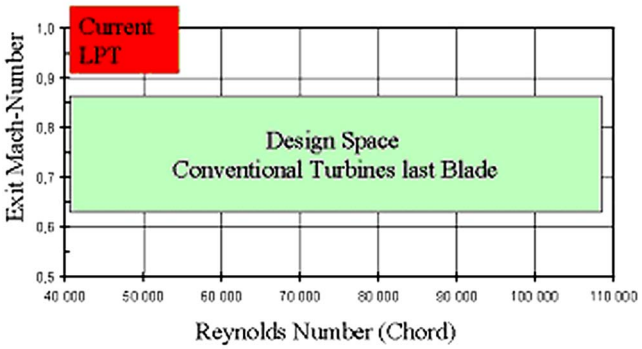


Fig. 2 Exotic combination of Mach and Reynolds numbers in the last blade

levels, as will be described later.

In the beginning of this project it was realized that this turbine features an extreme combination of very high Mach number level for LP turbines and very low Reynolds numbers, especially in the second stage. This is presented in Fig. 2. The Mach number of >1.0 is HPT-like, the Reynolds number of 50,000 (based on chord length) corresponds to LPTs for small jet engines.

Hence, there was concern with respect to fully separated flow on the airfoil suction sides and prediction quality of aerodynamic design tools.

Therefore, typical profile shapes where derived from the last blade. This was transformed into two cascades to confirm the CFD results. The cascades have been tested at the High Speed Cascade Wind Tunnel of the Universität der Bundeswehr München [4], and some results are presented here.

**Mechanical Boundary Conditions.** The most relevant parameter for the mechanical boundary conditions is $A^*n^2$. This is a characteristic number to assess whether the stress level of the design is within allowable structural limits. $A$ is the gas path area at turbine exit and $n$ is the turbine speed at blocktest condition, which comes up with the worst combination of high speed and high temperature. Here, the maximum value encountered is 6.9 (inch rpm)$^2$. The normal values for conventional LP turbines are typically below 3.0 (inch rpm)$^2$ (Fig. 3). This leads to typical design features for the blading design, especially a high area taper from hub to tip to reduce the stress levels. Furthermore, the stator vanes are subject to increased gasloads by the high pressure ratio. This has to be considered in the design of the airfoil shape.

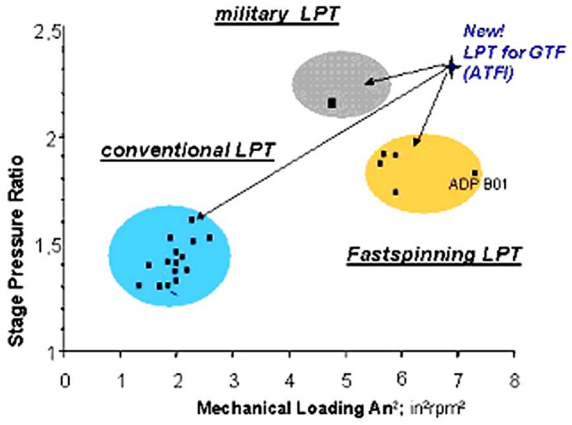


Fig. 3 LP turbine mechanical loading

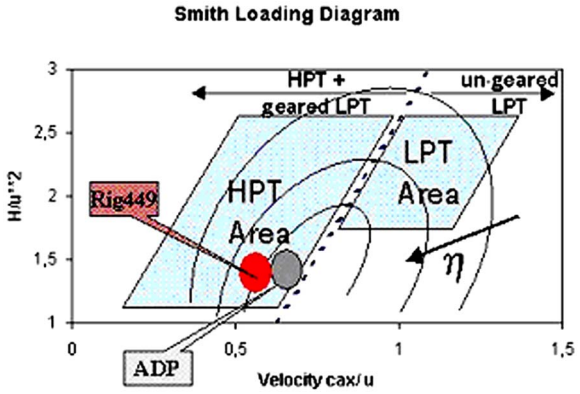


Fig. 4 Smith loading diagram

## Aerodynamic Design

**Gas Path.** The Smith turbine loading diagram in Fig. 4 shows that, due to the high circumferential velocity $u$, the turbine works in an area of higher efficiency levels. What is also seen is that this type of machine works in the design space of HPTs.

This means it has the positive aspect of a high circumferential velocity $u$ but is combined with the efficiency-wise detrimental high Mach number level in the gas path and on the airfoil surfaces. An additional positive characteristic is that the average blading acceleration exceeds values of $c_2/c_1 \approx 2.3$, while conventional modern turbines have accelerations of only around 1.8.

An important aspect for the overall optimization is the best possible blading efficiency without creating high TEC losses due to high blade exit Mach numbers and swirl in the absolute frame.

Due to the very high stress levels in the rotating parts, the overall optimization of the HPT/LPT and the cycle is essential. The best aerodynamic result will occur with a good mixture of low axial Mach numbers, moderate turning, and blade count. It is also very important to realize the maximum possible gas path steepness without getting flow separation in the interturbine duct. This increases the average circumferential velocity $u$, lowers the loading $\Delta H/u^2$, and the turbine length is minimized.

This is an example for a potential system optimization. If the parameter $A^* n^2$ has to be lowered, for example, by 10%, one way could be to decrease the exit area by 10%, another to reduce the speed by 5%. These choices would lead to principally different efficiency drops. Figure 5 shows the effects, which lead to the following conclusion: If it is reasonable from the systems side, it is better to change the speed and not the turbine exit area for getting the lower stress levels. The limiting factor can be the gear ratio for saving the optimum fan speed.

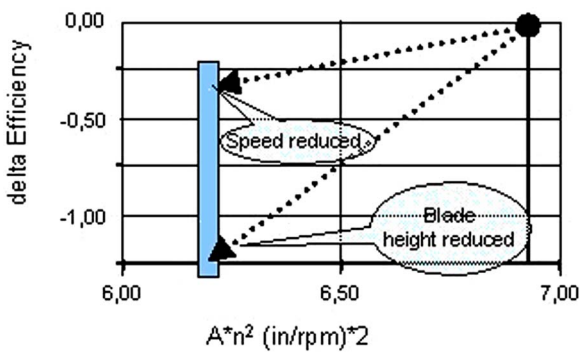


Fig. 5 Relation efficiency=f (speed; blade height)

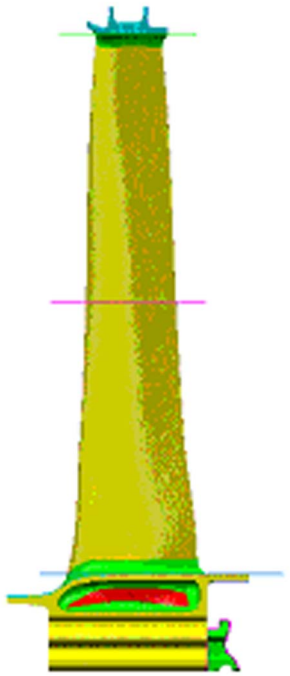

Fig. 6 Side view of second blade with area taper

**Airfoil Design.** Figure 6 gives an impression of the 3D-shaped blading for the LPT. High aspect ratios need strongly tapered profile shapes. The tip region needs very thin airfoil sections resulting in very high pitch-to-chord ratios ($>1.2$). For this blade, the area-ratio hub versus tip exceeds 3.5, compared to $\leqslant 2.0$ for typical conventional turbines. At the hub, this results in very thick airfoils sections with very low pitch-to-chord ratio (smaller than 0.6). Both conditions worsen the aerodynamic situation to perform low loss profiles, because this gives a further rise in the Mach number level. The aerodynamic design space for geometrical optimization is therefore very limited.

The favorable design characteristic here is the high aspect ratio ($h/b_{ax}$) of approximately 6, which is twice the value of the other typical small gas turbines. This reduces the extension of radial distortions related to the gas path height and the secondary losses decrease.

The additional challenge for this turbine is the cooling of the first stage (mixing losses, airfoil shape). This means that the turbine has to combine the whole complexity of high pressure turbines including intensive cooling with very low Reynolds numbers. The Reynolds number level is driven by the turbine size and especially by the mechanical boundary conditions.

The modern conventional low pressure turbines have relatively high efficiencies. This is possible mainly due to moderate Mach number levels. However, this high speed LP turbine has transonic flow for the whole blading over the complete radial span. This is driven by the very high stage pressure ratio. Figure 7 shows the comparison of typical Mach number distributions for a fast-spinning LPT, a conventional LPT blading, and a highly loaded transonic high pressure turbine.

The conventional blade shows exit Mach numbers $<1.0$, but local Mach numbers on the suction side may well exceed 1.0 locally in modern engines. The fast spinning and the high pressure turbine blade show exit Mach numbers near 1.0 and higher. This leads to typical phenomena for this loading class. Peak Mach numbers of 1.2 and higher on the suction side result in shocks. Therefore, complex shock boundary layer interactions occur, increasing the losses in the flow.

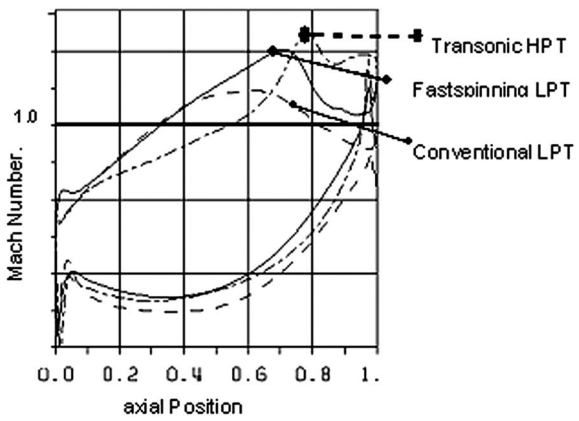


**Fig. 7 Comparison of typical pressure distributions for conventional LPT, high speed LPT, and HPT**

## Cascade Investigations

As stated above, the aerodynamic design of high Mach numbers and low Reynolds numbers inside the airfoil passage in combination with the strong mechanical requirements, especially in the rotor blades, proved to be quite challenging. It lead the aerodynamic design into regions with limited experience. Therefore, prior to the final design for the two-stage turbine, two cascade tests were performed in order to improve confidence for the design. Two especially critical sections of the last blade were investigated in a cascade test. For this, the hub (T132) and the tip section (T133) of this blade were chosen.

The hub section (T132) features a low pitch-to-chord ratio with high blockage and very low Reynolds number of about 60,000 based on chord length. The second airfoil (T133) is a typical tip section with high pitch-to-chord ratio, approximately sonic exit Mach conditions, and Reynolds numbers of about 77,000.

The High Speed Cascade Wind Tunnel is an open-loop test facility with an open test section. The whole wind tunnel is installed in a cylindrical pressure tank. The Mach number and Reynolds number can be varied independently from each other.

Profile pressure distributions at midspan as well as inlet and exit flow conditions (five-hole probe, wake traverses, and turbulence intensities) have been measured for the cascade. Schlieren pictures were also taken. Further details on the secondary flow structures have been obtained, performing oil flow visualizations of the blades at the endwalls. The measurements included various operating points.

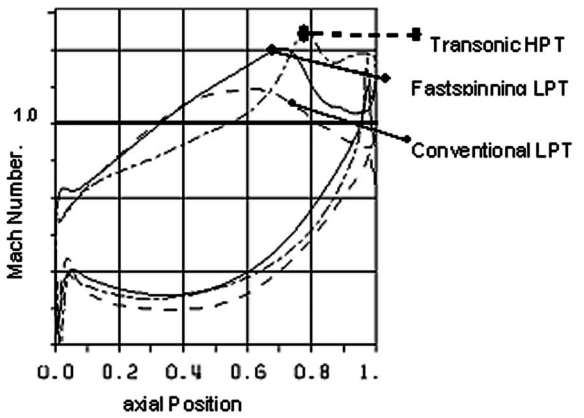


**Fig. 8 Measured and computed airfoil pressure distribution in the T132 cascade at nominal conditions**

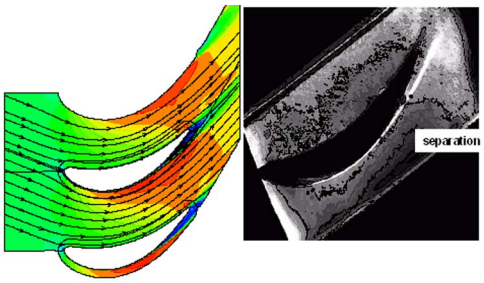


**Fig. 9 Comparison of Schlieren picture (experiment) and numerical solution of T132, $Re_{2th} \approx 60{,}000$; $Ma_{ex} \approx 0.8$; $Tu_{in} \approx 1.5\%$**

For the nominal conditions, the obtained pressure distribution is shown in Fig. 8. It is apparent that the flow on the suction side is fully separated for this operating point (see also Fig. 9). This behavior is well captured by the numerical simulation. Details about the numerical procedure can be obtained from [5,6].

In Fig. 9, where the two-dimensional flow field is shown, this separation can be also seen. The considerable size of the separation is displayed by both the numerical solution and the Schlieren picture. However, the turbulence level in the wind channel was limited to 1.6% for this operating point, which is significantly below the level to be expected for the last blade of the two-stage turbine. Although the danger of suction side flow separation for this blade is smaller in the turbine than in the cascade test, the blade built into the turbine was modified in order to reduce the separation tendency.

In Fig. 10 the Schlieren picuture of the T133 profile, which models the last blade tip section, is shown. In the design point this airfoil has an exit Mach number above one at a Reynolds number of approximately 77,000. The shock in the vicinity of the throat can be clearly seen. The pressure distribution proved to be very insensitive with respect to variations to higher as well as the lower Reynolds number in Fig. 10. No separation could be detected. Thus, this type of airfoil shape and pressure distribution was employed in the two-stage turbine.

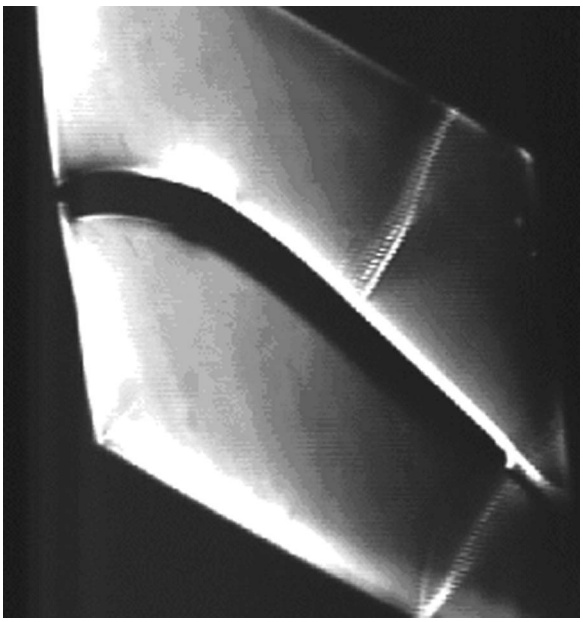

**Fig. 10 Cascade T133 Schlieren picture (density), $Re_{2th} \approx 65{,}000$; $Ma_{ex} > 1.0$; $Tu_{in} \approx 1.5\%$**

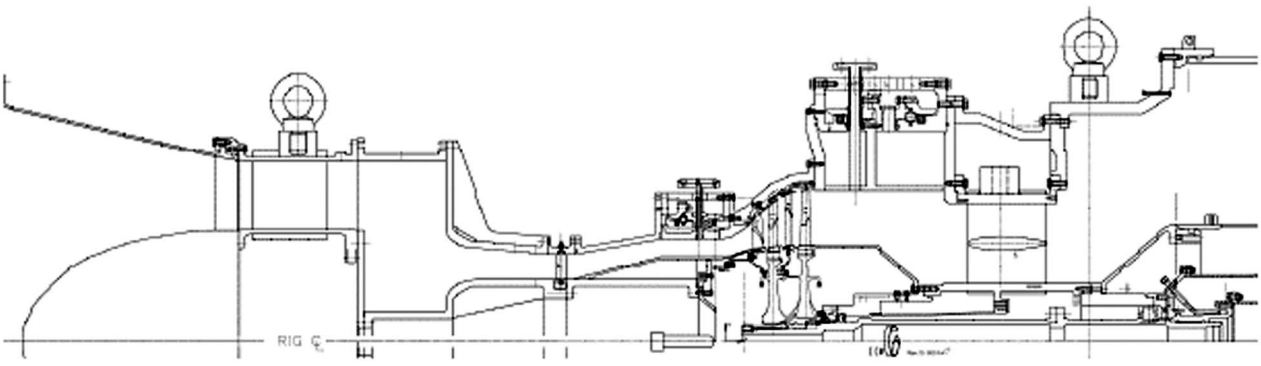

Fig. 11 Test facility with installed cold flow rig

## Coldflow Rig Tests

The two-stage test turbine was installed at the High Altitude Test Facility at the University of Stuttgart, Germany. The test rig is operated in a mode with a closed gas circuit in order to run the rig at Reynolds numbers typical for jet engines. The inlet and exit conditions can be separately adjusted to simulate different altitude levels and to cover the whole LPT map. Before the air enters the rig, the flow is homogenized in a large plenum chamber with an integrated flow rate nozzle. Figure 11 presents the installation in the test facility. The turbine power is transformed by a water brake.

In Fig. 12 a cross section of the test turbine is shown. To assess the inflow conditions, total pressure and temperature are measured in several radial and circumferential positions in the rig inlet duct. In the exit plane pressure and temperature probes with seven radial measurement positions are installed. Additionally, traversable five-hole probes were used to measure data for static pressure, total pressure, Mach number, and flow angles. The entire instrumentation in the rig exit plane is installed in a traverse gear and thus can be traversed circumferentially by two pitches of vane 2. Furthermore, vanes 1 and 2 are instrumented with pressure taps for wall pressure on the airfoil surfaces in three radial positions. Tests were conducted at different Reynolds numbers and LPT expansion ratios. Each condition includes a circumferential traverse over 1.2 pitches of vane 2.

As completion of the experiments the boundary layer flow was visualized with a color injection into the airflow. Therefore, injection pressure and viscosity had to be adjusted to the specific thermodynamic conditions of the gas flow. The injection was done for the reference Reynolds number.

**Test Results.** The coldflow rig has the geometry of the hot demonstrator component. The tests were carried out with an uncooled first stage (similarity of work-split, reaction, Mach number, Re number, etc., is realized by restaggering for the missing cooling flows).

In Fig. 13 the measured turbine map is displayed in terms of efficiency as a function of $\Delta H/T$ and speed. As can be obtained from this figure, the maximum efficiency is located exactly at the aero design point. For this point, the measured efficiency value is actually slightly above the prediction. The characteristics for higher pressure ratios shows no dramatic drop, so that mismatched engine conditions could be handled without operability problems. The off-design behavior also looks quite reasonable.

Since turbines not operating inside the normal design space pose high demands on the design system, the rig was also used to verify the prediction quality of the aero design tools. Some examples are discussed in the following section.

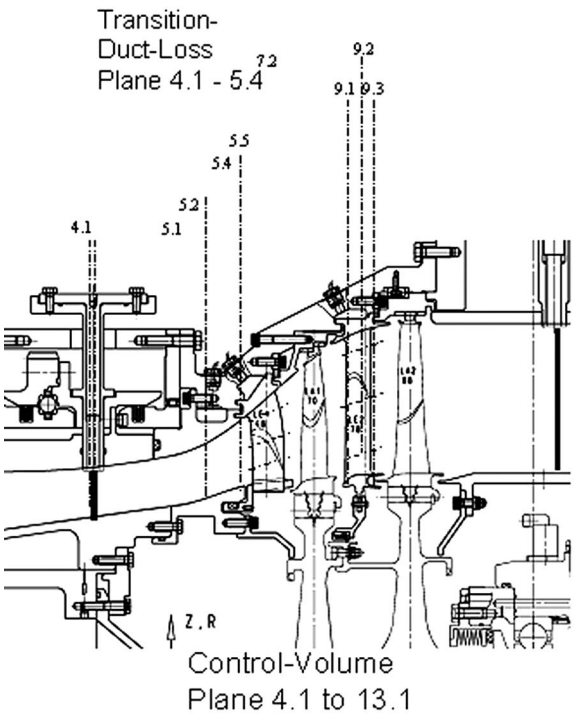


Fig. 12 Test rig with measurement positions

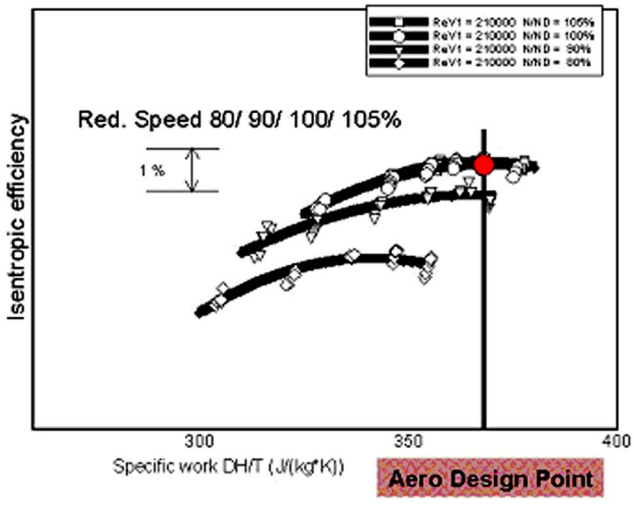


Fig. 13 Turbine characteristic for several speeds

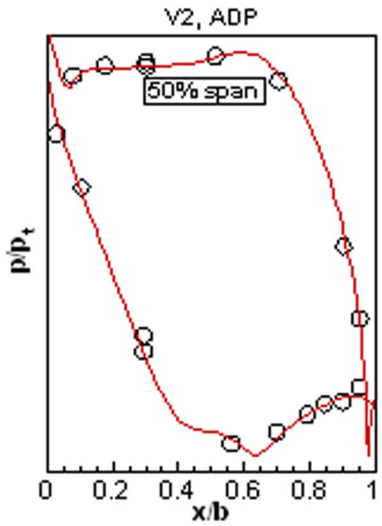


**Fig. 14 Pressure distribution on vane 2 mid-span**

In Fig. 14 the computed and measured pressure distributions are compared for the midsection of the second vane. The simulation agrees very well with the experimental data. Obviously the inflow conditions are captured as well as the boundary layer flow of the vane itself.

The flow at midspan is obviously fully attached (see also Fig. 15). The simulation slightly overpredicts the radial slope of the stream traces between 25% and 60% span. This is an indication that the computation predicts a thicker boundary layer than present in the experimental setup. The radial pressure gradient forces the slow boundary layer flow towards the hub, if the drag of the main flow is not strong enough to keep it on the ideal streamline. This indication of a slight boundary layer thickness overprediction is not critical, since it leads the aerodynamicist to a safe design.

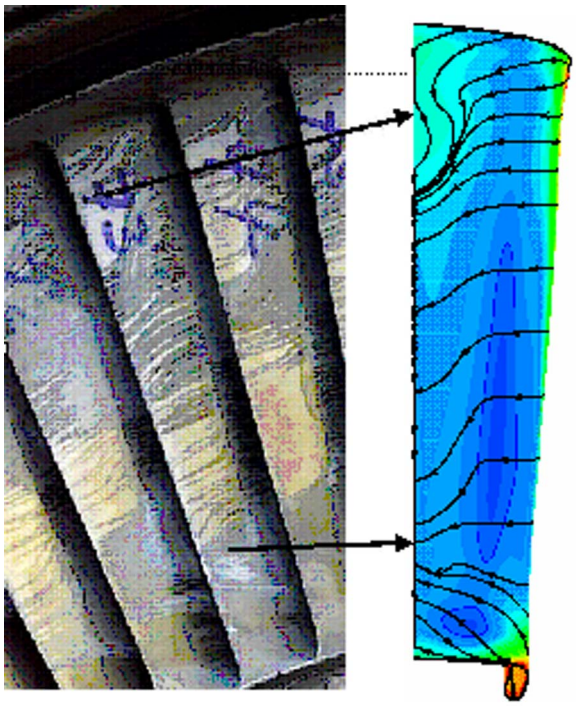

**Fig. 15 Flow visualization for second vane, comparison of color injection, and numerical simulation**

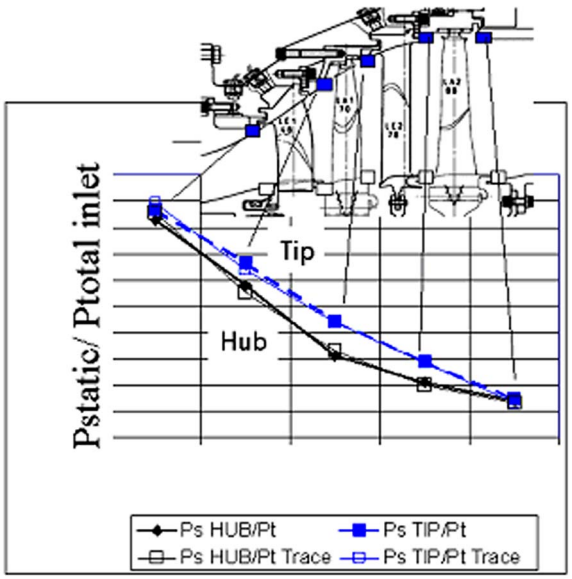


**Fig. 16 Normalized cavity pressures measurement versus 3D CFD**

Close to the hub the passage vortex system drives secondary flow up to about 20% span into the flow duct, which is quite well captured by the simulation. In the tip region, both Navier-Stokes computation and experiment exhibit a local separation zone in a region with interaction between the tip passage vortex and the main flow. Obviously, the separation in the test turbine is weak, since it differs between different airfoils.

In Fig. 16 the static duct pressures are displayed in order to check the work-split and reaction of the test turbine. The solid symbols characterize the measurement and the hollow symbols the simulation. Both agree well with each other. This gives confidence that no severe separations occur in the turbine and is verifying work-split and reaction.

Computations were performed for the ideal flow path (standard aero design procedure) and for the turbine geometry including the inner and outer air seals. A view of this numerical model can be seen in Fig. 17. It is setup using additional blocks for the cavities, which are connected to a main flow grid that uses the same parametrization as the standard computation (ideal flow path).

In Fig. 18 the radial distributions of the isentropic efficiency are shown. At midspan, both computations exhibit a very similar ef-

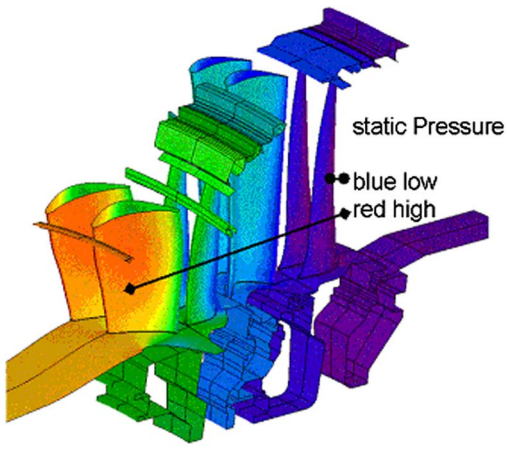


**Fig. 17 LP turbine 3D-CFD model including cavities**

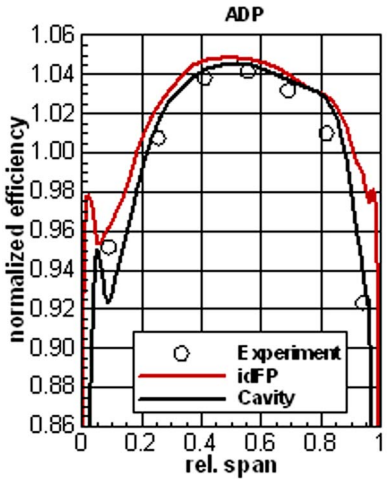


**Fig. 18 LP turbine component radial efficiency distribution with and without cavities (1 mm radial clearance)**

ficiency level, which also quite well corresponds to the experimental data. In the endwall regions, the ideal flow path computation overpredicts the efficiency. The cavity computation is closer to the measurement, because it captures additional loss mechanisms due to the presence of the cavities and the related leakage flows.

The data gathered for this test turbine show a good agreement between experiment and numerical simulation in terms of quantitative data as well as flow structure. This is of great importance for such designs, which reach beyond current experience.

## Conclusion

The high speed LPT is an key component for the geared turbofan concept. The LPT discussed in this paper is an exceptionally challenging turbine. Therefore, several investigation steps were taken in the aero design of this turbine. These steps are discussed in this paper.

In addition to the final, detailed investigations in a coldflow rig with engine-like dimensions, cascade tests were performed for two especially critical airfoil sections in order to check losses and boundary layer stability as well as the computation quality. Based on these results, the final airfoil design for the two-stage turbine was carried out.

The measurements inside the test turbine included efficiency level, the turbine characteristic, and profile pressure distributions. The results are very promising. In particular, the difficult combination of high Mach numbers and very low Reynolds numbers was shown as controllable. Very good turbine characteristics were measured in terms of the efficiency level, which turned out well above 90%, as well as the behavior in the turbine map. It was also shown that the MTU prediction tools are able to handle this turbine class. Taking the cavities into account showed a further improved prediction quality. These results represent an excellent base for the final definition for the PW800 engine and other similar products.

## Acknowledgment

The support for code development and validation as well as experimental and numerical investigation of the turbine rig through the German Ministry of Education and Research under the E3E 2 program is gratefully acknowledged. The numerical code TRACE used in this investigation was jointly developed by MTU Aero Engines and the Institute for Propulsion Technology of the German Aerospace Research Establishment (DLR). The authors further would like to thank UniBw Munich for their help in manufacturing the cascades and performing part of the experiments.

## Nomenclature

$c$, $c_{ax}$ = true chord, axial chord
$h$ = blade height
$h/b_{ax}$ = aspect ratio
$Ma_{is}$ = isentropic Mach number
$p$, $p_t$ = static pressure, total pressure
$u$ = circumferential velocity
$\Delta H/u^2$ = aeroloading parameter
$\Delta H/T$ = specific work ($J/(kg\,K)$)
$C_m/u$ = velocity ratio
$Re_2$ = Reynolds number with chord
$s/c$ = pitch/chord ratio
te, le = trailing/leading edge
$A$ = LPT gas path exit area: $A = Pi^*(D_{od}^2 - D_{id}^2)$
ADP = aerodynamic design point
ATFI = advanced technology fan integrator
CFTR = cold flow test rig
ER = expansion (pressure) ratio
HPT = high pressure turbine
idFP = ideal flow path
ID = inner diameter
ITD = interturbine duct
LPT = low pressure turbine
N = turbine speed (RPM)
OD = outer diameter
TEC = turbine exit casing

## References

[1] Broichhausen, K., Malzacher, F., and Niehuis, R., 1990, "Schnelllaufende Niederdruckturbinen für Neuzeitliche Antriebe," *Deutscher Luft—und Raumfahrtkongress/DGLR Jahrestagung*, October 1–4, Friedrichshafen, DGLR Paper No. 90-104.
[2] Niehuis, R., and Rued, K., 1997, "Entwicklung Schnelllaufender Niederdruckturbinen für Künftige Wirtschaftliche und Umweltschonende ADP Triebwerke," September, München, Germany.
[3] Rüd, K., Henrich, E., Westphal, V., and Hain, K., 2001, "Entwicklung und Bereitstellung Einer Hochbelasteten Schnelllaufenden Niederdruckturbine für die Erprobung in Einem Demonstratortriebwerk," *DGLR Jahrestagung*.
[4] Sturm, W., and Fottner, L., 1985, "The High-Speed Cascade Wind Tunnel of the German Armed Forces University Munich," 8th Symposium on Measuring Techniques for Transonic and Supersonic Flow in Cascades and Turbomachines, Genua.
[5] Gier, J., Ardey, S., and Heisler, A., 2000, "Analysis of Complex Three-Dimensional Flow in a Three-Stage LP Turbine by Means of Transitional Navier-Stokes Simulation," ASME Paper No. 2000-GT-645.
[6] Gier, J., Ardey, S., Eymann, S., Reinmöller, U., and Niehuis, R., 2002, "Improving 3D Flow Characteristics in a Multistage LP Turbine by Means of Endwall Contouring and Airfoil Design Modification, Part 2: Numerical Simulation and Analysis," ASME Paper No. GT-2002–30353.

**Toyotaka Sonoda**
Honda R&D Co. Ltd.,
Aircraft Engine R&D Center,
Saitama 351-0193,
Japan

**Toshiyuki Arima**
Honda R&D Co. Ltd.,
Wako Research Center,
Saitama 351-0193,
Japan

**Markus Olhofer**

**Bernhard Sendhoff**

Honda Research Institute Europe GmbH,
63073 Offenbach,
Germany

**Friedrich Kost**

**P.-A. Giess**

Institute of Propulsion Technology,
German Aerospace Center (DLR),
D-37073 Goettingen,
Germany

# A Study of Advanced High-Loaded Transonic Turbine Airfoils

*The development of high-performance turbine airfoils has been investigated under the condition of a supersonic exit Mach number. In order to obtain a new aerodynamic design concept for a high-loaded turbine rotor blade, we employed an evolutionary algorithm for numerical optimization. The target of the optimization method, which is called evolutionary strategy (ES), was the minimization of the total pressure loss and the deviation angle. The optimization process includes the representation of the airfoil geometry, the generation of the grid for a blade-to-blade computational fluid dynamics analysis, and a two-dimensional Navier-Stokes solver with a low-Re* k-ε *turbulence model in order to evaluate the performance. Some interesting aspects, for example, a double shock system, an early transition, and a redistribution of aerodynamic loading on blade surface, observed in the optimized airfoil, are discussed. The increased performance of the optimized blade has been confirmed by detailed experimental investigation, using conventional probes, hotfilms, and L2F system.* [DOI: 10.1115/1.2221325]

## Introduction

The target of a blade designer for turbine and/or compressor airfoils in gas turbine engines is to produce blade shapes that have low losses at the design flow conditions. Furthermore, minimal losses should also be obtained for a wide range of blade operating conditions, like incidence, Mach number, and Reynolds number.

In general, turbine airfoils have very thick, blunt trailing edges, as compared with those of compressor airfoils. In subsonic flow the trailing edge loss of the turbine airfoil is usually small compared to the boundary layer losses and it is often neglected for airfoils with thin trailing edges. However, it is well known that with increasing exit Mach number toward unity, the loss coefficient rises sharply and the base pressure falls together with the complex shock pattern formed around the trailing edge [1]. The loss usually continues to rise with the Mach number for low supersonic flow, but may level off and decrease at high exit Mach numbers for some types of blades [2]. It is also known that the trailing edge loss increases roughly linearly with trailing edge blockage and as a result becomes more important for thick trailing edges and/or high solidity blades, like a hub section in rotor blades.

The pressure side shock just downstream of the trailing edge will propagate toward the suction surface of the adjacent blade and may have a large effect on its pressure distribution and on the loss due to the shock-boundary layer interaction together with two reflected shocks through the generation of a separation bubble [3]. The generation of the bubble seems to be strongly related to the boundary layer property just upstream of the interaction point [3,4]. Also, the suction side shock may lead to a strong distortion of the static pressure for a downstream cascade.

Although the *basic* flow pattern of the transonic turbine is well understood, it is interesting and challenging to develop a new design concept for the further advancement of high-loaded transonic turbine airfoils. One approach to find new design concepts is to use modern numerical, global optimization techniques like evolutionary computation. The advantages of these methods are that they are able to identify a search direction in the huge parameter space, they are able to escape local optima, they do not require an analytical quality function, and they can operate successfully on noisy quality functions. Evolutionary algorithms have also been shown to produce robust solutions, i.e., solutions whose performance does not or only slightly deteriorate for variations of design conditions. Some papers on the two-dimensional (2D) optimization of compressor airfoils have been published [5,6]. However, hardly any literature can be found on the optimization of 2D turbine cascades. Shelton et al. [7] minimized the downstream shock strength in order to generate a more homogeneous flow field in the downstream blade row. However, the total pressure loss for the optimized airfoil is about 25% greater than the loss for the baseline airfoil, although the suction side shock strength is reduced as compared to the baseline case. Furthermore, their emphasis in the paper is on the application of their optimization techniques rather than on the physical details of the resulting blade design.

In this paper, we discuss the optimization results of the evolutionary strategy applied to a rotor hub section with a high trailing edge blockage for a high-loaded single stage turbine. The baseline airfoil cross section used in this research and the design parameters are shown in Fig. 1 and Table 1.

Contributed by the International Gas Turbine Institute (IGTI) of ASME for publication in the JOURNAL OF TURBOMACHINERY. Manuscript received October 1, 2003; final manuscript received March 1, 2004. IGTI Review Chair: A. J. Strazisar. Paper presented at the International Gas Turbine and Aeroengine Congress and Exhibition, Vienna, Austria, June 13–17, 2004, Paper No. 2004-GT-53773.

  

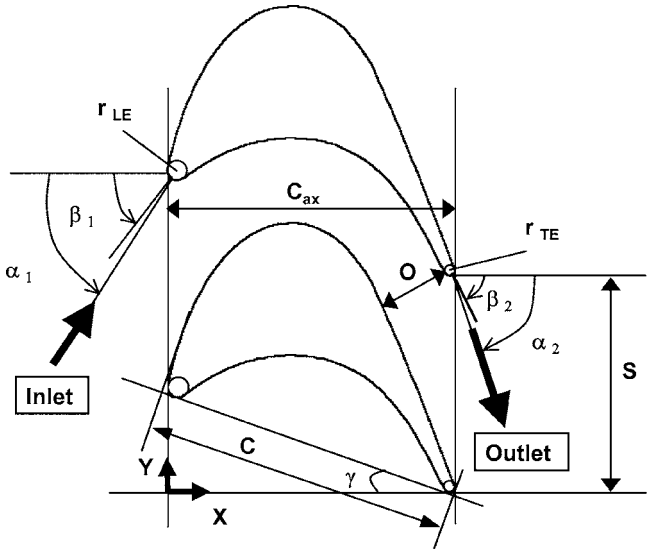


**Fig. 1 Baseline airfoil geometry and cascade parameters**

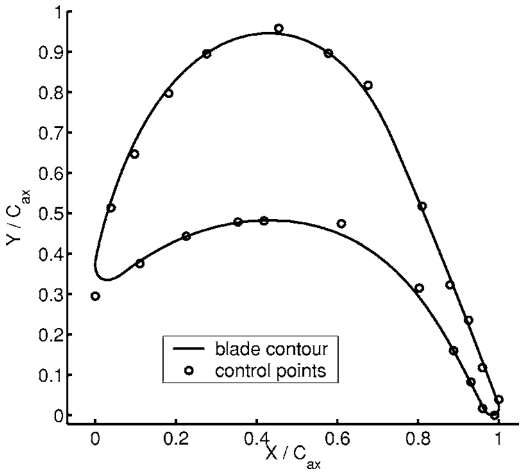


**Fig. 2 B-spline and initial blade**

This airfoil is designated the baseline (HL: high loaded) airfoil. The design outlet isentropic Mach number is 1.20 and the design outlet angle is 70 deg. The flow turning angle is 135 deg. The solidity and the throat blockage are about 1.4 and about 16%, respectively. They are higher than previously published ones [8,9]. The objective of the presented paper is to demonstrate the superior performance of the optimized turbine airfoils and to elucidate the reason of the higher performance, for which both extensive experimental tests as well as high-precision computational fluid dynamics (CFD) analysis are discussed.

## Design Approach

**The Evolutionary Algorithm.** Evolutionary algorithms belong to the class of global stochastic optimization algorithms. They are inspired by the principles of biological evolution and are based on a cyclic (generational) organization of the processes of reproduction, variation, and selection in a population of individuals, i.e., here designs of a blade shape.

In this paper, we use a special type of evolutionary algorithms called evolutionary strategy, where the process of variation is realized by adding normally distributed random numbers to the parameters that define the blade shape. Starting from a so-called parent population, offsprings are generated by randomly choosing individuals from the parent population and copying them to the offspring population until all λ individuals in this population are initialized. Thereafter, a normally distributed random vector is added to the parameter set of all offsprings, which are evaluated. Finally, the best $\mu$ individuals are selected to form the parent population of the following generation. The standard deviation of the normal distribution controls the width of the search and is itself subject to variations during the search. This principle of adaptation of the search width to the topology of the search space is referred to as *self-adaptation*. In this paper, we use the CMA (covariance matrix adaptation) method [10] for which the full covariance matrix of the normally distributed random vector is adapted. This allows the adaptation of the search direction independently from the chosen coordinate system of the search space, in other words correlations between design parameters can be taken into account during the search process. This method is known to have a high-convergence rate resulting in a reasonable overall calculation time. The presented blade geometry is the result of a strategy with $\mu=1$ parent individual and $\lambda=12$ offspring individuals in each population.

**Table 1 Design parameters of baseline (HL) cascade**

| Aerodynamics | | Geometry | |
|---|---|---|---|
| $Ma_{2is}$ | 1.2 | $C$ (mm) | 60 |
| $\alpha_2$ (deg) | 70 | $C_{ax}$ (mm) | 55.687 |
| $\alpha_1$ (deg) | 65 | $\beta_1$ (deg) | 58 |
| Turning angle (deg) | 135 | $\beta_2$ (deg) | 66.51 |
| | | $\gamma$ (deg) | 19.3 |
| | | $C/S$ | 1.413 |
| AVDR | 1.0 | $r_{TE}/C$ (%) | 1.76 |
| $Re_2$ | $\approx 9\times10^5$ | $2r_{TE}/O$ (%) | 15.4 |

**The Blade Profile Definition.** We encode the blade cross section by a third-order B spline. The control points and the resulting curve that represents the cross section of the blade are shown in Fig. 2. The circles show the control points of the third-order B spline; the solid line shows the resulting spline that describes the cross section of the blade. The number of control points is fixed to $p=23$ points. Each point is represented by its Cartesian coordinates. The dimension of the resulting parameter set, which is optimized, is therefore $n=46$. The initial set of control points for both optimizations is shown in Fig. 2. The 46 design parameters are stored in a vector, which is called a chromosome of an individual in the context of evolutionary computation.

**The Quality Function.** In order to evaluate the quality of each set of 46 design parameters, the spline curve is built out of the control points in the first step. In the next step, the geometric properties of the described cross section are calculated and used to determine whether the geometric constraints of the optimization are satisfied. Afterward, the aerodynamic properties are calculated using the Navier-Stokes flow solver, see the next section. The overall quality is then calculated by a weighted sum of the total pressure loss $\omega$, the deviation of the outflow angle from the target angle, and a penalty value in case the trailing edge thickness $r_{TE}$ is below a given minimal value. Therefore, the overall quality value $f$ is given by

$$f = \sum_{i=1}^{3} w_i t_i \rightarrow \text{minimize}$$

where the $w_i$ are weighting coefficients, which are fixed heuristically, and the $t_i$ are given as follows:

$$t_1 = \max(0, |\alpha_2 - \alpha_{2,\text{design}}| - \delta\alpha)$$

$$t_2 = \omega$$

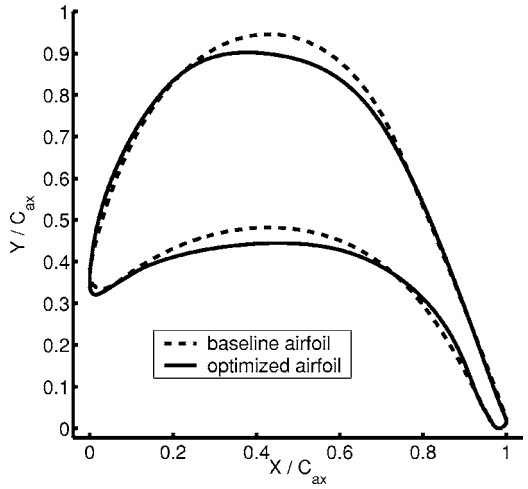


**Fig. 3 Baseline (HL) and optimized (ES) airfoil geometries**

$$t_3 = \max(0, r_{\text{TE,design}} - r_{\text{TE}})$$

The target outflow angle is given by $\alpha_{2,\text{design}}$, the tolerance range for the deviation is $\delta\alpha = 0.3$, and the minimal allowed radius of the trailing edge is given by $r_{\text{TE,design}} = (0.0176 \times \text{chord length})$.

The result of the optimization after about 130 generations of the algorithm is shown in Fig. 3. The optimized airfoil will be denoted in the following by "optimized ES" or in short by "ES." The stagger angle for the ES is slightly reduced by 1 deg and the maximum curvature point on the sunction side (SS) is significantly shifted toward the front side (from 40% to 25% of axial chord position). It is also interesting that the curvature around the middle part of the pressure side (PS) is slightly lower, while the shape between 75% and 90% of the axial chord position is slightly indented (compared to the HL blade). We can see the locally high concave curvature near the trailing edge. A redistribution of aerodynamic loading on the blade surface seems to be realized by the optimized ES airfoil.

**The Navier-Stokes Solver.** For the numerical analysis, a quasi-three-dimensional (Q3D) version of the Navier-Stokes flow solver HSTAR (Honda software for turbomachinery aerodynamics research) with a low Reynolds $k$-$\epsilon$ turbulence model proposed by Chien [11] has been used. The HSTAR Q3D solver was developed by Honda R&D, it is a modified 3D Navier-Stokes code for the purpose of calculating the aerodynamic performance of 2D cascades [12]. Two types of simulations were carried out. One for the evaluation of the airfoil geometries during the optimization and one for the detailed analysis of the flow physics after optimization. The axial velocity density ratio (AVDR) is set to one for all computations. The computational grids used in analyzing the flow physics are shown in Fig. 4. The grid consists of $541 \times 71$ cells, which is much finer than the one used in the optimization process ($191 \times 55$). The average $y+$ of the first grid point from the wall is about 0.5 for all calculations. In order to obtain a high resolution of the shock-boundary layer interaction, 200 cells are arranged on the suction surface and 100 cells on the pressure surface. This cell arrangement results in grid orthogonality in the uncovered region which is an important requirement for a CFD grid for the analysis of shock boundary layer interaction.

## Experimental Approach

**The Windtunnel for Straight Cascades (EGG).** The experiments reported in this paper were performed in the windtunnel for straight cascades at DLR Goettingen. The facility is of the blow-down type with an atmospheric inlet. Downstream of the cascade, the flow passes an adjustable diffuser and the main butterfly valve

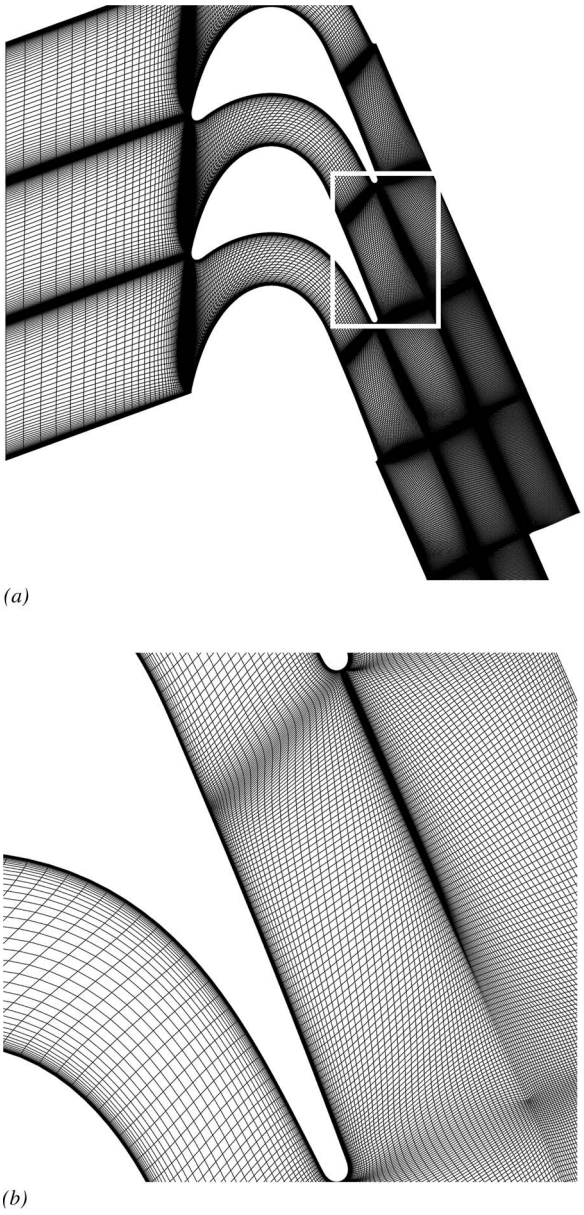

*(a)*

*(b)*

**Fig. 4 Computational grid used in numerical analysis: (*a*) overall; (*b*) enlargement**

and finally enters a large vacuum vessel (10,000 $m^3$). The Reynolds number cannot be varied independently, but is a function of the Mach number which is set by the adjustable diffuser. The cascade is mounted between two circular disks establishing the side walls of the flow channel. The inlet angle is adjusted by turning this assembly. The test section dimensions are ($380 \times 125$) $mm^2$, which allowed the cascade of the present tests to consist of 15 blades. The installed cascade had at least 14 blades within the flow. The periodicity was checked for ten pitches in subsonic flow and for six pitches at design Mach number of 1.2. A good periodicity has been achieved for all these measurements. Therefore, the wake measurements for the optimization condition were carried out over three pitches. More details on the windtunnel setup are available to the interested reader.[1]

**The Surface Pressure and Probe Measurements.** For surface pressure distribution measurements one of the blades mounted in

[1] http://www/dlr/de/at

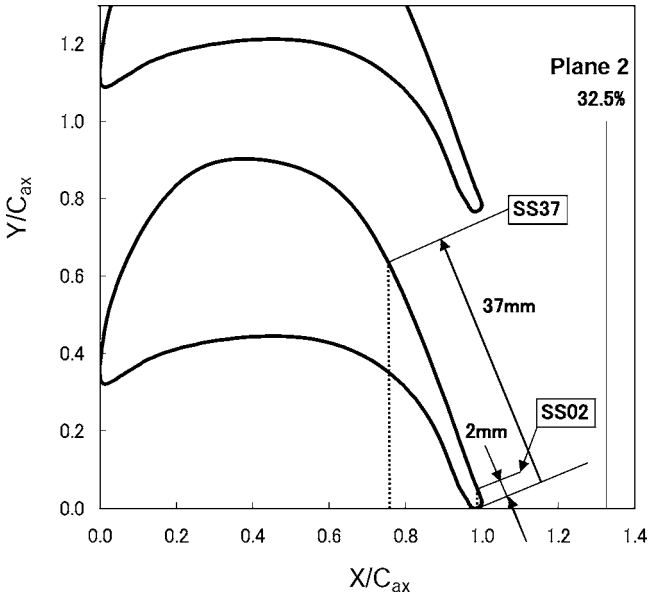


**Fig. 5 Measurement planes inside cascade and downstream**

the cascade center was substituted by an instrumented blade equipped with 30 pressure tappings. In order to determine the performance of the cascade, the wake flow was measured by traversing a wedge type probe far behind the cascade. From the data on the local inhomogeneous flow in the traverse plane, the properties of the equivalent homogeneous (mixed out) outlet flow are obtained by applying the equations of conservation of mass, momentum, and energy [13]. Inside the blade channels a flattened Pitot probe was used with a probe head size of 0.25 mm $\times$1 mm, enabling measurements in the boundary layers close to the blade surface. The measurement planes are shown in Fig. 5.

In the case of laser velocimetry by laser-two-focus (L2F) and Pitot-pressure measurements in the same plane, the L2F results (local Mach number and flow angle) and the Pitot pressure could be combined to obtain local flow data in the same way as from the wedge probe. Whereas, due to the size of the probe, reliable wedge probe measurements could be performed only further downstream, the combination of L2F and Pitot-pressure measurements allowed for investigations inside the cascade.

Pressures are measured with an accuracy of 0.1%, but to convert probe pressures into flow values a calibration is needed. Furthermore, the periodicity of the cascade flow suffers from reflected shocks in supersonic flow. Accordingly, the final accuracy of the measured flow data is only 1–2% for the Mach number and 0.5% for the loss.

**The Laser-Two-Focus Measurement Technique.** The measurement principle of L2F is rather simple. The L2F-measuring device generates two highly focused light beams in the probe volume which act as a "light gate" for tiny particles in the flow. The scattered light from the particles provides two successive pulses and from the time interval between the pulses the velocity perpendicular to the laser beams can be derived [14]. The two foci of the used L2F device have diameters of 8 $\mu$m and their separation is 210.8 $\mu$m. In order to increase the data rate, the flow has to be seeded. The necessary particles are oil droplets of 0.3 $\mu$m diameter which are produced by a special seeding generator and injected into the flow in the settling chamber.

At DLR Goettingen the laser-two-focus technique (L2F) is routinely applied to acquire flow field information for cascade and turbomachine flows [15]. The system measures 2D vectors of the fluid velocity. The present laser measurements were analyzed and the experimental uncertainties (on a 95% confidence level) were determined: The error bar for the Mach number was 0.003 outside the wakes and 0.006 inside. The error bar for the flow angle was 0.2 deg outside the wake and 0.4 deg inside.

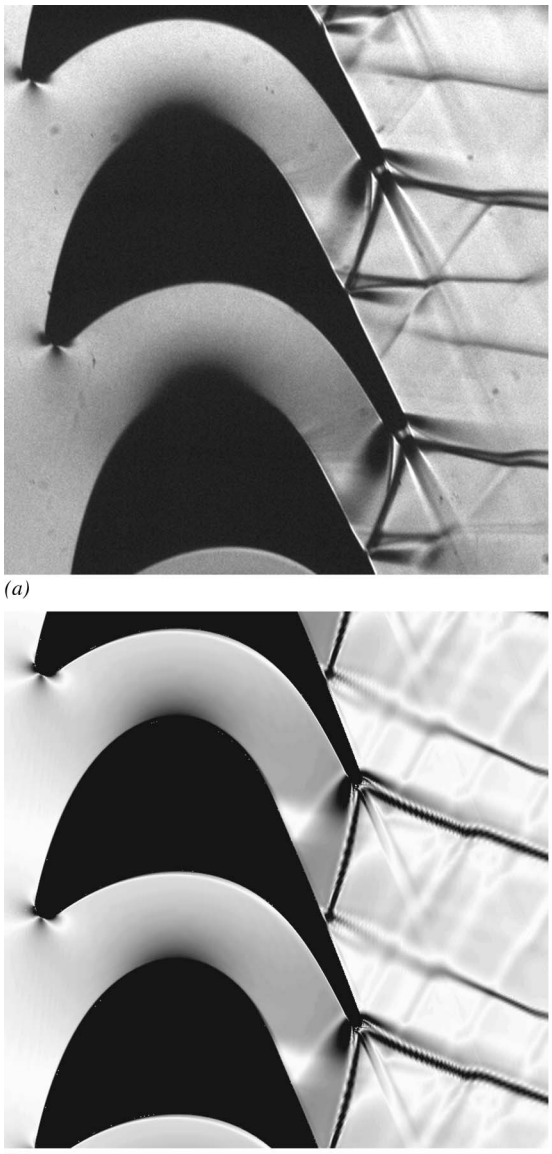


**Fig. 6 Schlieren photo of baseline cascade (HL) at $Ma_{2is}$=1.2, $\alpha_1$=65 deg: (*a*) EXP; (*b*) CFD**

## Validation of Design and Discussion

This presentation of the experimental (EXP) and/or numerical results (CFD) concentrates on the transonic case with isentropic exit Mach number $Ma_{2is}$=1.2, although a wide range of Mach numbers were investigated.

**The Flow Pattern for Baseline (HL) and Optimized (ES).** A qualitative view of a two-dimensional transonic flow field can be gained by Schlieren pictures which visualize the density gradients. Schlieren photos make shocks, wakes, and separation zones visible as well as regions of flow deceleration and acceleration. Figure 6 displays the experimental/numerical flow fields of cascade HL.

In Fig. 6(*a*), i.e., for the HL experiment, the conventionally designed blade HL shows one shock originating at the trailing edge of the neighboring blade, which impinges onto the suction side and is reflected as two shocks. This is a strong indication that

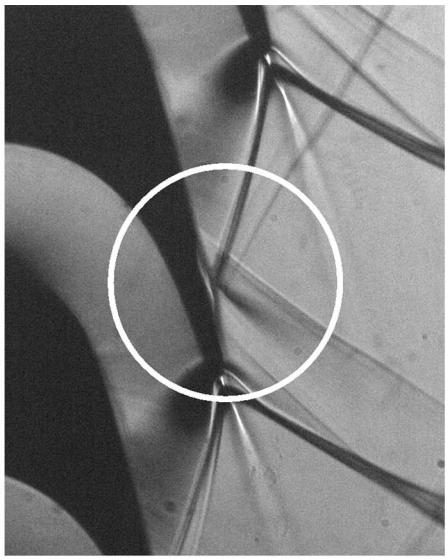

(a)

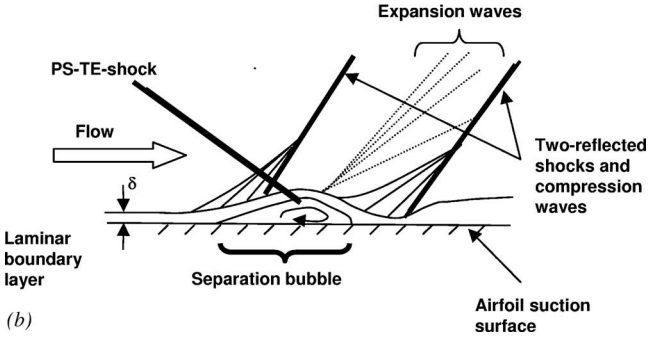


(b)

**Fig. 7 Generation of separation bubble by a shock boundary layer interaction at $Ma_{2is}=1.5$, $\alpha_1=65$ deg: (*a*) Schlieren photo near impingement; (*b*) schematic figure of a shock/boundary layer interaction**

a rather long separation bubble has been caused by the impinging shock [2]. Figure 7 shows the experimentally observed separation bubble near the impingement and a schematic figure of shock/boundary layer interaction. In order to better visualize the bubble (without changing the interaction), the Mach number for the Schlieren photo in Fig. 7(*a*) is higher than the one in Fig. 6(*a*). Such a long separation bubble may only exist if the upstream suction side boundary layer is still laminar. As shown in Fig. 6(*b*), CFD shows a similar pattern as EXP, but the two reflected shocks near the interaction point are not captured.

In the optimized airfoil (ES), an additional shock pattern is observed experimentally and numerically around just upstream of the trailing edge (TE) on the PS. Therefore, a double shock pattern is generated, as shown in Figs. 8(*a*) and 8(*b*). Figure 9 shows the reason why the second shock is induced for the optimized ES blade. There is a dimple near the trailing edge (TE) on PS. The depth of the dimple is very small (about 100 $\mu$m), while the manufacturing precision is about 20 $\mu$m. Due to the small dimple, the Mach number distribution near the TE on PS is significantly controlled to have a weaker TE shock. That is, the continuous increase of the Mach number toward the TE on PS is suppressed by the second shock that is generated around the dimple. Therefore, the Mach number from point A to point B is decreased. As a result, the absolute Mach number at point C, related to the strength of TE shock on PS, is decreased. One of the design concepts of the ES blade is to produce such a double shock system or multishock system just upstream of TE on PS. Additionally, there is a region of deceleration on the suction side upstream of the

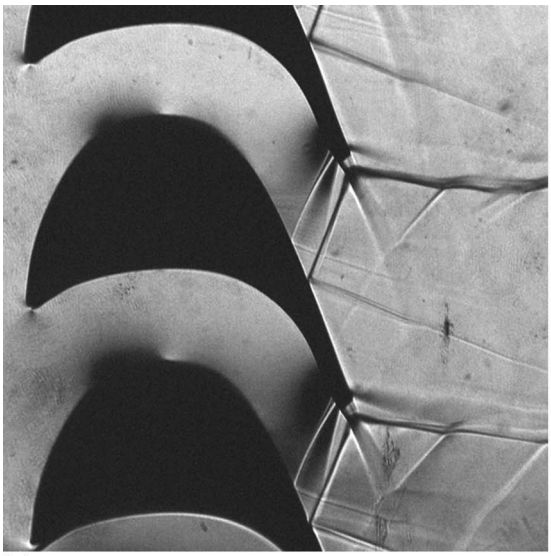

(a)

(b)

**Fig. 8 Schlieren photo of optimized cascade (ES) at $Ma_{2is}=1.2$, $\alpha_1=65$ deg: (*a*) EXP; (*b*) CFD**

throat (the white patch on the uppermost part of the suction side contour in Fig. 8(*a*)). The role of this "region of deceleration" will become clearer in the section "The Airfoil Surface Mach Number." Each shock impinging on the suction side gives rise to only one reflected shock, a clear hint that there is no separation bubble and that the boundary layer approaching the shock ought to be turbulent. In CFD, the double shock system is also captured. Overall there is a good qualitative agreement between EXP and CFD, see Fig. 8(*b*).

**The Airfoil Surface Mach Number.** Figure 10 shows the airfoil surface Mach number distributions for HL and ES airfoils at the design inlet flow angle of 65 deg. There are four interesting points for the optimized airfoil. First, the ES blade has a decelerated region in the front part of SS, as already shown in Fig. 8(*a*). The gradient seems to be small, but the decelerated region can be clearly identified by coupling EXP with CFD, as shown in Fig. 11. This decelerated region may lead to an early boundary layer transition for the ES blade. Second, the bubble around 85% of the axial chord for the HL blade cannot be observed for the optimized ES blade. Third, the ES blade has a smaller Mach number absolute level (i.e., higher-base pressure) on the pressure surface near

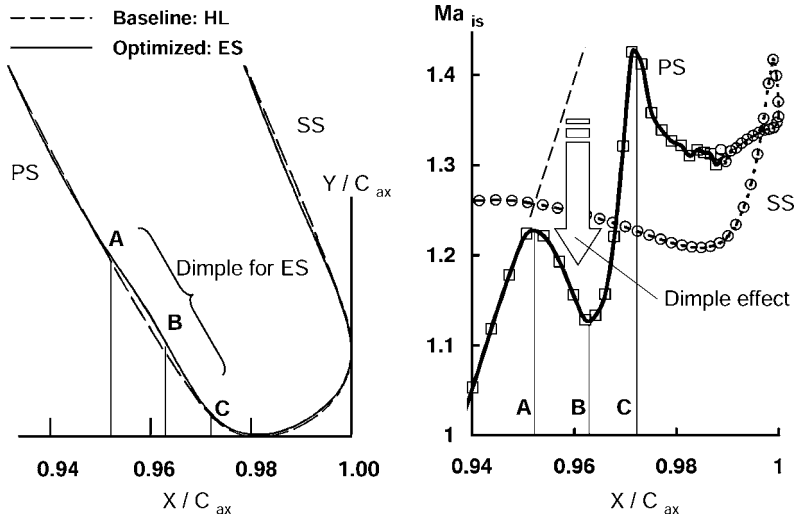


**Fig. 9 Computed effect of dimple on airfoil surface Mach number distribution for optimized cascade (ES) at $Ma_{2is}=1.2$, $\alpha_1=65$ deg**

the trailing edge compared to the HL blade. This may lead to a small trailing edge loss as well as to a weak shock generated at the pressure side just downstream of the trailing edge. Finally, a low-speed region is significantly extended toward downstream on the pressure surface. This is due to the locally high-concave curvature near the trailing edge, as already shown in Fig. 3.

Figure 11 shows the effect of the inlet flow angle on the surface Mach number distribution for both HL and ES airfoils, experimentally and numerically. There is a reasonably large discrepancy in the front part of the airfoil between EXP and CFD. This is due to the difference of AVDR between EXP (AVDR $\approx$ 0.90) and CFD (AVDR=1.0). In the case of the ES blade, EXP and CFD clearly show the decelerated region from about 30% to 50% of chord length, as already described above. As a result, the boundary layer transition can be observed for the ES blade. Thus, there seems to be no bubble for three inlet flow angles. The clearer flow patterns around the uncovered region on SS for the HL and ES blades are shown in Figs. 12 and 13, respectively. We can see that there is a bubble between 85% and 90% of the axial chord position for two inlet flow angles of 55 deg and 65 deg for the HL blade. In the case of a very positive incidence angle (the inlet flow angle is 70 deg) the boundary layer transition can be observed due to the high deceleration in the front part for the HL blade. In the case of the ES blade, the boundary layer is already turbulent (see Fig. 13).

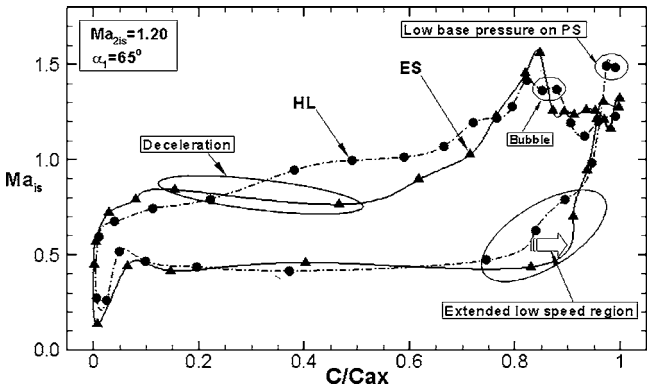


**Fig. 10 Measured airfoil surface Mach number distribution for baseline (HL) and optimized (ES) at design conditions at $Ma_{2is}=1.2$, $\alpha_1=65$ deg**

**The Boundary Layer Property.** It is highly probable that the transition of the boundary layer on the suction side took place in the mentioned deceleration region of the ES blade. This can be confirmed by the results of hot-film measurements displayed in Fig. 14. Here the normalized (mean) voltage shows a deep depression at suction surface length 42 mm and at the same position a peak can be observed in the rms value. These features are the footprint of a separation bubble that causes the boundary layer transition. We also note that the second peak of the rms value and the depression of voltage at suction surface length 84 mm mark the impingement of the main trailing edge shock onto the suction

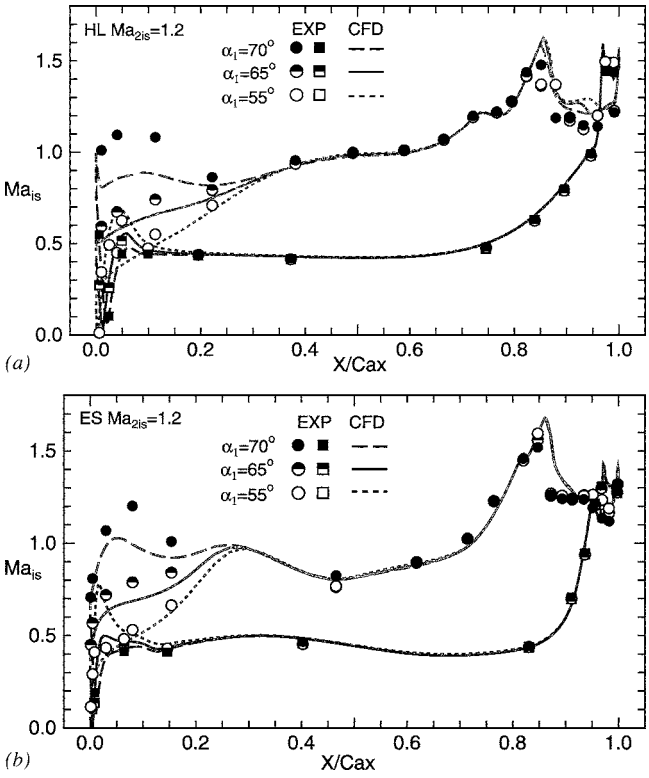


**Fig. 11 Comparison of CFD with EXP for airfoil Mach number distribution at $Ma_{2is}=1.2$: (*a*) baseline (HL); (*b*) optimized (ES)**

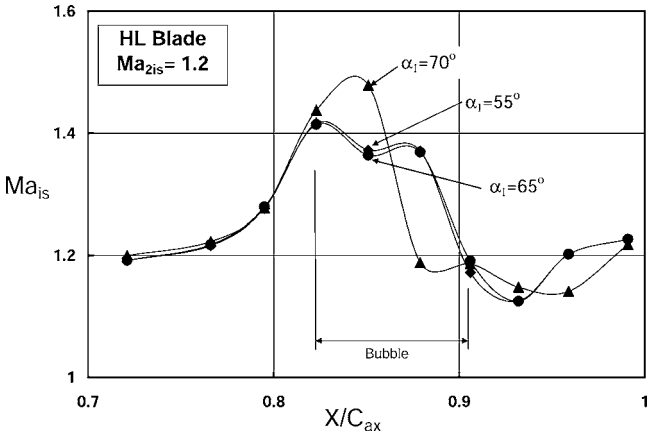


**Fig. 12 Measured suction surface Mach number distribution around uncovered region for baseline HL airfoil at $Ma_{2is}=1.2$**

side of the ES blade.

These different features of the ES blade compared to the HL blade result in a different development of the blade boundary layers and accordingly in different friction losses. Because of the much higher velocity on the suction side compared to the pressure side, the losses are mainly generated at the suction side. At design Mach number $Ma_{2is}=1.2$ the shock and the trailing edge losses should be already of more importance than the friction losses.

In Table 2 a comparison of the measured boundary layer thicknesses at suction side is presented. The two positions where results are shown are upstream of the shock impingement (SS-37) and 2 mm upstream of the trailing edge (SS-02). We can briefly summarize the observations as follows: At both positions the HL blade clearly shows the thinner boundary layer and accordingly the lower friction loss. The same conclusion can be drawn from

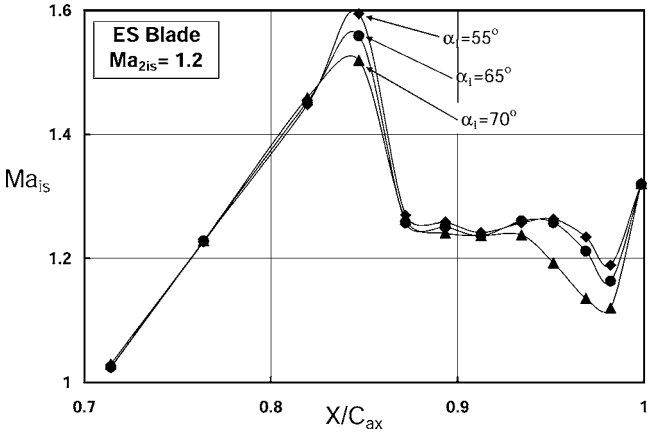


**Fig. 13 Measured suction surface Mach number distribution around uncovered region for optimized ES airfoil at $Ma_{2is}=1.2$**

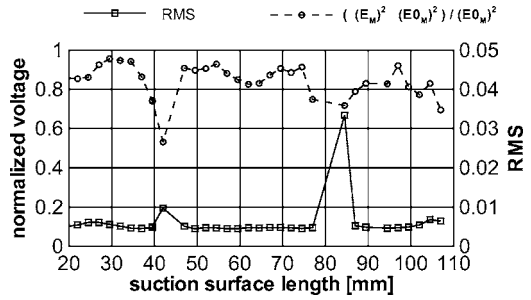


**Fig. 14 Hot-film measurements along the suction surface of optimized ES airfoil at $Ma_{2is}=1.2$, $\alpha_1=65$ deg**

**Table 2 Boundary layer thickness on SS at $Ma_{2is}=1.2$, $\alpha_1=65$ deg**

| | X/Cax | $\delta$ (mm) | |
|---|---|---|---|
| | | HL | ES |
| SS-37 | 0.759 | 0.211 | 0.820 |
| SS-02 | 0.993 | 0.921 | 2.126 |

Figs. 15 and 16 where the measured total pressure is displayed. In the vicinity of the suction side, the HL blade has a thinner boundary layer than the ES blade.

**The Total Pressure Loss.** In Fig. 15, the total pressure loss is close to zero outside the suction side boundary layer but rises sharply when approaching the wake (the plane SS-37 passes the trailing edge of the neighboring blade at a distance of 2 mm). Blade HL generates the bigger trailing edge loss compared to the ES cascade, although trailing edge thickness is very similar for the

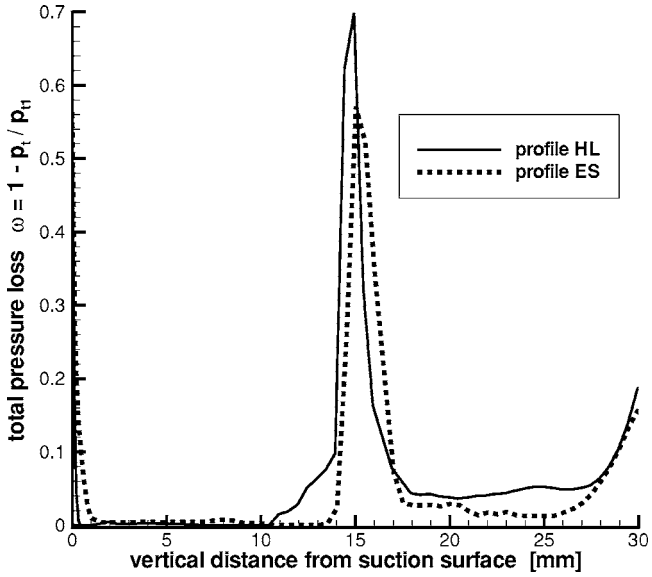


**Fig. 15 Measured total pressure loss coefficient in plane SS-37 at $Ma_{2is}=1.2$, $\alpha_1=65$ deg, $x/C_{ax}=0.759$**

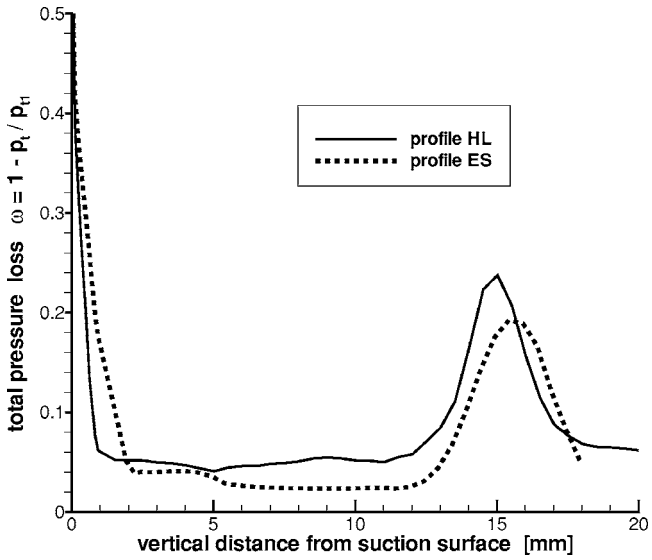


**Fig. 16 Measured total pressure loss coefficient in plane SS-02 at $Ma_{2is}=1.2$, $\alpha_1=65$ deg, $X/C_{ax}=0.993$**

two blade geometries. This is probably due to the Mach number reduction (maybe the base pressure for the ES blade is increased) at the trailing edge on the pressure side, as already shown in Fig. 10. This is related to the trailing edge of the ES blade: "a locally high concave curvature" and "a small dimple," as shown in Figs. 3 and 9, respectively. These specific shape properties have a positive influence. The total pressure loss from plane SS-37 to plane SS-02 (Fig. 16) between boundary layer edge and wake is caused by the shocks. Comparing these shock losses the HL cascade is worse than the ES cascade. The results of plane SS-02 further confirm that the trailing edge loss is bigger for the HL blade.

The mixed out flow losses downstream of the cascades were obtained from the wedge probe measurements. Therefore, they are independent of the measurements shown in the upper figures. The energy loss is derived from enthalpy and defined according to Horlock [16]. The results show that the energy loss of the ES cascade is smaller than the one of the baseline HL cascade. The improvement is about 12% (not shown here) at $Ma_{2is}=1.2$.

## Conclusions

An evolutionary optimization method, namely, evolutionary strategy, was applied to the design of a high-turning transonic turbine airfoil at supersonic exit Mach number of 1.20 together with a Navier-Stokes solver with Chien's low Reynolds $k$-$\varepsilon$ turbulence model. Furthermore, the aerodynamic characteristics for the baseline airfoil called HL and the optimized airfoil called ES were analyzed numerically as well as experimentally. The following conclusions can be drawn.

1. The superior performance of the optimized airfoil with 12% of energy loss reduction is gained at design exit isentropic Mach number of 1.2.
2. For the optimized airfoil, the trailing edge loss and the shock loss are improved, although the friction loss is worse than for the baseline. This means that the shock and trailing edge losses should be of higher importance than the friction loss in transonic turbine cascades. From the optimization point of view it might also indicate that there is a tradeoff between friction and shock/trailing edge loss.
3. The improvements of the trailing edge loss and shock loss are due to the reduction of the Mach number on the pressure side near the trailing edge. This is achieved by special geometric properties of the optimized blade: "a locally high concave curvature" and "a small dimple" on the pressure surface near the trailing edge. These properties lead to a "double shock system" and increase the base pressure.
4. In the case of the optimized airfoil, the boundary layer just upstream of the shock/boundary layer interaction point on the suction surface is fully turbulent due to a deceleration region of the front part of the airfoil. Therefore, no separation bubble is observed for three inlet flow angles, while in the case of the baseline airfoil, the separation bubble is observed for all inlet flow angles, except for an extreme positive flow angle of 70 deg.

## Nomenclature

AVDR = axial velocity density ratio: $AVDR=(\rho_2 u_2)/(\rho_1 u_1)$
$C$ = chord length
CFD = computational fluid dynamics
$E_M$ = time-averaged hot-film voltage with flow
$E0_M$ = time-averaged hot-film voltage without flow
EXP = experiment
$k$ = turbulent kinetic energy
Ma = Mach number
$O$ = throat length
$p$ = pressure
PS = pressure side
Re = Reynolds number based on chord length
RMS = root-mean square of hot-film voltage
$r$ = radius
$S$ = pitch length
SS = suction side
$u$ = velocity
$X$ = axial-chord-wise location
$Y$ = pitch-wise location
$y^+$ = dimensionless distance from wall
$\alpha$ = flow angle
$\beta$ = airfoil metal angle
$\gamma$ = stagger angle
$\delta$ = boundary layer thickness
$\delta\alpha$ = tolerance for exit flow angle
$\varepsilon$ = turbulent kinetic energy dissipation
$\mu,\lambda$ = population size (parent, offspring)
$\rho$ = density
$\omega$ = total pressure loss coefficient: $\omega=(p_{t1}-p_t)/p_{t1}$

### Subscripts

1 = inlet plane upstream of leading edge
2 = exit plane downstream of trailing edge
ax = axial direction
design = target values for optimization
is = isentropic entity
LE = leading edge
TE = trailing edge
$t$ = total

## References


[1] Sieverding, C. H., Stanislas, M., and Snoek, J., 1983, "The BASE Pressure Problem in Transonic Cascades," ASME Paper No. 83-GT-50.
[2] Graham, C. G., and Kost, F. H., 1979, "Shock Boundary Layer Interaction on High Turning Transonic Turbine Cascades," ASME Paper No. 79-GT-37.
[3] Stanewsky, E., 1973, "Shock Boundary Layer Interaction in Transonic and Supersonic Flow," Lecture Series 59 *Transonic Flow in Turbo-machines*, von Karman Institute, Brussel.
[4] Dietrichs, H.-J., Hourmouziadis, J., Malzacher, F., and Braeunling, W., 1987, "Flow Phenomena in Transonic Turbine Cascades; Detailed Experimental and Numerical Investigation," ISABE 87-7031.
[5] Koeller, U., Moenig, R., Kuesters, B., and Schreiber, H. A., 2000, "Development of Advanced Compressor Airfoils for Heavy-Duty Gas Turbines, Part 1: Design and Optimization," ASME J. Turbomach., **122**, pp. 397–405.
[6] Sonoda, T., Yamaguchi, Y., Arima, T., Olhofer, M., Sendhoff, B., and Schreiber, H. A., 2004, "Advanced High Turning Compressor Airfoils for Low Reynolds Number Condition, Part 1: Design and Optimization," ASME J. Turbomach., **126**(3), pp. 350–359.
[7] Shelton, M. L., Gregory, B. A., Lamson, S. H., Moses, H. L., Doughty, R. L., and Kiss, T., 1993, "Optimization of a Transonic Turbine Airfoil using Artificial Intelligence, CFD and Cascade Testing," ASME Paper No. 93-GT-161.
[8] Michelassi, V., Rodi, W., and Giess, P.-A., 1997, "Experimental and Numerical Investigation of Boundary-Layer and Wake Development in A Transonic Turbine Cascade," ASME Paper 97-GT-483.
[9] Jouini, D. B. M., Sjolander, S. A., and Moustapha, S. H., 2001, "Midspan Flow-Field Measurements for Two Transonic Linear Turbine Cascades at Off-Design Conditions," ASME Paper No. 2001-GT-0493.
[10] Hansen, N., and Ostermeier, A., 2001, "Completely Derandomized Self-Adaptation in Evolution Strategies," Evol. Comput., **9**(2), pp. 159–196.
[11] Chien, J. Y., 1982, "Predictions of Channel and Boundary Layers With a Low-Reynolds-Number Two Equation Model of Turbulence," AIAA J., **20**, pp. 33–38.
[12] Arima, T., Sonoda, T., Shirotori, M., Tamura, A., and Kikuchi, K., 1999, "A Numerical Investigation of Transonic Axial Compressor Rotor Flow Using a Low-Reynolds-Number k-$\varepsilon$ Turbulence Model," ASME J. Turbomach., **121**, pp. 44–58.
[13] Amecke, J., and Safarik, P., 1995, "Data Reduction of Wake Flow Measurements with Injection of an Other Gas," Forschungsbericht DLR-FB 95-32, Cologne.
[14] Schodl, R., 1980, "A Laser-Two-Focus (L2F) Velocimeter for Automatic Flow Vector Measurements in the Rotating Components of Turbomachines," ASME J. Fluids Eng., **102**, pp. 412–419.
[15] Kost, F., and Kapteijn, C., 1997, "Application of Laser-Two-Focus Velocimetry to Transonic Turbine Flows," *Proceedings 7th International Conference on Laser Anemometry—Advances and Applications*, University of Karlsruhe, Karlsruhe, Germany, September 8–11.
[16] Horlock, J. H., 1966, *Axial Flow Turbines*, Robert E. Krieger Publishing Company, Malabar, FL.

# Defining the Efficiency of a Cooled Turbine

**J. B. Young**
e-mail: jby@eng.cam.ac.uk

**J. H. Horlock**
e-mail: john.horlock1@btinternet.com

Hopkinson Laboratory,
Engineering Department,
Cambridge University,
Trumpington Street,
Cambridge, CB2 1PZ, UK

*Despite 40 years development of gas turbine cooling technology, there is no general agreement on the most appropriate definition of cooled turbine efficiency; the critical issue is the choice of a hypothetical "ideal" process. This paper reviews the definitions in use and presents new proposals for overcoming the problems. Attention is first focused on a stationary cooled cascade, and it is shown that the commonly used Hartsel efficiency definition (where the gas and coolant streams expand separately in the ideal process) is unsatisfactory. Three "mixed" efficiencies, referred to as the MP (mainstream-pressure), FR (fully reversible), and WP (weighted-pressure) efficiencies are then discussed. The MP ideal process involves mixing of the coolant and the mainstream to give an unchanged mainstream pressure before expansion. This definition, although sometimes used, is unsatisfactory because the efficiency is independent of the coolant supply pressures. The FR and WP efficiencies have not appeared in the literature previously. The FR efficiency is based on a fully reversible ideal process and has the soundest thermodynamic foundation. It is equivalent to a suitably defined rational efficiency and can be directly related to the various cooling losses. However, as it gives a significantly lower value than the Hartsell and MP definitions, it may not appeal to turbine manufacturers. The WP definition is a pragmatic alternative. In the WP ideal process the entropy increase associated with temperature equilibration of the mainstream and coolant flows is allowed in the mixing before expansion. All three mixed efficiencies can be applied to turbine stages with multiple coolant streams. Turbine manufacturers are urged to reconsider their current procedures with a view to standardizing on a thermodynamically sound definition of efficiency.* [DOI: 10.1115/1.2218890]

## 1 Introduction

Film cooling of the first few blade rows of a high-temperature gas turbine is standard practice. The cooling flow is introduced into the main flow through holes in the blade surface, slots in the trailing edge, and openings at the blade tips. Turbine performance is characterized, among other things, by the value of an "efficiency." The definition of efficiency is unambiguous for an uncooled turbine but this is not so when cooling is employed. Our purpose in this paper is to provide a critical review of the several definitions of cooled turbine efficiency and to present new proposals for overcoming the ambiguities.

There are two main uses of turbine efficiency, cooled or uncooled. In most turbine design offices the primary use is to compare different designs of turbine. In engine performance offices or in advanced project work the main use is to determine the actual power generated for the purpose of an engine performance or cycle calculation. This requires (i) the definition of the efficiency and its value and (ii) the calculation of the "ideal" power, as used in the definition, from known properties of the entry mainstream and coolant flows.

The definition of turbine efficiency therefore relates $P_{\text{gross}}$, the actual gross power output to $P_{\text{ideal}}$, the gross power produced in a hypothetical process which is in some sense ideal

$$\eta = \frac{P_{\text{gross}}}{P_{\text{ideal}}} \tag{1}$$

$P_{\text{gross}}$ is well-defined (see Sec. 2 below) and the main difficulty is in the specification of $P_{\text{ideal}}$. Here, a choice has to be made between several competing hypothetical processes, all of which have some claim to ideality. It is important to appreciate that cooled turbine efficiency, as defined by Eq. (1) and used throughout this paper, is a measure of the effectiveness of conversion into useful power of the combined power potential of the main flow and coolant streams. Because of the injection of coolant, ambiguities arise when the term efficiency is taken to refer to the mainstream expansion alone and this usage should be avoided. The efficiency of Eq. (1) therefore takes account of all losses experienced by the cooling flows between their supply stations and the locations at which they are injected into the main flow. The coolant supply stations are chosen by the designer and must be stated as part of the efficiency definition.

In a turbine, the main flow and multiple coolant streams differ in temperature, pressure, and chemical composition. For accuracy, calculation procedures often model the working fluid as a variable composition mixture of semi-perfect gases (i.e., $c_p$ and $c_v$ varying with temperature but not pressure). Any definition of efficiency must embrace such real gas effects; definitions which rely on perfect gas relations will be shown to be unsatisfactory.

## 2 Gross, Shaft, Windage, and Pumping Power

Although the major part of the paper concerns the various definitions of $P_{\text{ideal}}$, the relation of the gross power $P_{\text{gross}}$ to certain other power quantities merits some discussion.

Figure 1 shows a schematic diagram of a turbine rotor cooling system. Control volume $X$ comprises the mainstream (external) rotor blade passage from rotor inlet to stage outlet. Entering control volume $X$ are the mainstream gas with mass flow rate $m_g$ and mass flow-averaged state $g2$, and various coolant streams from the holes and slots on the blade surface with total mass flow rate $m_c$ and mass flow-averaged state $c2$. The fully mixed gases exit control volume $X$ at mass flow-averaged state 3. Control volume $Y$ comprises the internal rotor blade passages and the coolant supply system (ducting and preswirl nozzles, etc). Coolant with mass flow rate $m_c$ enters control volume $Y$ at mass flow-averaged state $c1$ and exits through the holes and slots at mass flow-averaged state $c2$.

Contributed by the Turbomachinery Division of ASME for publication in the JOURNAL OF TURBOMACHINERY. Manuscript received August 6, 2005; final manuscript received March 14, 2006. Review conducted by N. Cumpsty.

  

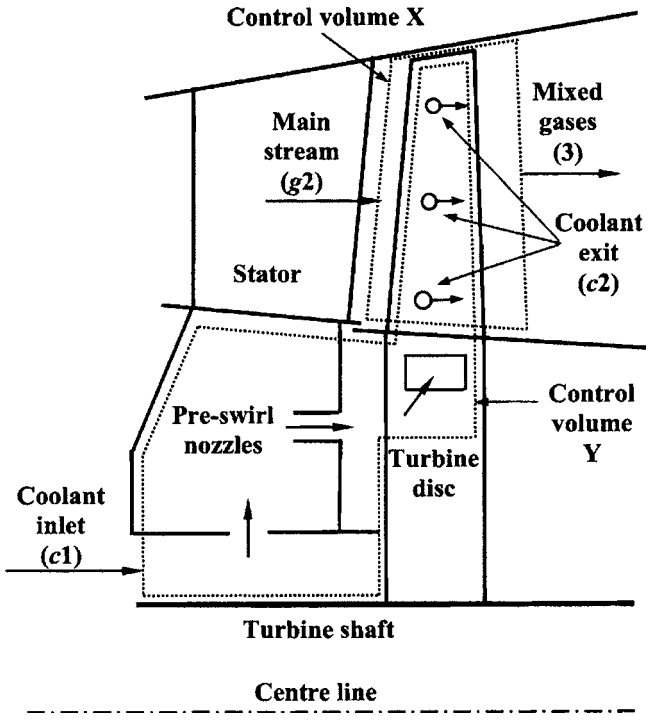


Fig. 1 Schematic diagram of a rotor blade cooling system

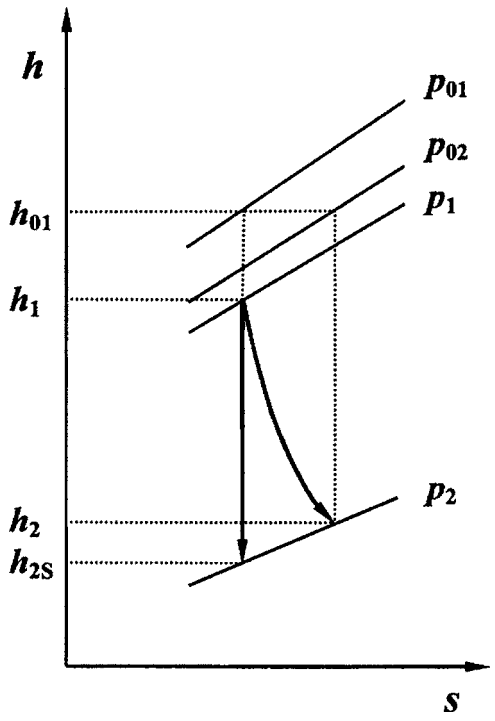


Fig. 2 Expansion through an uncooled turbine cascade

The power *outputs* from $X$ and $Y$ are denoted $P_X$ and $P_Y$ and are given by

$$P_X = m_g(\overline{UV_\theta})_{g2} + m_c(\overline{UV_\theta})_{c2} - (m_g + m_c)(\overline{UV_\theta})_3 \quad (2a)$$

$$P_Y = m_c(\overline{UV_\theta})_{c1} - m_c(\overline{UV_\theta})_{c2} \quad (2b)$$

where $U$ is the blade speed, $V_\theta$ is the absolute circumferential flow velocity, and the overbars denote values mass flow-averaged over the span or blade surface as appropriate. The negative of $P_Y$ is referred to as the "coolant pumping power" $P_{\text{pump}}$. It is the power required to pump the coolant from its mass flow-averaged entry state $c1$ to its mass flow-averaged exit state $c2$.

The sum of $P_X$ and $P_Y$ is referred to as the gross power, $P_{\text{gross}}$. Thus,

$$P_{\text{gross}} = P_X + P_Y = P_X - P_{\text{pump}} \quad (3)$$

The gross power is the total power produced by the mainstream and coolant flows and is equal to the combined drop in stagnation enthalpy of the mainstream plus coolant between stage inlet and stage outlet. The gross power from the turbine stage equals the shaft power plus the power for overcoming any windage loss on the turbine disk (usually estimated from empirical relations).

The shaft power (and hence the gross power and the stagnation enthalpy change) may be obtained experimentally via measurements of torque and speed. The gross power may also be obtained by calculation, and various methods are available to perform this task. The most accurate involve three-dimensional computational fluid dynamics (CFD) calculations of the flow through the whole turbine stage including the internal coolant flows. This is still a computationally expensive and time-consuming process, however, and various simplified approaches are also available, such as the one described by Young and Wilcock [1]. These calculation procedures are not actually relevant to the present paper, however, and will not be discussed further.

## 3 Uncooled Cascade and Turbine Efficiencies

We first review the efficiency definitions for uncooled turbine cascades and stages. It should be noted that the symbol $\varepsilon$ is used for cascade or blade row efficiency and $\eta$ for stage efficiency, with the subscript $u$ indicating that the definition applies to an uncooled expansion.

**3.1 The Uncooled Nozzle or Blade Row Cascade.** The cascade or blade row efficiency is mainly used in stationary cascade testing. There are two main definitions; see Horlock [2]. The *static-to-static* efficiency $(\varepsilon_u)_{SS}$ compares the actual *increase* in kinetic energy with the ideal *increase*. For the adiabatic expansion between static states 1 and 2 in Fig. 2,

$$(\varepsilon_u)_{SS} = \frac{h_1 - h_2}{h_1 - h_{2S}} = \frac{c_2^2 - c_1^2}{c_{2S}^2 - c_1^2} \quad (4)$$

where $c$ is the flow velocity relative to the blades. In contrast, the *total-to-static* efficiency $(\varepsilon_u)_{TS}$ compares the actual exit kinetic energy with the ideal exit value. Thus,

$$(\varepsilon_u)_{TS} = \frac{h_{01} - h_2}{h_{01} - h_{2S}} = \frac{c_2^2}{c_{2S}^2} \quad (5)$$

These efficiencies are related by $(\varepsilon_u)_{TS} = (\varepsilon_u)_{SS} + [1 - (\varepsilon_u)_{SS}] \times (c_1/c_{2S})^2$ and hence $(\varepsilon_u)_{TS} > (\varepsilon_u)_{SS}$.

**3.2 The Uncooled Turbine Stage.** The usual definition of uncooled stage efficiency is the *total-to-total* isentropic efficiency $(\eta_u)_{TT}$ based on entry and exit total conditions. Thus, with reference to Fig. 3,

$$(\eta_u)_{TT} = \frac{h_{01} - h_{03}}{h_{01} - h_{03S}} \quad (6)$$

In a multistage turbine with $c_1 \cong c_3$, $(\eta_u)_{TT}$ is approximately equal to the *static-to-static* isentropic stage efficiency $(\eta_u)_{SS}$, which (again with reference to Fig. 3) is defined by

$$(\eta_u)_{SS} = \frac{h_1 - h_3}{h_1 - h_{3S}} \quad (7)$$

Because the definitions of $(\eta_u)_{SS}$ and $(\varepsilon_u)_{SS}$ are similar, it is more convenient to use $(\varepsilon_u)_{SS}$ than $(\varepsilon_u)_{TS}$ when relating row effi-

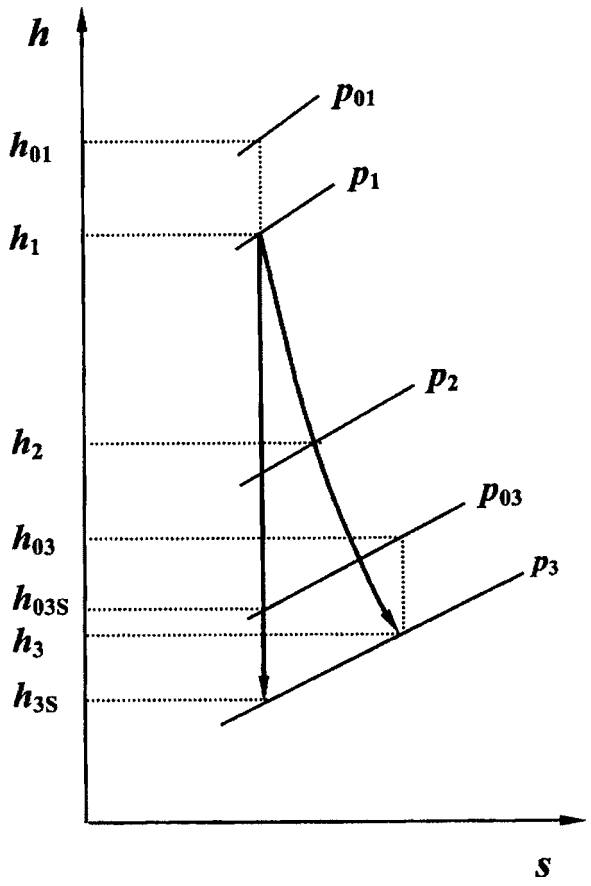


**Fig. 3 Expansion through an uncooled turbine stage**

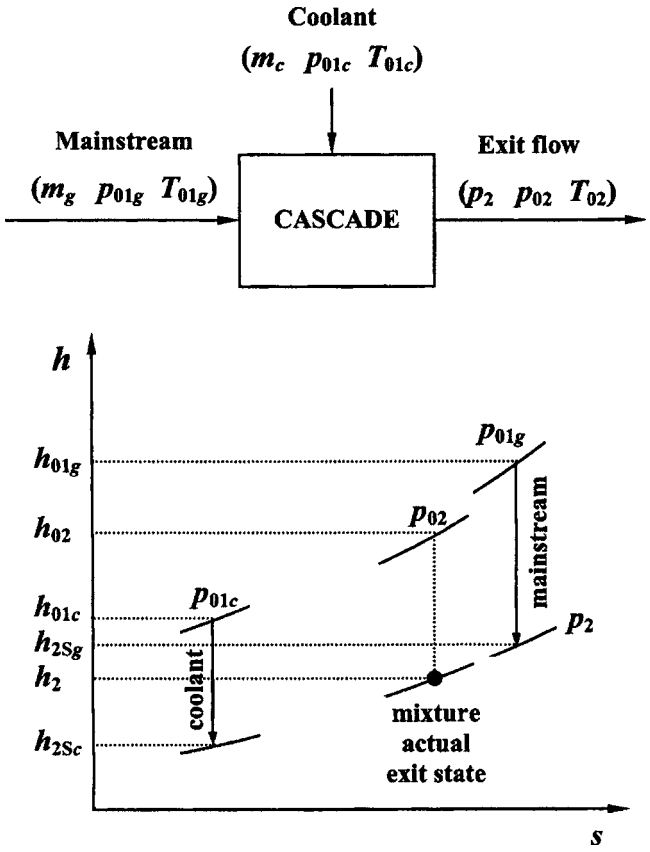


**Fig. 4 Illustrating the notation for Hartsel's cooled cascade. The mainstream gas, coolant, and mixture have different chemical compositions and therefore different sets of isobars on the (*h*-*s*) diagram.**

ciencies to the stage efficiency. Because of the so-called *reheat factor* resulting from the divergence of the isobars on the (*h*-*s*) diagram, the stage efficiency is greater than the mean of the row efficiencies. A similar effect leads to the overall efficiency of a multistage turbine being greater than the individual stage efficiencies.

The rational efficiency of an uncooled turbine is well-established in the literature but is seldom used. It is given by the actual work output divided by the maximum work that could be obtained between the entry and actual exit stagnation states. With reference to Fig. 3,

$$(\eta_u)_{\mathrm{RAT}} = \frac{h_{01} - h_{03}}{b_{01} - b_{03}} = \frac{h_{01} - h_{03}}{(h_{01} - h_{03}) - T_D(s_1 - s_3)}$$

$$\approx \frac{(\eta_u)_{TT}}{(\eta_u)_{TT} + (T_D/T_{03S})[1 - (\eta_u)_{TT}]} \tag{8}$$

where $b_0 = h_0 - T_D s$ is the steady-flow availability function and $T_D$ is the dead-state temperature. If $T_D = 25°\mathrm{C}$, then $T_D < T_{03S}$ and $(\eta_u)_{\mathrm{RAT}} > (\eta_u)_{TT}$. This reflects the fact that the ideal work is less than the isentropic enthalpy drop $(h_{01} - h_{03S})$ because it would be necessary to pump heat from the dead state at $T_D$ to raise the exit total temperature from $T_{03S}$ to $T_{03}$.

## 4 Cooled Cascade Efficiencies

We next consider how the uncooled efficiencies have to be changed when cooling flows are present. Initially, it is useful to consider a stationary cooled cascade because many of the concepts carry over to the case of a cooled turbine stage. The subscript *c* is used as a reminder that the efficiency definitions apply to cooled expansions.

**4.1 Hartsel's Cooled Cascade Efficiency.** Hartsel [3] considered a stationary cascade of turbine blades cooled by a single coolant stream. He suggested that the cascade efficiency should be defined by the expression

$$(\varepsilon_c)_{\mathrm{HART}} = \frac{\text{Exit } KE \text{ of actual mixed expansion}}{\text{Total exit } KE \text{ of separate unmixed isentropic expansions}} \tag{9a}$$

The denominator is calculated by assuming that the main gas flow and coolant stream expand isentropically without mixing from their supply stagnation conditions to the exit static pressure $p_2$. In the limit of zero coolant flow, Eq. (5) shows that $(\varepsilon_c)_{\mathrm{HART}} = (\varepsilon_u)_{TS}$, rather than $(\varepsilon_u)_{SS}$. This is important when comparing the efficiencies of cooled and uncooled blade rows.

With reference to Fig. 4 for notation, Eq. (9*a*) can be written as

$$(\varepsilon_c)_{\mathrm{HART}} = \frac{(m_g + m_c)(h_{02} - h_2)}{m_g(h_{01g} - h_{2Sg}) + m_c(h_{01c} - h_{2Sc})} \tag{9b}$$

where $m_g$ and $m_c$ are the mass flow rates of mainstream gas and coolant, respectively. The overall cascade flow is adiabatic so that the steady-flow energy equation gives $h_{02}$ from

$$(m_g + m_c)h_{02} = m_g h_{01g} + m_c h_{01c} \tag{10}$$

We now consider the special case when the mainstream gas and coolant behave as perfect gases, each with different (but constant) values of $c_p$ and $\gamma$. For the real cascade, we suppose that the main gas flow (supplied at $p_{01g}$ and $T_{01g}$) and the coolant stream (supplied at $p_{01c}$ and $T_{01c}$) are first mixed adiabatically to give total

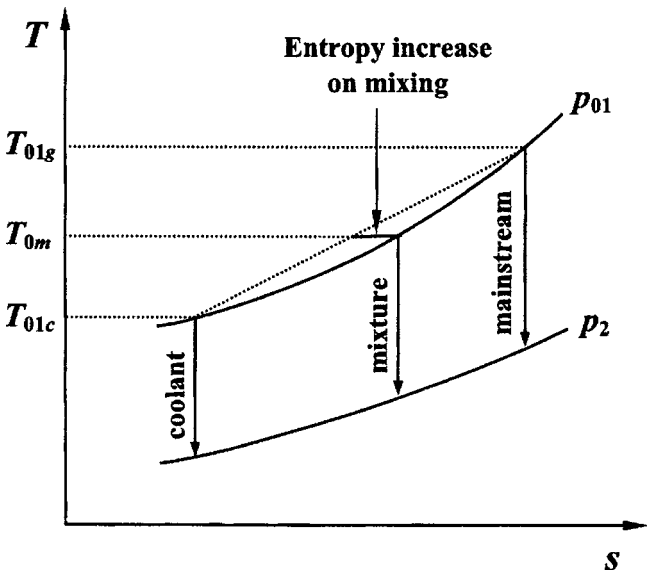


**Fig. 5 Illustrating Hartsel's approach for *identical* perfect gases with $p_{01g}=p_{01c}=p_{0m}=p_{01}$ and an isentropic mixed expansion. Note the entropy creation during constant pressure mixing.**

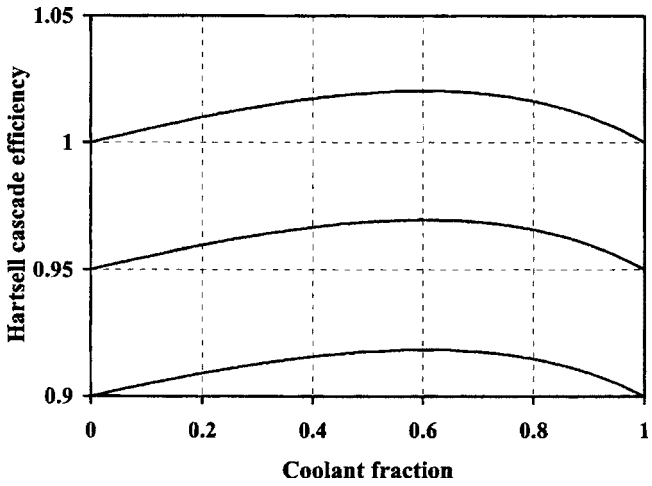


**Fig. 6 Hartsel cooled cascade efficiency $(\varepsilon_c)_{\mathrm{HART}}$ versus coolant fraction $\phi=m_c/(m_g+m_c)$ for gas properties and conditions as given in the text, and $(\varepsilon_m)_{\mathrm{TS}}=1.0$, 0.95, and 0.90 (upper, middle, and lower curves, respectively). The region of interest is $\phi<0.25$.**

conditions $p_{0m}$ and $T_{0m}$. After this, the mixture is expanded to the exit static pressure $p_2$ with a total-to-static efficiency of $(\varepsilon_m)_{TS}$. By using Eqs. (5), (9*b*), and (10) together with the usual perfect gas and isentropic relations, it can be shown that the Hartsel efficiency for the cascade is given by

$$(\varepsilon_c)_{\mathrm{HART}} = \frac{(\varepsilon_m)_{TS}\left(1+\dfrac{m_c c_{pc} T_{01c}}{m_g c_{pg} T_{01g}}\right)\left[1-\left(\dfrac{p_2}{p_{0m}}\right)^{(\gamma_m-1)/\gamma_m}\right]}{\left[1-\left(\dfrac{p_2}{p_{01g}}\right)^{(\gamma_g-1)/\gamma_g}\right]+\left(\dfrac{m_c c_{pc} T_{01c}}{m_g c_{pg} T_{01g}}\right)\left[1-\left(\dfrac{p_2}{p_{01c}}\right)^{(\gamma_c-1)/\gamma_c}\right]} \tag{11}$$

where, for the mixed flow, $\gamma_m=(m_g c_{pg}+m_c c_{pc})/(m_g c_{vg}+m_c c_{vc})$.

Here, $p_{0m}$ is not a uniquely defined pressure but depends on the details of the mixing. This is unlike $T_{0m}=T_{02}$, which follows from the perfect gas form of Eq. (10) and is independent of the mixing process (so long as it is adiabatic).

First, suppose that the mainstream gas and coolant are identical (so that $c_{pg}=c_{pc}=c_p$ and $\gamma_g=\gamma_c=\gamma_m=\gamma$), and that the supply stagnation pressures are equal (so that $p_{01g}=p_{01c}=p_{01}$). Suppose also that mixing is carried out such that $p_{0m}=p_{01}$. This would involve an overall increase in entropy; see the (*T*-*s*) diagram of Fig. 5. Equation (11) then gives the result that $(\varepsilon_c)_{\mathrm{HART}}=(\varepsilon_m)_{TS}$ for *all* coolant-to-gas ratios $m_c/m_g$. In particular, if the real mixed expansion is isentropic as in Fig. 5, then $(\varepsilon_c)_{\mathrm{HART}}=(\varepsilon_m)_{TS}=1.0$. It is thus impossible to have a Hartsel efficiency greater than unity with identical perfect gases.

Now, suppose that the gases, although perfect, have different values of $c_p$ and $\gamma$. To be specific, let $c_{pg}=1.20$ kJ/kgK, $c_{pc}=1.05$ kJ/kgK, $\gamma_g=1.32$, and $\gamma_c=1.38$. These values are typical of gas properties in a real gas turbine. As before, suppose that $p_{01g}=p_{01c}=p_{01}$, and that mixing occurs such that $p_{0m}=p_{01}$. Taking $T_{01c}/T_{01g}=0.5$ and $p_2/p_{01}=0.5$, Fig. 6 shows the variation of $(\varepsilon_c)_{\mathrm{HART}}$ with coolant fraction $\phi=m_c/(m_g+m_c)$ for three values of $(\varepsilon_m)_{TS}$, namely 1.0, 0.95, and 0.9. Evidently, for any nonzero coolant fraction $(\varepsilon_c)_{\mathrm{HART}}$ is greater than $(\varepsilon_m)_{TS}$, irrespective of the value of the latter. In particular, for an isentropic mixed expansion with $(\varepsilon_m)_{TS}=1.0$, the Hartsel efficiency exceeds unity.

In reality, $c_p$ and $\gamma$ are not constant but vary with temperature and chemical composition. Although it is not possible to write an explicit expression like Eq. (11) for such a general situation, calculations confirm that the conclusions remain the same.

This analysis shows that Eq. (9*a*) is not suitable as an efficiency definition for a cooled cascade. Even if an efficiency greater than unity were deemed acceptable, the behavior shown in Fig. 6 is clearly not. Differences in efficiency of the order of 0.5% are of great importance to the turbine designer, and variations of this magnitude arising from the efficiency definition itself are most undesirable. One way to avoid such problems is to specify the ideal process in terms of a mixed expansion, and some possibilities are now considered.

**4.2 Cascade Efficiency Definitions Based on Mixed Expansions.** Three proposals for modifying the denominator of Eq. (9*b*) are now described. All three include a mixing process before expansion, and two of the three involve irreversibility so that the reference process is no longer thermodynamically ideal.

In what follows, the mainstream gas and coolant are assumed to behave as semi-perfect gases. This is not strictly required but the analysis is less clear if the specific heats are taken to vary with pressure as well as temperature. For completeness, we assume there are *n* coolant streams, each supplied separately as shown in Fig. 7. For the *i*th stream, the supply stagnation pressure and temperature are $p_{01ci}$ and $T_{01ci}$, respectively, and the mass flow rate is $m_{ci}$.

The mixing process is defined to be adiabatic and the total temperature after mixing $T_{0m}$ can be calculated from the steady-flow energy equation, written for semi-perfect gases as

$$(1-\phi)\int_{T_{01g}}^{T_{0m}} c_{pg}(T')dT' + \sum_i \phi_i \int_{T_{01ci}}^{T_{0m}} c_{pc}(T')dT' = 0 \tag{12}$$

where $\phi_i=m_{ci}/(m_g+\Sigma m_{ci})$, $\phi=\Sigma\phi_i$ and the summation is over the *n* coolant streams. In contrast, the total pressure after mixing $p_{0m}$ depends on the details of the mixing process. In each of the three efficiency definitions, an assumption is therefore required to fix $p_{0m}$ (because the momentum equation is not being used). In the first, $p_{0m}$ is set equal to $p_{01g}$, in the second isentropic mixing is specified, and in the third a limitation is placed on the entropy

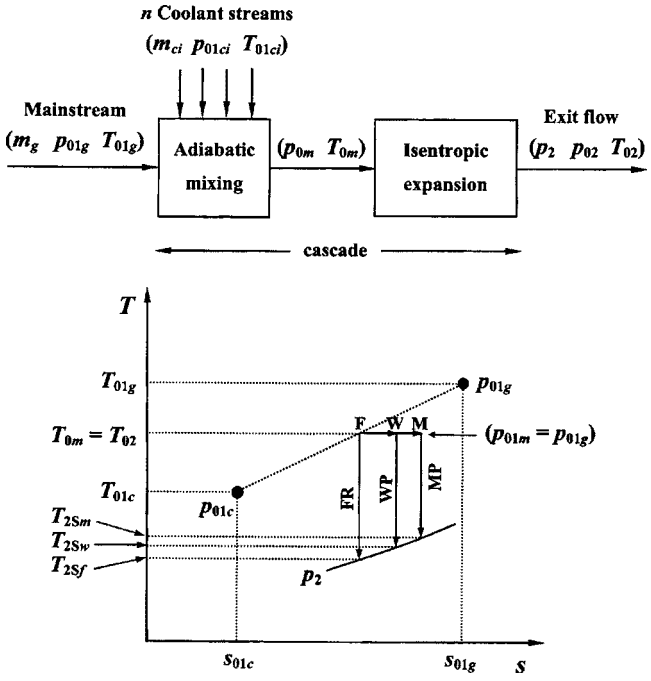


**Fig. 7 Illustrating the ideal processes in the MP, FR, and WP mixed cascade efficiency definitions. Note that (i) in the (*T-s*) diagram, only one coolant supply has been indicated; (ii) the dotted line defining point *F* is straight; and (iii) the WP expansion has been drawn assuming $p_{01c} > p_{01g}$.**

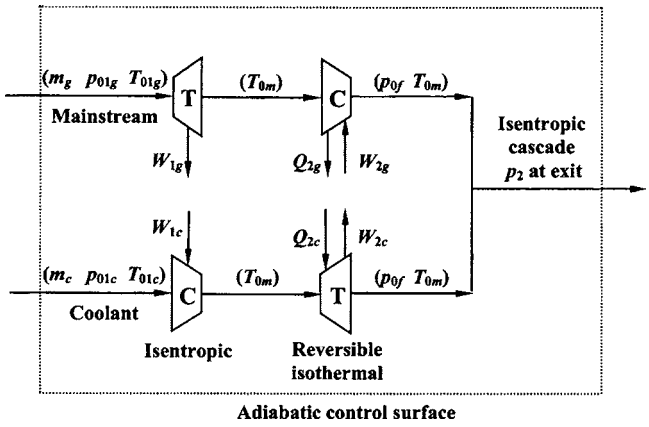


**Fig. 8 Conceptual fully reversible mixing process (for $p_{01c} > p_{01g}$) with $\sigma_T = \sigma_P = 0$. For semi-perfect gases it is easy to show that $W_{1g} = W_{1c}$, $W_{2g} = W_{2c}$ and $Q_{2g} = Q_{2c}$.**

generation.

In the mixing process, the entropy created per unit mass of mixture $\sigma$ is given by

$$\sigma = s_{0m} - \left[ (1-\phi) s_{01g} + \sum_i \phi_i s_{01ci} \right] \tag{13}$$

As shown in the Appendix, Eq. (13) may be written for semi-perfect gases as

$$\sigma = \sigma_T + \sigma_P + \sigma_C \tag{14}$$

where $\sigma_T$, $\sigma_P$, and $\sigma_C$ are given by

$$\sigma_T = (1-\phi) \int_{T_{01g}}^{T_{0m}} \frac{c_{pg}(T')}{T'} dT' + \sum_i \phi_i \int_{T_{01ci}}^{T_{0m}} \frac{c_{pc}(T')}{T'} dT' \tag{14a}$$

$$\sigma_P = (1-\phi) R_g \ln\left(\frac{p_{01g}}{p_{0m}}\right) + \sum_i \phi_i R_c \ln\left(\frac{p_{01ci}}{p_{0m}}\right) \tag{14b}$$

$$\sigma_C = -(1-\phi) R_g \ln(X_{gm}) - \phi R_c \ln(X_{cm}) \tag{14c}$$

In these equations $R$ denotes the specific gas constant, and $X_{gm}$ and $X_{cm}$ are the mole fractions of the mainstream gas and coolant after mixing, respectively.

The term $\sigma_C$ in Eq. (14) represents the diffusional entropy creation due to change in composition. As explained in the Appendix, it is essentially impossible (without the provision of semi-permeable membranes) to avoid this component of the mixing loss and instead produce useful work. A pragmatic approach is therefore to ignore $\sigma_C$ altogether because it is bound to occur in both the real and ideal processes. As shown by Young and Wilcock [1], this objective can be achieved very simply by evaluating the specific entropies of the components at the local mixture static pressure (rather than at their partial pressures). All references to mole fractions are then expunged from the equations and the term $\sigma_C$ does not appear. Rigorous thermodynamic analysis shows, however, that such a course of action is only justified if the mainstream gas and coolant behave as ideal gases (i.e., $c_{pg}$ and $c_{pc}$ do not depend on pressure).

*(i) The Mainstream-Pressure (MP) Mixed Efficiency*. What we refer to here as the *mainstream-pressure mixed efficiency* $(\varepsilon_c)_{\mathrm{MP}}$ is discussed by Kurzke [4] following Walsh and Fletcher [5]. It also has similarity to the *vane efficiency* used by Timko [6] in analyzing his annular cascade traverse measurements.

The Hartsel approach involved separate expansions of gas and coolant streams as shown in Fig. 5. In contrast, the MP ideal process, illustrated in the (*T-s*) diagram of Fig. 7, involves adiabatic mixing of the main flow at $(p_{01g}, T_{01g})$ with the coolant streams at $(p_{01ci}, T_{01ci})$ to give a mixed state $M$ $(p_{0m}, T_{0m})$, with $T_{0m}$ given by Eq. (12) and $p_{0m} = p_{01g}$ by *definition*. This mixing process is then followed by an isentropic expansion to the exit static pressure $p_2$. The cascade efficiency is defined by

$$(\varepsilon_c)_{\mathrm{MP}} = \frac{(h_{02} - h_2)}{(h_{0m} - h_{2Sm})} \tag{15}$$

where $(h_{02} - h_2)$ is the actual kinetic energy per unit mass of the mixture at cascade exit and $h_{2Sm}$ is the static specific enthalpy after the isentropic expansion.

Because the mixed state $M$ is defined to be $(p_{01g}, T_{0m})$, the denominator of Eq. (15) is independent of the $p_{01ci}$. This implies that any thermodynamic advantage which might be achieved by supplying coolant at high total pressure is assumed to be forfeited, *but is not charged as a loss*.

It can be seen that the choice $p_{0m} = p_{01g}$ is an arbitrary condition on which to base the ideal process. On its own, this might not preclude the MP efficiency as the efficiency of choice but the fact that the denominator of Eq. (15) is independent of the coolant supply pressures is worrying. It might be expected that changing the $p_{01ci}$ would have some effect, beneficial or otherwise, on the ideal as well as the actual process, but this is not reflected in the MP definition. We shall therefore turn our attention to two other ideal processes which have not previously been described in the literature. In these, the entropy creation is specified by defined physical criteria, resulting in values of the denominator which depend on the coolant as well as the mainstream supply conditions.

*(ii) The Fully Reversible (FR) Mixed Efficiency*. The most obvious way of fixing the state after mixing is to stipulate a fully reversible adiabatic mixing process so that $\sigma$, the total entropy generation, is zero. Then, the ideal process really is thermodynamically ideal. This is illustrated in the (*T-s*) diagram of Fig. 7 and Fig. 8 shows how the process might be achieved conceptually

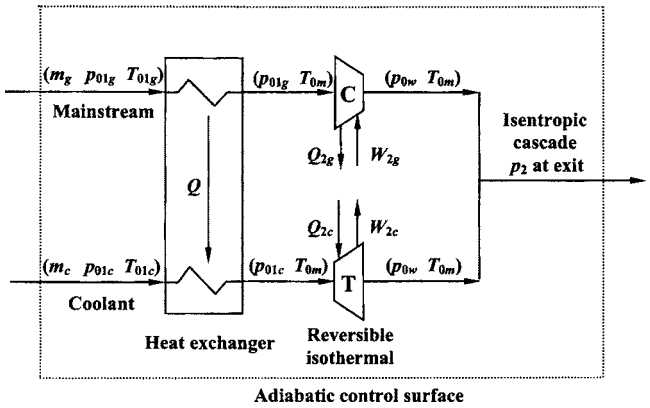


**Fig. 9 Conceptual partly reversible mixing process (for $p_{01c} > p_{01g}$) with $\sigma_T > 0$, $\sigma_P = 0$. For semi-perfect gases it is easy to show that $W_{2g} = W_{2c}$ and $Q_{2g} = Q_{2c}$.**

(for the case of a single coolant stream). The state after mixing, now denoted $F$, is $(p_{0f}, T_{0m})$, where $T_{0m}$ is given, as before, by Eq. (10) or (12) and $p_{0f}$ can be found by setting $\sigma = 0$ in Eq. (14). Taking $\sigma_C = 0$ as explained previously, we therefore have $(\sigma_T + \sigma_P) = 0$. For the general case where there are several coolant streams, it is then easily shown that $p_{0f}$ is given by

$$\frac{p_{0f}}{p_{01g}} = \exp\left(\frac{\sigma_T}{R}\right) \prod_i \left(\frac{p_{01ci}}{p_{01g}}\right)^{(\phi_i R_c/R)} \tag{16}$$

where $R = (1-\phi)R_g + \phi R_c$ is the specific gas constant of the mixture and the product is taken over all $n$ coolant streams. Finally, the FR cooled cascade efficiency is defined by

$$(\varepsilon_c)_{\mathrm{FR}} = \frac{(h_{02} - h_2)}{(h_{0f} - h_{2Sf})} \tag{17}$$

Although (for ideal gases) $h_{0f}$ in the denominator of Eq. (15) is equal to $h_{0m}$ in Eq. (15), it is evident that $h_{2Sf}$ in Eq. (17), unlike $h_{2Sm}$ in Eq. (15), depends on the coolant supply conditions through the value of $p_{0f}$.

Although $(\varepsilon_c)_{\mathrm{FR}}$ has every right to be called the *thermodynamic efficiency*, we avoid this terminology because the Hartsel efficiency is often referred to in this way.

*(iii) The Weighted-Pressure (WP) Mixed Efficiency*. It might be thought that the FR efficiency fulfills all the requirements of a cooled cascade efficiency because the reference process really does represent a thermodynamic ideal. It can be argued, however, that this is not the case because an ideal process with $\sigma = 0$ (as shown in Fig. 8) is not one to which the designer may aspire. In a stationary cascade there is obviously no possibility of transferring work between the two streams.

In turbomachinery practice no conscious attempt is made to recover the lost work associated with the process of bringing the gas and coolant streams to a common temperature. Indeed, the whole point of supplying low-temperature coolant is to maintain a substantial temperature difference between the blade metal and the hot gas, and the resulting heat transfer automatically results in entropy creation.

Such considerations provide an argument for excluding the entropy creation associated with thermal equilibration from the definition of cooled cascade efficiency. We therefore consider the process of entropy creation during mixing with a view to quantifying the *minimum practical thermal entropy production*, and illustrate in Fig. 9 how this might be achieved conceptually. Now, the isentropic turbo-compressor system of Fig. 8, which was used to bring the gas and coolant to a common temperature $T_{0m}$, is replaced by a frictionless heat exchanger in which the entropy generation is $\sigma_T$ *and there is no change in the total pressures* $p_{01g}$ *and* $p_{01c}$. A reversible isothermal turbo-compressor system then brings the two streams to a common state $W$ $(p_{0w}, T_{0m})$. The pressure $p_{0w}$ is defined by the condition $\sigma_P = 0$, i.e., zero loss in the turbo-compressor system. From Eq. (14*b*), $p_{0w}$ is therefore given by

$$\frac{p_{0w}}{p_{01g}} = \prod_i \left(\frac{p_{01ci}}{p_{01g}}\right)^{(\phi_i R_c/R)} \tag{18}$$

What we call the *weighted-pressure mixed cascade efficiency* is then defined by

$$(\varepsilon_c)_{\mathrm{WP}} = \frac{(h_{02} - h_2)}{(h_{0w} - h_{2Sw})} \tag{19}$$

The First Law ensures that $h_{0w} = h_{0f} = h_{0m}$. The static enthalpy after the isentropic expansion $h_{2Sw}$ will, however, depend on $p_{0w}$ which, itself, depends on the $p_{01ci}$ through Eq. (18).

If all the $p_{01ci}$ are equal to $p_{01g}$, it follows that $p_{0w} = p_{01g}$ and hence that $(\varepsilon_c)_{\mathrm{WP}} = (\varepsilon_c)_{\mathrm{MP}}$. This is an attractive aspect of the WP definition because, if two or more gases at the same total pressure but different total temperatures are, in reality, mixed at low speed, it would seem that the "best possible outcome" would indeed be one with zero pressure loss and entropy creation equal to $\sigma_T$. In more general cases $(\varepsilon_c)_{\mathrm{WP}}$ would be greater or less than $(\varepsilon_c)_{\mathrm{MP}}$ depending on the values of the $p_{01ci}$.

In the above description of the WP ideal process, it was argued that, although $\sigma_T$ is positive and unavoidable, the lowest possible (and therefore ideal) value of $\sigma_P$ is zero. This is not strictly true, however, because it is theoretically possible for $\sigma_P$ to be negative. Certainly, we cannot do better than achieve zero pressure loss on the cold side of the heat exchanger, but it is possible in the process of cooling a hot compressible flow for the pressure $p_{01g}$ to be increased on the mainstream gas side. Such a Rayleigh process was described by Shapiro [7], who referred to it as "aerothermopression." Shapiro showed that the stagnation pressure rise is proportional to the square of the flow Mach number and to the amount of heat transferred. Thus, in theory, a high-speed flow on the hot side would cause the stagnation pressure after the heat exchanger to exceed $p_{01g}$. In this situation $\sigma_P$ would be negative and the total entropy production rate $\sigma$ would be less than $\sigma_T$.

Although the introduction of an "aerothermopressor" into the WP process is theoretically conceivable, there are serious practical difficulties as Shapiro himself discovered after exhaustive experiments. We do note, however, that the mainstream gas flows in turbine cascades are at high, sometimes supersonic, Mach numbers, and that these are therefore conducive to some total pressure recovery. The WP process of Fig. 9 ignores this possibility by acknowledging that $\sigma_T$ represents an unavoidable positive contribution to the entropy creation, and taking the condition $\sigma_P = 0$ as a means of specifying the optimum total pressure $p_{0w}$ after mixing.

**Table 1 Properties for calculations**

| | $R$ (kJ/kgK) | $c_p$ (kJ/kgK) | $\gamma$ | $T_{01}$ (K) |
|---|---|---|---|---|
| Mainstream | 0.290 | 1.20 | 1.319 | 1800 |
| Coolant | 0.287 | 1.05 | 1.376 | 900 |

**4.3 Comparison of Cooled Cascade Efficiencies.** It is of interest to compare the magnitudes of the three mixed cascade efficiencies. Calculations were therefore carried out assuming the main flow and (single) coolant stream could be modeled as different perfect (not semi-perfect) gases with the properties given in Table 1. The pressure ratio $p_2/p_{01g}$ was fixed at 0.5.

The mainstream-pressure mixed efficiency $(\varepsilon_c)_{\mathrm{MP}}$ was taken as the reference efficiency because, as noted above, its value is independent of the coolant supply pressure (although not, of course, of coolant fraction $\phi$). Figure 10 shows how the weighted-

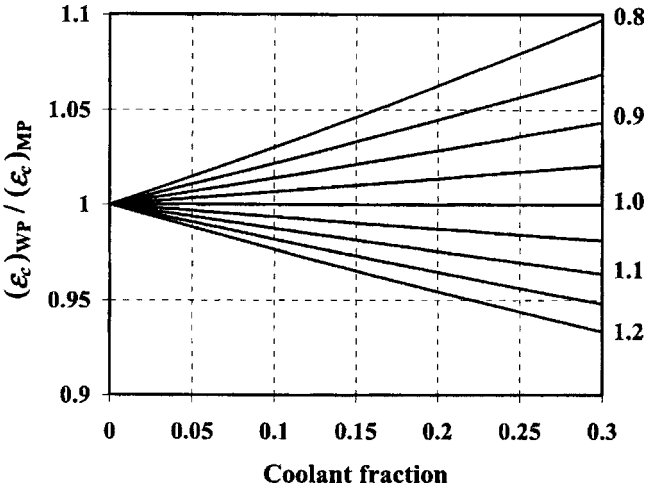


**Fig. 10 Ratio of WP to MP cascade efficiencies versus coolant fraction $\phi = m_c/(m_g+m_c)$ for the data given in Table 1 and a single coolant stream supplied at various pressures ($0.8 < p_{01c}/p_{01g} < 1.2$)**

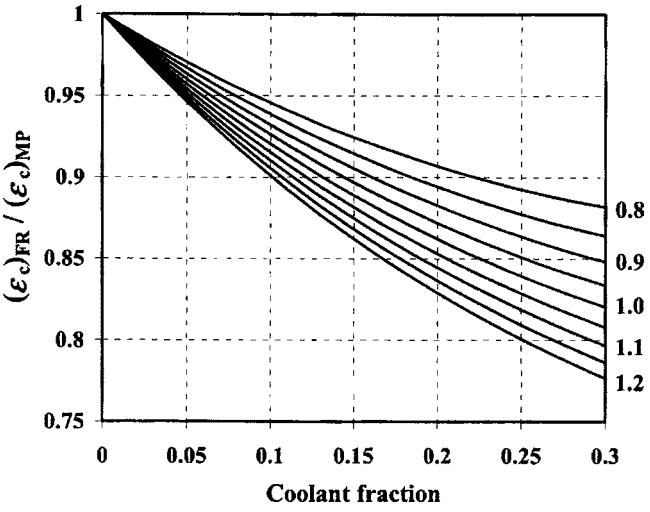


**Fig. 11 Ratio of FR to MP cascade efficiencies versus coolant fraction $\phi = m_c/(m_g+m_c)$ for the data given in Table 1 and a single coolant stream supplied at various pressures ($0.8 < p_{01c}/p_{01g} < 1.2$)**

pressure mixed efficiency $(\varepsilon_c)_{WP}$ varies with respect to this baseline case. For $p_{01c}=p_{01g}$ the two are equal for all values of $\phi$ as is evident from Eq. (18). However, for $p_{01c}>p_{01g}$ (the usual situation) the WP efficiency is less than the MP efficiency, the discrepancy increasing with increase of $\phi$ and also with increase of the ratio $p_{01c}/p_{01g}$.

Consideration shows that this is, indeed, the behavior expected of a cooled cascade efficiency. Thus, suppose $p_{01c}$ of an actual cooled cascade were raised to accommodate some extra flow resistance caused, perhaps, by redesign of the internal flow passages. If $T_{01g}$ and $T_{01c}$ remained the same, and if the static pressures and blowing ratios at the injection holes were likewise unchanged, then the cascade exit kinetic energy would be unaltered. The only difference would be that the coolant in the redesigned cascade would experience a "lossy" throttling process between the supply and injection stations. Clearly, therefore, the efficiency of the redesigned cascade should be lower because of the increase of $p_{01c}$ required to maintain the same cascade exit condition. Furthermore, the reduction in efficiency should depend both on the pressure increase required and the fraction of the total flow affected. The WP efficiency definition fulfills these requirements precisely but the MP definition does not.

Figure 11 is constructed in the same way as Fig. 10 but shows how the FR efficiency varies with respect to the MP baseline case. Because of the $\exp(\sigma_T/R)$ term in Eq. (16), the FR efficiency is greatly reduced compared to the other efficiencies. This is to be expected because the entropy production caused by thermal equilibration represents a large component of the total loss in any cooled cascade experiment.

## 5 Cooled Turbine Stage Efficiencies

The definitions of the various total-to-total efficiencies for a cooled turbine stage follow a similar approach to those given above for a cooled cascade, but with the stagnation pressure $p_{03}$ at stage outlet replacing the static pressure $p_2$ at cascade exit. We first discuss Hartsel's efficiency for a turbine stage as the role of the rotor coolant in the ideal process is clear; in other stage efficiency definitions in use it is more debatable.

**5.1 Hartsel's Efficiency.** The philosophy behind Hartsel's definition for cascade efficiency can be carried over to a turbine stage. There are now at least two separate coolant streams for the stator and rotor and, for the separate isentropic expansions, each stream expands from its supply condition to the specified common total pressure $p_{03}$ downstream of the stage as shown in Fig. 12. Modifying Eq. (9*b*) in an obvious manner and allowing for multiple coolant streams for both stator and rotor (i.e., including disk and platform cooling flows), the Hartsel stage efficiency can be written

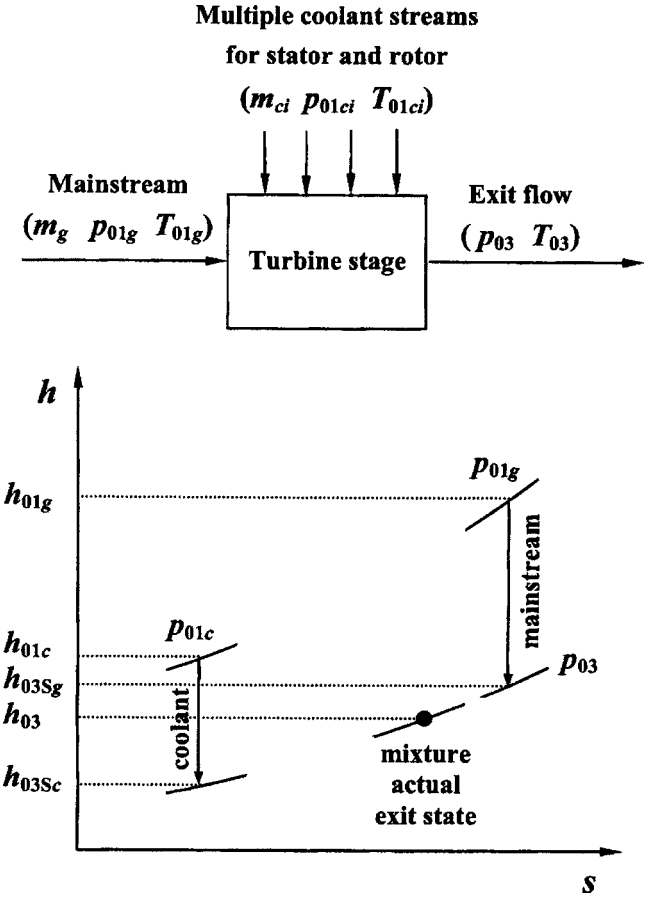


**Fig. 12 Illustrating the notation for Hartsel's cooled turbine stage. For simplicity, only one coolant supply is shown in the (*h-s*) diagram.**

$$(\eta_c)_{\mathrm{HART}} = \frac{P_{\mathrm{gross}}}{m_g(h_{01g} - h_{03Sg}) + \sum_{\mathrm{stator}} m_{ci}(h_{01ci} - h_{03Sci}) + \sum_{\mathrm{rotor}} m_{ci}(h_{01ci} - h_{03Sci})} \tag{20}$$

where the gross power is given by

$$P_{\mathrm{gross}} = \left(m_g h_{01g} + \sum_{\mathrm{stator}} m_{ci} h_{01ci} + \sum_{\mathrm{rotor}} m_{ci} h_{01ci}\right) - \left(m_g + \sum_{\mathrm{stator}} m_{ci} + \sum_{\mathrm{rotor}} m_{ci}\right) h_{03} \tag{21}$$

in which $h_{03}$ is the actual total specific enthalpy of the fully mixed flow at stage exit.[1]

Hartsel's stage efficiency suffers from exactly the same "real gas" problems as his cascade efficiency, and hence has limitations as a definition of efficiency. We therefore turn our attention to the three efficiencies based on mixed flow expansions.

**5.2 Stage Efficiency Definitions Based on Mixed Expansions.** It is straightforward to extend the mixed cascade efficiency definitions to a turbine stage. Initially, we take a purely thermodynamic view, acknowledging the work potential of every coolant stream, however minor. We also assume that the mainstream gas and coolant behave as semi-perfect gases. The notation is indicated in Fig. 13.

For the MP efficiency, it is assumed that to obtain $P_{\mathrm{ideal}}$ all coolant streams (stator, rotor, platform, disk etc.) are mixed adiabatically with the entering mainstream to give the state $M$. The total temperature $T_{0m}$ is given by Eq. (12) and the total pressure by $p_{0m}=p_{01g}$ (exactly as for the cascade efficiency). The mixture is expanded isentropically to the exit total pressure $p_{03}$ and the MP stage efficiency is defined by

$$(\eta_c)_{\mathrm{MP}} = \frac{P_{\mathrm{gross}}}{(h_{0m} - h_{03Sm})} \tag{22}$$

Just as with the cascade efficiency, the denominator of Eq. (22) is independent of the coolant supply pressures $p_{01ci}$.

It should be noted that in the form of this stage efficiency recommended by Kurzke [4], following Walsh and Fletcher [5], only those cooling flows upstream of the nozzle row throat are considered for the mixing process; it is argued that they are the only ones contributing to the actual turbine power output and therefore are the only ones that should be considered in the assessment of $P_{\mathrm{ideal}}$. Nevertheless, the work of Young and Wilcock [1] shows that the rotor coolant does make a contribution to the *gross* power. Indeed, the purpose of introducing preswirl vanes to guide the coolant onto the rotor disk is to increase that very contribution.

The authors suggest that turbine efficiency should be defined in such a way that the power potential of all the coolant streams should be included when calculating the ideal power. Whether or not this power potential is realized in practice is then reflected in the numerator of the efficiency definition. We believe that manufacturers should reconsider their current procedures with a view to standardizing on a thermodynamically sound definition.

For the FR efficiency, *all* coolant streams are mixed adiabatically with the entering mainstream gas in such a way that $(\sigma_T + \sigma_P)=0$. $T_{0m}$ is then given by Eq. (12), $p_{0f}$ by Eq. (16), and the FR stage efficiency by

$$(\eta_c)_{\mathrm{FR}} = \frac{P_{\mathrm{gross}}}{(h_{0f} - h_{03Sf})} \tag{23}$$

For the WP efficiency, *all* coolant streams are mixed with the mainstream such that $\sigma_P=0$. $T_{0m}$ is given by Eq. (12), $p_{0w}$ by Eq. (18), and the WP stage efficiency by

$$(\eta_c)_{\mathrm{WP}} = \frac{P_{\mathrm{gross}}}{(h_{0w} - h_{03Sw})} \tag{24}$$

**5.3 A Modified Rational Efficiency.** It is instructive to consider the rational efficiency of a cooled turbine stage in the light of the mixed efficiency definitions presented above. Modifying Eq. (8), we have

$$(\eta_c)_{\mathrm{RAT}} = \frac{P_{\mathrm{gross}}}{m_g b_{01g} + \sum_i m_{ci} b_{01ci} - \left(m_g + \sum_i m_{ci}\right) b_{03}} = \frac{P_{\mathrm{gross}}}{P_{\mathrm{gross}} + T_D \sum \Delta S_{CR}} \tag{25}$$

where $b_0=h_0-T_D s$ is the specific availability function with $T_D$ the dead-state temperature. The second expression is a standard rearrangement in terms of $\Sigma\Delta S_{CR}$ (the total rate of entropy creation between inlet and outlet states in the *actual* process due to irreversibilities) and this form matches well the approach recommended in Part 2 of Young and Wilcock [1] for estimating the cooling losses by calculating the various contributions $\Delta S_{CR}$. This form of cooled rational efficiency suffers from the same disadvantage as the uncooled version in that it is an efficiency based on the actual exit state (which itself varies with the efficiency it is being used to define) and, despite its solid thermodynamic foundation, it

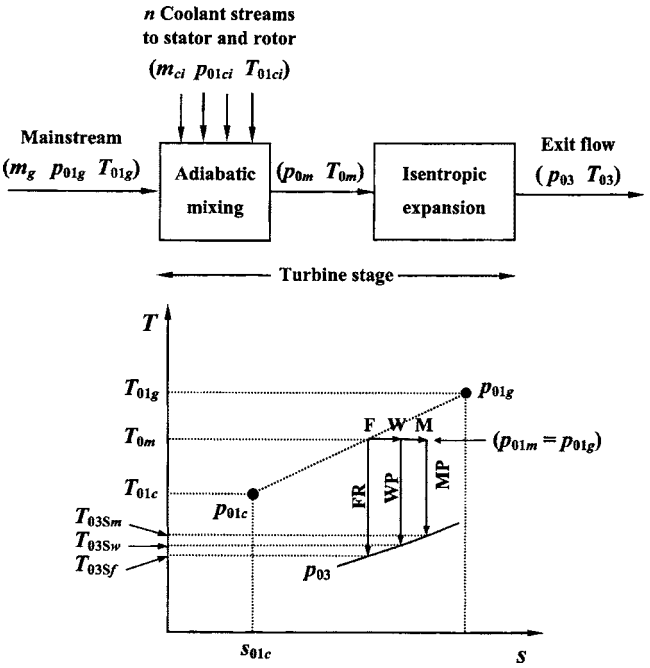


**Fig. 13 Illustrating the ideal processes in the MP, FR, and WP mixed stage efficiency definitions. In the (*T-s*) diagram, only one coolant supply (with $p_{01c}>p_{01g}$) has been indicated but in practice all coolant streams are included, however minor. Note that the dotted line defining point *F* is straight.**

[1]Sometimes (e.g., Kurzke [4], Timko [6]) the pumping power is added to $P_{\mathrm{gross}}$ in the numerator of Eq. (20) (i.e., $P_{\mathrm{gross}}$ is replaced by the $P_X$ of Eq. (3)) and a parallel modification is made to the denominator by the addition of an "isentropic" pumping power. We do not follow this practice here.

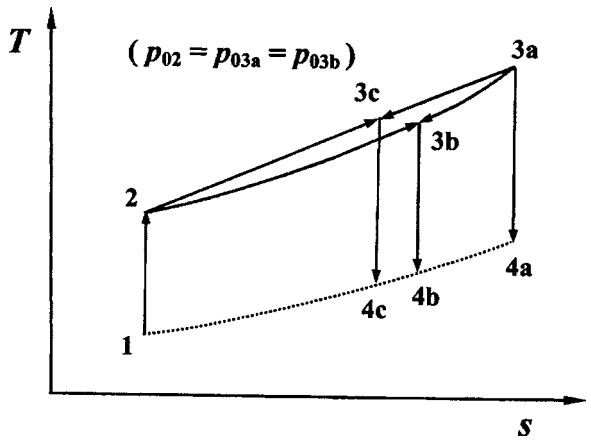


**Fig. 14 Three model perfect gas GT cycles with isentropic turbomachinery**

is rarely if ever used.

There is, however, no reason why $T_D$ should be taken as the standard ambient temperature of 25°C. Suppose, instead, that it were set equal to a temperature $\bar{T}$ defined by

$$\bar{T} = \frac{(h_{03} - h_{03S})}{(s_3 - s_{3S})} \tag{26}$$

where $(h_{03}, s_3)$ is the actual mass flow-averaged state at stage exit and $(h_{03S}, s_{3S})$ is the stage exit state corresponding to the ideal FR process; see Fig. 13 ($\bar{T}$ is approximately equal to the mean of $T_{03S}$ and $T_{03}$). By substituting Eq. (26) into the denominator of Eq. (25) and using the definition $b_0 = h_0 - T_D s$ with $T_D = \bar{T}$, it can be shown that the efficiency $(\eta_c)_{\mathrm{RAT}}$ of Eq. (25) is identical to the fully reversible mixed efficiency $(\eta_c)_{\mathrm{FR}}$.

This analysis shows that $(\eta_c)_{\mathrm{FR}}$ can therefore be written

$$(\eta_c)_{\mathrm{FR}} = \frac{P_{\mathrm{gross}}}{P_{\mathrm{gross}} + \bar{T} \sum \Delta S_{CR}} \tag{27}$$

showing that the FR efficiency can be related to the entropy creation terms precisely and unambiguously. Such an interpretation is of value in assessing the effect of the component losses on the efficiency. The only disadvantage seems to be that $\bar{T}$ is not exactly constant but varies (albeit very slightly) with the efficiency $(\eta_c)_{\mathrm{FR}}$ through the value of $T_{03}$.

## 6 Discussion and Conclusions

Various forms for the efficiency of cooled cascades and turbine stages have been discussed in this paper. The main point at issue is the definition of the quantity $P_{\mathrm{ideal}}$ to be used in the denominator of the expression for efficiency.

To put the discussion in a wider context, consider the model gas turbine cycles shown in Fig. 14. In all the cycles, it is assumed that the working fluid is the same perfect gas, the turbomachinery flows are isentropic, and the combustor is replaced by a constant pressure heater. Cycle A (1-2-3a-4a) is an uncooled cycle. Cycle B (1-2-3a-3b-4b) involves a cooling fraction $\phi$ which bypasses the heater and mixes with the heated fraction $(1-\phi)$ at constant pressure to give state 3b before entering the turbine. Cycle C (1-2-3a-3c-4c) is the same except that state 3c corresponds to mixing at constant entropy. It is easy to show [1] that the cycle efficiencies of A and B are the same, while the *cycle* efficiency of C is greater.

Consider cycle B. From its definition, its WP *turbine* efficiency is unity (because the heater exit, coolant, and mixed gas pressures are all equal), but its FR *turbine* efficiency is less than unity. Choice of the WP efficiency therefore implies that cycle B has the maximum efficiency possible. This, however, is untrue because cycle C (with a FR efficiency of unity) has a higher cycle efficiency resulting from the elimination of the "thermal equilibration" loss.

The authors argue that $P_{\mathrm{ideal}}$ should refer to a fully reversible FR process that provides the maximum possible gross power output from both mainstream gas and coolant flows; this in turn implies (for overall adiabatic flow) that the total entropy flow rate leaving the ideal turbine stage is equal to the total entropy flow rate entering.

The FR definition of efficiency leads, however, to values much lower than those currently presented by turbine manufacturers (around 5% less for cooling flow rates of about 10%). If such low efficiencies are unacceptable to turbine designers, then the weighted-pressure (WP) efficiency definition might prove acceptable. In this definition the ideal flow is not fully reversible, a minimum entropy generation (equal to that created during the thermal equilibration process) being allowed. The WP efficiency levels are only a little lower than those currently offered by industry, and are considerably higher than the FR values.

The thermal equilibration loss is not wholly inevitable and choice of the FR efficiency emphasizes its presence and provides an incentive to reduce it by improved design which, the authors believe, might be possible. Clearly, a temperature, difference between gas and coolant is essential to maintain the blades at the required safe temperature, but it is conceivable that the associated irreversibility might be reduced by attention to the entropy production mechanisms in the *thermal* boundary layers on the blade surfaces.

Finally, it is suggested that turbine manufacturers reconsider their current procedures with a view to standardizing on a thermodynamically sound definition which might then be universally accepted.

## Acknowledgment

The authors wish to thank Mr. P. Walsh and Dr. S. Gallimore of Rolls-Royce for sharing their expertise on turbine blade cooling technology, and to Dr. L. Torbidoni of Ansaldo for more general discussion. They are also grateful for comments from the reviewers and the associate editor.

## Nomenclature

$b$ = steady-flow availability function $(h - T_D s)$
$c_p$, $c_v$ = specific heat capacities
$h$ = specific enthalpy
$m$ = mass flow rate
$P_{\mathrm{ideal}}$ = ideal gross power
$P_{\mathrm{gross}}$ = actual gross power
$P_{\mathrm{pump}}$ = coolant pumping power
$p$ = pressure
$R$ = specific gas constant
$s$ = specific entropy
$T$ = temperature
$T_{\mathrm{D}}$ = dead-state temperature
$X$ = mole fraction
$\gamma$ = ratio of specific heat capacities $(c_p/c_v)$
$\varepsilon_u$, $\varepsilon_c$ = uncooled/cooled cascade or blade row efficiency
$\phi$ = coolant fraction
$\eta_u$, $\eta_c$ = uncooled/cooled stage efficiency
$\sigma$ = entropy created per unit mass of mixture

**Subscripts**

0 = total (stagnation)
$c$ = coolant
$ci$ = coolant stream $i$
FR = fully reversible
$g$ = mainstream gas
$m$ = mixed condition

MP = mainstream pressure
RAT = rational
S = state following an isentropic expansion
SS = static-to-static
TS = total-to-static
TT = total-to-total
WP = weighted pressure

## Appendix: Entropy Creation During Mixing

The gas exiting the hypothetical mixing control volume of Fig. 7 is a mixture of mainstream gas and coolant with mole fractions $X_{gm}$ and $X_{cm}$, respectively. Equation (13) for the rate of entropy creation per unit mass of mixture can therefore be written,

$$\sigma = (1-\phi)[s_g(X_{gm}p_{0m}, T_{0m}) - s_g(p_{01g}, T_{01g})] + \sum \phi_i[s_c(X_{cm}p_{0m}, T_{0m}) - s_c(p_{01ci}, T_{01ci})] \quad \text{(A1)}$$

If the gases enter and leave the control volume with high velocities, Eq. (A1) still holds because the total and static entropy are the same by definition. Assuming semi-perfect gases with $c_{pg}$ and $c_{pc}$ known functions of temperature, Eq. (A1) can be written,

$$\sigma = (1-\phi)\left[\int_{T_{01g}}^{T_{0m}} \frac{c_{pg}}{T'}dT' - R_g \ln\left(\frac{X_{gm}p_{0m}}{p_{01g}}\right)\right] + \sum_i \phi_i\left[\int_{T_{01ci}}^{T_{0m}} \frac{c_{pc}}{T'}dT' - R_c \ln\left(\frac{X_{cm}p_{0m}}{p_{0ci}}\right)\right] \quad \text{(A2)}$$

where $R_g$ and $R_c$ denote the specific gas constants. Rearranging gives

$$\sigma = \left[(1-\phi)\int_{T_{01g}}^{T_{0m}} \frac{c_{pg}}{T'}dT' + \sum \phi_i \int_{T_{01ci}}^{T_{0m}} \frac{c_{pc}}{T'}dT'\right] + \left[(1-\phi)R_g \ln\left(\frac{p_{01g}}{p_{0m}}\right) + \sum \phi_i R_c \ln\left(\frac{p_{01ci}}{p_{0m}}\right)\right] - \left[(1-\phi)R_g \ln(X_{gm}) + \sum \phi_i R_c \ln(X_{cm})\right] \quad \text{(A3)}$$

which is the same as Eq. (14) in the main text.

The final square-bracketed term in Eq. (A3) represents the rate of entropy creation due to the mixing of different gases and depends only on the composition. Had the supply gases been specified in terms of different components (e.g., $N_2$, $O_2$, $H_2O$, $CO_2$), both the algebraic form of the term and its numerical value would have been different.

Entropy creation due to diffusion is a genuine loss which can only be alleviated by performing the mixing more reversibly. Conceptually, this could be achieved using semi-permeable membranes as described in Part 1 of Young and Wilcock [1], but in practice such devices are not feasible. It is therefore expedient to ignore the loss in any definition of cascade or turbine efficiency on the basis that it is unavoidable. This also has the considerable advantage of removing all reference to mole fractions from the equations.

The above discussion only holds true if the mixture components behave as semi-perfect gases. If $c_{pg}$ and $c_{pc}$ are functions of $p$ as well as $T$, the final term in Eq. (A3) depends on these properties as well as the mole fractions. The cascade or turbine exit state then depends on the pressure at which the mixing occurs and the compositional entropy creation term must be retained. This is one reason why it is advantageous to adopt a semi-perfect gas model rather than a more complicated equation of state.

## References


[1] Young, J. B., and Wilcock, R. C., 2002, "Modelling the Air-Cooled Gas Turbine: Part 1, General Thermodynamics; Part 2, Coolant Flows and Losses," ASME J. Turbomach., **124**, pp. 207–213; 2002, ASME J. Turbomach., **124**, pp. 214–221.

[2] Horlock, J. H., 1973, *Axial Flow Turbines*, Krieger, Melbourne, FL.

[3] Hartsel, J. E., 1972, "Prediction of Effects of Mass-Transfer Cooling on the Blade-Row Efficiency of Turbine Airfoils," AIAA, 10th Aerospace Sciences Meeting, San Diego, Paper No. AIAA-72–11.

[4] Kurzke, J., 2002, "Performance Modelling Methodology: Efficiency Definitions for Cooled Single and Multistage Turbines," ASME Turbo-Expo 2002, Amsterdam, Paper No. 2002-GT-30497.

[5] Walsh, P. P., and Fletcher, P., 1998, *Gas Turbine Performance*, Blackwell Science, Oxford, U.K., pp. 225–229.

[6] Timko, L. P., 1980, "Energy Efficient Engine: High Pressure Turbine Component Test Perfomance Report," NASA Report No. CR-168289.

[7] Shapiro, A. H., 1953, *The Dynamics and Thermodynamics of Compressible Fluid Flow*, Ronald Press, New York.

# Direct Numerical Simulations of Transitional Flow in Turbomachinery

**J. G. Wissink**
e-mail: wissink@ifh.uni-karlsruhe.de

**W. Rodi**
e-mail: rodi@ifh.uni-karlsruhe.de

Institute for Hydromechanics,
University of Karlsruhe,
Kaiserstrasse 12,
D-76128 Karlsruhe, Germany

*An overview is provided of various direct numerical simulations (DNS) of transitional flows in turbine-related geometries. Two flow cases are considered: the first case concerns separating flow over a flat plate and the second case flows in turbine cascades. In the first case, in which* Re=60,000*, either an oscillating oncoming flow (1) or a uniform flow with and without oncoming turbulent free-stream fluctuations (2) is prescribed at the inlet. In both subcases (1) and (2), separation is induced by a contoured upper wall. In (1), the separated boundary layer is found to roll up due to a Kelvin-Helmholtz (KH) instability. This rolled-up shear layer is subject to spanwise instability and disintegrates rapidly into turbulent fluctuations. In (2), a massive separation bubble is obtained in the simulation without oncoming free-stream fluctuations. A KH instability is eventually triggered by numerical round-off error and is followed again by a rapid transition. With oncoming turbulent fluctuations, this KH instability is triggered much earlier and transition is enhanced, which leads to a drastic reduction in size of the separation bubble. The second case, concerning flow in turbine cascades, includes (1) flow in the T106 turbine cascade with periodically oncoming wakes at* Re=51,800 *and (2) flow and heat transfer in a MTU cascade with oncoming wakes and background turbulence at* Re =72,000*. In the simulation of flow in the T106 cascade with oncoming wakes, the boundary layer along the downstream half of the suction side is found to separate intermittently and subsequently rolls up due to a KH instability leading to separation-induced transition. At times when the wakes impinge separation is suppressed. In the simulations of flow around a MTU turbine blade, evidence of by-pass transition in the suction-side boundary-layer flow is observed while the pressure-side boundary layer remains laminar in spite of significant fluctuations present. In agreement with the experiments, the impinging wakes cause the heat transfer coefficient to increase significantly in the transitional suction-side region close to the trailing edge and by about 30% on the pressure side. The large increase in heat transfer in the pre-transitional suction-side region observed in the experiments could not be reproduced. The discrepancy is explained by differences in spectral contents of the turbulence in the oncoming wakes.* [DOI: 10.1115/1.2218517]

## 1 Introduction

Periodic unsteadiness, caused by rotor-stator interaction, and relatively low Reynolds numbers are characteristic for flow in certain turbomachinery components. Both phenomena directly affect blade boundary layer transition, the tendency to separation, heat transfer, and flow losses. While industrial computational fluid dynamics procedures are able to predict fairly accurately inviscid flow, the models in use for transition and turbulence, which are based on the Reynolds-averaged Navier-Stokes (RANS) equations, are still not sufficiently reliable and universal for coping with the complex phenomena cited above. The models need to be improved, and for this both an understanding of the underlying physical mechanisms and availability of high-quality data for testing the models are required. Direct numerical simulations (DNS) are now possible for idealized situations and can provide a wealth of information, but it is clear that this calculation method cannot be used in the design process, which will have to rely on RANS-based methods for a long time to come. In turbomachinery cascades, the focus is on flow periodicity caused by oncoming wakes of upstream rotor or stator blade rows that travel through the cascade, generating a very complex flow which is difficult to predict. These phenomena were investigated in the joint German Research Foundation (DFG) research program "Periodic Unsteady Flows in Turbomachinery" [1]. In this program, both experimental and numerical research was performed of flow in turbine-related geometries. In one subproject of the DFG research program, several direct numerical simulations of transitional flow in turbine-related geometries have been performed, and the present paper summarizes this work. Basically, two sets of DNS can be distinguished.

In the first set, boundary-layer separation flow was studied as a model for the flow along the suction side of a turbine blade. A contoured upper wall was used to induce an adverse streamwise pressure gradient along a flat plate mounted at the bottom, causing the boundary layer to separate. The effects of disturbances, added at the inlet to a uniform flow field, were studied. In the second set, a study was made of flows around turbine blades with and without periodically oncoming wakes. In one of the cases, the focus was on the interaction of wakes with a periodically separating boundary layer, while in the other case the aim was to elucidate the physical mechanisms that play a role in wake-induced by-pass transition and heat transfer.

More detailed background information on both sets of DNS and an overview of some of the literature can be found below.

## 2 Flat Plate Boundary-Layer Separation

In the first set of simulations, a flow over a flat plate with transition in a laminar separation bubble (LSB) was studied. In the presence of a strong enough adverse pressure gradient the laminar

Contributed by the Turbomachinery Division of ASME for publication in the JOURNAL OF TURBOMACHINERY. Manuscript received February 2, 2005; final manuscript received February 2, 2006. Review conducted by G. Walker. Paper presented at the Deutscher Luft- und Raumfahrtkongress 2004, Dresden, Germany.

  

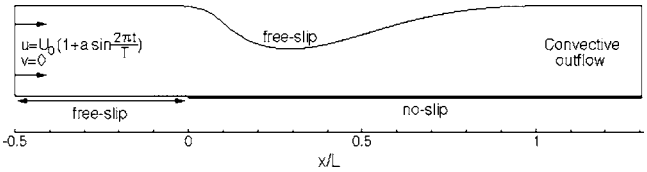


**Fig. 1 Computational domain at midspan**

boundary layer over a flat plate separates and forms a LSB. The separated boundary layer is very unstable and usually undergoes a fast transition to turbulence. Farther downstream, the turbulent wake-like flow may re-attach and slowly evolve into a turbulent boundary layer. Previously, DNS of LSB flow with steady inflow was performed by Alam and Sandham [2], Maucher et al. [3], and Spalart and Strelets [4]. To generate an adverse pressure gradient, required for the formation of a separation bubble, Alam and Sandham as well as Spalart and Strelets used suction through the upper boundary while Maucher et al. applied a special boundary condition for the free-stream velocity. In the simulation with steady inflow of Wissink and Rodi [5], the adverse pressure gradient was generated by the special shape of the upper wall (see Fig. 1). As in the simulation of Wissink and Rodi [5], Spalart and Strelets relied on small numerical round-off errors present in any LSB simulation to trigger natural modes. They detected a Kelvin-Helmholtz (KH) instability and found evidence of a low-frequency wavering mode in the separated boundary layer. Wissink and Rodi performed further LSB flow simulations in which they introduced oscillations and fluctuations to the oncoming flow [6–8]. In the present paper we aim to provide an overview and comparative study of these LSB simulations.

**2.1 Flow Configuration and Computational Aspects.** The computational geometry was chosen in accordance with experiments performed in a companion project at the Technical University of Berlin [9]. A direct comparison to the experiments is not possible because instantaneous velocity profiles at the inlet are not exactly known and because of the relatively high Reynolds numbers employed in the experiments. The special shape of the upper wall, illustrated in Fig. 1, generates a strongly adverse streamwise pressure gradient along the flat plate, due to which the boundary layer separates. By employing a free-slip boundary condition, separation along the upper wall was avoided. Along the lower wall, for $x<0$, free-slip boundary conditions were employed, while for $x>0$, no-slip boundary conditions were used. At the outlet, a convective outflow boundary condition was used, while in the spanwise direction periodic boundary conditions were employed. The Reynolds number, Re=60,000, is based on the mean inflow velocity $U_0$ and the length of the plate in the experiment $L$. The precise inflow boundary condition used depends on the situation simulated. Figure 1 shows the inlet boundary conditions employed in the simulations with oscillating external flow. At the inflow boundary of these simulations, an oscillating flow field $(u,v,w)=U_0(1+a\sin 2\pi t/T,0,0)$ was prescribed, where $a$ is the amplitude and $T$ is the period.

An overview of the simulations performed is provided in Table 1. After an initial period of approximately $\Delta T=6L/U_0$, in which the flow was allowed to develop, phase-averaged statistics were gathered for at least ten further periods of simulation. For the phase-averaging procedure, the period $T$ was divided into 256 equal phases: $\phi=0,1/256,\ldots,255/256$. For simulations O1 and O2, a grid-refinement study has been performed that shows a very good qualitative agreement of the simulations on various meshes and also a good quantitative agreement with respect to the most important phase-averaged quantities, such as the location of separation, the maximum reverse flow, the fluctuating kinetic energy, etc. The present paper reports on the best resolved simulations.

**Table 1 Overview of the simulations with oscillating inflow**

| Simulation | Grid | Size span | $a$ | $T$ |
|---|---|---|---|---|
| O1 | $966\times226\times128$ | $0.12L$ | 0.20 | 0.61 |
| O2 | $1286\times310\times128$ | $0.08L$ | 0.10 | 0.30 |
| O3 | $966\times226\times128$ | $0.12L$ | 0.05 | 0.30 |

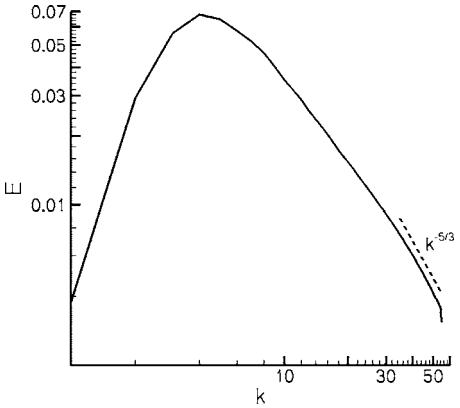


**Fig. 2 Energy spectrum of the free-stream disturbances added at the inlet**

In the simulations with free-stream disturbances, the inflow boundary conditions read: $(u,v,w)=U_0(1,0,0)+(u',v',w')$. The free-stream disturbances $(u',v',w')$ were obtained by interpolation from a snapshot of a separate large-eddy simulation (LES) of isotropic turbulence in a box and were kindly made available by Dr. Jochen Fröhlich of the University of Karlsruhe. Figure 2 shows a log-log plot of the energy spectrum of the free-stream disturbances added at the inlet. More information about the evolution of the disturbances as they travel through the inflow domain can be found in [8]. The integral length-scale associated with the free-stream disturbances is $\Lambda=0.019L$. An overview of the simulations with steady inflow and with free-stream disturbances is provided in Table 2. To allow the separated boundary layer to re-attach and assume typical characteristics of a turbulent boundary layer, the length of the flat plate ($l_x$) was chosen relatively large in simulations F2 and F3.

Both the simulations with oscillating inflow and with steady inflow were performed on the IBM SP-SMP of the Computing Center in Karlsruhe using up to 128 processors. The simulations with free-stream fluctuations were run on the Hitachi SR8000-F1 at LRZ (Leibniz Rechenzentrum) in Munich using 256 processors. The computational domain was subdivided in a number of equal-sized subdomains. To each of the subdomains one processor was assigned. This way, a near-optimal load-balancing was achieved. Communication between processors was performed using the standard Message Passing Interface (MPI) protocol. Typical runtimes for the simulations performed varied between one and three months of clock time.

**Table 2 Overview of the simulations with and without free-stream fluctuations. $l_x$ is the actual length of the flat plate used in the simulation, $x_{re}$ is the approximate location of re-attachment, and Tu is the turbulence level at the inlet.**

| Simulation | Grid | Size span | $l_x$ | $x_{re}$ | Tu (%) |
|---|---|---|---|---|---|
| F1 | $1038\times226\times128$ | $0.08L$ | $1.6L$ | $1.28L$ | 0 |
| F2 | $1926\times230\times128$ | $0.08L$ | $3.0L$ | $1.00L$ | 5 |
| F3 | $1926\times230\times128$ | $0.08L$ | $3.0L$ | $0.77L$ | 7 |

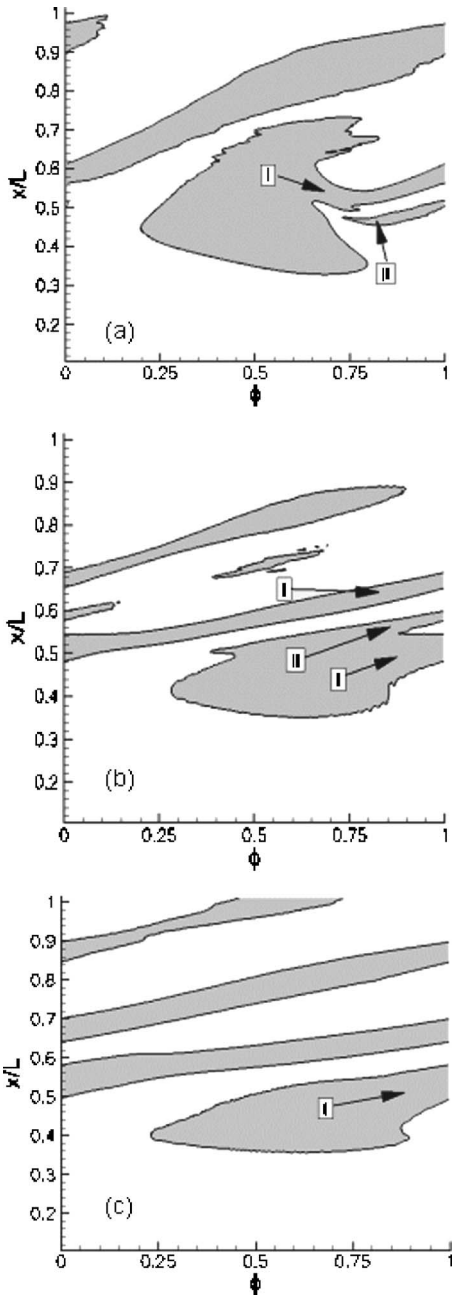


**Fig. 3 Evolution of the separation bubble during one period of inflow oscillation. The contours correspond to negative phase-averaged friction velocity. (*a*) Simulation O1, (*b*) simulation O2, and (*c*) simulation O3.**

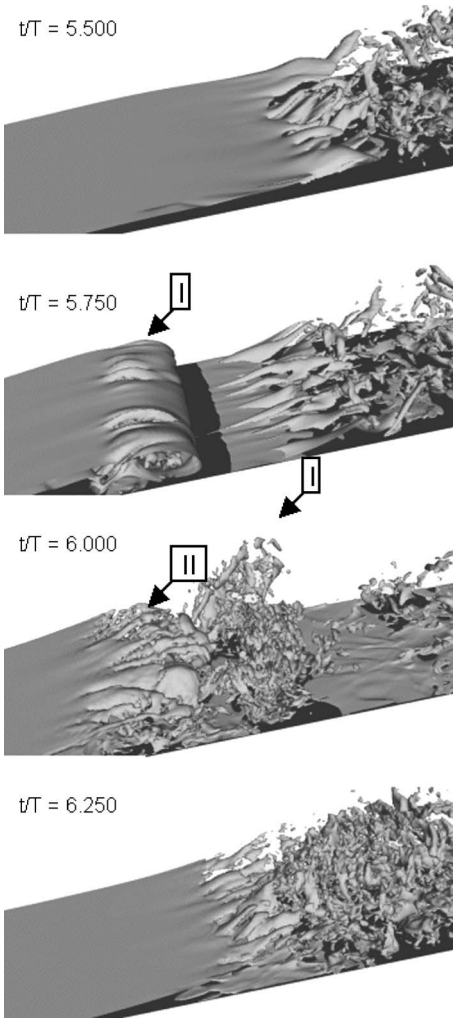


**Fig. 4 Simulation O1: sequence of isosurfaces of the spanwise vorticity. Label "I" identifies the roll of recirculating flow and label "II" the remainder of the separation bubble as discussed previously.**

### 2.2 Results

*2.2.1 Boundary Layer Separation With Oscillating Inflow*. In the presence of streamwise oscillating flow, the adverse streamwise pressure gradient, generated by the special shape of the upper wall, is alternately weakened and enhanced. As a result, the locations of separation and transition move back and forth. In Fig. 3, the location of the separation bubble is identified by contours of the negative phase-averaged friction velocity. The figure shows the evolution of the separation bubbles for the three simulations with oscillating external flow listed in Table 1. Owing to the large oscillation-amplitude and period in simulation O1, compared to simulations O2 and O3, the maximum streamwise extent of the separation bubble is much larger. In all three simulations, a large roll of re-circulating, turbulent flow (labeled "I") is shed as the oncoming flow decelerates (see also Figs. 4 and 5). In Figs. 3(*a*) and 3(*b*), the remainder of the separation bubble is labeled "II." In simulation O2, Region II intermittently merges with the newly formed separation bubble of the next period. In simulation O3, however, it was impossible to define Region II. This is explained by the small inflow-amplitude, which only mildly triggers the KH instability that is responsible for the roll-up of the shear layer and the formation of regions I and II. Hence, while Region II was already quite small in simulation O2, in simulation O3 it is even smaller and may completely merge with the newly formed bubble of the next period. In none of the three simulations, however, was Region I found to merge with the remainder of a bubble formed during another period. Along the flat plate, the number of separation bubble-remains—separated by patches of laminar flow—increases with decreasing inflow-oscillation period. For instance, at $\phi=0.5$, two such remains are observed for simulation O1, three for simulation O2, and four for simulation O3.

Figures 4 and 5 show a series of snapshots of the spanwise vorticity from simulations O1 and O3, which allow the illustration and comparison of the dynamics of the boundary layers during one period of inflow oscillation. Owing to the large period of $T=0.61L/U_0$ employed in simulation O1, in between the remains of two subsequently formed separation bubbles, a clearly visible patch of laminar boundary layer flow can be observed. The much smaller period of $T=0.30L/U_0$ in simulations O2 and O3 allows

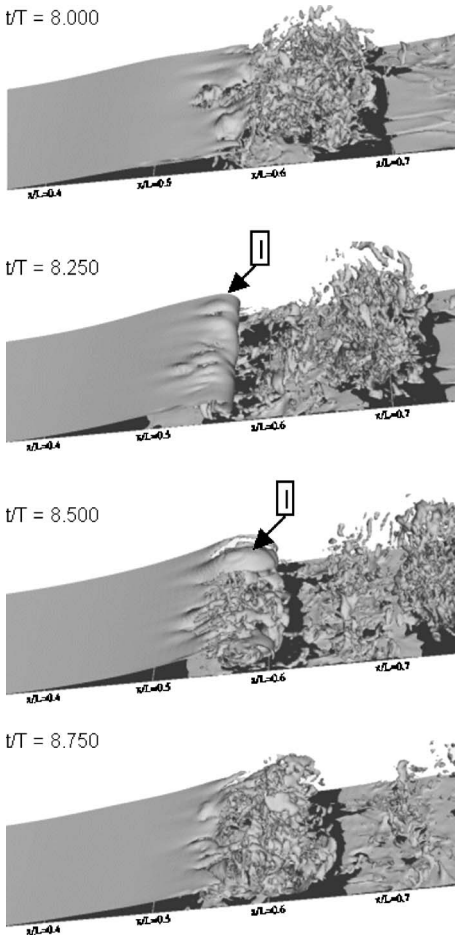


**Fig. 5 Simulation O3: sequence of isosurfaces of the spanwise vorticity. Label "I" identifies the roll of recirculating flow discussed previously.**

only a relatively small patch of laminar boundary layer flow to emerge, though at no time are subsequently formed separation bubbles observed to merge. In both simulations, the separated shear layer is found to roll up owing to a KH instability. The roll of recirculating flow (visible at $t/T=5.750$ in simulation O1 and at $t/T=8.500$ in simulation O3) is shed and subsequently very quickly becomes turbulent. As discussed in Wissink and Rodi [6], at least two types of elliptic instabilities—which may occur when two-dimensional flow with elliptical streamlines is subjected to three-dimensional disturbances—contribute to this very fast transition to turbulence of the recirculating flow.

In Fig. 6, a comparison is made of spectra of the $v$-velocity component gathered at various locations $P_1,\ldots,P_4$ in the time-averaged separated boundary layer. The points $P_1,\ldots,P_4$ are identified in the lower graphs, showing contours of the time-averaged spanwise vorticity. In all graphs, the peaks correspond to the oscillation-frequency (left-most peak) of the inflow and its higher harmonics. For each simulation, the maximum amplitude in each of the points $P_4$, located farthest away from the location of separation, is reached at a frequency of $f\approx 6.7U_0/L$, indicating that the most unstable modes of all three KH instabilities coincide. This is not surprising since in all simulations the thickness and strength of the shear layer is comparable. In simulations O1 and O3, at point $P_2$ the most unstable mode is reached at the smaller frequency of $f\approx 3.3U_0/L$. Apparently, the most unstable frequency becomes smaller as the location of the point where the time-signal is recorded is nearer to the location of separation.

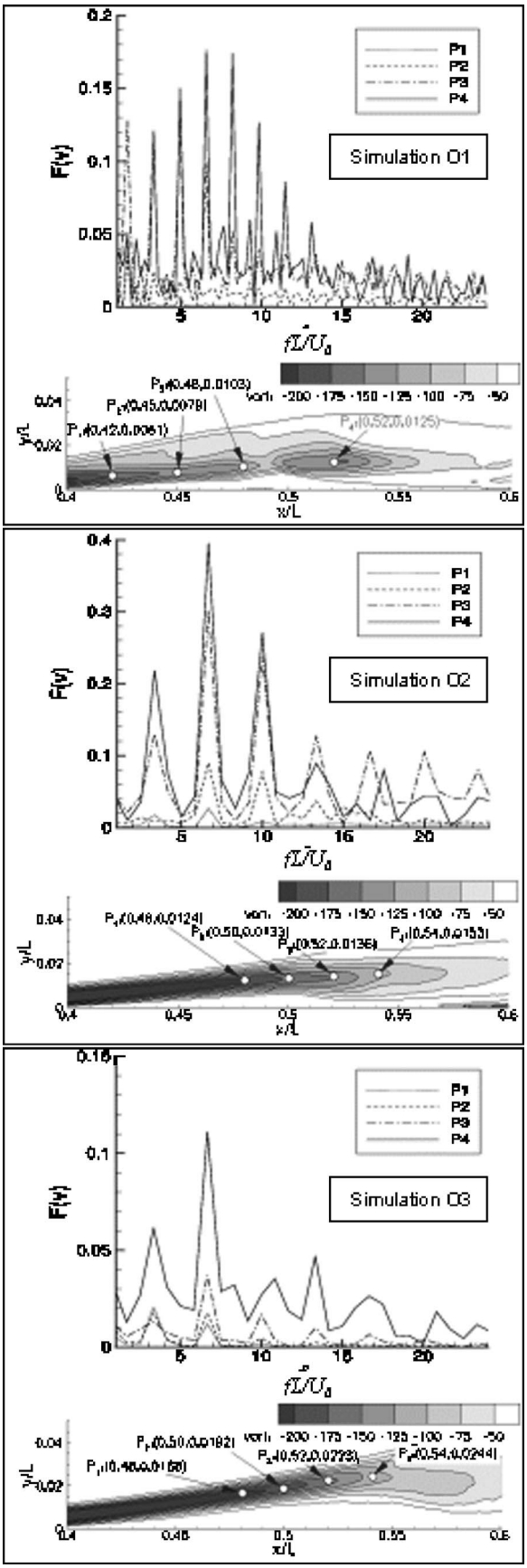


**Fig. 6 Spectra of the $v$-velocity at four points, $P_1-P_4$. The location of the points is identified in the lower graphs showing contours of the time-averaged spanwise vorticity.**

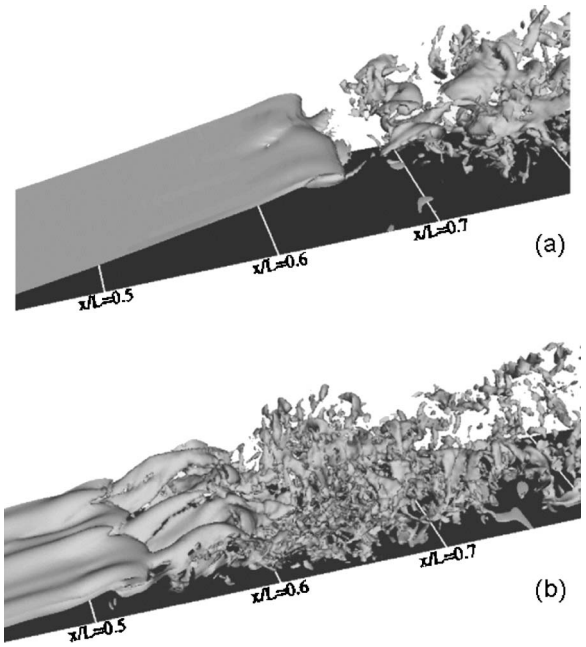


**Fig. 7 Isosurfaces of the spanwise vorticity. (*a*) Simulation F1 and (*b*) simulation F3.**

*2.2.2 Boundary-Layer Separation With Free-Stream Fluctuations*. The simulations with and without free-stream fluctuations stemming from a separate LES of isotropic turbulence in a box (see Fig. 2) are listed in Table 2. In simulation F1, without explicitly added fluctuations at the inlet, a KH instability is triggered by numerical round-off errors. The addition of free-stream fluctuations, 5% in simulation F2 and 7% in simulation F3, leads to a drastic reduction in size of the separation bubble compared to the one obtained in simulation F1. In Fig. 7, a comparison is made between simulation F1 and simulation F3. The figure shows snapshots of the instantaneous spanwise vorticity illustrating the presence of a KH instability in both simulations. In all simulations, the boundary layer separates near $x/L=0.37$. While in simulation F1 the shear layer rolls up at $x/L=0.63$, in simulation F3 the shear layer is found to roll up farther upstream, at $x/L=0.52$, corresponding to a much smaller separation bubble. Both figures illustrate that once the shear layer has rolled up, the transition to turbulence is almost instantaneous.

In Fig. 8, a comparison is shown of the time-averaged boundary-layer shape factor $H$ obtained in simulations F1, F2, and F3. It gives further evidence that the size of the separation bubble is quite sensitive to the amount of inflow fluctuations (see also Table 2, which provides the approximate location of re-attachment $x_{re}$). The difference in separation bubble size is reflected by the shape factor showing a peak of $H=16.4$ in simulation F2 as compared to a peak of $H=11.8$ in simulation F3. Upstream of the separation bubble, the shape factor takes on values around $H=2.4$, which are characteristic for a laminar boundary layer. Downstream of the separation bubble, the redeveloping turbulent boundary layer only very slowly assumes values around $H=1.7$ that are characteristic for a turbulent boundary layer. This reflects the effect of the wall-adjacent wake-like turbulent flow on the redeveloping boundary layer flow downstream of the separation bubble. Compared to both simulations F2 and F3, the shape factor of simulation F1—without free-stream disturbances—is much larger, assuming a peak value of $H=77.3$.

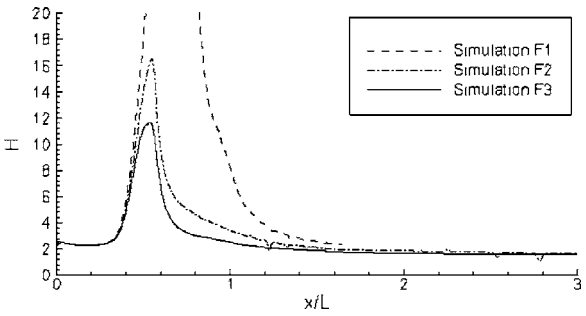


**Fig. 8 Time-averaged shape factor *H*; comparison of simulations F1, F2, and F3**

## 3 Flow Around Turbine Blades

In the second set of DNS, flow around low-pressure turbine (LPT) blades with periodically incoming wakes was studied. Generally, flows in turbine cascades are very complex and call for powerful computational tools and models. The aerodynamic performance of a turbine blade is affected strongly by disturbances carried by oncoming wakes generated by the preceding row of blades. Because of advances in computational power, recently, LES and DNS of flow in LPT cascades with oncoming wakes have become feasible [10–14]. Compared to a DNS, a LES is computationally less demanding and therefore appears to be an attractive alternative. Unfortunately, LES is found to be less accurate in predicting the details of boundary-layer transition including the location in the presence of impinging disturbances. This is partly due to the fact that in a LES, only the resolved part of the free-stream fluctuations physically impinges on the boundary layer resulting in a weaker triggering of boundary-layer instabilities [12]. A previous DNS of flow in a T106A LPT cascade has been performed by Wu and Durbin [13]. Their Reynolds number, based on the axial chord length and inflow conditions, was Re =148,000. They were the first to identify longitudinal vortical structures generated along the pressure side of the blade by impinging wakes. In the passage between two turbine blades, they discovered production of fluctuating kinetic energy at the apex of the strained wake, as predicted by Rogers [15]. In our DNS, we focus mostly on the study of boundary-layer development. Especially along the suction side, the presence of boundary-layer separation—inducing boundary-layer transition—or wake-induced by-pass transition has a major impact on heat transfer and losses.

**3.1 Flow Configuration and Computational Aspects.** The computational geometries were chosen in accordance with experiments performed in a companion project performed at the University of the Armed Forces in Munich [16] (T106A blades) and experiments performed earlier by Liu and Rodi [17,18] at the University of Karlsruhe (MTU blades), the latter focused on heat transfer. The numerical simulations were performed for a section of mid-span, which is approximately two-dimensional (see, for example, Fig. 9). In the $y$-direction, both upstream and downstream of the blades, periodic boundary conditions were applied. At the surface of the blades a no-slip boundary condition was employed. In the spanwise direction periodic boundary conditions were used, while at the outlet a convective outflow boundary condition was employed. Artificial wakes were introduced at the inlet, superposed on the mean flow $(u,v,w)=U(\cos\alpha,\sin\alpha,0)$, where $\alpha$ is the angle of attack (see Tables 3 and 4). The data used for the wakes stem from a separate simulation by Wu and Durbin of Stanford University [19] who performed LES of flow with a far-wake behavior.

The main parameters of the DNS performed of flow in the T106A LPT cascade with and without wakes are listed in Table 3. The Reynolds number—based on the inflow velocity and axial chord—is Re=51,800. In the simulation with wakes, the vertical distance between wakes is $P/2$, where $P=0.9306L$ is the pitch between blades and $L$ is the axial chord-length. The angle of at-

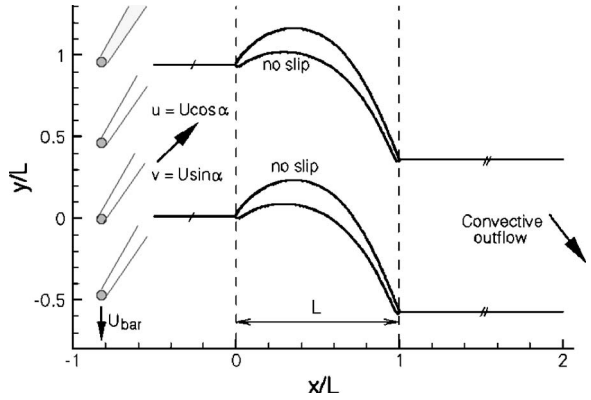


**Fig. 9 Computational domain of the T106A cascade at midspan**

tack for this flow problem is $\alpha=45.5$ deg. The period of the flow, $T=1.138L/U$, is equal to the time needed by the wakes to perform a vertical sweep through the inlet plane over a distance $P/2$.

The simulations of flow around and heat transfer from a model MTU turbine blade at Re=72000—based on inflow velocity and axial chord—are summarized in Table 4. In simulation M1 no wakes were at the inlet, which corresponds to Case A of the experiments, while in simulation M2 wakes were introduced, corresponding to Case C of the experiments with a wake-passing-frequency of $f=2.4U/L$. The angle of attack in both simulations was $\alpha=0$ deg. To reflect the setup in the experiments of Liu and Rodi [17,18], at the inflow the temperature $\theta$ of the oncoming flow was set to $\theta_0=0.7\theta_b$, while the temperature at the surface of the blades was assumed to remain constant at $\theta=\theta_b$. In the DNS, the heat transfer and its increase due to impinging wakes was studied. The local Nusselt number Nu defined by

$$Nu=\frac{hL}{\kappa}=-\frac{L}{\theta_b-\theta_0}\left.\frac{\partial\theta}{\partial n}\right|_w=-\frac{10}{3}\left.\frac{\partial(\theta/\theta_b)}{\partial(n/L)}\right|_w$$

with $h$ being the heat-transfer coefficient and $\kappa$ the thermal conductivity, was chosen as a nondimensional measure of heat transfer from the surface of the model turbine blade to the outer flow. To reflect the presence of background disturbances in the experiment with oncoming wakes, free-stream fluctuations of intensity Tu=4% were added to the inflow of the DNS. To be able to employ periodic boundary conditions in the $y$-direction of the DNS, it is necessary that the vertical distance between wakes is an integer divider of the pitch $P=L$ between blades. For this reason, the vertical distance between wakes in simulation M2 was chosen to be $P/2$, which is only an approximation of the distance of $0.567L$ in the experiments. As a result, the period of the flow in the DNS is $T=0.3676L/U$.

The computations of flow in turbine cascades were all performed on the Hitachi SR8000-F1 at LRZ in Munich using up to 256 processors.

**Table 3 Overview of the T106A LPT cascade simulations with and without oncoming wakes. The Reynolds number, based on the mean inflow *U* and axial chord-length *L* is Re=51,800 and the inflow angle is $\alpha=45.5$ deg. WD stands for the wake deficit and WHW stands for the wake half-width. No background fluctuations are added at the inlet.**

| Sim | Grid | Span | WD | WHW |
|---|---|---|---|---|
| T1 | $771\times256\times128$ | $0.25L$ | — | — |
| T2 | $1014\times260\times64$ | $0.20L$ | 25% | $0.03L$ |

**Table 4 Overview of the MTU turbine cascade simulations with and without oncoming wakes. The Reynolds number, based on the mean inflow and axial chord-length is Re =72,000 and the inflow angle is $\alpha=0$ deg. WD stands for the wake deficit, WHW stands for the wake half-width. Tu is the minimum turbulence level in the plane $x/L=0.20$, the spanwise size is $0.20L$. "Exp." refers to the experimental case simulated (see Liu and Rodi [15,16]).**

| Sim | Grid | WD | WHW | Tu | Exp. |
|---|---|---|---|---|---|
| M1 | $1254\times582\times128$ | — | — | 0% | A |
| M2 | $1254\times582\times128$ | 30% | $0.045L$ | 2.8% | C |

**3.2 Results.** Results from the simulations of the flow in the two different turbine cascades with oncoming wakes will now be discussed. The first case concerns the flow in the T106A cascade. The combination of low Reynolds number and a relatively high angle of attack of the inflow causes the flow around the T106A blades to separate along the suction side near the trailing edge resulting in separation induced transition. The separation is, however, periodically suppressed by impinging wakes. As in the flat plate simulations, the separated boundary layer exhibits a KH instability. The second case concerns flow and heat transfer in a MTU cascade. Here, incomplete by-pass transition of the boundary layer flow along the downstream half of the suction side is found to occur and an increase in laminar heat transfer from the pressure side is found to be promoted by longitudinal vortical structures.

*3.2.1 Flow in the T106 Turbine Cascade With Incoming Wakes.* Figure 10 shows the time-averaged wall-static pressure coefficient $C_p$ of (*a*) simulation T1 without wakes and (*b*) simulation T2 with wakes. Compared to experiment, in simulation T1 $C_p$ is reasonably well captured. Certain differences on the suction side can be attributed to discrepancies in the angle of attack, which was only approximately known in the experiment, and some minor compressibility effects. The difference between simulation T2 and experiment, shown in Fig. 10(*b*), is somewhat larger, which indicates that the physical presence of wake-generating cylinders in the experimental inlet region partly blocks the inflow, thereby reducing the mass flux through the passage. Consequently, the effective Reynolds number in the experiment also slightly reduces. The marked "kink" present along the suction side at $x/L=0.93$ (Fig. 10(*a*)) indicates that there is massive separation in the simulation without periodically impinging wakes. The much smaller kink at $x/L=0.88$ in Fig. 10(*b*) points to a much reduced average separation in simulation T2, which occurs only intermittently along the downstream half of the suction side.

The series of snapshots of the phase-averaged fluctuating kinetic energy shown in Fig. 11 illustrates the stretching and straining of the wakes and the production of fluctuating kinetic energy $k$ in the passage between blades. For each phase $\phi$, the location of the wakes is well-defined by an increased level of $k$. Production of fluctuating kinetic energy is concentrated at the apex of the strained wake and in the boundary layer along the downstream half of the suction side. As the wake approaches the leading edge of the blade, it begins to wrap around it. Especially near the suction side, immediately downstream of the leading edge, the wake is severely stretched, while its axis aligns with the surface of the suction side. As a consequence, in this region the wake impinges at virtually zero angle of attack. As the wake is stretched, the fluctuations carried by the wake are damped. Along the pressure side, near the leading edge the wake impinges at a relatively large angle of attack, which becomes increasingly smaller as the wake approaches the trailing edge of the blade. At the trailing edge itself, the angle between the wake-axis and the surface of the blade is virtually zero. As a result of the wakes impinging at the pressure side, longitudinal vortical structures are obtained (also observed for the MTU blade in Fig. 18).

Figure 12 shows two snapshots of vortical structures present in

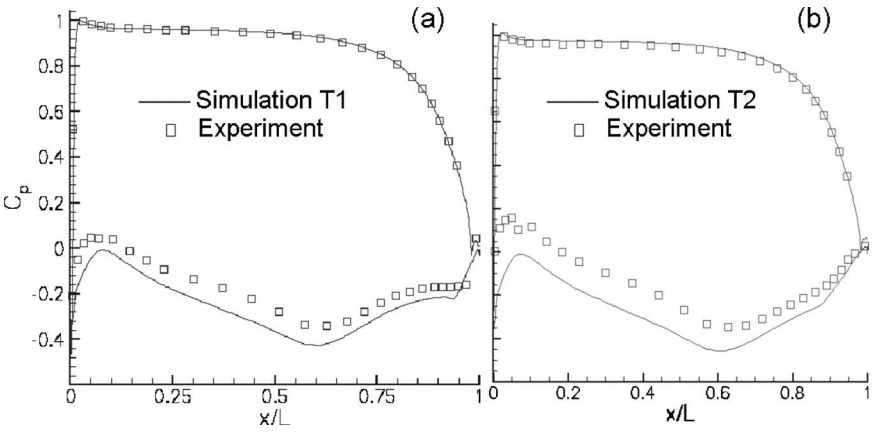


**Fig. 10 Wall static-pressure coefficient for simulations T1 (*a*) and T2 (*b*) and comparison to experiment [16]**

part of the passage between blades near the suction side. The vortical structures have been made visible using the $\lambda_2$ criterion of Jeong and Hussain [20], showing a negative isosurface of the second largest eigenvalue of the sum of the squares of the symmetric and anti-symmetric part of the velocity gradient tensor. The figure clearly shows the presence of relatively large-scale vortical structures carried by the periodically oncoming wakes. As already observed in Fig. 11, the wake impinges on the upstream half of the suction side at virtually zero angle of attack. While the wake is stretched, its vortical structures become elongated and very thin, thereby lessening its effect as it impinges on the suction-side boundary layer. The production of fluctuations in the passage between blades gives rise to an increase in vortical structures, visible, for instance, at $t/T=8.43$, adjacent to the upper boundary of the plotted section. In both snapshots, small scale vortical structures were present immediately upstream of the trailing edge, which indicates that the local boundary layer flow is no longer laminar.

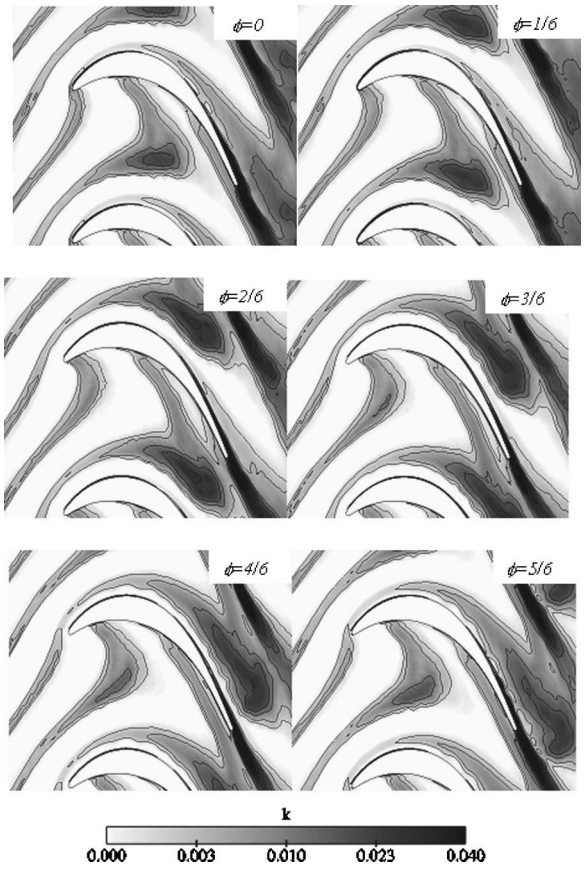


**Fig. 11 Phase-averaged fluctuating kinetic energy in the passage between blades (simulation T2)**

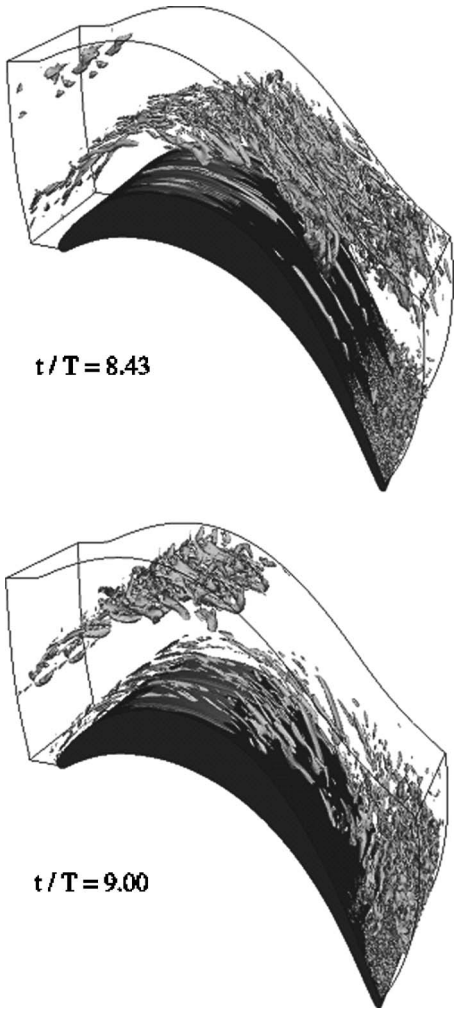


**Fig. 12 Simulation T2: snapshots showing instantaneous vortical structures near the suction side**

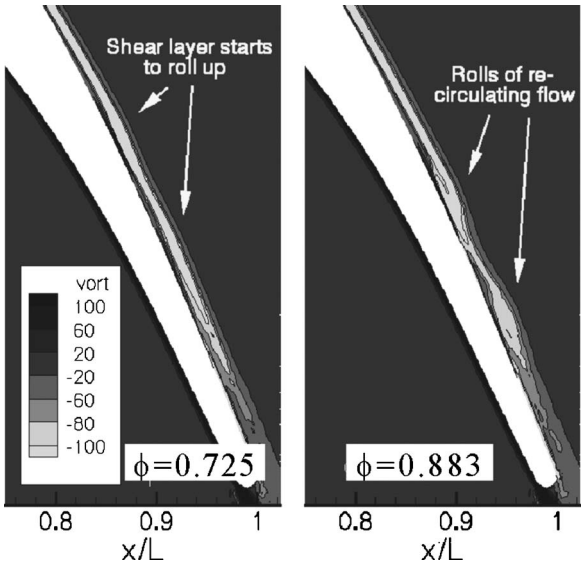


**Fig. 13 Simulation T2: Roll-up of separated shear layer**

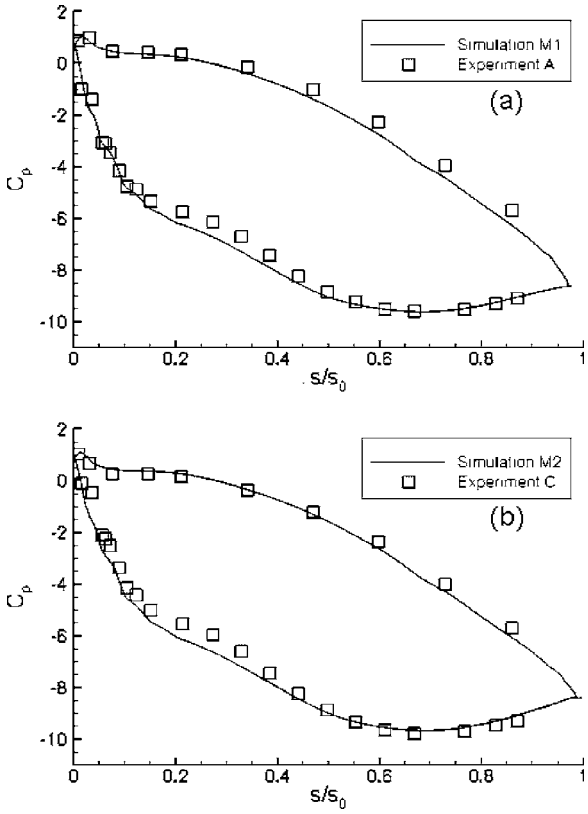


**Fig. 14 Wall static-pressure coefficient for simulations M1 (*a*) and M2 (*b*) as a function of the normalized wall coordinate $s/s_0$ and comparison to experiment**

In Fig. 13, two snapshots are shown providing a close-up of the separated shear layer along the downstream half of the suction side. The shear layer has been made visible using the phase-averaged spanwise vorticity. The figure clearly illustrates the roll-up of the separated shear layer owing to a KH instability triggered by an impinging wake, giving rise to the appearance of two recirculation zones. Inside the rolled-up shear layer, significant amounts of fluctuating kinetic energy are produced, causing separation-induced transition.

*3.2.2 Flow and Heat Transfer in the MTU Cascade*. In Fig. 14, the time-averaged wall-static pressure coefficient, $C_p=(p-p_{\text{ref}})/(1/2)u_{\text{ref}}^2$ of simulations M1 and M2 is compared to experiments A and C [17,18], respectively. The results obtained in both simulations compare well with the experiments. Compared with the T106 blade (Fig. 10) the favorable streamwise pressure gradient along the upstream half of the suction side is considerably stronger. As a consequence, the streamwise acceleration of the flow along the suction side of the MTU blade is relatively large. Though a small adverse pressure gradient region is present immediately upstream of the trailing edge on the suction side, it is not strong enough to induce boundary-layer separation.

Figure 15 shows snapshots of instantaneous vortical structures in the passage between the blades. As in Fig. 11, these structures have been made visible using the $\lambda_2$-criterion of Jeong and Hussain. Compared to the vortical structures carried by the wakes in simulation T2 of the T106 cascade, the vortical structures inside the wakes of simulation M2 are of a smaller scale. This is a direct consequence of the action of background disturbances, added at the inlet, on the coherent structures carried by the wakes, resulting in their partial destruction. As in simulation T2, an increase in vortical structures present in the middle of the cascade is observed, which is a consequence of fluctuating kinetic energy production at the apex of the wake.

In Fig. 16, the time-averaged shape factor $H$ along the suction side is shown for simulations M1 and M2. The shape factor obtained in simulation M2—with wakes—is in very good agreement with experiment. Upstream of $s/s_0=0.65$, where the streamwise pressure gradient is favorable, it assumes values larger than 2, which are characteristic for a laminar boundary layer. Farther downstream, in the neighborhood of the trailing edge, the values fall below 2, indicating that the flow is at least intermittently turbulent in this region. In simulation M1, without oncoming wakes and background fluctuations, the shape factor rises significantly in the region where the streamwise pressure gradient turns adverse. This indicates a tendency towards separation, but separation was in fact never observed. Along the pressure side—not illustrated here—there is hardly any difference in the shape factors found in simulations M1 and M2. In both simulations, downstream of $s/s_0=0.25$, a constant value of $H=2.35$ was obtained, indicating that the pressure-side boundary layer remains laminar.

Figure 17 shows the time-averaged local Nusselt number along the suction and pressure sides of the MTU blade. Along the suction side, the Nusselt number obtained in simulation M1—without wakes—is in good agreement with experiment A. The Nusselt number obtained in simulation M2—with wakes—is underestimated, especially in the laminar region, though the shape of the profile, which is related to the increase of Nu in the region where the boundary layer becomes intermittently turbulent, is reasonably well predicted. The underestimation of Nu is possibly explained by the spectrum of scales present in the disturbances added at the inflow. While small-scale structures in the outer flow are found not to be able to notably penetrate/disturb the suction-side boundary layer in the presence of a strongly favourable pressure gradient, large-scale disturbances might be more effective and are probably present in the experiment, leading to the observed increase in the heat transfer coefficient. There is evidence of the existence of a preferred free-stream fluctuation length-scale, which is particularly effective in promoting laminar heat transfer in the presence of an accelerating streamwise flow [21]. Along the pressure side, the Nusselt number obtained in simulations M1 and M2, respectively, is in good agreement with experiment. The moderate increase in Nu from Experiment A without wakes to Experiment C with wakes and background turbulence is quite well captured in the numerical simulations. The reason for this increase in Nu is most likely the increased transport of heat from the wall promoted by the wake-induced, streamwise vortical structures present along the pressure side. These structures can be seen in the two snap-

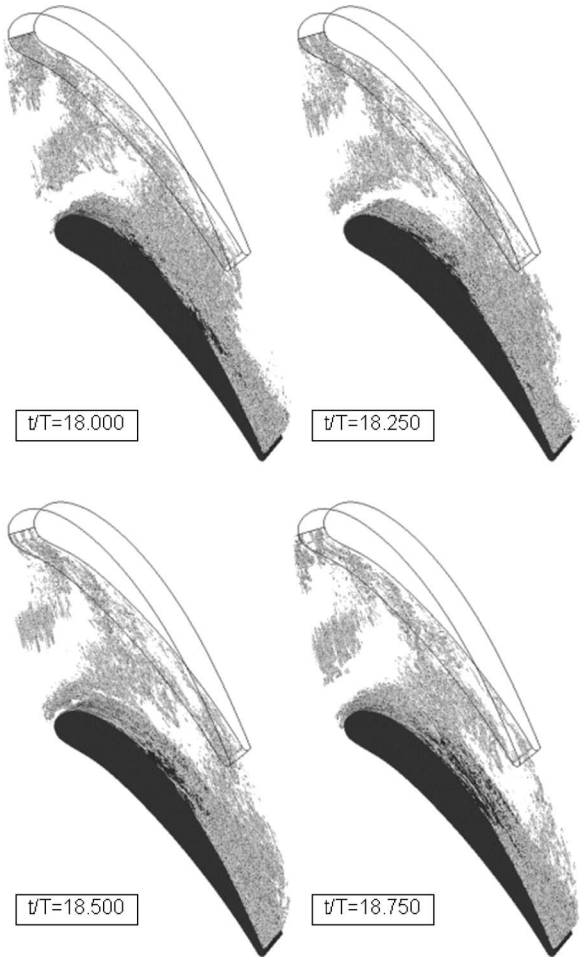


**Fig. 15 Simulation M2: Snapshots showing instantaneous vortical structures in the passage between blades**

shots shown in Fig. 18. The snapshots illustrate the evolution of the wake-induced structures along the pressure side of the blade (see also Wu and Durbin [10] and Wissink [11]) during one wake-passing period $T$.

Figure 19 illustrates the appearance of turbulent spots along the suction side, immediately upstream of the trailing edge. It shows two snapshots of instantaneous contours of the velocity component in the $y$-direction (see Fig. 9). Two separate turbulent spots are clearly visible, one lying on the periodic spanwise boundary and the other one a bit farther downstream. Though the snapshots

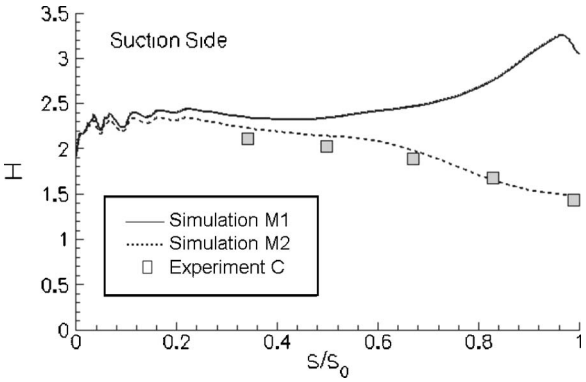


**Fig. 16 Time-averaged shape factor $H$ along the suction side and comparison to Experiment C**

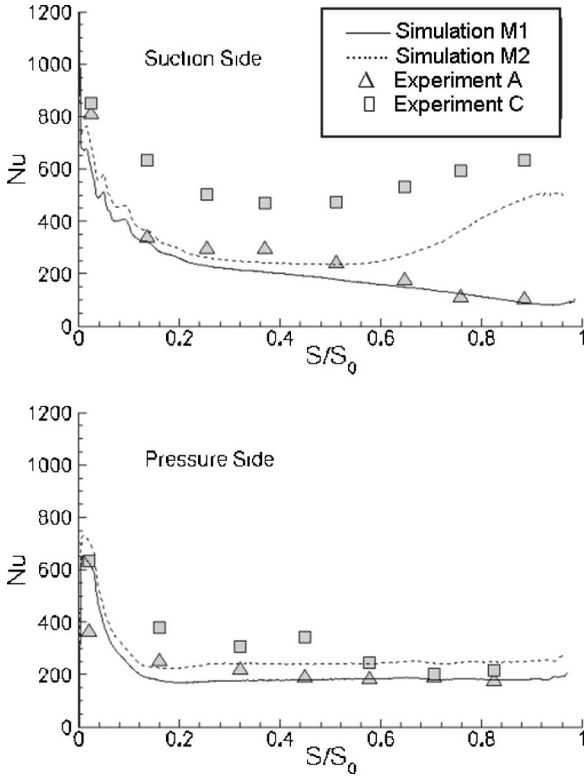


**Fig. 17 Simulations I & II: Time-averaged Nusselt number Nu as a function of the normalized wall-coordinate; comparison to experiments**

are relatively close to one another, they do illustrate the traveling downstream of the turbulent spots and provide proof of incomplete by-pass transition of the boundary layer flow along the suction side boundary layer of the MTU blade as opposed to separation-induced transition of the boundary layer flow along the suction side of the T106 blade.

## 4 Conclusions

The recent increase in computational power has made it possible to employ DNS for the study of transitional flow in turbine-related geometries. The application of DNS is still limited to flow with moderate Reynolds numbers and simplified geometries such as a two-dimensional geometry representing a model of the flow along the suction side of a turbine blade (discussed in Sec. 2) or a

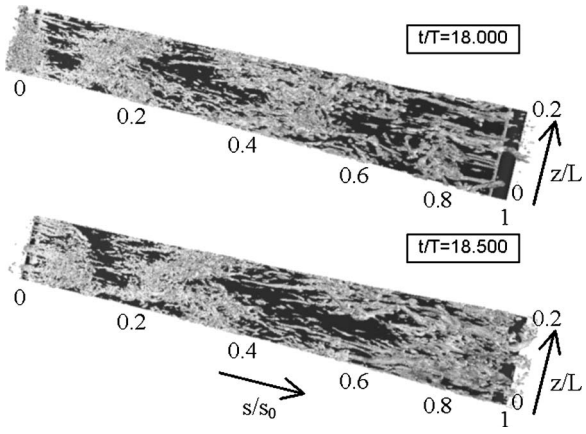


**Fig. 18 Simulation M2: Two snapshots showing instantaneous vortical structures along the pressure side of the blades**

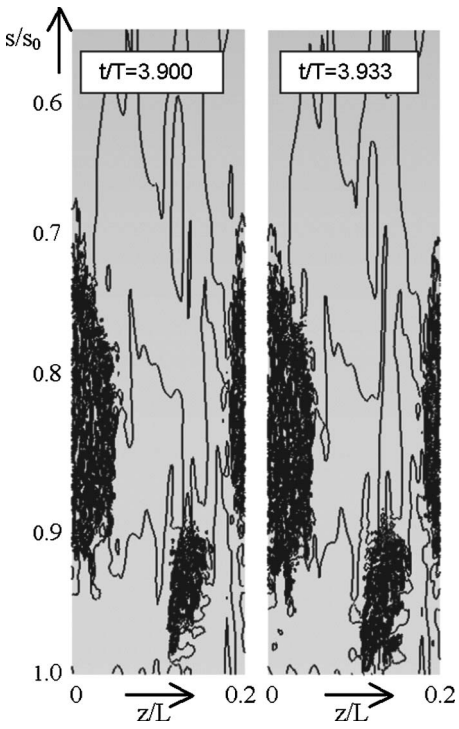


**Fig. 19 Contours of the instantaneous *v*-velocity, illustrating the appearance of turbulent spots near the trailing edge in the suction side boundary layer (simulation M2)**

section at midspan of one single turbine blade (see Sec. 3). To accurately describe the instantaneous flow in a two-dimensional section of a LP turbine passage using realistic operating conditions, approximately $100\times10^6$ grid points were found to be needed, combined with a time-step in the order of $10^{-5}L/U$. On average, it took several months of clock time to run one single simulation on a modern, massively parallel computer. Periodicity of the inflow signal, for instance, induced by prescribed inflow oscillations or by periodically impinging wakes, was used to gather phase-averaged statistics. Because, as observed above, the DNS were very expensive, only a moderate (but largely sufficient) number of periods was affordable during which phase-averaged statistics were gathered.

Though the computational power is not yet sufficient to tackle with DNS fully three-dimensional flow problems occurring in a real turbine, the simulations performed in two-dimensional geometries provide valuable data for the further development and improvement of models for transition to turbulence to be employed in Reynolds-averaged Navier Stokes simulations and allow the examination of physical mechanisms involved in boundary-layer transition. The DNS results of separating flow with oncoming disturbances, for instance, show that a Kelvin-Helmholtz instability plays a very important role in the early transition to turbulence, after which secondary instabilities take over. The same Kelvin-Helmholtz instabilities were observed to be triggered in the separated flow along the downstream half of the suction side in the T106A simulation with periodically oncoming wakes. On the other hand, in the MTU-blade simulation with oncoming wakes by-pass transition processes were found to play a very important role in the incomplete transition of the suction side boundary layer. Compared to the background fluctuations, the small-scale fluctuations carried by the periodically impinging wakes are relatively intense and cause the location of transition to alternately move up- and downstream. The streamwise vortical structures observed along the pressure side explain the increase in heat transfer from the model blade towards the outer flow. However, compared with experiment, the increase in laminar heat transfer caused by the wakes with small-scale fluctuations was partly underpredicted. In the near future, we will perform a further DNS of flow around the MTU blade to study the effect on the heat transfer of more realistic incoming wakes having larger-scale fluctuations.

Further DNS of turbomachinery flows are under way, and simulations of flow in a compressor cascade with incoming disturbances have already been carried out [22]. The expected further increase in computational power will make it possible to perform simulations at higher Reynolds numbers, to significantly increase the number of periods used for phase-averaging, to perform simulations using more than one turbine passage, and to calculate simulations with more complex three-dimensional geometries. Hence, the importance of DNS will grow with increasing computational power and, though it is highly unlikely that in the foreseeable future it will replace RANS as a standard tool for industrial applications, it is already an important tool in transition studies. Unfortunately, DNS results are sensitively dependent on the boundary conditions used. Hence, to obtain an accurate prediction of the flow, one would need to be able to prescribe the often very complex instantaneous boundary conditions with a high degree of accuracy. The main strength of DNS lies in its capability of accurately describing complex transitional and turbulent flow phenomena by resolving all relevant scales of motion, thereby allowing the extraction and study of all details of the flow.

## Acknowledgment

The authors would like to thank the German Research Foundation (DFG) for funding this project, the steering committee of the Supercomputing Facilities in Bavaria (HLRB) for granting computing time on the Hitachi SR8000-F1 at Leibniz Computing Center (LRZ) in Munich and the Computing Center of the University of Karlsruhe for granting access to the IBM SP-SMP supercomputer.

## Nomenclature

$a$ = amplitude of oscillating inflow
$C_p$ = pressure coefficient
$E$ = kinetic energy
$f$ = nondimensional frequency of Kelvin-Helmholtz mode
$F(v)$ = amplitude of Fourier mode of $v$-spectrum
$h$ = heat transfer coefficient
$H$ = shape factor
$k$ = fluctuating kinetic energy
$L$ = length of plate/axial chord length blade
$n$ = distance from turbine blade
Nu = local Nusselt number
$p$ = pressure
$P$ = pitch
Re = Reynolds number
$S$ = distance from leading edge measured along the surface
$S_0$ = distance from leading edge to trailing edge measured along the surface
St = Strouhal number
$T$ = period
Tu = turbulence level
$U_0$ = magnitude of time-averaged inlet velocity
$u$ = velocity component in $x$-direction
$v$ = velocity component in $y$-direction
$w$ = velocity component in $z$-direction
$x$ = $x$-coordinate
$y$ = $y$-coordinate

### Greek Symbols

$\alpha$ = angle of inflow with positive $x$-axis
$\phi$ = phase
$\kappa$ = thermal conductivity of air at 300 K

$\theta$ = temperature
$\theta_0$ = temperature of turbine blade
$\nu$ = kinematic viscosity

**Subscripts**

ref = reference
re = re-attachment
0 = inflow
$b$ = blade
$c$ = chord
$w$ = wall

## References


[1] Hourmouziadis, J., 2000, "Das DFG Verbundvorhaben Instationäre Strömung in Turbomaschinen," *Deutscher Luft und Raumfahrtkongress*, Leipzig, Germany, September 18–21, DGLR-JT2000-030.

[2] Alam, M., and Sandham, N. D., 2000, "Direct Numerical Simulation of 'Short' Laminar Separation Bubbles With Turbulent Reattachment," J. Fluid Mech., **410**, pp. 1–28.

[3] Maucher, U., Rist, U., Kloker, M., and Wagner, S., 2000, "DNS of Laminar-Turbulent Transition in Separation Bubbles," *High-Performance Computing in Science and Engineering*, E. Krause and W. Jäger, eds., Springer, Berlin.

[4] Spalart, P. R., and Strelets, M. Kh., 2000, "Mechanisms of Transition and Heat Transfer in a Separation Bubble," J. Fluid Mech., **403**, pp. 329–349.

[5] Wissink, J. G., and Rodi, W., 2002, "DNS of Transition in a Laminar Separation Bubble," *Advances in Turbulence IX*, I. P. Castro, P. E. Hancock, and T. G. Thomas, eds., CIMNE, Barcelona, pp. 727–730.

[6] Wissink, J. G., and Rodi, W., 2003, "DNS of a Laminar Separation Bubble in the Presence of Oscillating Flow," Flow, Turbul. Combust., **71**, pp. 311–331.

[7] Wissink, J. G., Michelassi, V., and Rodi, W., 2003, "Heat Transfer in a Laminar Separation Bubble Affected by Oscillating External Flow," *Turbulence, Heat and Mass Transfer-4*, K. Hanjalic, Y. Nagano, and M. J. Tummers, eds., Begell House, New York, pp. 199–206.

[8] Wissink, J. G., and Rodi, W., 2004, "DNS of a Laminar Separation Bubble Affected by Free-Stream Disturbances," in *Direct and Large-Eddy Simulation V*, R. Friedrich, B. J. Geurts, and O. Métais, eds., Kluwer Academic Publishers, Dordrecht, pp. 213–220.

[9] Lou, W., and Hourmouziadis, J., 2000, "Separation Bubbles Under Steady and Periodic-Unsteady Main Flow Conditions," *Proceedings of the 45th ASME International Gas Turbine & Aeroengine Technical Congress*, Munich, Germany, May 8–11.

[10] Wu, X., and Durbin, P. A., 2001, "Evidence of Longitudinal Vortices Evolved From Distorted Wakes in a Turbine Passage," J. Fluid Mech., **446**, pp. 199–228.

[11] Wissink, J. G., 2003, "DNS of Separating, Low Reynolds Number Flow in a Turbine Cascade With Incoming Wakes," Int. J. Heat Fluid Flow, **24**, pp. 626–635.

[12] Michelassi, V., Wissink, J. G., and Rodi, W., 2002, "Analysis of DNS and LES of Flow in a Low Pressure Turbine Cascade With Incoming Wakes," Flow, Turbul. Combust., **69**, pp. 295–329.

[13] Kalitzin, G., Wu, X., and Durbin, P. A., 2002, "DNS of Fully Turbulent Flow in a LPT Passage," *Engineering Turbulence Modelling and Experiments 5*, W. Rodi, and N. Fueyo, eds., Elsevier, New York.

[14] Raverdy, B., Mary, I., Sagaut, P., and Liamis, N., 2003, "High-Resolution Large-Eddy Simulation of Flow Around Low-Pressure Turbine Blade," AIAA J., **41**(3), pp 390–397.

[15] Rogers, M. M., 2002, "The Evolution of Strained Turbulent Plane Wakes," J. Fluid Mech., **463**, pp. 53–120.

[16] Stadtmüller, P., and Fottner, L., 2001, "A Test Case for the Numerical Investigation of Wake Passing Effects on a Highly Loaded LP Turbine Cascade Blade," ASME Paper 2001-GT-311.

[17] Liu, X., and Rodi, W., 1994, "Velocity Measurements in Wake-Induced Unsteady Flow in a Linear Turbine Cascade," Exp. Fluids, **17**, pp. 45–58.

[18] Liu, X., and Rodi, W., 1994, "Surface Pressure and Heat Transfer Measurements in a Turbine Cascade With Unsteady Oncoming Wakes," Exp. Fluids, **17**, pp. 171–178.

[19] Wu, X., Jacobs, R. G., Hunt, J. C. R., and Durbin, P. A., 1999, "Simulation of Boundary Layer Transition Induced by Periodically Impinging Wakes," J. Fluid Mech., **398**, pp. 109–153.

[20] Jeong, J., and Hussain, F., 1995, "On the Identification of a Vortex," J. Fluid Mech., **285**, pp. 69–94.

[21] Dullenkopf, K., and Mayle, R. E., 1995, "An Account of Free-Stream-Turbulence Length Scale on Laminar Heat Transfer," ASME J. Turbomach., Vol. **117**, pp. 401–406.

[22] Zaki, T. A., Durbin, P. A., Wissink, J. G., and Rodi, W., 2006, "Direct Numerical Simulation of By-Pass and Separation-Induced Transition in a Linear Compressor Cascade," ASME Paper GT2006-90885.

# Combustion Control by Vortex Breakdown Stabilization

**Christian Oliver Paschereit**
Hermann-Fottinger-Institute of Fluid Dynamics,
Technical University Berlin,
10623 Berlin, Germany

**Peter Flohr**
ALSTOM (Switzerland) Ltd.,
CH-5405 Baden, Switzerland

**Ephraim J. Gutmark**
Department of Aerospace Engineering and
Engineering Mechanics,
University of Cincinnati,
Cincinnati, OH 45221

*Flame anchoring in a swirl-stabilized combustor occurs in an aerodynamically generated recirculation region which is a result of vortex breakdown (VBD). The characteristics of the recirculating flow are dependent on the swirl number and on axial pressure gradients. Coupling with downstream pressure pulsations in the combustor affects the VBD process. The present paper describes combustion instability that is associated with vortex breakdown. The mechanism of the onset of this instability is discussed. Passive control of the instability was achieved by stabilizing the location of vortex breakdown using an extended lance. The reduction of pressure pulsations for different operating conditions and the effect on emissions in a laboratory scale model atmospheric combustor, in a high pressure combustor facility, and in a full scale land-based gas-turbine are described. The flashback safety, one of the most important features of a reliable gas turbine burner, was assessed by CFD, water tests, and combustion tests. In addition to the passive stabilization by the extended lance it enabled injection of secondary fuel directly into the recirculation zone where the flame is stabilized. Tests were conducted with and without secondary fuel injection. Measurements and computations optimized the location of the extended lance in the mixing chamber. The effect of variation of the amount of secondary fuel injection at different equivalence ratios and output powers was determined. Flow visualizations showed that stabilization of the recirculation zone was achieved. Following the present research, the VBD stabilization method has been successfully implemented in engines with sufficient stability margins and good operational flexibility. This paper shows the development process from lab scale tests to full scale engine tests until the implementation into field engines.* [DOI: 10.1115/1.2218521]

## Introduction

Modern design of low emission combustors is characterized by swirling air in the combustor's dome coupled with distributed fuel injection to maximize mixing. This design results in efficient combustion with extremely low emissions. The fuel distribution and mixing with the air stream play a critical role in the combustion process and in the performance of the system. Various flow dynamics processes control the mixing between fuel and air in diffusion flame configurations and the mixing between the fresh fuel/air mixture and hot combustion products and fresh air in premixed combustors. They include large-scale vortices that evolve in a separating shear layer downstream of a sudden expansion or bluff body flame holders, and swirling vortices that undergo vortex breakdown in swirl-stabilized combustors. Interaction between these vortices which are related to flow instabilities, acoustic resonant modes in the combustion chamber, and the heat release process was shown to cause undesired thermoacoustic instabilities in combustors [1].

The burner tested here stabilizes the flame near the burner outlet utilizing the sudden breakdown of the swirling flow, called vortex breakdown (VBD). The swirler consists of two halves of a cone, which are shifted to form two air slots of constant width [2]. This design produced a swirler which is a hybrid of radial and axial swirlers. Gaseous fuels are injected into the combustion air by means of fuel distribution tubes comprising two rows of small holes perpendicular to the inlet ports of the swirler. Complete mixing of fuel and air is obtained shortly after injection. During startup the EV burner is piloted by fuel supplied to a central fuel nozzle in the tip of the cone through a lance leading to a diffusion type flame.

Contributed by the International Gas Turbine Institute (IGTI) of ASME for publication in the JOURNAL OF TURBOMACHINERY. Manuscript received October 1, 2001; final manuscript received February 1, 2002. IGTI Review Chair: E. Benvenuti. Paper presented at the International Gas Turbine and Aeroengine Congress and Exhibition, Amsterdam, The Netherlands, June 3–6, 2002, Paper No. GT2002-30462.

The characteristics of combustion stabilization by vortex breakdown are controlled by the flow dynamics associated with this particular flow phenomenon. Vortex breakdown is defined as a flow instability that is characterized by the formation of an internal stagnation point on the vortex axis, followed by reversed flow [3]. It has been observed to occur in two distinct forms: spiral and bubble. The bubble form appears as a nearly axisymmetric rotating body of fluid. Downstream of the bubble, the core kinks and spirals downstream into a corkscrew manner. Subsequently, the core loses its coherence and collapses into turbulence. The spiral form of breakdown is similar to the second half of the bubble form but without the intermediate bubble stage. Instead, the core suddenly kinks, makes a few revolutions, and breaks into turbulence. Novak and Sarpkaya [4] have observed that in high-Reynolds number flows, vortex breakdown occurs when a slender vortex turns into three-dimensional form. Neither a stagnation point nor reversed flow is necessary for breakdown. No reverse flow region was found for Reynolds numbers approaching 300,000. Novak and Sarpkaya found breakdown to begin with a kink in the otherwise straight vortex core. At that point, the core began a tight spiral, often first splitting into two separate streams resulting in a double helix and then the spirals burst into fine scale turbulence. Upstream of the vortex breakdown location, the velocity profile is strongly jet-like with a peak velocity almost three times greater than the free-stream velocity. Very close downstream of breakdown the flow in the core may completely stagnate and then transition to a wave-like flow. Downstream of breakdown turbulence increases, axial velocities are substantially lower and reverse flow is possible [3]. Furthermore, the location of vortex breakdown is known to fluctuate in the flow direction [5].

Two major factors play a role in the vortex breakdown phenomenon, the swirl ratio and the presence of an adverse pressure gradient [3,6,7]. Performing experiments with vortices in tubes, Leibovich and others have shown that as the swirl ratio is increased, the location of breakdown moves upstream. Rusak and Lamb have developed a criterion based on the swirl ratio for axisymmetric

  

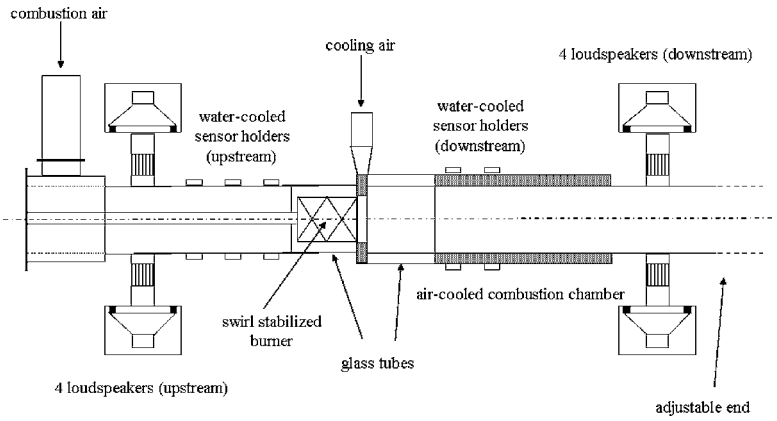


**Fig. 1 Schematic of the atmospheric test facility**

vortex breakdown. The swirl ratio, based on the maximum circumferential velocity over the maximum axial velocity, should be equal to $0.58 \pm 0.03$ at the point of breakdown. Any value greater than this will result in breakdown. Experimental data have shown good agreement with the theory [8,9]. The sensitivity of vortex breakdown to pressure gradients can cause coupling between pressure perturbations in the combustion chamber and the heat release from the flame which is anchored at the recirculating region produced by the breakdown, thus forming a feedback loop that may lead to combustion instability and a change in pollutants formation [10]. Free-stream flashback is another inherent feature of swirl-stabilized premixed combustion that is closely related to vortex breakdown due to the low velocity or even reversed flow caused by this phenomenon [11].

The present paper describes combustion instability that is associated with vortex breakdown. The mechanism of the onset of this instability will be described. Passive control of the instability was achieved by stabilizing the location of vortex breakdown using an extended lance. The reduction of pressure pulsations for different operating conditions and emissions in a laboratory scale model atmospheric combustor and in high pressure combustor facility are described. The flashback safety, one of the most important features of a reliable gas turbine burner, was assessed by CFD, water tests, and combustion tests. In addition an analysis assuming potential flow was performed.

## Experimental Setup

**Atmospheric Combustion Facility.** The atmospheric combustion facility is shown in Fig. 1. The test rig consists of a plenum chamber upstream of a swirl-inducing burner and a combustion chamber downstream of the burner. The plenum chamber contains perforated plates to reduce the turbulence level of the flow. The circular combustion chamber consists of an air-cooled double wall quartz glass to provide full visual access to the flame. The exhaust system is an air-cooled tube with the same cross section as the combustion chamber to avoid acoustic reflections at area discontinuities. The acoustic boundary conditions of the exhaust system can be adjusted from almost anechoic (reflection coefficient $|r| < 0.15$) to open end reflection.

Pressure fluctuations were measured using Brüel & Kjær water-cooled microphones. The wall-mounted water-cooled 1/4 in. condenser microphones were placed at an axial distance of $x/D = 0.69$. The holders consisted of a small orifice ($d = 0.5$ mm) open to the combustion chamber. The microphone diaphragm was placed in a small cavity and was heat radiation protected. The resonance frequency of the holder was larger than $f_{res} > 20$ kHz. Using condenser microphones rather than piezoelectric pressure probes gave the advantage of highly accurate phase and amplitude data which is necessary for acoustic measurements. The frequency response of the microphones in probe holders were compared

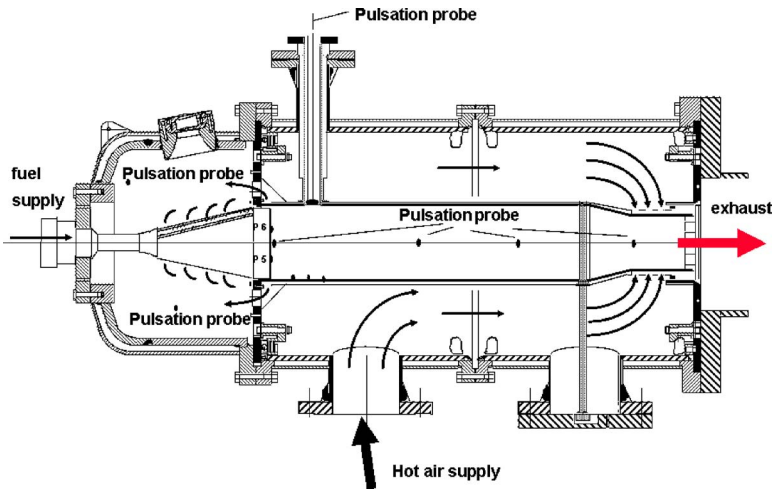


**Fig. 2 Schematic of the high pressure test facility**

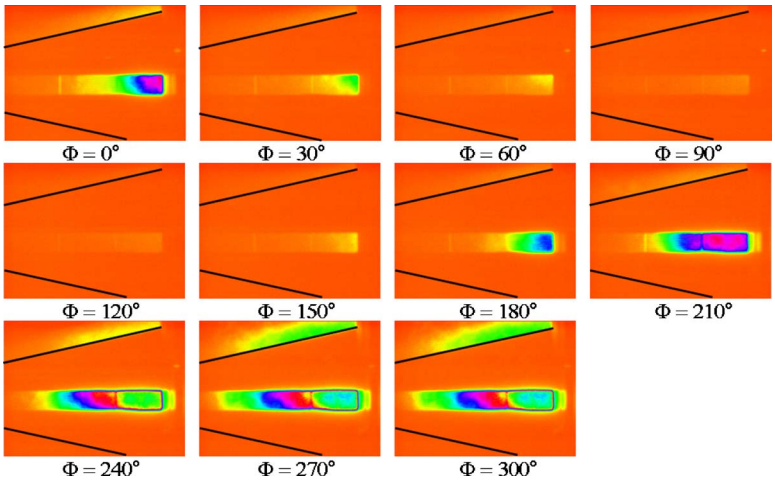


**Fig. 3 Flame motion in and out of the burner during a pilot instability cycle. Phase averaged pictures taken through a glass window in the burner are shown at intervals of 30 deg.**

against standard B&K microphones and showed good agreement. To compare pressure pulsations in the different test configurations one microphone at $x/D=2.5$ was used.

The operating conditions of the burner have been maintained by analyzing the exhaust gas composition using a physical gas analysis system. CO and $CO_2$ have been analyzed by using nondispersive infrared spectroscopy. The nitric oxides NO and $NO_2$, combined in $NO_x$, have been detected with a chemiluminescence analyzer. The detection of the remaining $O_2$ in the exhaust gas was made utilizing the paramagnetic properties of oxygen in the analyzing device. Carbon and oxygen balances were continuously computed and agreement within 0.2% was assured.

**High Pressure Combustion Facility.** The process of burner development and improvement includes combustion tests under 10 bars pressure. The facility is shown in Fig. 2. It allows quick, cost effective, and therefore extensive testing of single machine burners. The test rig consists of a plenum chamber upstream of the burner, two water-cooled tubular pressure vessels, and the rectangular chamber liner. The hot exhaust gases are quenched before the pressure reduction throttle and then discharged through the exhaust. The operating conditions of the burner have been maintained as in the atmospheric test rig by analyzing the exhaust gas composition.

The combustor liner is convectively cooled to prevent contamination of actual burner emissions by introducing additional film cooling air into the combustor and to avoid introduction of unrelated acoustic damping effects. Direct optical observation of the flame is provided by a video system mounted downstream of the burner. In addition, optical observation of the mixing zone through the burner slots is possible by a video system mounted upstream of the burner in the plenum.

## Results and Discussion

**Instability Mechanism.** Combustion instability was observed during a simulated start-up operation of the burner using the pilot stage of the burner at flame temperatures $T/T_n > 0.8$, where $T_n$ is the nominal flame temperature of the burner. Instability was also observed during switchover to premix fuel. Lower amplitude instabilities, reaching 30% of the peak levels in pilot and mixed operation, were also observed under simulated premix operation.

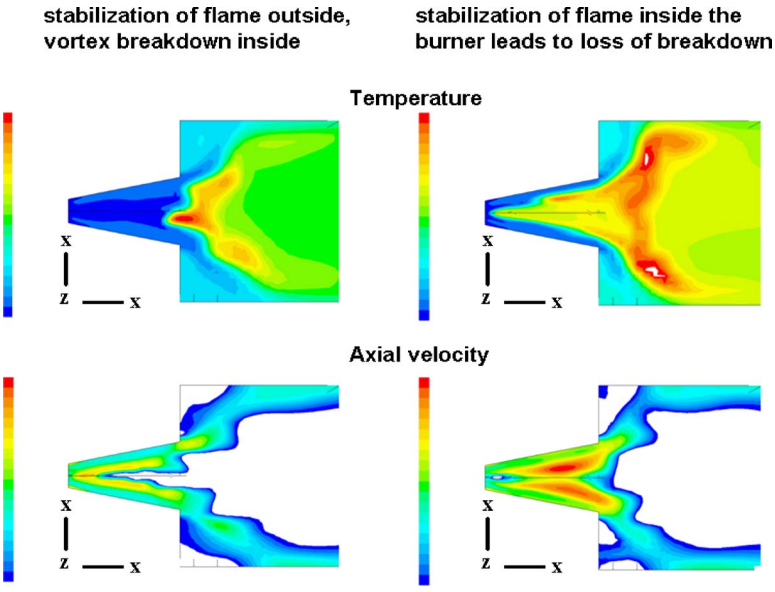


**Fig. 4 CFD simulation of the pilot instability**

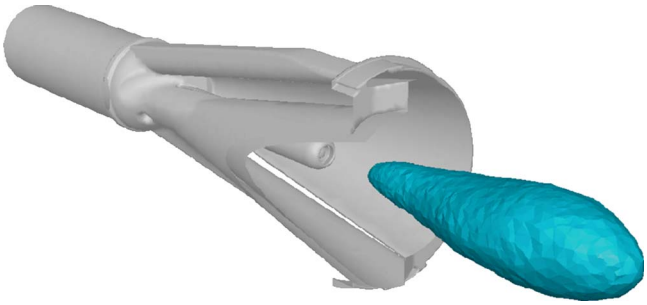

**Fig. 5 Burner with extended lance**

The instability was related to the fluctuating pilot flame position which occurred when the flame temperature was increased above $T/T_n > 0.8$ (Fig. 3). CFD simulations showed that the oscillations in flame location were related to the behavior of the vortex breakdown. When the flame was stabilized outside the burner, initiation of vortex breakdown was observed to occur inside the burner. When the flame was pushed into the burner by an increased pressure in the combustion chamber, the decreased density resulted in the prevention of the vortex breakdown (Fig. 4). Subsequent to the disappearance of the swirl-based stabilization mechanism, the flame exited the burner, stabilizing at the sudden expansion. The vortex breakdown was thus re-established and the instability cycle repeated itself.

**Passive Control of Instability.** In order to prevent the instability mechanism associated with large amplitude movement of the vortex breakdown location and the resulting flame oscillations in and out of the burner, passive control was applied to stabilize the vortex breakdown location. This stabilization was achieved by extending the pilot fuel lance into the burner. The concept was initially tested in an atmospheric combustor rig operating in piloted mode. Extension of the pilot fuel lance into the burner as shown in Fig. 5 resulted in a significant reduction of the pressure pulsations. The tests were performed using a fuel lance with an adjustable length which could be extended axially in order to determine an optimal length.

The tests showed that the optimum suppression of the pulsations occurred when the lance extension length was $x/L \approx 0.7$, where $L$ is the length of the burner (Fig. 6). However, variation of length was possible by ±25% without significant increase in pulsations. With 5% fuel injection through the long lance the oscillations were reduced by over 12 dB. It was imperative to ensure that the improvement of the operation in pilot mode will not result in degradation of the premixed operation. Atmospheric test rig results indicated no increase in $NO_x$ emissions and pulsations during premixed operation (Fig. 7). Added pilot fuel injection through the extended lance resulted in increase in $NO_x$ emissions. However, 5% fuel injection, which yielded a substantial decrease in the instability level, yielded acceptable penalty in $NO_x$ production due to the extremely low level at baseline conditions.

The main pulsation reducing mechanisms are:

(1) Stabilization of the vortex breakdown in the recirculation zone of the extended pilot lance
(2) Prevention of the periodically changing stabilization location of the pilot flame
(3) Introduction of streamwise vorticity to suppress the spanwise coherent structures which are the source of one of the mechanisms that drive thermoacoustic oscillations

The main advantage of extending the lance into the burner was the improved performance during start-up. Without the extended lance an increase of pulsations was observed when the burner power was increased at a constant flame temperature, and when the flame temperature was increased at a constant power (constant burner velocity) (Figs. 8 and 9). The typical normalized instability frequency at these conditions was $St = fD/U = 0.6$, where $f$ is the frequency of the instability, $D$ the burner diameter, and $U$ the burner exit velocity. Excitation of pressure oscillations was completely eliminated during start-up with pilot operation.

## Flashback Safety

An important feature of a reliable gas turbine burner in addition to its efficiency, emissions, flame stability, lean extinction limits, and pulsation behavior is its flashback safety. The effect of the extended lance on the flashback safety of the burner was assessed by using CFD simulations and by performing combustion tests at atmospheric and high pressure. In addition an analysis based on potential flow was performed. The flashback safety margins were assessed based on the stability boundaries of annular vortex breakdown to occur upstream of the lance tip. If an annular VBD was to propagate upstream of the lance tip it would have caused flame propagation into the burner and damage to the lance and the burner's structure.

**Analysis of Annular Breakdown.** The stability of the flow,

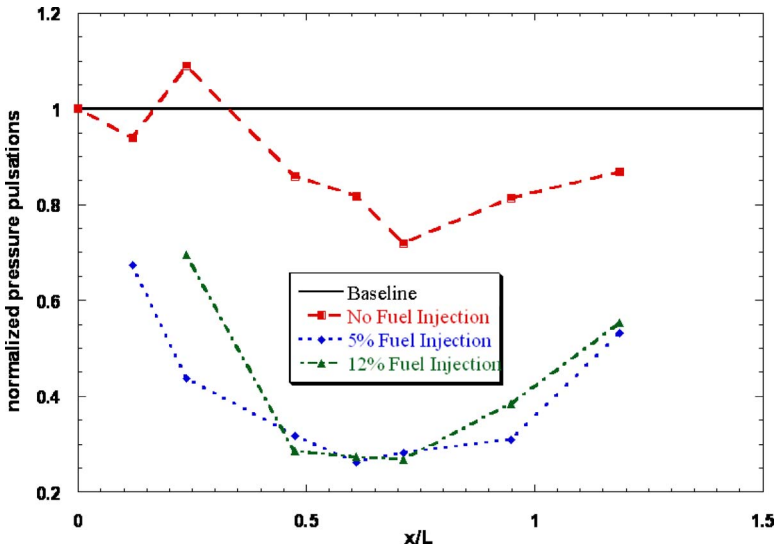


**Fig. 6 Suppression of pressure pulsations for different lance lengths**

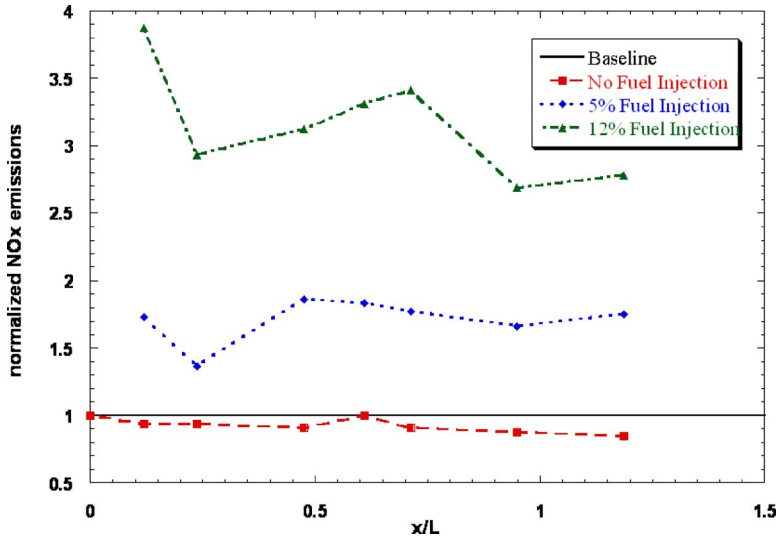


Fig. 7 $NO_x$ emissions for different lance lengths

inside the burner with extended fuel lance, near the lance tip was analyzed for the simplified configuration shown in Fig. 10. The analysis was based on potential flow approximations.

It was assumed that annular breakdown occurs near the lance tip. Upstream of this point the flow was assumed to be appropriately described by two concentric potential vortices, superimposed on a double plug-flow (see Fig. 10). The effect of the axially changing flow inside the double cone burner was neglected. While this assumption may seem to be a strong simplification when the entire flow inside the burner is considered, it should be appropriate for an analysis that is localized at the lance tip.

The continuity equations for the plug flow upstream and downstream of the annular breakdown are

$$r_1^2 - 1 = u_2(r_2^2 - R^2) \tag{1}$$

$$w_1(r_T^2 - r_1^2) = w_2(r_T^2 - r_2^2) \tag{2}$$

where the notation is defined in Fig. 10. All velocities have been nondimensionalized with the axial velocity $u_1$ close to the lance and all radii with the lance diameter $r_L$. The angular momentum of the inner potential vortex was defined as

$$\beta = \frac{u_\theta r}{u_1 r_L} \tag{3}$$

where $u_\theta$ is the azimuthal velocity at radius $r$. The angular momentum of the outer vortex is $\gamma\beta$. Assuming that both vortices have the same total pressure (equivalent to saying that the total velocities are continuous across $r=r_1$), it was determined that

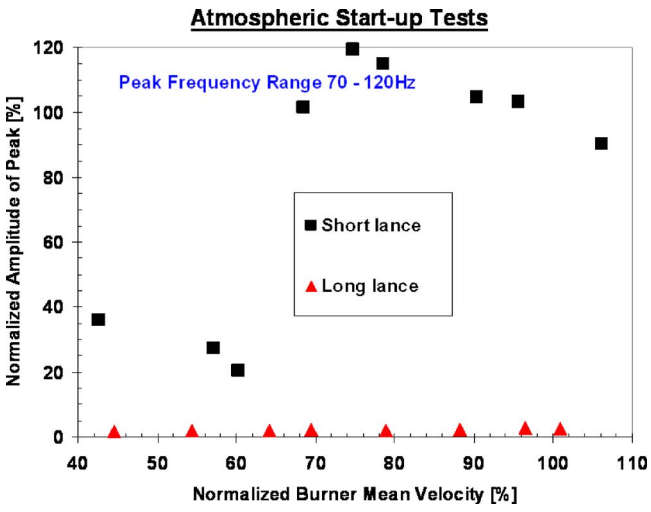


Fig. 8 Atmospheric startup test. Power variation.

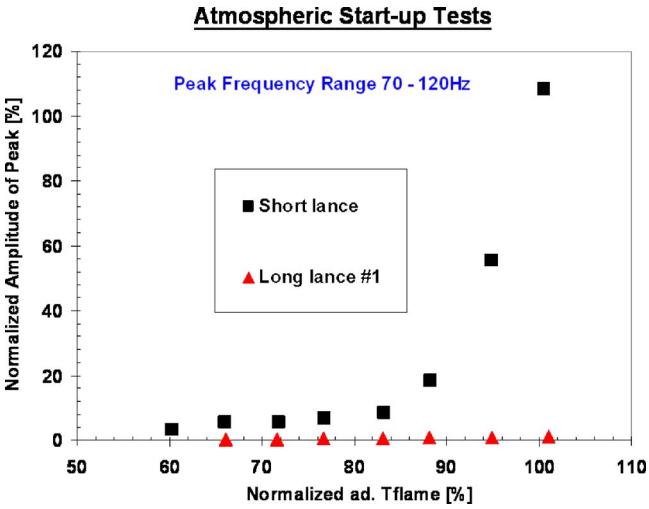


Fig. 9 Atmospheric start-up tests. Flame temperature variation.

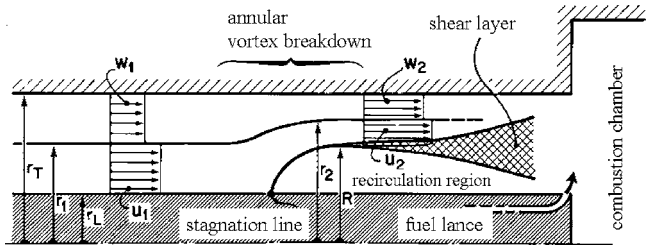


Fig. 10 Schematic of the configuration used for annular breakdown analysis

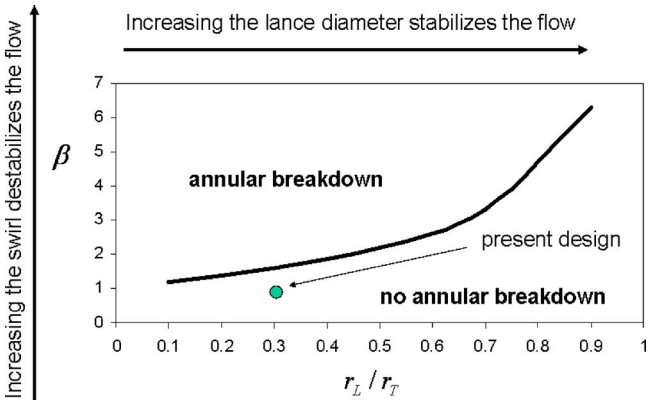


**Fig. 11 Critical swirl for a single vortex ($w_1 = u_1$). Present design shown to be in stable region.**

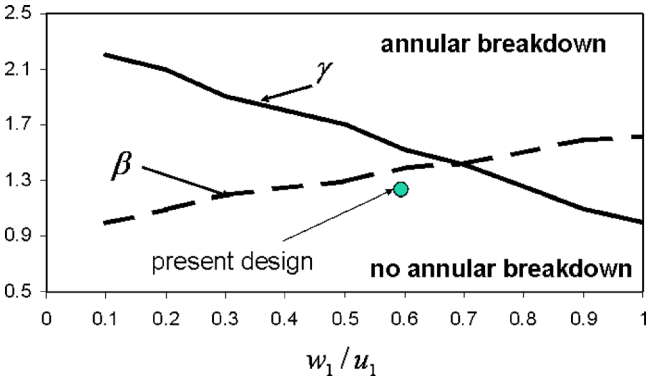


**Fig. 13 Critical swirl for two superimposed potential vortices with the geometric parameters ($r_1/r_L=2$, $r_T/r_L=3.4$)**

$$\gamma^2 = \frac{r_1^2(1-w_1^2)}{\beta^2} + 1 \tag{4}$$

Assuming constant pressure within the recirculating flow implies that the total velocity at the stagnation point is equal to the total velocity behind the breakdown

$$\beta^2 = \frac{u_2^2 R^2}{R^2 - 1} \tag{5}$$

Applying Bernoulli's equation on the stream surface between the two vortices, and using Eq. (4) leads to

$$-u_2^2 + w_2^2 + (\gamma^2 - 1)\frac{\beta^2}{r_2^2} = 0 \tag{6}$$

Equation (6) with (2) and (4) leads to

$$u_2^2 = w_1^2\left[\frac{r_t^2 - r_1^2}{r_T^2 - r_2^2}\right]^2 + [1 - w_1^2]\frac{r_1^2}{r_2^2} \tag{7}$$

Finally, conservation of momentum across the annular breakdown and using (2) and (4) leads to

$$(\beta^2+1)(r_t^2-1) - (1-w_1^2)\left[r_1^2 \log\frac{r_2^2}{r_1^2} + r_T^2\left(1 - \frac{r_1^2}{r_2^2}\right)\right]$$
$$= (\beta^2 + u_2^2)(r_T^2 - R^2) + \beta^2 \log R^2 \tag{8}$$

A solution can now be found with a simple root finding algorithm. $u_1$, $w_1$, $r_T$, $r_1$, and $r_L$ are assumed to be known. Estimating a value for $r_2$ leads to $u_2$, $R$, $\beta$, $\gamma$ from (7), (1), (5), and (4), respectively. $r_2$ is then corrected until (8) is fulfilled.

Figure 11 presents results for the generic (and strongly simplified) situation for which the annular flow around the lance can be described by a single potential vortex which is superimposed on a plug jet flow. The effect of swirl and variation in lance diameter (assuming a fixed outer diameter) was analyzed for this configuration. Figure 11 shows that increasing the swirling component in the flow has a destabilizing effect while an increase in lance diameter has a stabilizing effect. Figure 12 depicts results from water tunnel measurements. The flow parameter $\beta$, as well as the geometric parameters $r_L$, and $r_T/r_L$ can be estimated from analysis of the flow at the lance tip. The results indicate that the design for the standard lance is well below the critical level for which annular breakdown could be expected. The analysis of the experimental data of the velocity field at the lance tip revealed that it is more appropriate to consider two potential vortices for which the additional parameters $r_1/r_L$ and $w_1/u_1$ need to be introduced. In Fig. 13 the results of the generic case for two superimposed potential vortices (with the special constraint $r_1/r_L=2$, $r_T/r_L=3.4$) are presented. This approximation better describes the configuration near the lance tip of the burner. On the right of Fig. 13, $w_1/u_1=1$ and $\gamma=1$, i.e., the result for the single potential vortex is recovered. The critical swirl $\beta$ increased for increased axial flow ratio $w_1/u_1$. As the swirl ratio $\gamma$ is increased to values above one (a situation typical to such swirling flows), the critical swirl $\beta$ of the inner ring jet above which annular breakdown is observed decreases. It is interesting to note that there exists a maximum of possible *mean* swirl of the outer and inner flow that can be achieved in this configuration. It can be shown that the maximum is reached if the cross-sectional area of both potential vortices is equal. In both analyses, the present design was shown to dwell in the stable regime thus ensuring the potential for desired flashback safety.

**CFD and Water Tunnel Simulations.** CFD calculations were

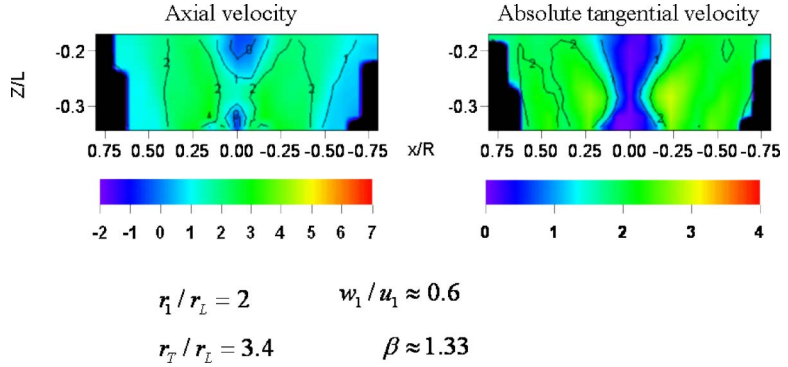


**Fig. 12 Normalized velocities near the lance tip measured in the water tunnel**

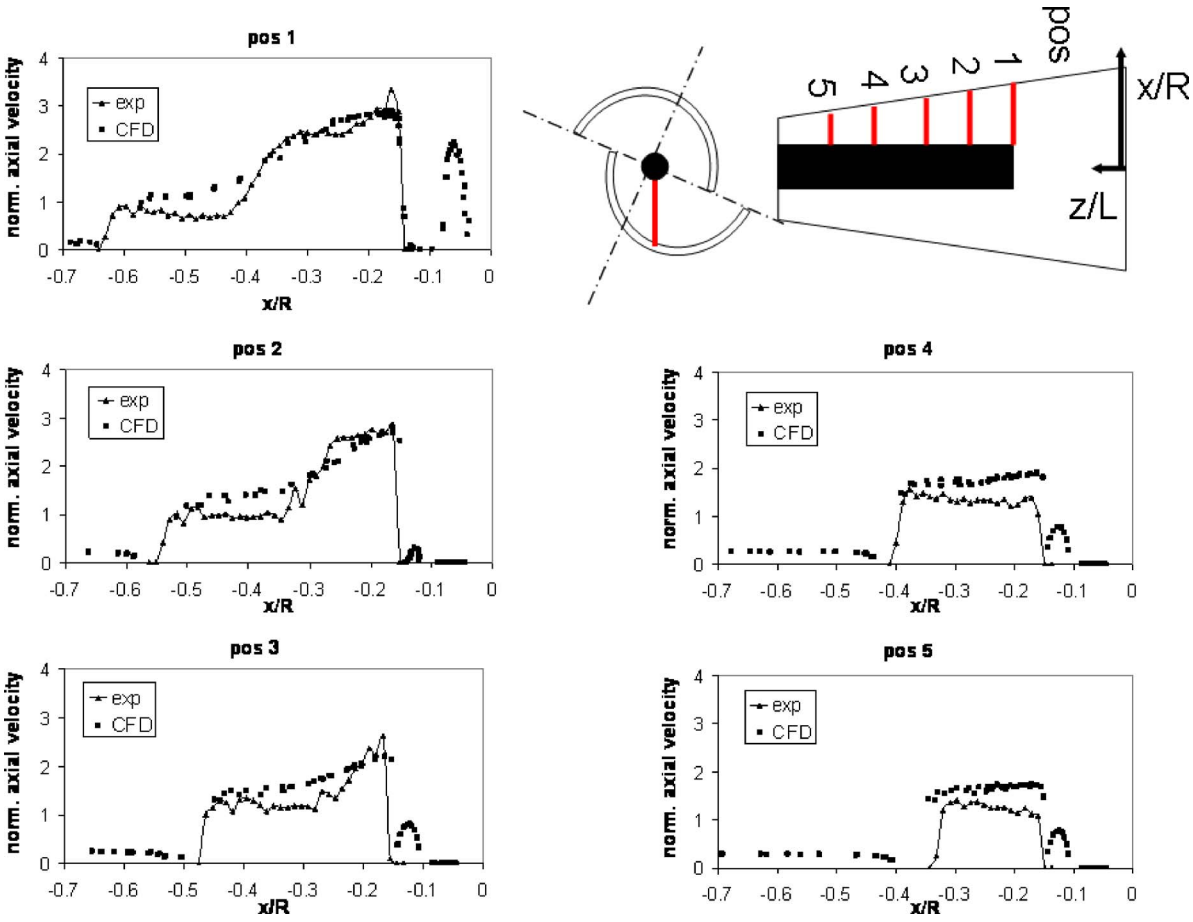


**Fig. 14 CFD calculations of the axial flow field around the extended lance compared with water tunnel measurements**

performed to investigate the position of the vortex breakdown as well as to check for recirculation regions along the extended lance to verify the burner's flashback safety. These calculations were performed for the case without combustion. The purpose was to ensure that there are no locations along the extended lance where the flame could stabilize. Figure 14 shows good agreement between the axial velocity profiles calculated using CFD and the water tunnel measurements. The flow field was mapped between the extended lance and the burner's walls. The flow was shown to be positive in the entire measurement and computational regime indicating that annular vortex breakdown did not occur, as predicted by the potential flow analysis in the previous section. CFD simulations and water tunnel measurements were also performed downstream of the extended lance tip (Fig. 15). The figure shows the comparison between CFD and water tunnel measurements of the axial and the absolute value of the tangential velocity components. The position of the vortex breakdown was identified to be well downstream of the tip of the extended lance where the axial velocity was reversed. This vortex breakdown location prevented the flame from being stabilized close to the lance tip with possible lance overheating. The CFD calculations of the highly turbulent swirling flow were in good agreement with the measurements in the water tunnel simulation and showed no recirculation regions at the lance.

**Combustion Tests.** The results of the atmospheric flashback safety tests were confirmed by tests conducted in the high pressure combustion rig. As the CFD and water tests indicated in atmospheric pressure conditions without combustion, the flame did not stabilize on the lance tip or upstream of it during high pressure combustion (Fig. 16).

Flashback safety tests were performed by adding gaseous fuel with high laminar flame speed (hydrogen) to the main fuel which was natural gas. The percentage of the additional fuel at the point when flashback occurs was a measure of the flashback safety of the tested burner. The resulting value was compared to the baseline flashback safety level of certified commercial burners. The burner is acceptable as "flashback safe" if the test results are within the margins allowed for certified burners. The flashback safety margin for certified burners is at 80% of the design target.

A number of different variants in terms of the extended lance length have been tested and compared against a design target defined for a standard burner. The results are summarized in Fig. 17. The tests were conducted at atmospheric conditions. The position that ensured flashback safety was also effective in suppression of pressure oscillations. All variants tested achieved the design target of 100%.

A forced atmospheric flashback test, in which a hydrogen igniter was mounted in the slots at the upstream part of the burner, confirmed the flashback safety of the burner (Fig. 18). The forced flashback tests proved flashback safety over a wide power range ($0.39<P/P_n<1$) and flame temperature range ($1<T/T_n<1.06$). When the igniter was switched on, the flame was forced to move into the burner. With the igniter switched off the flame was always pushed outside of the burner, again indicating the flashback safety of the extended lance.

## Engine Implementation

The operating behavior of the burner with the long lance was verified in a test engine. The main improvement of the long lance could be seen in the startup procedure. With the original burner

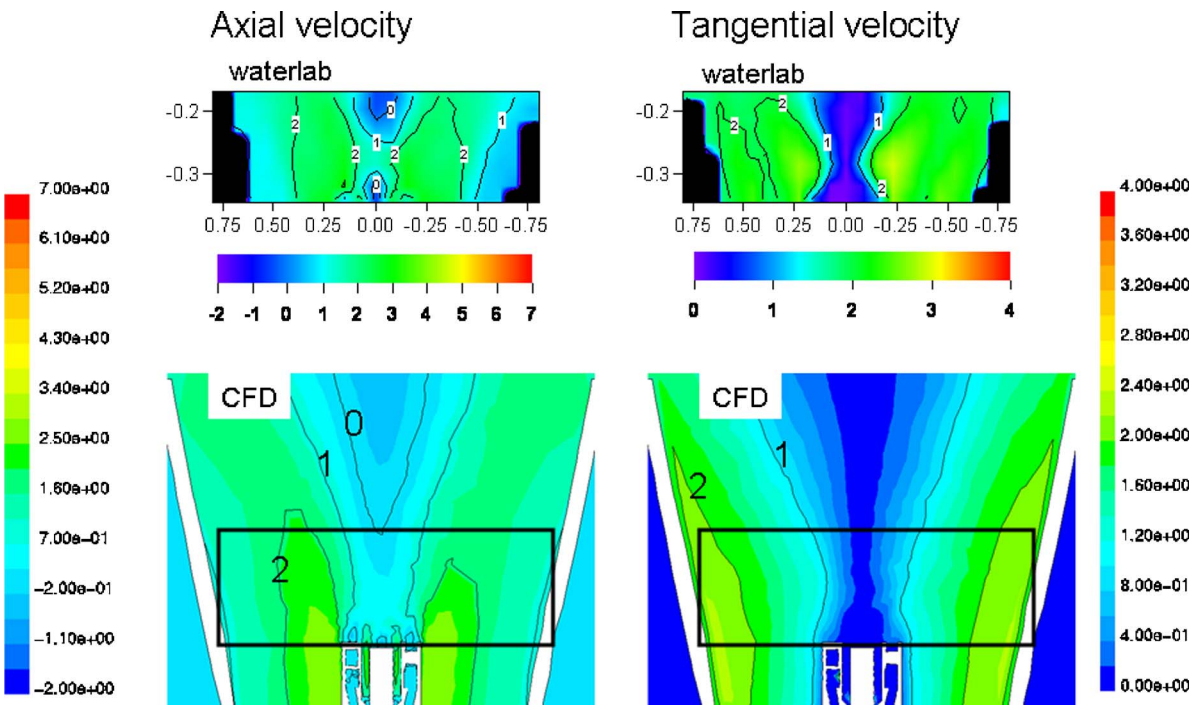


**Fig. 15 CFD calculations of the flow field downstream of the lance compared with water tunnel measurements**

high pulsation levels were observed during start-up at a normalized RPM range between 0.68 and 0.85 (Fig. 19). Using the long lance the start-up procedure was smooth and the pulsation levels were reduced by 90% (Fig. 20).

## Conclusions

This paper describes the source of combustion instability that is associated with vortex breakdown and a passive control method developed to suppress it. The tests were performed in an atmospheric combustor and were verified in combustion tests at 10 bar pressure and in a commercial engine.

The mechanism exciting the instability was investigated using CFD simulations. The simulations showed that the pressure oscillations were linked to fluctuations in the flame location, which were in turn affected by changes in the vortex breakdown characteristics. When the flame stabilized outside the burner, initiation of vortex breakdown could be observed inside the burner. When the flame was pushed by increased combustion pressure into the burner, the decreased density resulted in the elimination of vortex breakdown. Subsequent to the disappearance of this swirl-based stabilization mechanism, the flame exited the burner, stabilizing downstream of the burner's exit at the sudden expansion. As the burner temperature dropped and density increased, the internal vortex breakdown was re-established and the instability cycle repeated itself.

In order to prevent the instability mechanism which was shown to be associated with large amplitude movement of the vortex breakdown location and the resulting flame oscillations in and out of the burner, passive control was applied to stabilize the vortex

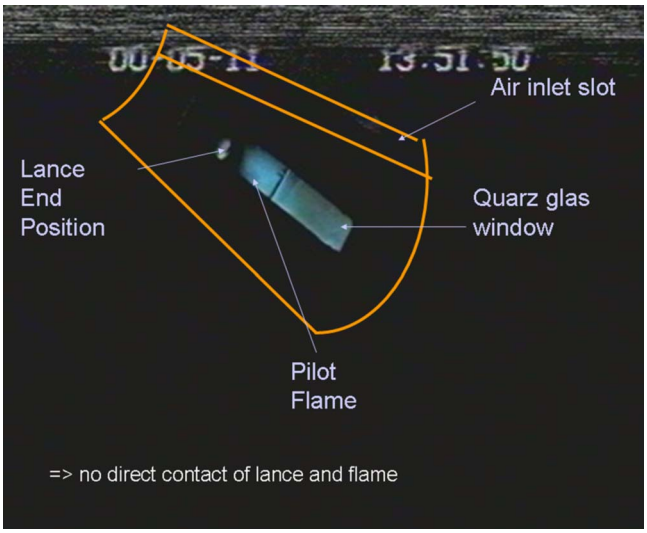


**Fig. 16 Video image of combustion in the high pressure rig, indicating that the flame is stabilized downstream of the extended lance**

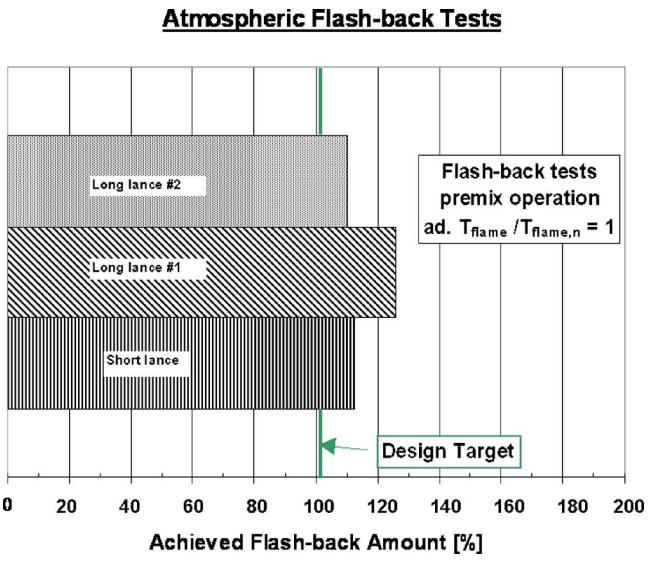


**Fig. 17 Atmospheric hydrogen flashback tests**

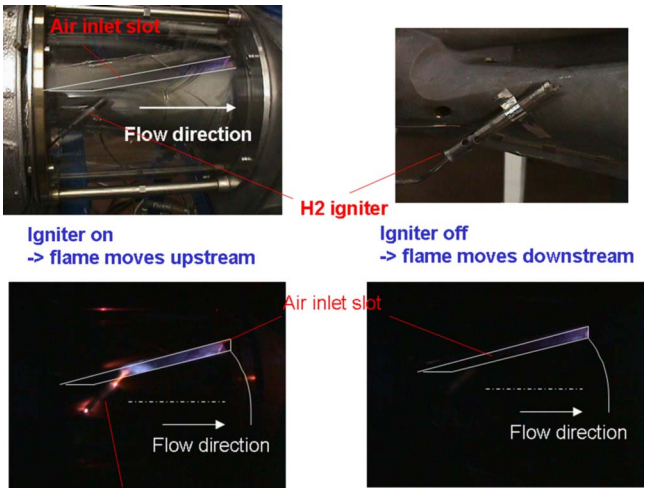


Fig. 18 Forced atmospheric hydrogen flashback test

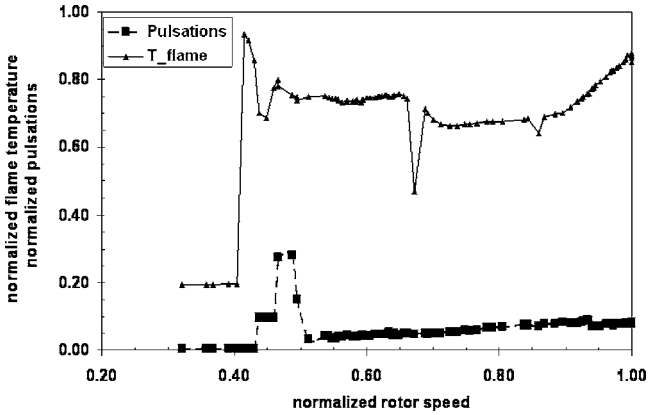


Fig. 20 Reduced pulsations in a start-up test in the test engine using the long lance

breakdown location. The stabilization was achieved by extending the pilot fuel lance into the burner. The concept was demonstrated in an atmospheric combustor rig. Extension of the lance into the burner eliminated the high pressure pulsations observed in mixed and purely piloted operation. The optimal extended lance length was approximately 70% of the burner's length. The pressure pulsations were suppressed by more than 12 dB in piloted operation. The improvement of the operation in pilot mode did not result in degradation of the premixed operation. Atmospheric test rig results indicated no increase in $NO_x$ emissions and pulsations.

The extended lance improved performance in the atmospheric test rig. Without the extended lance an increase of pulsations was observed when the burner power or the flame temperature was increased. The extended lance completely eliminated excitation of pressure oscillations for start-up conditions with pilot operation.

Other concerns associated with the extended lance were possible internal stabilization of flame on the lance and flashback safety. Potential flow analysis established criteria for the occurrence of annular vortex breakdown. Velocity measurements showed that the present conditions were subcritical and predicted that such breakdown will not occur. CFD simulations and water tunnel measurements showed that the position of the vortex breakdown was well downstream of the tip of the extended lance. This vortex breakdown location prevented the flame from being stabilized close to the lance tip with possible lance overheating. Hydrogen flashback tests confirmed that the extended lance did not adversely affect the flashback safety.

The stable operation of the burner with the long lance was verified in a high pressure test rig as well as in a test engine. The main improvement of the long lance could be seen in the start-up. With the original burner high pulsation levels were observed during start-up while the long lance yielded smooth start-up procedure and the pulsation levels were reduced by 90%. Flashback safety was verified in the high pressure tests in which the flame was shown to stabilize downstream of the lance tip.

The instability suppression by the extended lance was attributed to the following mechanisms: the stabilization of the vortex breakdown in the recirculation zone of the extended pilot lance, prevention of the periodical change in the stabilization location of the pilot flame, and the introduction of streamwise vorticity that suppressed the spanwise coherent structures which was one of the mechanisms that drove thermoacoustic oscillations.

## Acknowledgment

We gratefully acknowledge the help of Hanspeter Knöpfel for the atmospheric flashback and start-up tests, Peter Stuber for the medium pressure flashback tests, and Karin Bengtsson for the start-up tests in the test engine.

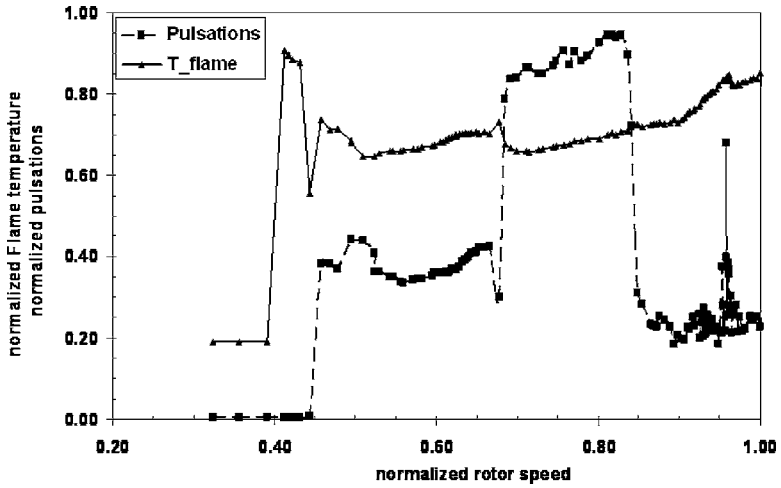


Fig. 19 Baseline start-up test in the test engine with the original burner configuration

## References


[1] Paschereit, C. O., Gutmark, E., and Weisenstein, W., 1999, "Coherent Structures in Swirling Flows and Their Role in Acoustic Combustion Control," Phys. Fluids, **9**, pp. 2667–2678.

[2] Doebbeling, K., Eroglu, A., Joos, F., and Hellat, J., 1999, "Novel Technologies for Natural Gas Combustion in Turbine Systems," in Eurogas 99, Ruhr University Bochum, Germany.

[3] Leibovich, S., 1978, "The Structure of Vortex Breakdown," Annu. Rev. Fluid Mech., **10**, pp. 45–88.

[4] Novak, F., and Sarpkaya, T., 1999, "Turbulent Vortex Breakdown at High Reynolds Numbers," AIAA Paper 99-0135.

[5] Gursul, I., and Xie, W., 1998, "Physics of Buffeting Flows Over Delta Wings," AIAA Paper 98-0688.

[6] Dixon, C. J., 1978, "The Mechanism of Vortex Control by Spanwise Blowing and Wing Geometry," Tech. Rept. Engineering Rept. No. LG 78-ER-0187, Lockheed-Georgia Co., Marietta, GA.

[7] Rusak, Z., and Lamb, D., 1998, "Prediction of Vortex Breakdown in Leading Edge Vortices Above Slender Delta Wings," AIAA Paper 98-2860.

[8] O'Neil, P. J., Roos, F. W., Barnett, R. M., and Hawk, J. D., 1989, "Investigation of Flow Characteristics of Developed Vortex," Tech. Report No. NADC-89114–60, McDonnell Aircraft Company.

[9] Menke, M., and Gursul, I., 1997, "Unsteady Nature of Leading Edge Vortices," Phys. Fluids, **9**(20), pp. 2960–2966.

[10] Paschereit, C. O., Gutmark, E., and Weisenstein, W., 1998, "Structure and Control of Thermoacoustic Instabilities in a Gas-Turbine Combustor," Combust. Sci. Technol., **138**, pp. 213–232.

[11] Lefebvre, A. H., 1988, *Gas Turbine Combustion*, Hemisphere, New York.

# On the Momentum and Thermal Structures of Turbulent Spots in a Favorable Pressure Gradient

**T. P. Chong**

**S. Zhong**
e-mail: shan.zhong@manchester.ac.uk

School of Mechanical,
Aerospace and Civil Engineering,
University of Manchester,
Manchester, Lancashire M60 1QD, UK

*This paper represents the results from an experimental investigation of the flow physics behind the difference in the transition zone length indicated by the momentum boundary layer and thermal boundary layer parameters observed on the suction surfaces of gas turbine blades. The experiments were carried out on turbulent spots created artificially in an otherwise laminar boundary layer developing over a heated flat plate in a zero pressure gradient and a favorable pressure gradient. A specially designed miniature triple wire probe was used to measure the streamwise velocity component U, transverse velocity component V and temperature T simultaneously during the passage of the spots. In this paper, the general characteristics of the ensemble-averaged velocity and temperature perturbations, rms fluctuations, and the second moment turbulent quantities are discussed and the influence of favorable pressure gradient on these parameters is examined. When a favorable pressure gradient is present, unlike in the velocity boundary layer where significant velocity fluctuations and Reynolds shear stress occur both on the plane of symmetry and the spanwise periphery, high temperature fluctuations (and turbulent heat fluxes) are confined in the plane of symmetry. The difference in the levels of velocity/temperature fluctuations at these two locations gives an indication of the effectiveness of momentum/heat transfer across the span of the spots. The results of this study indicate that the heat transfer within a spot is inhibited more than that of the momentum transfer at the presence of a favorable pressure gradient. This phenomenon is expected to slow down the development of a transitional thermal boundary layer, leading to a longer transitional zone length indicated by the heat transfer parameters as reported in the literature.* [DOI: 10.1115/1.2218520]

## Introduction

In boundary layer flows, there is a close relationship between surface heat transfer and skin friction. It has been a common practice for turbomachine designers to infer the surface heat transfer characteristics of a turbine blade directly from its velocity boundary layer via the Reynolds Analogy. However, based on experimental observations, although the Reynolds analogy holds for zero pressure gradient flow, its validity is questionable when a pressure gradient is present. It is found that a difference exists between the transition zone length deduced from the distribution of heat transfer coefficient and that from the shape factor for nonzero pressure gradient flows [1,2]. In particular, they found that the transition zone length deduced from the thermal boundary layer is longer than that from the momentum boundary layer at favorable pressure gradients (FPG); and the opposite is true at adverse pressure gradients.

The implication of the aforementioned discrepancy is significant in that it will lead to incorrect estimation of heat transfer distributions for turbine blades. In order to obtain a better understanding of this problem, a series of detailed measurements have been made to study the combined effects of freestream turbulence intensity and pressure gradients on both velocity and thermal boundary layers [3–6]. These investigations have yielded an improved understanding of the time-averaged intermittent flows and thermal structures of the transitional boundary layers. However, the physical mechanism that causes the different behavior in the transitional velocity and thermal boundary layers in reaction to the presence of a pressure gradient still remains to be understood.

Since the extent of a transition zone is closely related to the growth of *turbulent spots*, a better understanding of the transition process could be achieved by examining the growth and development of turbulent spots. The effects of pressure gradients on the structure of turbulent spots in unheated boundary layers have been relatively well studied [7–9]. The dependency of spot characteristics, such as the spreading angle, leading and trailing edge propagation rates, on the level of pressure gradients has been investigated and correlations for these parameters as functions of a pressure gradient parameter have been derived [10]. Since most of the available data are obtained through velocity measurements, a question that remains to be addressed is if the behavior of turbulent spots inferred by heat transfer parameters is identical to that by momentum parameters.

Recently, Zhong et al. [11] used both shear-sensitive and temperature-sensitive liquid crystals to visualize the spanwise growths of the turbulent spots and compared the spot spreading angles deduced from the surface shear stress and heat transfer rate, respectively. They found that in the zero pressure gradient (ZPG) flow, the spreading angles indicated by the two types of liquid crystals are almost identical. However, at favorable pressure gradients, the spreading angle indicated by the surface shear stress is larger than that by the surface heat transfer rate and this discrepancy increases as the level of the favorable pressure gradient increases. Since a larger spreading angle implies that the merging process of turbulent spots in the transitional zone is hastened, the transition zone length indicated by the momentum boundary layer is hence expected to be shorter.

The liquid crystal flow visualization experiments conducted by Zhong et al. provide some insights into the difference in the growth of transitional momentum and thermal boundary layers with favorable pressure gradients observed by Blair [1,3] and

Contributed by the International Gas Turbine Institute (IGTI) of ASME for publication in the JOURNAL OF TURBOMACHINERY. Manuscript received October 1, 2004; final manuscript received February 1, 2005. IGTI Review Chair: K. C. Hall. Paper presented at the ASME Turbo Expo 2005: Land, Sea and Air, Reno, NV, June 6–9, 2005, Paper No. GT2005-69046.

  

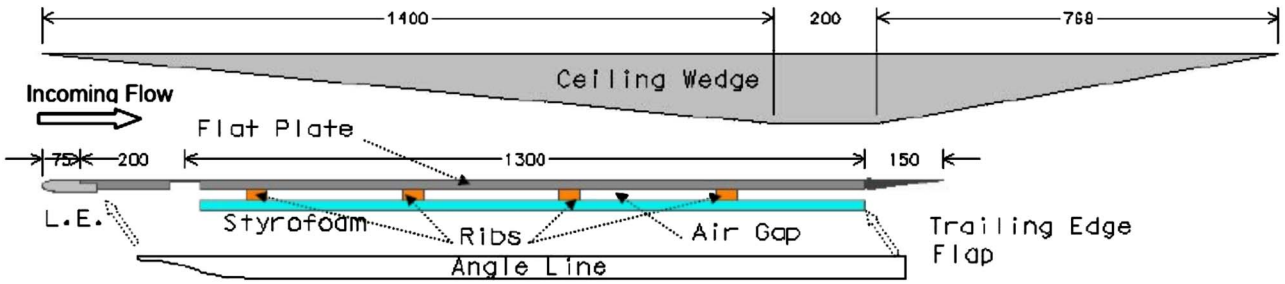


**Fig. 1 Schematic diagram showing the engineering drawing of the heater plate and the ceiling wedge insert for generating a FPG. All units in mm.**

Sharma [2]. However, their study was mainly confined to surface flow measurements. In the present experiment, a specially designed miniature triple-wire probe was used to measure simultaneously the velocity and temperature fluctuations of turbulent spots that were created artificially in a flat plate boundary layer. It is hoped that the results from this study could shed some light on the mechanism that is responsible for the difference in the growth of transitional momentum and thermal boundary layers developing under pressure gradients.

## Experimental Methods

**Experimental Setup.** The experiment was conducted in a low-turbulence close-returned wind tunnel at the Goldstein Research Laboratory, the University of Manchester. The test section of the wind tunnel has a cross-sectional area of 0.5 m by 0.5 m and a length of 3 m. The maximum velocity in the tests section is about 40 m/s and the turbulence intensity is about 0.03%. The wind tunnel is instrumented with a computer-controlled three-dimensional probe traverse mechanism. The accuracies of this traverse system are ±0.1, ±0.05, and ±0.1 mm in the streamwise, wall normal, and spanwise directions, respectively.

In order to create a thermal boundary layer, a specially designed heater plate was constructed. The heater plate consisted of three streamwise sections: a super-elliptical leading edge which was 75 mm in length, the main part of the test plate (1.5 m in length), which was heated, and a trailing edge flap (see Fig. 1). The whole plate was bolted to two angle lines and mounted to the wind tunnel side windows. The main part of the heater plate was made of four layers: a thin metallized plastic sheet, a paper-phenolic laminated flat plate, an air gap, and a styrofoam sheet. The combination of the last two layers minimized the thermal conduction through the backside of the flat plate. Four ribs were rigidly mounted on the backside of the laminate plate to form the air gap and also to strengthen the heater plate. The metallized plastic sheet was 0.1 mm thick and was used to heat the surface. It was bonded to the surface of the laminate flat plate using adhesive. The metallized sheet was heated using a dc power supply which was connected to the copper foil strips adhered to each side of the plate.

In the present experiment, the tests were conducted in a zero-pressure-gradient (ZPG) boundary layer and a favorable pressure gradient (FPG) boundary layer. In order to create the favorable pressure gradient along the test plate, an insert consisting of a convergent and divergent wedge-shaped block as shown in Fig. 1 was fixed onto the ceiling of the test section. The apex of the insert is located 250 mm right above the leading edge of the test plate. The acceleration generated by this wedge can be represented by a constant pressure gradient parameter, $K$, where

$$K = \frac{\nu}{U_\infty^2}\frac{dU_\infty}{dX} \tag{1}$$

In the present study, the FPG case had a value of $K$ equal to $0.56\times10^{-6}$ at an incoming free stream velocity of 10.5 m/s. In the ZPG case, the free stream velocity was 11 m/s. The distributions of the free stream velocity and the pressure gradient parameter for the FPG case are shown in Fig. 2(*a*). The displacement thickness $\delta_1$ and momentum thickness $\delta_2$ for the zero and favorable pressure gradient cases are shown in Fig. 2(*b*).

The turbulent spots were created artificially by injecting puffs of air with a loudspeaker through a 0.5-mm-diam orifice to the laminar boundary layer. The orifice was located at a distance of 275 mm downstream of the leading edge of the test plate. The local Reynolds numbers based on the momentum thickness are 310 and 300 for the zero and favorable pressure gradient cases, respectively. The loudspeaker was driven by a pulse generator which produced square waves with pulse duration of 0.8 ms. The spot generation frequency was adjusted for different measurement stations in order to maximize the number of spots captured during a given data sampling period while allowing sufficient amount of time for the boundary layer to resume its undisturbed laminar state after each spot has passed.

A miniature triple-wire probe, which consisted of an $x$ wire and a cold wire, was used to measure the velocity and temperature fluctuations produced by the spots in the boundary layer. The design criteria of the triple wire are described in [12]. A drawing illustrating the configuration of this triple wire is shown in Fig. 3. During the measurements, an overheat ratio of 1.3 was used for the $x$ wire. The choice of such a relatively low overheat ratio is a

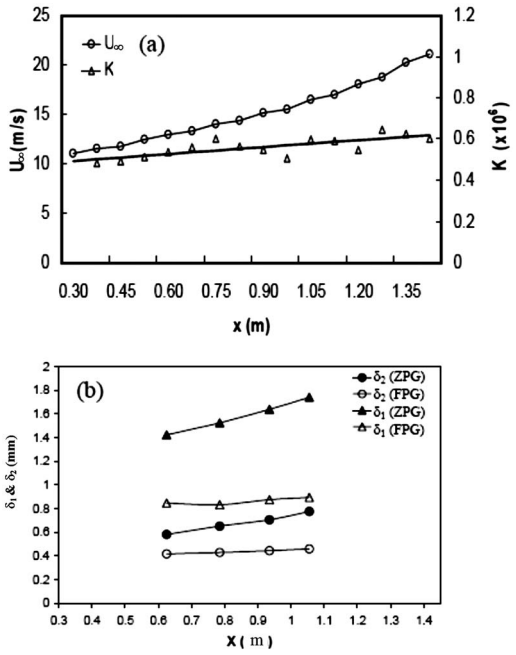


**Fig. 2 Distributions of (*a*) free stream velocity and *K* at FPG; (*b*) momentum and displacement thickness at ZPG and FPG**

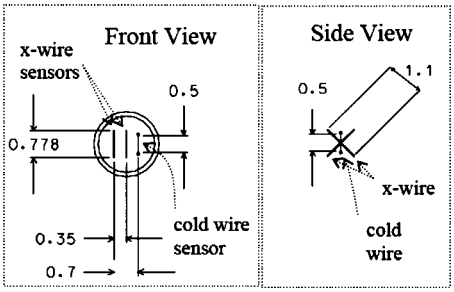


**Fig. 3 Engineering drawings of the triple wire. All units in mm.**

compromise between a reasonable velocity sensitivity and a minimal thermal interference between the wires. The calibration of the $x$ wire was carried out in situ and the procedure described in [13] was adopted. A constant current of 0.07 mA was applied to the cold wire for the temperature measurements. The cold wire calibration was carried out in a pipe rig in which the air stream was heated by a star-wound heater fixed inside the pipe. The velocity of the heated flow was about 10 m/s at the nozzle exit. In order to enable measurements closer to the wall, the triple-wire probe was tilted towards the test surface by 5 deg. In the present experiment, the nearest measurement point to the wall was 0.5 mm from the surface which corresponds to $y/\delta_{\text{tur}}=0.02$ (ZPG) or 0.038 (FPG) at the most downstream streamwise measurement station. Here $\delta_{\text{tur}}$ is the turbulent boundary layer thickness. To the best knowledge of the authors, the nearest measurement point to the wall in a similar study at ZPG that has been reported in the literature was at $y/\delta_{\text{tur}}=0.05$ [15].

The signals from the triple-wire were sampled at a frequency of 4 kHz after passing through a 2 kHz low-pass filter. A typical size of the samples was 120,000 containing about 120 turbulent spots. The measurements were made at a distance of $x_s=310$, 560, 660, and 780 mm from the loudspeaker in order to capture the streamwise growths of spots. Measurements were also made on a spanwise plane normal to the incoming flow direction at $x_s=660$ mm (ZPG) and 780 mm (FPG).

During the experiment, the surface of the test plate was kept at about 10°C above the free stream temperature. To ensure the accuracy of the results, the surface temperature was allowed to reach equilibrium before the measurement was taken. This usually required heating the test plate inside the running tunnel for at least 4–5 hours. It normally took approximately 3–4 hours. to complete the measurement for one pressure gradient case. The variations of the fluid temperature in the freestream were found to be less than 0.2°C during each test.

**Data Processing Method.** In the present study, the local temperature in the boundary layer was deduced from the voltage reading from the cold wire. A simple relationship exists between the voltage reading from the cold wire and the temperature $T$, which can be represented as

$$\boldsymbol{T}=\boldsymbol{C}_1\boldsymbol{E}_c+\boldsymbol{C}_2 \tag{2}$$

The coefficients $C_1$ and $C_2$ were determined from a best fit of the cold wire calibration curve.

The local temperature deduced from the cold wire was then used to correct the voltage readings from the $x$ wire using the following formula:

$$E_{\text{corr}}(x,y,z,t)=E(x,y,z,t)\left(\frac{T_{\text{wire}}-T_{\text{cal}}}{T_{\text{wire}}-T(x,y,z,t)}\right)^{0.5} \tag{3}$$

where $T_{\text{wire}}$ is the temperature of the $x$ wire, $T(x,y,z,t)$ is the temperature obtained from the cold wire and $T_{\text{cal}}$ is the fluid temperature during the calibration of the $x$ wire. Finally, a full velocity versus yaw-angle calibration technique described in Ref. [13] was employed to convert the corrected voltages from the $x$ wire into $U$ and $V$.

Let the temporal variations of the ensemble-averaged $U$, $V$, and $T$ at each measurement point be denoted by $\langle U(x,y,z,t_j)\rangle$, $\langle V(x,y,z,t_j)\rangle$, and $\langle T(x,y,z,t_j)\rangle$, respectively. The velocity perturbations $\tilde{\boldsymbol{U}},\tilde{\boldsymbol{V}}$ and temperature perturbation $\tilde{\boldsymbol{T}}$ caused by an ensemble-averaged turbulent spot relative to the undisturbed laminar boundary layer can be expressed as

$$\tilde{\boldsymbol{U}}(\boldsymbol{x},\boldsymbol{y},\boldsymbol{z},\boldsymbol{t}_j)=\frac{\langle \boldsymbol{U}(\boldsymbol{x},\boldsymbol{y},\boldsymbol{z},\boldsymbol{t}_j)\rangle-\boldsymbol{U}_L(\boldsymbol{x},\boldsymbol{y})}{\boldsymbol{U}_\infty(\boldsymbol{x})} \tag{4a}$$

$$\tilde{\boldsymbol{V}}(\boldsymbol{x},\boldsymbol{y},\boldsymbol{z},\boldsymbol{t}_j)=\frac{\langle \boldsymbol{V}(\boldsymbol{x},\boldsymbol{y},\boldsymbol{z},\boldsymbol{t}_j)\rangle-\boldsymbol{V}_L(\boldsymbol{x},\boldsymbol{y})}{\boldsymbol{U}_\infty(\boldsymbol{x})} \tag{4b}$$

$$\tilde{\boldsymbol{T}}(\boldsymbol{x},\boldsymbol{y},\boldsymbol{z},\boldsymbol{t}_j)=\frac{\langle \boldsymbol{T}(\boldsymbol{x},\boldsymbol{y},\boldsymbol{z},\boldsymbol{t}_j)\rangle-\boldsymbol{T}_L(\boldsymbol{x},\boldsymbol{y})}{[\boldsymbol{T}_W(\boldsymbol{x})-\boldsymbol{T}_\infty(\boldsymbol{x})]} \tag{4c}$$

where $U_L(x,y)$, $V_L(x,y)$, and $T_L(x,y)$ are the local values of $U$, $V$, and $T$ in the undisturbed laminar boundary layer, respectively. $T_w(x)$ is the local wall temperature and $T_\infty(x)$ the fluid temperature in the free stream.

Let the temporal variations of ensemble-averaged rms fluctuations of $U$, $V$, and $T$ at each measurement point be represented as $u'(x,y,z,t_j)$, $v'(x,y,z,t_j)$, and $\theta'(x,y,z,t_j)$, respectively, they can be calculated as

$$u'(x,y,z,t_j)=\sqrt{\frac{\sum_{i=1}^{N}[U(x,y,z,t_j)-\langle U(x,y,z,t_j)\rangle]^2}{N}} \tag{5a}$$

$$v'(x,y,z,t_j)=\sqrt{\frac{\sum_{i=1}^{N}[V(x,y,z,t_j)-\langle V(x,y,z,t_j)\rangle]^2}{N}} \tag{5b}$$

$$\theta'(x,y,z,t_j)=\sqrt{\frac{\sum_{i=1}^{N}[T(x,y,z,t_j)-\langle T(x,y,z,t_j)\rangle]^2}{N}} \tag{5c}$$

where $N$ is the total number of spots.

Similarly, the temporal variations of ensemble-averaged Reynolds shear stress $\langle uv\rangle$, Reynolds longitudinal heat flux $\langle u\theta\rangle$ and Reynolds cross stream heat flux $\langle v\theta\rangle$, can be calculated from the following equations

$$\langle uv\rangle=\sum_{i=1}^{N}\frac{\lfloor U(x,y,z,t_j)-\langle U(x,y,z,t_j)\rangle\rfloor\lfloor V(x,y,z,t_j)-\langle V(x,y,z,t_j)\rangle\rfloor}{N} \tag{6a}$$

$$\langle u\theta\rangle=\sum_{i=1}^{N}\frac{\lfloor U(x,y,z,t_j)-\langle U(x,y,z,t_j)\rangle\rfloor\lfloor T(x,y,z,t_j)-\langle T(x,y,z,t_j)\rangle\rfloor}{N} \tag{6b}$$

$$\langle v\theta\rangle=\sum_{i=1}^{N}\frac{\lfloor V(x,y,z,t_j)-\langle V(x,y,z,t_j)\rangle\rfloor\lfloor T(x,y,z,t_j)-\langle T(x,y,z,t_j)\rangle\rfloor}{N} \tag{6c}$$

The propagation rates of the turbulent spots can be obtained by plotting the *time of flight* versus the *integral arrival time* and

finding the slope of the best-fit line. In the present experiment, measurements were conducted at four streamwise stations on the plane of symmetry of the spots. The *time of flight* is the actual time that it takes for either the leading edge or the trailing edge of the spots to convect from a reference location $x_{\text{ref}}$ (the most upstream measurement point) to one of the remaining three streamwise locations. The *integral arrival time* is the time that is required for the spot to travel across the same distance at the local freestream velocity, i.e.

$$t_{\text{intergal}} = \int_{x_{\text{ref}}}^{x} \frac{dx}{U_\infty(x)} \tag{7}$$

A reliable detection algorithm is needed to detect the interface of each spot, thereby enabling the calculation of the spot propagation rates. In the present study, the algorithm described by Clark et al. [14] was employed to distinguish the interfaces between the turbulent flow inside the spot and its surrounding laminar boundary layer. In this method, a detector function was used to highlight the high frequency fluctuations associated with turbulence. It is defined as

$$D(x,y,z,t) = m(x,y,z,t)\left(\frac{\partial E(x,y,z,t)}{\partial t}\right)^2 \tag{8}$$

where $E(x,y,z,t)$ is the raw signal and $m(x,y,z,t)$ is the normalized signal magnitude, which is given by

$$m(x,y,z,t) = \frac{E(x,y,z,t) - E_{\min}(x,y,z)}{E_{\max}(x,y,z) - E_{\min}(x,y,z)} \tag{9}$$

The rate of change in the raw signal is obtained using the central difference scheme

$$\frac{\partial E(x,y,z,t)}{\partial t} = \frac{E(x,y,z,t_{j+1}) - E(x,y,z,t_{j-1})}{2\Delta t} \tag{10}$$

where $t$ is the signal sampling period. A smoothing function is then obtained from the detection function

$$C(x,y,z,t) = \frac{(\Delta t)^2}{1 + (\tau_s/\Delta t)} \sum_{j=i-(\tau_s/2\Delta t)}^{j=i+(\tau_s/2\Delta t)} w_j D(x,y,z,j\Delta t) \tag{11}$$

so as to eliminate zero crossings in the detection function within a turbulent spot. Here $\tau_s$ is the smoothing period and the weighting factor $w_j$ is defined as

$$w_j = \exp\left[-\left(\frac{0.625}{\tau_s/\Delta t}\right)\cdot|j-i|\right] \tag{12}$$

Finally, the turbulent portion of the signal produced by each spot is identified by employing a threshold to the smoothing function. In this study, this threshold value is chosen through a trial and error procedure until the interface between the turbulent and laminar region identified using this algorithm is consistent with that from visual inspection of the raw signal.

## Results

**General Features of Turbulent Spots at ZPG.** Figure 4 shows the sample signals of $U$, $V$, and $T$ acquired simultaneously on the plane of symmetry of the spots using the triple-wire probe along with the trigger pulses. $U$, $V$, and $T$ appear to be highly correlated among them in that the timing corresponding to the onset and rapid decay of turbulence in the spots appears to almost coincide. A stretch of the becalmed region trailing behind each spot is also evident in $U$ and $T$. It appears that in the present experiment a sufficient time interval has been given to allow the boundary layer to reassume its laminar state before the next spot arrives.

Figure 5(*a*) shows the variations of the spot leading edge propagation rate $C_l$ and trailing propagation rate $C_t$ with $y/\delta_{\text{tur}}$ on the plane of symmetry in the zero pressure gradient case. As shown in the figure, there is no appreciable difference between the propagation rates deduced from the velocity and the temperature data. In addition, the spots propagation rates found in the present study are similar to those obtained by other researchers in zero pressure gradient flows [10,14–20]. This can be taken as evidence that the spots under investigation in the present experiment resemble the "classical" turbulent spots studied by other researchers.

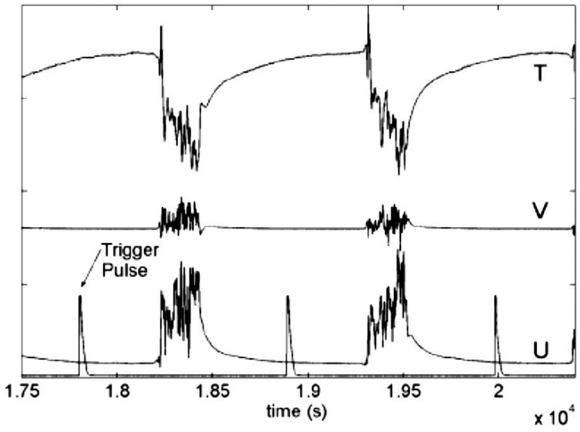


**Fig. 4 *U*, *V*, and *T* signals acquired simultaneously on the plane of symmetry of the spots along with the trigger pulses**

In this section, the general characteristics of the momentum and thermal structure of turbulent spots in the zero pressure gradient boundary layer are examined. Figures 6(*a*)–6(*i*) show the contours of $\tilde{U}/U_\infty$, $\tilde{V}/U_\infty$, and $\tilde{T}/\Delta T$, $u'/U_\infty$, $v'/U_\infty$, and $\theta'/\Delta T$ as well as those of $\langle uv\rangle/(U_\infty)^2$, $\langle u\theta\rangle/(U_\infty\Delta T)$, and $\langle v\theta\rangle/(U_\infty\Delta T)$ on the plane of symmetry of the spots at $x_s$=780 mm in the zero pressure gradient case. Here $\Delta T=(T_w-T_\infty)$.

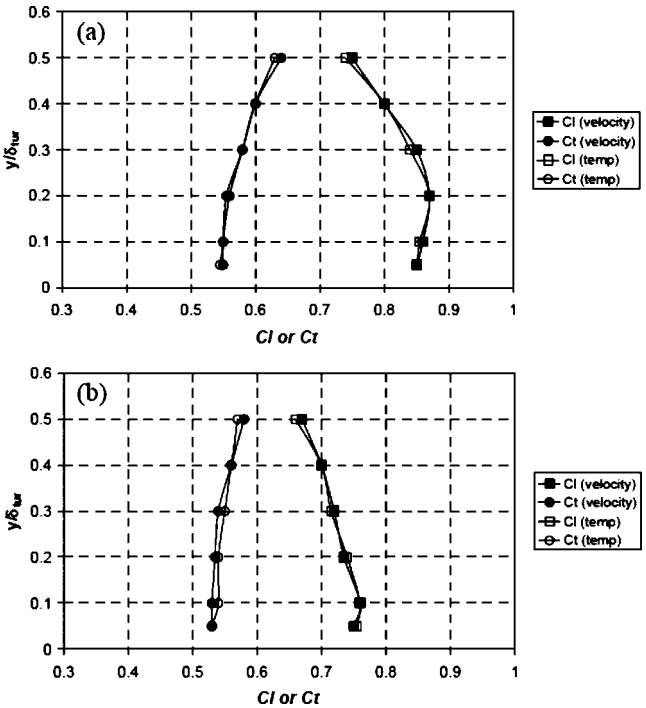


**Fig. 5 Comparison of $C_l$ and $C_t$ deduced from the velocity and temperature data in the (*a*) zero and (*b*) favorable pressure gradient boundary layer**

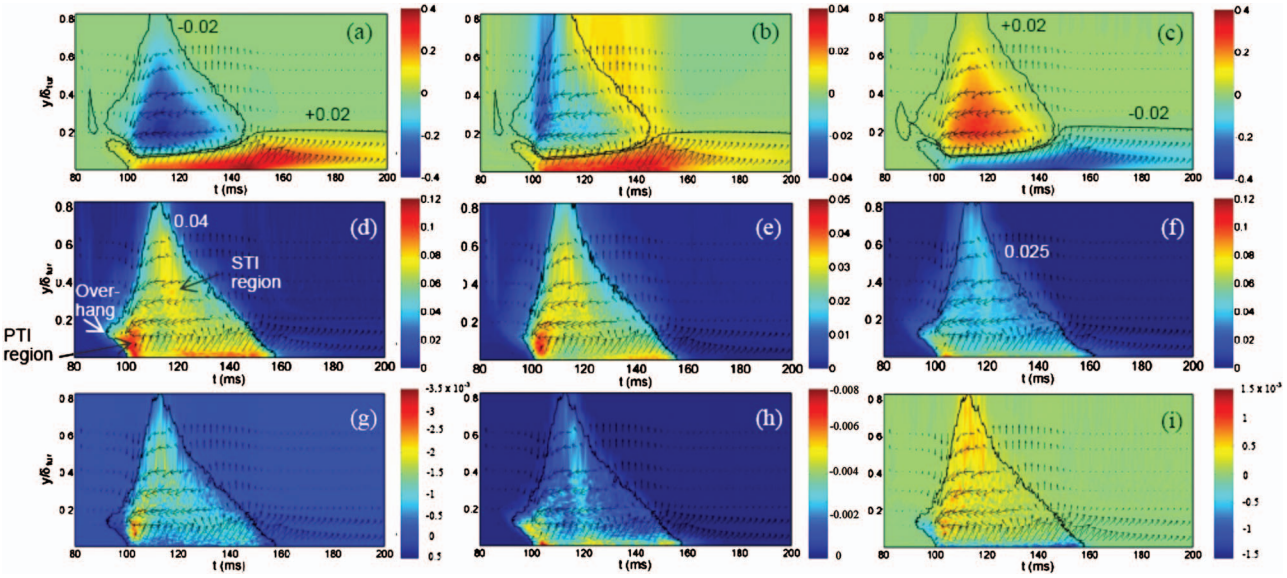


**Fig. 6 Contours of (*a*) $\tilde{U}/U_\infty$; (*b*) $\tilde{V}/U_\infty$; (*c*) $\tilde{T}/\Delta T$; (*d*) $u'/U_\infty$; (*e*) $v'/U_\infty$; (*f*) $\theta'/\Delta T$; (*g*) $\langle uv\rangle/U_\infty^2$; (*h*) $\langle u\theta\rangle/U_\infty\Delta T$; (*i*) $\langle v\theta\rangle/U_\infty\Delta T$ on the plane of symmetry of spots in the ZPG case at $x_s$=780 mm**

The $\tilde{U}/U_\infty$ contour in Fig. 6(*a*) resembles the same characteristics that were previously identified in an isothermal boundary layer [9]. In brief, the near wall region of the spot, including its becalmed region, exhibits a positive velocity perturbation, whereas the outer region exhibits a negative velocity perturbation. A criterion of $\tilde{U}/U_\infty=\pm0.02$ is adequate for defining the outer boundary of the ensemble-averaged spot.

The perturbation level of $\tilde{V}/U_\infty$ is about one-tenth of $\tilde{U}/U_\infty$ (see Fig. 6(*b*)). It appears that in the outer region, the arrival of the spot is characterized by a negative $\tilde{V}/U_\infty$ near the leading edge which is followed by a positive $\tilde{V}/U_\infty$ near the trailing edge. This is consistent with the observation made by Antonia et al. [15] In the near wall region, $\tilde{V}/U_\infty$ is found to be positive throughout the length of the spot and increases steadily towards the trailing edge. This is opposite to the results of Antonia et al. who found $\tilde{V}/U_\infty$ to be negative in this region. In the existing literature, the transverse velocity data of turbulent spots in the near wall region are very scarce hence the results are not conclusive. In the authors' opinion, however, a positive $\tilde{V}/U_\infty$ in the near wall region upon the arrival of a spot would be expected in accordance to the local thickening of the boundary layer. $\tilde{U}/U_\infty$ and $\tilde{V}/U_\infty$ can be combined to form perturbation velocity vectors which are superimposed onto various contours. A circulating motion inside the negative $\tilde{U}/U_\infty$ region of the spot is clearly seen and this is in line with the hypothesis made by Cantwell et al. [17] that the spot could be regarded as a large eddy in an averaged sense.

Figure 6(*c*) shows the temperature perturbation contour, $\tilde{T}/\Delta T$. Opposite to the $\tilde{U}/U_\infty$ contour, the local temperature was negatively perturbated throughout the course of spot passage in the near wall region. This indicates that the near wall fluid is cooler than the local laminar value due to an increased mixing caused by the passage of the turbulent spot. In the outer region, $\tilde{T}/\Delta T$ is always positive, indicating an amalgamation of warmer fluid there. The contour line with $\tilde{T}/\Delta T=\pm0.02$ perturbation seems to depict an almost identical shape of the spot as that with $\tilde{U}/U_\infty=\pm0.02$.

Similar to $\tilde{U}/U_\infty$, the characteristics of the $u'/U_\infty$ contour (see Fig. 6(*d*)) are the same as that previously identified in an isothermal boundary layer [9]. Regions with high turbulence intensity are seen to locate near the leading edge interface just below the leading edge overhang and also in the near wall region towards the trailing edge of the spot. There is also a region with a relative high turbulence intensity in the outer part of the spot. The region underneath the overhang has a typical intensity level of 10–12% and it is denoted as the "primary turbulence intensity (PTI)" region. The region in the outer part of the spot has a typical intensity level of 7–9% and it is denoted as the "secondary turbulence intensity (STI)" region. The above abbreviations are intended to categorize two major fluctuation levels, which usually confined themselves to specific locations within a spot. The PTI region is believed to be the source of streamwise turbulence breakdown for the spot. This is consistent with the observations made by Gad-el-Hak et al., Gutmark and Blackwelder, Glazer et al. [19–21]. Similar distributions of high fluctuation level are also observed in the $v'/U_\infty$ contour (Fig. 6(*e*)).

In general, the contour of $\theta'/\Delta T$ in Fig. 6(*f*) appears to be similar to that of $u'/U_\infty$ except that the fluctuation level is lower. A maximum $\theta'/\Delta T$ is again observed in the region underneath the leading edge overhang that coincides with the PTI region of $u'/U_\infty$. A criterion of $\theta'/\Delta T=0.025$ yields a spot shape similar to that with $u'/U_\infty=0.04$.

The $\langle uv\rangle/(U_\infty)^2$ contour is shown in Fig. 6(*g*). The interior of the turbulent spot is characterized by a negative turbulent shear stress and the downstream part of the PTI region has the highest negative value, indicating a maximum local turbulence production. Interestingly, the leading edge overhang has a low positive $\langle uv\rangle$ close to the laminar value. A low level of $\langle uv\rangle$ inside the overhang also confirms that turbulence was not generated locally. The leading edge overhang is likely to be composed of fluid which was ejected from the PTI region.

The longitudinal turbulent heat flux $\langle u\theta\rangle/(U_\infty\Delta T)$ contour shown in Fig. 6(*h*) has negative values throughout the spot. This is in agreement with the results from Antonia et al. High level of negative $\langle u\theta\rangle/(U_\infty\Delta T)$ is observed both in the PTI region and in the near wall regions up to the trailing edge. They are expected to be associated with vigorous longitudinal transport of turbulent heat flux in a turbulent spot.

A high level of cross-stream turbulent heat flux $\langle v\theta\rangle/(U_\infty\Delta T)$ is also observed in the region where a high level of $\langle uv\rangle/(U_\infty)^2$ is

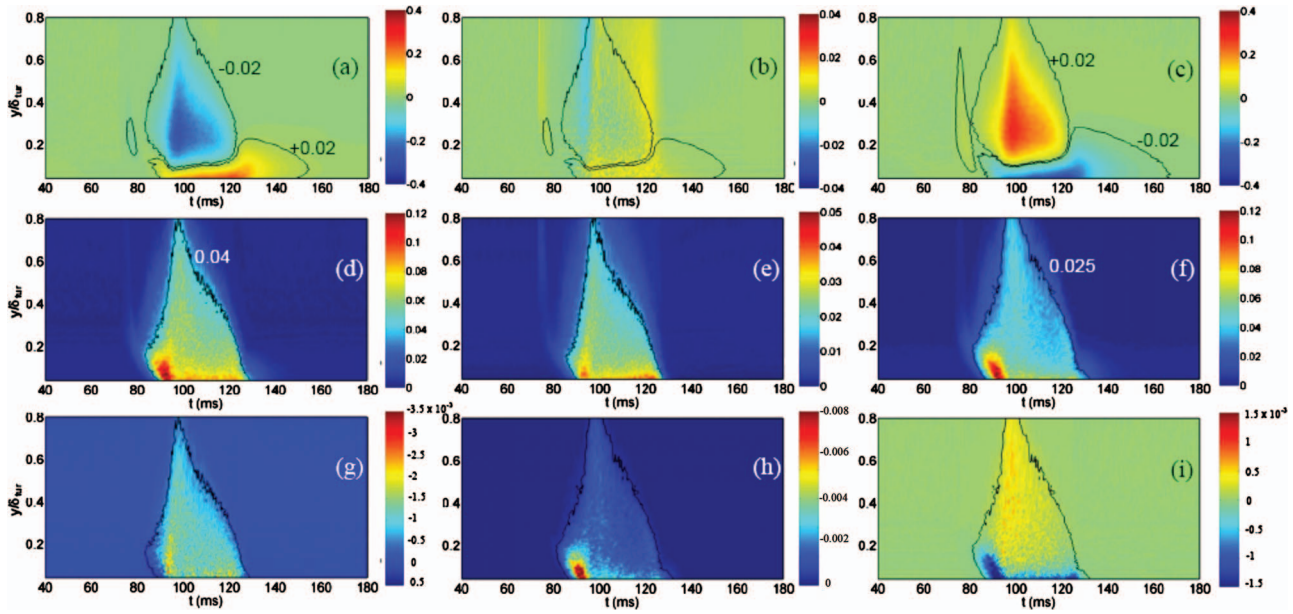


**Fig. 7 Contours of (*a*) $\tilde{U}/U_\infty$; (*b*) $\tilde{V}/U_\infty$; (*c*) $\tilde{T}/\Delta T$; (*d*) $u'/U_\infty$; (*e*) $v'/U_\infty$; (*f*) $\theta'/\Delta T$; (*g*) $\langle uv\rangle/U_\infty^2$; (*h*) $\langle u\theta\rangle/U_\infty\Delta T$; (*i*) $\langle v\theta\rangle/U_\infty\Delta T$ on the plane of symmetry of spots in the FPG case at $x_s$=780 mm**

found (see Fig. 6(*i*)). However, the entire near wall region and the region downstream to the PTI region are clearly dominated by a negative $\langle v\theta\rangle$. The rest of the spot is characterized by a positive $\langle v\theta\rangle$. Further discussions about the negative $\langle v\theta\rangle/(U_\infty\Delta T)$ will be made later in this paper.

**Characteristics of Spots on the Plane of Symmetry in FPG.** The leading edge and trailing edge propagation rates of the spot on the plane of symmetry in the FPG case are shown in Fig. 5(*b*). The propagation rates deduced from velocity and temperature data are almost identical. However, compared to the zero pressure gradient case, $C_l$ decreases whereas $C_t$ remains mostly unchanged for the FPG case. This implies that a reduction in the spot streamwise growth at the presence of a favorable pressure gradient is caused by a reduction in the leading edge propagation rate. This observation is consistent with the belief that the leading edge of the spot is in fact the locus of breakdown of laminar flow into turbulent flow and a favorable pressure gradient inhibits this local breakdown [7–9].

Figures 7(*a*)–7(*i*) show the contours of $\tilde{U}/U_\infty$, $\tilde{V}/U_\infty$, and $\tilde{T}/\Delta T$, $u'/U_\infty$, $v'/U_\infty$, and $\theta'/\Delta T$ as well as those of $\langle uv\rangle/(U_\infty)^2$, $\langle u\theta\rangle/(U_\infty\Delta T)$, and $\langle v\theta\rangle/(U_\infty\Delta T)$ on the plane of symmetry of the spots at $x_s$=780 mm in the FPG case. It can be seen that the magnitude of $\tilde{U}/U_\infty$, $\tilde{V}/U_\infty$, and $\tilde{T}/\Delta T$ reduces due to the presence of FPG. In addition, the shape of the spot depicted by the $\tilde{U}/U_\infty=\pm0.02$, and $\tilde{T}/\Delta T=\pm0.02$ perturbation contours indicates that the thermal boundary layer takes a longer time to reassume its laminar status than its velocity counterpart.

It is found that the level of $u'/U_\infty$ in the PTI and the STI regions responds differently to the presence of a FPG (see Fig. 7(*d*)); although the level of in the STI region decreases in the FPG case, the level in the PTI region is relatively unchanged. The inhibition of velocity fluctuations is more pronounced in the outer part of the boundary layer than in the near wall region due to the difference in sensitivity of the different parts of the layer to the presence of a favorable pressure gradient [9]. The response of $\theta'/\Delta T$ to the presence of a FPG is different. Comparing Fig. 7(*f*) with Fig. 6(*f*), one can see that the level of $\theta'/\Delta T$ in the PTI region increases in the FPG case. However, there is no obvious change in the level of $\theta'/\Delta T$ in the outer layer of the spot, indicating a greater resistance to the stabilizing effect imposed by the FPG in this region.

The inhibition effect which FPG exerts on the shear stress $\langle uv\rangle/(U_\infty)^2$ in the PTI region is apparent (see Fig. 7(*g*)). As a result, the leading edge overhang, which is induced by the dominant shear in the PTI region, becomes less pronounced in the FPG case. In contrast, there is a considerable increase in the level of $\langle u\theta\rangle/(U_\infty\Delta T)$ as shown in Fig. 7(*h*). Furthermore, $\langle v\theta\rangle/(U_\infty\Delta T)$ is seen to become increasingly negative in the near wall region and the leading edge such that positive $\langle v\theta\rangle/(U_\infty\Delta T)$ in the PTI region seen at ZPG almost diminishes and is replaced by a negative $\langle v\theta\rangle/(U_\infty\Delta T)$. The presence of negative $\langle v\theta\rangle/(U_\infty\Delta T)$ in the near wall region is peculiar since it is expected that a positive transverse velocity fluctuation $v$ is associated with a positive temperature fluctuation $\theta$ and vise versa. Negative $\langle v\theta\rangle/(U_\infty\Delta T)$ in the near wall region was also observed in transitional boundary layers [22,23].Such a similarity between an artificially generated turbulent spot and a transition boundary layer is not surprising since a transitional boundary layer is the amalgamation of randomly occurring turbulent spots. No explanation, however, has been given in the existing literature regarding why $\langle v\theta\rangle/(U_\infty\Delta T)$ in the near wall region is negative.

The authors of this paper believe that an increasing negative $\langle v\theta\rangle$ in the near wall region at FPG is not caused by the flow structure in the spot but an insufficient spatial resolution of the triple-wire probe in the measurement. The near wall region of a turbulent spot is believed to be populated with hairpin vortices whose legs are stretched along the wall. They are responsible for the low-speed streaks observed using various flow visualization techniques. The average spacing between low-speed streaks is known to be approximately 100 wall units, corresponding to the distance between the centers of neighboring hairpin vortices (see Fig. 8). There has been no data for the averaged width of the stretched hairpin vortices in the near wall region. But to allow for a finite spacing between the adjacent hairpin vortices and their legs with a finite width, the width of the stretched hairpin vortices is not expected to be greater than 50 wall units. Based on this assumption, the distance between the legs of hairpin vortices is

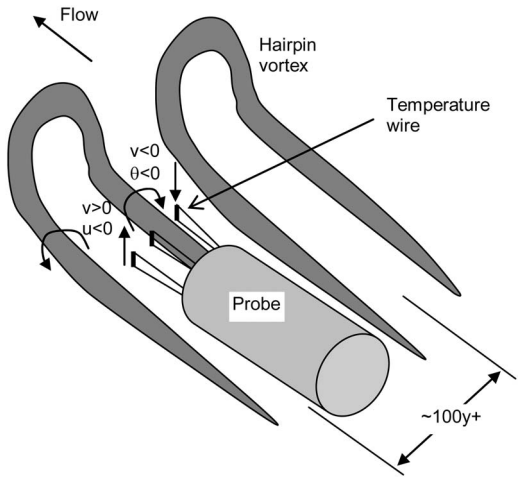


**Fig. 8 Schematic diagram showing the location of the sensors of the triple-wire probe relative to the hairpin vortices**

estimated to be 1.2 and 0.9 mm at ZPG at FPG, respectively. In the present experiments, the spanwise spacing between the temperature wire and the outer $x$ wire is 0.7 mm. It happens to be comparable to the distance between the legs of hairpin vortices at FPG. As such the triple wire tends to sit across one leg of each hairpin vortex. Imagine the center of the $x$ wire locates between the two legs of the hairpin, whereas the temperature wire at the outboard of one of the legs (see Fig. 8). When the $x$ wire senses a positive $v$, the temperature wire will pick up a negative $\theta$. Statistically, this scenario will result in a negative $\langle v\theta \rangle$ as measured with the triple wire. Consequently, the measurement of $\langle u\theta \rangle$ in the near wall region is in error. This is an inherent problem with the triple-wire probe since it is difficult to make the spacing between the wires physically smaller. Hence, in the following discussion, the attention will be focused on $u'/U_\infty$, $\theta'/\Delta T$, and $\langle uv \rangle/(U_\infty)^2$, which can be more accurately measured.

**Characteristics of Spots in Spanwise Planes in FPG.** Figures 9($a$) show the spanwise slices of $u'/U_\infty$ contour as the turbulent spot passes through the measurement plane at $x_s$=660 mm in the zero pressure gradient, whereas Figs. 9($b$) show the corresponding $\theta'/\Delta T$ contours. Note that the spanwise data for the ZPG case presented in this section are obtained at $x_s$=660 mm instead of at 780 mm. This is because that at the zero pressure gradient the wing tips of the spots are found to expand into the sidewall turbulence contamination zone at $x_s$=780 mm. Nevertheless, the results obtained on the plane of symmetry do not seem to be affected as found by Gostelow et al. [10]. At the favorable pressure gradient, this problem does not occur at $x_s$=780 mm as both the spreading angles of the turbulent spot and the side wall contamination zone are smaller.

It is seen that the spot grows both in height and width before its trailing edge arrives Fig. 9($a$4). After that the height of the spot decreases as the becalmed region takes over. High level of fluctuations initially occurs around the plane of symmetry. However, as the spot grows in width the region with high fluctuation levels gradually shifts outwards in the spanwise direction towards the wing tip. In the zero pressure gradient case, the level of velocity and temperature fluctuations is also high in the near wall region. The distributions of $u'/U_\infty$ and $\theta'/\Delta T$ contours at FPG are qualitatively similar to those at ZPG except the level of $\theta'/\Delta T$ in the wing tip is significantly lower (see Fig. 10).

In order to appreciate the difference in level of turbulence fluctuations across the spot, contours of $u'/U_\infty$ and $\theta'/\Delta T$ on a spanwise plane parallel to the test surface at $y$=0.07$\delta_{tur}$ at ZPG are shown in Fig. 11. It is seen clearly that the spot has a swept back leading edge and a slightly curved trailing edge. The level of $u'/U_\infty$ and $\theta'/\Delta T$ are higher near the leading edge than in the inner part of the spot. In addition, the level of $u'/U_\infty$ and $\theta'/\Delta T$

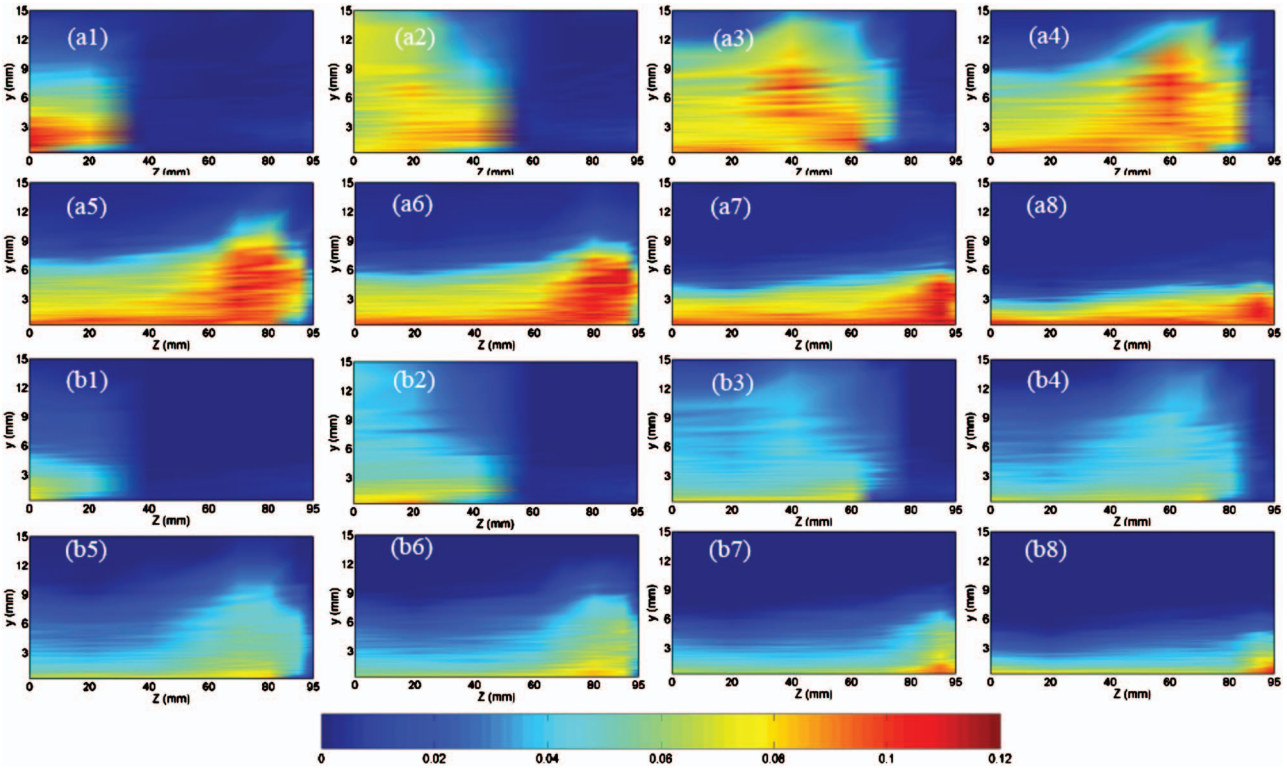


**Fig. 9 Ensemble-averaged ($a$1)–($a$8), $u'/U_\infty$ and ($b$1)–($b$8). $\theta'/\Delta T$ contours in the $y$–$z$ plane at $x_s$=660 mm, $t_0$=90, 99, 109, 115, 120, 123, 127, and 130 ms in the ZPG case.**

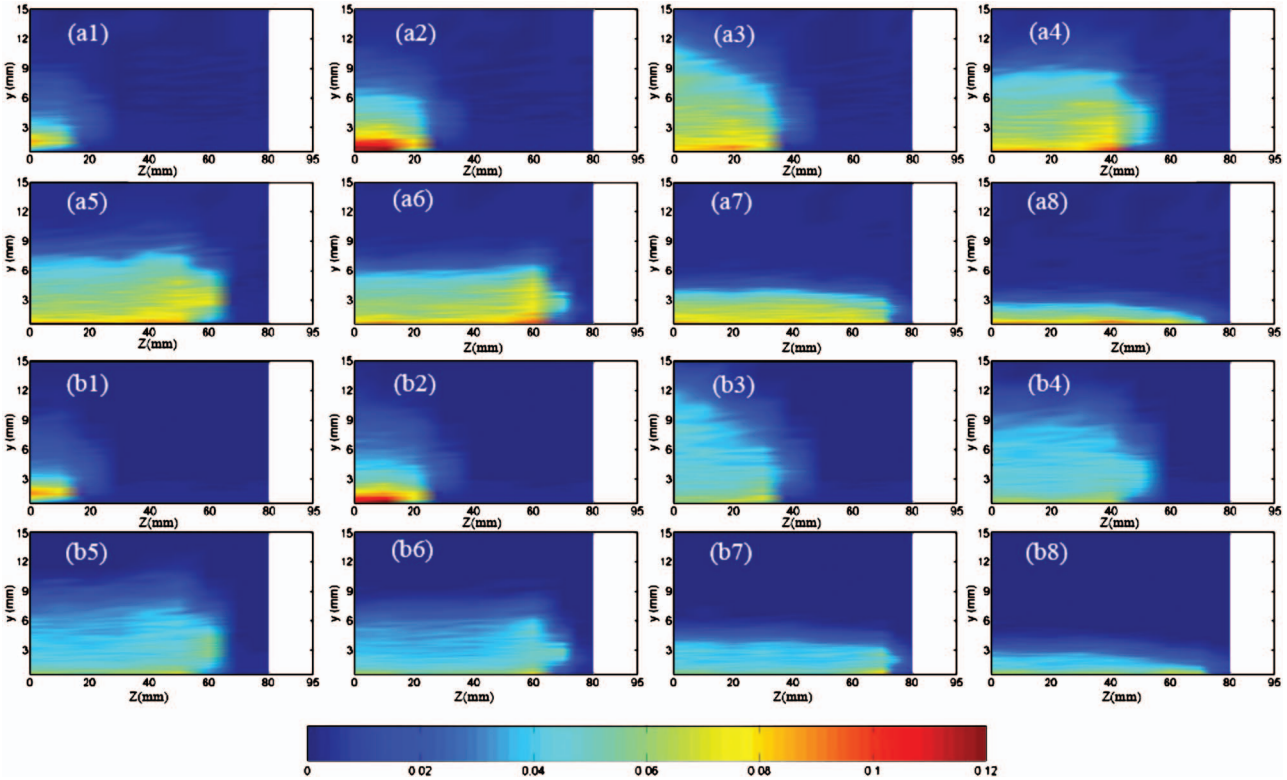


**Fig. 10 Ensemble-averaged (*a*1–*a*8) $u'/U_\infty$ and (b1–b8). $\theta'/\Delta T$ contours in the *y* - *z* plane at $x_s$=780 mm, $t_0$=88, 93, 97.8, 104, 110, 115, 121, and 124 ms in the FPG case.**

in the wing tip area is about the same as that on the plane of symmetry. However, there is a somewhat different picture for spots developing under FPG (see Fig. 12). It is seen that, although the level of $u'/U_\infty$ in the region of PTI (see Fig. 12(*a*)) is still comparable to that at the zero pressure gradient, the level of $u'/U_\infty$ at the spanwise periphery has been reduced to a certain extent. Furthermore, a higher temperature fluctuation $\theta'/\Delta T$is found in the region of PTI on the plane of symmetry (see Fig. 12(*b*)) whereas $\theta'/\Delta T$ at its spanwise periphery has been reduced substantially.

## Discussions

In order to investigate further how a favorable pressure gradient affects the streamwise growth of the spot, the characteristics of an ensemble-averaged spot on its plane of symmetry and two spanwise planes were investigated. The leading and trailing edge propagation rates of the spot on the plane of symmetry were examined first. It was found that $C_l$ and $C_t$ deduced from the velocity and temperature data are almost identical to each other in both the zero and favorable pressure gradient boundary layers. This

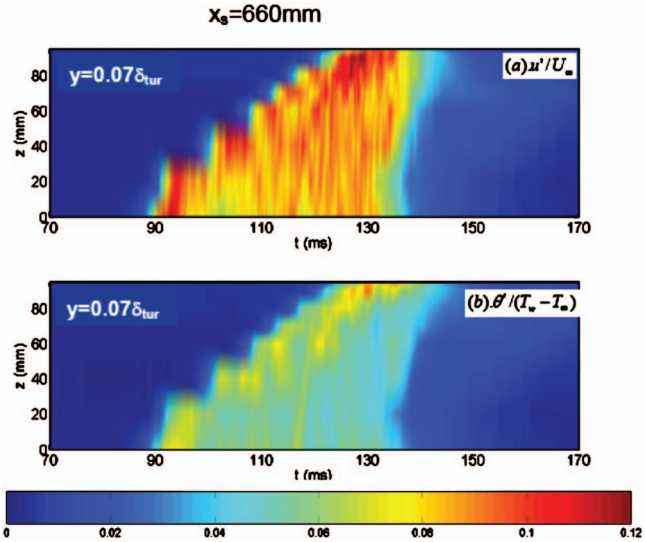


**Fig. 11 Ensemble-averaged (*a*) $u'/U_\infty$ and (*b*) $\theta'/\Delta T$ contours on the spanwise plane at $x_s$=660 mm, $y$=0.07$\delta_{tur}$ for the ZPG case**

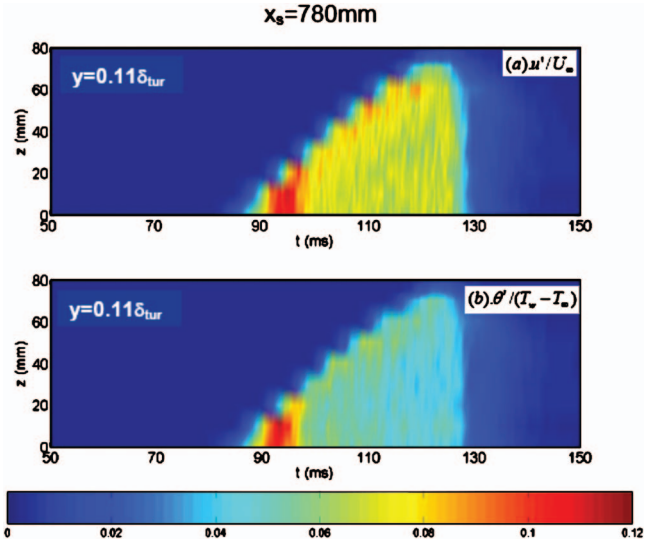


**Fig. 12 Ensemble-averaged (*a*) $u'/U_\infty$ and (*b*) $\theta'/\Delta T$ contours on the spanwise plane at $x_s$=780 mm, $y$=0.11$\delta_{tur}$ for the FPG case**

**Table 1 The differences in the levels of velocity fluctuations, Reynolds shear stresses, and temperature fluctuations between the PTI region and the spanwise peripheral of the spots in the ZPG and the FPG**

| Pressure gradient | $\Delta u'/U_\infty(\%)$ | $\Delta\langle uv\rangle/(U_\infty)^2(\%)$ | $\Delta\theta'/\Delta T(\%)$ |
|---|---|---|---|
| ZPG | 9 | 3 | 10 |
| FPG | 33 | 20 | 69 |

result is not surprising since the instantaneous variations in velocity and temperature appear to be highly correlated to each other on the plane of symmetry of the spot. It was then found that the difference between spot shapes depicted by the velocity and temperature perturbation contours is also minimal.

Nevertheless, some interesting features exist in the ways that $u'/U_\infty$ and $\theta'/\Delta T$ contours react to the presence of a favorable pressure gradient. First, comparing $u'/U_\infty$ and $\theta'/\Delta T$, one finds that $u'/U_\infty$ generally is associated with higher fluctuation levels than $\theta'/\Delta T$ in the zero pressure gradient case. However, at the favorable pressure gradient the level of $\theta'/\Delta T$ increases, whereas that of $u'/U_\infty$ stays almost constant such that $u'/U_\infty$ and $\theta'/\Delta T$ in the PTI region are at about the same levels (9–11%). Second, in the favorable pressure gradient flow significant velocity fluctuations and Reynolds shear stresses occur both in the PTI region and the spanwise periphery, whereas significant temperature fluctuations and turbulent heat fluxes (not shown here) are confined in the PTI region.

The second statement can be further appreciated if these differences are quantified. Here a new parameter is introduced to illustrate the difference between the regions of PTI and the spanwise periphery in terms of $u'/U_\infty$, $\theta'/\Delta T$ or $\langle uv\rangle/(U_\infty)^2$,

$$\Delta\psi = \frac{\bar{\psi}_{\mathrm{PTI}} - \bar{\psi}_{\mathrm{wing}}}{\bar{\psi}_{\mathrm{PTI}}} \tag{13}$$

where $\bar{\psi}_{\mathrm{PTI}}$ and $\bar{\psi}_{\mathrm{wing}}$ are the parameters of interest in the PTI region and at the spanwise periphery, respectively. Note that the temporal extent of $\bar{\psi}_{\mathrm{PTI}}$ is determined by applying a threshold value of $u'/U_\infty$, which is typically 10%. The PTI region within the corresponding time range is then averaged. For consistency, the corresponding time range is also applied to other quantities at the same flow condition. Since the intensity level varies considerably at the spot wing tip, a 0.5 ms period is used in calculating the level of $\bar{\psi}_{\mathrm{wing}}$ within the wing tip region which is associated with a significant intensity level. As shown in Table 1, $\Delta u'/U_\infty$ and $\Delta\langle uv\rangle/(U_\infty)^2$ are 9% and 3%, respectively, in the ZPG case and increase to 33% and 20% in the FPG case. In contrast, $\Delta\theta'/\Delta T$ is 10% in the ZPG caseand experiences a dramatic increase to 69% in the FPG case. A significant increase in $\Delta\langle u\theta\rangle/(U_\infty\Delta T)$ and $\Delta\langle v\theta\rangle/(U_\infty\Delta T)$ are also observed but the results will not be shown here.

In a turbulent spot, the 'primary turbulence intensity' region is considered as the 'agent' of destabilization that is responsible for the streamwise growth of the spot. It is also expected that a high turbulence intensity level occurs at the spanwise periphery of the spot to maintain its spanwise growth. The PTI region near the plane of symmetry is most likely to be the origin where high turbulence intensity in the spanwise periphery is produced in the first place. If this is true then a mechanism should exist which is responsible for transferring the momentum and heat energy across the span of the spot. The effectiveness of this mechanism can then be indicated by the level of turbulence fluctuations at the spanwise periphery in comparison to that in the region of PTI on the plane of symmetry.

In the zero pressure gradient case, similar levels of velocity and temperature fluctuations are found in the region of PTI on the plane of symmetry and at the spanwise periphery of the spot. This indicates that the turbulent momentum transfer process and the heat transfer process are in parallel to each other. However, at a favorable pressure gradient, although a similar level of velocity fluctuations is found in the region of PTI on the plane of symmetry and at the spanwise periphery of the spot, there is a significant reduction in the level of the temperature fluctuations at the spanwise periphery. This suggests that heat transfer across the spot is inhibited severely by the favorable pressure gradient.

It is rather peculiar at first sight that the temperature fluctuations in the near wall region in the favorable pressure gradient case are higher than in the zero pressure gradient case since it is expected that a favorable pressure gradient should inhibit turbulence. It is understood that the heat exchange process is by molecular conduction, whereas the momentum exchange can take place via pressure force [24]. Therefore, the momentum and heat transfer processes will respond differently to the presence of a pressure gradient. In the flow with a favorable pressure gradient, since the transport of temperature fluctuations to other parts of the spot is not as effective as the momentum fluctuation counterpart, most of the heat could be confined in the PTI region. The accumulation of thermal energy in the PTI region would then be manifested as an increase in $\theta'/\Delta T$, whereas $\theta'/\Delta T$ in the main body of the spot, particularly in the spanwise periphery, remains to be much lower.

The reduced ability of transporting heat across the span of a spot in the presence of a favorable pressure gradient is expected to slow down the development of the transitional thermal boundary layer. As such it will require a longer distance for a fully turbulent temperature profile to be established, as observed by Blair [1], hence a longer transition zone length indicated by the heat transfer parameter. This may also result in a smaller spot spreading angle in the thermal boundary layer than in the velocity boundary layer as found in the liquid crystal flow visualization experiments by Zhong et al. [11] However, this cannot be confirmed with the results from the present study since the cross span measurements were only conducted at one streamwise location.

## Conclusion

In this paper, results from an experimental investigation of the flow physics behind the difference in the transition zone length indicated by the momentum boundary layer and thermal boundary layer parameters commonly observed on the suction surfaces of gas turbine blades are represented. The experiments were carried out on turbulent spots created artificially in an otherwise laminar boundary layer developing over a heated flat plate in a zero pressure gradient and a favorable pressure gradient. A specially designed miniature triple-wire probe was used to measure the streamwise velocity $U$, transverse velocity $V$, and temperature $T$ simultaneously during the passage of the spots.

In this paper, the general characteristics of the ensemble-averaged velocity and temperature perturbations, rms fluctuations, and the second moment turbulent quantities are discussed and the influence of favorable pressure gradient on these parameters is examined. It is found that the leading edge and trailing edge propagation rates of the spots deduced from the velocity and temperature data on the plane of symmetry are almost identical at either the zero or the favorable pressure gradient. The general shapes depicted by the velocity and temperature parameters, such as the perturbation and rms fluctuation, are also very similar.

However, at the favorable pressure gradient, unlike in the velocity boundary layer where significant velocity fluctuations and Reynolds shear stresses occur both in the PTI region on the plane of symmetry and the spanwise periphery, high temperature fluctuations (and turbulent heat fluxes) are confined in the PTI region. The difference in the levels of velocity/temperature fluctuations at these two locations gives an indication of the effectiveness of momentum/heat transfer across the span of the spots. The results of this study show that the heat transfer within a spot is inhibited

more than that of the momentum transfer when a favorable pressure gradient is present. This phenomenon will slow down the spanwise growth of turbulent spots in the transitional thermal boundary layer, leading to a longer transitional zone length indicated by the heat transfer parameters as reported in the literature. This finding provides a deeper insight into the physics that is responsible for the unparalleled growth of momentum and thermal properties in a transitional boundary layer under the influence of favorable pressure gradients.

## Acknowledgment

The work reported in this paper is sponsored by the Engineering and Physical Science Research Council in the UK.

## Nomenclature

$C_l$ = leading edge propagation rate of turbulent spots
$C_t$ = trailing edge propagation rate of turbulent spots
$E$ = anemometer voltage, Volt
$K$ = pressure gradient parameter, $K = \nu / U_\infty^2 dU_\infty / dX$
$T$ = temperature, °C
$U$ = streamwise velocity, $ms^{-1}$
$U_\infty$ = freestream velocity, $ms^{-1}$
$V$ = transverse velocity, $ms^{-1}$
$x$ = streamwise distance from leading edge of test plate, m
$x_s$ = streamwise distance from spot generator, mm
$y$ = distance normal to the wall, mm
$z$ = spanwise distance from centerline, mm
$\delta$ = boundary layer thickness, mm
$\delta_1$ = displacement thickness, mm
$\delta_2$ = momentum thickness, mm
$\upsilon$ = kinematic viscosity, $m^2\,s^{-1}$

## References

[1] Blair, M. F., 1982, "Influence of Freestream Turbulence on Boundary Layer Transition in Favorable Pressure Gradients," ASME J. Eng. Power, **104**, pp. 743–750.
[2] Sharma, O. P., 1987, "Momentum and Thermal Boundary Layers on Turbine Airfoil Suction Surfaces," AIAA Paper No. 87–1918.
[3] Blair, M. F., 1992, "Boundary-Layer Transition in Accelerating Flows With Intense Free-Stream Turbulence: Part 1—Disturbances Upstream of Transition Onset; Part 2—The Zone of Intermittent Turbulence," ASME J. Fluids Eng., **114**, pp. 313–332.
[4] Mislevy, S. P., and Wang, T., 1996, "The Effect of Adverse Pressure Gradients on the Momentum and Thermal Structures in Transitional Boundary Layers. Part 1: Mean Quantities; Part 2: Fluctuating Quantities," ASME J. Turbomach., **118**, pp. 717–736.
[5] Wang, T., and Keller, F. J., 1997, "Intermittent Flow and Thermal Structures of Accelerating Transitional Boundary Layers, Part 1: Mean Quantities; Part 2: Fluctuation Quantities," ASME Paper Nos. 97-GT-4902, 97-GT-4903.
[6] Keller, F. J., and Wang, T., 1996, "Flow and Thermal Behavior in Transitional Boundary Layers With Streamwise Acceleration," ASME J. Turbomach., **118**, pp. 314–326.
[7] Wygnanski, I., 1981, "The Effects of Reynolds Number and Pressure Gradient on the Transitional Spot in a Laminar Boundary Layer," in *The Role of Coherent Structures in Modeling Turbulence and Mixing*, J. Jimenez, ed., Springer, New York, *Lecture Notes in Physics*, **136**, pp. 304–332.
[8] Katz, Y., Seifert, A., and Wygnanski, I., 1990, "On the Evolution of the Turbulent Spot in a Laminar Boundary Layer With a Favorable Pressure Gradient," J. Fluid Mech. **221**, pp. 1–22.
[9] Chong, T. P., and Zhong, S., 2005, "On the Three-Dimensional Structure of Turbulent Spots," ASME J. Turbomach., **127**, pp. 545–551.
[10] Gostelow, J. P., Melwani, N., and Walker, G. J., 1996, "Effects of Streamwise Pressure Gradient on Turbulent Spot Development," ASME J. Turbomach., **118**, pp. 737–743.
[11] Zhong, S., Chong, T. P., and Hodson, H. P., 2002, "On the Spreading of Turbulent Spots in Non-Isothermal Laminar Boundary Layers Under the Influence of Favorable Pressure Gradients," ASME Paper No. GT-2002-30222.
[12] Chong, T. P., 2004, "Development of Turbulent Spots Under the Influence of Favorable Pressure Gradients," Ph.D. thesis, School of Mechanical, Aerospace and Civil Engineering, University of Manchester, UK.
[13] Browne, L. W. B., Antonia, R. A., and Chua, L. P., 1989, "Calibration of X-Probes for Turbulent Flow Measurements," Exp. Fluids, **7**, pp. 201–208.
[14] Clark, J. P., Jones, T. V., and Lagraff, J. E., 1996, "On the Propagation of Naturally-Occurring Turbulent Spots," J. Eng. Math., **28** (1), pp. 1–19.
[15] Antonia, R. A., Chambers, A. J., Sokolov, M., and Van Atta, C. W., 1981, "Simultaneous Temperature and Velocity Measurements in the Plane of Symmetry of a Transitional Turbulent Spot," J. Fluid Mech., **108**, pp. 317–343.
[16] Sabatino, D. R., and Smith, C. R., 2002, "Simultaneous Velocity-Surface Heat Transfer Behavior of Turbulent Spots," Exp. Fluids, **33**, pp. 5–12.
[17] Cantwell, B., Coles, D., and Dimotakis, P., 1978, "Structure and Entrainment in the Plane of Symmetry of a Turbulent Spot," J. Fluid Mech. **87**, pp. 641–672.
[18] Sabatino, D. R., 1997, "Instantaneous Properties of a Turbulent Spot in a Heated Boundary Layer," M.Sc. thesis, Department of Mechanical Engineering and Mechanics, Lehigh University, Bethlehem, PA.
[19] Gad-el-Hak, M., Blackwelder, R. F., and Riley, J. J., 1981, "On the Growth of Turbulent Regions in Laminar Boundary Layers," J. Fluid Mech., **110**, pp. 73–99.
[20] Gutmark, E., and Blackwelder, R. F., 1987, "On the Structure of a Turbulent Spot in a Heated Laminar Boundary Layer," Exp. Fluids, **5**, pp. 217–229.
[21] Glazer, A., Katz, Y., and Wygnanski, I., 1989, "On the Breakdown of a Wave Packet Trailing the Turbulent Spot in a Laminar Boundary Layer," J. Fluid Mech., **198**, pp. 1–26.
[22] Sohn, K. H., and Reshotko, E., 1991, "Experimental Study of Boundary Layer Transition With Elevated Freestream Turbulence on a Heated Flat Plate," NASA, No. CR187068.
[23] Wang, T., Keller, J. F., and Zhou, D. D., 1992, "Experimental Investigation of Reynolds Stresses and Heat Fluxes in a Transitional Boundary Layer," ASME Paper No. HTD 226, pp. 61–70.
[24] Kays, W. M., and Crawford, M. E., 1983, *Convective Heat and Mass Transfer*, 3rd ed., McGraw–Hill, New York.

# The Importance of Shroud Leakage Modeling in Multistage Turbine Flow Calculations

**Budimir Rosic**
e-mail: br241@eng.cam.ac.uk

**John D. Denton**

**Graham Pullan**

Whittle Laboratory,
Cambridge University,
Cambridge CB3 0DY,
UK

*Three-dimensional steady multistage calculations, using the mixing plane approach, are compared with experimental measurement in a low-speed three-stage model turbine. The comparisons are made with two levels of shroud seal clearance, one representative of a real turbine and one with minimal seal clearance and almost no shroud leakage. Three different calculations are compared. The first computes the main blade path with no modeling of shroud leakage. The second includes a simple model of shroud leakage using sources and sinks on the end-walls, and the third is a multiblock calculation with all leakage paths and cavities computed. It is found that neglect of shroud leakage makes the computed velocity profiles and loss distributions significantly different to those measured. Simple modeling of shroud leakage gives some improvement but full calculation of the leakage flows and cavities is necessary to obtain good agreement between calculation and measurement.* [DOI: 10.1115/1.2181999]

## 1 Introduction

There are several levels of modeling complexity used in the design and analysis process of turbomachinery. Improved computational resources allow for the use of increased modeling complexity within design time frames. This improved modeling incorporates more flow physics which leads to designs with improved performance, and replaces more expensive and time consuming experiments.

A review of the main CFD methods in use, with discussion of their advantages and practical limitations is presented by Denton and Dawes [1]. Design methods based on three-dimensional (3D) steady Navier–Stokes (NS) solvers are currently in use and can predict the primary gas path flow reasonably well. The main limitation of the early single blade row 3D NS solvers, namely the need to apply inlet and exit boundary conditions, has been overcome by developing 3D multistage calculations. Multistage solvers have been developed by Ni and Bogoian [2], Adamczyk et al. [3], Hah and Wennerstrom [4], Dawes [5], Denton [6], Jennions and Turner [7]. The majority of current multistage solvers in practical use are steady, and they do not fully treat the real unsteady interaction between blade rows. Even though some of them have an unsteady mode, it is still impractical to use this as a standard design tool. Additional limitations of these 3D multistage solvers are: Neglected leakage and cavity modeling, limitations of turbulence and transition modeling, and limited number of grid points. In spite of these limitations, multistage 3D solvers can predict most of the flow features in the main passage and can adequately predict the overall efficiency.

In recent years, the physics of secondary path flows (shroud leakage, cavity, and cooling flows) and their interactions with the primary flow path has been intensively investigated. The importance of shroud leakage flow and its influence on overall turbine performance is presented by Denton and Johnson [8], Wallis et al. [9] and Pfau et al. [10]. Fundamentally, circumferential cavities on the hub and tip cannot support the blade-to-blade pressure gradients in the primary flow. The main passage flow periodically enters and leaves the cavity together with the leakage flow. This modifies the blade loading and pressure distribution near the end-walls. It also changes incidence and intensifies the secondary flows in the downstream blade row.

The main passage and leakage flow were traditionally treated separately in CFD. The over-shroud leakage flow fraction was determined using empirical relations, and an estimate of the loss introduced into a CFD calculation through correlations. The inadequacy of previous flow solvers in handling leakage is due to the geometrical complexity of the problem, coupled with a lack of understanding of how leakage flow passes through shroud cavities.

The acknowledged importance of shroud leakage effects in turbomachinery has led to the conclusion that they should be included in any 3D multistage calculation. This has led to a number of efforts to incorporate shroud leakage models, with varying degrees of complexity, into multistage simulation codes. These solvers can be divided into two categories. One is the so-called "black box" approach whereby the leakage flow is modeled by extracting and reinjecting fluid at an appropriate angle at the appropriate place on the end-walls upstream and downstream of a blade row. Lejambre et al. [11] modeled stator hub cavity flow and a bleed hole in a compressor stator row. The driving pressure gradient through the cavity is taken from the CFD solution. They used a one-dimensional (1D) model that accounts for the number of seals, the seal clearance, the drum rotor speed, and the cavity depth, to determine the leakage flow and loss through the cavity. Wellborn et al. [12] developed a similar simplified 1D model of the flow through shrouded stator cavities, and incorporated it into a fully 3D viscous primary flow solver. Similarly, Hunter and Orkwiss [13] discuss the use of source terms in a steady flow solver, to model the stator-shroud leakage in a turbine. The source terms were applied on grid cells directly above the cavity-mainstream interface. In all three of the aforementioned examples, the mass flux is applied pitch-wise uniformly over the extraction and injection slots and this is one of the essential limitations of such simple models in predicting leakage flow. Although, the aforementioned simple uniform or 1D shroud leakage models significantly improved the overall accuracy of the numerical predictions and showed an improved agreement with experiments, they cannot predict all aspects of the leakage flow, such as the circumferential variation of the flow and interaction between main passage and leakage flow inside the cavity.

Another approach for shroud leakage flow prediction includes attempts to model leakage flow geometry together with the main

Contributed by the International Gas Turbine Institute (IGTI) of ASME for publication in the JOURNAL OF TURBOMACHINERY. Manuscript received August 30, 2005; final manuscript received September 6, 2005. IGTI Review Chair: K. C. Hall. Paper presented at the ASME Turbo Expo 2005: Land, Sea, and Air, Reno, NV, June 6–9, 2005, Paper No. GT2005-68459.

  

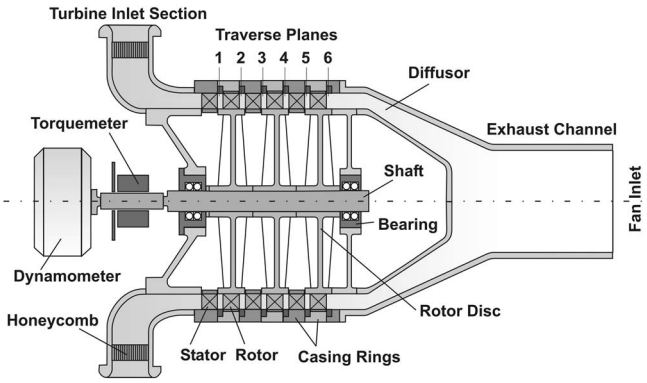


**Fig. 1 Schematic of model turbine.**

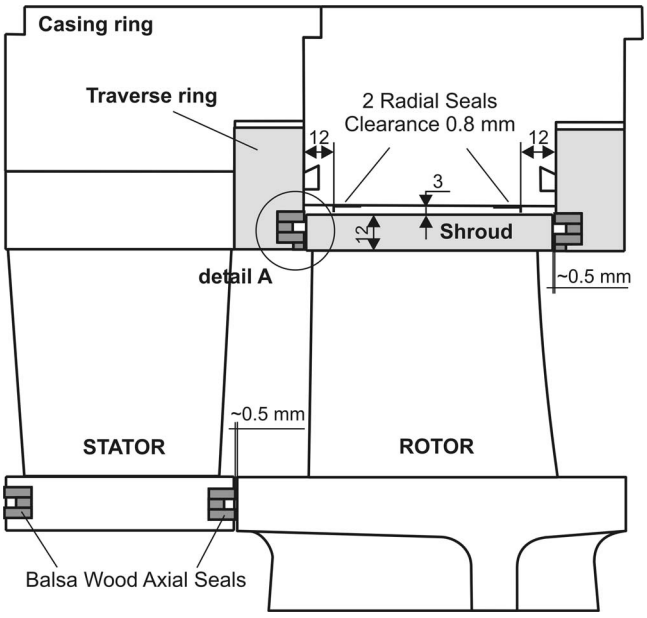


**Fig. 2 "Zero-leakage" shroud sealing arrangement**

blade passage. Wallis [9], used an unstructured 3D solver to model the leakage flowpath across a single blade in detail. Bohn et al. [14] used a 3D NS solver and multiblock approach to model inlet and exit shroud cavities both at stator hub and rotor tip but without modeling the leakage path. Peters et al. [15], Anker and Mayer [16] and Giboni et al. [17] investigated numerically and experimentally the interaction of labyrinth seal leakage flow and main passage flow in a 1.5 stage turbine, using a 3D solver with a block-structured grid. Although the general flow was predicted reasonably well in all cases, some flow phenomena near the endwalls were not captured. Gier and Stubert et al. [18] simulated flow in a three-stage low pressure turbine, including the entire shroud cavity geometry using a 3D multiblock solver. They compared numerical results with experiments. The blade surface static pressure distribution was presented together with isentropic efficiency, but other flow properties were not compared.

Neither of these approaches is satisfactory for the routine prediction of shroud leakage flow. Additional experimental validation and greater physical understanding must be acquired before the black box approach can be used with confidence to model the effects of a range of sealing geometries. The geometrical complexity of the problem requires advanced grid preprocessing, but the time required for grid generation and calculation makes the use of unstructured grid solvers still impractical for routine shroud leakage calculations. The "rectangularlike" shape of most cavities and leakage paths implies the use of the multiblock approach in multistage design tools for modelling leakage-mainstream flow interaction.

This paper discusses three different levels of complexity in treating shroud leakage flow numerically. The first computes the main blade path with no modeling of shroud leakage. The second includes a simple model of shroud leakage using sources and sinks on the end-walls, and the third is a multiblock calculation with all leakage paths and cavities computed. All results are compared with experimental measurements in a three-stage model turbine.

## 2 The Model Turbine and Experimental Methods

The experiments were carried out using a low-speed multistage air turbine, that was designed to represent the first few stages of a high pressure steam turbine (Fig. 1). Atmospheric air enters the inlet section radially and passes through a flow straightener before entering the turbine. Air is drawn through three turbine stages by a fan downstream of the turbine. Both stator and rotor blades were shrouded. The operating point, determined by the flow coefficient and rotational speed, is set by the fan power and dynamometer brake. The flow coefficient $V_x/U$ is calculated using the axial velocity at turbine inlet, which is measured indirectly using a mass flow measurement in the exhaust section and a density measurement at inlet.

Experiments were performed on 50% reaction blading at the design operation condition ($\phi=0.384$). The key rig geometrical and operational parameters are presented in Table 1. The blade parameters are taken at blade mid-height. The blading was designed to represent typical high pressure steam turbine conditions, and all parameters satisfy that condition. Only the Reynolds number, based on exit velocity and true chord, is significantly lower than that in a real turbine.

An experimental program consisting of two different rotor shroud configurations was performed. The first configuration (Configuration 1) was with a previously reported sealing arrangement (Wallis [9]) designed to minimize leakage flow. It comprises two axial abradable balsa wood seals each forming an axial clearance of approximately 0.5 mm with the shroud (Fig. 2, Detail A).

**Table 1 Turbine geometrical and operational parameters**

| | Design operating point data | Blade parameters | Stator | Rotor |
|---|---|---|---|---|
| Flow coefficient $\phi$ | 0.384 | Blade number | 40 | 38 |
| Stage loading $\Psi=\Delta h_0/U^2$ | 1.0 | True chord 1 (mm) | 89.73 | 105 |
| Design speed (rpm) | 830 | Aspect ratio ($h/l$) | 0.836 | 0.714 |
| Inlet Mach number | 0.045 | Pitch to chord ratio | 0.81 | 0.728 |
| Number of stages | 3 | Reynolds Number[a] | $2.53\times10^5$ | $2.97\times10^5$ |
| Interblade row spacing (mm) | 25 mm | | | |
| Blade height, $h$ (mm) | 75 mm | | | |
| Hub to tip ratio | 0.85 | | | |

[a]Based on true chord and exit velocity

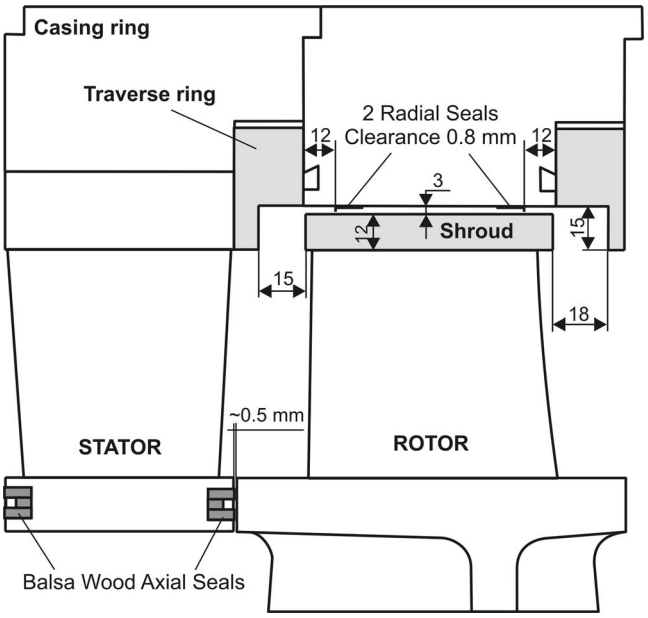


**Fig. 3 Shroud sealing arrangement with open cavities**

The actual clearance cannot be measured and the 0.5 mm is a best estimate subject to some uncertainty. The shroud forms a radial clearance of 3 mm with the casing. A stage with such a sealing arrangement is shown in Fig. 2.

The modified rotor sealing arrangement has opened inlet and exit rotor shroud cavities. This configuration (Configuration 2) is representative of commercial turbine design as it allows for the axial movement of the rotor shaft relative to the casing (Fig. 3). Using two approximately 0.8 mm clearance radial seals resulted in an overshroud leakage flow of approximately 2%. The stator hub sealing geometry was the same as in the first configuration.

To investigate the time-mean flow of the main passage, traverses were conducted using a five-hole pneumatic probe. The properties were measured by performing full-span area traverses over one blade pitch at an axial distance of 6 mm and 17 mm downstream of the stator and rotor trailing edge tip respectively (Fig. 1). The traverse grid was $37 \times 37$ uniformly spaced points in both radial and pitch-wise directions.

## 3 Multip Description

To calculate flow in the main passage without leakage and using a simple leakage model Denton's 3D multistage solver Multip was used. Multip is a Reynolds Averaged NS (RANS) finite volume solver, which uses the explicit SCREE scheme. Turbulence is modeled using a mixing length approach. Laminar to turbulent boundary layer transition can be modeled by assuming a laminar boundary layer up to a specified point on each blade and end-wall surface and a turbulent one downstream. The mixing plane approach allows reversed flow across the mixing plane, which may occur near the end-walls close to the leakage cavities. To accelerate convergence multigrid and spatially varied time steps are used.

Multip calculations without leakage modeling were used as the first level of calculations in this analysis. Figure 4 shows blade-to-blade views of the computational mesh for one stage. Both stator and rotor blades use $75 \times 49 \times 49$ grid points in axial, pitch-wise and span-wise directions, respectively. The grid is a structured sheared H-mesh type. The total number of grid points for three stages was approximately 1.5 million. Numerous comparisons with experimental data have shown that this grid is more than adequate for an accurate solution of the equations. The main limitation on accuracy, as with all such codes, comes from turbulence and transition modelling.

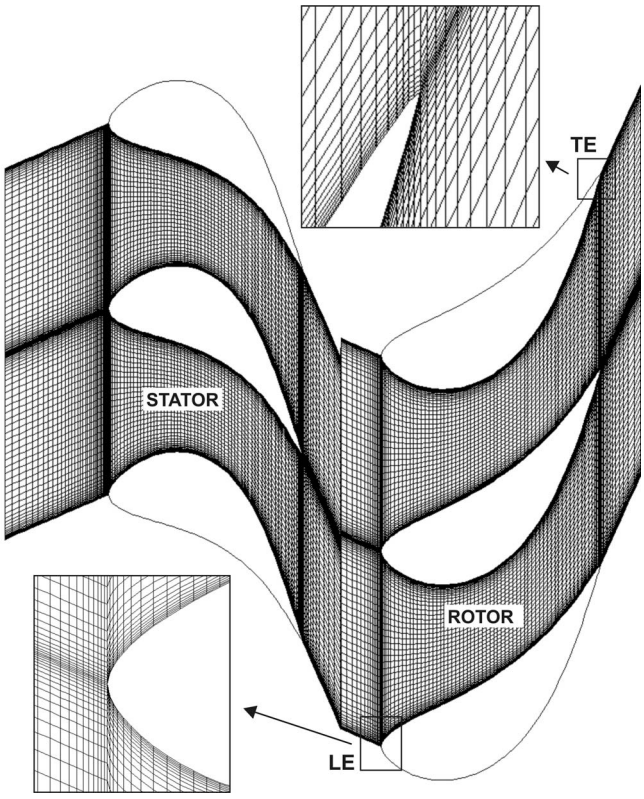


**Fig. 4 Multip computational grid**

## 4 Simple Shroud Leakage Model

The shroud leakage model in Multip is an extension of that first presented by Denton and Johnson [8]. The areas through which flow leaves the casing upstream of the shroud and re-enters the mainstream downstream of it are defined in the data, as illustrated in Fig. 5. The average of all flow properties is calculated over the

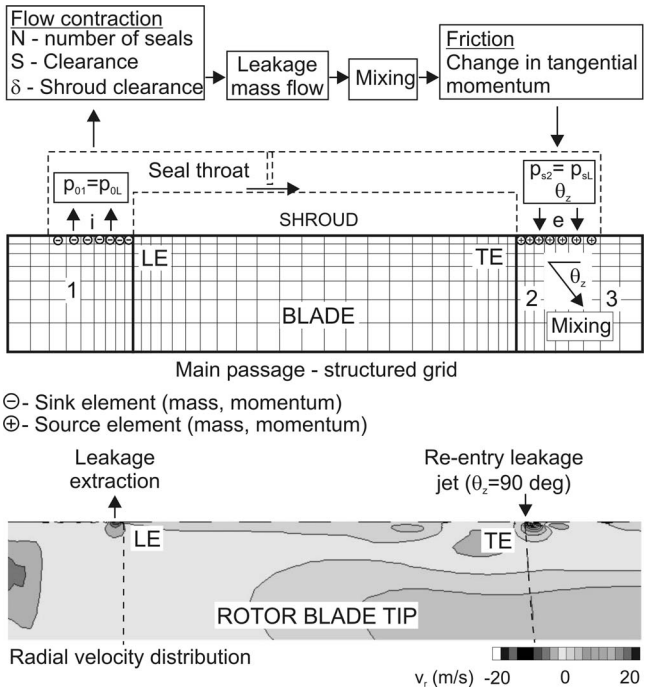


**Fig. 5 Schematic description of shroud leakage model**

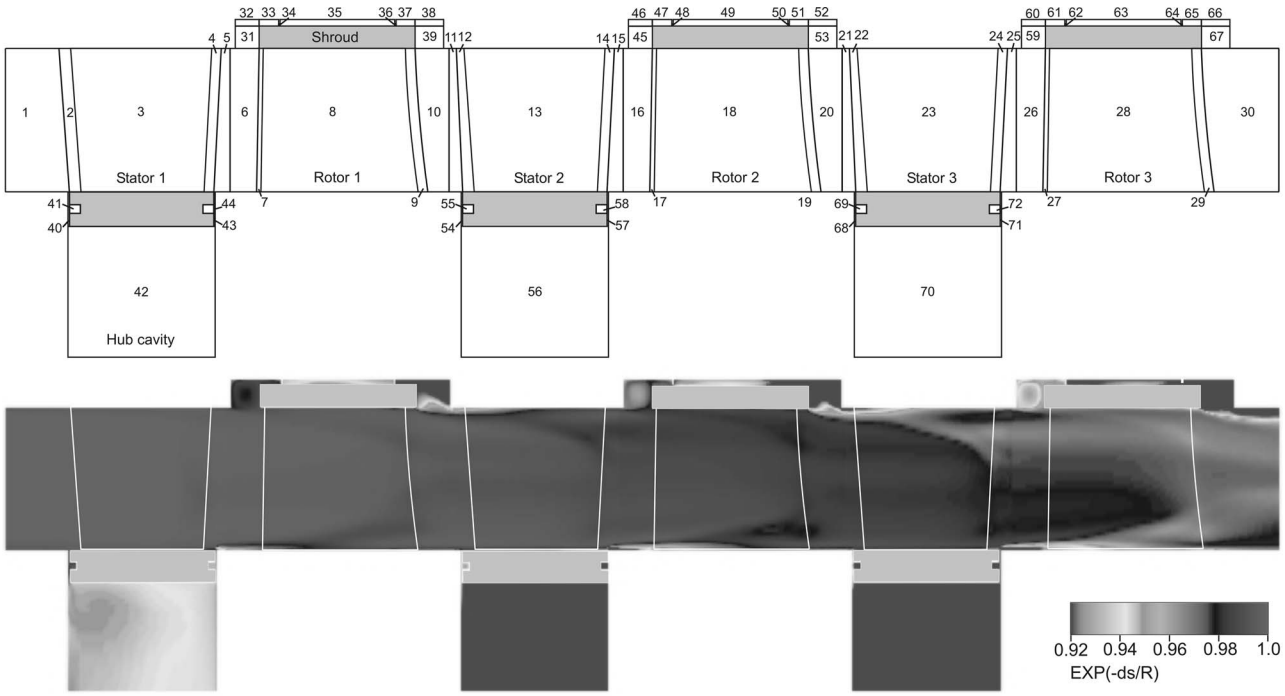


**Fig. 6 Tblock computational domain (Configuration 2)**

upstream area and the average static pressure is calculated over the downstream area. The tangential component of velocity plays no part in the leakage process, and so the leakage flow is driven by the difference between the stagnation pressure based on the meridional component of velocity upstream of the seal and the static pressure downstream of it. This pressure ratio and standard compressible flow relationships are used to calculate an isentropic seal-jet axial velocity and density. The leakage flow area is taken as the individual seal clearance divided by the square root of the number of seals and multiplied by a contraction coefficient $C_c$, usually taken to be 0.6. This enables the leakage mass flow rate to be calculated

$$\dot{m}_{\text{leak}} = \rho_{\text{jet}} v_{x,\text{jet}} \frac{2\pi r \delta}{\sqrt{N_{\text{seal}}}} C_C$$

It is important to know the tangential component of velocity and the stagnation temperature with which the leakage fluid re-enters the mainstream because these have a large influence on the mixing loss. These are obtained by estimating the skin friction coefficients on both the shroud surface and on the casing surface above the shroud. Converting these into surface shear stresses using the relevant relative tangential velocities enables the angular momentum and energy equations to be integrated along the length of the shroud to obtain the tangential velocity and absolute stagnation temperature of the re-entering fluid. In this way, the moving shroud is allowed to do work on the leakage flow increasing its stagnation temperature. The radial component of velocity with which the leakage flow re-enters the mainstream is obtained from continuity and the axial component is obtained from it by specifying the meridional angle $\theta_z$ of the re-entry flow, Fig. 5.

The leakage flows calculated above are modeled in the main flow solver by sources and sinks of mass momentum and energy on the casing walls. The mixing loss when the leakage flow re-enters the mainstream is automatically calculated by the main flow solver, because it satisfies conservation of mass, momentum and energy for each control volume.

## 5 Tblock Description

Recently, a new multiblock structured grid solver, Tblock, has been developed by the second author. This is a steady or unsteady RANS solver and uses the SCREE algorithm, the same numerical scheme used in Multip. Turbulence, laminar/turbulent transition and mixing planes at the interface between blade rows are also modeled in the same way in both codes. Tblock can be run in parallel with domain decomposition done on a block basis.

The code is aimed at predicting both main blade path and secondary gas path flows in turbomachinery, although it can be used to calculate other types of flow. The solver overcomes most of the limitations of the simple shroud leakage model in calculating complex geometries, and was used for the third level of calculations in this paper including the shroud leakage flow path. The flow field is divided into as many "cuboid" blocks as are necessary to represent the geometry and each block is solved separately. Information passes between blocks using different types of interfaces treated as "patches" (inlet and exit boundary, solid boundary, mixing plane, and periodic boundary). The method is tolerant of extreme levels of grid distortion, and when necessary can interpolate the flow data from one patch onto another, which may lie on a noncontiguous face and may have a different number of grid points.

Two configurations, one with minimized shroud leakage flow (Fig. 2) and another one with open shroud inlet and exit cavities (Fig. 3) were modeled using Tblock. Simulations were completed modeling all three stages including rotor tip shroud and stator hub leakage paths. Figure 6 presents the flow domain decomposition for Configuration 2.

The domain was divided into 72 blocks. The main blade passage was modelled using Multip type of geometry using 75 grid points in the axial, and 49 grid points in both pitch-wise and radial directions. The leakage flow paths were divided into the necessary number of rectangular blocks using structured H meshes. The whole domain consists of 3.3 million grid points. The simulation was run in parallel using 12 2.8 GHz processors, and a fully con-

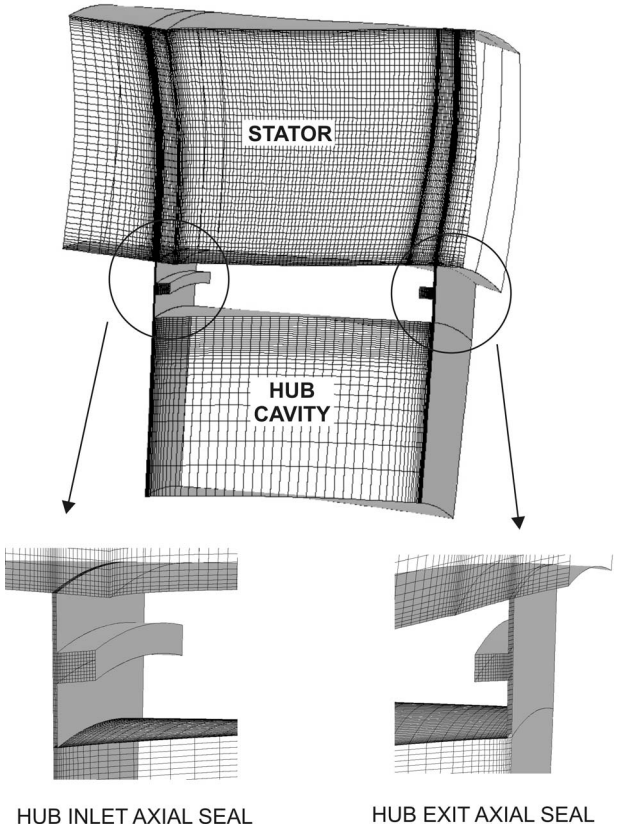


**Fig. 7 Tblock-stator grid structure**

verged solution was obtained in 5 h. Figure 6 also shows the calculated entropy generated through the whole domain. The contours presented the pitch-wise averaged values of entropy. The significant contribution of the leakage paths in the process of loss generation can be seen. The detailed grid and block structure used to model each stator blade passage is presented in Fig. 7. The hub cavity is modeled as a large plenum with rotating walls to simulate rotor disks. In the model turbine, the stator hub was sealed using balsa wood (Fig. 2, Detail A) forming inlet and exit axial seals with about 0.5 mm clearance, and this geometry was reproduced in the CFD mesh (Fig. 7). The rotor shroud for both configurations was modeled in a similar way.

## 6 Experimental and Numerical Results

For both configurations, experimental, and numerical results are presented using span-wise distribution of the pitch-wise averaged yaw angle and axial velocity for Stator 1 and Stator 3, and relative yaw angle downstream Rotor 2 and Rotor 3. Axial velocity was nondimensionalized by the passage mass averaged value. Total pressure was nondimensionalized by the total pressure drop across the whole turbine to give a total pressure coefficient:

$$C_{po} = \frac{p_{\text{oin}} - p_o}{p_{\text{oin}} - p_{\text{oex}}}$$

Total pressure coefficient contours are only presented for the third stator, although measurements were performed after each blade row. The measurement plane covers one pitch from 2% to 97% span. The white areas on the contour plots of experimental data indicate regions not covered by the traverse. The flow in the first stator is not affected by any change in downstream tip shroud leakage flow, and all three models predict it reasonably well. Figure 8 shows measured and predicted values for $C_{po}$ using the Tblock solver (Configuration 1).

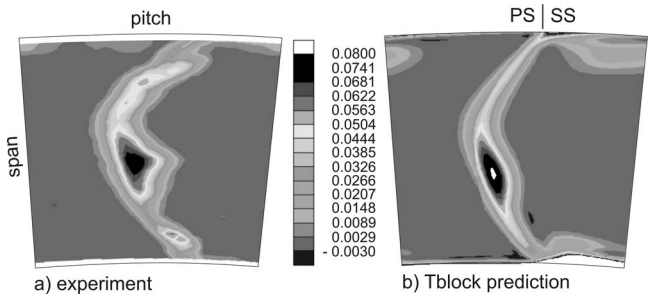


**Fig. 8 $C_{po}$ contours downstream of the first stator**

Laminar flow in the first stator causes the formation of a separation bubble on the blade suction side, and a single strong loss core at the mid-span. None of the solvers in this analysis can predict boundary layer transition but it can be specified. Figure 9(*a*) shows the flow visualization of the first stator suction side as evidence of the separation bubble. The blade surfaces were painted red and the end-walls green. Figure 9(*b*) shows the Tblock prediction. Low aspect ratio and blade lean generate a flow field dominated by secondary flows and low momentum end wall fluid (green) migrates form both end-walls to mid-span. The size of the separation bubble and hence of the loss core in Fig. 8(*b*) is very dependent on the assumed transition point and it is unlikely that this could be predicted a priori. Figure 8 shows reasonable agreement on the location and size of the loss core obtained using a guessed transition point.

In order to compare the results of different numerical approaches to leakage flow modelling, Multip and Tblock solutions of the main passage flow without leakages were first analyzed. The results, not presented here, show close agreement between the two solvers. The same values for all numerical parameters, and inlet and exit boundary conditions were used. Also, the same number of grid points was used to model the blade passage.

**6.1 Configuration 1.** In comparing calculated and measured flow patterns, it must be remembered that the real clearance is not known with great accuracy and that it varies significantly around the circumference.

The first test case presents flow in an environment where the influence of the leakage flow is reduced as much as possible, by closing inlet and exit cavities and reducing axial seal clearance (Fig. 2), within the mechanical constraints of the model turbine. The estimated clearance was 0.5 mm.

Figure 10(*a*) shows measured contours of total pressure coefficient downstream of the third stator. The most distinctive flow feature is a strong loss core at the mid-span position and a weaker loss core toward the hub. As is typical for a low aspect ratio blade

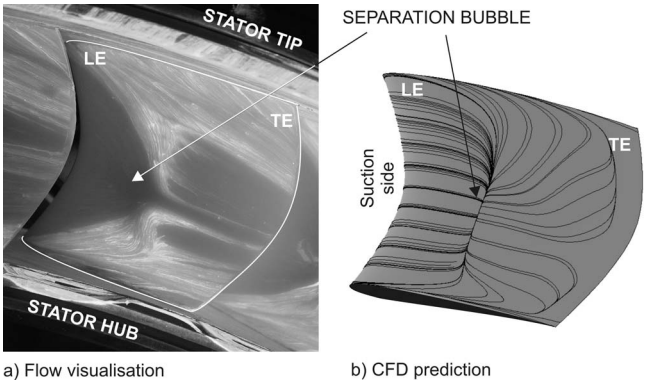


**Fig. 9 Flow visualization and predicted streamlines on the suction side of Stator 1**

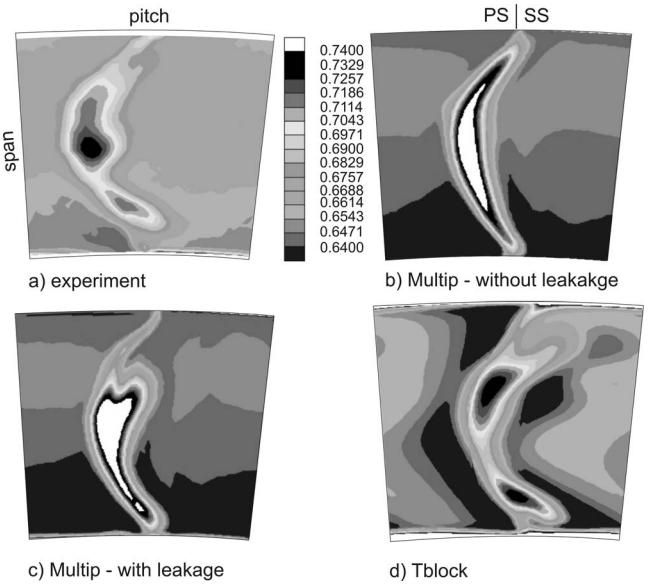


**Fig. 10 $C_{po}$ contours-Stator 3 (Configuration 1)**

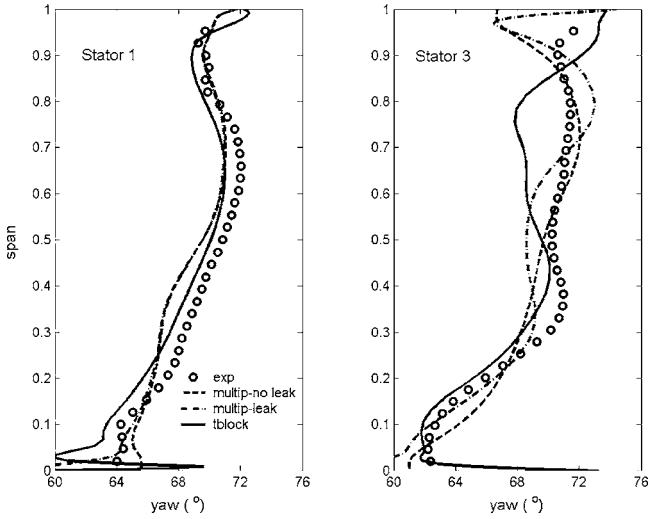


**Fig. 11 Measured and predicted pitch-wise averaged yaw angle (Configuration 1)**

and 3D blade design, strong secondary flows migrate from the hub and casing to the mid-span on the blade suction surface. The radial pressure gradient causes the nonsymmetric span-wise penetrations of the hub and casing secondary flows. Because of that, the loss core associated with the casing passage vortex merges with other low momentum fluid from the blade wake to form the strong mid-span loss core.

Although the seal clearances on the hub and tip were minimized, evidence of leakage flow is present. For such a seal configuration Tblock predicted tip shroud leakage of 0.9%. Figures 10(*b*) presents result of a Multip simulation for the case without leakage flow, and Fig. 10(*c*) shows a Multip prediction with the simple leakage model included. In the simulation without leakage flow the loss core is not so concentrated in the mid span but is spread out and covers a much bigger proportion of the span. The inclusion of the hub and tip leakage flows intensifies the secondary flows and their radial migration through the blade passage and the central loss core is shown in Fig. 10(*c*). Total pressure contours obtained using Tblock modeling the leakage flow path fully are presented in Fig. 10(*d*). The main loss core is much better predicted and the hub loss core is also reproduced.

In the case of the first stator (Fig. 8) the total pressure level in the whole traverse plane is very well predicted together with loss core strength. As the traverse plane progresses through the domain, small differences in blade exit angles and loss coefficients produce small but significant differences in the level of stagnation pressure. As a result, there is a difference in the average level of total pressure for the free stream region away from the wake.

The span-wise distribution of pitch-wise averaged values of absolute yaw angle and axial velocity downstream the first and third stators are shown in Figs. 11 and 12. All three levels of simulations showed a high level of agreement with experimental results in predicting yaw angle and axial velocity distribution. Downstream of the first stator, the profiles are almost identical for the whole span.

Since in this configuration the size of the inlet and exit cavities is minimized and the leakage flows are as small as possible the leakage and main passage flow interaction is more predictable by the simple shroud leakage model, because the interaction is localized over a small circumferential area (~0.5 mm clearance). As a result, we do not anticipate large differences between any of the three computations. The increased overturning and underturning predicted by Tblock downstream of Stator 3 (Fig. 11) is possibly because it overpredicts the leakage flow due to an overestimate of the real clearance.

Figure 12 shows the distribution in circumferentially averaged nondimensional axial velocity downstream of the first and third stator for experiments and three levels of predictions. The good agreement is evident for all three predictions downstream of the first stator. Downstream of the third stator, all models give good predictions up to 60% of the span from the hub. The errors in the Tblock prediction outboard of this are again probably due to an overestimate of the leakage.

The relative yaw angle distribution downstream of the rotors, shown in Fig. 13, is well predicted for both Rotor 2 and Rotor 3 along most of the span. Differences in results at the hub are due to a different seal clearance used in the calculations, compared with the unknown real clearance value. The high overturning predicted by Tblock very close to the casing is believed to be the correct trend although the experimental data was not obtained close enough to the casing to confirm this.

Differences between predicted and measured values in the region close to the hub for both yaw angle and axial velocity are due to the position of the traverse plane, which is located very close to

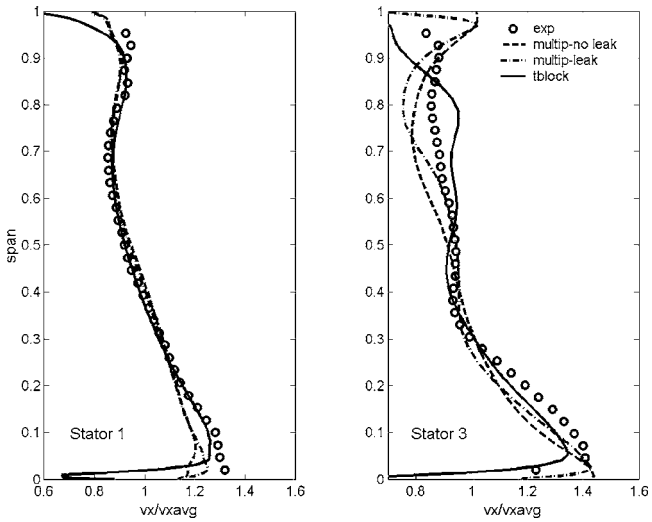


**Fig. 12 Measured and predicted pitch-wise averaged axial velocity (Configuration 1)**

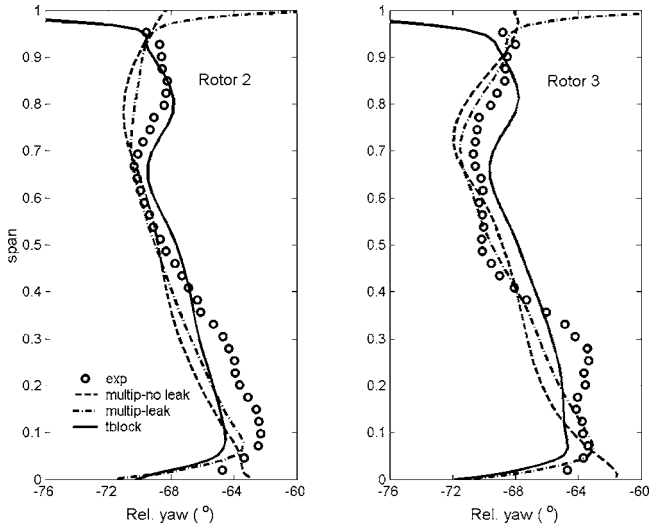


**Fig. 13 Measured and predicted pitch-wise averaged relative yaw angle (Configuration 1)**

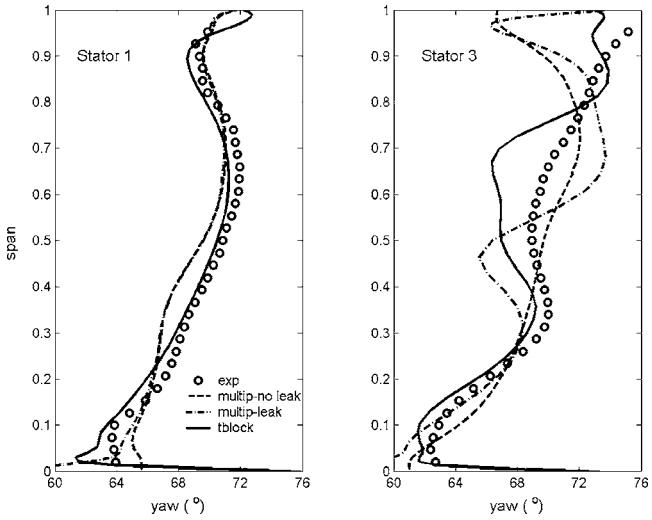


**Fig. 15 Measured and predicted pitch-wise averaged yaw angle (Configuration 2)**

the stator hub leakage re-entry cavity. The very intensive mixing process in the mainstream close to the cavity causes very strong gradients in flow properties.

There is a general tendency for the experimental profiles to be smoother than the computed ones. This may be due to high levels of free-stream turbulence causing enhanced mixing.

**6.2 Configuration 2.** In order to compare the performance of the different numerical approaches to modeling leakage flow, simulating flow in a real high pressure turbine geometry, the second test was performed. Stage geometry is presented in Fig. 3. The sealing arrangement on the stator hub is the same as in Configuration 1 but with a increased length of inlet and exit rotor shroud cavities, representative of a real turbine.

Opening the cavities and an increased leakage flow caused even more intensive secondary flows than with closed cavities. It resulted in a much stronger loss core at mid span as it is shown in Fig. 14(*a*). The region of concentrated low momentum fluid is asymmetric. The low momentum flow associated with casing endwall boundary layers and leakage has migrated completely to the mid-span. The loss core at the hub was not changed and it is very similar to that associated with Configuration 1, due to unchanged hub geometry. The Multip calculation without leakage does not predict even the general shape of the low momentum area, which confirms that the process of loss core formation in such a blade design is driven mainly by leakage flows.

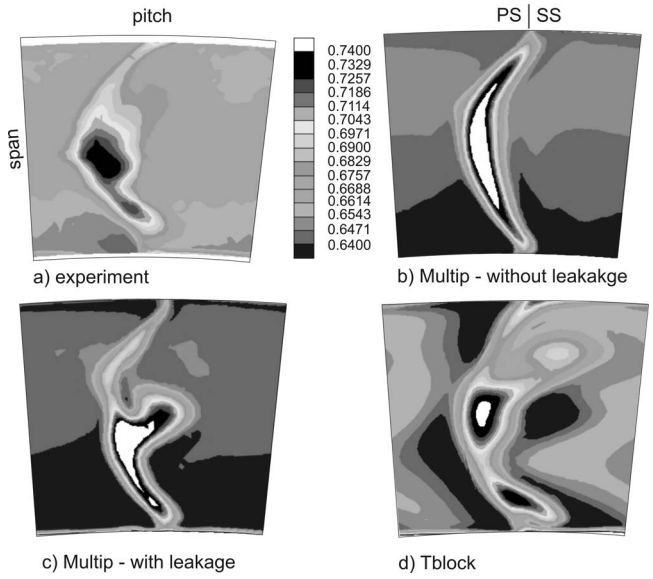


**Fig. 14 $C_{po}$ contours-Stator 3 (Configuration 2)**

The simple leakage model calculation was performed by redistributing the position of sink end source elements on the tip endwall in accordance with increased length of inlet and exit cavity. Also, the radial seal clearance was increased (0.8 mm). Increased radial seal clearance resulted in increased leakage flow. The simple leakage model does not model flow in the exit shroud cavity. In a real cavity, the main passage flow periodically enters the cavity and mixes out with leakage flow weakening the leakage jet formed under the last labyrinth seal throat. Therefore, the simple leakage model predicts a much stronger leakage jet, which causes stronger radial movement of casing low momentum fluid than is measured and shifts the position of the loss core closer to the hub (Fig. 14(*c*)).

Again, only the third level of calculations—which models the full leakage flow path—can predict main flow features reasonably well (Fig. 14(*d*)). The main loss core is positioned at the same span-wise location as in the experiments. The hub loss core did not migrate enough towards mid-span.

Figure 15 shows the radial distribution of the yaw angle for the first and third stator. All three calculations showed good agreement with experiments for the first stator. For the third stator, good agreement between experiments and predicted values, for all three levels of computations is evident up to 40% span. Multip calculation with the simple leakage model predicted stronger secondary flows and did not predict the overturning in the near casing region caused by increased leakage flow. Tblock shows a less smooth variation than the experiments but with the correct overall trend.

The radial distribution of the non-dimensional axial velocity is given in Fig. 16. As in the case with closed cavities, good agreement between experimental values and predictions was achieved for the first stator. The Tblock prediction of axial velocity distribution downstream of Stator 3 is very close to the measured distribution, but again it is less smooth.

Figure 17 compares measurements and three calculations of the relative yaw angle behind Rotors 2 and 3. Although in the case of the closed cavities (Fig. 13), all three models predicted the radial distribution well, in the case of the open cavities the limitations of the first two models became obvious. In the region close to the

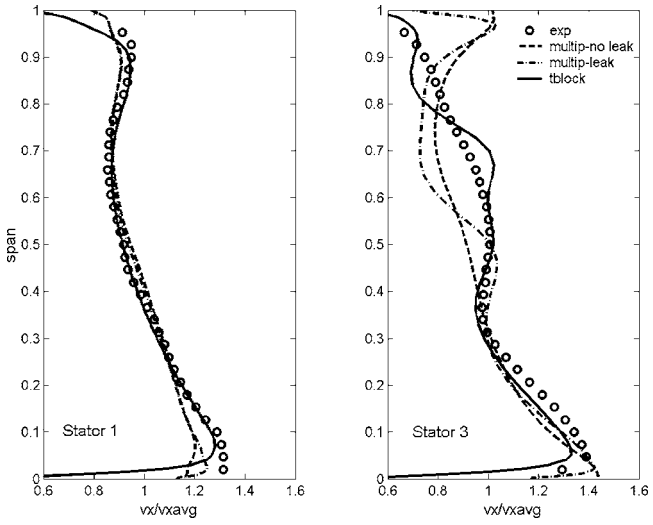


**Fig. 16 Measured and predicted pitch-wise averaged axial velocity (Configuration 2)**

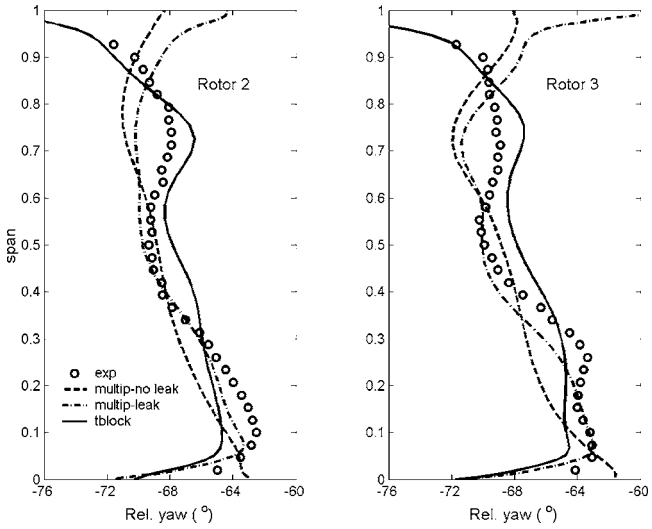


**Fig. 17 Measured and predicted pitch-wise averaged relative yaw angle (Configuration 2)**

casing and the rotor shroud exit cavity, none of the Multip calculations was able to predict the correct trend in the main passage flow angle caused by mixing of the leakage flow. Again, the overturning predicted by Tblock very close to the casing is believed to be the correct trend.

The measured difference in yaw angle downstream of the third stator between the case with closed cavities and minimized leakage (Fig. 11), and the case with open cavities on the tip (Fig. 15) is approximately 4° in the near-tip region. The accuracy required to capture such small differences in flow properties presents a significant challenge to current steady 3D multistage solvers. Without such accuracy, the correct prediction of leakage flow influence on the main passage flow is almost impossible.

Although Tblock can capture most of the main flow features, there is some possibility for further improvements. The flow in the cavities is highly unsteady and turbulent in its nature. The turbulence level in the cavities is unknown and the applied mixing length limit was a best guess based on previous experience. The overall effect of multiple mixing planes and high levels of freestream turbulence on the transport of flow information is not certain. It is unclear if better agreement with experiments can be achieved using a mixing plane approach in a multistage environment, or if a much more expensive full unsteady calculation is required.

In spite of the inherent limitations of a mixing plane approach, acceptable agreement between measured and predicted overall turbine efficiency can still be realised. The measured difference in overall turbine efficiency between the closed and open shroud cavity configurations was 1.16%. Tblock predicted a reduction in efficiency of 1.00%, while Multip, with simple leakage model, gave an 0.80% reduction. As Multip does not calculate cavity flows this could explain the underprediction of the reduction in efficiency.

## 7 Flow in the Shroud Exit Cavity

One of main limitations of simple leakage models is that they cannot predict circumferential variation in leakage and complex main passage flow interaction and flow in cavities. To illustrate that, Fig. 18 shows the predicted radial velocity distribution in the shroud exit cavity using Tblock, for three different circumferential locations, close to the rotor blade pressure side, mid-passage and close to suction side. The process in the cavity is highly influenced by the blade-to-blade pressure gradient. Close to the pressure side (Fig. 18(*a*)), the blue color indicates main stream flow entering the cavity. The leakage flow jet formed under the second seal throat, stays attached to the cavity downstream end-wall. Main passage flow mixes in the cavity with the leakage flow and forms a vortical structure which occupies most of the cavity space. Starting from the mid passage (Fig. 18(*b*)) until the suction side, flow starts to leave the cavity and re-enters main passage. This structure repeats in the next rotor blade pitch.

It is very difficult to measure flow properties in a cavity, and because of that, CFD calculations—which can model the full ge-

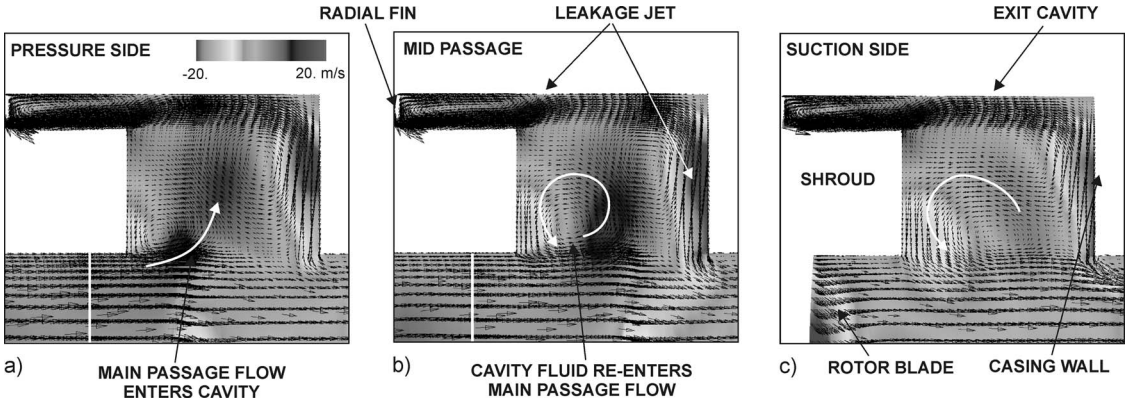


**Fig. 18 Radial velocity distribution in the shroud exit cavity**

ometry of leakage flow path—are of the greatest importance in understanding the physics of this complex interaction. Increased computational resources allow such calculations to be incorporated into a design process trying to optimise leakage path geometry and leakage-mainstream interaction.

## 8 Conclusions

Comparison of measurements and 3D calculations shows that the flow in shrouded, low aspect ratio turbines is dominated by shroud leakage. This is especially true as regards the loss distribution. The rotor shroud leakage flow greatly increases the secondary flow in the downstream stators and drives low energy fluid towards mid-span.

With very low values of shroud leakage the flow is reasonably well modelled by a simple 1D model of the leakage flow, using sources and sinks on the casing. However, for more representative real clearances, full 3D modelling of the seal and cavity flows is necessary in order to obtain reasonable agreement.

The measured differences in flow angles between two cases, open and closed cavities, are of the order of a few degrees. Therefore, the correct prediction of the leakage and main passage flow interaction requires highly accurate 3D multistage solvers. In practice, the accuracy of all predictions of leakage flow is likely to be limited by the accuracy with which the operating seal clearance is known, especially since the latter is likely to vary around the circumference.

There is a general tendency for the pitch-wise average experimental flow properties to vary more smoothly with radius than do the predicted ones. It is suggested that this may be due to neglect of free stream turbulence, and hence of span-wise mixing, in the calculations.


## Acknowledgment

The authors would like to thank Siemens Power Generation for funding this work. Also, we would like to thank Ashley Peterson and Kevin Reid of the Whittle Laboratory for technical support during the writing of this paper.


## Nomenclature

$C_C$ = contraction coefficient
$C_{po}$ = total pressure coefficient
$h$ = blade height
$l, l_x$ = chord length, axial chord length
$N$ = number of seals
$p_{\text{oin}}$, $p_{\text{oex}}$ = turbine inlet and exit total pressure
$r$ = radius
$S$ = seal clearance
$V$ = absolute velocity
$U$ = blade speed
$\delta$ = shroud clearance
$\rho$ = density

## References


[1] Denton, J. D., and Dawes, W. N., 1999, "Computational Fluid Dynamics for Turbomachinery Design," Proc. Inst. Mech. Eng., Part C: J. Mech. Eng. Sci., **213**, pp. 107–124.
[2] Ni, R. H., and Bogoian, J. C., 1989, "Prediction of 3D Multistage Turbine Flowfield Using a MultiGrid Euler Solver," Paper No. AIAA-89-0203.
[3] Adamczyk, J. J., Celestina, M., Beach, T. A., and Barnett, M., 1990, "Simulation of Viscous Flow Within a Multistage Turbine," ASME J. Turbomach., **112**, pp. 370–376.
[4] Hah, C., and Wennerstrom, A. J., 1991, "Three-Dimensional Flowfields Inside a Transonic Compressor With Swept Blades," ASME J. Turbomach., **113**.
[5] Dawes, W. N., 1992, "Towards Improved Throughflow Capability: The Use of 3D Viscous Flow Solvers in a Multistage Environment," ASME J. Turbomach., **114**.
[6] Denton, J. D., 1992, "The Calculation of Three-Dimensional Viscous Flow Through Multistage Turbomachinery," ASME J. Turbomach., **114**.
[7] Jennions, X. X., and Turner, Y. Y., 1993, "Three-Dimensional Navier-Stokes Computations of Transonic Fan Using an Explicit Flow solver and an Implicit $k$-$\varepsilon$ Solver," ASME J. Turbomach., **115**(2).
[8] Denton, J. D., and Johnson, C. G., 1976, "An Experimental Study of the Tip Leakage Flow Around Shrouded Turbine Blades," CEGB Report No. R/M/N848, Marchwood Engineering Laboratories, UK.
[9] Wallis, A. M., Denton, J. D., and Demargne, A. A. J., 2000, "The Control of Shroud Leakage Flows to Reduce Aerodynamic Losses in a Low Aspect Ratio, Shrouded Axial Flow Turbine," ASME Paper No. 2000-GT-475.
[10] Pfau, A., Kalfas, A. I., and Abhari, R. S., 2004, "Making Use of Labyrinth Interaction Flow, ASME Paper No. GT2004-53797.
[11] Le Jambre, C. R., Zacharias, R. M., Biederman, B. P., Gleixner, A. J., and Yetka, C. J., 1998, "Development and Application of a Multistage Navier-Stokes Solver—Part II: Application to a High-Pressure Compressor Design," ASME J. Turbomach., **120**, pp. 215–223.
[12] Wellborn, S. R., Tolchinsky, I., and Okiishi, T. H., 2000, "Modeling Shrouded Stator Cavity Flows in Axial-Flow Compressors," ASME J. Turbomach., **122**, pp. 55–61.
[13] Hunter, S. D., and Orkwis, P. O., 2000, "Endwall Cavity Flow Effects on Gaspath Aerodynamics in an Axial Flow Turbine. Part II: Source Term Model Development," ASME Paper No. 2000-GT-513.
[14] Bohn, D. E., Balkowski, I., Ma, H., and Tuemmers, C., 2003, "Influence of Open and Closed Shroud Cavities on the Flowfield in a 2-Stage Turbine with Shrouded Blades," ASME Paper No. GT2003-38436.
[15] Peters, P., Breisig, V., Giboni, A., Lerner, C., and Pfost, H., 2000, "The Influence of the Clearance of Shrouded Rotor Blades on the Development of the Flowfield and Losses in the Subsequent Stator," ASME Paper No. 2000-GT-478.
[16] Anker, J. E., and Mayer, J. F., 2002, "Simulation of the Interaction of Labyrinth Seal Leakage Flow and Main Flow in an Axial Turbine," ASME Paper No. GT-2002-30248.
[17] Giboni, A., Wolter, K., Menter, J. R., and Pfost, H., 2004, "Experimental and Numerical Investigation into the Unsteady Interaction of Labyrinth Seal Leakage Flow and Main Flow in a 1.5-Stage Axial Turbine," ASME Paper No. GT2004-53024.
[18] Gier, J., Stubert, B., Brouillet, B., and de Vito, L., 2003, "Interaction of Shroud Leakage Flow and Main Flow in a Three-Stage LP Turbine," ASME Paper No. GT2003-38025.

# Toward Defining Objective Criteria for Assessing the Adequacy of Assumed Axisymmetry and Steadiness of Flows in Rotating Cavities

**G. D. Snowsill**

**C. Young**

Rolls-Royce plc,
P. O. Box 31,
Derby, DE24 8BJ, UK

*The need to make a priori decisions about the level of approximation that can be accepted—and subsequently justified—in flows of industrial complexity is a perennial problem for computational fluid dynamics (CFD) analysts. This problem is particularly acute in the simulation of rotating cavity flows, where the stiffness of the equation set results in protracted convergence times, making any simplification extremely attractive. For example, it is common practice, in applications where the geometry and boundary conditions are axisymmetric, to assume that the flow solution will also be axisymmetric. It is known, however, that inappropriate imposition of this assumption can lead to significant errors. Similarly, where the geometry or boundary conditions exhibit cyclic symmetry, it is quite common for analysts to constrain the solutions to satisfy this symmetry through boundary condition definition. Examples of inappropriate use of these approximating assumptions are frequently encountered in rotating machinery applications, such as the ventilation of rotating cavities within aero-engines. Objective criteria are required to provide guidance regarding the level of approximation that is appropriate in such applications. In the present work, a study has been carried out into: (i) The extent to which local three-dimensional features influence solutions in a generally two-dimensional (2D) problem. Criteria are proposed to aid in decisions about when a 2D axisymmetric model is likely to deliver an acceptable solution; (ii) the influence of flow features which may have a cyclic symmetry that differs from the bounding geometry or imposed boundary conditions (or indeed have no cyclic symmetry); and (iii) the influence of unsteady flow features and the extent to which their effects can be represented by mixing plane or multiple reference frame approximations.* [DOI: 10.1115/1.2185124]

## Introduction

Computational fluid dynamics (CFD) is increasingly being used to support engineering design, and a number of special interest groups have embraced the need to establish common modeling approaches, e.g., [1]. In the field of internal flow analysis, CFD is used to establish the boundary conditions for metal temperature predictions on critical rotating components within the core of gas turbines.

It is worth defining precisely what is meant by internal flow analysis in the context of the gas turbine: this is the study of all the air flows within the core of a gas turbine that are not part of the main gas path. They comprise the cooling and ventilating flows within the rotors and the ducts supplying cooling air to these spaces. They are typically bounded by the surfaces of the compressor and turbine rotors and by the static structures supporting the bearing systems.

This particular application area has lagged behind analysis of the turbomachinery components and of external aerodynamics. This tardiness can largely be attributed to the complex geometries encountered and the extreme stiffness of the governing equation set. In contrast to "ordinary" CFD, where the flow is dominated by pressure/momentum, most internal cavity flows are dictated by a combination of viscous pumping from rotating disks and very significant regions of recirculation. Thus, computation times required to achieve satisfactory convergence are typically *one to two orders of magnitude greater* than for, for example, a turbine stage calculation with a comparable number of computational cells. Once it is also appreciated that the geometric complexity of internal flow problems typically requires very detailed meshing, it is perhaps unsurprising that this field of CFD has proved resistant historically.

In order to make progress in this difficult area, a very tempting option is to simplify the problem under consideration. In the earliest simulations of rotating cavity flows, attempts to solve the time-averaged Navier-Stokes equations at all were by-passed in favor of momentum-integral solutions [2]. Although providing excellent computational efficiency, such solutions are acknowledged to be limited in applicability [3] and there is always the suspicion that one "needs to know the answer in order to write the program."

As computational resources have improved, developers and practitioners have naturally aspired to greater generality. The first step was to solve for the full RANS (Reynolds-averaged Navier-Stokes) equations but with severe restraints on the geometries that could be modeled (e.g., axisymmetric cavities of rectangular cross section [4]). This has progressed through structured and unstructured grids and general geometries so that, today, it is possible to model such cavities with all geometric complexity resolved explicitly, the flow field fully three-dimensional (3D) and unsteady if required. Nevertheless, the time requirements both for setting up and for solving such problems remain fearsome even on modern

Contributed by the International Gas Turbine Institute (IGTI) of ASME for publication in the JOURNAL OF TURBOMACHINERY. Manuscript received October 1, 2004; final manuscript received February 1, 2005. IGTI Review Chair: K. C. Hall. Paper presented at the ASME Turbo Expo 2005: Land, Sea and Air, Reno, NV, June 6–9, 2005, Paper No. GT2005-68539.

  

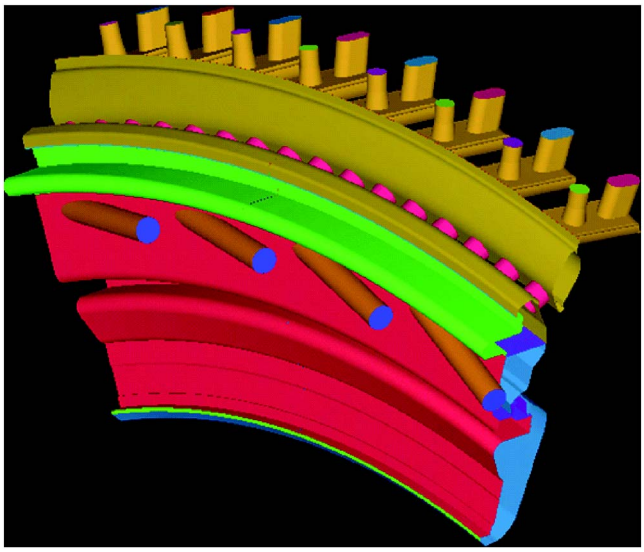

**Fig. 1 CFD model of an HPT preswirl/receiver hole system: three-repeat sectors shown for clarity**

multiprocessor machines. For example, the model of a typical aero-engine preswirl system, shown in Fig. 1, employs a mesh constructed from ~3 M hexahedral cells and required in excess of 1000 h of CPU time on 12 GHz×2.5 GHz processors to reach an unsteady cyclic solution.

In industrial applications, the biggest motivation for carrying out a CFD analysis is to influence the evolution of a design. In this context, there is still a need to simplify the models used wherever this can be justified. However, the difference is that now we introduce simplifying assumptions more as a matter of choice, not necessity; and we aim to carry out the most cost-effective analysis, not the only one that is practical. It is, of course, vital that practitioners understand what the consequences of such simplifications are so that informed decisions can be made.

## Disadvantages of Simplification

In general, all fluid flows are 3D and unsteady and, therefore, require all four dimensions to fully describe them. They also contain motions on a variety of length and time scales from large (comparable to the physical dimensions of the flow domain) to small (molecular).

An approximation that is universal, at least in industrial CFD, is to accept that only relatively large-scale fluid motion will be explicitly resolved, the effects of very small-scale motion being represented by some form of turbulence model. This is a very reasonable approach, but it must be remembered that turbulence models have a range of applicability that needs to be recognized. This is discussed further below.

Dimensional simplification is more controversial. It is only in very special cases that one or more dimensions can be ignored. An oft-used but nevertheless valuable illustration is the problem of balancing a pencil on its sharp end. A simple feat in a degenerate dimensional space, but clearly, as a real-world problem, this is very challenging.

Removing any of the four dimensions makes it much more straightforward. Solving as a steady problem would suggest that this is extremely simple. Removing just one of the spatial dimensions leaves an easier (but still very tough) problem but is highly misleading since an infinite number of possible real solutions are immediately excluded.

To sum up, any simplification that applies a constraint on the dimensionality of the solution will, as a minimum, prevent a number of possible solutions from being achieved. What is required is a way of determining whether the solution observed in Nature is amongst those that are excluded.

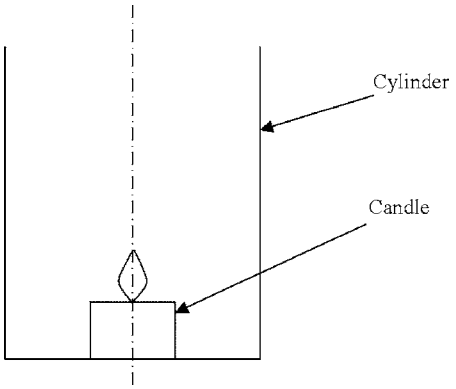


**Fig. 2 Schematic arrangement of burning candle in a cylindrical vessel**

## Two-Dimensional Versus Three-Dimensional

The most commonly used simplification is probably, in reality, the most dangerous. There are two insidious elements in rotating cavity analysis:

1. Very frequently, the geometry under consideration is, to a large extent, axisymmetric. Nonaxisymmetric features tend to be restricted to bolts, holes (generally used for introduction of cooling air), etc. However, boundary pressures/temperatures are rarely axisymmetric where there is an interface with the main gas path.
2. A very important use for the results of these analyses is to provide boundary conditions for metal temperature calculations, for which only circumferentially averaged air temperatures are typically required.

For these reasons, two-dimensional (2D) axisymmetric models are very commonly adopted for such analysis. Occasionally, this is appropriate but very often it is not.

Consider the example shown in Fig. 2. This illustration is based on a demonstration performed by Professor Alan Turner at Sussex University several years ago. A lighted candle is placed at the bottom of a glass cylinder that is open only at the top. The geometry here is clearly axisymmetric as are the boundary conditions. Furthermore, the boundary conditions are steady. A simple experiment shows, however, that nature *does not* choose an axisymmetric or a steady solution to this problem. In fact, as can be judged from Fig. 3, the flow is highly 3D and unsteady; the slight nonuniformity of the flame gives rise to quite complex buoyancy-induced flows into and out of the cylinder.

A particularly insidious aspect of this particular problem is that it is perfectly possible to set up an axisymmetric analysis that will apparently converge (see Fig. 4). Translating this experience to the sorts of application that are encountered on a daily basis in the simulation of gas turbine air systems, one may consider the flow within a rotating cavity. Such an example is presented in Fig. 5, which shows a typical rotor-stator cavity with the sort of geometry one might expect to find in an HP compressor rear cone.

Again, the geometry is very nearly axisymmetric, the only 3D features being the discrete preswirl holes and the protruding static bolt heads. It is extremely common practice for such holes to be represented as a slit, the width of the slit being chosen to give the appropriate mass flow and velocity into the cavity. Furthermore, it is not uncommon for the presence of protruding features, such as bolt heads, to be either omitted completely or represented by a momentum sink or local roughness. However, consider the differ-

**Fig. 3 Nonaxisymmetric and unsteady buoyant flow driven by a burning candle**

ence between the distribution of predicted wall temperature on the rotor and stator with imposed axisymmetry and the one where the 3D features have been explicitly represented within a 3D model. See Figs. 6 and 7.

It is very clear that, although the calculated flow field gives rise to a fairly axisymmetric adiabatic wall temperature in both cases

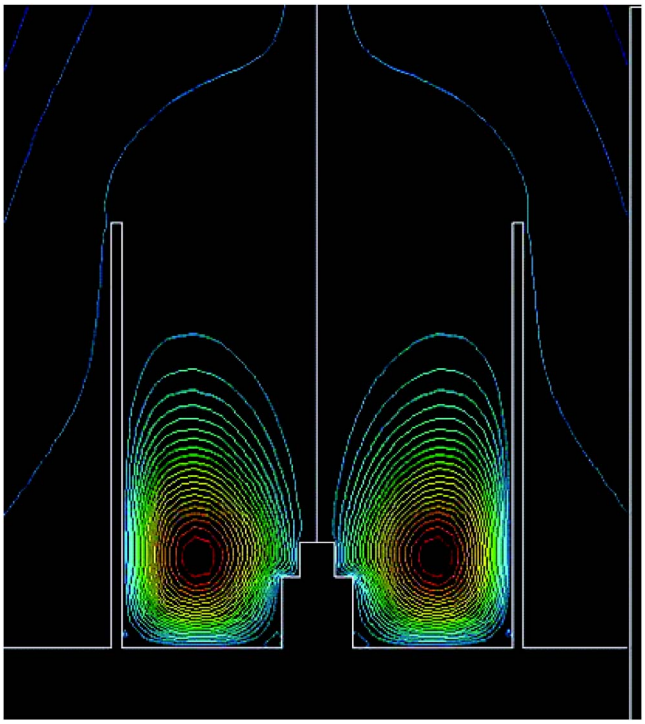

**Fig. 4 Stream function predictions of axisymmetric buoyancy-driven flow**

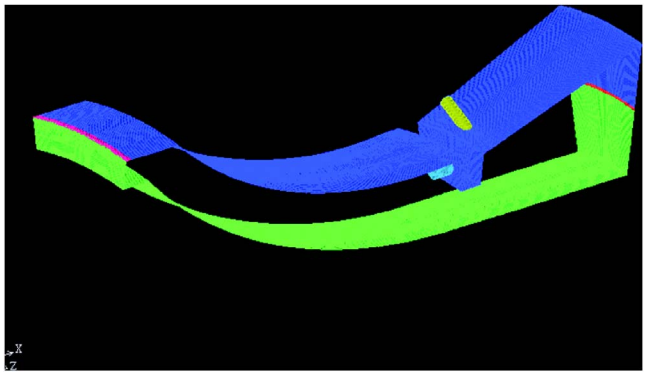

**Fig. 5 HP compressor rear cone model**

(often used as a justification for this approach), the solution is actually very different from the one where axisymmetry is imposed.

There are some essential axioms:

1. Even if all the geometry and all the boundary conditions are axisymmetric, the real flow field need not be axisymmetric (and, indeed, will only be so in special cases).
2. Even where the flow field is *mostly* axisymmetric, it is not, in general, the same flow field that would be reached by *imposing* axisymmetry.
3. In many cases, the imposition of axisymmetry constrains the solution to take a form that is unlikely to be realized in nature. And, there is a corollary: The adoption of a 2D axi-

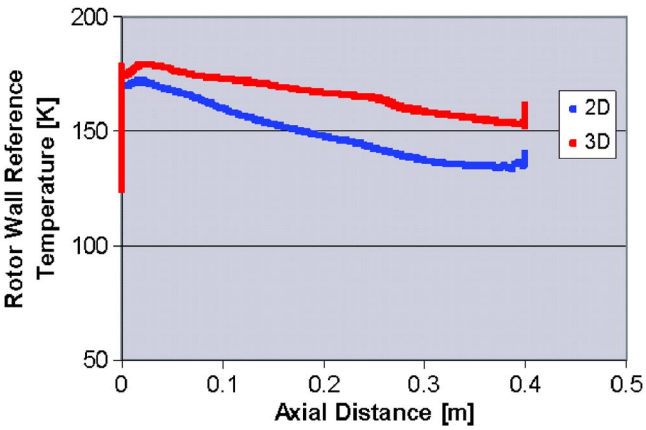


**Fig. 6 Comparison of 2D and 3D rotor wall temperatures**

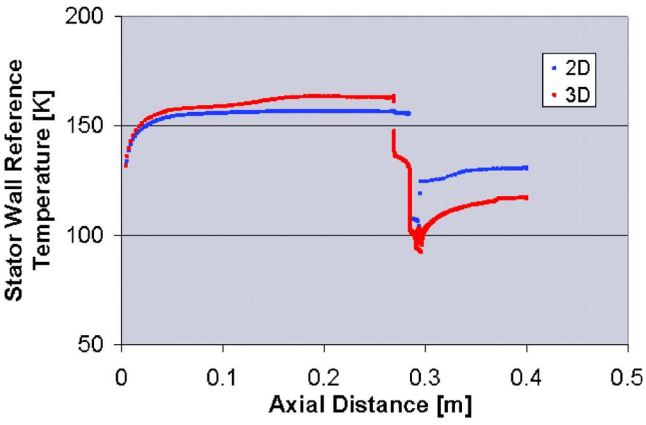


**Fig. 7 Comparison of 2D and 3D stator wall temperatures**

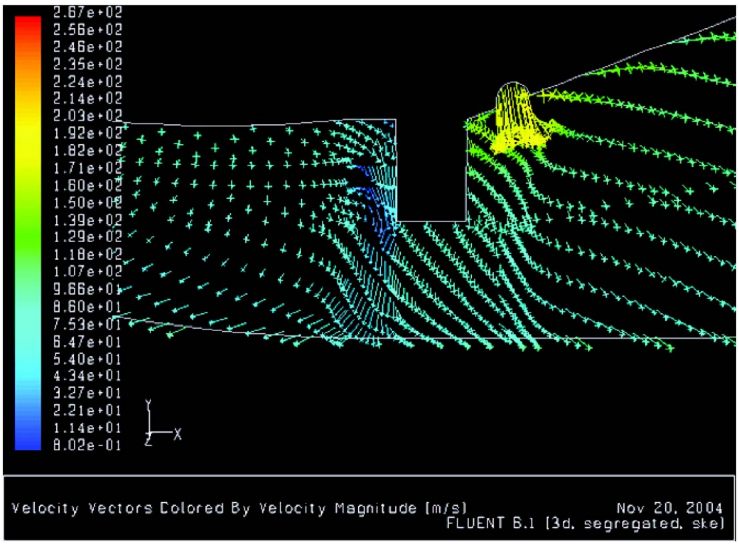


**Fig. 8 Prediction of strong radial velocities in the 3D drive cone flow solution**

symmetric approach is a modeling choice that must be critically appraised, just as is a choice of turbulence model or meshing strategy. It is essential that this assumption be validated before any results can be accepted, just as any other modeling choice.

Although not exactly a corollary, a further observation (which really stems from axiom 3) is that, if the solution forced by the imposition of axisymmetry is extremely unphysical, achievement of that solution may require considerably more computational effort than a 3D solution—even allowing for the much larger mesh. Having said all this, it is perhaps surprising that anyone would want to do any axisymmetric CFD. We freely confess that we have done 2D axisymmetric analysis and will probably do so again because, for the right problem, the speed advantage is worth having. What is required is a set of guidelines that allow practitioners to assess whether an axisymmetric approach is likely to be fruitful coupled with a willingness to carry out some validation to demonstrate that the solution is sufficiently close to the "real" one.

We can offer the following framework for approaching these problems. We do not pretend that at the current point in time these are all encompassing, but it is hoped that they provide a reasonable starting point. Some necessary but *not sufficient* conditions are as follows:

(a) It must be possible to produce a converged axisymmetric solution. The main reason for including this is that some practitioners have stated that the CFD code will, itself, determine the viability of the approach by refusing to reach convergence unless the 2D solution is valid. This is not the case; however, it has certainly proved true in our experience that failure to achieve a converged solution is a good indication that there is no valid axisymmetric solution.

(b) Geometry and boundary conditions are axisymmetric. Clearly the presence of nonaxisymmetric elements ought to be a strong disincentive to the production of an axisymmetric model. In practice, the influence of nonaxisymmetric elements needs to be carefully assessed: a stationary protrusion in a flow with little swirl may be expected to have little effect. The same protrusion in highly swirling flow would have a strong influence on the flow in the cavity. A useful exercise is to estimate the drag of such features and compare it to the total drag of the axisymmetric surfaces. If the total contribution of the discrete features is small ($<5\%$ of the total), then it is reasonable to assume that the effect of the features is largely localized.

In addition to any drag, discrete features can lead to mixing of the flow in a way that is impossible in a true axisymmetric flow. This is true of the drive cone cavity example cited earlier in which the static bolt heads deflect the predominantly tangential flow. This gives rise to strong localized inboard flows in the vicinity of these static features, which cannot properly be represented by momentum sinks or accommodated within the constraints of an axisymmetric flow field. The presence of these regions of strong inflow in the 3D solution is typically shown in the vector plot presented in Fig. 8.

Clearly, some engineering judgement is required in assessing whether such effects are likely to be important although the approach illustrated here of building a very stylized (and hence computationally efficient) model to explore the problem has been shown to be very valuable.

(c) No destabilizing buoyancy effects should be present. In general, this means that the temperature gradient $dT/dr$ should be negative.

(d) No requirement for streamlines to cross. Surprisingly, this requirement causes great confusion. If a flow field is to be axisymmetric, there is no way for one flow to cross another. This imposes profound restrictions on the way flows are able to mix within a cavity, which is, in general, unphysical. Consider the simple rotor-stator cavity example shown in Fig. 9, where the flow entering via the separate, static cooling air holes impinges directly on a rotor. In the 2D axisymmetric simulation of this flow, the inlet slot flow crosses the cavity, preventing any fluid inboard of the nozzle radius leaving the cavity, as can be seen from the streamlines in Fig. 10.

It is important to realize that the imposition of axisymmetry makes it *impossible* for this flow to go anywhere else. This rather simplistic representation of a flow constrained by the requirement for noncrossing streamlines may be compared to the altogether more complex 3D flow represented by pathlines originating from the inlet nozzle, shown in Fig. 11. This imposes a very important limitation on the way in which temperature (or any other transported scalar quantity) is distributed around a cavity. Since streams cannot cross, the only way isolated surfaces can be influ-

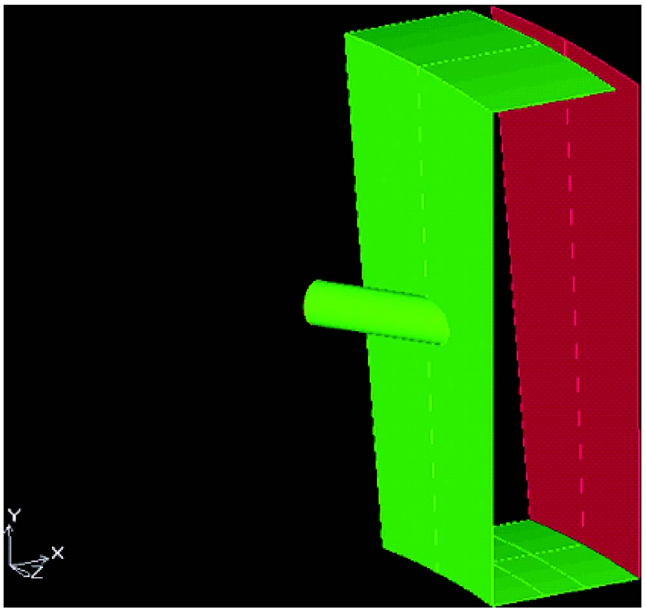


**Fig. 9 Simple rotor-stator cavity geometry**

enced by certain streams is by diffusion. This is a much weaker transport mechanism than the convection that would take place in the "real" 3D flow. Since any flow into or out of the cavity will have an overriding influence on the distribution of flow in the cavity, there needs to be confidence that this influence is not preventing the real flow from developing.

In general, it has to be accepted that the imposition of axisymmetry is really a far-reaching decision. It has much greater influence on the outcome of an analysis than a similar assumption in, for instance, stress/thermal analysis where the errors in assuming axisymmetry are generally confined to regions very close to 3D features. In order to be justifiable, we need to be sure that the benefits in solution speed are really worthwhile and that the errors incurred can be tolerated. Very often the latter will require a 3D model to be created anyway so that the real benefits of the approach may only be realized where repeated runs are required. Where the consequences of uncertainty are safety or commercially critical, the assumption of axisymmetry may not be justifiable at any price.

## 3D Sector Models

Once the requirement to undertake a 3D modeling approach has been accepted, analysts will generally still try to resist reality for a little longer by attempting to model only a sector of the real geometry, appealing to whatever level of symmetry is present. This could be regarded as "2.5-D" (two-and-a-half dimensional). This approach has been used very commonly and is probably the all-round "best buy," offering useful savings when compared to a full 360 deg 3D analysis. In our experience, excellent results can be achieved with an accuracy that, in general, exceeds our capability to validate against measurements made in the hostile environment of a gas turbine. Why, then, are we bothering to discuss this here? There are circumstances where this can still go wrong, usually because of poor modeling choices but occasionally due to nature being uncooperative.

It is generally felt to be appropriate and sufficient to identify all of the cyclic features in a geometry. If there are (say) 32 bolts in a flange and 16 air holes, the usual approach would be to assemble a model of a 22.5 deg sector (1/16). Is this always sufficient? Jakoby et al. [5] describe an experiment where there is a strong pressure fluctuation that bears no apparent relation with any cyclic feature in the rig. It is surmised that this phenomenon is responsible for the lack of success to date in matching a CFD solution to the experimental data. Where, then, can we go wrong?

In imposing a cyclic boundary condition on a sector model we are doing two very important things:

(a) We are *imposing* a symmetry on all characteristics of the flow. In a 1/4 sector model, we are imposing a periodicity of order 4 on any flow behavior in the cavity. If any element of the model tends to produce fluctuations close to this order, the symmetry condition is likely to enhance it.

(b) We are suppressing any fluctuations that have an order $<4$. Thus, in the experiment referred to above, a sector model cannot be expected to reproduce the behaviour observed.

This leads to some very interesting questions. If consideration

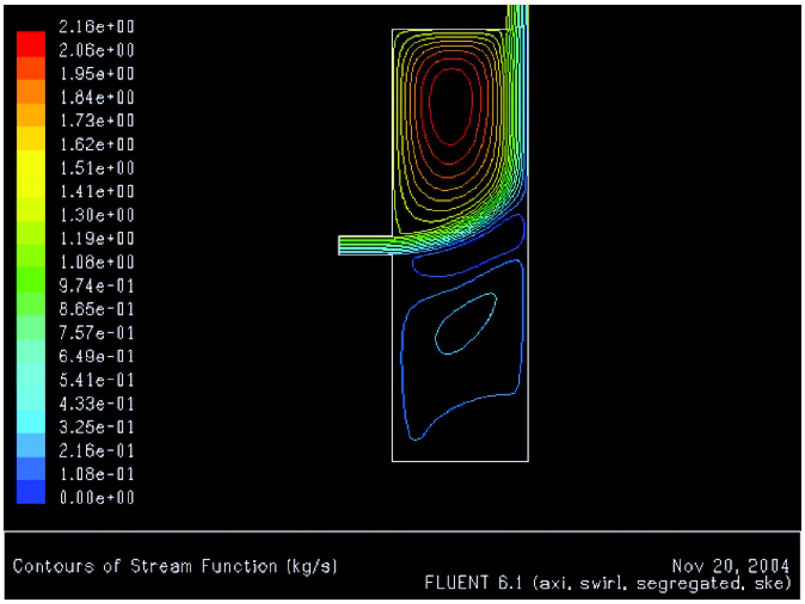


**Fig. 10 Contours of stream function in the axisymmetric flow simulations**

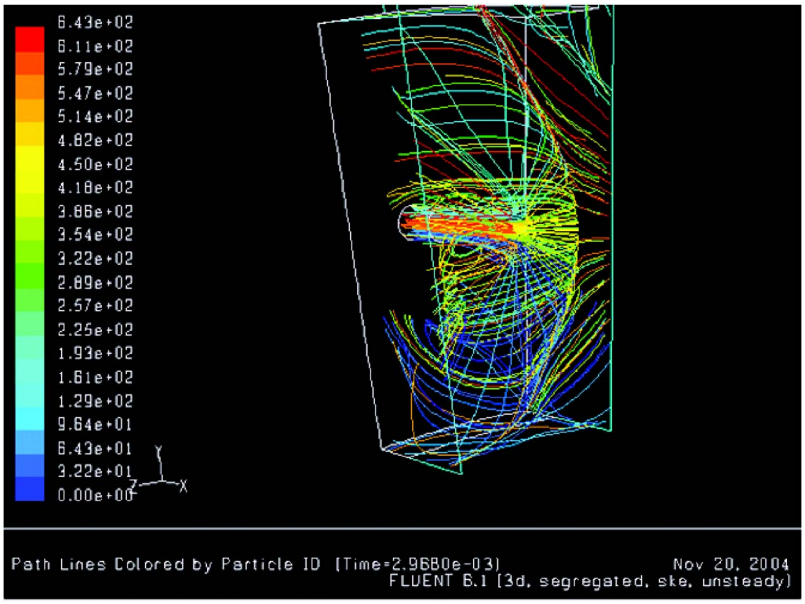


**Fig. 11 Pathline predictions created using a 3D sector model of the simple cavity**

of the cyclic symmetry of the model results in a sector that is not an integral subdivision of 360 deg, does this introduce a periodicity that is unrelated to the rotation of the machine but purely to the phasing of the model? It is possible that the only reliable solution is to insist on only modeling the full 360 deg. In some complex cases, this may currently be impractical so the next best choice is to be wary of the dangers.

A common dilemma is that, in real machines, we have rotating and static features circumferentially distributed that do not share any convenient common factors. This results in the question of how far we can go in rounding up or down the number of these features to permit the creation of a sector model.

The most important thing to remember here is the reason why the real machine does not have convenient multiples of these features: if, for example, a turbine had two rotor blades for every nozzle guide vane, one would expect to see destructive pressure perturbations at least at some operating conditions. This is perhaps the most helpful way to approach this problem. If we apply some license and alter numbers of features to achieve 1:2, 2:3, etc. ratios between them, this will allow much smaller sectors of geometry to be used. If the perturbations in *the parameters of interest* remain small, then this is generally a good indication that the assumption is good enough. Of course, the key here lies in the parameters of interest and clearly such a model could never be used to investigate phenomena such as the destructive pressure perturbations referred to above.

## Steady/Unsteady

Many issues of apparent unsteadiness can be resolved by suitable choice of reference frame. It is tempting to regard this observation as self-evident, but our experience suggests that this is not necessarily so. If all the discrete, 3D features in a geometry are either rotating or stationary, the appropriate choice of rotating or stationary reference frame is all that is required to recover a steady problem from what may otherwise appear to be an unsteady one. The real problem arises when both rotating and static features exist in the domain.

Much confusion arises simply from the difficulty in answering the question: when is a 3D feature not a 3D feature? Or more precisely, when is a 3D feature unlikely to give rise to 3D flow phenomena that are significant and relevant to the flow under investigation. Is it reasonable to represent certain features by some sort of circumferentially averaged property of the flow domain rather than explicitly model them in their full 3D glory? Given the preceding discussion, this may seem to be dangerous ground. However, there is a very important philosophical distinction between a 2D representation of geometry and/or boundary conditions and the imposition of two-dimensionalness on the flow field itself. Provided the flow is able to respond to the imposed boundary conditions in a physically realistic way, it is often reasonable to model the effect of the discrete features rather than the features themselves. (In fact, we suspect that this is what many people visualize when they propose a fully axisymmetric model.)

Clearly, in order for this approach to be valid, we need to have some basis for assessing the importance of each feature to the final solution and some experimental data on which to base the simplified model of the discrete features (and against which to validate the model). Our practice is to use simplified, highly stylized models. This enables the effects of different modeling assumptions to be assessed without the investment of detailed geometric modeling.

As with 2D axisymmetric analysis, the most useful measure is to assess the drag imposed by a particular feature and to compare it to the drag of the smooth surfaces. If the drag of a feature is $<5\%$ of the total, then it is generally safe to assume that the effect will be highly localized. If the drag is between 5% and 10%, then it is unlikely to be acceptable to neglect the effect but could be quite acceptable to include the influence simply as a momentum sink term (representing the drag). Beyond this, we feel that the appropriate action is to model the feature explicitly.

A subtle but essential point: do not forget to reevaluate the drag with the flow field that results from including the additional drag. If the conclusion is that significant influence arises from features on both rotating and stationary surfaces, then there is no option but to adopt some sort of unsteady approach. Even here there are important choices to be made.

In order to model discrete, 3D features on both rotating and stationary elements, it is clearly necessary to decompose the flow domain into two or more subdomains, each of which must be solved relative to an appropriate frame of reference. The aim of this decomposition is to solve the flow in a reference frame in which the 3D features in question are stationary. Typically, the flow adjacent to the stator will be solved in a stationary reference frame while the flow adjacent to the rotor will be solved relative

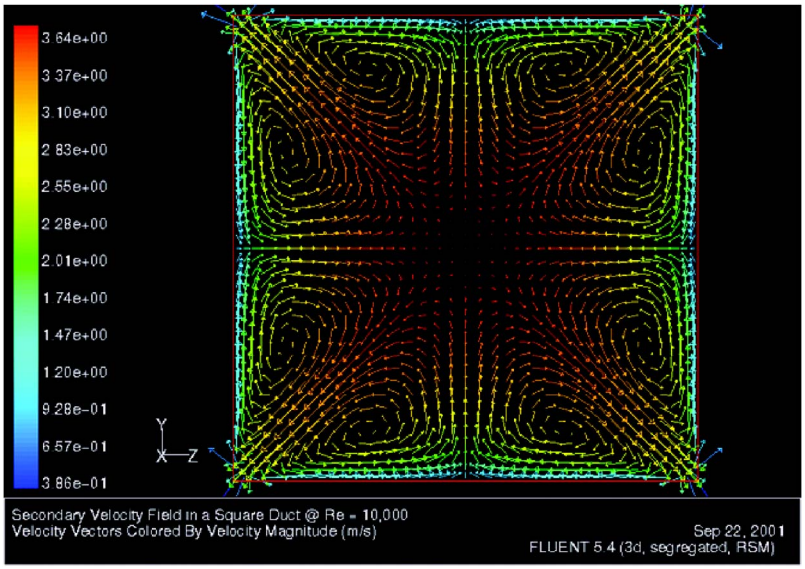


**Fig. 12 Secondary flow behavior in a square-sectioned duct**

to a rotating frame of reference. (We assume that the practitioner will avoid the pitfall of specifying nonaxisymmetric rotating features in a stationary frame of reference, permitted by many CFD codes but with unphysical results.)

The relative passing frequency of nonaxisymmetric features in a rotor-stator (or rotor-rotor) cavity gives rise to unsteady flow behavior. Depending on the relative motion, size, and proximity of the nonaxisymmetric features, the strength of the induced transient behavior can vary between being so weak as to be negligible to being the dominant effect driving the entire flow. Consequently, the level of sophistication used in interfacing the various subdomains in a multireference frame application should be consistent with the relative importance of the transient behavior to the application under investigation.

In applications where the interactions arising from the differential rotation are judged to be weak and remote from the region of principal interest, it may be appropriate to undertake a quasi-steady solution. In such an approach, the steady-state flow is solved in the respective frames of reference and account is taken of the reference frame differences in the calculational cells adjacent to the subdomain interface(s).

At the opposite extreme, in applications where transient interactions are judged to be strong, the only course of action is to undertake a transient simulation in which the differential rotation of the boundary geometry is explicitly resolved. This is achieved by simulating the relative motion of the respective subdomains during each interval of the transient solution. This more sophisticated—and computationally expensive—approach is typically employed in the modeling of preswirl systems, where differentially rotating components with nonaxisymmetric features are in close proximity to one another.

To date, no clear guidance has emerged concerning the demarcation between where the quasi-steady and fully unsteady approaches should be used. In the absence of better information, the authors' practice has been to establish the amplitude of transient oscillations using a stylized—relatively easily meshed—representation of the problem under consideration. Based on these results, the judgement has been taken that if the parameters under consideration, e.g., rotor torque, vary by more than ±5% over the transient cycle, an unsteady analysis is warranted.

It should be noted that the mixing plane treatment, which circumferentially averages flow behaviour at subdomain interfaces has been omitted from the foregoing discussion. While this approach has been used with some success in main annulus flows, where a dominant axial flow direction exists, its underlying assumption of unidirectional axial behavior renders it unsuitable in rotating cavity flows.

## Turbulence Modeling

Selection of an appropriate turbulence model is another way in which substantial aspects of the physical fluid behavior are potentially suppressed. There are several levels of approximation that are generally accepted.

Turbulence can be modeled explicitly. Direct numerical simulation (DNS) is increasingly an option that can be considered [6] provided the geometric complexity does not make the model size prohibitive. In principle, no aspect of the behavior of the fluid should be suppressed, provided the spatial and temporal resolution is adequate. In practice, the geometric complexity generally does still make the model size prohibitive.

Large eddy simulation (LES) is often claimed to provide most of the benefit of DNS but with less calculational overhead. Clearly, though, there is a requirement to validate this approach for any given application since the contribution of the very small-scale turbulence represented by the subgrid-scale model can be very significant [7]. Experience when applying this method to internal flow has shown that a very fine calculational mesh is still required for LES.

The Reynolds-averaged Navier-Stokes (RANS) approach is almost universal in industrial CFD applications, primarily to avoid the massive computational overhead of LES/DNS but also because RANS has been well validated for a wide range of flows. Although all commercial CFD codes provide a multitude of turbulence models, the real choice for most flows is between isotropic and anisotropic models.

Included in isotropic models are most of the "flavors" of the $k$-$\varepsilon$ model [8–10], which probably accounts for most of the industrially complex RANS CFD carried out at present. An observation that we would make at this juncture is that there appears to be very little to choose between the various alternatives. For any given application, it is probably better to choose one and stick with it, making due allowance for its known deficiencies. This leaves more time to invest on other sensitivity studies rather than resurveying the full range of turbulence models. In spite of claims to the contrary, $k$-$\varepsilon$ has been shown in a number of applications to work very well in rotating cavity problems, e.g., [11–13].

The main difficulty with the $k$-$\varepsilon$ model is the implicit assumption that the turbulence it purports to represent is isotropic. A

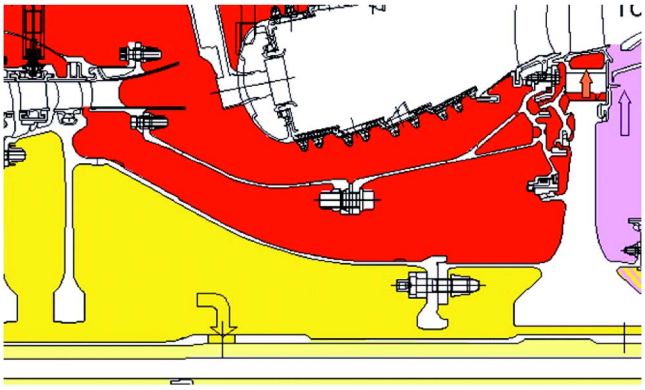

**Fig. 13 Typical aero-engine drive cone cavity geometry**

classic example of the shortcomings of isotropic turbulence models is fully developed flow in a duct of noncircular cross section. Figure 12 shows the secondary flow field in a square-sectioned duct, predicted using a Reynolds stress model (RSM) [14]. These secondary flows, which appear in Fig. 12, are driven by the anisotropic turbulent stresses, which clearly could not be captured using a treatment such a $k$-$\varepsilon$ in which the potential for anisotropy of the turbulence has been excluded.

Other examples are in the area of flows through constrictions where the flow contraction results in significant anisotropy in the turbulence. Where anisotropy is important, the most practical option is RSM [15]. In practice, adoption of the RSM treatment is often resisted due to the order of magnitude increase in computing time. It must be remembered, however, that the purpose of CFD is generally to save time by "right first time" design or by removing the requirement for experiments. Producing the wrong answer quickly is often a distraction and all too often does not, in fact, save any time. It is possible that use of RSM, if it results in a better solution, still represents the best investment.

## Stylized/Simplified Models

This is an issue that can be related to the foregoing and one which is often very helpful in making useful informed judgements about the seriousness of some of the compromizes made. Much of the difficulty in carrying out internal flow CFD results from the geometric complexity of the models. The eternal dilemma for CFD analysts is that, while capture of model detail makes the results more useful by reducing modeling uncertainties, it makes those results more difficult to obtain. The suppression of geometric/modeling detail makes models easier to run, but no one believes the results. If the purpose of the analysis is only to find out whether the real analysis should be 2D or 3D, steady or unsteady, sector or full 360 deg, the requirement for a geometrically rigorous model can be significantly relaxed. The model shown in Fig. 5 actually represents a much more complex geometry, as shown in Fig. 13.

As can be seen, the stylized model requires far fewer mesh points to produce a good model and can be used to assess the relative importance of the different elements of the model without a large overhead in computing time. In fact, the "real" model would generally be produced while running the stylized model(s). By making use of the results of the stylized model, the confidence that the real model will deliver useful results is greatly increased.

## Validation

The need for demonstrably validated modeling methods in safety-critical applications of CFD should not be underestimated. In recent years, significant progress has been made toward establishing a rational framework to underpin the validation process, e.g., [16]. With the increasingly diverse use of CFD, the primary objective of physical testing is often the acquisition of data for CFD model validation. A disconcerting corollary of this is that CFD is itself increasingly used in the design of such experiments. For instance, instrument placement is often defined on the basis of results from the same CFD model that is to be the subject of the validation exercise.

Clearly, a CFD solution compromised by inappropriate assumptions of degenerate dimensionality is likely to result in the definition of a correspondingly flawed experiment. Consequently, many of the potential pitfalls previously referred to are also relevant to the experimental community. Where this use of CFD is unavoidable, it is imperative that any simplifications are well founded and based on sound knowledge rather than judgement.

## Conclusions

The application of CFD to industrially complex situations in order to achieve the basis of a right first time design process is rapidly becoming a reality. Consequently, the modeling compromises that have been habitually made on the basis of computational necessity must increasingly be called into question. In this work, we have attempted to share some of the thoughts and practices that we have found useful. Moreover, our aim was to stimulate consideration of how to build on our own personal experiences and prejudices.

In the coming years, the internal flow CFD community must not shrink from the decision to make simplifying assumptions where appropriate. Our aim should be to clarify where the true boundaries of our assumptions lie. If we fail to rise to this challenge, the urgent requirements to maximize engine efficiency and minimize environmental impact will surely be compromised.

## Acknowledgment

The authors wish to thank Rolls-Royce plc for giving their permission for this work to be published and to Richard Scott who performed some of the calculations.

## References

[1] Casey, M., and Wintergerste, T., eds., 2000, Best Practice Guidelines, European Research Community on Flow, Turbulence and Combustion Special Interest Group on Quality and Trust in Industrial CFD, Version 1.0, January.
[2] Owen, J. M., and Rogers, R. H., 1995, *Flow and Heat Transfer in Rotating-Disc Systems*, Vols. 1 and 2, Research Studies Press, Taunton, UK.
[3] Goulas, A., Heritage, J., and Versteeg, H. K., 1986, Cranfield Fluid Engineering Unit Course Notes, Fluid Flow Computations for Engineers, Cranfield Institute of Technology. December.
[4] Gosman, A. D., and Ideriah, F. J. K., 1976, TEACH-T: A General Computer Program for Two-Dimensional Turbulent Recirculating Flows, Department of Mechanical Engineering, Imperial College, London.
[5] Jakoby, R., Zierer, T., Lindblad, K., Larsson, J., deVito, L., Bohn, D. E., Funcke, J., and Decker, A., 2004, "Numerical Simulation of the Unsteady Flow Field in an Axial Gas Turbine Rim Seal Configuration," ASME Paper No. GT2004-53829.
[6] Muldoon, F., and Acharya, S., "Numerical Simulation of a Film Cooling Jet," ASME Paper No. GT2004-53502.
[7] Sun, Z., Kilfoil, A., Chew, J. W., and Hills, N. J., 2004, "Numerical Simulation of Natural Convection in Stationary and Rotating Cavities," ASME Paper No. GT2004-53528.
[8] Launder, B. E., and Spalding, D. B., 1972, *Lectures in Mathematical Modelling of Turbulence*, Academic Press, London.
[9] Yakhot, V., and Orszag, S. A., 1986, "Renormalisation Group Analysis of Turbulence—I: Basic Theory," J. Phys.: Condens. Matter, **2**, pp. 3–51.
[10] Shih, T.-H., Liou, W. W., Shabbir, A., and Zhu, J., 1995, "A New k-$\varepsilon$ Eddy Viscosity Model for High Reynolds Number Turbulent Flows: Model Development and Validation," Comput. Fluids, **24**(3), pp. 227–238.

[11] Young, C., 2003, "The Application of CFD to Underpin Material Selection for Gas Turbine Rotors," *Proceedings of the Thermal and Fluids Analysis Workshop (TFAWS) 2003*, Aug. 18–22 NASA Langley Research Centre, Hampton, VA.
[12] Wang, Y. Y., Young, C., Snowsill, G. D., and Scanlon, T. J., 2004, "Study of Airflow Features Through Step Seals in the Presence of Disengagement due to Axial Movement," ASME Paper No. GT2004-53056.
[13] Evans, J., Stevens, L. M., and Kang, M.-K. B., "Prediction of Velocities and Heat Transfer Coefficients in a Rotor-Stator Cavity," ASME Paper No. GT2004-53639.
[14] Launder, B. E., Reece, G. J., and Rodi, W. J., 1975, "Progress in the Development of a Reynolds Stress Turbulence Closure," J. Fluid Mech., **68**(3), pp. 537–566.
[15] Rayer, Q. G., and Snowsill, G. D., 1998, Validation of FLUENT against Incompressible and Compressible Flow Through Orifices, I. Mech. E. Seminar Publication: CFD in Fluid Machinery Design, No. S546/010/98.
[16] American Institute of Aeronautics and Astronautics, 1998, "Guide for the Verification and Validation of Computational Fluids Dynamics Simulations," AIAA Paper No. G-077-1998.

**Anthony J. Smalley**
Mechanical and Materials Engineering Division,
Southwest Research Institute,
P.O. Drawer 28510,
San Antonio, TX 78228-0510
e-mail: tony@tonysmalleyconsulting.com

**Massimo Camatti**
Turbocompressors & Steam Turbines Division,
Nuovo Pignone,
Via Felice Matteucci,
2 Firenze, 50127 Italy
e-mail: Massimo.camatti@np.ge.com

**Dara W. Childs**
Department of Mechanical Engineering,
Turbomachinery Laboratory,
Texas A&M University,
College Station, TX 77843-3254
e-mail: dchilds@turbo-lab.tamu.edu

**Justin R. Hollingsworth**
Mechanical and Materials Engineering Division,
Southwest Research Institute,
P.O. Drawer 28510,
San Antonio, TX 78228-0510
e-mail: jhollingsworth@swri.org

**Giuseppe Vannini**
Turbocompressors & Steam Turbines Division,
Nuovo Pignone,
Via Felice Matteucci,
2 Firenze, 50127 Italy
e-mail: Giuseppe.vannini@np.ge.com

**Jeremy J. Carter**
Engine and Vehicle Research Division,
Southwest Research Institute,
P.O. Drawer 28510,
San Antonio, TX 78228-0510
e-mail: jcarter@swri.org

# Dynamic Characteristics of the Diverging Taper Honeycomb-Stator Seal

*This paper introduces a variant on the honeycomb-stator seal, which can extend the already strong stabilizing influence of this seal geometry for centrifugal compressors. The paper presents predicted and measured dynamic characteristics, demonstrating how a clearance, which diverges axially from inlet to outlet, increases the maximum effective damping of a honeycomb-stator seal, even though the average clearance is increased. The results also show a strong negative direct stiffness at zero and low frequency for this seal geometry (termed the "diverging taper honeycomb seal (DTHCS)"). The predictions are made with ISOTSEAL, software developed at The Texas A&M Turbomachinery Laboratory. (This code was developed within the Turbomachinery Laboratory and is not a commercial product (not for sale).) The test data, also obtained at the Turbomachinery Laboratory, confirm the nature and magnitude of both these dynamic characteristics with close fidelity. However, measured leakage falls significantly below predicted leakage. The frequency dependence of the seal dynamic characteristics and the strong negative static stiffness require careful attention in rotor dynamics analysis.* [DOI: 10.1115/1.2218891]

## 1 Introduction

Centrifugal compressors have demonstrated time and again their potential for subsynchronous vibrations excited by working fluid forces within the gas flow path. Conditions which make this phenomenon more likely to occur include: high head, high density, high speed, high power (size), and high ratio of running speed to first natural frequency. While high discharge pressure characterizes some of the most well-known and severe examples (e.g., Ekofisk, 530 bar), some large propane compressors in refrigeration service with discharge pressures of only 15 to 25 bar have raised concerns with evidence of self-excited subsynchronous vibrations.

A substantial amount of research has established that labyrinth seals within the compressor are a significant source of destabilizing excitation. Their potential for negative effective damping at the first natural frequency increases with high inlet swirl, with high ratio of running speed to first natural frequency, with flow length, and with high pressure differential across the seal. Either the labyrinth balance piston or the labyrinth center seal in back-to-back designs can make a particularly significant destabilizing contribution [1,2]. Reducing inlet swirl to a labyrinth balance piston by means of swirl brakes or shunt holes has proved effective in reducing this destabilizing effect [3–5].

Alternatives to the labyrinth balance piston design have shown their value, including the pocket damper seal or TAMSEAL [6,7] and the honeycomb-stator seal [1]. Tests and analysis for the honeycomb-stator seal have demonstrated high effective damping that remains positive for a wider range of subsynchronous frequencies than the labyrinth seal.

The honeycomb-stator seal employs a pattern of closely spaced holes in the stator surface of hexagonal shape (when viewed from directly above the surface). Derived from aircraft engine technology, the honeycomb-stator seal has some disadvantages from a manufacturing and procurement point of view, and the material hardness of the aircraft technology seals creates concerns regarding the result of a rub. The use of aluminum for construction

Contributed by the International Gas Turbine Institute (IGTI) of ASME for publication in the JOURNAL OF TURBOMACHINERY. Manuscript received October 1, 2003; final manuscript received March 1, 2004. IGTI Review Chair: A. J. Strazisar. Paper presented at the International Gas Turbine and Aeroengine Congress and Exhibition, Vienna, Austria, June 13–17, 2004, Paper No. 2004-GT-53084.

  

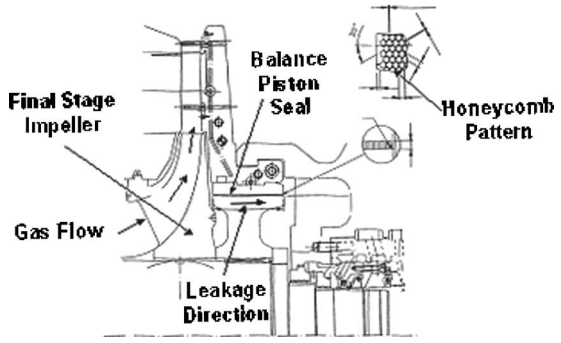


**Fig. 1 Side elevation of honeycomb-stator balance piston seal for large centrifugal compressor in propane refrigeration service**

and/or the use of closely spaced circular holes [8] (which has demonstrated comparable stabilizing capability) represent options to reduce these concerns.

The present paper addresses the honeycomb-stator seal and, in particular, a variant whose radial clearance increases linearly from inlet to outlet. It illustrates the geometry of the diverging taper honeycomb seal (DTHCS), and shows that adding a diverging taper in the flow direction to a honeycomb-stator seal can significantly enhance its positive damping characteristics. It also shows how the taper exaggerates the tendency for this seal to exhibit a negative stiffness at low and zero frequencies and discusses the implications. The paper compares predictions and measurements of effective stiffness and damping for a DTHCS operating in air at different clearances, pressures, and rotational speeds with encouragingly close agreement.

## 2 Configuration

Figure 1 shows a honeycomb-stator balance piston located behind the last stage in a large, straight-through, centrifugal compressor designed for propane refrigeration service. The balance piston sets the radius at which pressure acting axially on the compressor transitions from discharge pressure to suction pressure. Since flow through the balance piston seal must return via an internal or external line to compressor inlet, the compressor's performance is influenced significantly by the amount of gas at discharge pressure, which flows through the balance piston as leakage.

Figure 2 shows schematically how a honeycomb-stator seal with a diverging taper differs geometrically from a constant clearance ("straight") honeycomb-stator seal; the main difference is that the clearance at exit is higher than the clearance at inlet—

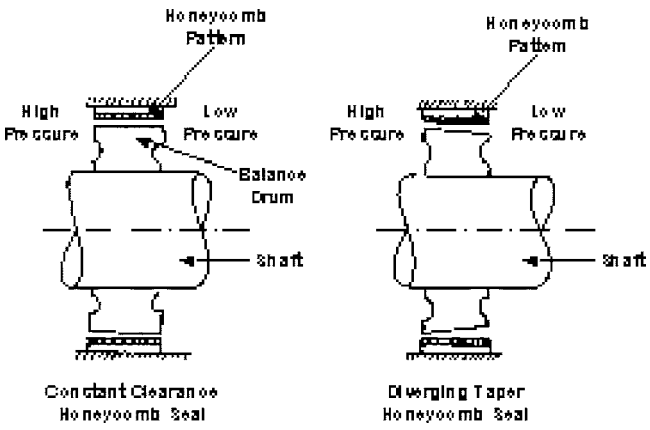


**Fig. 2 Schematic comparison between straight and diverging taper honeycomb-stator seals**

**Table 1 Key dimensions of test seal configurations**

| | | |
|---|---|---|
| Length | 85.71 mm | 85.71 mm |
| Test Shaft Diameters | 114.295 mm | 114.071 mm |
| Inlet Clearance | 0.1198 mm | 0.2316 mm |
| Outlet Clearance | 0.2158 mm | 0.3276 mm |
| Cell Depth | 2.6 mm | 2.6 mm |
| Cell Face Spacing | 1.6 mm | 1.6 mm |

typically by a factor of 2 or more. As will be shown, the beneficial result of the taper is to increase effective damping of the seal—even when the taper increases the seal's mean clearance. An intuitive rationalization is that the diverging taper concentrates the axial pressure drop near the inlet. Radial eccentricity of the rotating element relative to the stator causes the axial pressure distribution to vary circumferentially. Concentrating the axial pressure variation near the inlet also ensures concentrating this circumferential pressure variation near the inlet, and so the net radial pressure forces can act over a larger axial length of the seal. The circumferential acoustic response of gas film pressure to normal relative velocity of stator and rotor has a strong influence on the honeycomb-stator seal's damping. The honeycomb-stator cell depth directly affects the effective compliance of the gas volume and, thereby, the acoustic response. Again, concentrating axial pressure drop near seal inlet maximizes the sensitivity of film forces to the circumferential acoustic response.

Table 1 shows the length, diameter, clearance, and honeycomb dimensions of two test seals. A single stator whose bore increases linearly from inlet to outlet is combined with two shafts, which have different (but axially uniform) diameters. The 0.124 mm difference in diameter yields two test seal configurations: one whose clearance diverges from 0.1198 to 0.2158 mm (low clearance), and one whose clearance diverges from 0.2316 to 0.3276 mm (high clearance). Test seal length and diameter had to fit the existing test rig and, thereby, differ from the target application. The test objective was, therefore, to build general confidence in the predictability of a diverging clearance seal's characteristics. Pressure ratio, surface speed, and ratio of inlet to outlet clearances, as tested, remained close to the target application. Table 2 shows the originally planned test conditions; these were all completed for the high clearance seal but could be completed for the low clearance seal only under the 8 bar test condition. This will be discussed further in Sec. 4. Section 3 characterizes the test seal and Sec. 4 details the tests and the confirmatory test results.

## 3 Dynamic Characteristics

The computer program ISOTSEAL, developed by the Texas A&M Turbomachinery Laboratory [9], was used to predict all honeycomb seal characteristics in this paper. This isothermal, bulk flow analysis solves the film-wise momentum and continuity equations. A zero-order concentric solution establishes the axial pressure distribution, and linear perturbation provides complex derivatives of pressure with respect to dynamic radial displacement of the rotating element. The pressure derivatives appropriately integrated over the surface area yield stiffness and damping coefficients. The holes in one film surface increase effective gas compressibility,

**Table 2 Planned test condition matrix**

| Test Case | Speed (RPM) | Upstream Pressure (Bar) | Surface Speed |
|---|---|---|---|
| 1 | 12,000 | 8 | 71.95 |
| 2 | 12,000 | 17 | 71.95 |
| 3 | 17,000 | 8 | 101.9 |
| 4 | 17,000 | 17 | 101.9 |
| 5 | 22,000 | 8 | 131.9 |
| 6 | 22,000 | 17 | 131.9 |

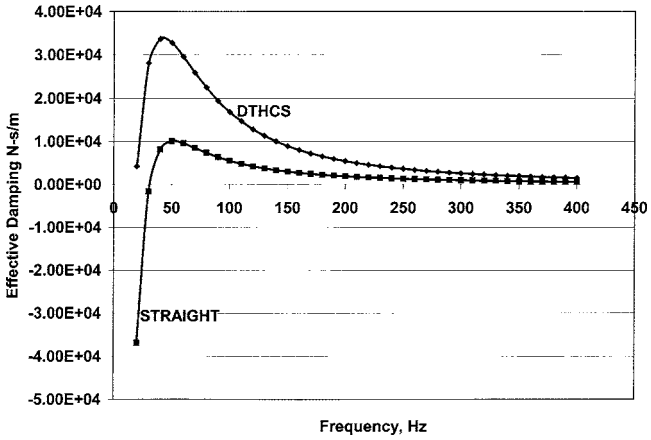


**Fig. 3 Predicted effective damping of test configuration; diverging taper honeycomb-stator seal compared to a straight seal; 22,000 rpm; 17 bar upstream and 1 bar downstream pressure $C_{in}$=0.1 mm; $C_{out}$=0.21 mm**

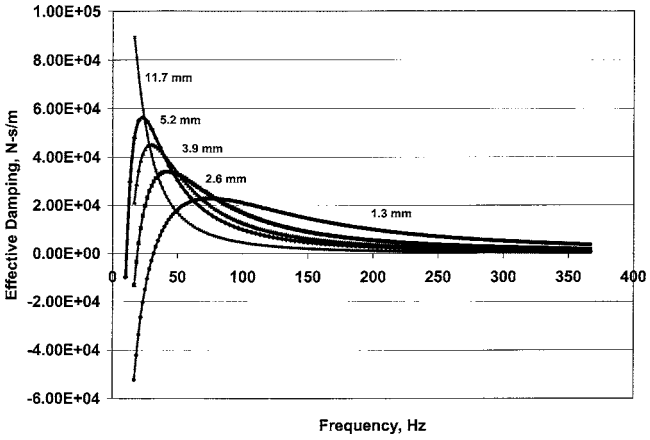


**Fig. 5 Predicted damping of the test seal as a function of frequency for different cell depths; 22,000 rpm; 17 bar upstream and 1 bar downstream pressure $C_{in}$=0.1 mm; $C_{out}$=0.21 mm**

reduce film-wise acoustic velocity, and significantly influence the frequency-dependent stiffness and damping characteristics.

Figure 3 shows the variation of effective damping with excitation frequency for both the test DTHCS and for a straight seal with the same clearance at inlet. The definition of effective damping is as follows:

$$C_{\text{effective}} = C_{xx} - K_{xy}/\omega \tag{1}$$

Thus, in this definition, the direct damping is reduced by a contribution from the destabilizing cross coupling of the seal.

Although the diverging taper seal's mean clearance is one and a half times that of the straight seal, its predicted damping exceeds the highest straight seal damping over a wide frequency range, making it possible to increase the damping near the subsynchronous frequency where it is needed. In addition, the frequency where effective damping transitions from positive to negative is at least 30 percent lower for the diverging taper seal when compared to the straight seal, broadening the frequency range over which this seal makes a positive contribution to stability.

Figure 4 shows how the effective stiffness varies with frequency, both for the DTHCS, and for the straight seal. Effective stiffness is defined as follows:

$$K_{\text{effective}} = K_{xx} + \omega C_{xy} \tag{2}$$

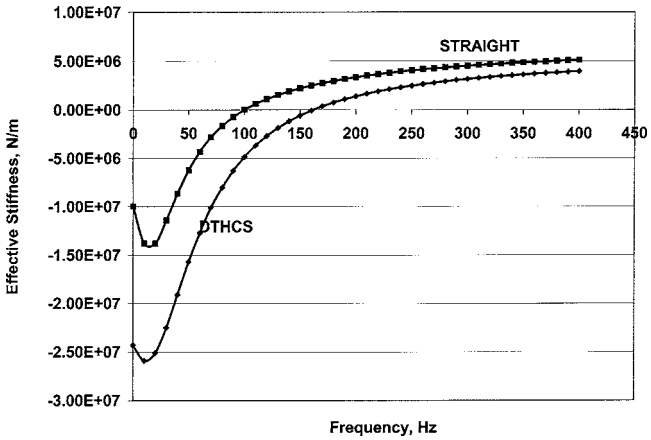


**Fig. 4 Predicted effective stiffness of test configuration; diverging taper honeycomb-stator seal compared to a straight seal; 22,000 rpm; 17 bar upstream and 1 bar downstream pressure $C_{in}$=0.1 mm; $C_{out}$=0.21 mm**

Figure 4 shows that both straight and tapered seals have a negative effective stiffness over a wide band of frequencies below 150 Hz. The DTHCS negative stiffness at zero frequency (nearly 2.5 times more negative than the straight seal) can influence the static deflection of the rotor in its supports, and for a sufficiently soft rotor system could make the system statically unstable. It will be shown that the rotor-bearing system for the target straight-through compressor had substantial margin relative to static instability, but the potential for static instability should be considered in any application of the honeycomb-stator seal, straight or tapered. An additional concern is the potential to drop the first critical speed into a region where the seal's effective damping is negative. Camatti et al. [10] recently reported instability on a back-to-back compressor caused by such an unintentional divergence in the center division-well seal.

Figure 5 shows how the depth of the honeycomb-stator cell influences predicted effective damping of the DTHCS. The peak damping clearly increases with increasing cell depth, but the peak becomes narrower and its frequency drops, emphasizing the need to match the frequency range of increased damping to the frequency range of concern for subsynchronous vibration in the specific application. The choice of 2.6 mm cell depth provides high damping over a broad frequency range.

## 4 Testing and Test Results

Figure 6 shows the test rig (described in detail by Childs and Hale [11]). In summary, a stiff rotor is mounted in very stiff hydrostatic bearings. High-pressure air is supplied to a central feeding groove between the sealing gaps of two nominally identical test seals. To achieve the high-pressure ratio across the seal required for the target application, the gas exhausts to atmosphere for these tests. Hydraulic shakers drive the seal's stator in two orthogonal directions, with a force measured by load cells and adjusted to achieve relative motion between stator and rotor of about one-tenth the clearance. Stator motion relative to the rotor is measured by eddy current displacement probes at both ends of the seal, in the same orthogonal planes as the applied shaker forces. Stator motion is constrained normal to the rotor by stabilizing bars. Accelerometers on the stator measure its acceleration along the orthogonal $x$ and $y$ axes. Processing the measurements of input force, rotor-stator relative displacement, and stator acceleration vectors over a range of excitation frequencies yields complex dynamic coefficient matrix elements for the test seal. Tare complex dynamic stiffness coefficients for the assembly, which are used to correct for the exit labyrinth seals, hoses, stabilizer bars, etc., are

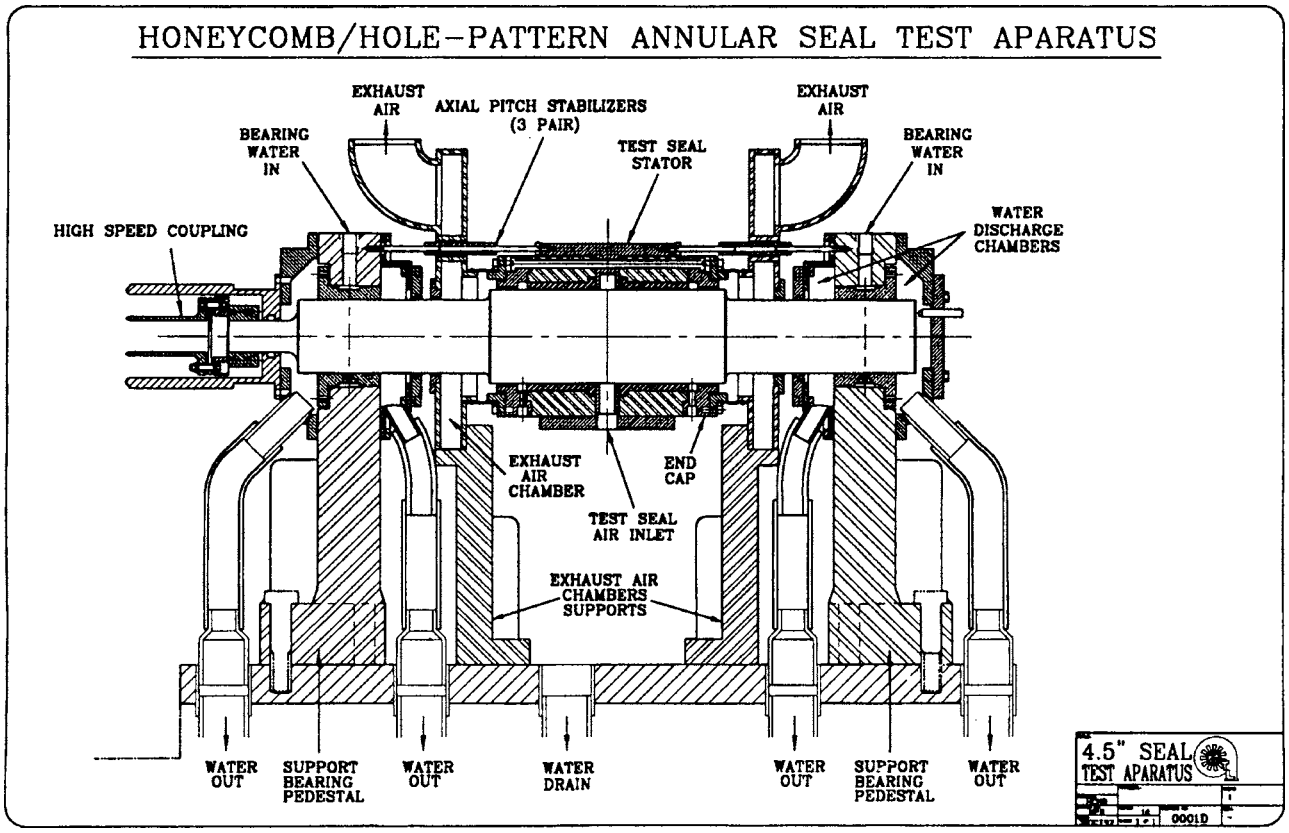


**Fig. 6 TAMU turbomachinery lab air seal test rig**

obtained by testing a seal pair with greatly enlarged clearances. The resulting coefficients for a single seal are simply half those obtained for the dual seal assembly.

Table 3 presents the specific characteristics of the seal as tested, including supply pressure, speed, low or high clearance, and summary predictions for straight and tapered configuration. The seal was tested at two clearances, three speeds, and three pressures in almost complete combination. However, the highest supply pressure combined with the tightest clearance produced a negative stiffness strong enough to pull the stator hard against the rotor, so this combination could not be tested and is not included in Table 3. For reduced supply-pressure cases, the shaker stiffness was sufficient to overcome the seal's negative stiffness. Table 1 shows the clearance values used in these predictions, which result from averaging diameter and bore measurements at a series of angles to account for small out of roundness in the stator.

Figures 7–10 compare predicted and measured values for effective stiffness and damping in two orthogonal directions under four test conditions. These figures present two high-clearance tests and two low-clearance tests over a range of speeds and pressures, from lowest to highest, keeping the volume of data presented manageable, while truly representative of the entire test data set. These figures show consistently good agreement between predictions and measurements, both in magnitude and characteristic behavior. In particular, the frequency and magnitude of the peak effective damping are well predicted, as are low-frequency trends to negative effective stiffness and damping.

Table 4 compares measured and predicted leakage under all conditions tested. Measured leakage lies consistently below predicted by between 20% and 35%. Leakage significantly impacts compressor efficiency and throughput, and the low leakage discrepancy is in the preferred direction. As a contributory factor to this discrepancy, the high-pressure ratio causes choking or sonic velocity to occur at some axial position in the seal. With a diverging taper, leakage is clearly influenced by the axial location where choking sets in. While not explaining the discrepancy, leakage

**Table 3 Summary of operating conditions and predicted characteristics for seals as tested**

| Pressure Bara | Speed RPM | Clearance | Straight $K_{eff}$ at 20 Hz | Diverging $K_{eff}$ at 20 Hz | Straight $C_{eff}$, Max | Diverging $C_{eff}$, Max | Straight Frequency of $C_{eff}$, Max | Diverging Frequency of $C_{eff}$, Max | Straight Flow Kg/s | Diverging Flow, Kg/s |
|---|---|---|---|---|---|---|---|---|---|---|
| 7.841 | 10200 | High | $-1.65E+06$ | $-2.76E+06$ | 2770 | 3260 | 80 | 80 | 0.0569 | 0.0768 |
| 7.901 | 17000 | High | $-1.63E+06$ | $-3.43E+06$ | 1670 | 2880 | 100 | 100 | 0.0569 | 0.0742 |
| 8.115 | 22000 | High | $-1.48E+06$ | $-3.37E+06$ | 1090 | 2250 | 130 | 110 | 0.0569 | 0.0742 |
| 18.250 | 10200 | High | $-2.35E+06$ | $-6.91E+06$ | 4650 | 8040 | 90 | 80 | 0.1423 | 0.1851 |
| 18.250 | 17000 | High | $-3.90E+06$ | $-6.70E+06$ | 3990 | 5310 | 110 | 110 | 0.1377 | 0.1851 |
| 18.250 | 22000 | High | $-3.69E+06$ | $-8.04E+06$ | 2710 | 5310 | 130 | 110 | 0.1377 | 0.1790 |
| 7.083 | 10200 | Low | $-2.90E+06$ | $-7.55E+06$ | 6110 | 14400 | 40 | 30 | 0.0202 | 0.0309 |
| 7.239 | 17000 | Low | $-2.83E+06$ | $-7.79E+06$ | 2300 | 10500 | 60 | 50 | 0.0202 | 0.0309 |
| 7.281 | 22000 | Low | $-4.62E+06$ | $-7.61E+06$ | 2910 | 8070 | 60 | 50 | 0.0191 | 0.0309 |

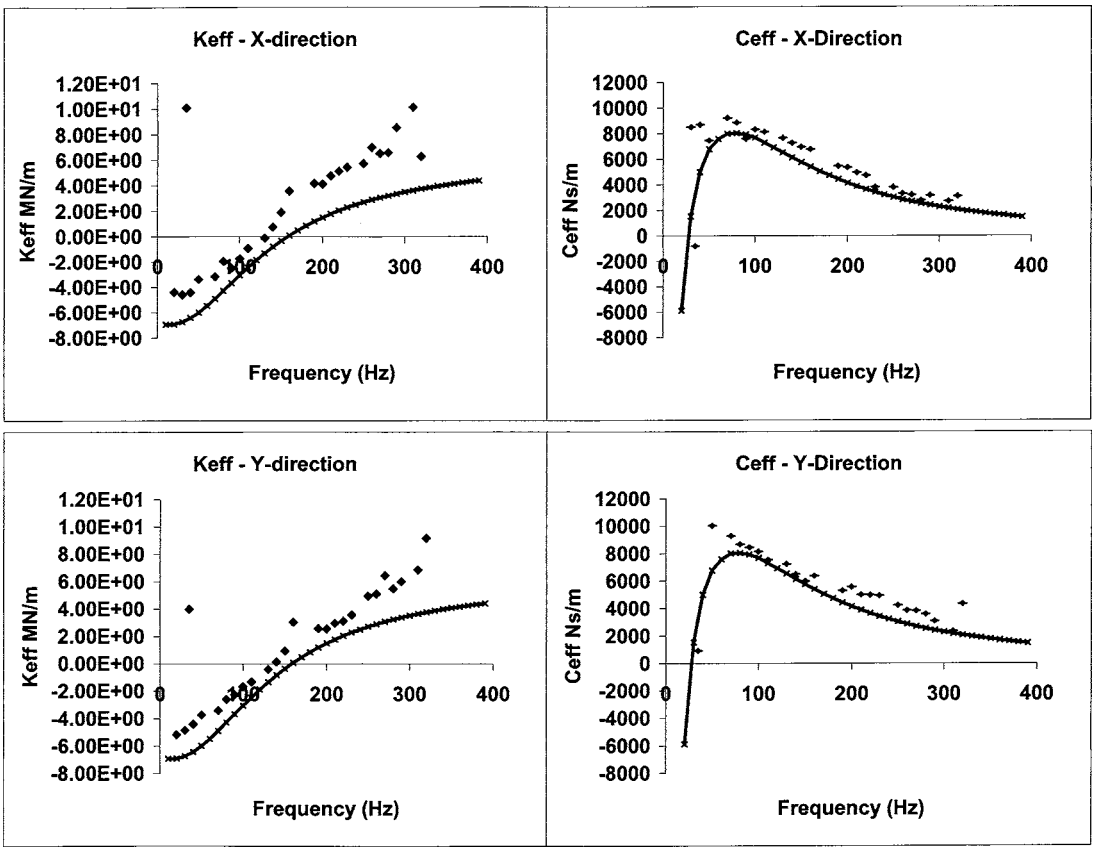


**Fig. 7 Comparison of predicted (line) and measured (data points) characteristics for the DTHCS at 10,200 rpm under 18.25 bar supply pressure with high clearance**

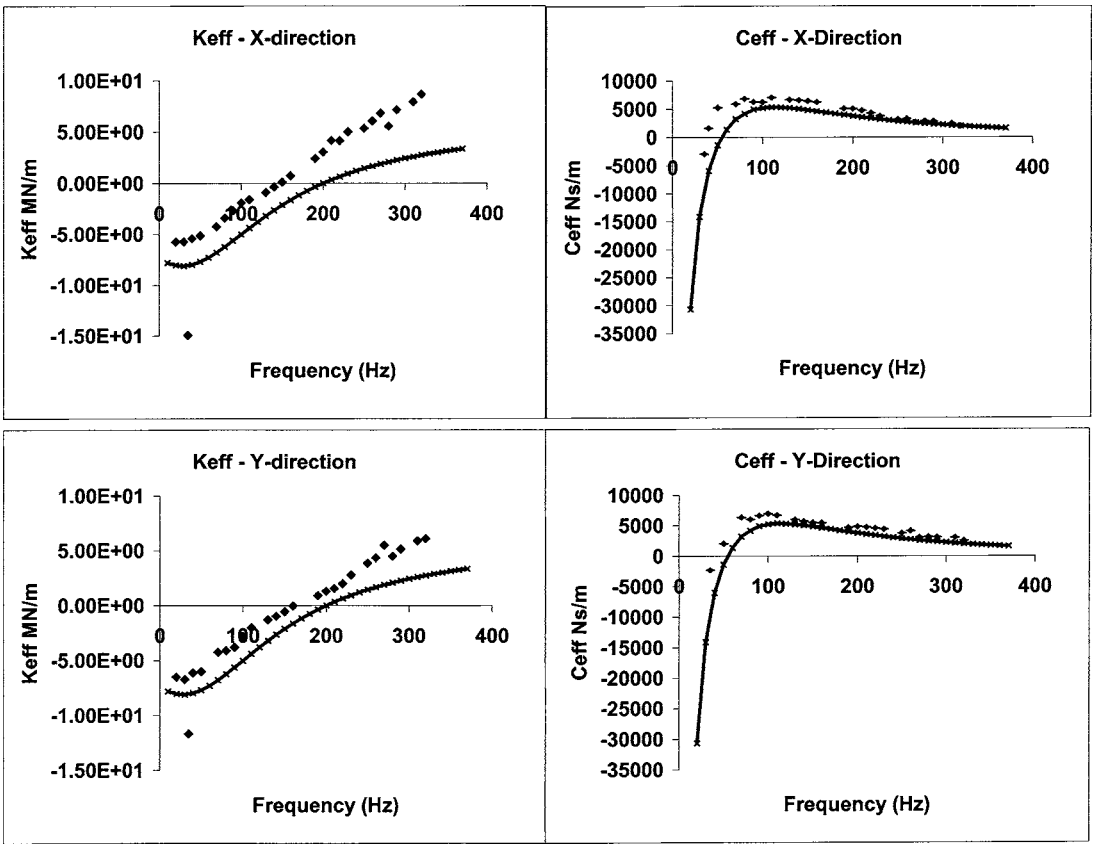


**Fig. 8 Comparison of predicted (line) and measured (data points) characteristics for the DTHCS at 22,000 rpm under 18.25 bar supply pressure with high clearance**

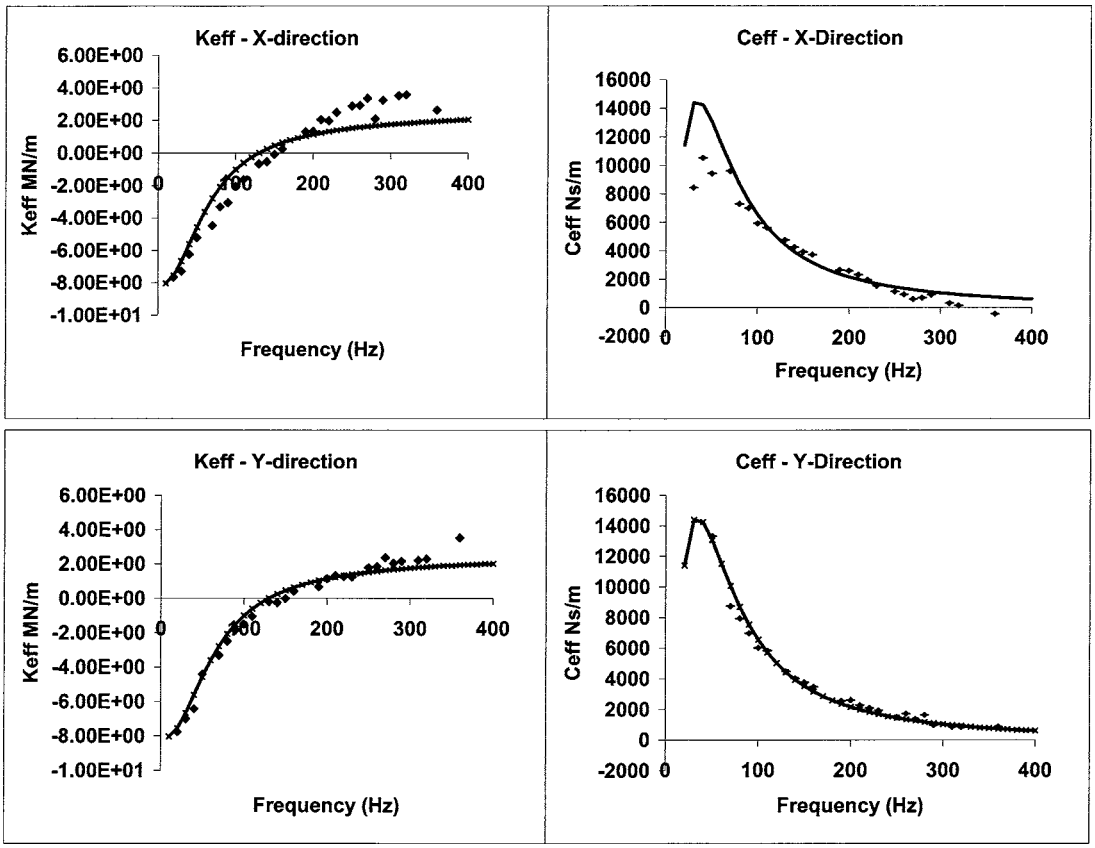


**Fig. 9 Comparison of predicted (line) and measured (data points) characteristics for the DTCHS at 10,200 rpm under 7.083 bar supply pressure with low clearance**

data in Table 3 show that flows predicted for a constant clearance equal to the inlet clearance match the measured data much more closely than the Table 4 data. Based on this observation, using a constant clearance solution just for leakage predictions may provide a working approach to bounding the flow uncertainty for balance pistons with diverging taper and high-pressure ratios across them.

## 5 Predictions for Target Compressor

Figure 11 compares the log decrement, as defined by Lund [12] at the first natural frequency of the target 65 MW compressor, predicted for several different balance piston configurations, including a labyrinth seal, a labyrinth with straight and reverse flow shunt holes, a straight honeycomb-stator seal, and a diverging taper honeycomb-stator seal (optimized for this application). Figure 11 shows that the most negative log decrement results from the conventional labyrinth. The straight honeycomb-stator design makes the predicted log decrement less negative. However, for this example, only the diverging taper honeycomb-stator seal provides a prediction of positive log decrement, and remarkably increases predicted log decrement by 0.6 relative to the plain labyrinth. This compressor in question has three side streams, which combined with the first stage suction stream, lead to gas compression through four different pressure ratios from individual stream suction to final discharge. The highest of these pressure ratios is close to 20—between first suction and final discharge. This leads to a similar pressure ratio across the balance piston. Damped natural frequencies were predicted for this compressor, accounting for aerodynamic excitation based on the following adaptation of the Wachel [13] method to account for the side streams:

$$(K_{XY})_i = 63{,}000^* \frac{\text{Mole Weight}}{10} \sum_{j=1}^{N_S} \frac{(\text{Horsepower})_{i,j}}{\text{rpm}^* D_i^* h_i} \left(\frac{\rho_D}{\rho_S}\right)_j \tag{3}$$

for wheel $i$, streams $j=1$ *to* $(N_S)_i$.

As predicted and confirmed by test, the DTHCS also develops a strong static negative stiffness. For the target application, the static deflection of the rotor in response to an external force of 4454 Newtons, applied at the balance piston location, is 15.06 microns without the addition of this negative stiffness; with the negative stiffness included, the deflection increases to 21.84 microns. The negative stiffness of the DTHCS essentially acts in parallel with the positive bearing stiffness; the effective system stiffnesses with and without the negative stiffness contribution are 296 and $204 \times 10^6$ N/m, respectively, indicating about 30% reduction caused by the DTHCS. Thus, while the influence of the DTHCS negative stiffness is apparent, the system maintains a strongly positive system stiffness. Any DTHCS application should include a comparable check on its possible contribution to static instability of the rotor-bearing system. In addition, the first damped natural frequency prediction must include all honeycomb dynamic coefficients, evaluated at the natural frequency. This may require an iterative process, to ensure the natural frequency and frequency of honeycomb seal evaluation are the same.

The diverging taper honeycomb-stator seal was maintained as an option if the full load string tests of the target propane compressor should indicate a need for it. The balance piston configuration used in the string tests was a labyrinth with reverse flow shunt holes—Case 3 in Fig. 11. The propane compressor was tested over a range of conditions and exhibited small subsynchronous vibrations, but these never exceeded 5 microns, leading to a decision that the reverse flow shunt hole labyrinth would not be

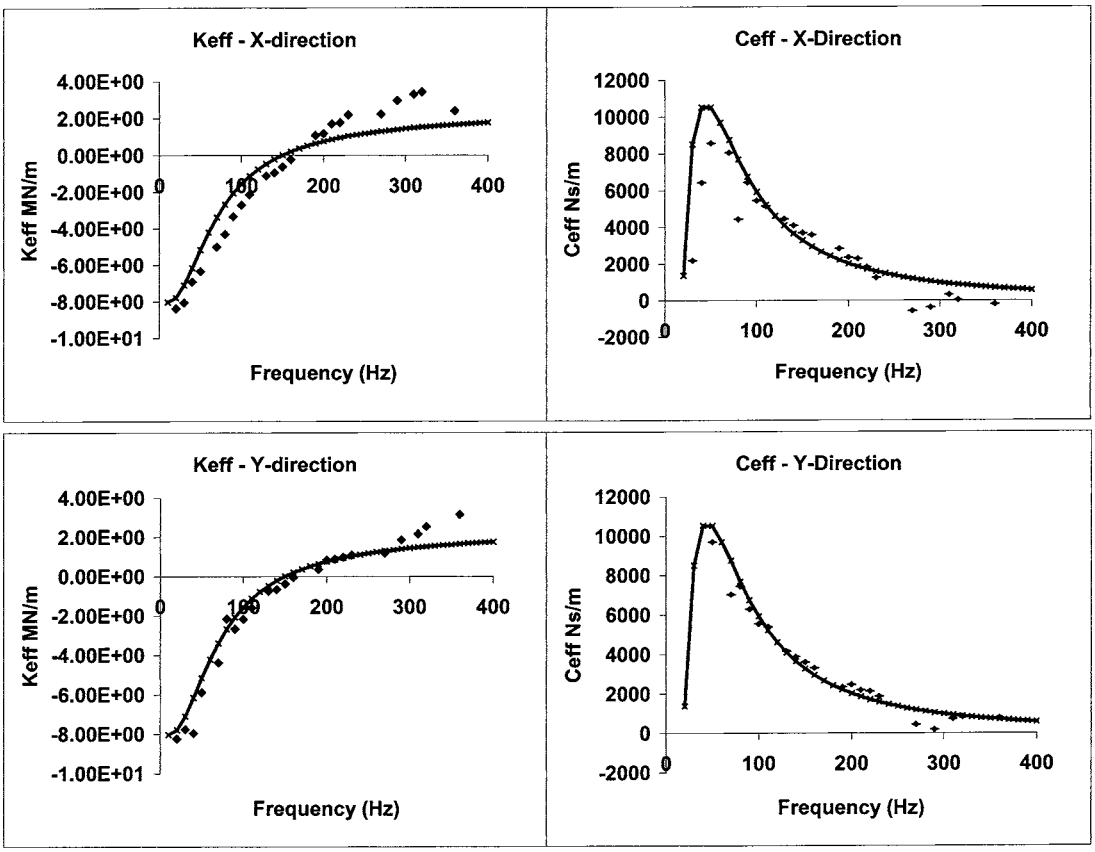


**Fig. 10 Comparison of predicted (line) and measured (data points) characteristics for the DTHCS at 17,000 rpm under 7.239 bar supply pressure with low clearance**

replaced with the diverging taper honeycomb-stator seal, since performance and vibration characteristics were acceptable without it.

## 6 Conclusions

- The diverging taper honeycomb-stator seal offers distinct advantages in achievable, effective, damping relative to a straight or constant clearance honeycomb-stator seal with the same minimum clearance.
- The peak effective damping can be a factor of 2 or more higher than that for the straight seal. Test results confirm that the computer program, ISOTSEAL, predicts effective stiffness and effective damping of the DTHCS with good accuracy over a range of conditions, sufficient for use as an engineering tool.
- For the conditions tested (very high pressure ratio across the seal), measured leakage is consistently lower than predicted leakage, by an amount in the range of 20 to 35%.
- Although physically inconsistent, predicted leakage with constant clearance equal to the minimum clearance of the diverging taper seal comes much closer to the measured data. By combining this with the leakage prediction for a diverging taper seal, the uncertainty in leakage may be bounded for these high-pressure ratio conditions.
- The diverging taper honeycomb-stator seal also has a distinct negative static stiffness, which must be considered when designing for a particular application. Other positive

**Table 4 Comparison of measured and predicted leakage for all tests**

| Clearance | Pressure Bara | Speed RPM | Measured Kg/s | Predicted Kg/s |
|---|---|---|---|---|
| High | 7.841 | 0200 | 0.0626 | 0.0768 |
| High | 7.901 | 17000 | 0.0620 | 0.0742 |
| High | 8.115 | 22000 | 0.0606 | 0.0742 |
| High | 18.255 | 10200 | 0.1409 | 0.1851 |
| High | 18.255 | 17000 | 0.1378 | 0.1851 |
| High | 18.255 | 22000 | 0.1332 | 0.1790 |
| Low | 7.083 | 10200 | 0.0230 | 0.0309 |
| Low | 7.239 | 17000 | 0.0212 | 0.0309 |
| Low | 7.281 | 22000 | 0.0199 | 0.0309 |

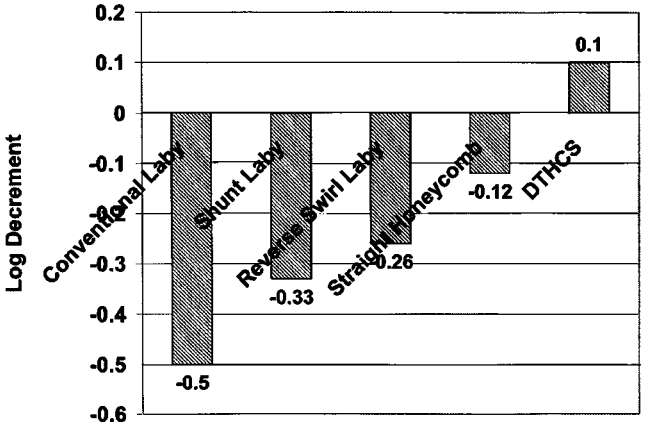


**Fig. 11 Comparison of predicted log decrement for various configurations of balance piston seal in target propane compressor**

stiffnesses acting on the rotor must be sufficient to provide a net positive system stiffness. In addition, care must be taken that the first natural frequency does not drop excessively, creating a negative effective damping for the seal at the natural frequency.

- For the particular application considered, the negative stiffness from the balance piston reduces positive system stiffness by about 30%. Thus, the system preserves positive static stability, and the effective damping at the first natural frequency is positive, large, and effective.
- However, the recent industrial test of a high pressure compressor under full load [10] clearly showed the need to evaluate seal stator and balance drum deformation under operating loads for the possibility of divergence, excessive negative stiffness, and reduction of the first natural frequency into a negative damping region. If a particular application exhibits this characteristic, corrective action must then be taken to eliminate, reduce, or compensate for the excessive structural deformation.

## Acknowledgment

The authors wish to acknowledge Shell Global Solutions for encouraging this investigation; Nuovo Pignone for supporting the testing and encouraging publication of this unique data set; and Southwest Research Institute® for supporting a number of supplementary analyses in the paper.

## Nomenclature

$C_{\text{effective}}$ = $C_{xx} - K_{xy}/\omega$
$C_{\text{in}}, C_{\text{out}}$ = inlet and outlet seal clearances
$C_{xx}$ = direct damping coefficient
$C_{xy}$ = cross-coupled damping coefficient
$D_i, h_i$ = diameter and flow passage width for wheel
$\rho_D/\rho_S$ = the ratio of discharge to suction density for wheel $i$
$(\text{Horsepower})i,j$ = power for wheel $i$ to compress stream $j$
$K_{\text{effective}}$ = $K_{xx} + \omega C_{xy}$
$K_{xx}$ = direct stiffness coefficient
$K_{xy}$ = cross-coupled stiffness coefficient
$(K_{XY})_i$ = cross-coupling for wheel $i$
$N_S$ = number of streams passing through wheel $i$
RPM = speed, revolutions per minute

## References

[1] Childs, D. W., Jordan, L. T., and Vance, J. M., 1997, "Annular Gas Seals and Rotordynamics of Compressors and Turbines," Proceedings 26th Turbomachinery Symposium, Houston, TX, pp. 201–220.
[2] Memmott, E. A., 1996, "Stability of an Offshore Natural Gas Centrifugal Compressor," 15th Machinery Dynamics Seminar, CMVA, Banff, Alberta, Canada.
[3] Memmott, E. A., 1994, "Stability of a High Pressure Centrifugal Compressor Through Application of Shunt Holes and a Honeycomb Labyrinth," 13th Machinery Dynamics Seminar, CMVA, Toronto, Canada.
[4] Memmott, E. A., 1998, "Stability Analysis and Testing of a Train of Centrifugal Compressors for High Pressure Gas Injection," ASME Paper No. 98-GT-378.
[5] Miller, H. F., 2002, "Centrifugal Pipeline Compressor Technology Evolution-High Pressure Pipeline Applications," GMRC Gas Machinery Conference, Nashville, TN.
[6] Vance, J. M., and Schultz, R. R., 1993, "A New Damper Seal for Turbomachinery," ASME 14th Biennial Conference on Mechanical Vibration and Noise, Albuquerque, NM, ASME, New York, DE-Vol. 60, pp. 139–148.
[7] Vance, J. M., and Li, J., 1996, "Test Results of a New Damper Seal for Vibration Reduction in Turbomachinery," ASME J. Eng. Gas Turbines Power, **118**, pp. 843–846.
[8] Yu, Z., and Childs, D. W., 1998, "A Comparison of Experimental Rotordynamic Coefficients and Leakage Characteristics Between Hole-Pattern Gas Damper Seals and a Honeycomb Seal," ASME J. Eng. Gas Turbines Power, **120**(4), pp. 778–783.
[9] Kleynhans, G. F., and Childs, D. W., 1997, "The Acoustic Influence of Cell Depth on the Rotordynamic Characteristics of Smooth-Rotor/Honeycomb-Stator Annular Gas Seals," ASME J. Eng. Gas Turbines Power, **119**(4), pp. 949–957.
[10] Camatti, M., Vannini, G., Fulton, J. W., and Hopenwasser, F., 2003, "Instability of a High Pressure Compressor Equipped With Honeycomb Seals," Proceedings Thirty-Second Turbomachinery Symposium, pp. 39–48.
[11] Childs, D., and Hale, K., 1994, "A Test Apparatus and Facility to Identify the Rotordynamic Coefficients of High-Speed Hydrostatic Bearings," ASME J. Tribol., **116**, pp. 337–344.
[12] Lund, J. W., 1974, "Stability and Damped Critical Speeds of a Flexible Rotor in Fluid-Film Bearings," J. Eng. Ind., **96**, pp. 509–517.
[13] Wachel, J. C., and von Nimitz, W. W., 1980, "Assuring the Reliability of Offshore Gas Compression Systems," European Offshore Petroleum Conference and Exhibition, London, England, EUR 205.

# Rotordynamic Force Coefficients of Pocket Damper Seals

**B. Ertas**
Vibrations/Dynamics Laboratory,
Rotating Equipment Group,
GE Global Research,
1 Research Circle,
Niskayuna, NY 12309
e-mail: ertas@research.ge.com

**A. Gamal**
e-mail: ajmg@tamu.edu

**J. Vance**
e-mail: jvance@tamu.edu

Mechanical Engineering Department,
Texas A&M University,
College Station, TX 77843-3123

*This paper presents measured frequency dependent stiffness and damping coefficients for 12-bladed and 8-bladed pocket damper seals (PDS) subdivided into four different seal configurations. Rotating experimental tests are presented for inlet pressures at 69 bar (1000 psi), a frequency excitation range of 20–300 Hz, and rotor speeds up to 20,200 rpm. The testing method used to determine direct and cross-coupled force coefficients was the mechanical impedance method, which required the measurement of external shaker forces, system accelerations, and motion in two orthogonal directions. In addition to the impedance measurements, dynamic pressure responses were measured for individual seal cavities of the eight-bladed PDS. Results of the frequency dependent force coefficients for the four PDS designs are compared. The conclusions of the tests show that the eight-bladed PDS possessed significantly more positive direct damping and negative direct stiffness than the 12-bladed seal. The results from the dynamic pressure response tests show that the diverging clearance design strongly influences the dynamic pressure phase and force density of the seal cavities. The tests also revealed the measurement of same-sign cross-coupled (cross-axis) stiffness coefficients for all seals, which indicate that the seals do not produce a destabilizing influence on rotor-bearing systems.*
[DOI: 10.1115/1.2221327]

## 1 Introduction

Present day turbomachinery requires the use of annular gas seals to impede flow of the working fluid from high-pressure regions to low-pressure regions. This is a necessity for achieving the thermodynamic efficiency and energy density indicative of modern day compressors and turbines. The most common type of annular gas seal is the labyrinth seal, which is used in turbines, compressors, and pumps. Some undesirable effects of labyrinth seals are the low-direct damping and high-cross-coupled stiffness forces that have little contribution to mitigating synchronous vibration response and also degrade the dynamic stability of rotor-bearing systems. Gas labyrinth seals possess negligible added mass terms and can generally be expressed by the reaction force model [1] as shown in Eq. (1). This equation relates the seal forces due to rotor motion and velocity through direct $(K_{XX}, K_{YY}, C_{XX}, C_{YY})$ and cross-coupled $(K_{XY}, K_{YX}, C_{XY}, C_{YX})$ linear force coefficients.

$$-\begin{bmatrix} F_X \\ F_Y \end{bmatrix} = \begin{bmatrix} K_{XX} & K_{XY} \\ K_{YX} & K_{YY} \end{bmatrix} \cdot \begin{bmatrix} X \\ Y \end{bmatrix} + \begin{bmatrix} C_{XX} & C_{XY} \\ C_{YX} & C_{YY} \end{bmatrix} \cdot \begin{bmatrix} \dot{X} \\ \dot{Y} \end{bmatrix} \quad (1)$$

Another type of annular gas seal that can be represented by the reaction force equation in Eq. (1) is the pocket damper seal (PDS). The development of the PDS [2] was driven by the need for a gas seal that possesses favorable rotordynamic characteristics, unlike the labyrinth seal. The PDS work in 1993 by Vance and Schultz showed significant positive direct damping and encouraged a decade of research focused on understanding and predicting the rotordynamic behavior of PDS. This work included the following milestones: Li and Vance [3] conducted the first rotating tests, Ransom [4] measured direct and cross-coupled coefficients, Laos [5] investigated a PDS with eight circumferential pockets, Li et al. [6] focused on direct and cross-coupled coefficients, and Vance et al. [7] observed the behavior for higher-frequency excitation. Although these series of tests provided significant insights into the effects of clearance ratio, rotor speed, excitation frequency, pressure ratio, and seal geometry; the tests were conducted for low inlet pressures not representative of centrifugal compressor pressures in the industry.

The main objective of this work was to experimentally investigate the effect of clearance ratio, pressure ratio, rotor speed, and excitation frequency on rotordynamic force coefficients at high inlet pressures of 69 bar (1000 psig) and rotor speeds to 20,200 rpm.

## 2 Test Seals

The 12-bladed seal, shown in Fig. 1, was manufactured by inserting bar stock into eight angular slots machined into the seal body where they were powder brazed in an oven under high temperature, followed by the machining of the inactive plenums. The 12-bladed seal was fabricated using this method due to the small blade-to-blade-spacing of the cavities in combination with the large cavity depth of 35.56 mm (1.4 in.). Two different configurations were tested with the 12-bladed PDS: (1) 1:1 clearance ratio and (2) 1:2 clearance ratio. The 1:1 clearance ratio represents the ratio of the inlet blade clearance area from the rotor surface to the exit blade annular clearance area from the rotor surface. For the 1:1 case both the inlet and exit areas are equivalent therefore labeling the configuration as a "straight through" seal with no notches. The second configuration, (the 1:2 clearance ratio) utilizes curvilinear notches (as shown in Fig. 1) on the exit blade making the exit clearance area from the rotor equal to two times the inlet clearance, which is referred to as a diverging clearance configuration.

The next set of seals tested were the eight-bladed PDS configurations, shown in Fig. 2. Unlike the 12-bladed seal the eight-bladed seal was manufactured from a single piece of round stock, therefore a brazing process was not required. Also, the eight-bladed seal was fabricated with different shaped cavities, rectangular notches rather than curvilinear notches, and rectangular blade profiles. The eight-bladed seal was tested for two clearance ratios, 1:1 clearance ratio (straight through configuration) and a 1:1.5 clearance ratio (diverging clearance). This seal is composed of four circumferential rows of eight equally spaced cavities, axially separated by three inactive plenums (no cavities). Four pressure taps were machined into the two middle cavities for pressure transducers, which will be discussed later. All test seal configurations possessed a 0.127 mm (0.005 in.) radial clearance from the rotor.

Contributed by the International Gas Turbine Institute (IGTI) of ASME for publication in the JOURNAL OF TURBOMACHINERY. Manuscript received October 1, 2005; final manuscript received February 1, 2006. IGTI Review Chair: R. S. Abhari. Paper presented at the ASME Turbo Expo 2006: Barcelona, Spain, May 8–11, 2006, Paper No. GT2006-91058.

  

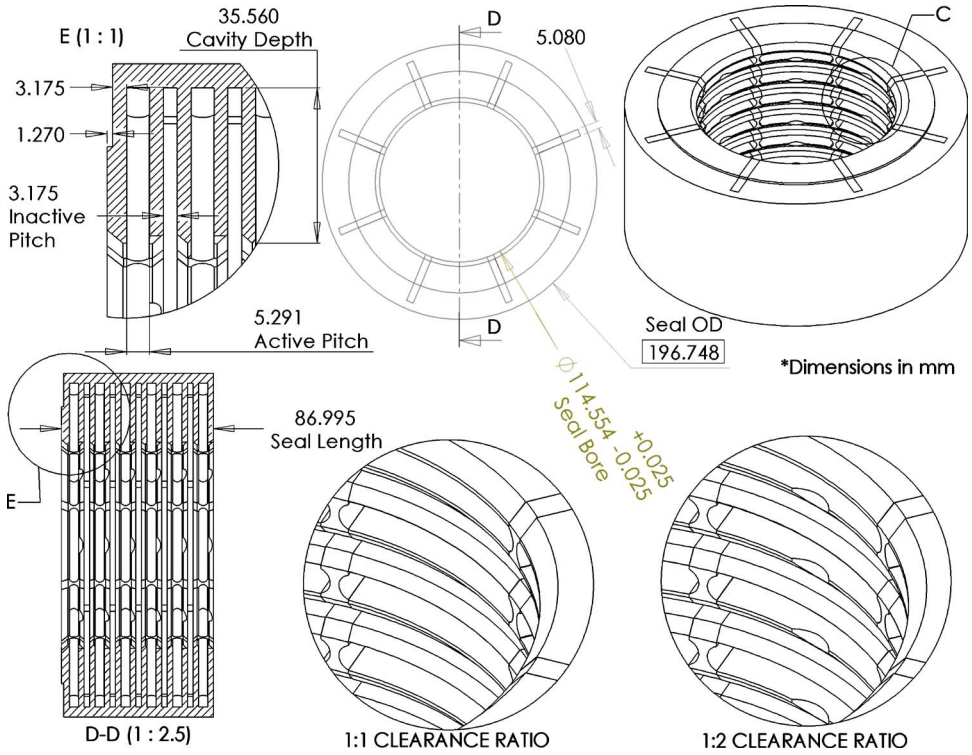


**Fig. 1 Twelve bladed PDS**

## 3 Experimental Test Rig

The main requirements for the testing were: (1) a test facility to support experiments at 68.9 bar (1000 psi); (2) the ability to asynchronously excite the system at variable frequencies up to 300 Hz in two orthogonal directions; and (3) rotor speeds of 10,200–20,200 rpm. The test rig layout is shown in Fig. 3. The high-pressure test rig was originally developed [8] to test hydrostatic bearings, but was later modified [9] to support testing of annular gas seals. A variable frequency motor drives the test rig through a gearbox. The rotor is supported by two hydrostatic water bearings and possesses a first natural frequency well above the test frequency range of 20–300 Hz.

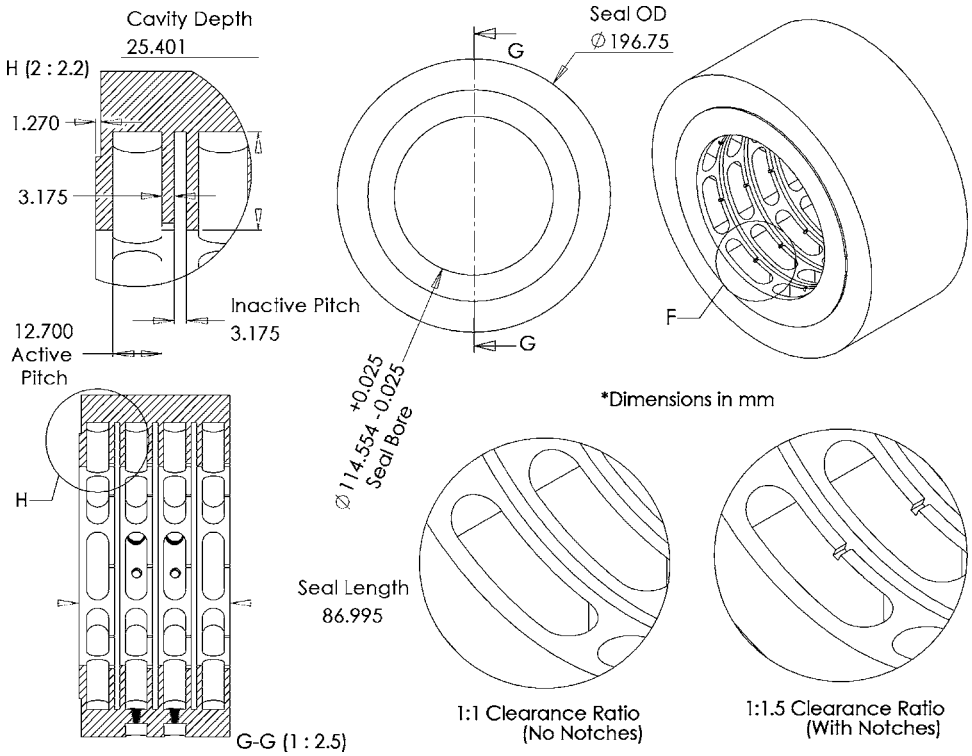


**Fig. 2 Eight bladed PDS**

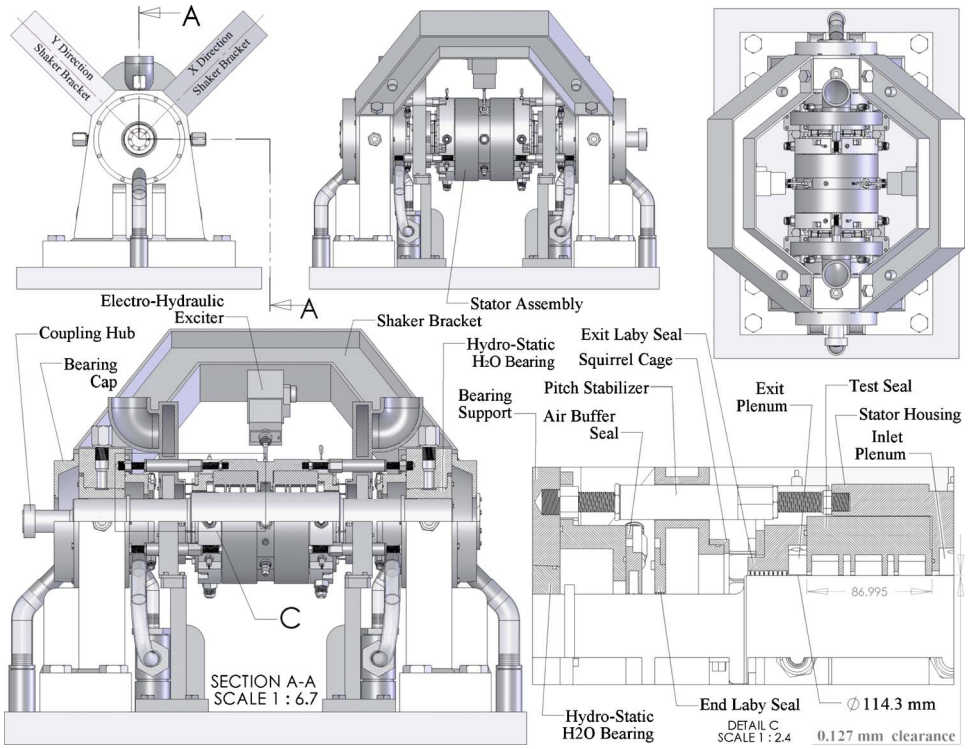


**Fig. 3 High-pressure annular gas seal test rig [12]**

The stator housing is a floating (suspended around rotor) assembly that interfaces the test rig at the bearing supports by the use of six pitch stabilizers (three on each end). To limit the axial thrust in the test rig the test seals are mounted in a back-to-back configuration where the inlet air is supplied at the center plenum (between the test seals) of the stator assembly. A preswirl ring was not used during testing. Several static and dynamic measurements were required during experiments. Figure 4 shows an isometric view of the stator assembly. The static measurements included static inlet pressure taken at the center inlet plenum of the stator housing, temperature at the inlet plenum, static back pressures at the exit of the test seals, and finally the exit gas temperature at the

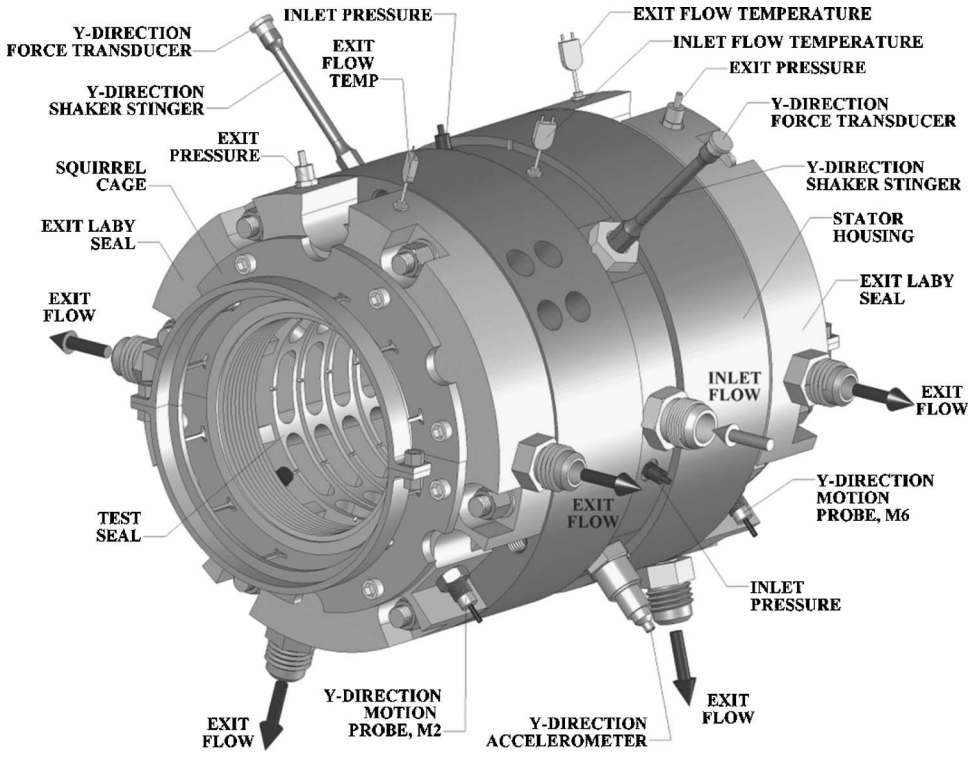


**Fig. 4 Stator housing isometric view with instrumentation**

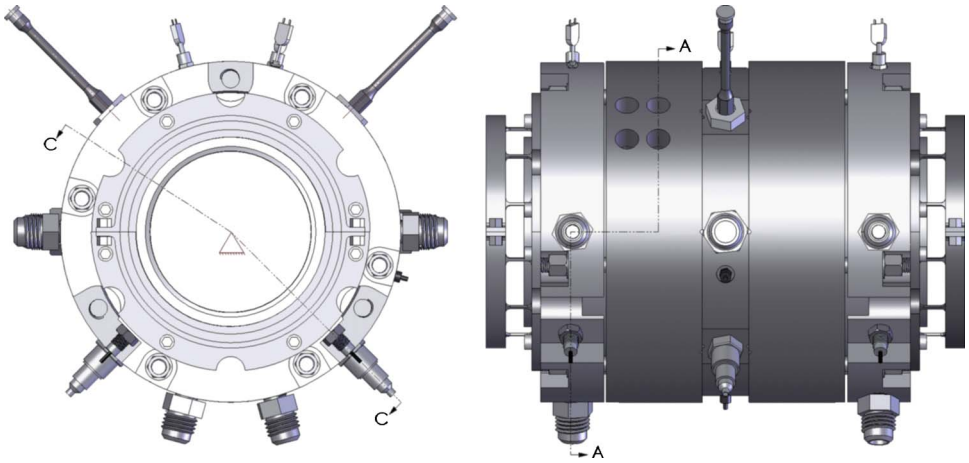


**Fig. 5 Stator housing front and side views**

test seal exit. The back pressure to the test seals was controlled by a valve that varies the flow through the three ports on each labyrinth seal. The exit pressure for the two labyrinth seals was controlled within 0.69 bar of one another. Each labyrinth seal possessed a radial clearance of 0.102 mm (0.004 in.) from the rotor and was required to hold the back pressure during testing.

Figure 5 shows the standard views of the stator assembly and Fig. 6 represents the A-A cross-sectional front view showing the instrumentation for dynamic measurements. The first method of testing performed in the experiments was the system impedance method, which required the measurement of the external system dynamic forces, stator displacement motion, and stator acceleration. The forced excitation was achieved using two orthogonally mounted electrohydraulic shakers, which possess a static preload capability of 4.448 kN, a 0-pk dynamic force output of 4.448 kN, and a frequency range of 1000 Hz. Four proximity probes were installed through the laby seals, two in line with the *X* direction and two in line with the *Y* direction, which were used to measure the relative motion between the stator housing and the rotor. The static eccentricity of the test seal was controlled to 0.0025 mm, while the 0-pk excitation was 0.0228 mm.

In addition to the impedance method dynamic cavity pressures were measured in combination with relative stator-rotor vibration. The dynamic pressure readings were used to better understand the dynamics and differences between the various PDS seal configurations.

## 4 Impedance Method

The method used to determine frequency dependent force coefficients was the system impedance method [8]. It is labeled as an impedance method because the method measures the total system impedance, which is comprised of the pitch stabilizers, exit labyrinth seals, squirrel cage radial stiffeners, and the test seals. The first step in the derivation was to develop the equations of motion for the stator housing assembly shown in Fig. 6. Note that the

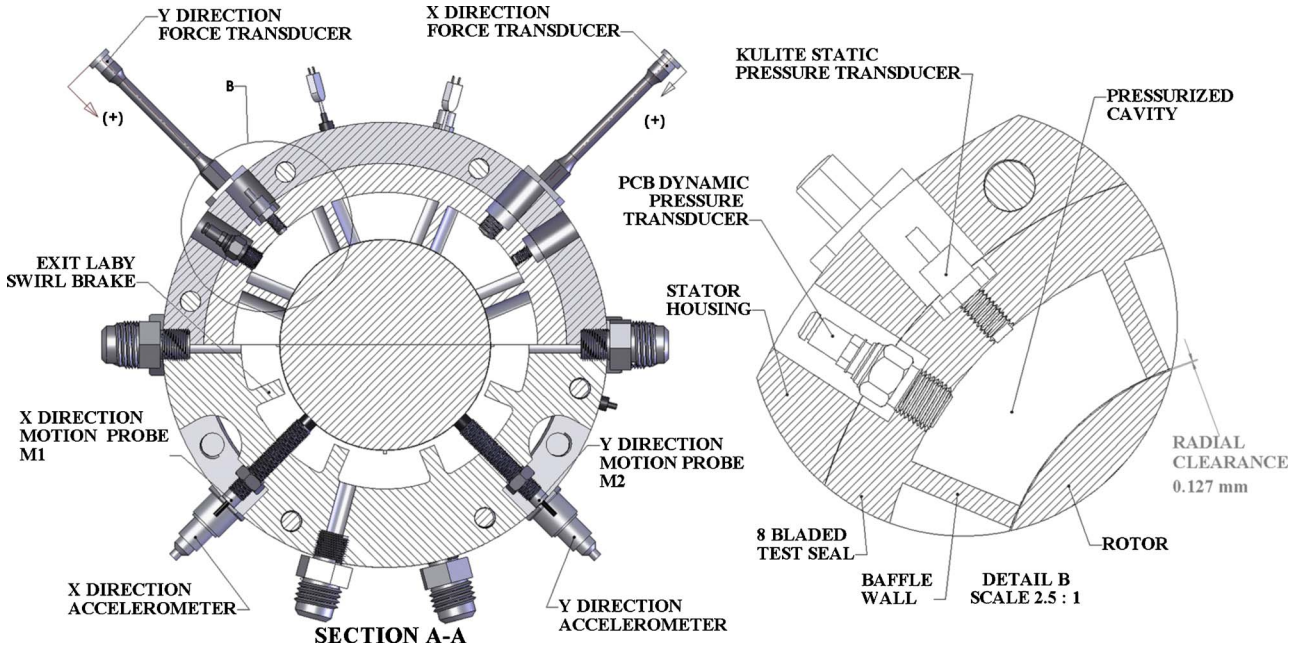


**Fig. 6 Dynamic measurements**

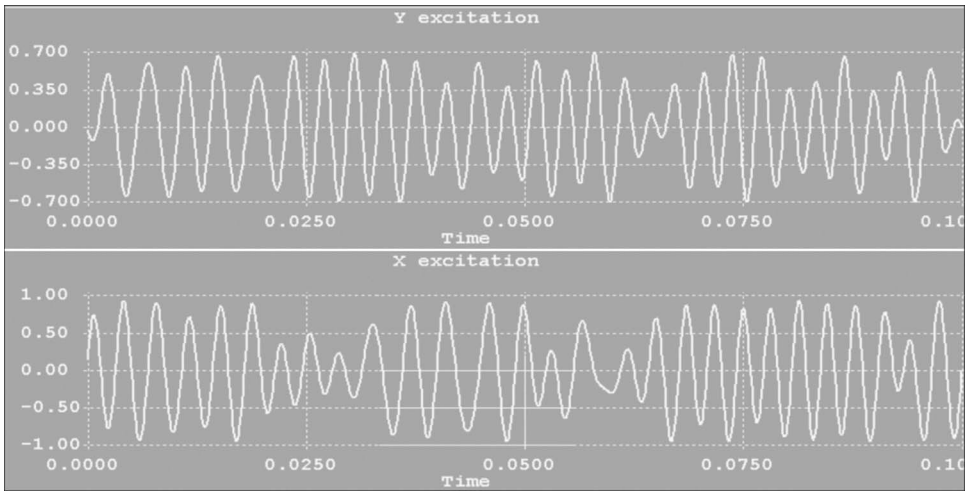


**Fig. 7** ***X*** **and** ***Y*** **direction pseudorandom forced excitations**

complex equations of motion are derived in the frequency domain, and that each equation possesses a real component (determines stiffness) and an imaginary component (determines damping). Equations (2) and (3) show the $X$ direction force equations, where Eq. (2) represents the direct equation of motion and Eq. (3) represents the cross-coupled equation of motion. Equations (4) and (5) show the $Y$ direction equations of motion. The left-hand side of Eqs. (2)–(5) is the effective force components (Eqs. (6)–(9)), which are defined as the dynamic shaker forces minus the stator inertia forces from the system, where $M$ is the stator assembly mass and $A_{ij}$ is the measured system acceleration from the accelerometers.

$X$ Direction equations of motion

$$F_{xx} - MA_{xx} = (K_{xx} + j\omega C_{xx}) \cdot D_{xx} + (K_{xy} + j\omega C_{xy}) \cdot D_{xy} \quad (2)$$

$$F_{yx} - MA_{yx} = (K_{xx} + j\omega C_{xx}) \cdot D_{yx} + (K_{xy} + j\omega C_{xy}) \cdot D_{yy} \quad (3)$$

$Y$ Direction equations of motion

$$F_{yy} - MA_{yy} = (K_{yy} + j\omega C_{yy}) \cdot D_{yy} + (K_{yx} + j\omega C_{yx}) \cdot D_{yx} \quad (4)$$

$$F_{xy} - MA_{xy} = (K_{yy} + j\omega C_{yy}) \cdot D_{xy} + (K_{yx} + j\omega C_{yx}) \cdot D_{xx} \quad (5)$$

Effective forces in $X$ direction

$$f_{xx} = F_{xx} - MA_{xx} \quad (6)$$

$$f_{yx} = F_{yx} - MA_{yx} \quad (7)$$

Effective forces in $Y$ direction

$$f_{yy} = F_{yy} - MA_{yy} \quad (8)$$

$$f_{xy} = F_{xy} - MA_{xy} \quad (9)$$

Also note that each force equation has a contribution of direct coefficients and cross-coupled coefficients.

The next step is to define direct and cross-coupled impedances (Eqs. (10)–(13)). Substituting Eqs. (6)–(13) into Eqs. (2)–(5) yields the final equation of motion in matrix form (Eq. (14)). The force matrix of Eq. (14) and the displacement matrix are terms that are measured during testing. These measurements can be used to solve for the impedances (Eqs. (15)–(18)), which are composed of stiffness and damping terms.

Direct and cross-coupled impedance for $X$ direction

$$H_{xx} = K_{xx} + j\omega C_{xx} \quad (10)$$

$$H_{xy} = K_{xy} + j\omega C_{xy} \quad (11)$$

Direct and cross-coupled impedance for $Y$ direction

$$H_{yy} = K_{yy} + j\omega C_{yy} \quad (12)$$

$$H_{yx} = K_{yx} + j\omega C_{yx} \quad (13)$$

Final equation of motion in matrix form

$$\begin{bmatrix} f_{xx} & f_{yx} \\ f_{xy} & f_{yy} \end{bmatrix} = \begin{bmatrix} H_{xx} & H_{xy} \\ H_{yx} & H_{yy} \end{bmatrix} \cdot \begin{bmatrix} D_{xx} & D_{yx} \\ D_{xy} & D_{yy} \end{bmatrix} \quad (14)$$

Direct impedance in $X$ direction

$$H_{xx} = \frac{f_{xx} \cdot D_{yy} - f_{yx} \cdot D_{xy}}{D_{xx} \cdot D_{yy} - D_{yx} \cdot D_{xy}} \quad (15)$$

Cross-coupled impedance in $X$ direction

$$H_{xy} = \frac{f_{xx} \cdot D_{yx} - f_{yx} \cdot D_{xx}}{D_{xy} \cdot D_{yx} - D_{yy} \cdot D_{xx}} \quad (16)$$

Direct impedance in $Y$ direction

$$H_{yy} = \frac{f_{yy} \cdot D_{xx} - f_{xy} \cdot D_{yx}}{D_{yy} \cdot D_{xx} - D_{yx} \cdot D_{xy}} \quad (17)$$

Cross-coupled impedance in $Y$ direction

$$H_{yx} = \frac{f_{yy} \cdot D_{xy} - f_{xy} \cdot D_{yy}}{D_{xy} \cdot D_{yx} - D_{yy} \cdot D_{xx}} \quad (18)$$

The force excitation used in the tests was a pseudorandom complex frequency waveform tailored to contain several frequencies in the signal that acts as the reference input signal from which all other signals are phased. A waveform was constructed for each of the PDS configurations by performing single frequency amplitude tests for $X$ and $Y$ directions to determine the amplitude ratio between the different frequency components. Unlike single frequency excitation tests, which require a separate test for each frequency, performing a test using a multitone excitation yields results for multiple frequencies, therefore requiring only one shake test. Figure 7 illustrates an example excitation waveform in the $X$ and $Y$ directions, which were administered independently. Each test contained 32 0.1 s long excitations resulting in 3.2 s of data collection in each direction.

Figure 8 shows dynamic measurements recorded for a $Y$ direction excitation of the stator assembly. Measurements shown in this figure include forces in the $X$ and $Y$ directions ($FX$ and $FY$), stator accelerations ($AX$ and $AY$), and stator motion relative to the rotor surface (M1, M5, M2, and M6). The black time trace represents the $Y$ direction shaker force input, and the red trace shows the vibration response of the stator assembly in the $Y$ direction. Also

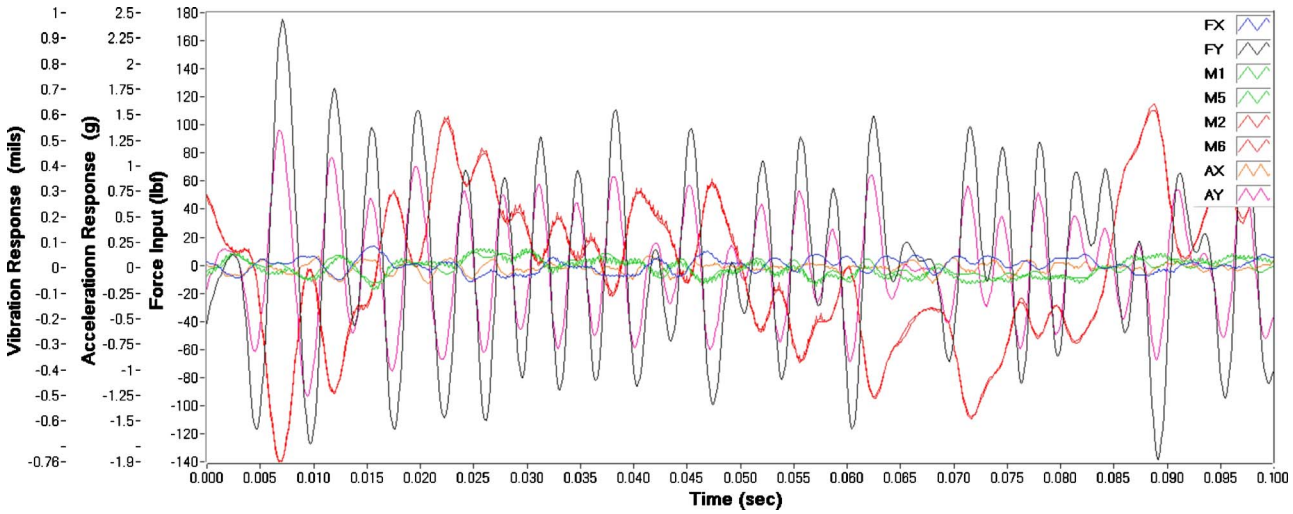


**Fig. 8 Experimental measurements: Impedance method [12]**

shown in Fig. 8 is the stator acceleration measurement used to subtract the inertial forces. The four impedance functions were generated through independent excitations int the $X$ and $Y$ directions.

Before determining the test seal coefficients, one must realize that the impedance measured in the procedure described above is the system impedance, which is composed of contributions from the entire mechanical system such as the pitch stabilizers, exit labyrinth seals, and the radial squirrel cage stiffeners. Extracting the PDS force coefficients will require a separate assembly of the test rig and a baseline test using baseline or blank inserts in place of the test seals. The objective of the baseline test is to measure the contribution of all other components in the system other than the test seals. This is achieved by replacing the test seals by smooth baseline seals (Fig. 9) with large clearances from the rotor resulting in negligible effects from the inserts. After measuring the system impedance with the baseline inserts $[H_{ij}]_{\mathrm{BL}}$ it is subtracted from the system impedance with the test seals $[H_{ij}]_{\mathrm{TS}}$ yielding the resultant test seal impedance $[H_{ij}]_R$ (Eq. (19)). A baseline test was conducted for all combinations of pressure ratios and rotor speeds.

$$\begin{bmatrix} H_{xx} & H_{xy} \\ H_{yx} & H_{yy} \end{bmatrix}_R = \begin{bmatrix} H_{xx} & H_{xy} \\ H_{yx} & H_{yy} \end{bmatrix}_{\mathrm{TS}} - \begin{bmatrix} H_{xx} & H_{xy} \\ H_{yx} & H_{yy} \end{bmatrix}_{\mathrm{BL}} \tag{19}$$

## 5 Pressure Measurements

The objective of the dynamic pressure measurements was to gain a deeper understanding of the dynamic behavior between the different PDS configurations. Figure 10 shows a cross-sectional view (defined in Fig. 5) of the eight-bladed PDS. The testing scheme involved shaking the stator assembly with respect to the rotor in the $Y$ direction and measuring vibration motion, static inlet pressure, static back pressure, static cavity pressures, inlet flow temperature, and dynamic cavity pressures. Note that the dynamic pressures were measured for the cavity inline with the $Y$ direction stinger. The excitation signal was chosen to be a fixed sine wave for the frequency range of 20–200 Hz and all tests were conducted with the same pressure differential 31.7 bar (460 psi) with an inlet plenum pressure of 68.9 bar (1000 psi). An example measurement of the cavity dynamics is shown in Fig. 11. This figure shows the front control panel for data acquisition, where all the results are displayed for cavities 3 and 5.

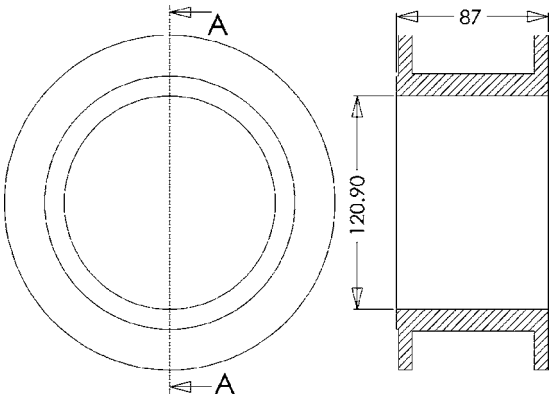


**Fig. 9 Baseline insert**

The methodology for experimentally determining the direct cavity coefficients was based on two equations (Eqs. (20) and (21)). These equations define the direct stiffness and damping contributions from a single cavity in a PDS, where $A_p$ is the projected area of a single cavity, $y$ is the 0-pk vibration amplitude, $\omega$ is the vibration frequency, and $P_{S,C}$ are the pressure components with respect to the displacement and velocity. To better understand the terms in Eqs. (20) and (21) refer to the example vibration signal and pressure signals shown in Fig. 12. Consider a sinusoidal motion $Y(t)$ with two different types of cavity pressure signals $P_1(t)$ and $P_2(t)$. The $P_2(t)$ signal is considered to have a phase angle that leads the vibration motion by an angle $90 > \phi 2 > 0$ and the $P_1(t)$ signal leads the vibration by an angle $90 > \phi 1 > 180$. These time trace signals can be represented as rotating vectors with the reference zero angle defined at $Y(t)$. The $Y$ direction displacement therefore is related to the stiffness coefficient and the $\dot{Y}$direction represents the velocity, which relates to the damping coefficient. Next, the two pressure signals $P_1(t)$ and $P_2(t)$ can be decomposed into the two directions defined by $Y$ and $\dot{Y}$. The dynamic pressure $P_2(t)$ has both components in line with the displacement and velocity whereas $P_1(t)$ possesses a component in phase with the velocity but 180 deg out of phase with the displacement. When the pressure components are in phase with the displacement and velocity, they produce a positive reaction force against the stator displacement and velocity, hence yielding positive stiffness and damping terms. For phase angles between 180 deg and 90 deg the cavity pressure $P_1(t)$ resolves into positive damping and negative stiffness terms.

$$\text{Direct damping:} \quad C_{yy} = \frac{P_S \cdot A_P}{\omega \cdot y} \tag{20}$$

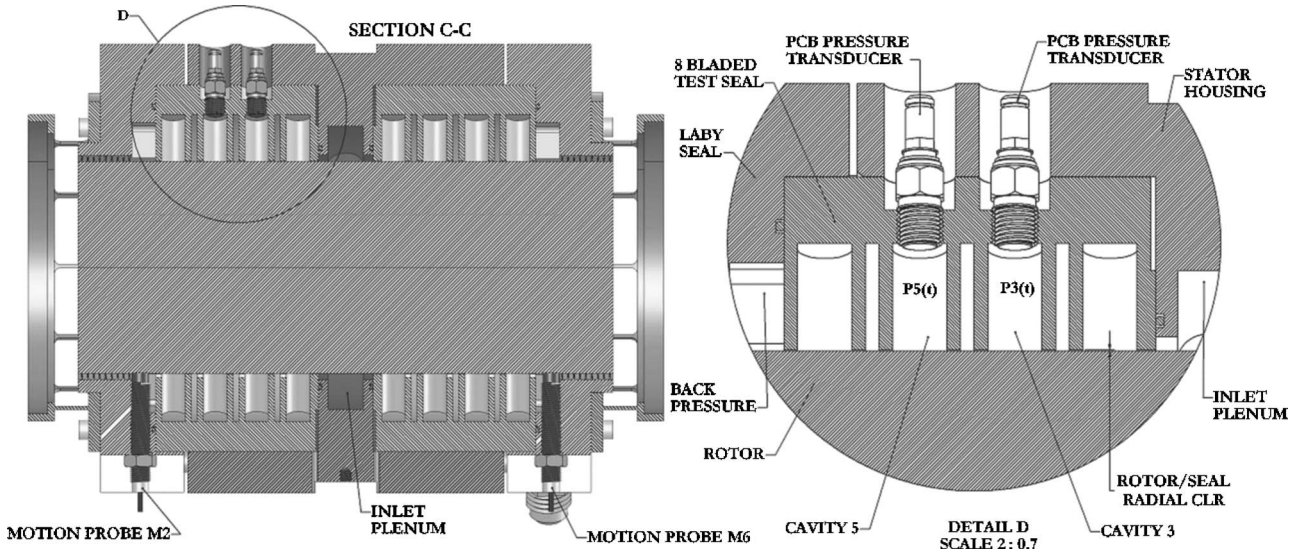


**Fig. 10 Dynamic cavity pressures**

$$\text{Direct stiffness:} \quad K_{yy} = \frac{P_C \cdot A_P}{y} \tag{21}$$

## 6 Rotordynamic Coefficients

This section presents asynchronous frequency dependent rotordynamic coefficients for various rotor speeds and pressure ratios. Each plot shows results for a single rotor speed but different clearance ratios (CR) and pressure ratios ($PR = P_{out}/P_{in}$). All tests were performed with a 69 bar inlet pressure. Figures 13 and 14 show the direct stiffness and damping coefficients for the straight-through and diverging clearance eight-bladed PDS configurations at 10,200 rpm and 20,200 rpm, respectively. The effect of pressure ratio in the straight through configuration seems to be most

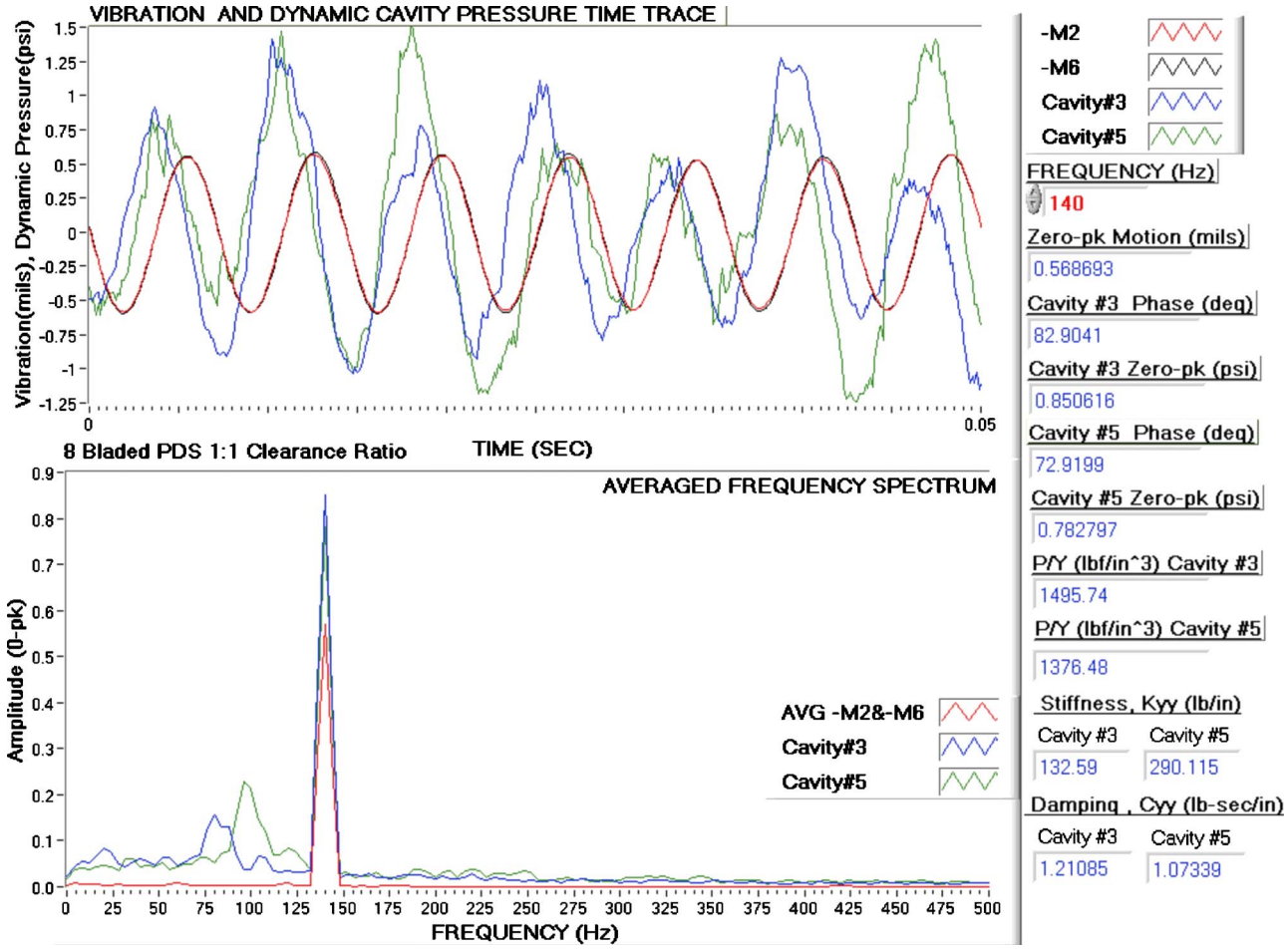


**Fig. 11 Experimental measurements: Dynamic pressure response method**

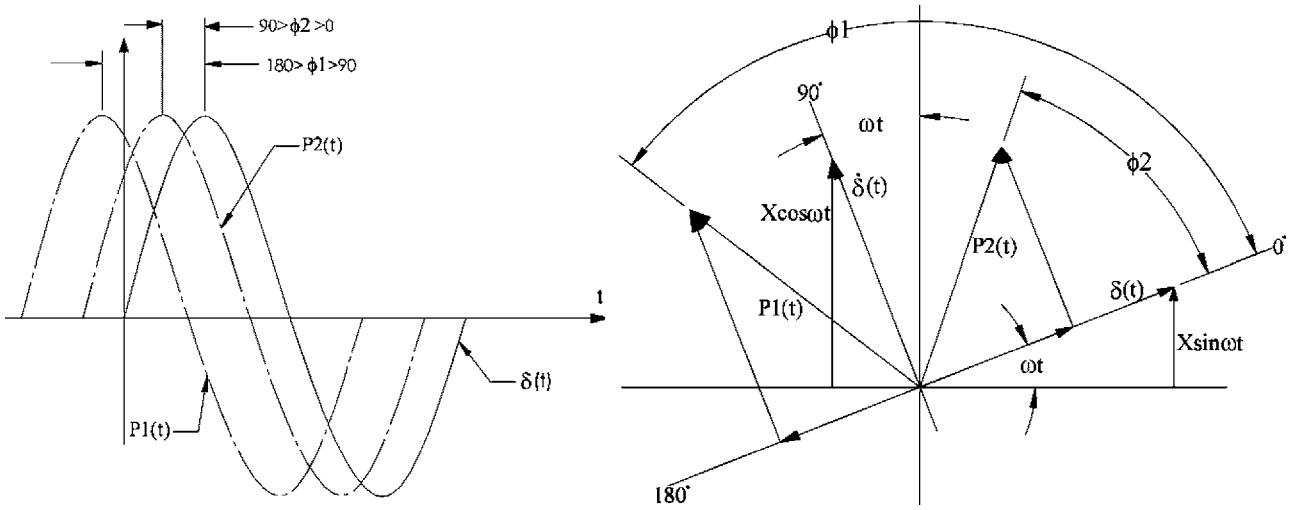


**Fig. 12 Phasor plot: Dynamic pressure response**

prominent at lower frequency ranges of 20–80 Hz, but for higher frequencies the effect of pressure ratio on the direct damping is small. The damping plots in these figures suggests that the parameter which influences the damping capacity the most is the clearance ratio, when comparing the 1:1 clearance ratio cases with the 1:1.5 clearance ratio test. The rotor speed has very little if any effect on the direct damping values of the eight-bladed results in Figs. 13 and 14. Also shown in Figs. 13 and 14 are the results for the direct stiffness of the eight-bladed PDS configurations. The stiffness results show almost identical values for the high-pressure and medium-pressure ratio cases, whereas the low-pressure case of PR= ~0.1 and clearance ratio 1:1 shows lower stiffness even though the pressure differential across the seal is larger.

The diverging 1:1.5 clearance ratio seal possesses negative stiffness throughout the entire frequency range and is significant in magnitude, especially at low frequencies. The direct force coefficients of the 12-bladed PDS results are plotted with two cases from the eight-bladed PDS results at 10,200 rpm (Fig. 15). The results shown in Fig. 15 indicate that increasing the number of blades results in smaller valued direct stiffness and damping. Note that the pressure ratio of the 12-bladed PDS are on the order of ~0.2 compared to ~0.5. The results for high-pressure ratios (smaller pressure differentials) for the 12-bladed PDS yielded even smaller valued coefficients that were within the uncertainty of the data, and are therefore not presented here.

The direct damping of all the tested seals decreases with increasing frequency and is almost maximized around the frequency where most multistage compressors have stability problems (50–80 Hz). This behavior makes these seals ideal for application in combination with squeeze film dampers, which usually decreases the first eigenvalue frequency due to the compliant bearing supports. The behavior is opposite from that of honeycomb or hole-pattern seals, which lose their effective damping at lower frequencies around 50 Hz as shown by Sprowl and Childs [10]. The negative stiffness behavior of the diverging clearance seals typically lowers the first critical speed of a compressor about 5% and also contributes toward making the seal compatible with a squeeze film bearing support dampers.

Next, the cross-coupled stiffness coefficients for the eight-bladed and 12-bladed PDS configurations are shown in Figs. 16 and 17. The main conclusion from these results is that the cross-

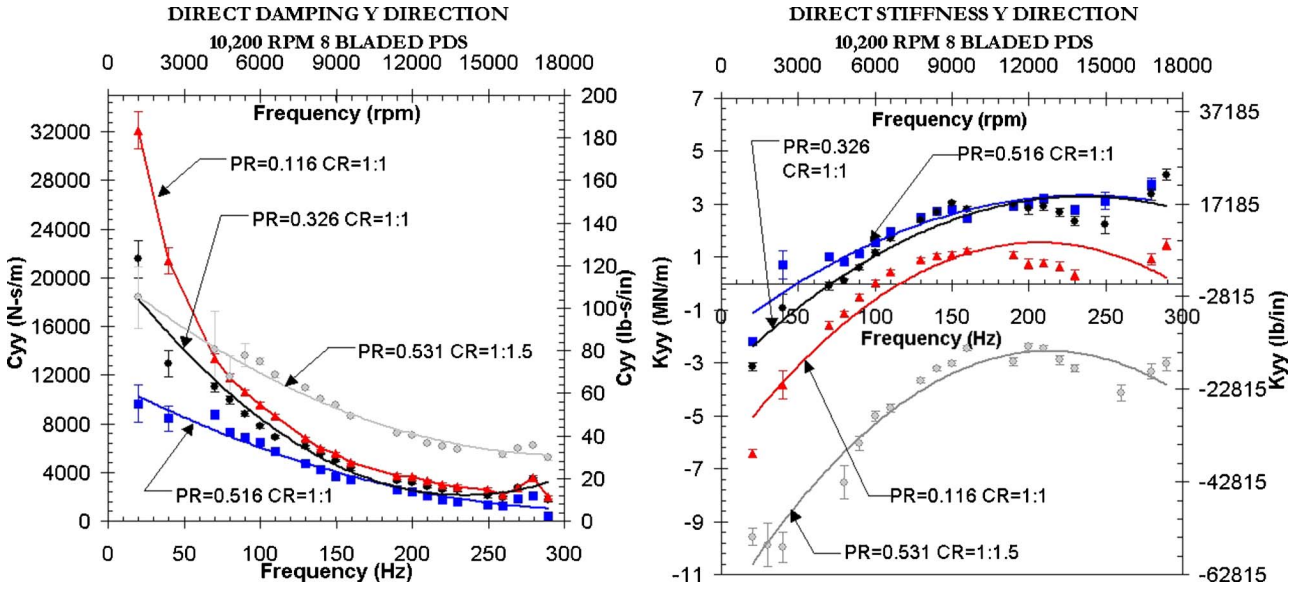


**Fig. 13 Direct stiffness and direct damping: 8 bladed PDS 10,200 rpm**

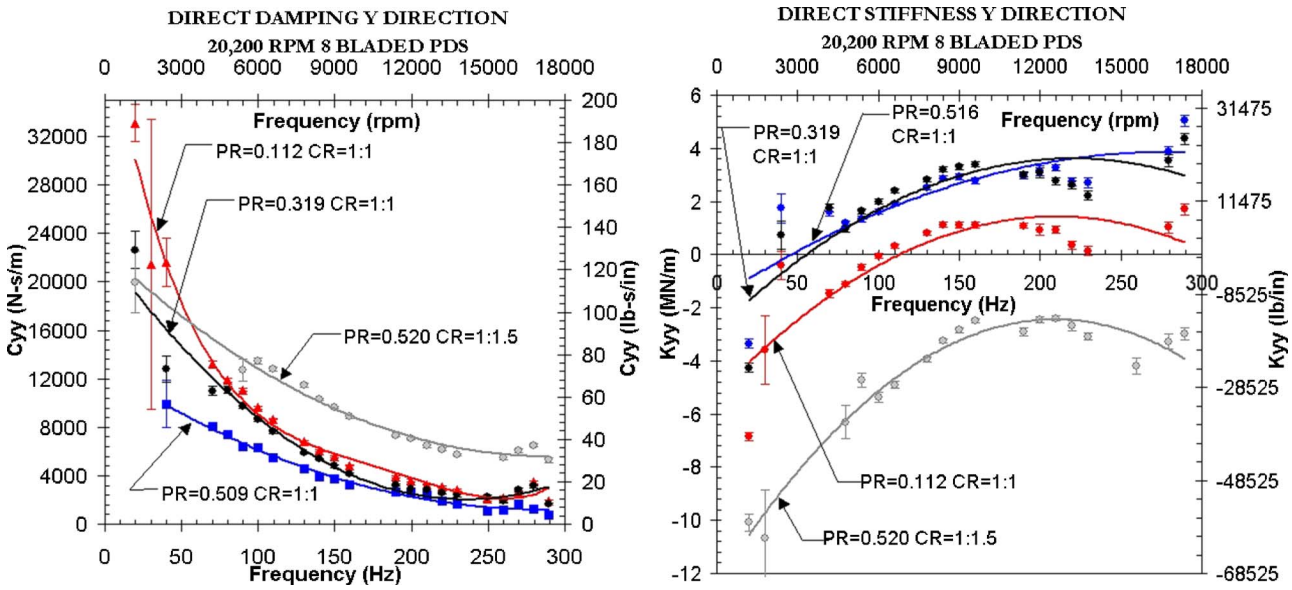


**Fig. 14 Direct stiffness and direct damping: 8 bladed PDS 20,200 rpm**

coupled stiffness coefficients are small in magnitude compared to the direct stiffness and are of the same sign, indicating a stabilizing effect rather than a destabilizing effect on rotor-bearing systems. The measurement of same sign stiffness coefficients of PDS for high-speed operation (15,200 rpm) was verified through separate static displacement tests [11] by measuring stator displacement and internal static cavity pressures. Static tests were successfully conducted given that the negative stiffness of the PDS were smaller in magnitude of the baseline stiffness of the test rig, namely, the positive stiffness of the pitch stabilizers and electrohydraulic shakers. Gamal [12] also verified this result through nonrotating static tests, by measuring displacement and external shaker forces. The last impedance plot is the cross-coupled damping of the 12-bladed PDS (Fig. 18). These coefficients are of little importance due to significantly small magnitudes and the fact that they act like direct stiffness.

## 7 Dynamic Pressure Response

In the previous section it was shown that the diverging eight-bladed PDS possessed significantly more direct negative stiffness and more positive direct damping compared to the straight-through eight-bladed PDS. The following experiments were conducted to determine the reason for the change in coefficients by measuring two metrics: (1) dynamic pressure phase of individual seal cavities and (2) the cavity force density.

The dynamic pressure phase for cavities 3 and 5 in line with the *Y* direction shaker stinger is shown in Fig. 19. Although the pressure phases for the two cavities are similar at lower frequencies (generating positive damping and negative stiffness), the straight through 1:1 clearance ratio (CR) cavity shows more frequency dependence. Furthermore, the straight through seal cavities transition from negative stiffness to positive stiffness at 100 Hz for

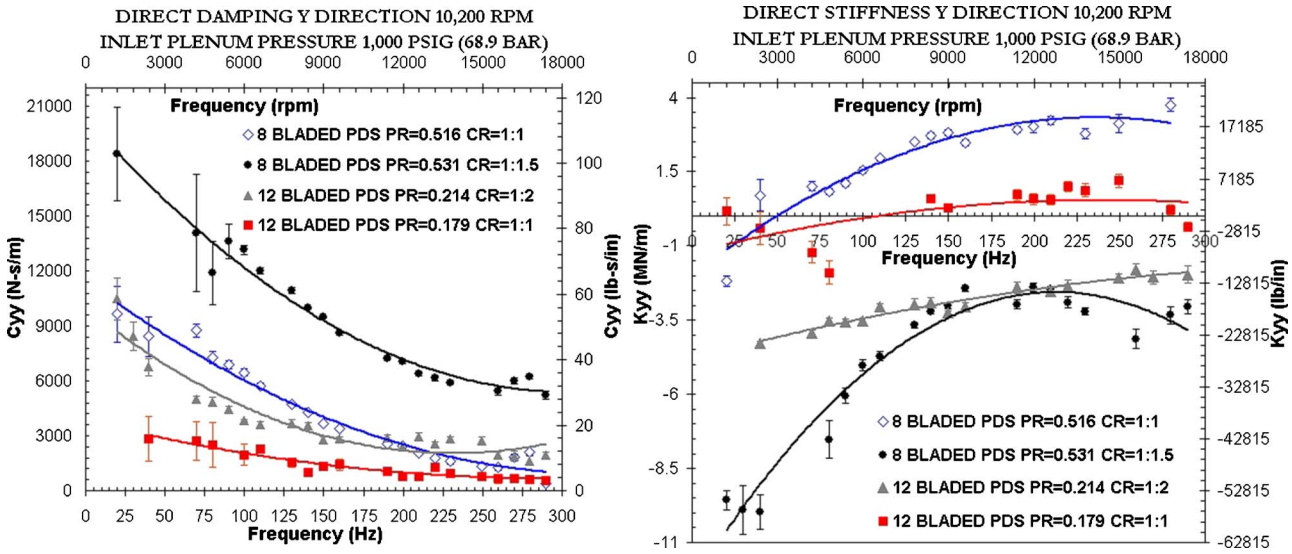


**Fig. 15 Direct stiffness and direct damping: 8 bladed PDS versus 12 bladed PDS**

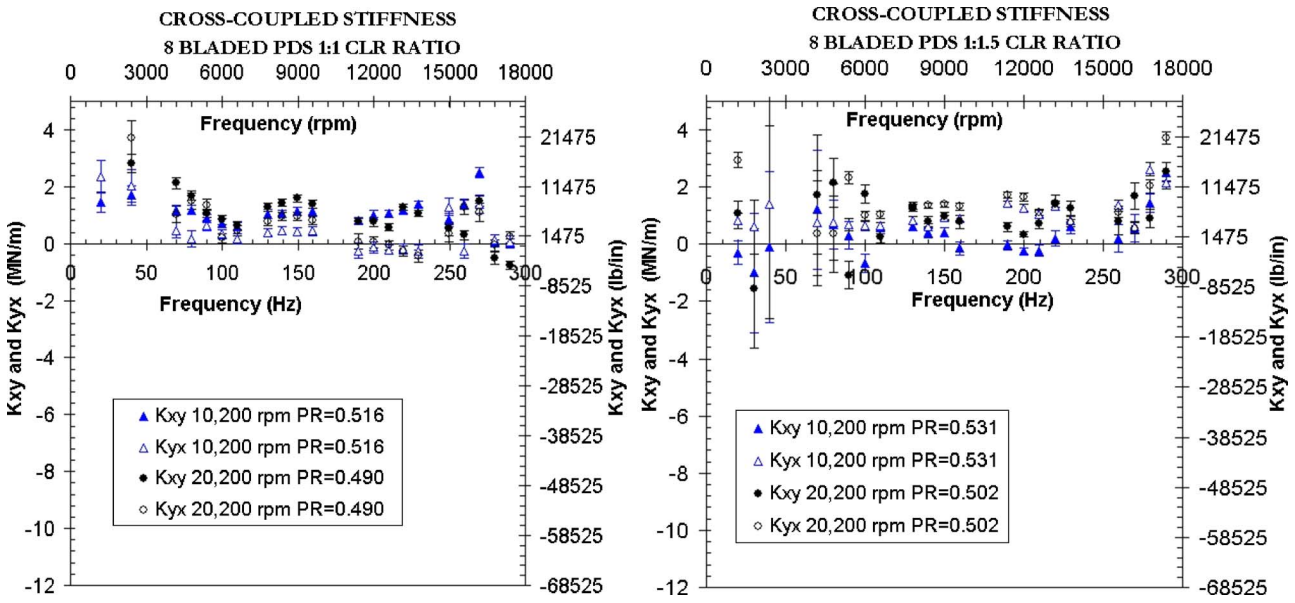


**Fig. 16 Cross-coupled stiffness: 8 bladed PDS**

cavity 5 and 130 Hz for cavity 3. The second plot shown in Fig. 19 displays the force density, which is defined by $|P/Y|$, where $P$ is the 0-pk dynamic pressure and $Y$ is the 0-pk vibration amplitude. The force density is defined as the cavity force generated per unit volumetric displacement of a pressurized cavity control volume. The magnitude of the force density from the diverging cavities were measured to be three times the force density of the straight through cavities.

The stiffness and damping of an individual cavity was defined in Eqs. (20) and (21), and can be calculated by using the force density, pressure phase, and projected cavity area (Fig. 20). The diverging seal cavity configuration was shown to possess almost twice the damping of the straight-through cavities and exhibited significantly more negative stiffness. This behavior is expected and was closely predicted by theory [13].

It is important to note the pressure resonances at ~80 Hz and ~95 Hz, as shown in Fig. 11 for the straight-through PDS. These are locations where the force density has a local maximum for the third cavity and a local minimum for the fifth cavity (Fig. 19). The damping plot in Fig. 20 also shows deviations in the data at 80 Hz and 100 Hz. Figure 20 illustrates that the third cavity increases in damping at 80 Hz and cavity 5 shows a local decrease in damping at 100 Hz. The frequency where the force density shows maximums and minimums is clearly seen in all the frequency spectra of the cavity pressure measurements. Initially the asynchronous frequencies observed from the pressure probes were thought to be acoustic frequencies, but this hypothesis was discarded because of the difference of the frequencies in the two cavities. Since the cavities possess the same geometry and the temperature from cavity three to cavity five is changing no more than 1 °F, the acoustic frequencies should be very close, given that they are a function of temperature [13]. However, the frequencies shown in Fig. 11 display frequencies with a ~15 Hz separation indicating that the resonances in the force density are attributed to another phenomena. One major difference between the two cavities is the static pressure, which also materializes as a variation in gas density. This variation yields differences in cavity flow velocities, where cavity 3 possesses a lower flow velocity than cavity 5. It is interesting to note that the 95 Hz frequency in cavity 5 is ~16%

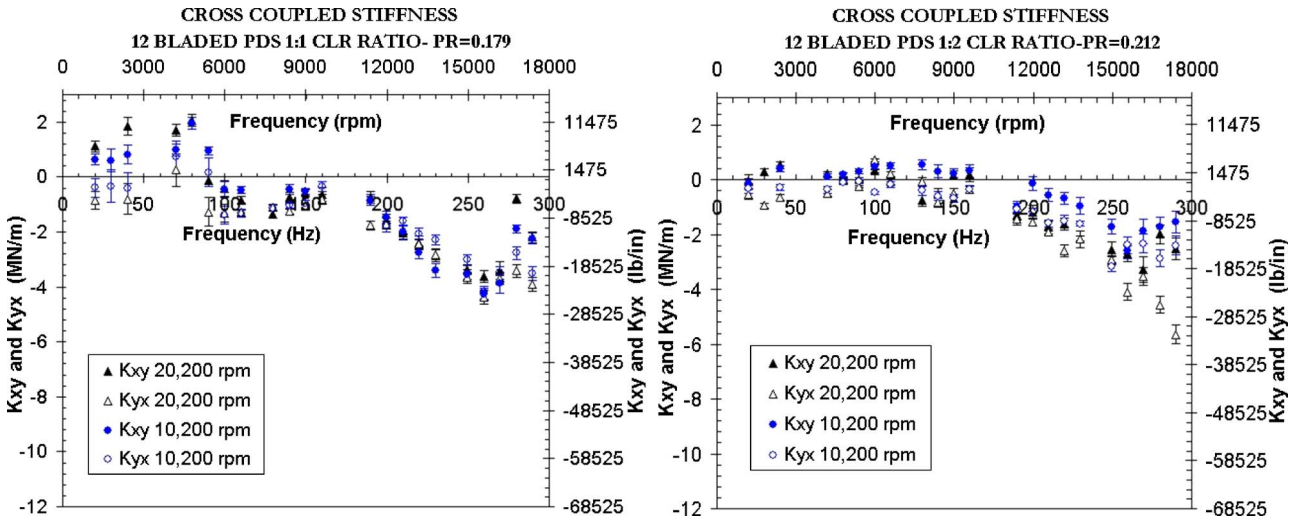


**Fig. 17 Cross-coupled stiffness: 12 bladed PDS**

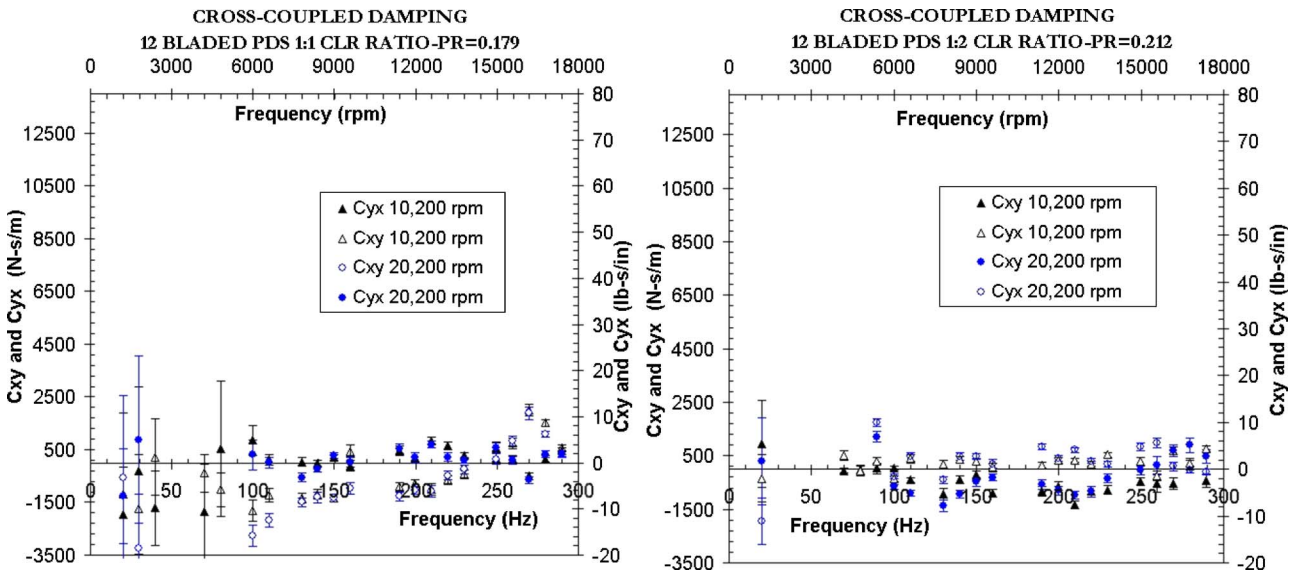


**Fig. 18 Cross-coupled damping: 12 bladed PDS**

higher than the asynchronous 80 Hz frequency of cavity 3 and that the flow velocity in cavity 5 is ~14% higher than the flow velocity for cavity 3. The ratio of velocities and frequencies are similar and imply a direct linear relation between the two. The asynchronous frequencies are most likely related to a vortex shedding phenomena, which can be described by a nondimensional Strouhal number (Eq. (22)). This equation relates the wake shedding frequency ($f$) to the flow velocity ($V$) using a characteristic length $L_c$ and the Strouhal number (St). Using the axial pitch of the cavity for the characteristic length, the Strouhal number becomes ~0.11. The pressure resonances had a minimal effect on individual cavity coefficients and its influence on overall seal coefficients was not observed for this seal design.

$$\mathrm{St} = \frac{f \cdot L_c}{V} \tag{22}$$

## 8 Conclusion

Several conclusions can be formulated from the results presented here. First, it was shown that all PDS configurations generated positive direct damping and same sign cross-coupled stiffness coefficients. These two characteristics are favaorable for bounding synchronous vibration response through critical speed transitions and supressing subsynchronous rotor whirl instabilities. This is especially true for multistage centrifugal compressors that typically possess a first natural frequency between 50 Hz and 80 Hz, which is where the PDS generates maximum damping. The second major conclusion was the effect of clearance ratio on direct stiffness and direct damping. The addition of a downstream notch on the exit blade yielded large valued negative direct stiffness coefficients whereas the straight through seals generated

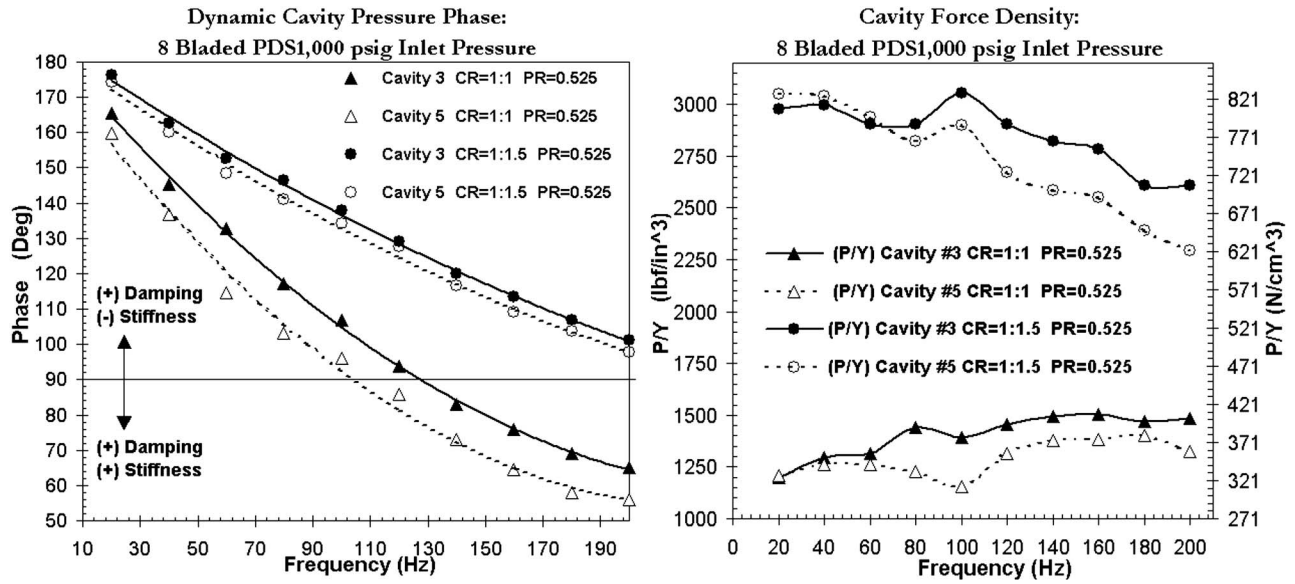


**Fig. 19 Cavity pressure phase and force density: 8 bladed PDS**

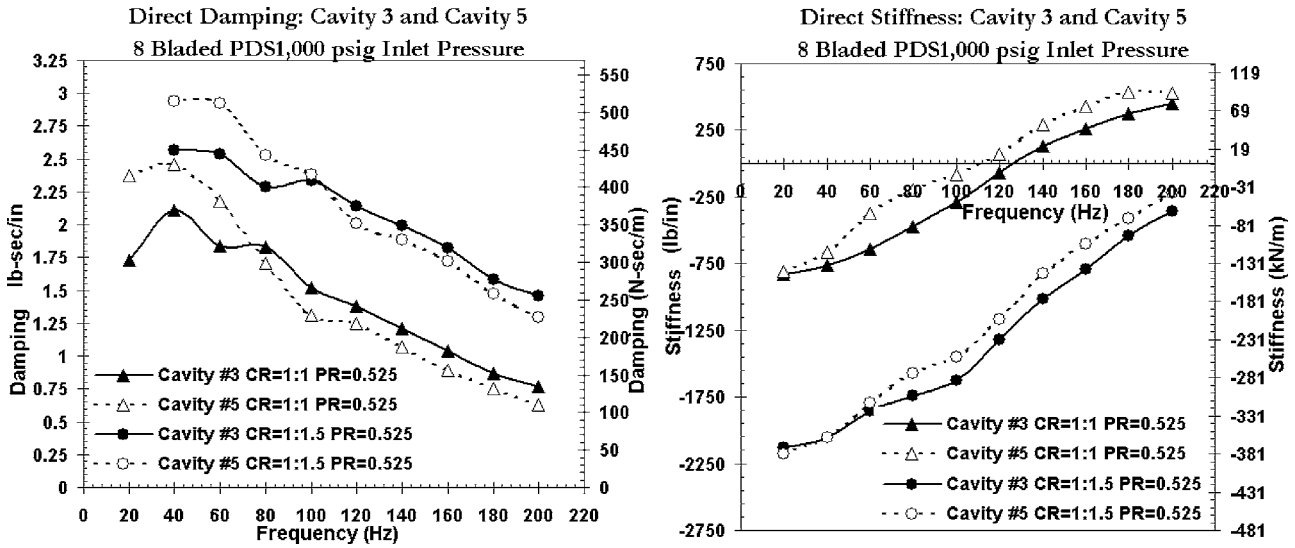


**Fig. 20 Cavity coefficients: 8 bladed PDS**

small valued negative and positive direct stiffness coefficients. The notch was also shown to increase direct damping by a factor of 2 for both seals.

## Acknowledgment

The authors would like to thank Professor Dara Childs of Texas A&M University Turbomachinery Laboratory for allowing the use of his test facility, and Dr. Fouad Zeidan for providing the test seals and the ancillary hardware.

## Nomenclature

$F_{xx}$ = shaker force in $X$ direction for $X$ direction excitation
$F_{xy}$ = shaker force in $Y$ direction for $X$ direction excitation
$F_{yy}$ = shaker force in $Y$ direction for $Y$ direction excitation
$F_{yx}$ = shaker force in $X$ direction for $Y$ direction excitation
$D_{xx}$ = stator motion in $X$ direction for $X$ direction excitation
$D_{xy}$ = stator motion in $Y$ direction for $X$ direction excitation
$D_{yy}$ = stator motion in $Y$ direction for $Y$ direction excitation
$D_{yx}$ = stator motion in $X$ direction for $Y$ direction excitation
$f_{xx}$ = effective force in $X$ direction for $X$ direction excitation
$f_{xy}$ = effective force in $Y$ direction for $X$ direction excitation
$f_{yy}$ = effective force in $Y$ direction for $Y$ direction excitation
$f_{yx}$ = effective force in $X$ direction for $Y$ direction excitation
$A_{xx}$ = stator acceleration in $X$ direction for $X$ direction excitation
$A_{xy}$ = stator acceleration in $Y$ direction for $X$ direction excitation
$A_{yy}$ = stator acceleration in $Y$ direction for $Y$ direction excitation
$A_{yx}$ = stator acceleration in $X$ direction for $Y$ direction excitation
$H_{xx}$ = direct impedance in $X$ direction
$H_{xy}$ = cross-coupled impedance in $X$ direction
$H_{yy}$ = direct impedance in $Y$ direction
$H_{yx}$ = cross-coupled impedance in $Y$ direction
$K_{xx}$ = direct stiffness in $X$ direction
$K_{xy}$ = cross-coupled stiffness in $X$ direction
$K_{yy}$ = direct stiffness in $Y$ direction
$K_{yx}$ = cross-coupled stiffness in $Y$ direction
$C_{xx}$ = direct damping in $X$ direction
$C_{xy}$ = cross-coupled damping in $X$ direction
$C_{yy}$ = direct damping in $Y$ direction
$C_{yx}$ = cross-coupled damping in $Y$ direction
$M$ = stator mass
$\omega$ = excitation frequency of electrohydraulic shaker
$A_P$ = projected area of pressurized seal cavity on rotor surface
$y$ = 0-peak excitation amplitude of stator housing for dynamic pressure tests
$P_C$ = dynamic pressure component in phase with stator displacement
$P_S$ = dynamic pressure component in phase with stator velocity

## References

[1] Childs, D. W., 1993, *Turbomachinery Rotordynamics*, John Wiley and Sons, New York.
[2] Vance, J. M., and Schultz, 1993, "A New Damper Seal for Turbomachinery," *Vibration of Rotating Systems*, ASME, New York, DE-Vol. 60, pp. 139–148.
[3] Li, J., and Vance, J. M., 1995, "Effects of Clearance and Clearance Ratio on Two and Three Bladed TAMSEALS, TRC-Seal-4-95," Turbomachinery Laboratory Research Progress Report, Texas A&M University, College Station.
[4] Ransom, D., Li, J., San Andrés, L., and Vance, J. M., 1998, "Experimental Force Coefficients for a Two-Bladed Labyrinth Seal and a Four Pocket Damper Seal," J. Tribol., **28**, pp. 98–109.
[5] Laos, H. E., 1999, "Rotordynamic Effect of Pocket Damper Seals," Ph.D. dissertation, Texas A&M University, College Station, TX.
[6] Li, J., Aguilar, R., San Andrés, L., and Vance, J. M., 2000, "Dynamic Force Coefficients of a Multiple Blade, Multiple-Pocket Gas Damper Seal: Test Results and Predictions," J. Tribol., **122**, pp. 317–322.
[7] Vance, J. M., Sharma, A., and Jayakar, N., 2002, "Effect of Frequency and Design Parameters on Pocket Damper Seal Performance," *Proceedings of Fluid Structure Interactions*, New Orleans, LA, ASME, New York, No. 23, pp.

208–217.
[8] Childs, D. W., and Hale, K., 1994, "A Test Apparatus and Facility to Identify the Rotordynamic Coefficients of High Speed Hydrostatic Bearings,"J. Tribol., **116**, pp. 337–334.
[9] Dawson, M., 2000, "A Comparison of the Static and Dynamic Characteristics of Straight-Bore and Convergent Tapered-Bore Honeycomb Annular Gas Seals," M. S. thesis, Texas A&M University, College Station, TX.
[10] Sprowl, T. B., and Childs, D. W., "A Study of the Effects of Inlet Preswirl on the Dynamic Coefficients of a Straight-Bore Honeycomb Gas Damper Seal," ASME Paper No. GT2004-53328.
[11] Ertas, B., and Vance, J., "The Influence of Same Sign Cross-Coupled Stiffness on Rotordynamics," ASME Paper No. DETC2005-84873.
[12] Gamal, A., 2003, "Analytical and Experimental Evaluation of the Leakage and Stiffness Characteristics of High Pressure Pocket Damper Seals," M.S. thesis, Texas A&M University, College Station, TX.
[13] Ertas, B., 2005, "Rotordynamic Force Coefficients of Pocket Damper Seals," Ph.D. dissertation, Texas A&M University, College Station, TX.
[14] Lucas, M. J., Noreen, R. A., Sutherland, L. C., Cole, J. E., and Junger, M. C., 1997, *Handbook of the Characteristics of Turbomachinery Cavities*, ASME, New York.

# Analysis of Airfoil Trailing Edge Heat Transfer and Its Significance in Thermal-Mechanical Design and Durability

**F. J. Cunha**

**M. T. Dahmer**

Pratt & Whitney,
United Technologies Corporation,
East Hartford, CT 06108

**M. K. Chyu**
Department of Mechanical Engineering,
University of Pittsburgh,
Pittsburgh, PA 15261
e-mail: mkchyu@engr.pitt.edu

*The trailing edge section of modern high-pressure turbine airfoils is an area that requires a high degree of attention from turbine performance and durability standpoints. Aerodynamic loss near the trailing edge includes expansion waves, normal shocks, and wake shedding. Thermal issues associated with trailing edge are also very complex and challenging. To maintain effective cooling ensuring metal temperature below design limit is particularly difficult, as it needs to be implemented in a relatively small area of the airfoil. To date, little effort has been devoted to advancing the fundamental understanding of the thermal characteristics in airfoil trailing edge regions. Described in this paper are the procedures leading to closed-form, analytical solutions for temperature profile for four most representative trailing edge configurations. The configurations studied are: (1) solid wedge shape without discharge, (2) wedge with slot discharge, (3) wedge with discrete-hole discharge, and (4) wedge with pressure-side cutback slot discharge. Comparison among these four cases is made primarily in the context of airfoil metal temperature and resulting cooling effectiveness. Further discussed in the paper are the overall and detail design parameters for preferred trailing edge cooling configurations as they affect turbine airfoil performance and durability.* [DOI: 10.1115/1.2220047]

## Introduction

In modern high-pressure turbine airfoils, the aft section of the airfoil denoted as the trailing edge section is an area that requires a high degree of attention from turbine designers and researchers. This is particularly true because of the fundamental role that airfoil trailing edges have on the overall design of all turbines in operation today for aircraft engines and electrical generating power plants.

Airfoil trailing edges provide a degree of blockage in the gas flow path, contributing to the overall degradation of turbine performance and efficiency. Along the turbine airfoil external walls, there are pressure profiles on the pressure (concave) and suction (convex) sides that lead to pressure differences between the pressure and suction sides at the airfoil trailing edge. These pressure profiles result in expansion waves in blade passage, trailing edge normal shocks, and wake shedding as illustrated in Fig. 1 [1,2]. All these effects contribute to increasing turbine losses. Thus, the illusive theoretical goal of the aerodynamic Kutta-condition [3], requiring the gas flow to leave the airfoils smoothly at the trailing edge, is impossible to achieve with today's technology and cooling requirements. The thickness of airfoil trailing edges is directly related to the turbine aerodynamic performance as it affects the gas path aerodynamic losses. Airfoil cooling in this region is also extremely difficult to achieve, as it needs to be implemented effectively in a relatively small area of the airfoil. Without cooling, however, the trailing edge metal temperatures would reach metal temperatures as high as the melting temperatures of most superalloys.

Innovative ideas are required to obtain the most practical and effective means to cool these airfoil regions. Low or inadequate trailing edge cooling can lead to high thermal strains, as airfoil trailing edges respond thermally faster than other parts of the airfoil. This is due to the heat capacity of relatively small trailing edge mass when compared to the rest of the airfoil. Resulting thermal mismatch within the airfoil walls can lead to excessive thermal-mechanical cyclic loading, which can be exacerbated with long dwell times at high temperatures during cruising and continuous power generation for aircraft and land-based turbines, respectively. This dwell effect can manifest itself as creep blade growth with thermal-mechanical crack nucleation and overall crack progression.

From a phenomenological point-of-view, creep growth can occur close to the apex of the trailing edge. Nearby thermal strains give rise to stress intensities and subsequent trailing edge thermal-mechanical cracking nucleation. As the centrifugal force remains constant, the colder portions of the airfoil begin sharing the load as the hottest portions of the blade start the process of stress-relaxation. This interaction is commonly referred to as the airfoil load shakedown [4]. Load sharing could eventually lead to a state of potential overstress in the cold regions of the airfoil with substantial plastic deformation. The interaction of events can eventually culminate in catastrophic structural failure. Attention is thus required in the design process to avoid exceeding the endurance limits of the material. This is a major concern for turbine designers and researchers as airfoils are designed fundamentally using deterministic means for crack initiation before crack propagation [5].

Advances in materials science have continued along with advances in blade cooling technology for airfoil trailing edge designs. Materials of construction for these airfoils have, therefore, become an important part of materials science development and testing. As the rotor inlet temperatures have increased in the last 20 years, there have been considerable advances in alloy composition and casting technology. Early equiaxed nickel and cobalt alloys have been displaced by single-crystal nickel superalloys for the most advanced military and commercial gas turbine engines. Even in land-based power generation turbines, directionally solidified and single-crystal alloy castings are now finding their way

Contributed by the International Gas Turbine Institute (IGTI) of ASME for publication in the JOURNAL OF TURBOMACHINERY. Manuscript received October 1, 2004; final manuscript received February 1, 2005. IGTI Review Chair: K. C. Hall. Paper presented at the ASME Turbo Expo 2005: Land, Sea and Air, Reno, NV, June 6–9, 2005, Paper No. GT2005-68108.

  

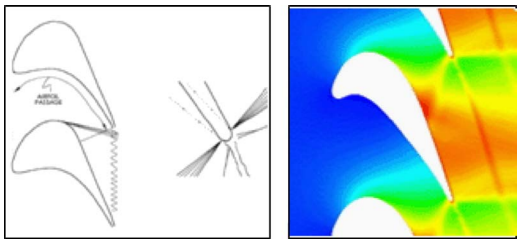

**Fig. 1 Typical shock structures in high-pressure turbine airfoils: (*a*) from Kuhne [8], and (*b*) from Eisemann [9]**

as first stage turbine components. Similarly, to these developments, metallic and thermal barrier coatings have excelled and are now regarded as prime-reliant features in all advanced turbine designs. Even with these advances, the oxidation, creep, and fatigue resistance of trailing edges are still being challenged by the adverse and compounding effects of vibrational stresses. These dynamic effects occur in extreme hot rotating environments with harmonically varying pressure fields.

To bring trailing edge designs within the available design space, several fabrication methods are used today. These include: (1) internal cooling schemes to bring the metal temperature within design limits; (2) internal aluminide coatings to prevent internal oxidation; (3) external metallic bond coatings to prevent external oxidation and aluminum content depletion; (4) thermal barrier coatings to reduce external thermal loading; (5) structural design features and devices integrated in the cooling schemes to reduce thermal, bending, panel, and vibratory stresses; and (6) optimization of trailing edge thickness and airfoil wedge angles to minimize film cooling degradation and aerodynamic losses. All these aspects need to be assembled together to balance the design and satisfy the stringent design requirements in terms of heat transfer, structures, and performance.

The durability design factors affecting the configuration of existing and future turbine airfoil trailing edges are the subject matter of this paper. The presentation will be applicable to airfoil trailing edges found in both aircraft and land-based engines. Four most representative configurations will be presented as introductory to analyzing their relative merits in terms of durability. As such, the interplay between geometrical features and airfoil metal temperatures will be described and explained using closed-form, analytical models. Trailing edge cooling schemes will be presented in the context of metal temperature or resulting cooling effectiveness, as it affects all other design parameters, including creep, thermal-mechanical fatigue, oxidation, spallation, and performance. The four configurations studied are: (1) solid wedge shape without discharge, (2) wedge with slot discharge, (3) wedge with discrete-hole discharge, and (4) wedge with pressure-side cut-back slot discharge.

## Analytical Models

**Case 1: Solid Trailing Edge without Internal Cooling.** As way of introduction, a simple wedge model shown in Fig. 2 is considered. In this figure, the airfoil trailing edge is represented by a wedge-fin type of configuration without internal convective cooling. Different cooling schemes will be considered in subsequent models.

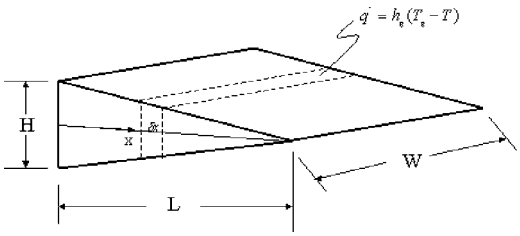


**Fig. 2 Trailing edge analytical model without internal convective cooling**

If an infinitesimal control volume of Fig. 2 is considered, the mathematical expression, which physically states that the energy being stored in the control volume is equal to the heat being transferred to the system by external convection, and conducted away from the system by thermal conduction, can be given as follows:

$$\underbrace{-\frac{\partial}{\partial x}\left(-kA\frac{\partial T}{\partial x}\right)\delta x}_{\text{Conduction}} + \underbrace{h_g(T_g - T)P\,\delta x}_{\text{External Convection}} = \underbrace{\rho A c\frac{\partial T}{\partial t}\delta x}_{\text{Energy Storage}} \tag{1}$$

where

$$A = (HW)\left(\frac{L-x}{L}\right)$$

$$P = 2\left[W + H\left(\frac{L-x}{L}\right)\right]u$$

$$u = 2\left\{1 + \left(\frac{H/2}{L}\right)^2\right\}^{1/2}$$

It should be noted that in expression (1), the conduction cross-sectional area $A$, and the corresponding perimeter $P$, of the control volume are functions of the axial distance $x$. Other geometrical attributes are depicted in Fig. 2. Variables, $T$ and $T_g$, denote metal temperature and external gas temperature, respectively. The thermo-physical variables $k$, $\rho$, and $c$, denote the metal thermal conductivity, density, and specific heat capacity properties, respectively. In the right-hand side, time is denoted by variable $t$. The right-hand-side term of expression (1) will vanish if one considers the steady state condition only for the control volume. Further, the simplification for large $W$ leads to the following equation:

$$\frac{d}{dx}\left[(L-x)\frac{dT}{dx}\right] + \left[\left(\frac{h_g}{k}\right)\left(\frac{L}{H}\right)(2u)\right](T_g - T) = 0 \tag{2}$$

Equation (2) is further simplified by a change of variables, using $\theta = T - T_g$ and $y = L - x$, to obtain the fundamental modified Bessel equation of order zero:

$$y^2\frac{d^2\theta}{dy^2} + y\frac{d\theta}{dy} - E^2 y\theta = 0 \tag{3}$$

where

$$E^2 = \left[\left(\frac{h_g}{k}\right)\left(\frac{L}{H}\right)(2u)\right]$$

To solve this second-order differential equation, two boundary conditions are required. The first boundary condition is located at the base of the wedge model of Fig. 2, at $x=0$, and requires that $T=T_b$ or $\theta=\theta_b$ where the subscript $b$ stands for a base quantity. The other boundary condition comes from the requirement that the metal temperature at the apex of the wedge model, at $x=L$, be finite. The solution of Eq. (3) then becomes

$$\frac{\theta(x)}{\theta_b} = \frac{I_0[2E(L-x)^{1/2}]}{I_0(2EL^{1/2})} \tag{4a}$$

or

$$T(x) = T_g - (T_g - T_b)\frac{I_0[2E(L-x)^{1/2}]}{I_0(2EL^{1/2})} \tag{4b}$$

Solutions (4*a*) and (4*b*) are equivalent. Either solution is fundamental in that it assumes a form that will appear again as the homogeneous solution for problems involving different cooling

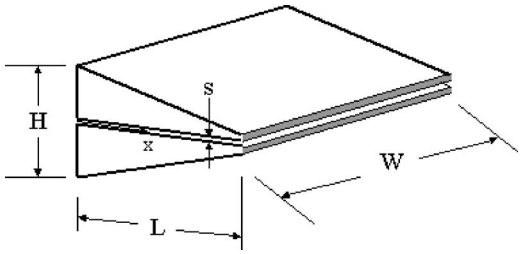


**Fig. 3 Trailing edge model with centerline slot**

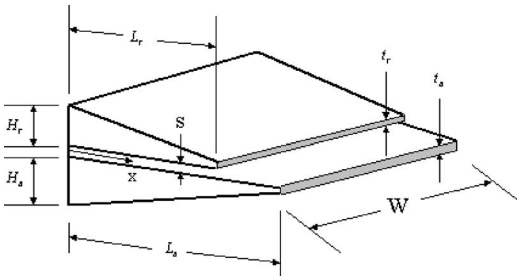


**Fig. 5 Cut-back trailing edge model with slots**

schemes. These fundamental solutions will always follow the form of solution (4) with different interpretations for the argument $E$ of the Bessel function of second kind and order zero: $I_0$. Variations of the model of Fig. 1 with different internal cooling schemes are now considered.

**Case 2: Trailing Edge With Centerline Slot Discharge.** Following the steps outlined previously for the analysis of the model in Fig. 2, the next model depicted in Fig. 3 is analyzed in similar fashion.

The governing equation is derived as per Eq. (3) with the addition of the nonhomogeneous term $S$ which accounts for the slot cooling effect. As noted before, the homogeneous solution is provided by Eq. (4). In this case, argument $E$ is modified to account for the internal cooling effect of the centerline slot.

The internal heat transfer coefficient, denoted by $h_c$, is assumed constant. In subsequent sections, expressions to relate this internal heat transfer coefficient to geometrical attributes of the cooling passage will be discussed. It is sufficient to say here that the coefficient is considered known and that the sink effect is the particular solution of Eq. (5), defined by the source term $S$ as follows:

$$y\frac{d^2\theta}{dy^2} + \frac{d\theta}{dy} - E^2\theta = S \tag{5}$$

where

$$y = L\left(1 - \frac{s}{H}\right) - x$$

$$E^2 = \left(\frac{h_g}{k}\right)\left(\frac{L}{H}\right)(2u) + 2\left(\frac{h_c}{k}\right)\left(\frac{L}{H}\right)$$

$$S = 2\left(\frac{h_c}{k}\right)\left(\frac{L}{H}\right)[T_g - T_c(x)]$$

The complete solution of Eq. (5) will be presented in a subsequent section wherein more details about the coolant temperature distribution are provided.

**Case 3: Trailing Edge With Arbitrary Openings in a Centerline Discharge.** In the cooling configuration shown in Fig. 4, discrete cooling holes with arbitrary shapes are considered. The formulation follows that performed when the model of Fig. 2 was considered. The resulting governing equation is similar to Eq. (5), with parameters modified to account for the new cooling arrangement.

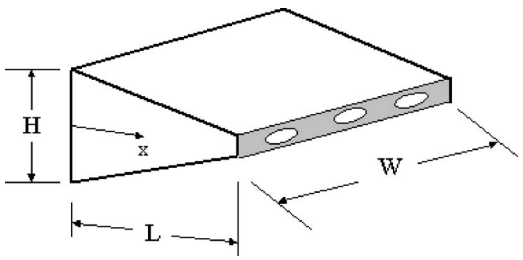


**Fig. 4 Trailing edge model with cooling holes**

In this treatment, the geometrical parameter $A_H$ denotes the cross sectional area of an arbitrarily shaped cooling hole with $P_H$ as the perimeter of the cooling hole. The term $N_H$ denotes the number of cooling holes in the radial span. The new governing parameters for this configuration become:

$$y = L\left(1 - \frac{A_H N_H}{WH}\right) - x$$

$$E^2 = \left(\frac{h_g}{k}\right)\left(\frac{L}{H}\right)(2u) + \left(\frac{P_H N_H}{W}\right)\left(\frac{h_c}{k}\right)\left(\frac{L}{H}\right)$$

$$S(x) = \left(\frac{P_H N_H}{W}\right)\left(\frac{h_c}{k}\right)\left(\frac{L}{H}\right)[T_g - T_c(x)]$$

The complete solution of Eq. (5) will be presented in a subsequent section wherein more details about the coolant temperature distribution are provided.

**Case 4: Trailing Edge Cut-back Design With Pressure Side Discharge.** This cooling configuration deviates from centerline discharge as the pressure side of the trailing edge has a cut-back leading to a pressure-side ejection of the coolant into the main gas stream. The model shown in Fig. 5 has the trailing edge of the airfoil extended all the way on the suction (bottom) side with a cut-back located on the pressure (top) side. The pressure-side cut-back is probably one of the most utilized cooling configurations for today's airfoils. This permits a significantly thinner trailing edge, approximately 0.76 mm (0.030 in.) versus 1.27 mm (0.050 in.) for the centerline discharge. Therefore, the aerodynamic losses associated with the cut-back design attain the lowest values among all the cases analyzed here.

The governing equation is similar to that given by Eq. (5). For simplicity, the defining governing parameters for this configuration are divided into two parts: one for a side defined up to $x < L_T$; and, the other for the suction side defined by $L_T \leq x \leq L_B$, This leads to: For $x < L_T$:

$$y = \frac{H}{M} - x$$

$$M = \left(\frac{H_T - t_T}{L_T}\right) + \left(\frac{H_B - t_B}{L_B}\right)$$

$$E^2 = \left(\frac{\overline{h_g}(u_T + u_B) - 2h_c}{kM}\right)$$

$$S(x) = \left(\frac{2h_c}{kM}\right)[T_g - T_c(x)]$$

with $\overline{h_g} = (h_{g,T} + h_{g,B})/2$

$$u_T = \left[1 + \left(\frac{H_T - t_T}{L_T}\right)^2\right]^{1/2}$$

$$u_B = \left[1 + \left(\frac{H_B - t_B}{L_T}\right)^2\right]^{1/2}$$

and for $L_T \leqslant x \leqslant L_B$:

$$y = \frac{H_B}{M} - x$$

$$M = \left(\frac{H_B - t_B}{L_B}\right)$$

$$E^2 = \left(\frac{h_{g,B}(u_B) - h_c}{kM}\right)$$

$$S(x) = \left(\frac{h_c}{kM}\right)[T_g - T_c(x)]$$

For the particular solution of Eq. (5), it is necessary that the term $S$ be obtained. In this case, the external conditions, $T_g$ and $h_g$, are assumed known constants for simplicity and convenience, while the coolant temperature $T_c$ needs to be determined.

If one considers a fluid control volume at the same axial distance as that for the control volume shown in Fig. 2, and assuming that the heat flux $q''$ is a known constant, again for simplicity and convenience; an expression for the coolant heat pick-up can then be written as follows:

$$\rho V A c_P \frac{dT_C}{dx}\delta x = q''(x)\,\delta A_{C,S} \tag{6}$$

where

$$q''(x) = q''_T(x) + q''_B(x) \quad x < L_T$$

$$q''(x) = q''_B(x) \quad L_T \leqslant x \leqslant L_B$$

It should be noted that the heat fluxes $q''_T$ and $q''_B$ denote the respective heat fluxes from the top and bottom parts of the cooling passage. The quantity $\delta A_{c,s}$ denotes the control volume internal surface area of the cooling passage. The governing equation (6) has a single inlet boundary condition at $x=0$ as $T_c = T_{c,i}$ or $\theta = \theta_{c,i}$ and the solution becomes:

$$\theta_c = \theta_{c,i} + \Delta\theta_c(x) \tag{7}$$

where

$$\Delta\theta_c = \frac{q''\Delta A_{C,S}}{\rho V A c_P}$$

Even though the calculation of the trailing edge metal temperature is an important step in the durability design process, it is equally important to determine the cooling flow rate through the trailing edge. After all, the cooling flow rate is directly related to the internal heat transfer capability of the cooling design. To estimate the trailing edge cooling flow, one needs to consider the inlet coolant flow rate, at the root of the supply cavity, denoted here as $m_{\text{Root}}$, as well as the tip-cooling flow rate at the tip, denoted as $m_{\text{tip}}$, and flow variation through the trailing edge feed cavity. The linear function of cooling flow rate distribution from the root to the tip as flow exits the trailing edge leads to the following flow relationship:

$$m(r) = m_{\text{Root}}(1 - ar) \tag{8}$$

where

$$a = \frac{1}{L_H}\left(1 - \frac{m_{\text{Tip}}}{m_{\text{Root}}}\right)$$

with $L_H$ as the blade span radial height. Note that if there is no communication between the tip holes and the trailing edge supply cavity, the term $a$ in Eq. (8), is equal to the reciprocal of the blade span radial height, and the trailing edge flow distribution varies linearly from a finite mass flow rate, at the root section to no-flow condition at the tip.

The temperature of the coolant inside the feed cavity is obtained by considering an infinitesimal small control volume ($dr$) in the supply cavity. This consideration leads to the following energy balance:

$$mc_P\frac{dT_c}{dr} = \frac{dQ}{dr} + \frac{mr\omega^2}{Jg_c} \tag{9}$$

where $Q$ denotes the total heat transfer onto the corresponding trailing edge section of radial span $L_H$.

The trailing edge coolant flow rate of Eq. (8) is then introduced in Eq. (9). The resulting expression is integrated from root to any other radial section of the airfoil. This yields an expression for the coolant temperature increase in terms of heat transfer, and rotational pumping, as a function coolant flow rate. The result is:

$$T_c(r) = T_{c,\text{Root}} + \left(\frac{Q_{\text{Total}}}{aL_H m_{\text{Root}} c_p}\right)\ln\left(\frac{1 - ar_{\text{Root}}}{1 - ar}\right) + \frac{(r^2 - r^2_{\text{Root}})\omega^2}{2Jg_c c_p} \tag{10}$$

This expression allows for calculation of the temperature increase of the coolant in the supply cavity before entering the trailing edge passages, and it should be used as $T_{c,i}$ for Eq. (7) presented previously.

Finally, when the particular solution Eq. (7) is substituted in Eq. (5) for evaluating source term $S$, the following complete solution is obtained:

$$\theta(x) = \frac{I_0[2E(L-x)^{1/2}]}{I_0(2EL^{1/2})}\left[\theta_b - \left(\frac{E_c}{E}\right)^2\theta_{c,i}\right] + \left(\frac{E_c}{E}\right)^2[\theta_{c,i} + \Delta\theta_c(x)] \tag{11a}$$

or

$$T(x) = T_g - \left\{\frac{I_0[2E(L-x)^{1/2}]}{I_0(2EL^{1/2})}\left\{[(T_g - T_b\,] - \left(\frac{E_c}{E}\right)^2(T_g - T_{c,i})\right\} + \left(\frac{E_c}{E}\right)^2[(T_g - T_{c,i}) + \Delta T_c(x)]\right\} \tag{11b}$$

Solutions (11$a$) and (11$b$) are equivalent, and applicable to all the configurations studied. The parameters $E^2$ and $E_c^2$ for each configuration are summarized in Table 1.

## Analytical Solutions and Their Implication in Trailing Edge Design

To illustrate the realistic characteristics of each design, Table 2 gives representative magnitudes of key variables associated with the parameters listed in Table 1. With these data, the temperature distributions based on Eq. (11$b$) for all four configurations are given in Fig. 6. One notable finding is that the solid trailing edge yields the highest metal temperatures approaching 1260°C (2300°F). As per solution (4), using the ratio of Bessel functions requires that the metal temperature profile increase monotonically.

The same trend is observed for the centerline discharge cases of the slot and discrete cooling openings. Based on the input data from Table 2, the maximum temperature occurs at the end of the trailing edge with 1202°C (2196°F) and 1214°C (2219°F) for the slot and discrete cooling openings, respectively. This decrease in metal temperature is a sole function of the sink effect provided by the cooling configuration, as the base temperature and all other conditions are kept constant for all cases considered. One relevant

**Table 1 Parameters for different models**

| Configuration | $E^2$ | $E_c^2$ |
|---|---|---|
| Solid wedge model (Fig. 2) | $\left[\left(\frac{h_g}{k}\right)\left(\frac{L}{H}\right)(2u)\right]$ | 0 |
| Wedge with slot cooling (Fig. 3) | $\left(\frac{h_g}{k}\right)\left(\frac{L}{H}\right)(2u)+2\left(\frac{h_c}{k}\right)\left(\frac{L}{H}\right)$ | $2\left(\frac{h_c}{k}\right)\left(\frac{L}{H}\right)$ |
| Wedge with cooling holes (Fig. 4) | $\left(\frac{h_g}{k}\right)\left(\frac{L}{H}\right)(2u)+\left(\frac{A_{S,H}N_H}{W}\right)\left(\frac{h_c}{k}\right)\left(\frac{L}{H}\right)$ | $\left(\frac{A_{S,H}N_H}{W}\right)\left(\frac{h_c}{k}\right)\left(\frac{L}{H}\right)$ |
| Cut-back wedge with slot cooling (Fig. 5) | $\left(\frac{h_g^-(u_T+u_B)-2h_c}{kM}\right), x<L_T; \left(\frac{h_{g,B}(u_B)-h_c}{kM}\right), L_T\leq x\leq L_B$ | $\left(\frac{2h_c}{kM}\right), x<L_t$ $\left(\frac{h_c}{kM}\right), L_T\leq x\leq L_B$ |

design feature for the centerline discharge configurations is that the cooling design affects the metal temperatures monotonically. That is, if the metal temperature is considered elevated for particular design application; then, the only variable to be iterated upon is the coolant passage heat transfer coefficient to reduce the metal temperature at the end of the trailing edge. This implies overall that either the size of the coolant passage need to be increased, or the features inside the passage need to be modified to enhance the magnitudes of internal heat transfer coefficient. Alternatively, higher coolant flow rates may be increased to enhance cooling. This approach is viable only if sufficient supply pressure is available.

For the configuration with a pressure-side ejection cut-back trailing edge, the limitations associated with the thicker trailing edge of the centerline designs are removed. As shown in Fig. 6, the metal temperature profile does not increase monotonically for pressure side ejection designs. This allows for several alternative design options to optimize the cooling configuration. These are: (1) size of the cooling passage can be increased, (2) internal cooling features inside the cooling passage could be selected to enhance internal heat transfer, (3) trailing edge thickness could be made thinner, (4) pressure side lip thickness could be made thinner, (5) pressure side land roughness could be increased to augment coolant heat transfer, and (6) slot film effectiveness could be increased with higher coverage. From this set of design features, only two features, namely, (1) and (2), can be used realistically for centerline discharge designs, whereas, all features, (1) through (6), can be used for pressure-side ejection cut-back trailing edge designs. There are also benefits of improved aerodynamic performance with thinner trailing edge. In addition, the thermal-mechanical fatigue and creep life capability is also improved as metal temperature distributions are improved for the entire trailing edge region of the airfoil.

**Table 2 Boundary conditions for trailing edge examples**

| Configuration | Solid | Centerline Slot | Centerline Holes | Cut-Back PS Ejection |
|---|---|---|---|---|
| Figure | 2 | 3 | 4 | 5 |
| $T_g$ | 2300 | 2300 | 2300 | 2300 |
| $\Delta T_{c,T}$, $\Delta T_c$ | 50 | 50 | 50 | 50 |
| $\Delta T_{c,B}$ | | | | 150 |
| $T_{c,\text{in.}}$ | 1600 | 1600 | 1600 | 1600 |
| $T_{\text{base}}$ | 1900 | 1900 | 1900 | 1900 |
| $h_g$ or $h_{g,t}$ | 2000 | 2000 | 2000 | 2000 |
| $h_{g,B}$ | | | | 1000 |
| $h_c$ | 2000 | 2000 | 2000 | |
| $h_{c,T}$ | | | | 2000 |
| $h_{c,B}$ | | | | 2500 |
| $k$ | 12 | 12 | 12 | 12 |
| $L_T$ or $L$ | 0.12 | 0.12 | 0.12 | 0.08 |
| $L_B$ | | | | 0.12 |
| $H_T$ or $H$ | 0.06 | 0.06 | 0.06 | 0.03 |
| $H_B$ | | | | 0.03 |
| $t_T$ | | | | 0.01 |
| $t_B$ | | | | 0.029 |
| $P_H$ | | 0.05 | | |
| $d_h$ | | | 0.015 | |
| $W$ | | | 2.5 | |
| $S$ | | 0.015 | | 0.015 |

Notes: $h_g$, $h_g$: BTU/(h ft$^2$ °F), k: BTU/(hr ft °F); BTU/(h ft$^2$ °F)=5.68 W/(m$^2$ K), BTU/(h ft °F)=1.73 W/(m K); All length dimensions in inches: and temperatures in °F; 1 in.=0.0254 m, °F=32+(9/5)°C.

## Cooling Considerations in Trailing Edge Design

**Combined Centerline Discharge and Pressure Side Cut-back.** Cooling high-pressure turbine airfoils are cooled internally with compressor air that enters a blade inlet plenum just before flowing into the blade internal cavities. However, some designs may use cooling media other than air. For instance, in closed-loop cooling combined cycle power plants, the cooling medium is steam [6–9]. Regardless of the cooling medium, the overall design procedures that govern the airfoil trailing edge cooling remain the same.

To illustrate various facets of trailing edge design, this part of discussion begins with considering a typical high-pressure turbine blade configuration from Lee [10], shown in Fig. 7. Air enters an inlet plenum located underneath the blade. Cooling air passes onto the blade as rotating forces pump the flow towards blade internal cavities and eventually to the trailing edge. It should be noted that in the embodiment of Fig. 7, the trailing edge configuration is made up of two cooling arrangements: (1) the pressure side cut-back with slots, located in the upper portion of the blade; and (2) the centerline discharge with round openings located in the lower portion of the blade. The combination of these two trailing edge cooling schemes in one component is the essence of this design.

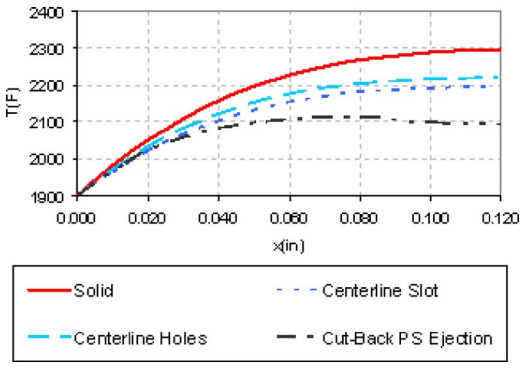


**Fig. 6 Metal temperature results for different configuration**

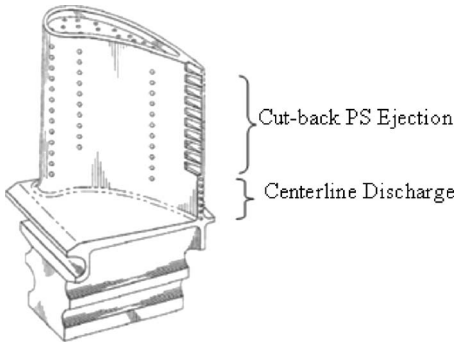


**Fig. 7 Typical high-pressure turbine blade showing trailing edge cooling openings and pressure-side ejection slots, from Lee [10]**

In line with the material presented in the previous sections, the combination of slots and round openings at the trailing edge provides a performance improvement due to the thin trailing edge in the upper portion of the airfoil.

The use of centerline discharge with cooling holes in the lower portion of the blade is practical, as the gas path temperatures can be considerably reduced at the lower radial portion of the airfoil. This effect is aided by hot gas-path migration to the blade tip, and stage profile attenuation. The advantage of a thicker trailing edge at the lower portions of the blade stems from the structural requirements. In general, high centrifugal stresses exist in the lower regions and it may be necessary to add material to the blade at the trailing edge to, among other considerations, decelerate the thermal response of the airfoil trailing edge relative to the rest of the airfoil and endwalls. In this way, both creep and thermal-mechanical material fatigue resistance can be increased. Thus, it should be recognized that a combination of trailing cooling schemes may provide preferred arrangements for specific designs, as suggested here for the model of Fig. 7. However, there are many other trailing edge design configurations in operation today as listed in references [10–14].

**Internal Cooling Near Trailing Edge.** In an attempt to describe other relevant details associated with trailing edge design, attention is given to the design depicted in Fig. 8, from Hill et al. [15]. This figure illustrates a cross sectional area of a typical high-pressure turbine blade. It is observed from this cross section that

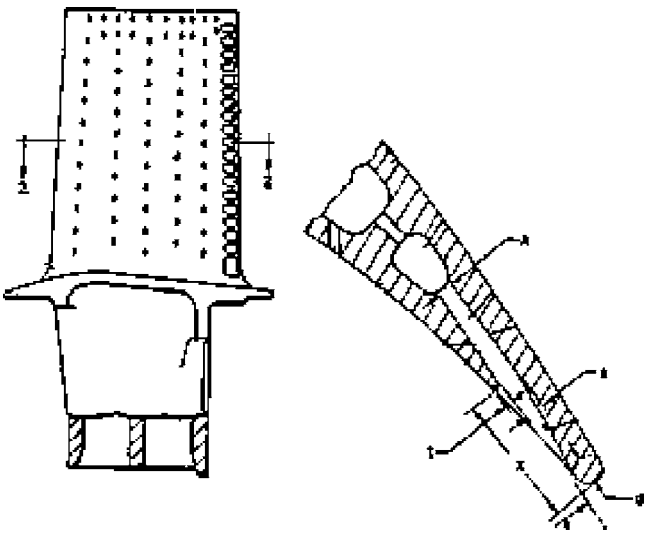

**Fig. 8 Typical high-pressure turbine blade showing cross-sectional area and trailing edge detail, from Hill et al. [15]**

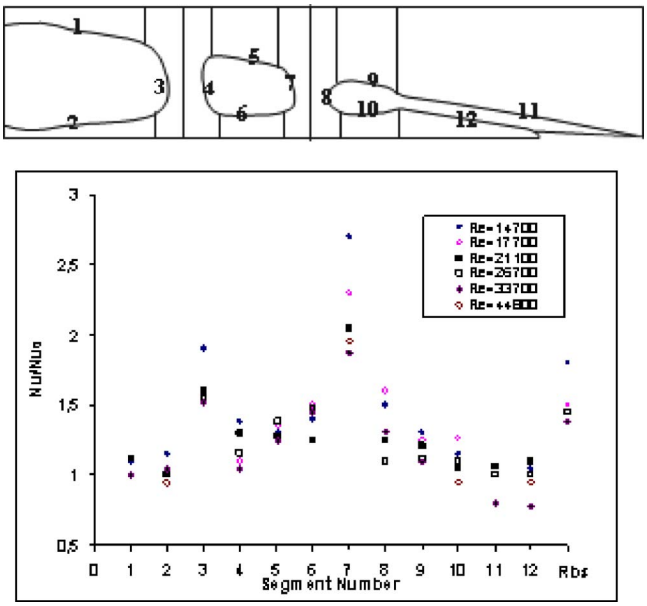


**Fig. 9 Localized heat transfer enhancement on different segments in trailing edge cavities, from Chyu et al. [16]**

there exists a supply cavity that provides cooling air through a series of impingement cross-over holes. The cooling circuit ends at the trailing edge pressure side slots in a cut-back arrangement.

In Fig. 8, it should also be noted that, tip pressure side film holes are in communication with the trailing edge supply cavity. Tip cooling is done through film cooling holes located close to the blade tip. Even though the function of these tip holes is to cool the blade tip with air film, preventing tip oxidation, it reduces the flow to the trailing edge. Clearly, such flow interaction is accounted for during trailing edge cooling requirements as previously expressed by Eq. (10). Inside the trailing edge internal cavities, there are a large number of cooling features that can be explored in the design space to enhance internal cooling. For instance, internal trailing edge cooling configurations may consist of more than one set of impingement rows with internal cooling features, such as pedestals and/or trip strips or turbulators.

Impingement cooling configurations have been used extensively in the gas turbine industry. In general, cooling air is allowed to pass through cross-over openings (i.e., circular holes, racetrack holes, elliptical holes, or slots) leading to jet impingement on the downstream airfoil ribs and surrounding walls. In these designs, coolant flow acceleration is high through cross-over impingement openings. As a result, coolant flow Mach number profiles, which are related directly to the local velocity and static pressure always assume nonuniform, or step-wise characteristics, as the coolant flow crosses these openings. Step-wise or nonuniform coolant profiles are undesirable as they lead to spatial nonuniformity in internal heat transfer coefficients at the walls of the blade. Such nonuniformity is evident in a recent study by Chyu et al. [16], as shown in Fig. 9. Segment number 7, which is subjected to direct impingement of the accelerated flow exited from the first set of cross-over holes, experiences the highest overall heat transfer coefficient, nearly 3 to 4 times of those surfaces without direct impingement. This finding suggests that there are regions in the blade walls, which attain relative lower metal temperatures due to high internal heat transfer coefficients. Meanwhile, other areas may attain relatively higher metal temperatures due to lower internal heat transfer coefficients. Thus, step-wise profiles of coolant jets could lead to step-wise metal temperature differences, which, in turn, can lead to high thermal strains. In parallel to these temperature and heat transfer differences, rela-

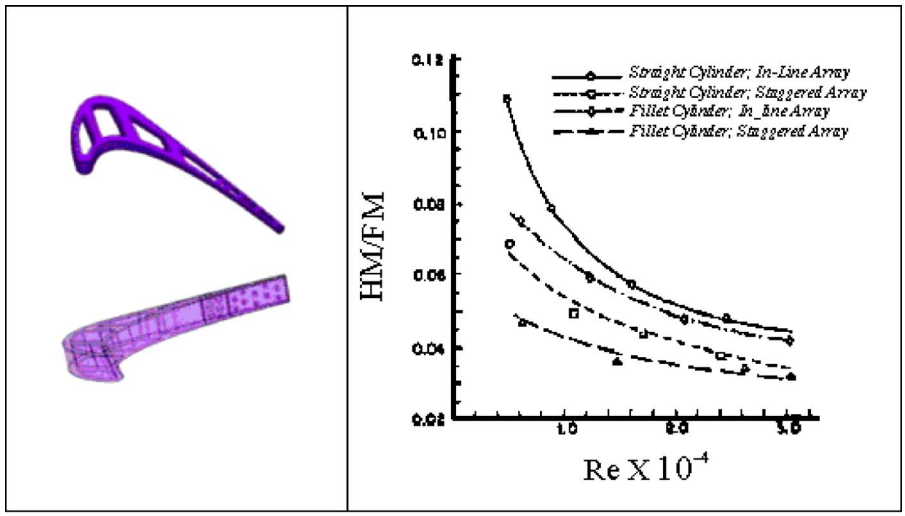


**Fig. 10 Pedestal trailing edge configuration and test results. (*a*) Transparent view of blade showing pedestal bank at trailing edge. (*b*) Effect of Reynolds number on performance index (HM/FM) in straight pins with fillets, from Chyu [21].**

tively fast blade trailing edge thermal response during take-off or power loading can further exacerbate undesirable thermal-mechanical effects of metal fatigue at the airfoil trailing edge [17].

It is, therefore, necessary to design a trailing edge cooling configuration that improves the internal profiles for Mach number, static pressure, and internal heat transfer coefficient distributions. In this regard, internal features, such as pedestals provide distinct advantages. Optimal designs may include internal pedestals with many different cross-sectional areas, such as: circular, oval, race-track, square, rectangular, diamond, clover-leaf cross sections, just to mention only a few. In this context, Zukauskas [18] suggested how the Reynolds number, based on pin or pedestal diameter, may be used to characterize the flow passing through the trailing edge internal chambers in terms of corresponding Nusselt numbers for assessing the internal heat transfer capability. However, certain correction measure is needed here, as Zukausas's correlations are primarily for two-dimensional tube bundles and without taking account of pin-endwall interaction. The corresponding internal heat transfer enhancement or heat multiplier (HM) is then normalized by the smooth channel Dittus-Boelter correlation to assess the effectiveness of the cooling design. Similarly, in this context, the pressure drops through a bank of pedestals, lead to the notion of the friction multiplier (FM) normalized with Blasius resistance formula from the experimental results of Ishida et al. [19].

The corresponding relationships provided by Refs. [18,19] for the heat and friction multipliers, HM and FM, respectively, can fully characterize the trailing edge cooling design with pin-fins, in terms of cooling effectiveness. The spacing and location of these internal cooling features are then optimized to ensure the elimination of step-wise distributions of metal temperatures in the airfoil trailing edge walls. These features are presented here as representations of typical design procedure; however, there are many other features or combination of features that could be used effectively as well. In all design cases, experimental correlations are needed to assess a multitude of cooling feature characteristics. Some of these correlations are compiled by Han et al. [20].

The overall procedure for designing airfoil trailing edges with optimum heat transfer characteristics rely on the knowledge of the corresponding heat and friction multipliers, HM and FM. In many instances, plots of FM/HM versus Re are used to compare the performance of different configurations. One such plot is shown in Fig. 10, based on mass-transfer measurements conducted by Chyu [21]. Using a well-established analogy between heat transfer and mass transfer [22], the results of these experiments for different cooling features can be used to assess heat transfer characteristics of the overall cooling design. Information as such, also known as performance index, is useful in the design process as they relate heat transfer characteristics of different cooling features with available pressure gradients and flow requirements.

**External Cooling Near Trailing Edge.** In conjunction with the internal heat transfer, the heat transfer characteristics on external airfoil surface near the trailing edge also needs to be evaluated in detail. As mentioned earlier, the performance of the airfoil is affected considerably by the thickness of the trailing edge. It is, therefore, necessary to have an airfoil trailing edge with minimum thickness and with a cooling configuration that allows for lower coolant flow rate while not exceeding the metal temperatures required for the metal durability in terms of oxidation, creep, and fatigue. Meanwhile, one would like to have cast-in features as much as possible to avoid machining cost and process time.

In examining possibilities for film cooling for the design of Fig. 10, one recognizes that the airfoil has trailing edge cavities and slots in communication with the supply cavity. The slot outlet is disposed at a cut-back downstream edge of the pressure-side wall with a thickness $t$. A number of channels with width $s$, as the slot outlet allows for discharge cooling air over the extended back-surface suction-side wall or the so-called "land." If a film cooling parameter $P$ is defined as a dimensionless air flow parameter directly proportional to the cut-back distance $x$ and inversely proportional to the slot $s$ and the cooling flow rate ratio, one obtains the relation $P=x/(Ms)$ with $M$ being the blowing parameter defined as the ratio of coolant to gas mass flux ratio: $M=(\rho_c v_c)/(\rho_g v_g)$. This film cooling parameter $P$ is critical in film effectiveness calculations, as it has been used to correlate the film cooling effectiveness $\eta_F$ at the trailing edge as shown in Fig. 11.

Higher values of the film cooling parameter $P$ imply greater cut-back distances and less air flow for an equivalent film cooling effectiveness $\eta_F$. It has been recognized that high film effectiveness can be maintained over significantly longer cut-back distances with less air if the ratio $t/s$ is low [16]. According to Fig. 11, the value of $\eta_F$ can remain constant as $x$ increases, if the value of the ratio $t/s$ is decreased. This implies that if all other parameters affecting $P$ are held constant, the cut-back distance $x$ could be increased significantly without loss of film cooling effective-

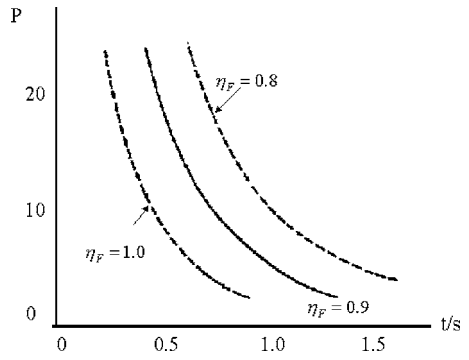


**Fig. 11 Dimensionless flow parameter *P* as function of ratio of cut-back lip thickness-to-slot for different film cooling effectiveness, from Hill et al. [16]**

ness over the length of the cut-back portion, if the ratio $t/s$ is decreased. Alternatively, or in combination, the coolant flow rate could be reduced and the cut-back distance increased. In this context, Goldstein [23] also presented experimental results for film effectiveness of various $t/s$ ratios and the blowing parameter $M$ of unity. These results are shown in Fig. 12.

To maximize the benefits for this configuration several desirable geometrical attributes will lead to an optimized design in terms of film cooling coverage. These are: (1) reduction of pressure-side lip thickness $t$ and (2) enlargement of slot $s$, provided that both are consistent with structural strength requirements. The combination of geometrical attributes (1) and (2) can then lead to minimum cooling flow rates for the pressure-side cut-back trailing edge configurations. The limit on the cooling flow rate would then come from the metal temperature ahead of the cut-back distance. As seen in Fig. 6, the metal temperature increases monotonically with distance from the supply cavity up to the onset of cut-back ($x \sim 0.08''$), the effect of trailing edge film cooling takes place after this point.

The metal temperature profile with pressure-side cut-back may not increase monotonically toward the trailing edge, as is the case for the centerline discharge configurations. The surface of the pressure side land could also be made aerodynamically rough to enhance the coolant heat transfer coefficient on that surface. Thus, the preferred selection of distance $x$, lip thickness $t$, slot $s$, and blowing parameter $M$, leads to a pressure-side cut-back trailing edge configuration, which becomes attractive for airfoil durability and overall aerodynamic performance. This paper has summarized insight into the relevant characteristics affecting the design of trailing edge configurations for high-pressure turbine airfoils.

## Conclusions

Presented in this paper are closed-form, analytical models of airfoil temperature for four most representative trailing edge configurations. These include: (1) solid wedge shape without discharge, (2) wedge with centerline slot discharge, (3) wedge with centerline discrete-hole discharge, and (4) wedge with pressure-side cut-back slot discharge. These analytical solutions for metal temperature provide fundamental insight into the relevant characteristics affecting the design of trailing edge configurations for high-pressure turbine airfoils.

Based on the information gained from the analysis, the relevant design features can be summarized as follows: (1) size of the cooling passage, (2) internal cooling features inside the cooling passage, (3) trailing edge thickness, (4) pressure-side lip thickness, (5) roughness on pressure side land, and (6) slot film coverage. From this set of features, only two, namely (1) and (2), can be used effectively for centerline discharge configurations, whereas all features, (1) through (6), can be used effectively for the pressure side cut-back configurations. For the cut-back design, there are also the added benefits of improved aerodynamic performance due to thinner trailing edges. The life capability to resist thermal-mechanical fatigue and creep is also improved as metal temperature distributions are more evenly distributed over the entire trailing edge region for the cut-back designs.

Overall design parameters were introduced to illustrate how these parameters can be selected during the optimization cycle for the trailing edge designs. This process leads to the search of detail design features and geometrical attributes, which can be judiciously selected in concert with the available design space. In this regard, cooling effectiveness becomes a strong function of the convective efficiency using internal cooling features to temper step-wise pressure and coolant Mach number distributions inside the trailing edge passages. The film cooling effectiveness and corresponding film coverage defined in terms of geometrical lip-to-slot ratio $t/s$ and blowing ratio are also important design parameters. These are influential in maintaining desired film cooling effectiveness while minimizing trailing edge cooling flow for specified trailing edge cut-back distances.

## Nomenclature

$A$ = area
$c$ = specific heat
$C_p$ = fluid specific heat at constant pressure
$E$ = cooling parameter
$f$ = friction factor
$g_c$ = gravitational constant

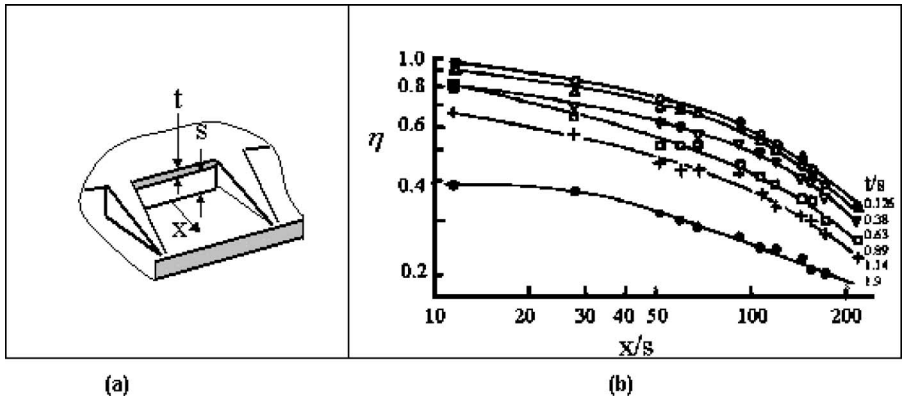


**Fig. 12 Cut-back trailing edge configuration and test results. (*a*) Schematic showing locations of relevant geometrical parameters. (*b*) Effect of *x/s* and *t/s* parameters on trailing edge film effectiveness, from Goldstein [23].**

$h$ = heat transfer coefficient
$H$ = trailing edge height at the base
$I_0$ = Bessel function of second kind, order zero
$J$ = mechanical to thermal energy conversion factor
$k$ = thermal conductivity
$L$ = length
$m$ = flow rate
$M$ = slope parameter
$N$ = number of cooling openings
Nu = Nusselt number
$P$ = perimeter
Pr = Prandtl number
$r$ = radius
Re = Reynolds number
$s$ = slot height
$S$ = sink parameter
$t$ = time or thickness
$T$ = temperature
$Q$ = total heat transfer
$q$ = heat flux
$u$ = trailing edge slope parameter
$V$ = velocity
$x$ = axial distance
$y$ = $L-x$
$W$ = width

**Greek Symbols**

$\delta$ = small change
$\Delta$ = finite change
$\phi$ = cooling effectiveness
$\eta$ = film effectiveness
$\theta$ = dimensionless temperature
$\rho$ = density
$\omega$ = speed

**Subscripts**

$B$ = bottom
$B$ = base
$c$ = coolant
$d$ = pin diameter
$g$ = gas
$h$ = holes
$L$ = longitudinal
$n$ = longitudinal
$o$ = smooth plate or channel
$P$ = transverse
$S$ = surface
$T$ = top

## References


[1] Kuhne, C. M., 2003, "Reduced Shock Transonic Airfoil," US Patent No. 2003/0072649A1, April.
[2] Eisemann, K. M., 2003, "Uncooled Data Reduction," Pratt & Whitney Internal Documentation, Pratt & Whitney, East Hartford, CT.
[3] Karamcheti, K., 1980, *Principles of Ideal-Fluid Aerodynamics*, R. E. Krieger Pub., Malabor, FL, Chap. 13.
[4] Maclachlan, D. W., and Knowles, D. M., 2002, "The Effect of Material on the Analysis of Single Crystal Turbine Blades: Part I-Material Model," *Fatigue and Fracture Engineering Material Science 25*, Blackwell Science Ltd., Oxford, pp. 385–398.
[5] Maclachlan, D. W., and Knowles, D. M., 2002, "The Effect of Material on the Analysis of Single Crystal Turbine Blades: Part II-Component Analysis," *Fatigue and Fracture Engineering Material Science 25*, Blackwell Science Ltd., Oxford, pp. 385–398.
[6] Langston, L., 2004, "A Year of Turbulence," Power and Energy, **6**, pp. 29–33.
[7] Cunha, F. J., 1994, "Integrated Steam/Gas Cooling System for Gas Turbines," US Patent No. 5,340,274, August.
[8] Jacala, A., Davis, R. M., Sullivan, M. A., Chyu, R. P., and Staub, F., 1996, "Closed Circuit Steam Cooled Bucket," US Patent No. 5,536,143, July.
[9] Cunha, F. J., DeAngelis, D. A., Brown, T. A., Chopra, S., Correia, V. H. S., and Predmore, D. R., 1997, "Turbine Stator Vane Segments Having Combined Air and Steam Cooling Circuits," US Patent No. 5,634,766.
[10] Lee, C.-P., 2001, "Turbine Blade Trailing Edge Cooling Openings and Slots," US Patent No. 6,174,135B1, Jan. 16.
[11] Cunha, F. J., Dahmer, M. T., and Chyu, M. K., 2005, "Thermal-Mechanical Life Prediction System for Anisotropic Turbine Components," ASME Paper No. GT2005-68107.
[12] Braddy, B. T., 1981, "Film Cooled Airfoil Body," US Patent No. 4,303,374, Dec.
[13] Starkweather, J. H., 1998, "Turbine Blade," US Patent No. 5,813,836, Sept.
[14] Manning, R. F., Acquaviva, P. J., and Demers, E., 1981, "Series Impingement Cooled Airfoil," US Patent No. 6036441.
[15] Cunha, F. J., and DeAngelis, D. A., 2000, "Cooling Circuits for Trailing Edge Cavities in Airfoils," US Patent No. 6,056,505, May.
[16] Hill, E. C., Liang, G. P., and Auxier, T., 1986, "Airfoil Trailing Edge Cooling Arrangement," US Patent No. 4,601,638, July.
[17] Chyu, M. K., Uysal, U., and Li, P.-W., 2002, "Convective Heat Transfer in a Triple-Cavity Structure Near Turbine Blade Trailing Edge," ASME Paper No. IMECE2002-32405.
[18] Zukauskas, A. A., 1972, "Heat Transfer from Tubes in Cross Flow," Adv. Heat Transfer, **8**, pp. 116–133.
[19] Ishida, K., and Hamabe, K., 1985, "Effect of Pin-Fin Aspect Ratio and Arrangement on Heat Transfer and Pressure Drop of Pin Fin Duct for Airfoil Internal Cooling Passage," ASME Paper No. 85-WA/HT-62.
[20] Han, J. C., Dutta, S., and Ekkad, S., 2000, *Gas Turbine Heat Transfer and Cooling Technology*, 1st ed., Taylor and Francis, New York, Chap. 1.
[21] Chyu, M. K., 1990, "Heat Transfer and Pressure Drop for Short Pin-Fin Arrays With Pin-Endwall Fillet," ASME J. Heat Transfer, **112**, pp. 926–932.
[22] Eckert, E. R. G., 1976, "Analogies to Heat Transfer Processes," *Measurements in Heat Transfer*, E. R. G. Eckert and R. J. Goldstein, eds., Hemisphere Publishing Corp., New York, Chap. 1.
[23] Goldstein, R. J., 1976, "Film Cooling," Adv. Heat Transfer, **7**, pp. 357–358.

# The Dynamics of the Horseshoe Vortex and Associated Endwall Heat Transfer—Part I: Temporal Behavior

**T. J. Praisner**
Turbine Aerodynamics,
United Technologies Pratt and Whitney,
400 Main Street, S/S 169-29,
East Hartford, CT 06108

**C. R. Smith**
Department of Mechanical Engineering,
Lehigh University,
19 Memorial Drive West,
Bethlehem, PA 18015

*Instantaneous flow topology and the associated endwall heat transfer in the leading-edge endwall region of a symmetric airfoil are presented. An experimental technique was employed that allowed the simultaneous recording of instantaneous particle image velocimetry flow field and thermochromic liquid-crystal-based endwall heat transfer data. The endwall flow is dominated by a horseshoe vortex that forms from reorganized impinging boundary layer vorticity. A relatively small vortex is shown to be a steady feature of the corner region, while a secondary vortex develops sporadically immediately upstream of the horseshoe vortex. The region upstream of the horseshoe vortex is characterized by a bimodal switching of the near-wall reverse flow, which results in quasiperiodic eruptions of the secondary vortex. The bimodal switching of the reverse flow in the vicinity of the secondary vortex is linked to the temporal behavior of the down-wash fluid on the leading edge of the foil. Frequency analysis of the flow field and endwall heat transfer data, taken together, indicate that the eruptive behavior associated with the horseshoe vortex occurs at a frequency that is essentially the same as the measured turbulence bursting period of the impinging turbulent endwall boundary layer.*
[DOI: 10.1115/1.2185676]

## Introduction

When a turbulent boundary layer approaches a bluff-body obstruction, the body-generated adverse-pressure gradient precipitates a separation process that forces the impinging boundary layer vorticity to reorganize into a horseshoe vortex. The horseshoe vortex circumscribes the leading edge of the bluff body with legs extending downstream, and is characterized by significant aperiodic unsteadiness (Devenport and Simpson [1], Agui and Andreopoulos [2], Praisner et al. [3]). In turbomachinery applications, the leg of horseshoe vortex on the pressure side of the airfoil has been shown to have high aerodynamic losses associated with it (Sjolander [4], Langston et al. [5], Sharma and Butler [6]). The leading-edge region of turbulent juncture flows is of particular interest in turbomachinery applications because the presence of the horseshoe vortex system has been found to increase local endwall heat transfer rates by as much as 300% above flat plate levels (Graziani et al. [7], Blair [8], Hippensteele and Russell [9], Giel, et al. [10], Kang et al. [11]). High heat transfer rates in leading-edge regions of high-pressure turbines are known to cause thermal-mechanical fatigue, spalling of thermal barrier coatings, and airfoil endwall/platform burning.

In recent years, the primary focus of juncture-flow studies has been the documentation of the time-mean flow field. As shown in Fig. 1, earlier studies have reported a time-mean symmetry plane flow topology that included a primary horseshoe vortex (HV), a counter-rotating secondary vortex (SV) upstream of the horseshoe vortex, a tertiary vortex (TV) upstream of the secondary vortex, and a small vortex in the corner region of the juncture (CV) (Hunt et al. [12], Praisner et al. [3]). However, it is difficult to gain a physical appreciation of the complex three-dimensional structure of the turbulent, bounded flow and its resulting impact on surface heat transfer by viewing time-mean data alone.

Devenport and Simpson [1] investigated the time-averaged structure of a turbulent juncture flow for both a 3:2 elliptical leading edge and a NACA 0020 airfoil. Their surface oil-flow visualizations revealed an impinging boundary layer separation point at $x=0.5D$ (where $x$ is the distance upstream of the foil leading edge and $D$ is the leading-edge diameter) and the existence of a line of low shear at $x=0.28D$. Their study detected a bimodal distribution of the fluctuating velocity components in the region of the horseshoe vortex, which they attributed to the impingement of fluctuating momentum and vorticity quantities from the outer region of the boundary layer. They also reported an average quasiperiodic frequency for the fluctuating velocity components.

Agui and Andreopoulos [2] performed endwall oil-flow visualizations for a cylindrical bluff body. Their results for the separation point of the impinging boundary layer agreed with those from Devenport and Simpson [1] and Dickinson [13]. Using smoke visualizations, Agui and Andreopoulos concluded that large-scale structures from the impinging boundary layer interact strongly with the HV and cause it to "wander" in a mostly streamwise direction. Their visualizations indicated strong, aperiodic outward eruptions of wall fluid upstream of the HV, which subsequently lead to the formation of a smaller counter-rotating vortex. However, they did not observe the corner vortex that was reported by earlier researchers (Hunt et al. [12], Blair [8], Ishii and Honami [14]).

Praisner et al. [3] recorded spatially and temporally resolved heat transfer data on the endwall for a turbulent juncture flow. They reported on a series field-wise instantaneous heat-transfer measurements that revealed the time-dependent spatial patterns of Stanton number upstream of a rectangular bluff body. Using Particle Image Velocimetry (PIV) measurements, they proposed an interaction model to explain the mechanisms that cause both high RMS fluctuations and elevated heat transfer for $x/x_{sep} \approx 0.5$. Their determination of the location of the boundary layer separation

Contributed by the International Gas Turbine Institute (IGTI) of ASME for publication in the JOURNAL OF TURBOMACHINERY. Manuscript received October 1, 2004; final manuscript received February 1, 2005. Assoc. Editor: K. C. Hall. Paper presented at the ASME Turbo Expo 2005: Land, Sea, and Air, Reno, NV, June 6–9, 2005, Paper No. GT 2005-69088.

  

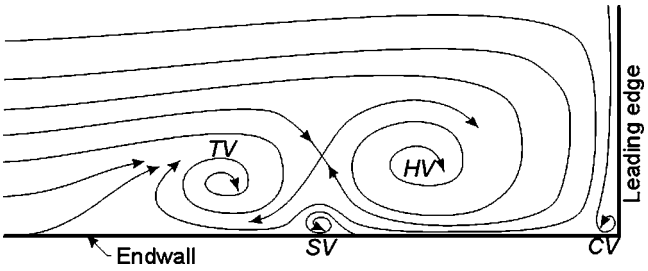


**Fig. 1 Schematic representation of the time-mean symmetry-plane streamline topology in a turbulent endwall flow**

point, the low shear/high RMS region, and the region of overall heat transfer augmentation compared well with previous consensus estimates. In addition, they observed local, instantaneous heat transfer excursions up to 200% higher than the impinging turbulent boundary layer.

While there exists some level of agreement in the results of the aforementioned studies, discrepancies still remain. These discrepancies include the instantaneous and time-mean flow topologies and most importantly, the mechanisms which give rise to elevated heat transfer levels in the leading-edge regions of turbulent endwall flows. The objective of this present study was to identify the unsteady mechanisms that give rise to the high endwall heat transfer rates so that they may be better understood and modeled in turbomachinery. An additional intent was to provide benchmark quality data for RANS- and LES-based codes that might be employed for the prediction of endwall heat loads. The assessment technique discussed in the present paper offers a unique capability for a better physical understanding of complex turbulent flows by simultaneously combining PIV and LC techniques. Part II of this study (Praisner and Smith [15]) presents time-mean flow field and heat transfer results.

## Experimental Setup

The present experiments were conducted in a closed circuit water channel as described by Acarlar and Smith [16]. The salient features of the channel include flow through a 1.75:1 contraction passing into a 5.0 m long $\times$ 0.9 m wide $\times$ 0.4 m test section. Flow speeds from 0.03 m/s to 1.20 m/s are possible with ±2% spanwise uniformity and a maximum turbulence intensity of 0.5%.

Figure 2 shows the experimental configuration employed in the present study. A cylinder with a 15.08 cm diameter and a 5:1 trailing-edge fairing was employed as a bluff body. The intent of this configuration was not to simulate a specific turbomachinery geometry, but instead to provide a generic test case. The body was mounted on a flat test plate with localized heating applied in the

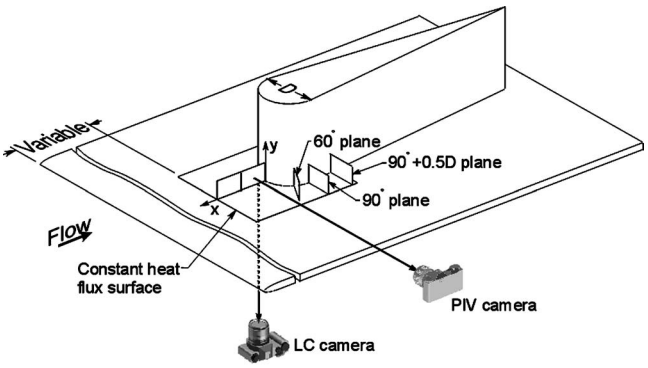


**Fig. 2 Experimental setup illustrating the configuration employed to record simultaneous flow-field and endwall heat transfer data**

endwall region. The cylinder fairing was employed to minimize temporal fluctuation of the stagnation line at the leading edge caused by vortex shedding. A uniform heat-flux condition was generated on the endwall using a galvanically heated 0.051 mm stainless-steel foil stretched over a thin air cavity in the test plate. The thin air cavity provides nearly perfect insulation on the inner surface of the uniform heat-flux surface when the outer surface is exposed to the water flow. Thus, essentially all heat transfer from the foil is into the water boundary. In addition, the insulating air cavity provided a dry environment for the application of thermochromic liquid crystals (LC) for monitoring the temperature variations of the heating surface (i.e., the foil).

The application of the LC to the *nonflow* side of the stainless-steel sheet allowed the simultaneous recording of: (1) flow-field data (high-density particle image velocimetry, PIV) and (2) high-resolution instantaneous heat transfer distributions on the endwall. This simultaneous recording process is accomplished by viewing the LC images on the underside of the test plate, while the PIV views are recorded using a camera positioned along side the water channel, as shown schematically in Fig. 2. The frequency response of the composite sensing sheet (stainless steel, black paint and LCs) was determined to be greater than 100 Hz (Praisner et al. [17]), which is approximately ten times greater than the temporal frequencies of the resolvable structures in the flow field. This thin temperature-sensing sheet was also shown to incur negligible lateral smearing of the local surface temperature field (Praisner et al. [17]).

There are a variety of phenomena which may impact the accuracy of wide-band thermochromic liquid crystal temperature measurements, including irregularities in liquid crystal and black paint layers, reflective components from light sources, and variations in the lighting/viewing angle across the surface. A wide-band calibration technique was employed for this study, which accounted for these and other sources of uncertainty by employing a point-wise calibration of the entire endwall surface (Praisner [18], Sabatino et al. [19]). The resultant instantaneous temperature distributions were employed to establish spatially and temporally resolved convective heat transfer coefficient distributions presented in the form of Stanton number using the conventional equation

$$\mathrm{St} = \frac{\left(\dfrac{q''}{T_w - T_\infty}\right)}{\rho U_\infty C_p} \tag{1}$$

Here $T_\infty$ is the impinging free-stream temperature, $\rho$ is evaluated at $T_{\mathrm{film}}=(T_{w\text{-avg}}+T_\infty)/2$, $T_w$ is the local wall temperature and $T_{w\text{-avg}}$ is the spatially averaged wall temperature from a single realization. The mean uncertainty of the Stanton numbers was established, using the method of Kline and McClintok [20], as approximately ±4.7%, varying between ±3.6% and ±7.9 (see Sabatino et al. [19], for a detailed assessment).

High image-density PIV (Adrian [21], Rockwell et al. [22]) was employed to establish velocity-field realizations which are temporally and spatially correlated with the surface heat transfer measurements. For each spatial plane considered (Fig. 2), the interrogated PIV images produced vector fields of nominally $100\times50$ vectors, with image dimensions of $0.5D\times0.25D$. This provided approximately 12 vectors across the diameter of the horseshoe vortex (HV) on the symmetry plane. The uncertainty of the measured velocity fields was experimentally estimated by Praisner [18] as ±2%, which is supported by Adrian [20]. Details of the test section construction, calibration, and PIV system can be found in Praisner et al. [17].

The spatial planes on which PIV data were collected are also shown in Fig. 2. Two fields-of-view on the symmetry plane were necessary to span one leading-edge diameter upstream of the bluff body, while single fields of view were employed for the 60 deg,

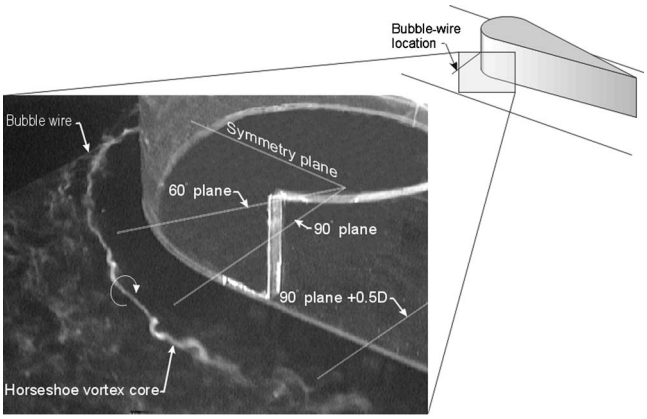


**Fig. 3 Hydrogen-bubble visualization of the horseshoe vortex core in a turbulent endwall flow formed with a faired cylinder**

90 deg, and 90 deg+0.5$D$ planes. A thumbnail version of Fig. 2, with the corresponding PIV plane colored red, is included in select figures of this report to help orient the reader.

The approach flow test plate (the endwall surface) used a 5:1 elliptical leading edge to smoothly initiate the impinging boundary layer, and a 213 cm development length prior to the leading edge of the bluff body. Heating of the endwall started 190 cm downstream of the leading edge of the test plate and 15 cm upstream of the bluff body leading edge. A uniform endwall heat flux level at the base of the bluff body was maintained at 10,500 W/m$^2$.

The endwall boundary layer was tripped at the leading edge of the endwall test plate. The free-stream velocity, $U_\infty$, was held constant at 14.7 cm/s for all studies, giving a Reynolds number based on the cylinder diameter of $2.44\times10^4$, which is at the low end of the typical range for high-pressure turbines. The corresponding undisturbed (with the bluff body removed) boundary-layer parameters at the stream-wise location of the bluff body leading edge were $\delta$=5.2 cm, $\mathrm{Re}_x=3.20\times10^5$, $\mathrm{Re}_\theta$=814, and $H$=1.28. The results presented here were obtained with a free-stream turbulence of 0.5%.

In addition, qualitative flow visualization data of the endwall region were obtained using hydrogen-bubble and laser-illuminated particle visualization techniques, and were used to guide the interpretation of the quantitative PIV and LC data.

## Results

Figure 3 shows a view (viewing obliquely from downstream) of the horseshoe vortex core marked by hydrogen bubbles. The bubble wire was positioned transverse to the impinging flow, approximately 0.9 cm above the endwall and 2.8 cm upstream of the bluff body (the approximate location of the center of the HV on the symmetry plane). The bottom edges of the planes for which PIV data were obtained are indicated on the endwall in this figure. One can observe that the HV maintains a well-defined core until a point just downstream of the 90 deg plane (note that the vortex core is a region of low pressure due to the rotation, which "traps" the bubbles in the core). Beyond this point, the vortex appears to break down, as indicated by the spiral distortion, which develops immediately downstream of the 90 deg plane, followed by dispersion of the bubble markers.

While Fig. 3 is a single instantaneous image, this pattern of vortex breakdown was generally characteristic of the flow behavior of the HV core. In a series of visualization studies employing both hydrogen-bubble and dye injection, the HV core was observed to consistently break down before reaching the 90 deg +0.5$D$ plane. It should also be noted that the quality of flow visualizations carried out with tracer techniques varied widely

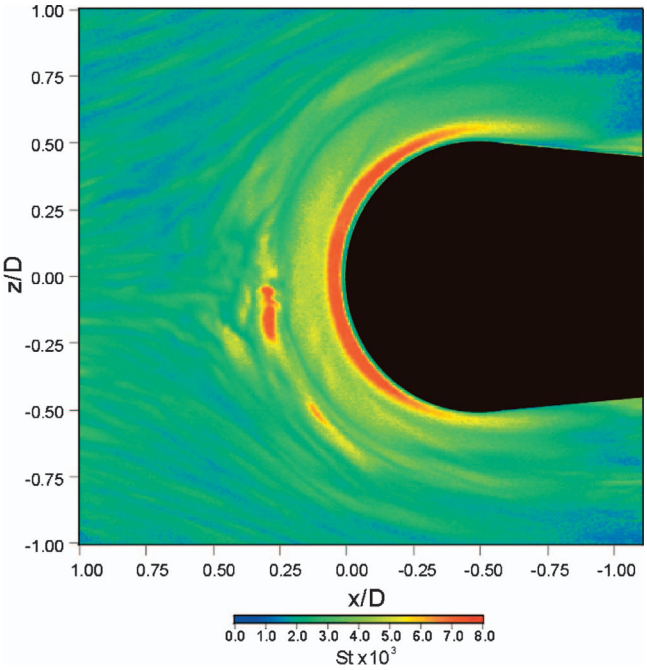


**Fig. 4 Snapshot of an instantaneous Stanton number distribution on the endwall. Flow is from left to right.**

with time. The varying quality of the visualizations was caused by oscillations of the HV, which are thought to be induced by the inherent fluctuating momentum within the turbulent endwall boundary layer. This finding is consistent with results reported by Ishii and Honami [14] and Devenport and Simpson [1].

Figure 4 is an instantaneous realization of the Stanton number distribution on the endwall. This figure illustrates the thermal streak-spacing behavior created by the impinging turbulent boundary layer immediately upstream of the endwall separation point (roughly $x/D\approx0.5$ on the symmetry plane), just prior to the leading edge of the bluff body. Cross-stream auto correlations of the instantaneous Stanton number data at $x/D$=1.00, 0.75, and 0.50 indicate that the thermal streak spacing increases, respectively, from 104 $z^+$ to 106 $z^+$ and finally to 160 $z^+$. This type of increase in hydrodynamic streak spacing was reported previously by Schraub and Kline [23] for turbulent boundary layers experiencing adverse pressure gradients.

Figure 4 reveals that the most spatially extensive, or primary, region of high heat transfer is a band (shown as red) located immediately upstream of the leading edge of the bluff body ($x/D\approx0.05$). The level of instantaneous heat transfer augmentation in this primary band is as much as 300% higher than the impinging turbulent boundary layer. Hydrogen bubble flow visualizations revealed that the primary band of high heat transfer is caused by outer-region boundary layer fluid that impinges on the leading edge, and then flows down the face of the bluff body, impinging on the endwall (Praisner [18]). Additionally, this primary band of high heat transfer was found to be temporally stable, demonstrating little change. The isolated region of high heat transfer (the small red region at $x/D\approx0.27$) near the symmetry plane, referred to here as the secondary band, displays heat transfer levels that are, at the depicted instant in time shown, equally as high as the primary band of high heat transfer. However, this secondary band or region of high heat transfer was found to be much more transient in its development and behavior.

Simultaneous flow-field and endwall heat transfer data for a selected instant are shown in Fig. 5, which is a composite image of instantaneous symmetry-plane vorticity distribution juxtaposed with the corresponding instantaneous endwall Stanton number distribution. The HV is clearly marked by the strong concentration

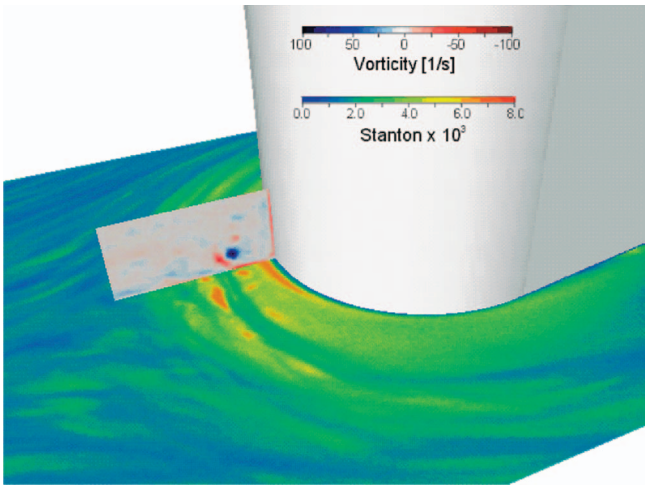


**Fig. 5 Instantaneous symmetry-plane flow-field data with the corresponding instantaneous endwall heat transfer distribution**

of positive vorticity. This composite image substantiates initial visualization studies, which suggested that the HV resides immediately above a region of relatively low heat transfer, separating two bands of high heat transfer. Figure 5 also illustrates that a transverse region of high heat transfer upstream of the HV is in fact spatially coincident with the SV, and not the HV.

A temporal visualization sequence illustrating the eruptive process on the symmetry plane in the vicinity of the HV is shown in Fig. 6. Laser-illuminated neutrally buoyant particles were employed with digital video recording to visualize the temporal behavior of the flow for this figure. The primary vortical structures, HV, SV, and TV, are labeled in Fig. 6(*a*) and the sense of the local streamline flow is sketched on each image for clarity. Note that initially the reverse-flow fluid path is under the HV, passing over the SV and then merging with the flow under the TV. As shown in Fig. 6(*b*), the flow streamlines suddenly switch to a flow topology where the reverse flow under the HV now primarily feeds the SV, with a stagnation flow developing on the endwall immediately between the SV and the TV. By Fig. 6(*c*), the SV is erupting away from the endwall, being replaced by an inrush of fluid from the far-wall region. The eruptive process is nearly complete in Fig. 6(*d*) as the SV ejects into the far-wall region, and is completely replaced by the inrush of outer fluid. While other more subtle modes of interaction were observed upstream of the HV, the eruptive process shown in Fig. 6 was the most pronounced and energetic mode. Evaluation of numerous visualization sequences, such as those shown in Fig. 6, revealed that during these eruptive processes, the horseshoe vortex is characterized by motions in the symmetry plane within a limited streamwise envelope of $\pm 0.04D$.

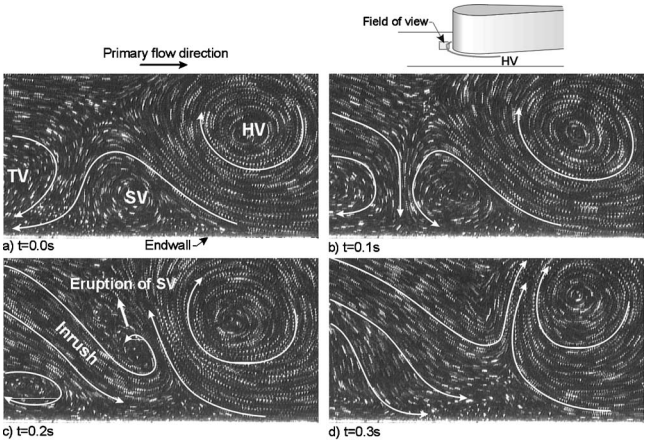


**Fig. 6 Temporal sequence of laser-illuminated particle visualizations of the symmetry-plane flow topology**

The aforementioned visualizations illustrate the existence in a turbulent juncture flow (in an instantaneous sense) of a dominant horseshoe vortex, a counter-rotating secondary vortex, a co-rotating tertiary vortex, and a small corner vortex. These results compare well with the time-mean symmetry-plane topology reported by Ishii and Honami [14].

Figure 7 is a sequence of instantaneous vorticity-streamline images in the symmetry plane (generated from PIV data), juxtaposed with the corresponding instantaneous surface heat transfer along a line where the symmetry plane intersects the endwall. While streamline topologies for individual PIV frames are of limited physical significance, they are useful for tracking flow patterns that are consistent across sequential realizations. The sequence in Fig. 7 illustrates the response of the endwall heat transfer to an eruptive process in the vicinity of the HV on the symmetry plane. Note that the streamline topologies in this figure are quite similar to the flow topologies of Fig. 6. The time between each realization is 0.2 s or 9 $t^+$. An interaction parameter (IP), defined in Eq. (2) below, is tracked for each frame in Fig. 7,

$$\mathrm{IP} = \frac{\Gamma}{aU_\infty} \tag{2}$$

The red bar in each bar chart in Fig. 7 corresponds to the IP for each frame shown. The interaction parameter, is a grouping of the circulation strength ($\Gamma$) of the HV as calculated about a contour of constant vorticity equal to approximately half the peak level in the vortex, the vertical distance from the center of the HV to the endwall ($a$) as deduced from streamline plots, and the free-stream velocity ($U_\infty$). This interaction parameter characterizes the strength of the local surface pressure gradient created by the presence of the vortex, which is directly responsible for the creation of inviscid-viscous interactions (Doligalski et al. [24]) (i.e., the stronger the vortex, or the closer its proximity to the surface, the greater the interaction of the vortex with the viscous fluid in proximity to the endwall).

In Fig. 7(*a*) the heat transfer levels in the vicinity of the SV are relatively low due to the feeding of fluid from under the HV, over the SV, and then back under the TV. This is essentially the same flow topology depicted in the visualization of Fig. 6(*a*). The interaction parameter at this point indicates a high value of 1.6, which coincides with the initiation of the ejection of the SV. By Fig. 7(*b*), the SV begins to lift away from the endwall surface, followed closely by the initiation of an inflow of outer-region fluid into the near-wall region just upstream of the SV. This interchange of fluid results in a sudden rise in the heat transfer in the region immediately upstream of the SV. As the ejection of the SV continues in Fig. 7(*c*), the inrush of replacement fluid becomes more pronounced, as does the associated heat transfer. Finally, by Fig. 7(*d*), following the ejection of the parcel of negative-vorticity SV fluid into the outer region, the heat transfer near the origin of the SV begins to decrease. Note that during this ejection process the IP for the HV continually decreases as the HV strength decreases, due to a cross cancellation with the vorticity of the ejecting SV, and the HV moves further from the endwall. The flow will relax until the HV gains strength from the main flow, moves toward the endwall again (thus increasing the IP), another interaction with the endwall fluid is precipitated, and the cycle repeats. The results in Fig. 7 quantitatively illustrate that the in-rush of replacement fluid during the process of SV lift-off and ejection is responsible for the sudden rise in the associated endwall heat transfer.

The temporal sequence shown in Fig. 7 supports the original report of Devenport and Simpson [1] that a bimodal switching of the flow exists in the region upstream of the HV. The current results indicate that the saddle point shown in Fig. 1 above the SV marks the confluence of two opposing flows. These opposing

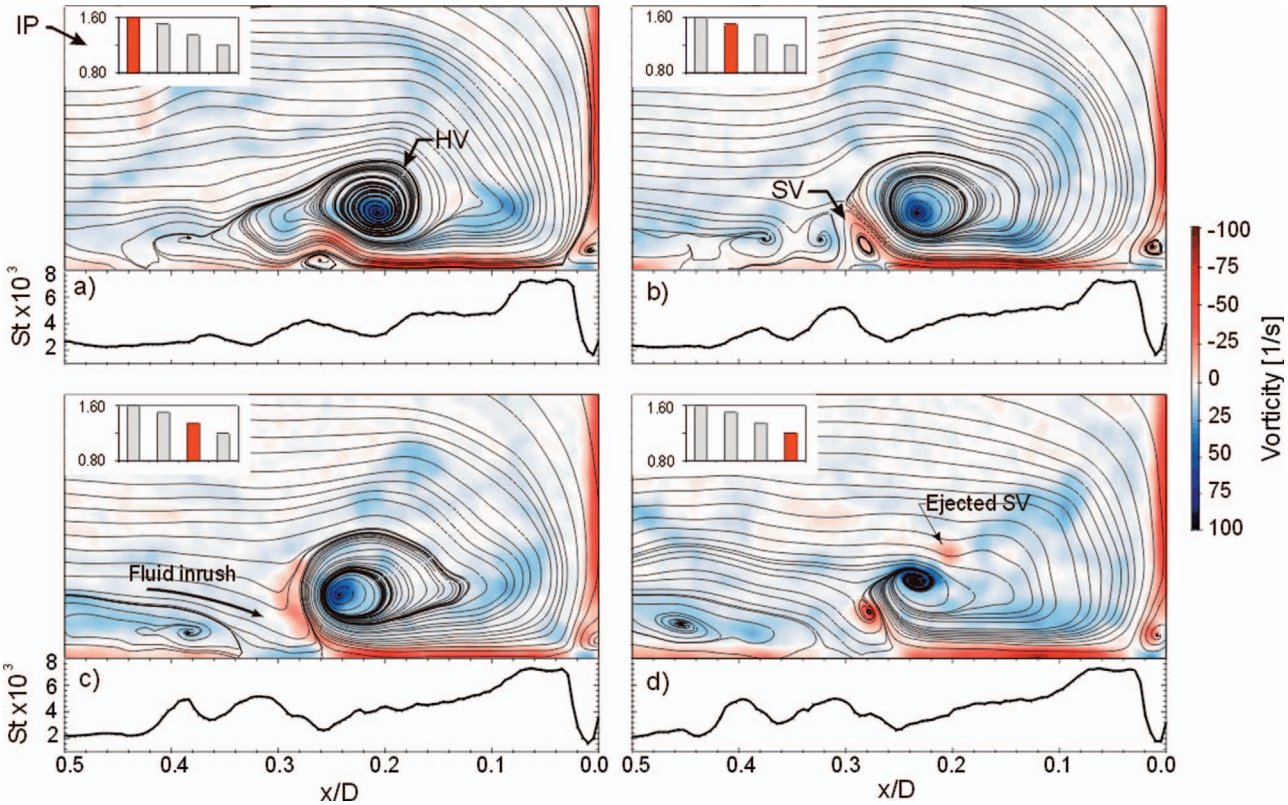


**Fig. 7 Temporal sequence of four instantaneous realizations of symmetry-plane streamlines and vorticity distributions with the corresponding endwall heat transfer distributions. Time between frames is 0.2 s or 9$t^+$.**

flows are formed from: (1) the near wall fluid of the impinging boundary layer, and (2) outer-region fluid that has impinged on the face of the leading edge of the foil, and then turned by the endwall to flow upstream under the HV. The interaction of these two opposing flows gives rise to two modes of interaction upstream of the HV. In the first mode, as shown in Figs. 6(*a*) and 7(*a*), the near-wall reverse flow under the horseshoe vortex travels upstream (over the secondary vortex which may or may not be present) to eventually feed under, and then into, the tertiary vortex. In this mode of reverse flow, outer-region fluid does not penetrate the near-wall region. In this first mode, all of the reverse-flow fluid originates from the downwash of fluid on the leading edge of the foil. This mode dominates the near-wall flow topology for approximately 80% of the time, only disrupted by a quasi-periodic switching to a second mode of reverse flow.

In the second mode of interaction, the reverse-flow region beneath the horseshoe vortex switches from feeding upstream under the tertiary vortex, to a mode in which it feeds only into the secondary vortex and horseshoe vortex. At this point, cool outer-region flow typically penetrates to the endwall surface, causing a local increase in endwall heat transfer.

So, it is the competition between the impinging inflow and the reversed flow (passing under the HV) that creates the bimodal flow patterns observed in sequences such as those shown in Figs. 6 and 7. It should be noted that, as the thermal boundary layer for the present study is substantially thinner than the momentum boundary layer, the mode switching has an exaggerated effect on the instantaneous heat transfer pattern shown in Fig. 7. Thus, when the SV is ejected from the near-wall region, the cool replacement fluid from the outer region of the impinging boundary layer results in a rapid elevation in local heat transfer.

In an instantaneous sense, the band of high heat transfer that develops under the secondary vortex (at $x/D \approx 0.27$ on the symmetry plane in Fig. 4) is characterized by transversely segmented regions of high heat transfer. This segmentation suggests that eruptive events like those depicted in Figs. 6 and 7, occur separately in cross-stream-localized regions upstream of the body, and are apparently the result of the transversely segmented "streak" flow structures comprising the near-wall region of the impinging turbulent boundary layer.

A sequence of vorticity/heat transfer behavior is shown in Fig. 8 for the 90 deg plane (perpendicular to the mean flow direction). In this sequence, the time between frames is 0.2 s or 9.2 $t^+$. For the sake of simplicity, a local axis system, denoted by $x'$, similar to that used for the symmetry-plane information is used to spatially reference the off-symmetry-plane data. Because the instantaneous streamlines in the off symmetry-plane PIV data (the primary flow component is out-of-plane) are deduced from projections of the instantaneous three-dimensional flow vectors onto the PIV plane, they yield limited insight into the flow behavior and were not included in Fig. 8.

Figure 8(*a*) illustrates the vorticity field, with a concentration of positive vorticity (blue) indicating the location of the HV, but with slightly lower heat transfer than the comparable region in Figs. 7 and 8. This is not surprising considering that the main component of velocity in this region is essentially perpendicular to the data plane. In Fig. 8(*b*), a relatively weak interaction (compared to the symmetry-plane interactions) between the HV and the near-wall fluid is evidenced by the focusing of near-wall wall vorticity (red) into a SV. Note that the subsequent lifting of the SV away from the surface (Fig. 8(*c*)) and ejection of the SV (Fig. 8(*d*)) is associated with the development of a region of elevated heat transfer between $0.35 < x'/D < 0.48$. The strength and lateral scale of the HV is also observed to increase during this process. So, the strengthening of the vortex and subsequent ejection of near-wall fluid appears to be the primary mechanism that causes the formation of the secondary band of high heat transfer between the sym-

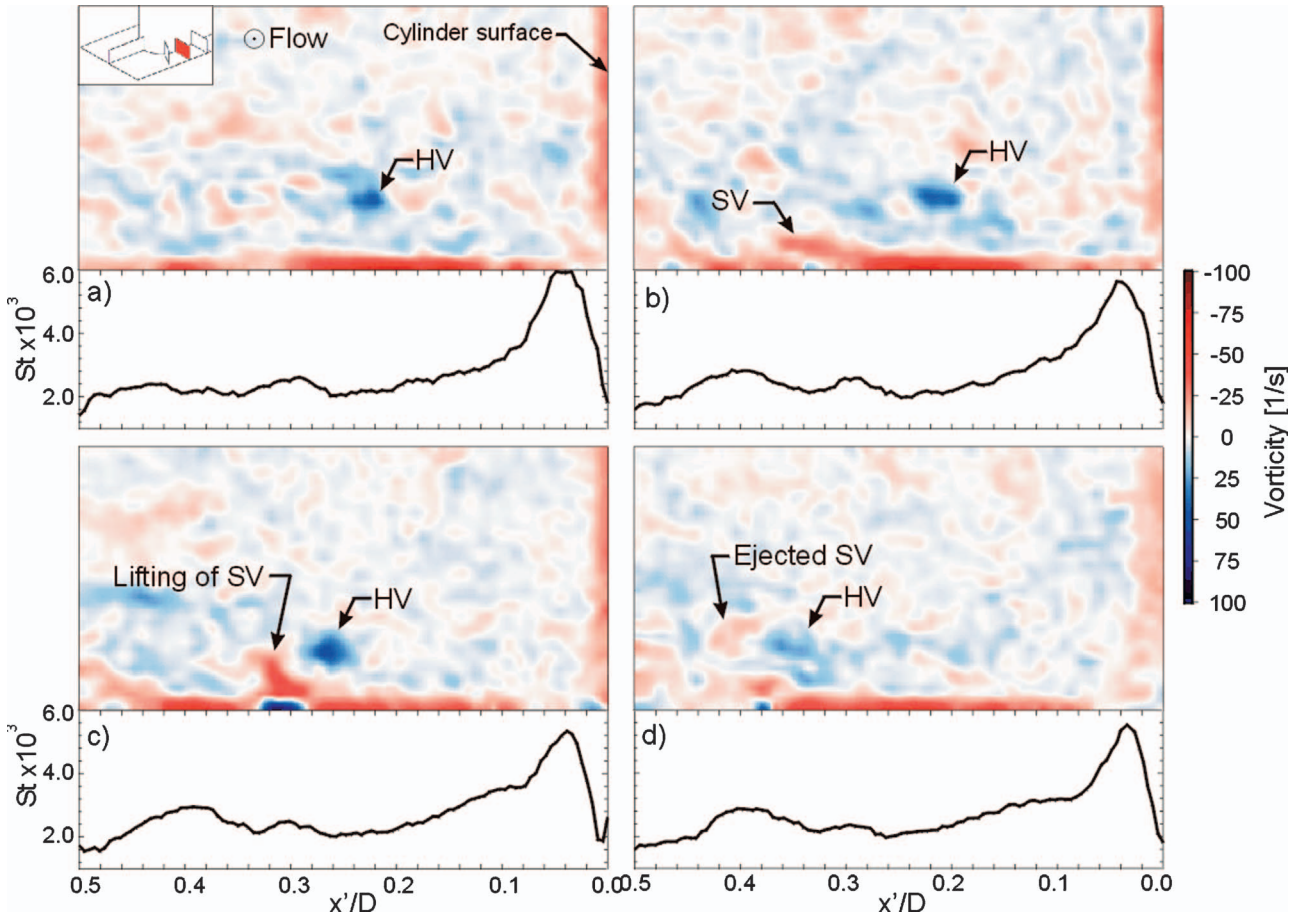


**Fig. 8 Temporal sequence of vorticity distributions and the associated endwall heat transfer on the 90 deg plane. Time between instances is 0.2 s or 9$t^+$. Note, the bulk flow is toward the viewer.**

metry and 90 deg planes. As the vortex/near-wall fluid interaction becomes weaker as the 90 deg plane is approached, the secondary band of high heat transfer becomes more muted.

Figure 9 is a schematic illustrating a process used to construct three-dimensional time-space images from sequences of simultaneously recorded vorticity and endwall heat transfer data. These 3D images illustrate contours of constant vorticity, creating regions of time-space vorticity behavior. In a similar manner, the symmetry-plane Stanton number data was extracted from each instantaneous image and compiled in a two-dimensional $x$-$t$ plane to form a planar representation of the spatial-temporal behavior of the symmetry plane heat transfer. The color maps for the PIV and LC time-space images were chosen to produce clear color discrimination between the contours of vorticity and endwall Stanton number.

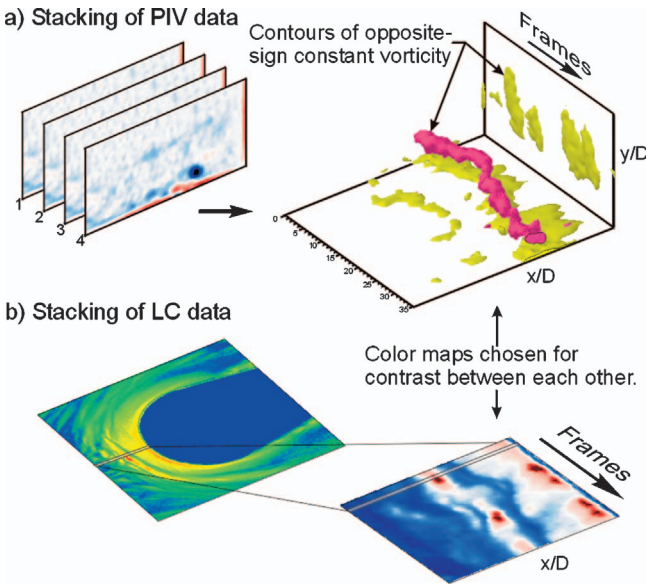


**Fig. 9 Schematic illustrating the stacking of flow-field and endwall heat transfer data in the time dimension to form time-space constructs**

Figure 10 shows time-space constructs for two different sets of PIV and LC data in the symmetry plane. The value of constant vorticity in both images is $\pm 25\ s^{-1}$ and the color map for the LC space-time construct is adjusted to highlight regions of high heat transfer (red areas). All of the data are plotted against time in wall units, based on the characteristics of the unobstructed impinging turbulent boundary layer.

An examination of the temporal relationships between the type of eruptive events shown in Figs. 6 and 7 reveal a consistent temporal pattern for both high-vorticity and high Stanton-number events. This temporal behavior is most evident in Fig. 10($a$) from the endwall Stanton number distribution and the vorticity patterns near the endwall and leading-edge surfaces. In Fig. 10($a$), note how a region of high negative vorticity develops on the face of the bluff body near $y/D \approx 0.15$ at $t^+ \approx 70$, which reflects a localized acceleration of the down-wash fluid. This acceleration of the down-wash fluid is caused by the impingement of relatively high momentum fluid from the log and wake regions of the upstream boundary layer (deduced from instantaneous PIV data). This downwash acceleration proceeds down the face of the bluff body

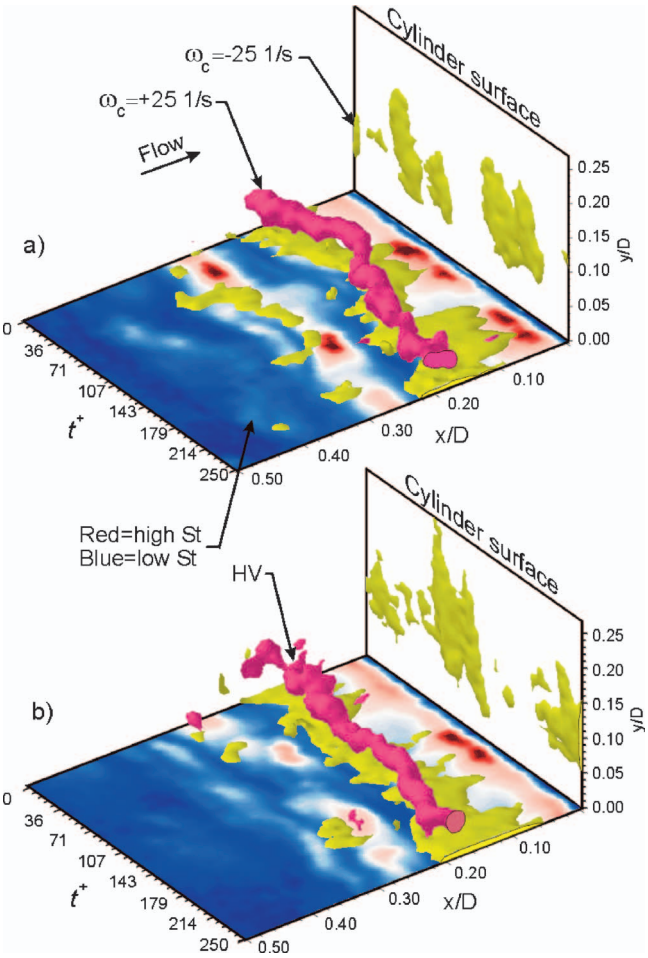


**Fig. 10 Combined time-space constructs of symmetry-plane flow-field and heat transfer data from two separate data sets illustrating quasiperiodic eruptive events**

(as evidenced by the skewed orientation in the time-space image) and lasts for approximately 30 $t^+$ units. The downwash acceleration is followed closely (30 $t^+$ units later) by a second acceleration event, which displays a similar time-space pattern. Immediately following this pair of downwash events, a pair of locally isolated regions of high heat transfer appears in the endwall corner region. The spacing and position of these high heat transfer events suggests that they develop as a result of the downwash acceleration events. Approximately 120 $t^+$ units after the first two downwash events occur, a second set of more closely spaced, similar downwash events occurs. This again results in the subsequent development of two closely spaced regions of high heat transfer on the endwall at $t^+ \approx 200$.

In addition to the coupled downwash-heat transfer events near the bluff body juncture, two other regions of high heat-transfer develop upstream of the HV at approximately $t^+=25$ and $t^+=150$. Note that these upstream high heat transfer events display a temporal separation period ($t^+ \approx 120$) that is similar to that between the downwash events. Comparable, but weaker, temporal behavior is also evident in Fig. 9(*b*).

From an examination of the time-space constructs of Fig. 10, it is unclear whether the heat transfer events upstream of the HV either temporally precede or possibly follow the pronounced downwash events near the bluff body. However, the streamline topologies of Fig. 7 indicate that the fluid that eventually comprises the eruptive SV originates from the downwash region. This suggests that the high heat transfer events developing upstream *follow* the downwash events in the corner region. Consistent temporal spacing between these downwash and high heat transfer events was observed in three sets of time-space constructs (another data construct is not shown in this paper), suggesting that there is a correlation between the observed downwash acceleration events and the subsequent eruptive interactions of the HV.

**Table 1 Auto correlation results for the five planes of data collected as well as for the undisturbed impinging turbulent boundary layer (TBL)**

| | Endwall St number | Bluff-body vorticity | Endwall vorticity |
|---|---|---|---|
| Symmetry plane [$t^+$] | 136 | [a] | 113 |
| | 126 | 125 | 134 |
| 60 deg plane [$t^+$] | [b] | 135 | 120 |
| | [b] | 133 | [a] |
| 90 deg plane [$t^+$] | [a] | 120 | 121 |
| | [a] | 115 | 110 |
| 90 deg+0.5$D$ plane [$t^+$] | 98 | 110 | 125 |
| | [a] | 118 | 133 |
| Juncture average: | 120 | 122 | 122 |
| Undisturbed TBL [$t^+$] | 116 | NA | 108 |

[a]No clear correlation.
[b]Heat transfer data not investigated.

A series of two-dimensional auto correlations were performed on time-space constructs of the endwall heat transfer beneath each PIV plane, the foil-surface vorticity, and the endwall vorticity. This was done for each of the planes considered in this set of experiments (Fig. 2). The time period of the dominant peak in each respective autocorrelation was then assessed, and is given in Table 1. Note that two sets of simultaneous data were recorded for all planes examined, while one set was recorded for the base turbulent boundary layer. The nature of the eruptive events in the turbulent endwall region appears to be quasiperiodic, with the average of the time periods comparing well with the primary bursting period of the impinging turbulent boundary layer (TBL). Additionally, the time periods for the undisturbed boundary layer compare well with the commonly accepted bursting period of 100 $t^+$ units for canonical turbulent boundary layers (Lu and Smith [25]). These results support the concept that the strongest turbulent events in the impinging TBL, termed "bursts" by Kim, Kline, and Reynolds [26] (which result in high negative Reynolds stresses within the boundary layer), can give rise to regions of disparate momentum in the wall-normal direction which, ultimately influence the eruptive events in the endwall region.

## Conclusions

The present study illustrates that the endwall juncture region is dominated by a horseshoe vortex that is characterized by significant quasiperiodic unsteadiness. The quasiperiodic nature of the flow modes in the vicinity of the horseshoe vortex is a result of sporadic acceleration of the downwash fluid on the face of the bluff body. Downwash and eruptive events are observed to create two bands of distinctly elevated heat transfer:

(1) A primary band of high heat transfer very near the leading edge that is created by fluid flowing down the face of the leading edge and impinging on the endwall in the corner region.
(2) A secondary band that is associated with upstream eruptions of secondary vortices, and the subsequent penetration of outer region fluid to the endwall.

The location of a saddle point above the SV (Fig. 1) marks a point of equilibrium between the opposing impinging turbulent boundary layer fluid and the near-wall reverse flow that passes beneath the HV. The dominant mode of interaction between these opposing flows is one in which the impinging outer-region fluid passes over the HV, while the reverse-flow fluid under the HV

remains within the near-wall region. This mode is disrupted by a sudden quasiperiodic increase in the reverse flow beneath the HV, precipitated by a downwash event accelerating toward the corner region. This increased local flow rate typically causes the HV to strengthen and move into closer proximity of the endwall, causing a strengthening of the SV. As the SV grows in strength, it mutually interacts with the HV, which results in an induced, inviscid-type interaction between the HV and the SV, which culminates in the SV moving rapidly away from the surface, reflected as an ejection of the SV away from the endwall and into the outer region flow. As the secondary vortex separates from the endwall and ejects outward, a portion of the outer-region flow diverts toward the endwall and under the reverse flow, replacing the fluid in the region formerly occupied by the secondary vortex.

Finally, the eruptive events shown in Fig. 6 and 7 occur with a mean time period between events of 115–120 $t^+$ units, based on the viscous time scale of the impinging turbulent boundary layer. This period is essentially the same as the measured bursting period in the undisturbed impinging turbulent boundary layer, and appears to reflect the influence of the impinging turbulence in controlling the temporal behavior of the endwall flow.

## Acknowledgment

The authors wish to thank the Air Force Office of Scientific Research for its support of this research under Contract No. F49620-93-1-0217.

## Nomenclature

$a$ = proximity of vortex core to endwall
$C_p$ = specific heat
CV = corner vortex
$D$ = leading-edge diameter
$h$ = convective heat transfer coefficient $h=q''/A/(T_s-T_\infty)$
$H$ = boundary layer shape factor
HV = horseshoe vortex
N = Newton
$q''$ = heat Flux $W/m^2$ K
$Re_D$ = Reynolds number based on $D$, $Re_D=U_\infty D/\nu$
St = Stanton number $St=h/(\rho U_\infty C_p)$
SV = secondary vortex
$T$ = temperature
TBL = turbulent boundary layer
TV = tertiary vortex
$t^+$ = nondimensional time $t^+=t(u_\tau)^2/\nu$
$U_\infty$ = free-stream velocity
$x$ = direction upstream from leading edge of bluff body
$x_{sep}$ = separation point of the endwall boundary layer
$x'$ = direction normal to the surface of the bluff body
$y$ = endwall-normal distance
$z$ = cross-stream distance from symmetry plane

### Greek Symbols

$\delta$ = boundary layer thickness
$\Gamma$ = vortex circulation strength
$\rho$ = fluid density
$\tau$ = wall shear
$\mu$ = dynamic viscosity
$\nu$ = kinematic viscosity
$\omega$ = vorticity

## References

[1] Devenport, W. J., and Simpson, R. L., 1990, "Time-Dependent and Time-Averaged Turbulence Structure Near the Nose of a Wing-Body Junction," J. Fluid Mech., **210**, pp. 23–55.
[2] Agui, J. H., and Andreopoulos, J., 1992, "Experimental Investigation of a Three-Dimensional Boundary Layer Flow in the Vicinity of an Upright Wall Mounted Cylinder," ASME J. Fluids Eng., **114**, pp. 566–576.
[3] Praisner, T. J., Seal, C. V., Takmaz, L., and Smith, C. R., 1997, "Spatial-Temporal Turbulent Flow-Field and Heat Transfer Behavior in End-Wall Junctions," Int. J. Heat Fluid Flow, **18**(1), pp. 142–151.
[4] Sjolander, S. A., 1975, "The Endwall Boundary Layer in an Annular Cascade of Turbine Nozzle Guide Vanes," Carleton University, Deptartment of Mechanical and Aeronantal Engineering, Ottawa, Canada, TR ME/A 75–4.
[5] Langston, L. S., Nice, M. L., and Hooper, R. M., 1976, "Three-Dimensional Flow Within a Turbine Cascade Passage," ASME Paper No. 76-GT-50.
[6] Sharma, O. P., and Butler, T. L., 1987, "Predictions of Endwall Losses and Secondary Flows in Axial Flow Turbine Cascades," ASME J. Turbomach., **109**, pp. 229–236.
[7] Graziani, R. A., Blair, M. F., Taylor, J. R., and Mayle, R. E., 1980, "An Experimental study of Endwall and Airfoil Surface Heat Transfer in a Large Scale Turbine Blade Cascade," ASME J. Eng. Power, **102**, pp. 257–267.
[8] Blair, M. F., 1974, "An Experimental Study of Heat Transfer and Film Cooling on Large-Scale Turbine Endwalls," ASME J. Heat Transfer, **96**, pp. 524–529.
[9] Hippensteele, S. A., and Russell, L. M., 1988, "High Resolution Liquid-Crystal Heat-Transfer Measurements on the Endwall of a Turbine Passage with Variations in Reynolds Number," NASA Technical Memorandum 100827.
[10] Giel, P. W., Thurman, D. R., VanFossen, G. J., Hippensteele, S. A., and Boyle, R. J., 1998, "Endwall Heat Transfer Measurements in a Transonic Turbine Cascade," ASME J. Turbomach., **120**, pp. 305–313.
[11] Kang, M., Kohli, A., and Thole, K. A., 1999, "Heat Transfer and Flowfield Measurements in the Leading Edge Region of a Stator Vane Endwall," ASME J. Turbomach., **121**, pp. 558–568.
[12] Hunt, J. C. R., Abell, C. J., Peterka, J. A., and Woo, H., 1978, "Kinematical Studies of the Flows Around Free or Surface-Mounted Obstacles; Applying Topology to Flow Visualization," J. Fluid Mech., **86**, pp. 179–200.
[13] Dickinson, S. C., 1988, "Time Dependent Flow Visualization in the Separated Region of an Appendage-Flat Plate Junction," Exp. Fluids, **6**, pp. 140–143.
[14] Ishii, J., and Honami, S., 1986, "A Three-Dimensional Turbulent Detached Flow With a Horseshoe Vortex," ASME J. Eng. Gas Turbines Power, **108**, pp. 125–130.
[15] Praisner, T. J., and Smith, C. R., 2006, "The Dynamics of the Horseshoe Vortex and Associated Endwall Heat Transfer—Part II: Time-Mean Results," ASME J. Turbomach., **128**, pp. 755–762.
[16] Acarlar, M. S., and Smith, C. R., 1987, "A Study of Hairpin Vortices in a Laminar Boundary Layer," J. Fluid Mech., **175**, pp. 1–41.
[17] Praisner, T. J., Sabatino, D. R., and Smith, C. R., 2001, "Simultaneously Combined Liquid-Crystal Surface Heat Transfer and PIV Flow-Field Measurements," Exp. Fluids, **30**, pp. 1–10.
[18] Praisner, T. J., 1998, "Investigation of Turbulent Juncture Flow Endwall Heat Transfer and Fluid Flow," Ph.D. thesis, Lehigh University, Department of Mechanical Engineering and Mech.
[19] Sabatino, D. R., Praisner, T. J., and Smith, C. R., 2001, "A High-Accuracy Calibration Technique for Thermochromic Liquid Crystal Temperature Measurement," Exp. Fluids, **28**, pp. 497–505.
[20] Kline, S. J., and McClintock, F. A., 1953, "Describing Uncertainties in Single-Sample Experiments," Mech. Eng. (Am. Soc. Mech. Eng.), **75**, pp. 3–8.
[21] Adrian, R. J., 1991, "Particle-Imaging Techniques for Experimental Fluid Mechanics."
[22] Rockwell, D., Magness, C., Towfighi, J., Akin, O., and Corcoran, T., 1993, "High Image-Density Particle Image Velocimetry Using Laser Scanning Techniques," Exp. Fluids, **14**, pp. 181–192.
[23] Schraub, F. S., and Kline, S. J., 1965, "A Study of the Structure of the Turbulent Boundary Layer With and Without Longitudinal Pressure Gradients," Report MD-12, Stanford University, Stanford California.
[24] Doligalski, T. L., Smith, C. R., and Walker, J. D. A., 1994, "Vortex Interactions With Walls," Annu. Rev. Fluid Mech., **26**, pp. 573–616.
[25] Lu, L. J., and Smith, C. R., 1990, "Use of Flow Visualization Data to Examine Spatial-Temporal Velocity and Burst-Type Characteristics in a Turbulent Boundary Layer," J. Fluid Mech., **232**, pp. 303–340.
[26] Kim, H. T., Kline, S. J., and Reynolds, W. C., 1971, "The Production of Turbulence Near a Smooth Wall," J. Fluid Mech., **50**, 133–160.

# The Dynamics of the Horseshoe Vortex and Associated Endwall Heat Transfer—Part II: Time-Mean Results

**T. J. Praisner**
Turbine Aerodynamics,
United Technologies Pratt and Whitney,
400 Main Street, N/S 169-29,
East Hartford, CT 06108

**C. R. Smith**
Department of Mechanical Engineering,
Lehigh University,
19 Memorial Drive West,
Bethlehem, PA 18015

*Time-mean endwall heat transfer and flow-field data in the endwall region are presented for a turbulent juncture flow formed with a symmetric bluff body. The experimental technique employed allowed the simultaneous recording of instantaneous particle image velocimetry flow field data, and thermochromic liquid-crystal-based endwall heat transfer data. The time-mean flow field on the symmetry plane is characterized by the presence of primary (horseshoe), secondary, tertiary, and corner vortices. On the symmetry plane the time-mean horseshoe vortex displays a bimodal vorticity distribution and a stable-focus streamline topology indicative of vortex stretching. Off the symmetry plane, the horseshoe vortex grows in scale, and ultimately experiences a bursting, or breakdown, upon experiencing an adverse pressure gradient. The time-mean endwall heat transfer is dominated by two bands of high heat transfer, which circumscribe the leading edge of the bluff body. The band of highest heat transfer occurs in the corner region of the juncture, reflecting a 350% increase over the impinging turbulent boundary layer. A secondary high heat-transfer band develops upstream of the primary band, reflecting a 250% heat transfer increase, and is characterized by high levels of fluctuating heat load. The mean upstream position of the horseshoe vortex is coincident with a region of relatively low heat transfer that separates the two bands of high heat transfer.*
[DOI: 10.1115/1.2185677]

## Introduction

When a turbulent boundary layer approaches a bluff-body obstruction, the cross-stream-discrete adverse pressure gradient creates a three-dimensional separation, which rapidly reorganizes the boundary-layer vorticity into a leading-edge horseshoe vortex. Early recognition of the importance of horseshoe vortices in the leading-edge region of endwall juncture flows was presented by Langston et al. [1] and Sjolander [2], based on experimental studies of turbulent endwall flows in turbomachinery cascades. The leading-edge region of turbulent juncture flows is of particular interest in turbomachinery applications because the presence of a horseshoe vortex system has been found to increase local endwall heat transfer rates by as much as 300% above canonical flat plat flows (Graziani et al. [3], Blair [4], Hippensteele and Russell [5], Giel et al. [6], Kang et al. [7]). The high heat transfer rates in leading-edge regions of turbomachinery airfoils are known to cause thermal mechanical fatigue, spalling of thermal barrier coatings, and airfoil endwall/platform burning.

Hunt et al. [8] employed endwall oil-flow and smoke visualizations to determine the symmetry-plane flow topology for an endwall flow formed with a rectangular block. Their measurements identified the existence of a primary horseshoe vortex (HV), a counter-rotating secondary vortex (SV) upstream of the horseshoe vortex, a tertiary vortex upstream of the secondary vortex (TV), and a small vortex in the corner region of the juncture (Fig. 1 in Praisner and Smith [9]).

Eckerle and Langston [10] conducted wind tunnel experiments to investigate the turbulent horseshoe vortex system formed at the base of a cylindrical bluff body, reporting flow-field data obtained over a series of planes ranging from the symmetry plane (0 deg) to the 90 deg plane. They reported an impinging boundary-layer separation point at $x=0.5D$ ($D$ is the leading-edge diameter of the bluff body) upstream of the cylinder, a value that is supported by a number of other studies (Dickinson [11], Devenport and Simpson [12], Pierce and Shin [13], Ireland and Jones [14], Lewis et al. [15], Praisner et al. [16]). Unlike other researchers, they reported that no HV existed on the symmetry plane or the 5 deg plane. From surface oil-flow visualizations, they concluded that the HV did not form until approximately the 15 deg plane. They argued that because there is only one saddle point of attachment and one of separation on the endwall, there could not exist a multiple vortex system such as that proposed by Hunt et al. [8] and Blair [17].

Pierce and Shin [13] investigated the development and growth of the HV using a cylinder with a 2.3:1 faired trailing edge in a wind tunnel. Using LDV, they measured the time-mean flow on the symmetry plane and in cross-stream planes at 43%, 100%, 150%, and 200% of the bluff body chord. They reported an endwall boundary-layer separation location at $x=0.5D$ with a single dominant vortex (HV) present. Based on vorticity calculations, the HV legs and a smaller co-rotating vortex were identified in all of the downstream cross-flow planes. The strength of the HV was reported to decrease with increasing downstream position, while increasing in length scale.

Over the past three decades, significant progress has been made in determining the salient features of time-mean endwall heat transfer in turbulent juncture flows. Endwall heat transfer measurements in a turbulent endwall flow obtained by Graziani et al. [3] indicate increases in Stanton number of up to 33% relative to the undisturbed boundary layer in the region immediately upstream of the leading edge of a turbine blade model. In contrast, Ireland and Jones [14] used thermochromic liquid crystal thermography to map highly resolved time-mean endwall convective heat transfer coefficients for a turbulent endwall flow formed with

Contributed by the International Gas Turbine Institute (IGTI) of ASME for publication in the JOURNAL OF TURBOMACHINERY. Manuscript received October 1, 2004; final manuscript received February 1, 2005. Assoc. Editor: K. C. Hall. Paper presented at the ASME Turbo Expo 2005: Land, Sea, and Air, Reno, NV, June 6–9, 2005, Paper No. GT2005-69091.

  

a cylindrical bluff body. They noted increases in Stanton number up to 250% higher than the impinging flat plate values, with the highest heat flux occurring on the symmetry plane at $x/D=0.04$. Following this point of highest heat flux, the heat flux monotonically decreased with upstream distance from the bluff body, reaching a plateau in the symmetry-plane heat transfer at $x/D=0.24$. This reported monotonic variation in symmetry-plane heat transfer behavior contrasts with the bimodal behavior reported by Blair [17]. Employing a liquid-crystal-based measurement technique, Hippensteele and Russell [5] reported increases in Stanton number of just over 200% near the leading edge of a rectilinear cascade of turbine blades. In a study similar to that of Graziani et al. [3], Blair [17] reported increases in Stanton number of approximately 100% near turbine blade leading edges and 60% on the suction side of the blades. Both increases were attributed to the presence of the HV.

More recently, Lewis et al. [15] obtained time-resolved pointwise measurements in a juncture flow for both a modified (3:2 elliptical nose) NACA 0020 airfoil and a faired cylinder. They noted that for both bluff bodies the symmetry-plane Stanton number decreased monotonically with upstream distance. They observed that $x_{sep}=0.5D$ and a plateau in the Stanton number at $x=0.27D$. This Stanton number plateau corresponded to the location of both a low-shear line and the region of highest RMS fluctuations in Stanton number. They postulated that the high RMS values at this location were due to a bimodal switching of the flow. The authors reported a maximum augmentation of the time-mean heat transfer of approximately 200% compared to the upstream boundary layer.

In a unique study, Yoo et al. [18] used a square bluff body and flat plate made of cast naphthalene to measure the time-mean mass transfer in the turbulent juncture region. They reported an increase in the mass transfer rate of more than 150% versus the undisturbed boundary layer, with a bimodal distribution on the symmetry-plane and a secondary peak at $x=0.45D$. When referenced to the separation location, the position of the secondary peak coincides with the low-shear line reported by Devenport and Simpson [12] and the symmetry-plane plateau of heat transfer reported by Ireland and Jones [14].

There are a number of disagreements in the results of the aforementioned studies, which include the characteristics of the time-mean flow topologies, the levels of heat-transfer augmentation, and key features of the endwall heat transfer distributions in the leading-edge region. The goals of the present study are to: (1) provide an improved understanding of the physical mechanisms that give rise to elevated levels of endwall heat transfer in juncture regions, and (2) quantify the salient features of both the time-mean flow field and endwall heat transfer for a turbulent juncture flow. Results that address the first goal are presented in Praisner and Smith [9], while results that address the second goal are presented in the present manuscript.

## Experimental Setup

The experimental setup employed for the results presented here is described in Part I of this paper (Praisner and Smith [9]) and in more detail in Praisner et al. [19]. In brief summary, the present experiments were carried out in a closed circuit, water channel with flow speeds from 0.03 m/s to 1.20 m/s, ±2% spanwise uniformity, and a maximum turbulence intensity of 0.5%.

Figure 1 shows the experimental configuration employed in this study. A 15.08 cm diameter cylinder with a 5:1 trailing-edge fairing was used as a bluff body mounted on a flat test plate, with localized heating applied in the enwall region. A turbulent endwall boundary layer was assured by tripping the approach boundary layer just after the leading edge of the test plate, allowing a development length to the juncture of 213 cm.

A uniform heat-flux condition was generated on the endwall by galvanically heating a stainless-steel foil stretched over a thin air cavity in the test plate. The thin air cavity provided essentially a perfect insulation for the backing of the uniform heat-flux surface and also a dry environment for the application of thermochromic liquid crystals for monitoring the surface temperature of the foil.

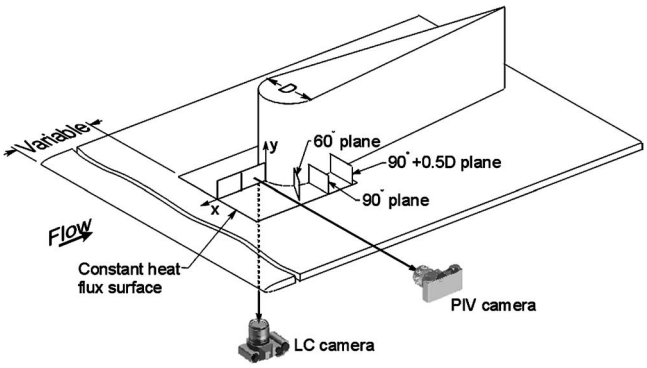


**Fig. 1 Experimental setup illustrating the configuration employed to record simultaneous flow-field and endwall heat transfer data**

The application of the liquid crystals (LCs) to the nonflow side of the stainless-steel sheet allowed the simultaneous recording of (1) flow-field data (high-density PIV) and (2) high-resolution instantaneous heat transfer distributions on the endwall. More details concerning the experimental apparatus are given in Praisner et al. [19] and Praisner and Smith [9].

Instantaneous surface-temperature maps of the endwall were created from recorded LC images via the pointwise calibration technique reported by Sabatino et al. [20]. The resultant temperature distributions were employed to determine the convective heat transfer coefficient distributions, presented in the form of Stanton number:

$$\mathrm{St}=\frac{\left(\dfrac{q''}{T_w-T_\infty}\right)}{\rho U_\infty C_p} \tag{1}$$

where $T_\infty$ is the impinging free-stream temperature, $\rho$ is evaluated at $T_{\mathrm{film}}=(T_{w\text{-avg}}+T_\infty)/2$, $T_w$ is the local wall temperature and $T_{w\text{-avg}}$ is the spatially averaged wall temperature from a single realization. The mean uncertainty of the St was established as approximately ±4.7%, varying between ±3.6% and ±7.9 (see Sabatino et al. [20], for a detailed assessment).

High image-density PIV (Adrian [21], Rockwell et al. [22]) was employed to establish velocity-field realizations simultaneously with the surface heat transfer measurements. For each spatial plane considered in Fig. 1, the interrogated PIV images provided instantaneous vector fields of nominally $100\times50$ vectors, with image dimensions of $0.5D\times0.25D$. The uncertainty of the measured velocity fields was experimentally estimated by Praisner [23] to be ±2%.

The spatial planes on which PIV data were collected are shown in Fig. 1. Due to spatial resolution requirements, two fields-of-view were used to span one diameter upstream of the tapered cylinder on the symmetry plane, while single fields of view were employed for the 60 deg, 90 deg, and 90 deg+0.5$D$ planes. A thumbnail version of Fig. 1, with the corresponding PIV plane colored red, is included in select figures of this paper to help orient the viewer.

The free-stream velocity, $U_\infty$, was held constant at 14.7 cm/s for all studies, giving a Reynolds number based on the leading-edge diameter of $2.44\times10^4$, which is at the lower end of the typical range for high-pressure turbines. The corresponding undisturbed (with the bluff body removed) turbulent boundary-layer parameters at the streamwise location of the bluff body leading edge were: $x=213$ cm, $\delta=5.2$ cm, $\mathrm{Re}_x=3.20\times10^5$, $\mathrm{Re}_\theta=814$, and

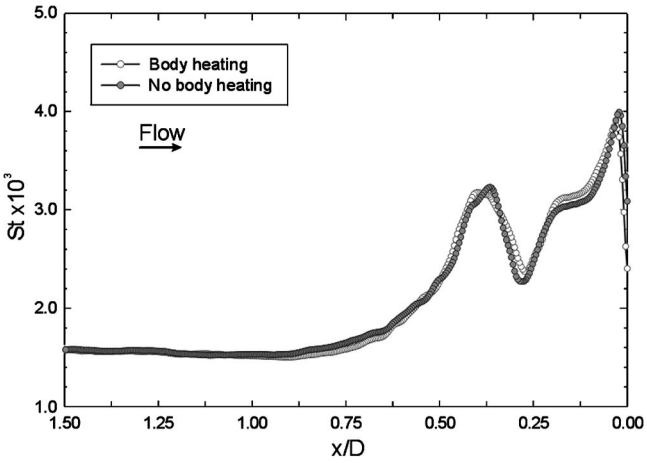


**Fig. 2 Time-mean symmetry-plane Stanton number distributions illustrating the effects of bluff body heating on endwall heat transfer**

$H=1.28$ (as deduced from the measured upstream boundary layer). The results presented here were obtained with a free-stream turbulence level of 0.5%.

## Results

An initial test was performed with and without heating applied to the leading-edge region of the bluff body to investigate the effects of bluff body heating on endwall heat transfer. For these tests, a 15.4 cm wide ($D$) rectangular bluff body was employed to allow for a more simplified heating arrangement. While the geometry for this test was not the same as that shown in Fig. 1, it was deemed similar enough for evaluation of body-heating effects. Figure 2 is a comparison of time-mean endwall heat-transfer results on the symmetry-plane obtained with and without heating of the bluff body. Except for the region between $x/D=0.00$ and $x/D\approx0.05$, the two curves are within ±5% of each other. The close agreement between the two data sets in Fig. 2 suggest that body-heating effects are minimal, even on the symmetry plane.

A composite image of the time-mean vorticity and streamline data on the symmetry plane, complemented by selected $u$-velocity profiles, is shown in Fig. 3. Two PIV fields-of-view, each averaged over 72 instantaneous realizations, were combined to create this figure. The $u$-velocity profiles have been selected to illustrate the progressive nature of the three-dimensional separation in this plane. One can observe the development of a classical separation of the impinging boundary layer in the progression of the $u$-velocity profiles between $x/D=0.85$ and $x/D=0.45$. The location of the endwall boundary layer separation point occurs between $0.45<x/D<0.55$ as indicated by the $u$-velocity profiles. This compares well with the $x_{sep}=0.50D$ reported by Devenport and Simpson [12]. The $u$-velocity profile in the vicinity of the SV ($x/D=0.27$) in Fig. 3 illustrates the general location of the point of minimal wall shear, which conflicts with Reynolds analogy given the high convective heat transfer coefficients in this region (see Fig. 7 below).

The time-mean symmetry-plane horseshoe vortex shown in Fig. 3 is characterized by a stable-focus streamline topology, and a mean location of $x/D\approx0.18$ and $y/D\approx0.06$, estimated by interrogation of the streamline topology. Evidence of a time-mean tertiary vortex is found only in the symmetry-plane data. A stable focus streamline topology on this plane supports the existence of this structure in a time-mean sense. The flow in the corner region ($0.0<x/D<0.05$) of the symmetry plane is dominated by a small (approximately 25% of the horseshoe vortex diameter) corner vortex, which remains a steady flow feature (see Part I, Praisner and Smith [9]). The corner vortex is revealed to be the primary vortex in a "jet-maze" type of three-dimensional flow separation similar to an endwall flow with a laminar approach boundary layer and low Reynolds number. The corner vortex apparently forms as a result of the separation of the boundary layer formed on the face of the bluff body by downwash fluid. Finally, the vorticity/streamline topology in Fig. 3 is consistent with the four-vortex model suggested by Ishii and Honami [24].

Figure 4 shows a comparison of the time-mean vorticity fields obtained for each of the four primary PIV planes adjacent to the bluff body, as indicated in Fig. 1. For reference, vorticity contours equal to one-half of the peak vorticity of the HV (in the respective plane) are also shown. For the symmetry-plane results, Fig. 4($a$), a bimodal distribution similar to that reported by Devenport and

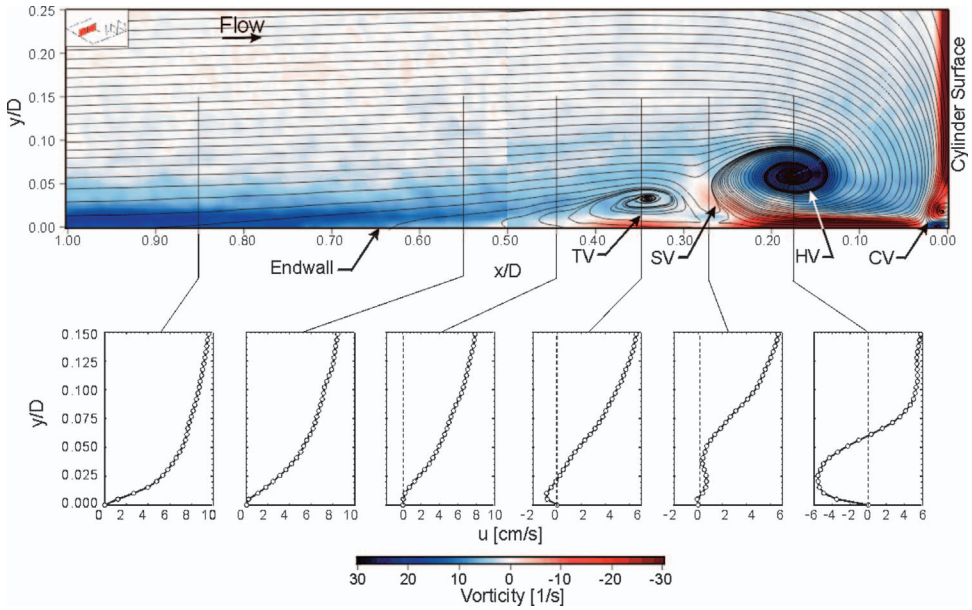


**Fig. 3 Time-mean symmetry-plane vorticity and streamline topologies deduced from PIV data. Select *u*-velocity profiles are also shown.**

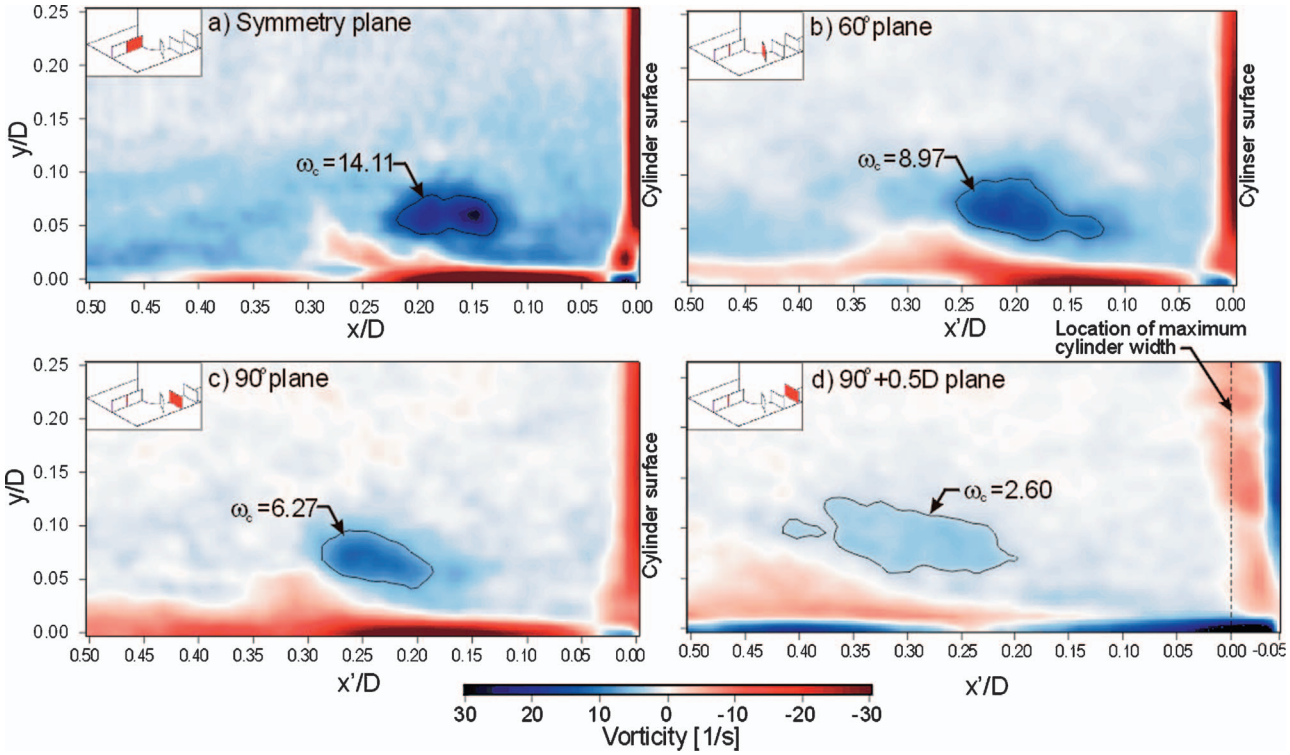


**Fig. 4 Time-mean vorticity for the four flow-field measurement planes adjacent to the bluff body**

Simpson [12] is evident, as indicated by the two adjacent dark blue, high-vorticity regions within the isovorticity contour. The presence of the SV is evidenced by the concentration of negative vorticity (red) at $x/D=0.25$, while the CV is revealed as a strong concentration of negative vorticity in the corner region. Note that the presence of the TV is not readily evident from the vorticity field alone, although the streamlines in Fig. 3 suggest that it exists just upstream of the SV, at approximately $x/D \approx 0.35$.

In Fig. 4(*b*), the overall levels of vorticity (normal to the plane) are attenuated compared to those observed for the symmetry-plane, although a similar topological appearance is present. In Fig. 4(*c*), the HV and the SV are even less well defined than for the previous planes. From a study of the temporal characteristics of these flow structures (Praisner and Smith [9]), both the HV and SV are observed to move in wider spatial envelopes of motion with increasing downstream distance. Viscous dissipation, as well as the reorientation of the vortex axes away from the initial source of impinging boundary layer vorticity are thought to be the reasons for the weaker and less organized flow structures observed in Figs. 4(*c*) and 4(*d*).

While a bimodal vorticity distribution is evident for both the symmetry and 60 deg planes of Fig. 4, the distribution for the 90 deg and 90 deg+0.5*D* planes is less clear, with the vorticity of the HV extending over a broader region, and a markedly lower magnitude (≈80% less than for the symmetry plane). There is a roughly linear decrease in the peak vorticity of the horseshoe vortex with downstream distance from the symmetry plane, while the center of the vortex moves respectively away from the endwall and the bluff body. By the 90 deg+0.5*D* plane the center of the horseshoe vortex core is approximately 40% higher above the end wall and its horizontal location is approximately 70% farther from the bluff body than its original position in the symmetry plane.

The time-mean vorticity distribution for the 90 deg+0.5*D* plane

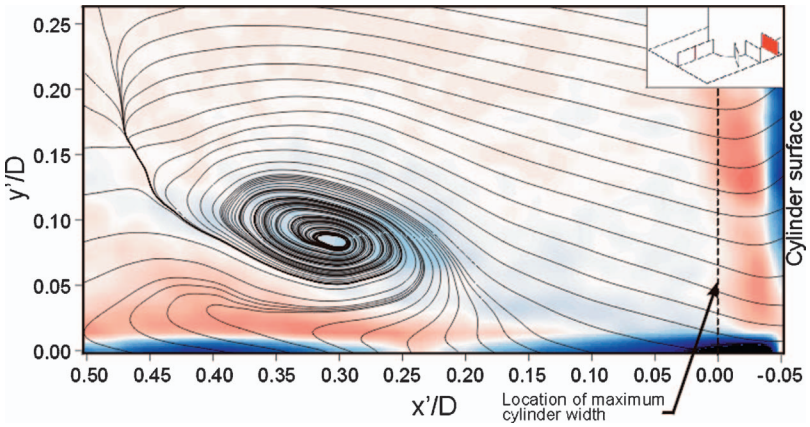


**Fig. 5 Time-mean vorticity and streamline topologies for the 90 deg+0.5*D* measurement plane. Vorticity levels are the same as those shown in Fig. 4.**

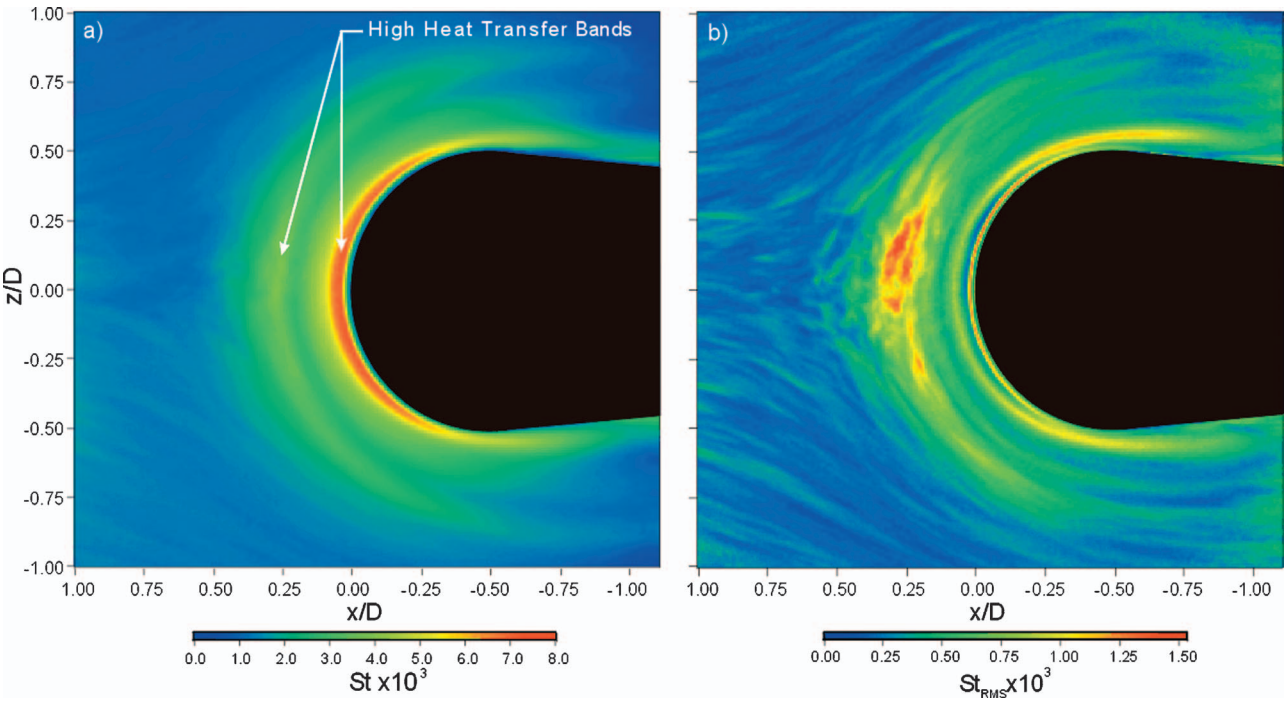


**Fig. 6 Time-mean (*a*) and RMS (*b*) endwall heat transfer distributions in the form of Stanton number**

is shown again in Fig. 5, superposed here with the corresponding streamlines. The vorticity distribution, especially the shape of the HV, compares well to the results of Pierce and Shin [13] for a plane 40% downstream along their 2.4:1 faired cylinder (the 90 deg+0.5*D* plane is 20% downstream for the 5:1 tapered cylinder considered in this study). The spatially averaged *u*-velocity component of the flow is toward the bluff-body surface ($u_{\text{mean}}$ =2.15 cm/s), and the streamlines reveal an unstable-focus topology. Note, that the rotational sense of the HV is still positive (clockwise in Fig. 5), however the streamlines are found to spiral outwards from the center in an unstable-focus pattern that is indicative of a vortex undergoing compression (Perry and Steiner [25]). Evidence of vortex *compression* in a time-mean sense is consistent with the vortex breakdown observed in flow visualizations reported in Part I of this paper (Praisner and Smith [9]).

The streamline topologies for the time-mean flow in the three upstream planes (for brevity, not all shown here) display topologies that indicate *vortex stretching*, similar to that in Fig. 3. The change from vortex stretching in the 90 deg plane to vortex compression 0.5*D* downstream is a result of the adverse pressure gradient that exists due to the tapering of the bluff body fairing. A similar type of behavior to that shown in Fig. 5 might be expected for a horseshoe vortex exposed to the adverse pressure gradient on the suction side of an airfoil following the cross-passage migration of the vortex in turbine cascades, as reported by a number of researchers (Langston et al. [1], Gregory-Smith and Cleak [26]). Resolution of the vortex breakdown process in an adverse pressure-gradient may prove critical to the accurate prediction of aerodynamic losses and heat transfer associated with the horseshoe vortex.

The time-mean endwall heat transfer, computed from 350 instantaneous LC images, is shown in Fig. 6(*a*). The primary band of elevated heat transfer, immediately adjacent to the bluff body, displays a peak value of $\text{St}=7.2\times10^{-3}$, which corresponds to an increase of approximately 350% over the impinging turbulent boundary layer. This augmentation is substantially higher than the values of roughly 200% reported by Hippensteele and Russell [5] and Lewis et al. [15]. This variance possibly reflects the order of magnitude variation between the Reynolds numbers of the present study and the previous investigations. The secondary band of high heat transfer, which develops near $x/D=0.27$ on the symmetry plane, moves slightly away from the body as it circumvents the body, extending downstream to $x/D\approx-0.50$. This secondary band corresponds to a 250% increase in heat transfer over the impinging boundary layer, and is coincident with the location of the secondary vortex in the time-mean flow field data shown in Fig. 3.

Figure 6(*b*) shows the root mean square (RMS) behavior of the endwall heat transfer averaged over 350 instantaneous images. Note that all the RMS data are relative to the local mean value at each point. The region in the vicinity of $x/D=0.27$ and between $-0.25<z/D<0.25$ displays the highest RMS values ($\text{St}_{\text{RMS}}\approx1.30\times10^{-3}$), indicative of the area of largest temporal variations. In addition, the corner region, corresponding to the position of the CV, displays peaks in $\text{St}_{\text{RMS}}$ of similar magnitude to the region near $x/D=0.27$. These areas of elevated RMS behavior are separated by a band of relatively low heat load fluctuation, which corresponds to the reverse-flow region that resides beneath the HV. The steadier behavior of the reverse-flow region beneath the HV is illustrated in the temporal sequences of instantaneous flow-field PIV data in Part I of this paper.

Figure 7 shows the time-mean flow-field, wall shear, Stanton number, and RMS Stanton number data on the symmetry-plane. The zero-shear point observed at $x/D=0.02$ corresponds to the endwall stagnation point of the leading-edge downwash fluid. As this leading-edge downwash fluid stagnates on the endwall, and is subsequently advected upstream, the negative shear reaches a minimum of $-0.26\ \text{N/m}^2$ at $x/D=0.16$, immediately under the HV. A second point of zero shear occurs at $x/D=0.23$, corresponding to the separation of the reverse-flow fluid beneath the horseshoe vortex. A region of maximum positive shear then occurs in the vicinity of the secondary vortex. This region is also characterized by high heat transfer levels and high values of $\text{St}_{\text{RMS}}$, indicating a region of significant unsteady behavior. It should be noted that a RANS-based simulation of endwall flow typically will not predict the inherent unsteadiness of the flow structures, and subsequnelty, the high heat transfer rates in the vicinity of the SV.

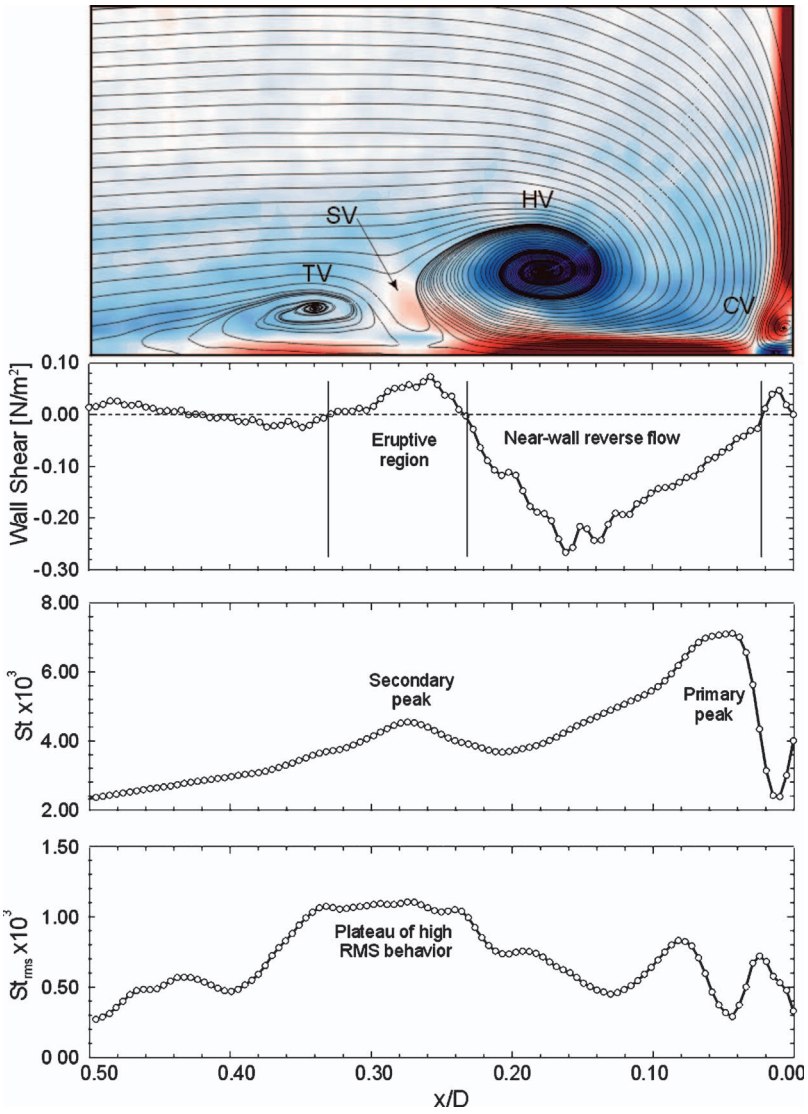


**Fig. 7 Spatially aligned flow-field and endwall heat transfer data on the symmetry plane**

The two bands of high heat transfer that circumscribe the leading edge of the bluff body are evidenced in Fig. 7 by the two peaks in the time-mean Stanton number data. The RMS Stanton number behavior associated with the primary peak in high heat transfer reflects fluctuations of ±12% about the local mean. However, the upstream plateau in the RMS Stanton number, which is within the eruptive region, coincides with the secondary peak in Stanton number, reflecting fluctuations as high as ±24% about the local mean. As mentioned in Part I (Praisner and Smith [9]), the bimodal nature of the Stanton number distribution shown in this figure is thought to be a result of the relatively thin impinging thermal boundary layer (due to localized heating only in the endwall region) relative to the momentum boundary layer. As a result of this thin thermal boundary layer, the impinging outer region fluid that replaces the endwall fluid during the ejection of the SV is markedly cooler than if the thermal boundary layer was of a comparable thickness to the momentum boundary layer.

As illustrated by Fig. 7, the location of the horseshoe vortex coincides with a region of relatively low heat transfer that separates the two bands of high heat transfer. A local minimum in Stanton number occurs at $x/D=0.22$, within the reverse flow region beneath the HV, and immediately preceding (in the sense of the reverse flow) the point of zero-shear at $x/D=0.23$. This local Stanton-number minimum near the reverse-flow boundary-layer separation point is consistent with results reported by Puhak et al. [27] using a numerical simulation of three-dimensional laminar boundary-layer separation.

Finally, Fig. 8 is an oblique view of time-averaged flow-field and endwall heat transfer data. In this figure the spatial relationships between the time-mean vorticity in each measurement plane, and the associated mean endwall Stanton number are illustrated. Note that all four vorticity planes shown indicate that the secondary band of high Stanton number occurs outboard of the HV and beneath the SV. In addition, the lower Stanton number regions seem to correlate with the locations of the co-rotating HV and TV.

As demonstrated in Fig. 4, Fig. 8 shows how the strength of the HV, as indicated by the regions of concentrated positive vorticity (blue), decreases from the symmetry plane to the 90 deg+0.5$D$ plane. The most marked reduction in strength, which occurs downstream of the 60 deg plane, is hypothesized to be due to a significant reduction in the entrainment of boundary layer vorticity into the HV, as well as continued viscous dissipation of the initially concentrated vorticity. The decreased entrainment of vorticity is a result of the HV legs becoming extended in the streamwise direction as they wrap around the bluff body (and thus cross stream to the vorticity source), which results in viscous dissipation

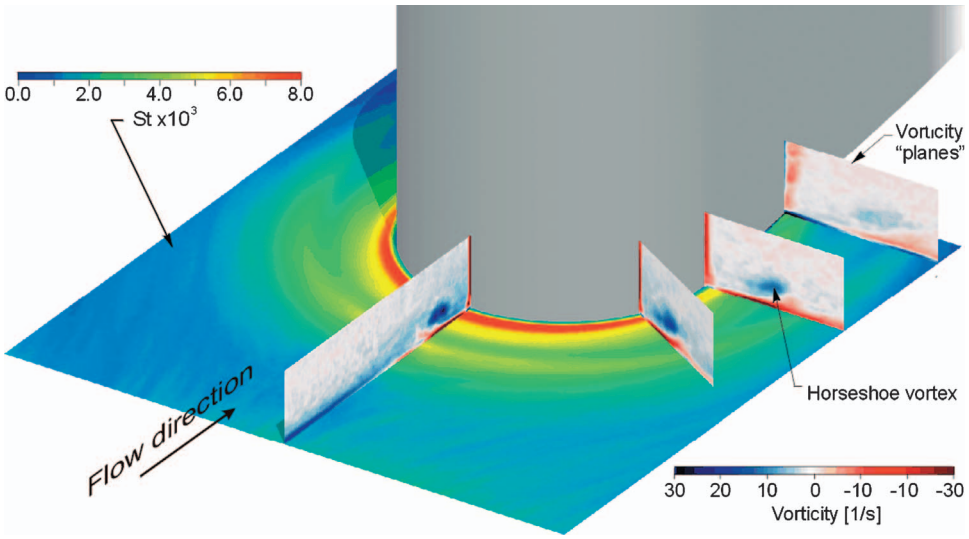


**Fig. 8 Construct of time-mean vorticity and endwall heat transfer data. Image is to scale.**

dominating the evolution of the vortex as it extends downstream. As Fig. 8 shows, the elevated endwall heat transfer stimulated by the HV also decreases significantly in conjunction with this downstream reduction in HV strength.

## Conclusions

The time-mean flow field on the symmetry plane is characterized by the presence of a horseshoe, secondary, tertiary, and corner vortices. The separation point of the impinging turbulent boundary layer develops on the symmetry plane at $x/D \approx 0.50$. The time-mean symmetry-plane horseshoe vortex is characterized by a bimodal distribution of vorticity, and a stable-focus streamline topology. While a bimodal HV vorticity distribution is reflected by both the symmetry and 60 deg planes, no clear distribution is apparent for both the 90 deg and 90 deg+0.5$D$ planes, where the horseshoe vortex is characterized by broader and weaker vorticity concentrations. The peak vorticity of the horseshoe vortex decreases almost linearly with distance from the symmetry plane, while the height of the HV above the end wall, and its distance from the bluff body, both increase. While not obvious in the time-mean streamline topology, the existence of a secondary vortex is reflected by a focused region of negative vorticity between the horseshoe and tertiary vortices. The secondary vortex is characterized by a length scale roughly half the size of the horseshoe vortex and is of opposite-sign rotation. Evidence of a time-mean tertiary vortex is apparent only in the time-mean symmetry-plane streamline data.

The time-mean endwall heat-transfer data in the leading-edge region are characterized by two bands of high convective heat transfer levels. The band of highest Stanton number occurs in the corner region of the juncture, has a peak corresponding to a 350% increase over the impinging turbulent boundary layer and reflects RMS variations on the symmetry plane of ±12% about the local mean. A secondary band of high Stanton number, near $x/D = 0.27$ on the symmetry plane, reflects a 250% increase in heat transfer, with RMS fluctuations of ±24% of the local mean. This secondary band is coincident with the location of the secondary vortex in the time-mean flow field data. As reported in Part I (Praisner and Smith [9]), the aperiodic generation and ejection of the SV by the interaction of the HV with the near wall flow results in a subsequent interaction between an outer region replacement flow, and the endwall reverse flow. This aperiodic interaction process creates the high levels of flow and thermal unsteadiness in this region.

## Acknowledgment

The authors wish to thank the Air Force Office of Scientific Research for its support of this research under Contract No. F49620-93-1-0217.

## Nomenclature

- $a$ = proximity of vortex core to endwall
- $C_p$ = specific heat
- CV = corner vortex
- $D$ = leading-edge diameter
- $h$ = convective heat transfer coefficient $h=q''/A/(T_s-T_\infty)$
- $H$ = boundary layer shape factor
- HV = horseshoe vortex
- N = Newton
- $q''$ = heat flux W/m$^2$ K
- $\mathrm{Re}_D$ = Reynolds number based on $D$, $\mathrm{Re}_D=U_\infty D/\nu$
- St = Stanton number $\mathrm{St}=h/(\rho U_\infty C_p)$
- SV = secondary vortex
- $T$ = temperature
- TBL = turbulent boundary layer
- TV = tertiary vortex
- $t^+$ = nondimensional time $t^+=t(u_\tau)^2/\nu$
- $U_\infty$ = free-stream velocity
- $x$ = direction upstream from leading edge of bluff body
- $x_{\mathrm{sep}}$ = separation point of the endwall boundary layer
- $x'$ = direction normal to the surface of the bluff body
- $y$ = endwall-normal distance
- $z$ = cross-stream distance from symmetry plane

### Greek Symbols

- $\delta$ = boundary layer thickness
- $\Gamma$ = vortex circulation strength
- $\rho$ = fluid density
- $\tau$ = wall shear
- $\mu$ = dynamic viscosity
- $\nu$ = kinematic viscosity
- $\omega$ = vorticity

## References


[1] Langston, L. S., Nice, M. L., and Hooper, R. M., 1976, "Three-dimensional Flow Within a Turbine Cascade Passage," ASME Paper No. 76-GT-50.

[2] Sjolander, S. A., 1975, "The End Wall Boundary Layer in an Annular Cascade of Turbine Nozzle Guide Vanes," Carleton University, Department of Mechanical and Aeronautical Engineering, Ottawa, Canada, TR ME/A 75-4.

[3] Graziani, R. A., Blair, M. F., Taylor, J. R., and Mayle, R. E., 1980, "An Experimental Study of Endwall and Airfoil Surface Heat Transfer in a Large Scale Turbine Blade Cascade," ASME J. Eng. Power, **102**, pp. 257–267.

[4] Blair, M. F., 1994, "An Experimental Study of Heat Transfer in a Large-scale Turbine Rotor Passage," ASME J. Turbomach., **116**, pp. 1–12.

[5] Hippensteele, S. A., and Russell, L. M., 1988, "High Resolution Liquid-Crystal Heat-Transfer Measurements on the End Wall of a Turbine Passage With Variations in Reynolds Number," NASA Technical Memorandum 100827.

[6] Giel, P. W., Thurman, D. R., VanFossen, G. J., Hippensteele, S. A., and Boyle, R. J., 1998, "Endwall Heat Transfer Measurements in a Transonic Turbine Cascade," ASME J. Turbomach., **120**, pp. 305–313.

[7] Kang, M., Kohli, A., and Thole, K. A., 1999, "Heat Transfer and Flowfield Measurements in the Leading Edge Region of a Stator Vane Endwall," ASME J. Turbomach., **121**, pp. 558–568.

[8] Hunt, J. C. R., Abell, C. J., Peterka, J. A., and Woo, H., 1978, "Kinematical Studies of the Flows Around Free or Surface-Mounted Obstacles; Applying Topology to Flow Visualization," J. Fluid Mech., **86**, pp. 179–200.

[9] Praisner, T. J., and Smith, C. R., 2006, "The Dynamics of the Horseshoe Vortex and Associated Endwall Heat Transfer—Part I: Temporal Behavior," ASME J. Turbomach., **128**, pp. 747–754.

[10] Eckerle, W. A., and Langston, L. S., 1987, "Horseshoe Vortex Formation Around a Cylinder," ASME J. Turbomach., **109**, pp. 278–284.

[11] Dickinson, S. C., 1988, "Time Dependent Flow Visualization in the Separated Region of an Appendage-Flat Plate Junction," Exp. Fluids, **6**, pp. 140–143.

[12] Devenport, W. J., and Simpson, R. L., 1990, "Time-Dependent and Time-Averaged Turbulence Structure Near the Nose of a Wing-Body Junction," J. Fluid Mech., **210**, pp. 23–55.

[13] Pierce, F. J., and Shin, J., 1992, "The Development of a Turbulent Junction Vortex System," ASME J. Fluids Eng., **114**, pp. 559–565.

[14] Ireland, P. T., and Jones, T. V., 1986, "Detailed Measurements of Heat Transfer on and Around a Pedestal in Fully Developed Passage Flow," Proceedings, 8th International Heat Transfer Conference, C. L. Tien et al., eds., Hemisphere Publishing, Washington, D.C., Vol. 3, pp. 975–980.

[15] Lewis, D. J., Simpson, R. L., and Diller, T. E., 1994, "Time-Resolved Surface Heat Flux Measurements in the Wing/Body Junction Vortex," J. Thermophys. Heat Transfer, **8**(4), pp. 656–663.

[16] Praisner, T. J., Seal, C. V., Takmaz, L., and Smith, C. R., 1997, "Spatial-Temporal Turbulent Flow-Field and Heat Transfer Behavior in End-Wall Junctions," Int. J. Heat Fluid Flow, **18**(1), pp. 142–151.

[17] Blair, M. F., 1984, "An Experimental Study of Heat Transfer and Film Cooling on Large-scale Turbine Endwalls," ASME J. Heat Transfer, **106**, pp. 524–529.

[18] Yoo, S. Y., Goldstein, R. J., and Chung, M. K., 1993, "Effects of Angle of Attack on Mass Transfer From a Square Cylinder and its Base Plate," Int. J. Heat Mass Transfer, **36**(2), pp. 371–380.

[19] Praisner, T. J., Sabatino, D. R., and Smith, C. R., 2001, "Simultaneously Combined Liquid-Crystal Surface Heat Transfer and PIV Flow-Field Measurements," Exp. Fluids, **30**, pp. 1–10.

[20] Sabatino, D. R., Praisner, T. J., and Smith, C. R., 2001, "A High-Accuracy Calibration Technique for Thermochromic Liquid Crystal Temperature Measurement," Exp. Fluids, **28**, pp. 497–505.

[21] Adrian, R. J., 1991, "Particle-Imaging Techniques for Experimental Fluid Mechanics," Annu. Rev. Fluid Mech., **23**, pp. 261–304.

[22] Rockwell, D., Magness, C., Towfighi, J., Akin, O., and Corcoran, T., 1993, "High Image-Density Particle Image Velocimetry Using Laser Scanning Techniques," Exp. Fluids, **14**, pp. 181–192.

[23] Praisner, T. J., 1998, "Investigation of Turbulent Juncture Flow Endwall Heat Transfer and Fluid Flow," Ph.D. thesis, Lehigh University, Department of Mechanical Engineering and Mechanics.

[24] Ishii, J., and Honami, S., 1986, "A Three-dimensional Turbulent Detached Flow With a Horseshoe Vortex," ASME J. Eng. Gas Turbines Power, **108**, pp. 125–130.

[25] Perry, A. E., and Steiner, T. R., 1987, "Large-Scale Vortex Structures in Turbulent Wakes Behind Bluff Bodies, Part 1. Vortex Formation," J. Fluid Mech., **174**, pp. 233–270.

[26] Gregory-Smith, D. G., and Cleak, J. G. E., 1992, "Secondary Flow Measurements in a Turbine Cascade With High Inlet Turbulence," ASME J. Turbomach., **114**, pp. 173–183.

[27] Puhak, R. I., Degani, A. T., and Walker, J. D. A., 1995, "Unsteady Separation and Heat Transfer Upstream of Obstacles," J. Fluid Mech., **305**, pp. 1–27.

# Large Eddy Simulation of Flow and Heat Transfer in the 180-Deg Bend Region of a Stationary Gas Turbine Blade Ribbed Internal Cooling Duct

**Evan A. Sewall**
e-mail: esewall@vt.edu

**Danesh K. Tafti**

Mechanical Engineering Department,
Virginia Tech,
Blacksburg, VA 24061

*Large eddy simulation of the 180 deg bend in a stationary ribbed duct is presented. The domain studied includes three ribs upstream of the bend region and three ribs downstream of the bend with an outflow extension added to the end, using a total of 8.4 million cells. Two cases are compared to each other: one includes a rib in the bend and the other does not. The friction factor, mean flow, turbulence, and heat transfer are compared in the two cases to help explain the benefits and disadvantages of the wide number of flow effects seen in the bend, including flow separation at the tip of the dividing wall, counter-rotating Dean vortices, high heat transfer at areas of flow impingement, and flow separation at the upstream and downstream corners of the bend. Mean flow results show a region of separated flow at the tip of the dividing region in the case with no rib in the bend, but no separation region is observed in the case with a rib. A pair of counter-rotating Dean vortices in the middle of the bend is observed in both cases. Turbulent kinetic energy profiles show a 30% increase in the midplane of the bend when the rib is added. High gradients of heat transfer augmentation are observed on the back wall and downstream outside wall, where mean flow impingement occurs. This heat transfer is increased with the presence of a rib. Including a rib in the bend increases the friction factor in the bend by 80%, and it increases the heat transfer augmentation by approximately 20%, resulting in a trade-off between pressure drop and heat transfer.*
[DOI: 10.1115/1.2098769]

## Introduction

Flow inside cooling ducts in gas turbine blades is highly turbulent and is often complicated by the presence of ribs, which are placed in the ducts to increase turbulence and augment heat transfer. The 180-deg bends that connect two passages further complicate the flow by reversing its direction. Prediction of the flow through these cooling passages has been sought through the use of Reynolds averaged Navier–Stokes turbulence modeling for closure in the Navier–Stokes equations, but the lack of consistency and accuracy in these simulation methods brings about the motivation to use more detailed calculations, such as large eddy simulations (LES), to predict the complicated flow. The added computational expense has proven to be worth the cost because of the significant increase in computational accuracy and reliability. The resources required have, up to this point, limited internal computational domains of ribbed ducts to those of fully developed periodic flows, but current supercomputers are capable of adequately resolving the large scales in these time-dependent calculations.

The goal of this paper is to present mean flow, turbulence, friction factor, and heat transfer results from two LES calculations of the 180-deg bend region of a ribbed internal cooling duct. The domain consists of three hydraulic diameters (three ribs) of the upstream pass, a bend region connecting the upstream and downstream passes, and three hydraulic diameters (three ribs) in the downstream leg. The duct cross section is square, ribs are attached to opposite walls in an in-line configuration, and a constant temperature boundary condition is applied on all walls and ribs. A comparison is made of a case with a rib in the bend and without a rib in the bend.

**Previous Works.** A heat transfer experiment by Metzger and Sahm [1] and a mass transfer experiment by Park and Lau [2] in smooth 180-deg bends both showed a steep increase in heat transfer, reaching a maximum value at the exit of the bend leading into the second pass. A PIV study by Schabacker and Bölcs in a 180 -deg bend region with smooth walls pointed out several large scale flow structures in the duct, including recirculation zones in the upstream and downstream corners, a large separation bubble hugging the inside wall downstream of the divider tip, and a set of counter-rotating vortices (Dean-type secondary motion) in a plane parallel to the dividing wall. The maximum value of turbulent kinetic energy in the bend was found in the shear layer between the separation bubble and downstream shear flow and had a magnitude of 28% [3]. A comparison of divider thicknesses in a smooth bend showed that the width of the divider has a significant effect on the size and location of the separation bubble at the tip of the dividing wall, as well as the shape of the counter-rotating Dean vortices. Peak values of turbulence are lower than those reported by Schabacker and Bölcs, falling closer to 20% [4]. A smooth channel study by Mochizuki et al. (1994) showed flow visualization of laminar flow in a bend region and found that the flow is highly three dimensional and significantly affected by the recirculation region in the upstream corner [5]. An infrared thermography study of the bend region in smooth ducts reported that bend effects do not reach more than 1 $D_h$ upstream from the turn. The highest heat transfer occurred on the downstream part of the bend, immediately before flow entered the downstream leg. A

Contributed by the International Gas Turbine Institute (IGTI) of ASME for publication in the JOURNAL OF TURBOMACHINERY. Manuscript received October 1, 2004; final manuscript received February 1, 2005. IGTI Review Chair: K. C. Hall. Paper presented at the ASME Turbo Expo 2005: Land, Sea, and Air, Reno, NV, June 6–9, 2005, Paper No. GT2005-68518.

  

second peak in heat transfer was observed about 1.5 channel widths downstream of the bend, corresponding with reattachment of the separation bubble on the inside wall [6].

An attempt to calculate the flow characteristics around a 180-deg bend using a $k$-$\varepsilon$ model was reported by Besserman and Tanrikut. This study showed that an advanced treatment of the boundary conditions was essential when the $k$-$\varepsilon$ model was used [7]. Calculations of smooth U bends have been reported in several studies using more advanced models, including $k$-$\omega$ [8] and Reynolds-stress models [2,9].

A few experimental studies have reported flow measurements in 180-deg bends connecting ribbed ducts. PIV measurements by Son et al. [10] showed results for a bend with ribs on one wall, and LDV measurements by Liou et al. [11] focused primarily on the effects of rotation. Most other flow measurement studies focused on ducts with 45-deg ribs [12–15].

A wide number of heat transfer studies have been published on 180-deg bends with 90-deg ribs. In addition to the two mentioned in the previous paragraph, these studies include a 180-deg bend with one ribbed wall and a rib in the bend [16,17], one with ribs on opposite walls and no rib in the bend [18], another with ribs on opposite walls and no rib in the bend but with an aspect ratio of 2:1 [19], and one with two opposite rib roughened walls and no rib in the bend [20].

A computational study on a two-pass duct with 90-deg ribs was reported by Zhao and Tao [21]. They used a $k$-$\varepsilon$ model with wall functions to simulate the flowfield and obtained reasonably good agreement between numerical and experimental results. More calculations of 180-deg bends have been reported of studies with 45-deg ribs [22–27].

Internal flow calculations using large eddy simulations (LES) have rarely been used in domains other than periodic calculations of fully developed flow in ribbed ducts [28–40] because of the requirements in computational resources. Flow and pressure characteristics in smooth 90-deg pipe bends were explored by Teng et al. [41] and Rütten [42]. Recently, LES calculations have been extended to include developing flow in a ribbed duct [43,44], and a series of full two-pass channel calculations with smooth walls and 45- and 90-deg ribs was carried out by Murata and Mochizuki [45–48]. No rib was included in the bend in these studies.

**Objective.** The objective of this study is to provide a detailed view of the flow and heat transfer in a stationary 180-deg bend connecting two ducts with in-line 90-deg ribs, using information from LES calculations and comparing them with experiments and previous findings. In this study, a comparison is made between a configuration with and without a rib in the bend, and the goal is to determine the benefit of increased heat transfer with the included rib over the friction factor penalty incurred. The comparison will be made in terms of the friction factor across the bend and the differences in the flowfield, turbulence, and heat transfer between the two cases.

## Computational Model and Governing Equations

The computational domain used for studying the 180-deg bend region, shown in Fig. 1, extends from three ribs in the upstream leg to three ribs downstream and is followed by a smooth extension region. In Case 1, no rib is included in the bend, and in Case 2, a rib is included. The duct surfaces, as well as the ribs, are heated with a constant temperature boundary condition. The governing flow and energy equations are nondimensionalized by a characteristic length scale, given by the channel hydraulic diameter ($D_h$), a characteristic velocity scale, given by the channel bulk velocity ($\overline{u_{\text{in}}}$), and a characteristic temperature scale, given by ($T_s - T_{\text{in}}$).

The equations governing the flow are the time-dependent Navier–Stokes and energy equations in transformed coordinates, $\boldsymbol{\xi} = \boldsymbol{\xi}(\mathbf{x})$. The equations, as well as all results presented in this paper, are given in terms of non-dimensional variables:

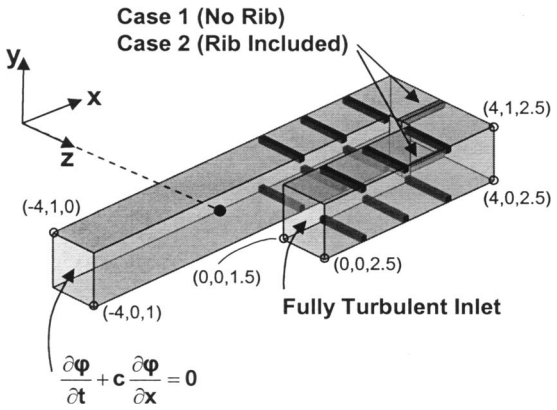


**Fig. 1 The 180 deg bend domain consists of three ribs upstream and downstream of the bend. An extension region is included downstream to negate effects from the outflow boundary condition. The dividing wall is $\frac{1}{2}$ $D_h$ in width, and the duct cross-sectional area is 1 $D_h^2$ throughout the bend. A comparison is made between having no rib in the bend (Case 1) and having a rib in the bend (Case 2).**

Continuity:

$$\frac{\partial}{\partial \xi_j}(\sqrt{g}\bar{U}^j) = 0, \tag{1}$$

Momentum:

$$\frac{\partial}{\partial t}(\sqrt{g}\bar{u}_i) + \frac{\partial}{\partial \xi_j}(\sqrt{g}\bar{U}^j\bar{u}_i) = -\frac{\partial}{\partial \xi_j}(\sqrt{g}(\mathbf{a}^j)_i\bar{p}), + \frac{\partial}{\partial \xi_j}\left(\left(\frac{1}{\text{Re}} + \frac{1}{\text{Re}_t}\right)\sqrt{g}g^{jk}\frac{\partial \bar{u}_i}{\partial \xi_k}\right) \tag{2}$$

and Energy:

$$\frac{\partial}{\partial t}(\sqrt{g}\bar{\theta}) + \frac{\partial}{\partial \xi_j}(\sqrt{g}\bar{U}^j\bar{\theta}) = \frac{\partial}{\partial \xi_j}\left(\left(\frac{1}{\text{PrRe}} + \frac{1}{\text{Pr}_t\text{Re}_t}\right)\sqrt{g}g^{jk}\frac{\partial \bar{\theta}}{\partial \xi_k}\right), \tag{3}$$

where $\mathbf{a}^i$ are the contravariant basis vectors (the notation $(\mathbf{a}^j)_k$ is used to denote the $k$th component of vector $\mathbf{a}^j$. $(\mathbf{a}^j)_k = \partial \xi_j / \partial x_k$), $\sqrt{g}$ is the Jacobian of the transformation, $g^{ij}$ are the elements of the contravariant metric tensor, $\sqrt{g}U^j = \sqrt{g}(\mathbf{a}^j)_k u_k$ is the contravariant flux vector, $u_i$ is the Cartesian velocity vector, and $\theta$ is the non-dimensional temperature. The overbar denotes grid filtered quantities with an implicit top-hat filter, $\bar{G}$.

The inverse of the non-dimensional eddy-viscosity, $\text{Re}_t$, is modeled as:

$$\frac{1}{\text{Re}_t} = C_s^2(\sqrt{g})^{2/3}|\bar{S}|, \tag{4}$$

where $|\bar{S}|$ is the magnitude of the strain rate tensor and the Smagorinsky constant $C_s^2$ is obtained via the Dynamic subgrid stress model [49]. The model is described in more detail in [50]. The turbulent Prandtl number used in the heat transfer model is $\text{Pr}_t = 0.5$.

The three boundary conditions imposed on the walls are the following:

$$\mathbf{u} = 0 \tag{5}$$

$$\nabla p \cdot \mathbf{n} = 0 \tag{6}$$

$$\theta_s = 1 \tag{7}$$

The inlet velocity and temperature boundary (identified as "Fully Turbulent Inlet" in Fig. 1) is represented by a series of time-dependent frames extracted from a location immediately downstream of the fifth rib in the developing flow calculation [43], giving the entire channel a length of eight ribs. The frames span a region of $\frac{1}{4}$ time unit and are repeated continuously. A comparison of the time average of the mean and turbulent quantities of the frames to that of the developing flow region from where they were extracted yielded a negligible difference. The autocorrelation spatially averaged across each frame settled to a value less than 0.2 for all quantities, and doubling the number of frames to span a region of $\frac{1}{2}$ time unit only decreased the autocorrelation to a value of 0.1. The time span of $\frac{1}{4}$ time unit was determined to be a sufficiently long time based on these criteria. The last 2% of frames in the set were linearly interpolated between the previous frame and the first frame to produce a smooth transition as the sequence of frames was repeated. A convective outflow boundary condition is used as shown in Fig. 1, where $c$ is the convective flow velocity and is the same as the mean flow velocity.

The governing equations for momentum and energy are discretized with a conservative finite-volume formulation using a second-order central difference scheme on a non-staggered grid topology. The Cartesian velocities, pressure, and temperature are calculated and stored at the cell center, whereas contravariant fluxes are stored and calculated at the cell faces. For the time integration of the discretized continuity and momentum equations, a projection method is used. The temporal advancement is performed in two steps, a predictor step, which calculates an intermediate velocity field, and a corrector step, which calculates the updated velocity by satisfying discrete continuity. The energy equation is advanced in time by the predictor step. Details about the algorithm, functionality, and capabilities can be found in Tafti [51].

The computer program GenIDLEST (Generalized Incompressible Direct and Large-Eddy Simulations of Turbulence) used for these simulations has been applied to fully developed flow and heat transfer in a ribbed duct geometry [50], with rotation and buoyancy effects [52,53], and in a channel with 45-deg ribs [54]. It has also been applied to both stationary and rotating developing flow [43,44]. In all of these cases, it has been consistently established through comparison with experiments that predictions of mean flow, turbulent quantities, and heat transfer, are accurate to within ±10% of experiments and in some cases within experimental uncertainty.

## Computational Details

The calculation domain presented in this paper is a 180-deg bend connecting two straight ribbed ducts. Each ribbed section has similar grid distribution as the $96^3$ resolution periodic channel presented in Tafti [50]. A grid independence study between a periodic channel with $96^3$ and $128^3$ grid points showed no significant differences between the low and high resolution cases when the Dynamic Smagorinsky subgrid scale model is used. Both meshes predicted the local and mean heat transfer augmentations within experimental uncertainty on the ribbed and smooth walls. For this reason and because of the domain size, the $96^3$ mesh is used for each rib. The total mesh size for this calculation is $8.4 \times 10^6$ computational cells.

The channel aspect ratio is 1:1, and the geometric ratios governing the rib placement are $e/D_h = 0.1$ and $P/e = 10$, which is typical in many computational and experimental studies. A constant temperature boundary condition is imposed on both the walls and the ribs, and the Reynolds number based on the inlet velocity, which is also the bulk fluid velocity, is 20,000. The Prandtl number in this study is 0.7.

The non-dimensional time step in the calculations is set to $5 \times 10^{-5}$. The diffusion terms are treated implicitly, and the average $L_1$ residual norm of global mass balance is converged to $1 \times 10^{-8}$, while the momentum and energy equations are converged to $1 \times 10^{-7}$. The calculations utilized 152 processors of an IA-64 Itanium Linux cluster. Each time step took about 0.5 $\mu$s/grid node of wall clock time.

Each calculation was initiated by assuming initial conditions similar to a fully developed channel and integrating in time until the flow reached a statistically stationary state. The time evolution of bulk quantities such as Nusselt number, wall heat flux, friction drag losses, and form drag losses were observed until all values reached a uniform state. Once stationary conditions were established, sampling to obtain mean and turbulent quantities was carried out for approximately 11.5 time units. Initial mean quantities were obtained by sampling over one time unit before obtaining turbulent statistical quantities. The sampling time was doubled by using the $y$ symmetry of the duct and by presenting the averaged and turbulent quantities for $\frac{1}{2}$ of the duct cross section. The coordinate system used for reporting results is shown in Fig. 1.

The local Nusselt number as related to the *non-dimensional* heat flux and non-dimensional temperature is calculated as:

$$\mathrm{Nu} = \frac{q''}{\theta_s - \theta_{\mathrm{ref}}} \tag{8}$$

where $q''$ is the non-dimensional heat flux at the walls, $\theta_s = 1$ is the surface boundary condition, and $\theta_{\mathrm{ref}}$ is the reference temperature defined as:

$$\theta_{\mathrm{ref}} = \frac{\int\int |u_1| \theta dA_x}{\int\int |u_1| dA_x}, \tag{9}$$

where $\theta$ is the non-dimensional temperature defined as:

$$\theta = \frac{T - T_{\mathrm{in}}}{T_s - T_{\mathrm{in}}}. \tag{10}$$

The surface-averaged Nusselt number is area weighted as:

$$\overline{\mathrm{Nu}} = \frac{\int\int_{\Omega} \mathrm{Nu} \cdot dS}{\int\int_{\Omega} dS}, \tag{11}$$

where $S$ denotes the surface under consideration.

The Fanning friction factor is calculated in terms of the non-dimensional pressure gradient as:

$$f = -\frac{1}{2}\frac{\Delta p}{\Delta L}. \tag{12}$$

The reference value for the Nusselt number is obtained from the Dittus–Boelter correlation:

$$\mathrm{Nu}_0 = 0.023 \cdot \mathrm{Re}^{0.8} \cdot \mathrm{Pr}^{0.4} \tag{13}$$

and the reference value for the friction factor is [55]:

$$f_0 = 0.046 \cdot \mathrm{Re}^{-0.2}. \tag{14}$$

## Results

Table 1 shows the friction factor and heat transfer augmentation in the ribbed sections and the bend. The section numbers correspond to the diagram above the table. The first value shown is the heat transfer augmentation or friction factor augmentation for Case 1, while the second value, in parentheses, represents Case 2. The third value is the percent change from Case 1 to Case 2. The table shows that the heat transfer augmentation is much higher in the downstream leg than in the upstream leg. The maximum heat

**Table 1 Averaged heat transfer and friction in the bend**

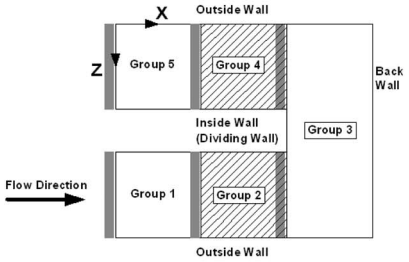


$Nu_o = 0.23\ Re^{0.8}\ Pr^{0.4}$

$f_o = 0.046\ Re^{-0.2}$

| Section # | Nu / Nu$_o$ Ribbed Wall | Inside Wall | Outside Wall | f / f$_o$ |
|---|---|---|---|---|
| Case 1 -- No Rib in Bend (Case 2 – Rib in Bend) % Change from Case 1 to Case 2 | | | | |
| 1 | 2.27 (2.24) -1% | 1.79 (1.77) -1% | 1.59 (1.59) 0% | 9.77 (9.85) +1% |
| 2 | 2.42 (2.38) -2% | 1.91 (1.87) -2% | 1.64 (1.67) +2% | 20.56 (20.96) +2% |
| 3 | 3.03 (3.62) +19% | | | 20.44 (37.22) +82% |
| 4 | 3.12 (3.36) +8% | 2.68 (3.26) +22% | 2.97 (3.06) +3% | 37.02 (35.84) -3% |
| 5 | 3.02 (2.84) -6% | 2.51 (2.56) +2% | 2.66 (2.63) -1% | -0.55 (3.94) -716% |
| Dividing Wall = 3.60 Nu / Nu$_0$ (4.37) +21% | | | Back Wall = 2.94 Nu / Nu$_0$ (3.42) +16% | |

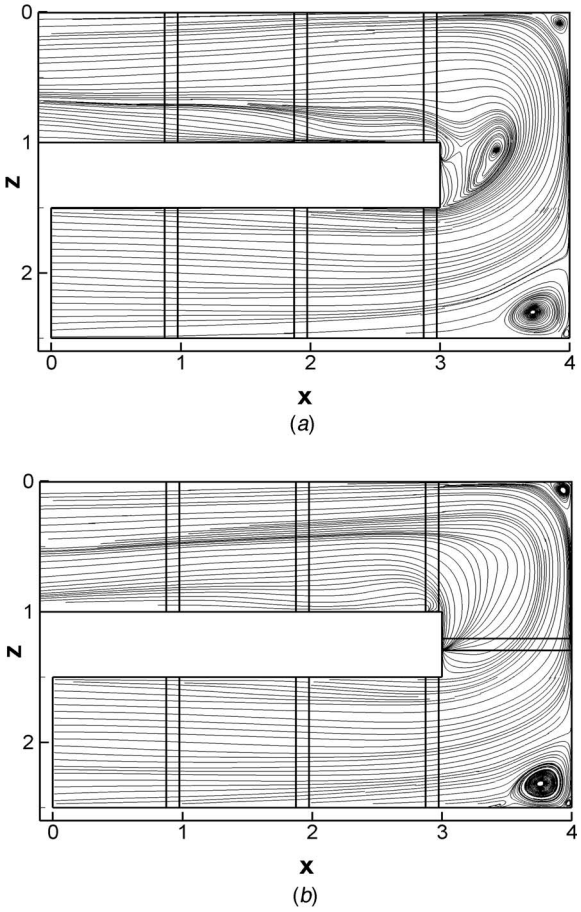


**Fig. 2 The prominent features of the bend for (*a*) Case 1 and (*b*) Case 2 include separation at the end of the dividing wall and recirculation at the upstream and downstream corners, resulting in impingement of highly accelerated flow on the back wall and outside wall of the downstream leg.**

transfer is found on the ribbed walls. In the upstream leg of the duct, the inside wall has a higher heat transfer augmentation than the outside wall in both cases, and in the downstream leg, the heat transfer augmentation on the outside wall is higher than the inside wall, but only in Case 1. In Case 2, the inside wall actually shows more heat transfer.

The heat transfer augmentation on the ribbed wall in the bend region is 19% higher in Case 2. The section immediately downstream of the bend is also a region of high heat transfer. In Case 1, the heat transfer peaks in this region. Downstream of the bend, the addition of the rib (Case 2) also significantly increases the heat transfer on the inside wall, in this case by 22%. The outside wall in the downstream leg of both cases experiences high heat transfer due to flow impingement. The friction factor is also much higher in the bend. The fully developed calculations show the area averaged friction factor augmentation to have a value of 8.6 across a single rib pitch. In this case, the value is slightly higher upstream of the bend (section 1) but has a significantly larger value across the entrance and exit ribs and the bend itself (sections 2–4). The last rib in the upstream leg leading into the bend (section 2) shows a friction factor augmentation about 2–3 times as large as that of the fully developed channel in both cases, and in the bend (section 3), the friction factor increases by a factor of 2 when the rib is added (Case 2).

A very large pressure drop is seen in both cases across the first rib in the downstream duct (section 4), with a value of more than four times that of the fully developed ribbed duct in both cases. It is interesting to note that the friction factor only changed significantly in the immediate vicinity of the rib in the bend. In Case 1, downstream of the bend a slight pressure recovery similar to that found in the calculation of the developing region [43,44] results in a negative friction factor, while in Case 2 only a small friction factor is shown.

A comparison of the basic flow effects in the 180-deg bend can be seen in streamlines plotted in the symmetry plane, as shown in Fig. 2. In both cases, a large recirculation zone is seen in the upstream corner of the bend, as well as a smaller zone in the downstream corner. High heat transfer augmentation results from flow impingement on the back and downstream outside walls due to redirection of the flow around the bend. In Case 1, a large recirculating bubble is observed at the tip of the dividing wall. This zone is not observed, however, in Case 2 because of the high acceleration in the streamwise direction as a result of the addition of the ribs. The recirculating zones in the corner and the separated flow at the divider tip have also been shown in the PIV study in [3] and the LDV study in [4].

Another feature of the mean flow is a pair of counter-rotating Dean vortices in the midplane of the bend, which is oriented parallel to the dividing wall. The Dean vortices have been reported in many studies of flow through smooth 180-deg bends [3,4,7,9,10]. Vector plots of the Dean vortices are shown in Fig. 3 for both

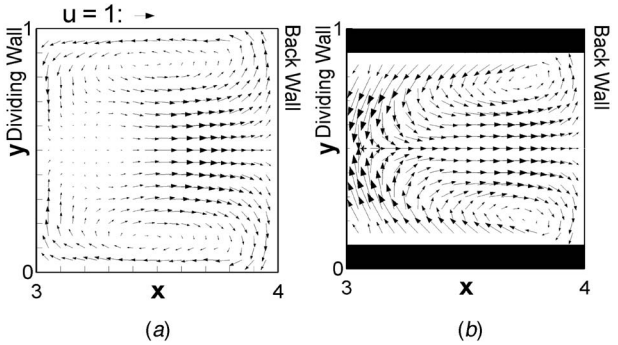


**Fig. 3 A pair of counter-rotating Dean vortices at the midplane of (*a*) Case 1 and (*b*) Case 2 shows impingement on the back wall. Case 1 shows a low velocity in the recirculation bubble near the dividing wall.**

cases. In Case 1, the peak velocity is found near the back wall, with a low velocity seen in the region near the large recirculation bubble shown previously. In Case 2, however, the recirculation strength near the dividing wall is much stronger due to the high vertical velocity above the ribs. The horizontal velocity towards the back wall is similar to that of Case 1.

A comparison of the streamwise velocity and streamwise turbulence is shown in Fig. 4. Two vertical locations are considered: one at $\frac{1}{4}$ of the channel height ($y=0.25$) and the other at the midchannel height ($y=0.50$). The LDV data of Sewall et al. [56], which was taken in a duct with geometry and flow conditions exactly the same as Case 1, is also shown in the figure.

In the middle plane of the bend, the streamwise velocity is nominally negative, and positive values indicate backward flow. In Case 1, both experiments and computations show the presence of a recirculating region at the inner wall of the bend, whereas the presence of the rib in the bend prevents the separation and recirculation. Besides this effect, the ribs in the bend also tend to produce a more uniform flow in the bend particularly at $y=0.25$ near the ribbed wall. The comparisons of mean flow velocity show very good agreement with LDV data.

Streamwise turbulence comparisons show the highest turbulence near the inside wall, peaking at 55% in this case, and the lowest turbulence near the back wall, dipping below 15% in the figure. Towards the center of the duct, the turbulence in both cases is approximately equal. The measured values are in close agreement with the computations, although the measurements show a trajectory of the shear layer which is slightly closer to the inside wall of the bend. Because the measurement plane is directly on top of the ribs, the distributions of streamwise turbulence intensities are not very different between Case 1 and Case 2.

Turbulent kinetic energy in the midplane of the bend (Fig. 5) shows the effect of adding a rib in the bend. Unlike the distribution of streamwise intensities as shown in Fig. 4, the distribution of turbulent kinetic energy is strongly affected by the presence of the rib in the bend through the differences in cross-stream and spanwise fluctuations. In Case 1, turbulence as high as 35% from the shear layers on the ribs upstream of the bend is shown to be transported towards the center of the dividing wall by the action of the secondary Dean vortices. In Case 2, the turbulence is further augmented by the ribs in the bend and reaches over 45%. In a 180-deg bend connecting two smooth ducts, the turbulent kinetic energy peaks at 20% [3,4]. In Case 1, a vertical layer of relatively high turbulence (20% surrounded by 15%) indicates the presence of the shear layer formed from flow separation off of the dividing wall as flow enters the bend. In Case 2, the shear layer is not seen explicitly and the turbulence is much higher. In both cases, the turbulence near the back wall is very low, between 5% and 10%.

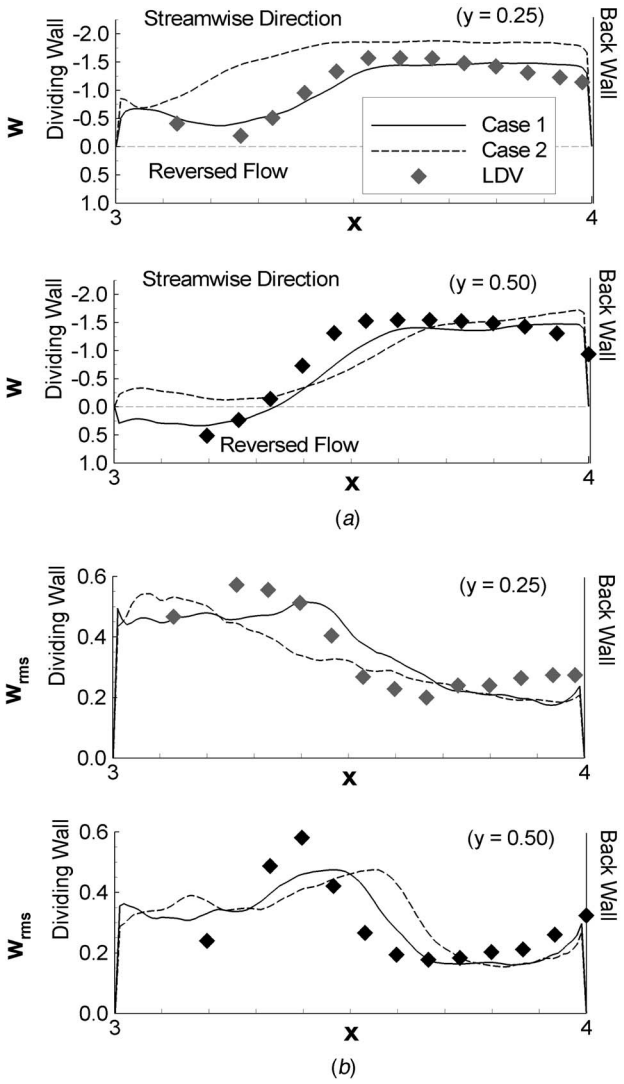


**Fig. 4 The (*a*) streamwise velocity and (*b*) streamwise rms quantity are compared between Case 1 (solid line) and Case 2 (dashed line). The LDV measurements correspond to the calculations in Case 1.**

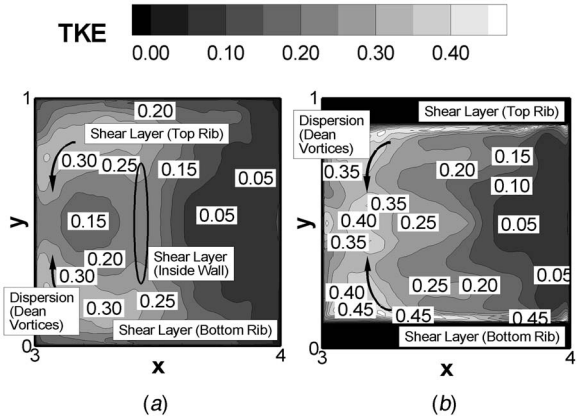


**Fig. 5 Turbulent kinetic energy in the bend in (*a*) Case 1 and (*b*) Case 2 shows the combination of shear layers as well as transport of turbulence up along the inside wall from the motion of the Dean vortices.**

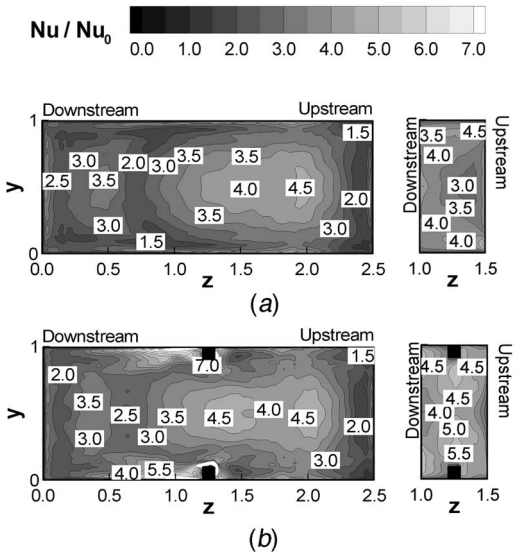


**Fig. 6 Heat transfer augmentation on the back wall and tip of the dividing wall with (*a*) Case 1 and (*b*) Case 2 shows the difference in heat transfer augmentation near the top and bottom walls and the higher heat transfer augmentation on the tip of the dividing wall due to the presence of the rib.**

As a result of the mean and turbulent flow effects, the dividing wall and back wall of the bend show large gradients of heat transfer augmentation. Flow from the upstream duct impinges on the back wall, and due to the motion of the counter-rotating Dean vortices, the fluid is swept back towards the inside wall where it increases the heat transfer augmentation on the end of the dividing wall near the ribbed walls in both cases. These effects can be seen in Fig. 6. In both cases, the peak heat transfer augmentation on the center of the back wall has a value of 4.5, but in Case 2 the heat transfer near the ribs reaches over 7.0. The presence of the rib also increases the heat transfer augmentation on the dividing wall tip. The maximum augmentation in Case 2 reaches 5.5, while the maximum in Case 1 is only 4.0, which is 27% less than that of Case 2. The edges of the back wall show low heat transfer near the ribbed walls in Case 1 but show much higher heat transfer in the same area in Case 2.

Figure 7 shows a series of comparisons between the mass transfer experiments of Han et al. [20] at Re=30,000 and the LES calculations in the upstream and downstream legs of the duct. The rib size ($e/D_h$) and spacing ($P/e$) and in-line rib configuration with ribs on opposite walls are the same as those in the present study. A number of studies in the fully developed region of ribbed ducts have shown a very weak dependence of heat transfer augmentation ratios on Reynolds number (Re=30,000 in the experiments) that is certainly within experimental uncertainty [56–59]. In the study by Han et al. [20], averaged heat transfer augmentation values in the bend yielded essentially no difference between Reynolds numbers of 15,000 and 30,000. The experimental uncertainty was reported to be ±8%, and the calculated heat transfer augmentation is expected to be well within the range of the experimental values. A study of smooth 180-deg bends comparing divider thickness of $\frac{1}{2}\,D_h$ (calculations) and $\frac{1}{4}\,D_h$ (experiments) [4] concluded that a larger dividing wall thickness would decrease the turbulent kinetic energy downstream of the bend and reduce the heat transfer augmentation. However, in ribbed ducts the level of turbulence is much higher than that encountered in smooth ducts, and the effect of the thickness of the dividing wall may not have a large effect on the average heat transfer augmentation downstream of the bend.

The experimental measurements of Han et al. [20] were taken along three lines on the ribbed wall of the duct. The inner line was

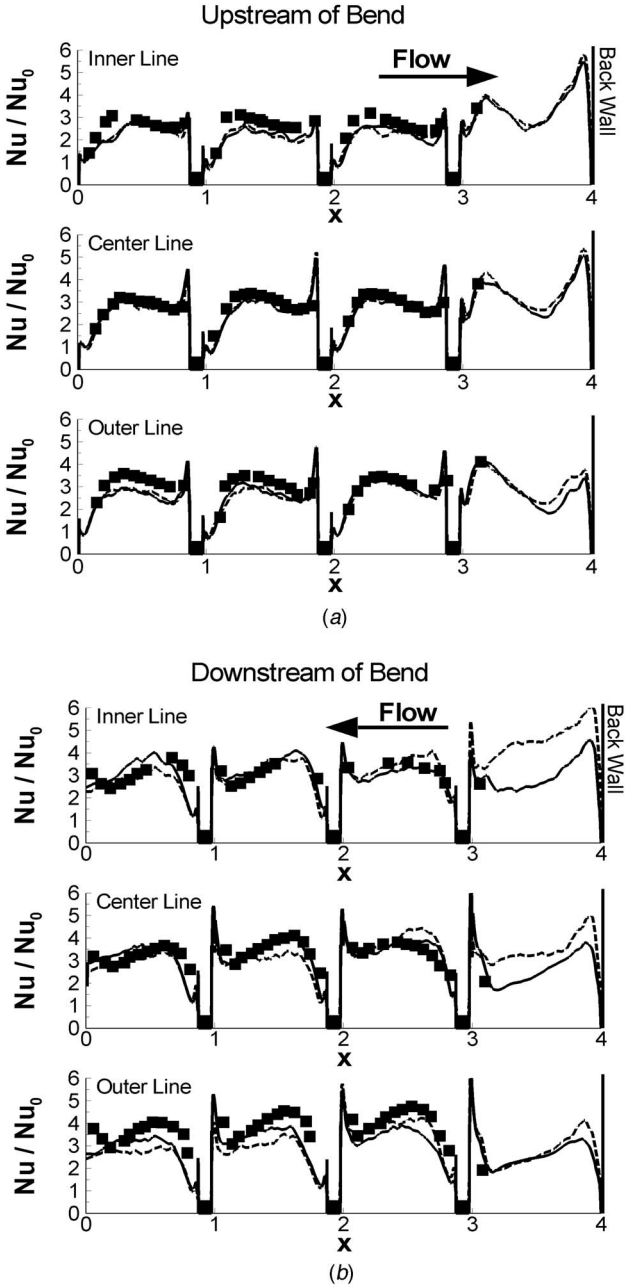


**Fig. 7 Heat transfer comparisons with Han et al. [20] along an inner line, center line, and outer line in the (*a*) upstream leg and (*b*) downstream leg of the ribbed wall show good agreement between the mass transfer experiments and heat transfer results. The measurements of Han et al. did not have a rib in the bend (Case 1), and the dashed lines denote the LES calculations of Case 2.**

measured midway between the centerline and inside wall, and the outer line was measured midway between the centerline and outside wall. The first three plots show comparisons along the ribbed wall of the upstream side of the bend, where flow is in the $+x$ direction, and the last three are downstream of the bend, where flow is in the $-x$ direction. The upstream calculations (Fig. 7(*a*)) show that the bend has relatively little effect on the upstream flow. An increase in heat transfer augmentation is seen downstream of the last rib, and a very high value can be seen in the corner at the back wall. Downstream of the bend (Fig. 7(*b*)), the heat transfer is shifted more towards the outside wall than it was upstream. Here,

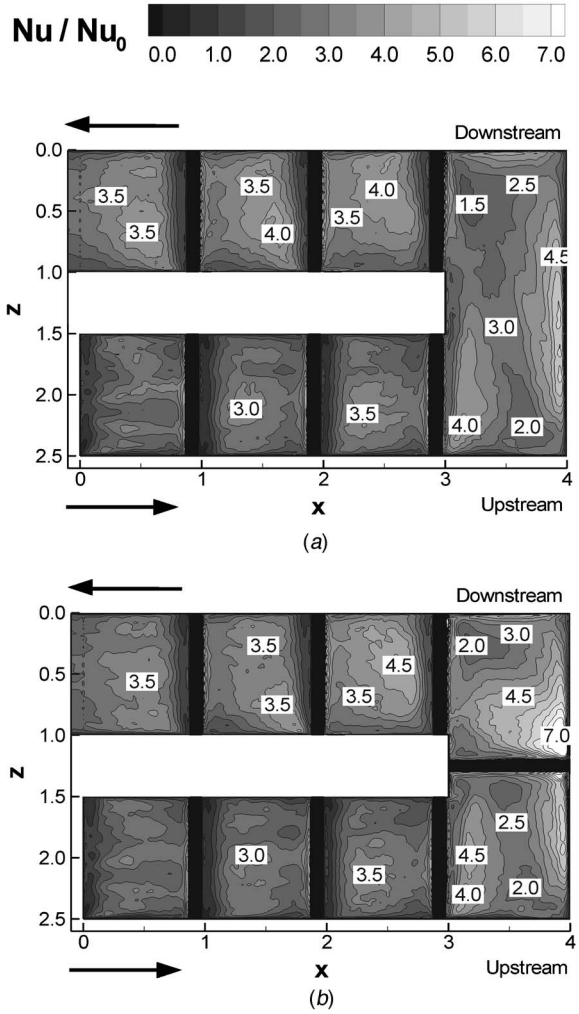


**Fig. 8 The heat transfer augmentation on the ribbed wall in (*a*) Case 1 and (*b*) Case 2 shows the high heat transfer in the immediate vicinity of the rib and a slightly increased heat transfer augmentation downstream.**

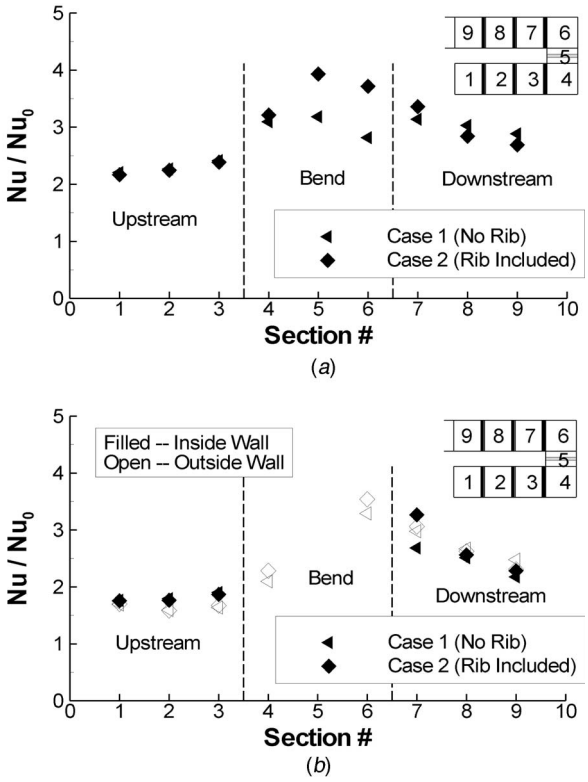


**Fig. 9 Average heat transfer augmentation on (*a*) the ribbed walls and (*b*) the inside and outside walls shows the increase in heat transfer due to the rib.**

the outside line shows a much higher heat transfer augmentation than it did on the upstream side. Also, the inner two curves show a low heat transfer augmentation downstream of the first rib in the downstream leg, but this value is found to increase after the second rib. The only significant difference between the two LES cases is found on the downstream side of the bend, where the inclusion of the rib increases the heat transfer significantly.

Figure 8 shows the heat transfer augmentation on the ribbed wall of both cases. In the upstream section, the heat transfer augmentation is nearly identical in both cases. For Case 2, the peak heat transfer increases significantly along the back wall, as well as in the downstream half of the bend, where greater flow acceleration due to the added ribs causes stronger flow impingement on the outside wall than in Case 1. At the entrance to the second pass of the duct, the effect of the included rib is manifest through a higher peak heat transfer value in Case 2 in the reattachment region downstream of the first rib. Heat transfer downstream of the following ribs becomes similar between the two cases, indicating that the added rib in Case 2 only increases the heat transfer augmentation in the bend and immediately downstream.

Averaged heat transfer along the ribbed wall is shown in Fig. 9(*a*). The presence of the rib increases the bend heat transfer dramatically, but the increase in heat transfer is not seen past the entrance to the downstream leg. In the bend, the rib is shown to increase heat transfer augmentation by 20–30%. Figure 9(*b*) shows the sidewall heat transfer. The addition of the rib slightly increases the outside wall heat transfer on both the upstream and downstream sides, but in the downstream leg the rib increases the heat transfer on both the inside and outside walls. The inside wall is increased significantly, and it actually has a value larger than the outside wall in Case 2, as well.

## Conclusions

Large eddy simulations are shown to be an effective prediction tool for highly turbulent flows in the 180-deg bend region of a ribbed duct. Two configurations were compared in this study, one without a rib in the bend and the other with a rib included in the bend, and the conclusions are as follows:

- Both cases showed a pair of counter-rotating Dean vortices in the midplane of the bend, while only Case 1 showed a large recirculation zone at the tip of the dividing wall.
- The friction factor increases by a factor of 2 across the last rib in the upstream leg of the bend in both cases. The friction factor is approximately four times as large as that of a straight ribbed duct across the first rib in the downstream leg.
- Upstream of the bend, the ribbed wall and smooth wall heat transfer are unaffected by the addition of the rib in the middle of the bend. In this region, however, the average heat transfer on the back wall increases by 16%, and the heat transfer on the tip of the divider wall increases by 21%. The ribbed wall also experiences a jump of nearly 20% when the rib is added in the bend.
- Downstream of the bend, the heat transfer is about 8% higher on the ribbed wall in Case 2 (added rib), but it is also higher on the inside and outside walls. In addition, the inside wall has a higher heat transfer augmentation than the outside wall in Case 2, while the opposite is true in Case 1.

- Adding a rib to the bend increases the friction factor by 82%, while it only increases the heat transfer by 20%. Though the trade-off is significant, it may still be advisable to place a rib in the bend if the 20% increase in heat transfer is worth the pressure loss incurred by doing so.

## Acknowledgment

This research was supported by the U.S. DOE, Office of Fossil Energy, National Energy Technology Laboratory. Any opinions, findings, conclusions, or recommendations expressed herein are those of the author and do not necessarily reflect the views of the DOE. This work was also supported by National Computational Science Alliance under MCA98N042N and utilized the Teragrid Linux cluster at the National Center for Supercomputing Applications.

## Nomenclature

$D_h$ = hydraulic diameter, characteristic length
$e$ = rib height
$f$ = fanning friction factor
$k$ = thermal conductivity
$\Delta L$ = change in streamwise position between two pressure measurements
$\underline{\mathrm{Nu}}$ = local Nusselt number
$\overline{\mathrm{Nu}}$ = spatially averaged Nusselt number
$P$ = rib pitch
$p$ = non-dimensional pressure
Pr = Prandtl number $(=\mu C_p/k)$
$q''$ = non-dimensional heat flux on duct walls and ribs
Re = Reynolds number $(=\bar{u}_{\mathrm{in}} D_h/v)$
$T$ = temperature, characteristic temperature is $(T_s - T_{\mathrm{in}})$
TKE = turbulent kinetic energy described by: TKE $=(\overline{u'^2}+\overline{v'^2}+\overline{w'^2})/2\bar{u}_{\mathrm{in}}^2$
$\mathbf{u}$ = Cartesian velocity vector $(u,v,w)$ or $(u_1,u_2,u_3)$
$\bar{u}_{\mathrm{in}}$ = inlet flow velocity/mean bulk flow velocity, characteristic velocity
$\mathbf{x}$ = physical coordinates $(x,y,z)$ or $(x_1,x_2,x_3)$
$\Omega$ = heat transfer surface area
$\theta$ = non-dimensional temperature, $(T-T_{\mathrm{in}}/T_s-T_{\mathrm{in}})$
$\boldsymbol{\xi}$ = computational coordinates $(\xi,\eta,\zeta)$

### Subscripts

$s$ = surface
in = inlet to calculation domain; average bulk velocity
rms = root mean square
$t$ = turbulent Reynolds number and Prandtl number
0 = smooth duct

## References

[1] Metzger, D. E., and Sahm, M. K., 1986, "Heat Transfer Around Sharp 180-deg Turns in Smooth Rectangular Channels," ASME J. Heat Transfer, **108**, pp. 500–506.
[2] Park, C. W., and Lau, S. C., 1998, "Effect of Channel Orientation of Local Heat (Mass) Transfer Distributions in a Rotating Two-Pass Square Channel With Smooth Walls," ASME J. Heat Transfer, **120**, pp. 624–632.
[3] Schabacker, J., and Bölcs, A., 1998, "PIV Investigation of the Flow Characteristics in an Internal Coolant Passage With Two Ducts Connected by a Sharp 180° Bend," ASME Paper No. 98-GT-544.
[4] Liou, T.-M., Tzeng, Y.-Y., and Chen, C.-C., 1999, "Fluid Flow in a 180-deg Sharp Turning Duct With Different Divider Thicknesses," ASME J. Turbomach., **121**, pp. 569–576.
[5] Mochizuki, S., Takamura, J., Yamawaki, S., and Yang, W.-J., 1994, "Heat Transfer in Serpentine Flow Passages With Rotation," ASME J. Turbomach., **116**, pp. 133–140.
[6] Cardone, G., Astarita, T., and Carlomagno, G. M., 1998, "Wall Heat Transfer in Static and Rotating 180[d] Turn Channels by Quantitative Infrared Thermography," Rev. Gen. Therm., **37**, pp. 644–652.
[7] Besserman, D. L., and Tanrikut, S., 1992, "Comparison of Heat Transfer Measurements With Computations for Turbulent Flow Around a 180-deg Bend," ASME J. Turbomach., **114**, pp. 865–871.
[8] Song, B., and Amano, R. S., 2000, "Application of Non-Linear $k$-$\omega$ Model to the Turbulent Flow Inside a Sharp U-Bend," ASME Paper No. 2000-GT-0225.
[9] Gu, X., Wu, H.-W., Schock, H. J., and Shih, T. I.-P., 2002, "Two-Equation Versus Reynolds-Stress Modeling in Predicting Flow and Heat Transfer in a Smooth U-Duct With and Without Rotation," ASME Paper No. GT-2002-30616.
[10] Son, S. Y., Kihm, K. D., and Han, J.-C., 2002, "PIV Flow Measurements for Heat Transfer Characterization in Two-Pass Square Channels With Smooth and 90° Ribbed Walls," Int. J. Heat Mass Transfer, **45**, pp. 4809–4822.
[11] Liou, T.-M., Chen, M.-Y., and Tsai, M.-H., 2002, "Fluid Flow and Heat Transfer in a Rotating Two-Pass Square Duct With In-Line 90-deg Ribs," ASME J. Turbomach., **124**, pp. 260–268.
[12] Tse, D. G. N., and Steuber, G. D., 1997, "Flow in a Rotating Square Serpentine Coolant Passage With Skewed Trips," ASME Paper No. 97-GT-529.
[13] Iacovides, H., Jackson, D. C., Kelemenis, G., Launder, B. E., and Yuan, Y.-M., 2001, "Flow and Heat Transfer in a Rotating U-Bend With 45° Ribs," Int. J. Heat Fluid Flow, **22**, pp. 308–314.
[14] Chanteloup, D., Juaneda, Y., and Bölcs, A., 2002, "Combined 3D Flow and Heat Transfer Measurements in a 2-Pass Internal Coolant Passage of Gas Turbine Airfoils," ASME Paper No. GT-2002-30214.
[15] Servouse, Y., and Sturgis, J. C., 2003, "Heat Transfer and Flow Field Measurements in a Rib-Roughened Branch of a Rotating Two-Pass Duct," ASME Paper No. GT2003-38048.
[16] Ekkad, S. V., and Han, J.-C., 1997, "Detailed Heat Transfer Distributions in Two-Pass Square Channels With Rib Turbulators," Int. J. Heat Mass Transfer, **40**, pp. 2525–2537.
[17] Ekkad, S. V., Pamula, G., and Shantiniketanam, M., 2000, "Detailed Heat Transfer Measurements Inside Straight and Tapered Two-Pass Channels With Rib Turbulators," Exp. Therm. Fluid Sci., **22**, pp. 155–163.
[18] Chandra, P. R., Han, J. C., and Lau, S. C., 1988, "Effect of Rib Angle on Local Heat/Mass Transfer Distribution in a Two-Pass Rib-Roughened Channel," ASME J. Turbomach., **110**, pp. 233–241.
[19] Mochizuki, S., Murata, A., Shibata, R., and Yang, W.-J., 1999, "Detailed Measurements of Local Heat Transfer Coefficients in Turbulent Flow Through Smooth and Rib-Roughened Serpentine Passages With a 180° Sharp Bend," Int. J. Heat Mass Transfer, **42**, pp. 1925–1934.
[20] Han, J. C., Chandra, P. R., and Lau, S. C., 1988, "Local Heat/Mass Transfer Distributions Around Sharp 180 Deg Turns in Two-Pass Smooth and Rib-Roughened Channels," ASME J. Heat Transfer, **110**, pp. 91–98.
[21] Zhao, C. Y., and Tao, W. Q., 1997, "A Three Dimensional Investigation on Turbulent Flow and Heat Transfer Around Sharp 180-Deg Turns in Two-Pass Rib-Roughened Channels," Int. J. Heat Mass Transfer, **24**, pp. 587–596.
[22] Bonhoff, B., Tomm, U., Johnson, B. V., and Jennions, I., 1997, "Heat Transfer Predictions for Rotating U-Shaped Coolant Channels With Skewed Ribs and With Smooth Walls," ASME Paper No. 97-GT-162.
[23] Stephens, M. A., and Shih, T. I.-P., 1997, "Computation of Compressible Flow and Heat Transfer in a Rotating Duct With Inclined Ribs and a 180-Degree Bend," ASME Paper No. 97-GT-192.
[24] Shih, T. I.-P., Lin, Y.-L., Stephens, M. A., and Chyu, M. K., 1998, "Flow and Heat Transfer in a Ribbed U-Duct Under Typical Engine Conditions," ASME Paper No. 98-GT-213.
[25] Jang, Y.-J., Chen, H.-C., and Han, J.-C., 2000, "Flow and Heat Transfer in a Rotating Square Channel With 45° Angled Ribs by Reynolds Stress Turbulence Model," ASME Paper No. 2000-GT-0229.
[26] Lin, Y.-L., Shih, T. I.-P., Stephens, M. A., and Chyu, M. K., 2001, "A Numerical Study of Flow and Heat Transfer in a Smooth and Ribbed U-Duct With and Without Rotation," ASME J. Heat Transfer, **123**, pp. 219–232.
[27] Al-Qahtani, M., Jang, Y.-J., Chen, H.-C., and Han, J.-C., 2002, "Prediction of Flow and Heat Transfer in Rotating Two-Pass Rectangular Channels With 45 -Deg Rib Turbulators," ASME J. Turbomach., **124**, pp. 242–250.
[28] Ciofalo, M., and Collins, M. W., 1992, "Large-Eddy Simulation of Turbulent Flow and Heat Transfer in Plane and Rib-Roughened Channels," Int. J. Opt. Comput., **15**, pp. 453–489.
[29] Braun, H., Neumann, H., and Mitra, N. K., 1999, "Experimental and Numerical Investigation of Turbulent Heat Transfer in a Channel With Periodically Arranged Rib Roughness Elements," Exp. Therm. Fluid Sci., **19**, pp. 67–76.
[30] Murata, A., and Mochizuki, S., 2000, "Large Eddy Simulation With a Dynamic Subgrid-Scale Model of Turbulent Heat Transfer in an Orthogonally Rotating Rectangular Duct With Transverse Rib Turbulators," Int. J. Heat Mass Transfer, **43**, pp. 1243–1259.
[31] Murata, A., and Mochizuki, S., 2001, "Comparison Between Laminar and Turbulent Heat Transfer in a Stationary Square Duct With Transverse or Angled Rib Turbulators," Int. J. Heat Mass Transfer, **44**, pp. 1127–1141.
[32] Murata, A., and Mochizuki, S., 2001, "Effect of Centrifugal Buoyancy on Turbulent Heat Transfer in an Orthogonally Rotating Square Duct With Transverse or Angled Rib Turbulators," Int. J. Heat Mass Transfer, **44**, pp. 2739–2750.
[33] Murata, A., and Mochizuki, S., 2003, "Effect of Cross-Sectional Aspect Ratio on Turbulent Heat Transfer in an Orthogonally Rotating Rectangular Duct With Angled Rib Turbulators," Int. J. Heat Mass Transfer, **46**, pp. 3119–3133.
[34] Jordan, S. A., 2003, "The Turbulent Character and Pressure Loss Produced by Periodic Symmetric Ribs in a Circular Duct," Int. J. Heat Fluid Flow, **24**, pp.

795–806.
[35] Cui, J., Patel, V., and Lin, C.-L., 2003, "Large-Eddy Simulation of Turbulent Flow in a Channel With Rib Roughness," Int. J. Heat Fluid Flow, **24**, pp. 372–388.
[36] Saha, A. K., and Acharya, S., 2003, "Flow and Heat Transfer in an Internally Ribbed Duct With Rotation: An Assessment of LES and URANS," ASME Paper No. GT2003–38619.
[37] Tyagi, M., and Acharya, S., 2004, "Large Eddy Simulations of Flow and Heat Transfer in Rotating Ribbed Duct Flows," ASME Paper No. GT2004-53401.
[38] Ahn, J., Choi, H., and Lee, J. S., 2004, "Large Eddy Simulation of Flow and Heat Transfer in a Channel Roughened by Square or Semicircle Ribs," ASME Paper No. GT2004-53924.
[39] Watanabe, K., and Takahashi, T., 2002, "LES Simulation and Experimental Measurement of Fully Developed Ribbed Channel Flow and Heat Transfer," ASME Paper No. GT-2002-30203.
[40] Takahashi, T., and Watanabe, K., 2004, "Large Eddy Simulation of Flow and Heat Transfer in a Rectangular Channel With Crossed Angled Ribs," ASME Paper No. GT2004-53673.
[41] Tang, X.-L, Qian, Z.-D., Wu, Y.-L., Liu, S.-H., and Yang, F., 2004, "An Improved Dynamic Subgrid-Scale Stress Model," J. Hydrodynam., **16**, pp. 276–282.
[42] Rütten, F., Meinke, M., and Schröder, W., 2001, "Large-Eddy Simulations of 90° Pipe Bend Flows," J. Turbul., **2**, pp. 1–14.
[43] Sewall, E. A., and Tafti, D. K., 2004, "Large Eddy Simulation of the Developing Region of a Stationary Ribbed Internal Turbine Blade Cooling Channel," ASME Paper No. GT2004-53832.
[44] Sewall, E. A., and Tafti, D. K., 2004, "Large Eddy Simulation of the Developing Region of a Rotating Ribbed Internal Turbine Blade Cooling Channel," ASME Paper No. GT2004-53833.
[45] Murata, A., and Mochizuki, S., 2004, "Large Eddy Simulation of Turbulent Heat Transfer in a Rotating Two-Pass Smooth Square Channel With Sharp 180° Turns," Int. J. Heat Mass Transfer, **47**, pp. 683–698.
[46] Murata, A., and Mochizuki, S., 2004, "Effect of Rib Orientation and Channel Rotation on Turbulent Heat Transfer in a Two-Pass Square Channel With Sharp 180° Turns Investigated by Using Large Eddy Simulation," Int. J. Heat Mass Transfer, **47**, pp. 2599–2618.
[47] Murata, A., and Mochizuki, S., 2004, "Centrifugal Buoyancy Effect on Turbulent Heat Transfer in a Rotating Two-Pass Smooth Square Channel With Sharp 180-Deg Turns," Int. J. Heat Mass Transfer, **47**, pp. 3215–3221.
[48] Murata, A., and Mochizuki, S., 2004, "Aiding and Opposing Contributions of Centrifugal Buoyancy on Turbulent Heat Transfer in a Two-Pass Transverse- or Angled-Rib-Roughened Channel With Sharp 180° Turns," Int. J. Heat Mass Transfer, **47**, pp. 3721–3743.
[49] Germano, M., Piomelli, U., Moin, P., and Cabot, W. H., 1991, "A Dynamic Subgrid-Scale Eddy Viscosity Model," Phys. Fluids A, **3**, pp. 1760–1765.
[50] Tafti, D. K., 2005, "Evaluating the Role of Subgrid Stress Modeling in a Ribbed Duct for the Internal Cooling of Turbine Blades," Int. J. Heat Fluid Flow, **26**, pp. 92–104.
[51] Tafti, D. K., 2001, "GenIDLEST—A Scalable Parallel Computational Tool for Simulating Complex Turbulent Flows," *Proceedings of the ASME Fluids Engineering Division, FED*, ASME-IMECE, New York, p. 256.
[52] Abdel-Wahab, S., and Tafti, D. K., 2004, "Large Eddy Simulation of Flow and Heat Transfer in a 90° Ribbed Duct With Rotation—Effect of Coriolis Forces," ASME Paper No. GT2004-53796.
[53] Abdel-Wahab, S., and Tafti, D. K., 2004, "Large Eddy Simulation of Flow and Heat Transfer in a 90° Ribbed Duct With Rotation—Effect of Buoyancy Forces," ASME Paper No. GT2004-53799.
[54] Abdel-Wahab, S., and Tafti, D. K., 2004, "Large Eddy Simulation of Flow and Heat Transfer in a Staggered 45° Ribbed Duct," ASME Paper No. GT2004-53800.
[55] Incropera, F. P., and DeWitt, D. P., 2002, *Fundamentals of Heat and Mass Transfer*, 5th ed., Wiley, New York.
[56] Sewall, E. A., Tafti, D. K., Graham, A., and Thole, K. A., 2005, "Experimental Validation of Large Eddy Simulations of Flow and Heat Transfer in a Stationary Ribbed Duct," Int. J. Heat Fluid Flow, **27**, pp. 243–258.
[57] Han, J. C., 1988, "Heat Transfer and Friction Characteristics in Rectangular Channels With Rib Turbulators," ASME J. Heat Transfer, **110**, pp. 321–328.
[58] Fann, S., Yang, W.-J., and Zhang, N., 1994, "Local Heat Transfer in a Rotating Serpentine Passage With Rib-Roughened Surfaces," Int. J. Heat Mass Transfer, **37**, pp. 217–228.
[59] Taslim, M. E., and Wadsworth, C. M., 1997, "An Experimental Investigation of the Rib Surface-Averaged Heat Transfer Coefficient in a Rib-Roughened Square Passage," ASME J. Turbomach., **119**, pp. 381–389.

**Hiroshi Nakayama**
Daido Institute of Technology,
Minami-ku, Nagoya, 457-8530, Japan
e-mail: hnaka@daido-it.ac.jp

**Masafumi Hirota**
Department of Micro-Nano System Engineering,
Nagoya University,
Chikusa-ku, Nagoya 464-8603, Japan
e-mail: hirota@mech.nagoya-u.ac.jp

**Hideomi Fujita**
Department of Mechanical Engineering,
Meijo University,
Tenpaku-ku, Nagoya 468-8502, Japan
e-mail: hdfujita@ccmfs.meijo-u.ac.jp

**Takeshi Yamada**
Akashi Works,
Kawasaki Heavy Industries,
Kawasaki-cho, Akashi 673-8666, Japan
e-mail: yamada_take@khi.co.jp

**Yusuke Koide**
Tokai Works,
Du pont-Toray,
Shinpo-cho, Tokai 476-8567, Japan
e-mail: yusuke_koide@td-net.co.jp

# Fluid Flow and Heat Transfer in Two-Pass Smooth Rectangular Channels With Different Turn Clearances

*Flow characteristics in stationary two-pass channels with a sharp* 180-deg *turn have been measured using LDV (laser Doppler velocimeter), directing special attention to the influence of the size of the turn clearance on the flow structure. The main features of the flow, flow separation and recirculation, secondary flow, turbulence intensities, measured with* $\mathrm{Re}=3.5\times10^4$ *for three turn clearances, are presented. A close comparison of the velocity data with local Sherwood number distributions on the channel walls reveals that the wall-normal velocity mainly dominates the heat transfer in the channel, but the wall-parallel component also contributes locally to heat transfer after the turn.*
[DOI: 10.1115/1.2101854]

## 1 Introduction

The two-pass channels with a rectangular cross section connected by a sharp 180-deg turn are widely applied in industrial practices; the typical applications are ventilation piping system, flow passages in various heat exchangers, and internal cooling passages of an advanced gas-turbine blade. The flow passing through a sharp turn develops highly three-dimensional structures with the secondary flow induced by the centrifugal force, which is yielded in U-bends [1] as well, and with the flow separation and recirculation that are inherent in the sharply turning channels. As a result, the local heat transfer characteristics also tend to be very complicated even under a stationary condition.

Detailed data on heat transfer in the two-pass channels are indispensable for a critical design of thermal equipment used under a severe thermal condition. In response to such demand, over the past decades a number of studies were conducted on forced convection heat transfer in such two-pass channels with a sharp turn under the stationary condition. As the typical studies on the heat transfer characteristics in those channels, Metzger et al. [2] first studied overall heat transfer characteristics in two-pass smooth rectangular channels by varying the divider location and the turn clearance at the turn. Chyu [3] presented heat transfer results in both two- and three-pass channels with 180-deg turn. They showed that heat transfer coefficient at the first turn has already reached the thermally developed condition. Han et al. [4], Ekkad et al. [5–7], Wang et al. [8], and Mochizuki et al. [9] investigated the influence of the ribs attached on the channel walls: they reported the combined effects of the rib angle and rib orientation on heat transfer characteristics in the sharp turn channels. Astarita et al. [10] showed the local heat transfer coefficients in smooth two channels with different aspect ratios and constant turn clearance.

Although the detailed data on flow characteristics are also important for a better understanding of the complex heat transfer mechanism in those channels, only few results are found in open literature because of considerable difficulties in measuring them with high accuracy. Schabacker et al. [11,12] first measured mean and fluctuating velocity fields in two-pass square smooth and ribbed channel by using a stereoscopic digital PIV (particle image velocimetry) system. They showed the influences of the turn and the ribs on the overall flow characteristics. Liou et al. made a series of experimental studies on the velocity distributions in a 180-deg sharp turning duct using LDV [13–15]; their attention was directed to the influence of the divider wall thickness. Son et al. [16] also made a PIV flow measurement in a two-pass square channel with smooth and ribbed walls. Recently, numerical simulations with RANS (Reynolds-averaged Navier-Stokes) model [17,18] and LES (large eddy simulation) [19] were conducted on this type of channel flow, and detailed turbulence characteristics were made clear; however, experimental data that can be compared with numerical ones are still quite scarce.

Among the investigations on heat transfer characteristics conducted to date, the present authors made a series of experiments to make clear the effect of channel geometry on the heat transfer using the naphthalene sublimation method [20–23]. In particular, they found that the size of the turn clearance exerted a great influence on the local heat transfer characteristics inside and after the turn section. Their results suggested that, by changing the turn clearance, the distributions of the secondary flow and the characteristics of the flow separation and reattachment around the turn could be modified significantly. Although it is of fundamental interest and of practical importance to make clear the influence of the turn clearance on the flow characteristics in two-pass channels with a 180-deg sharp turn, very few discussions have been made hitherto on this issue.

In view of the above situation, this study aims at a comprehensive investigation on the influence of the turn clearance upon the

Contributed by the Heat Transfer Division of ASME for publication in the JOURNAL OF TURBOMACHINERY. Manuscript received May 10, 2004; final manuscript received May 2, 2005. Review conducted by J.-C. Han.

  

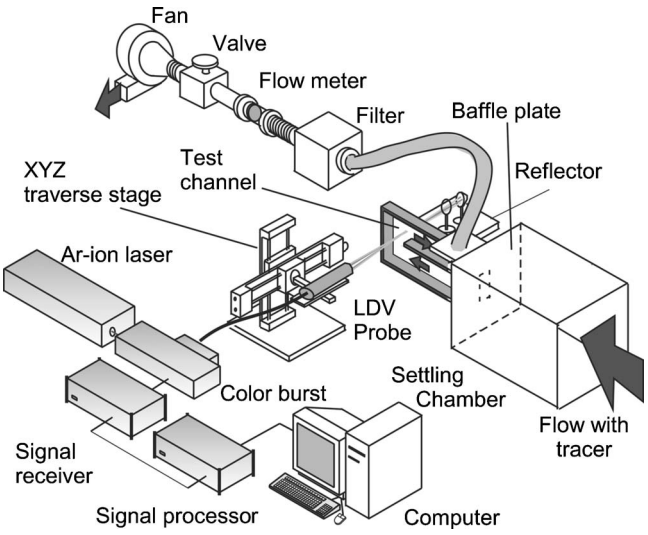


**Fig. 1 Schematic diagram of the experimental apparatus**

flow characteristics in sharp-turn connected two-pass channels under a stationary condition. The geometry of the test channels is essentially the same as that used in the earlier study on heat (mass) transfer [21]; the aspect ratio of the channel cross section is 2, and three turn clearances are tested under a Reynolds number of $3.5\times10^4$. In this paper, the distributions of mean velocities and turbulence intensities in a symmetrical plane of the channels and in several cross sections in and after the turn are presented, directing attention to the influence of the turn clearance on the separation and recirculation of the flow and on the evolution of the longitudinal vortices after the turn. Then, by comparing the near-wall flow characteristics with the local Sherwood number distributions [21] closely, the flow parameters that dominate the heat transfer in and after the turn are examined.

## 2 Experimental Apparatus and Procedure

Figure 1 shows a schematic diagram of the experimental apparatus. The flow loop is substantially the same as that used in the earlier mass-transfer experiment [20–23]. The apparatus is operated in a suction mode. Air flows into the test channel through a settling chamber in which the entrance condition of the flow is set up. A baffle plate is equipped at the entrance of the test channel, which helps to form a sharp-edged contract flow inlet condition [22]. Details of the channel entrance are explained later.

As shown in Fig. 2, the test channel is a two-pass channel with

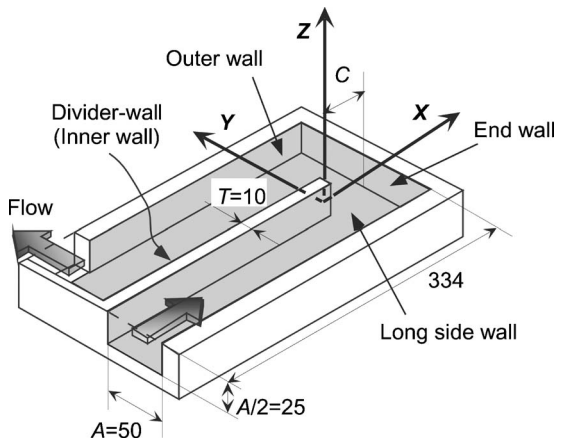


**Fig. 2 Details of the test channel and coordinate system**

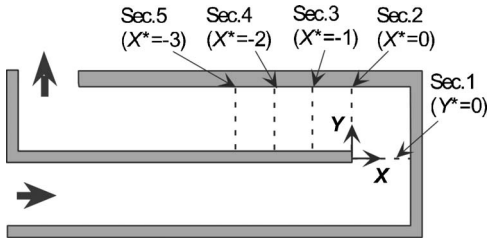


**Fig. 3 Measurement cross sections normal to the streamwise axis**

a rectangular cross section connected by a sharp 180-deg turn; all the channel walls are made of transparent acrylic plates to allow optical access. The cross section in the straight sections before and after the turn is $50\times25$ mm. The divider (inner) wall is 10 mm thick and its tip has a square configuration [21]. By changing the length of this divider wall, the turn clearance ("*C*" in Fig. 2) is set at 30, 50, or 70 mm, i.e., $C^*=C/A=0.6$, 1.0, 1.4, where *A* denotes the spanwise (long-side) length of the channel cross section (=50 mm). The distance between the channel entrance and the end wall is 334 mm for all the turn clearances; thus, the distance between the channel entrance and the divider-wall tip changes from 264 mm (=7.93 $d_h$) to 304 mm (=9.13 $d_h$), depending on *C*. Note that the condition of $C^*=1.0$, i.e., the turn clearance is equal to the channel width *A*, a standard turn geometry that has been commonly used in most of the preceding studies.

The coordinate system is also shown in Fig. 2. The origin is at the center of the divider-wall tip; thus, the turn entrance and exit are located at $X^*=0$ for all *C*. In this study, we first measured the velocity distributions in a symmetric plane of the channel ($Z^*=0$), then measured them in several cross sections that were normal to the streamwise axis. Detailed measurement cross sections are illustrated in Fig. 3; six cross sections, sections 1–6, starting from the turn entrance were set up in a channel.

The two-component backscatter fiber LDV system (TSI Inc.) was used to measure the mean velocities and turbulence intensities. A probing volume was about 1.27 mm in length and 0.088 mm in diameter, based on $1/e^2$ extent of laser light intensity. The LDV system was mounted on *X*-*Y*-*Z* traversing stage as shown in Fig. 1, providing a spatial resolution of the probing location of 0.025 mm. In order to improve the Doppler signals, a reflector that consisted of a corner cube prism and a lens was used in the measurements. The reflector was settled opposite to the LDV probe as shown in Fig. 1; it collects and reflects the light scattered by seeding particles and can virtually form the forward scatter receiver configuration. Due to the interference between the channel wall and the light beam, the closest measurement point to each wall was 3 mm from the wall. In order to measure the secondary flow vectors and the turbulent kinetic energy, which consist of two and three velocity components, respectively, two independent velocity measurements were conducted by rotating the test section 90 deg around the *X* axis. We confirmed carefully that quantitatively similar results were obtained for the same velocity component measured by those independent measurements. To keep sufficiently high data rates, the coherence window was not applied and the cross correlation between two velocity components, i.e., Reynolds stresses, was not measured in the present study.

Seeding particles were water droplets with diameters of 1–5 $\mu$m supplied by a nebulizer. The traceability of the seeding particles to the fluctuating velocity was evaluated based on the method proposed by Hjelmfelt et al. [24], and it was found that, with a gain of 0.9, the seeding particles could follow the fluctuating velocity with a frequency up to 2.2 kHz. It was also confirmed that the velocity that was added to the particles by the centrifugal force in flowing around the turn section was as small

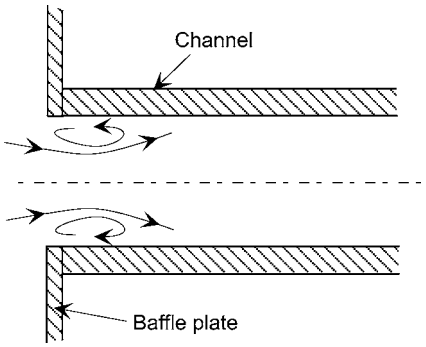


**Fig. 4 Entrance configuration of the channel**

as 0.08% of $U_b$ [25]. These results show that the seeding particles used in this study can follow the turbulent fluid motion quite accurately, and it is expected that unbiased velocities will be measured by LDV with these particles. About 10,000 realizations were ensemble averaged to calculate mean velocities and turbulence intensities at each measuring location. The realizations were sufficient to be sure of statistical convergence [14]. The data that were out of a range of $\pm 3\sigma$ were eliminated in calculating the statistical quantities. The uncertainties involved in the measured values of mean velocity and turbulence intensity were estimated to be at most $0.03U_b$ and $0.06U_b$, respectively [26]. In a preliminary experiment, the influence of the Reynolds number on flow characteristics was examined, and it was found that it does not appear for $\mathrm{Re} > 2\times 10^4$. Therefore, the present experiment was conducted under a single Reynolds number of $3.5\times 10^4$. This Reynolds number is the same as that adopted in the earlier mass-transfer experiments [20–23].

Figure 4 shows the details of the entrance configuration of the channel. Similar to the mass-transfer experiments, a baffle plate was placed at the channel entrance to form a sharp-edged configuration, which ensured that the flow entering the test section had an abrupt contraction-entrance condition [21,22]. This flow-inlet condition was selected rather arbitrarily to simulate the channels used in compact heat exchangers that have a wide range of flow-inlet conditions [27]. The velocity distributions measured in the $Z^*=0$ plane at $X^*=-3$ in the straight section before the turn are shown in Fig. 5. This position corresponds to 5.5 $d_h$ upstream from the

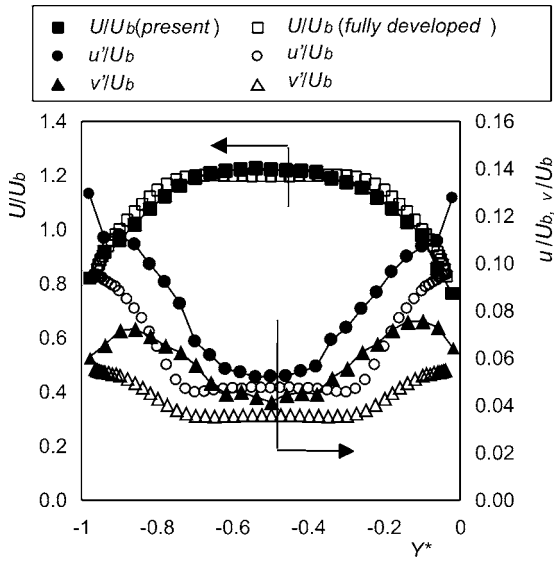


**Fig. 5 Velocity distributions before the turn ($Z^*=0$ plane at $X^*=-3$)**

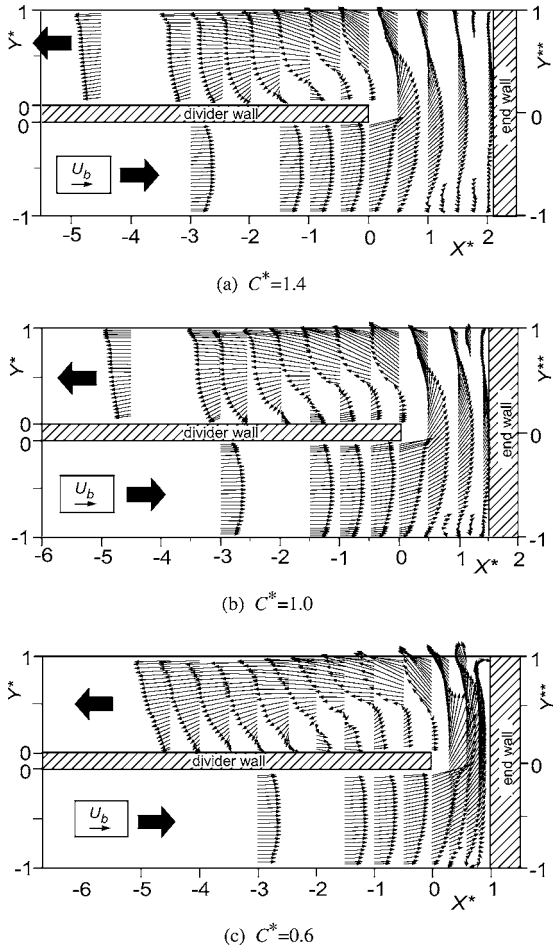


**Fig. 6 Mean velocity vector diagram. (a) $C^*=1.4$; (b) $C^*=1.0$; (c) $C^*=0.6$.**

channel entrance: we made the verification on the symmetry of the velocity distribution in the $Z$ direction. The results obtained in a fully developed turbulent flow in a rectangular straight duct with an aspect ratio of 2 are presented together for comparison [28]. The distribution of the primary flow velocity $U/U_b$ in the present channel agrees well with that of the fully developed condition, but the strong turbulence ($u'/U_b$) produced by the sharp-edged inlet is still maintained at the turn entrance. Since additional measurements were not made in this position, detailed characteristics of the flow, such as the turbulence length scale and the presence of the secondary flow of the second kind, are not clarified.

## 3 Results and Discussion

**3.1 Flow Characteristics in a Symmetric Plane.** At first, in order to grasp the global view of the flow field, the flow characteristics observed in the symmetric plane of the channels, the plane of $Z^*=0$, are presented.

*3.1.1 Overview of Mean Velocity Field.* The mean velocity vector diagrams obtained for $C^*=1.4$, 1.0, 0.6 are shown in Figs. 6(*a*)–6(*c*), respectively. As described above, in the straight section before the turn, the mean velocity distribution at $X^*=-3$ agrees with that of the fully developed turbulent flow. In a region of $-1<X^*<0$ near the turn section, the flow with higher velocity is deviated to the divider-wall side, and thus the mean velocity shows asymmetric distribution with respect to the spanwise centerline of this section. This means that the influence of the turn on the flow begins to appear in the region before the turn entrance. Such a deflection of the mean velocity near the turn entrance is a

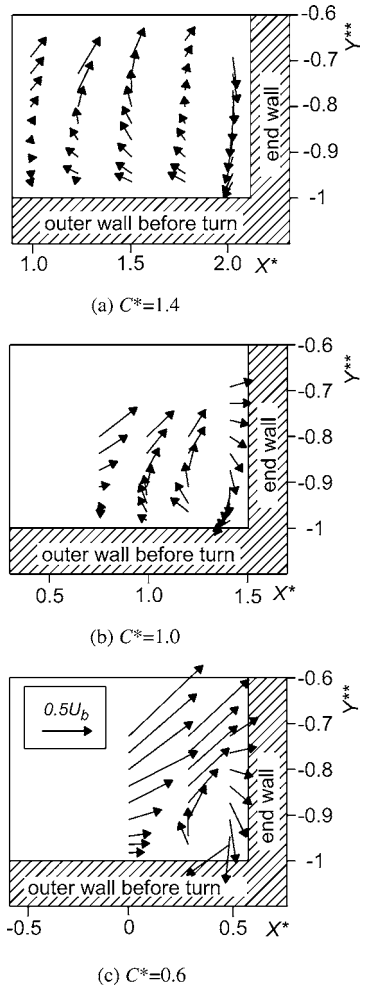


**Fig. 7 Magnified vector diagram at the first outer corner ($Z^*=0$); (a) $C^*=1.4$; (b) $C^*=1.0$; (c) $C^*=0.6$**

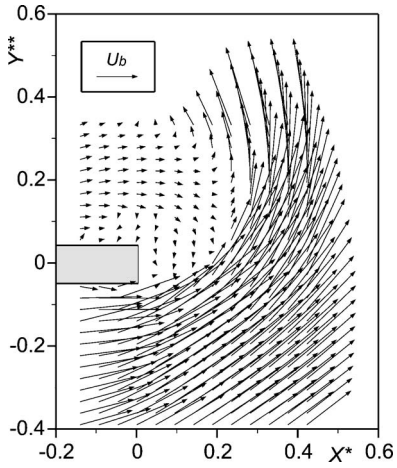


**Fig. 8 Magnified velocity vectors near divider wall tip ($C^*=1$)**

phenomenon peculiar to the channel with a sharp turn, and it is caused by the influence of the pressure gradient near the turn entrance that is favorable in the divider-wall side and adverse in the outer-wall side [29]. At the turn entrance ($X^*=0$), the values of the normalized primary flow velocity $U/U_b$ at $Y^*=-0.02$, which is the measuring point located nearest the upstream edge of the divider wall, are 1.5, 1.6, and 2.1 for $C^*=1.4$, 1.0, and 0.6, respectively. The acceleration of the flow at the turn entrance becomes larger as the turn clearance is decreased.

In the turn section ($X^*>0$ and $-1<Y^{**}<1$), the flow impinges on the end wall and most of this impinging flow proceeds downstream to the second outer corner. The impinging flow is, however, partly reversed upstream and forms a recirculation zone in the first outer corner as observed in Fig. 7, which is the magnified vector diagrams in the first corner. As $C^*$ is decreased, this recirculation zone shrinks, whereas the flow and resulting clockwise vortex in it become stronger. The recirculation zone is also formed in the second corner of the turn section, in which the flow impinging on the outer wall is partly reversed toward the end wall. The velocity $U$ of this reversed flow measured at a location 3 mm apart from the end and outer walls, which is the measuring point located nearest these walls, is $0.38U_b$, $0.14U_b$, and $0.03U_b$ for $C^*=0.6$, 1.0, and 1.4, respectively. These results suggest that the clockwise vortex at the second corner become stronger as $C^*$ is decreased, but the vortex in the second corner is rather weak compared to that in the first corner for all $C^*$.

The flow is separated at the tip of the divider wall. As shown in Fig. 8, which shows magnified velocity vector diagrams around the divider-wall tip measured by PIV [30], the flow is separated at the upstream edge of the divider-wall tip and the reversal flow gets into this upstream edge. The separated flow reattaches on the divider wall; thus, a recirculation zone (separation bubble) with a relatively large-scale is formed along this wall. Such a large-scale separation bubble is also found in the results reported by Liou et al. [13,14]. The height (a scale in the $Y$ direction) of the separation bubble for $C^*=1.0$ is about one-half of the second-pass width, and is consistent with the observation by Liou et al. [13] for the similar channel configuration. As the turn clearance is decreased, the height of the separation bubble becomes larger and the reattachment point on the divider wall moves downstream. Moreover, the velocity of the reverse flow inside the separation bubble increases with the decrease of $C^*$.

In order to examine the scale of the separation bubble after the turn quantitatively, the stream function $\psi$ has been defined by Eq. (1) following the proposal of Hsieh et al. [31], and its contour maps are shown in Fig. 8.

$$\psi = \frac{1}{U_b}\int_0^{Y^*} U\, dY^* \tag{1}$$

It should be noted that $\psi$ defined here is not a stream function in the strict sense because of the three-dimensional nature of the present flow field. In this paper, however, we term $\psi$ as stream function for convenience and examine the influence of $C$ on the separation bubble based on $\psi$. Figure 9 shows the distributions of $\psi$ after the turn. The outer edge of the separation bubble is defined as the line of $\psi=0$, and the reattachment point of the separated flow as the intersection of this line and the divider wall. The $Y$ coordinate of the maximum height of the separation bubble is $Y^*=0.42$, 0.55, and 0.66, and the reattachment point is located at $X^*=-1.9$, $-2.4$, and $-3.6$ for $C^*=1.4$, 1.0, and 0.6, respectively. Here, it should be noted that, as described later, the separation bubble has a three-dimensional shape and thus the reattachment lengths in the plane of $Z^*=0$ are not necessarily the maximum ones. From the results shown in Figs. 6 and 9 however, it would be reasonable to consider that the separation bubble becomes larger in scale as the turn clearance is decreased. Such a growth of the separation bubble with the decrease of $C$ is ascribable to an increasing inertia force in passing through the narrower turn clearance, which prevents the separated flow from reattaching on the divider wall within a short distance. As shown later, the reattachment point defined here is well correlated with the local maximum of Sh on the divider wall for all $C$.

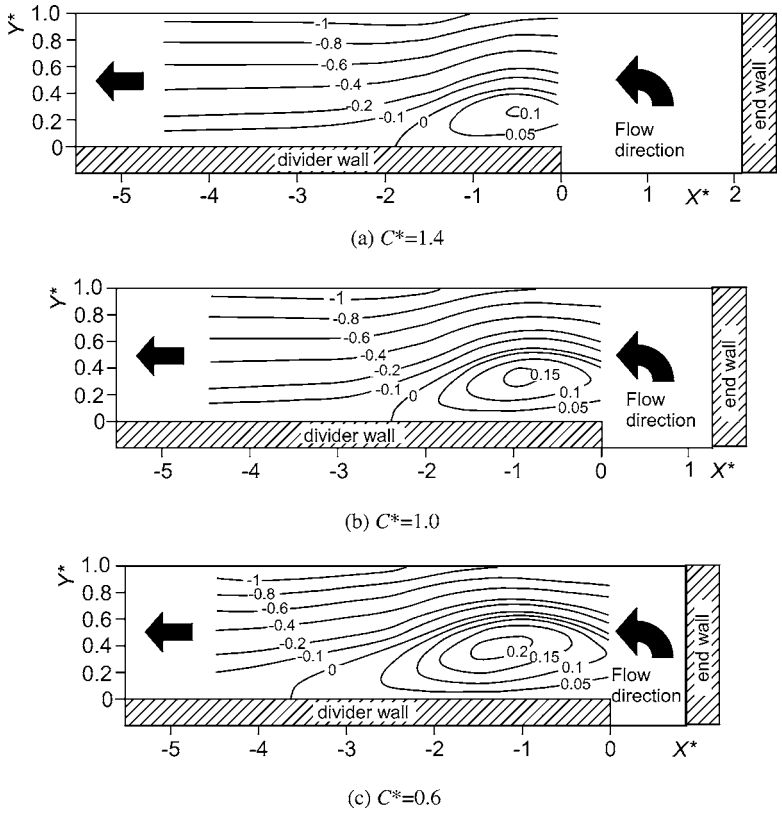


**Fig. 9 Contour map of $\psi(Z^*=0)$; (a) $C^*=1.4$; (b) $C^*=1.0$; (c) $C^*=0.6$**

*3.1.2 Flow Characteristics After the Turn.* Next, in order to examine the influence of the turn clearance on flow characteristics after the turn more closely, the distributions of mean velocities $U$ and $V$, and of turbulent kinetic energy $k/U_b^2$ with different $C^*$ are compared in Fig. 10. In this figure, the distributions at $X^*=0$, $-1$, $-2$, $-3$, and $-4.5$ ($U$ and $V$ only) are presented; these locations cover the whole streamwise length of the separation bubble for all $C^*$.

As observed in Fig. 10(*a*), which compares the primary flow velocity $U/U_b$, the distributions of $U/U_b$ with different $C^*$ agree with one another at the front edge of the divider wall. In the region of $X^* \leqslant -1$, the distributions of $U/U_b$ for $C^*=1.4$ almost agree with those for $C^*=1.0$ except for the inside of the separation bubble ($0<Y^*<0.5$). As for $C^*=0.6$, however, both the acceleration of $U$ near the outer wall and the reverse flow inside the recirculation zone are much intensified. As a result, $\partial U/\partial Y$ retains quite large values throughout the test section. This is caused by the growth of the separation bubble and resulting decrease of the substantial cross-sectional area of the flow passage, which causes intense flow acceleration in the outer-wall side.

In the distributions of the spanwise mean velocity $V/U_b$ shown in Fig. 10(*b*), the influence of $C^*$ is observed at $X^*=0$ and $-1$, which are relatively near the turn section, at which the flow directing outwards ($V>0$) appears in $Y^*>0.4$ and shows larger values in the channel of $C^*=0.6$. This corresponds to the acceleration of the flow in passing through the narrower turn clearance. In the downstream region of $X^* \leqslant -2$, the values of $V/U_b$ and the influence of $C^*$ on them are quite small.

The turbulent kinetic energy $k/U_b^2$ presented in Fig. 10(*c*) shows sharp peaks along the shear layer around the separation bubble at $X^*=0$ and $-1$. As the flow proceeds downstream, these peaks lower and the region of relatively large $k$ is diffused in the $Y$ direction. Such a tendency of $k$ distribution is qualitatively similar to that observed in turbulent flow behind a backward-facing step [32]. Similar to the case of $U/U_b$, the distributions of $k$ in the channel of $C^*=1.4$ and 1.0 agree quantitatively with each other except for the inside of the recirculation zone, whereas the values for $C^*=0.6$ are generally larger. This tendency is observed more clearly in the region of $X^* \leqslant -2$. These large values of $k$ for $C^*=0.6$ can be attributed to such a large velocity gradient $\partial U/\partial Y$ as described above, and it is originally caused by the larger separation bubble formed along the divider wall.

**3.2 Flow Characteristics in Cross Sections Normal to the Streamwise Axis.** In this section, the distributions of the primary flow velocity, secondary flow vectors, turbulent kinetic energy, and fluctuating velocity intensities obtained in the cross sections located inside and after the turn are presented.

*3.2.1 Primary and Secondary Flow Velocities.* Figures 11(*a*)–11(*c*) show the secondary flow vectors (upper half) and the primary flow velocity contour maps (lower half) for $C^*=1.4$, 1.0, and 0.6, respectively. In the contour maps of the primary flow velocity, the numerical values denote $V/U_b$ in section 1 (midplane of the turn section, $Y^{**}=0$), and $-U/U_b$ in sections 2–5 (straight section after the turn). Therefore, in all the contour maps shown here, the negative values correspond to the reverse flow, and the flow reversal regions are shown in gray. The left periphery and the right periphery of the figures correspond to the divider wall and the outer wall (end wall in section 1) of the channel, respectively. In order to compare the secondary flow velocities with different $C^*$ after the turn ($X^*=0$, $-1$, and $-2$) quantitatively, the magnitude of the secondary flow velocity $(V^2+W^2)^{0.5}/U_b$ in the planes of $Z^*=0$ and $Z^*=0.65$ are presented in Figs. 12(*a*) and 12(*b*), respectively.

At first, the results in the channel of $C^*=1.0$ with a standard turn clearance (Fig. 11(*b*)) are examined in detail. In section 1, the midplane of the turn section, there appear strong secondary currents ($U/U_b=1.1$) that are directing outwards (toward the end

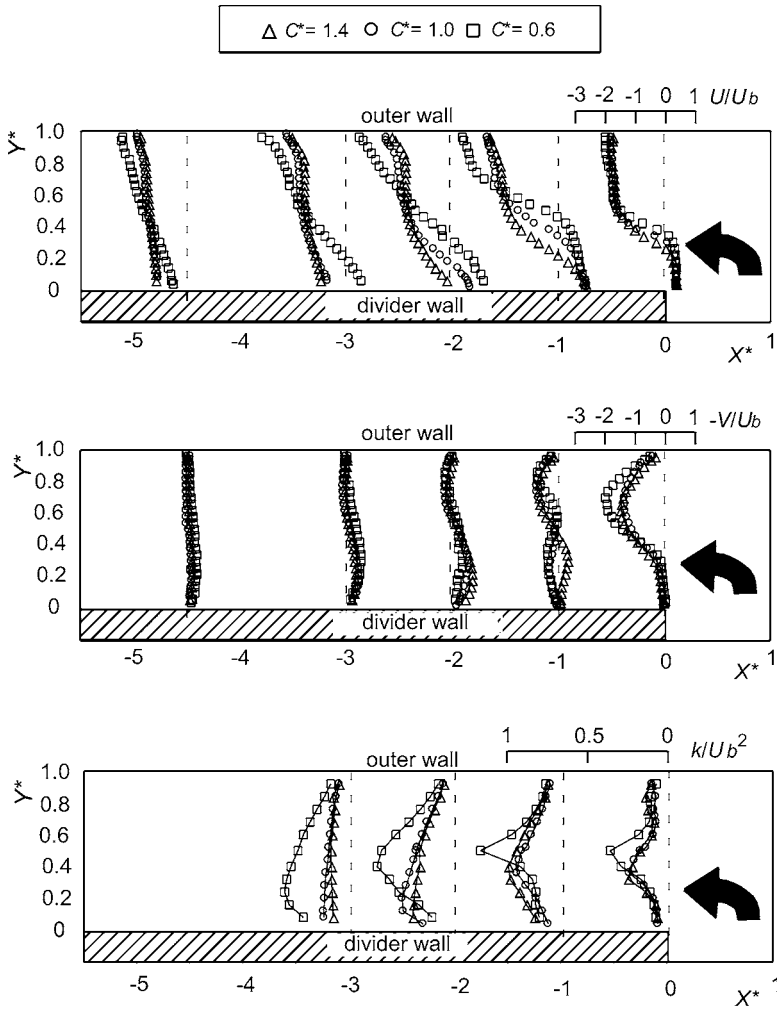


**Fig. 10 Flow characteristics after the turn ($Z^*=0$). (*a*) Primary flow velocity $U/U_b$; (*b*) secondary flow velocity $V/U_b$; (*c*) turbulent kinetic energy $k/U_b^2$.**

wall) along the $X$ axis. The maximum primary flow velocity $V/U_b$ is attained at $X^*=0.3$, the location deviated to the divider-wall side from the center of the cross section. Since the region near the divider wall ($X^*<0.2$) is occupied by the separated reverse flow, the velocity gradient $\partial V/\partial X$ in the separation shear layer is considerably large and it contributes to produce strong turbulence as described later.

At the turn exit (section 2) the flow reversal region near the divider wall further expands. The outer edge of this flow reversal region, i.e., the contour of $U/U_b=0$, is distorted toward the outer wall; thus, the separation bubble has a convex shape in this cross section. On the other hand, near the outer wall the secondary flow produces a clear longitudinal vortex that is rotating in the counterclockwise direction in this figure. This secondary flow transports the high momentum fluid near the outer wall to the vicinity of the long-side wall. Consequently, $-U/U_b$ near the long-side wall becomes larger than that near the $Y$ axis, and the maximum value of $-U/U_b$(=1.83) is attained at $Y^*=0.6$ and $Z^*=-0.64$. These characteristics of the primary and the secondary flow distributions are qualitatively similar to those reported by Liou et al. [13,14].

In section 3 ($X^*=-1$), as observed in Fig. 9 as well, the separation bubble occupies larger part of the cross section than that in section 2 and the reverse flow velocity in it is further increased. Due to the decrease of the substantial cross-sectional area, the primary flow in the outer-wall side is more accelerated and the maximum $-U$ is twice as large as $U_b$. On the other hand, the secondary flow velocity is generally smaller than that in section 2, and the longitudinal vortex is not observed so clearly; this means that the effect of the centrifugal force is diminishing in this cross section. After section 3, the secondary currents directing outwards along the $Y$ axis become weaker, while the flow proceeding toward the divider wall is enhanced by the reattachment of the separated flow. In particular, the increase of $V$ is remarkable near the long-side wall in section 4. These tendencies of the secondary flow distributions within a few $d_h$ after the turn are qualitatively similar to those reported by Son et al. [16]. In response to such a change of the secondary flow distributions, the shape of the reverse flow region is also changed in the streamwise direction; in sections 2 and 3 it has a convex shape bulging to the outer-wall side, but in section 4 it is curved in the opposite direction. These features of the reverse flow region suggest that the separation bubble formed after the turn has a three-dimensional shape, and thus the reattachment lengths in the plane of $Z^*=0$ are not necessarily the maximum ones. In this study, however, the detailed spanwise variation of the reattachment lengths is not clarified due to the limitation of the point-by-point measurement with LDV.

In section 5, both the reverse flow region near the divider wall and the longitudinal vortex in the outer-wall side disappear. As for the primary flow, the tendency that the high velocity region is deflected to the outer-wall side is still observed. However, the feature that $-U$ near the long-side wall is larger than that near the $Y$ axis is not observed; this is correlated with the disappearance of the longitudinal vortex in this cross section.

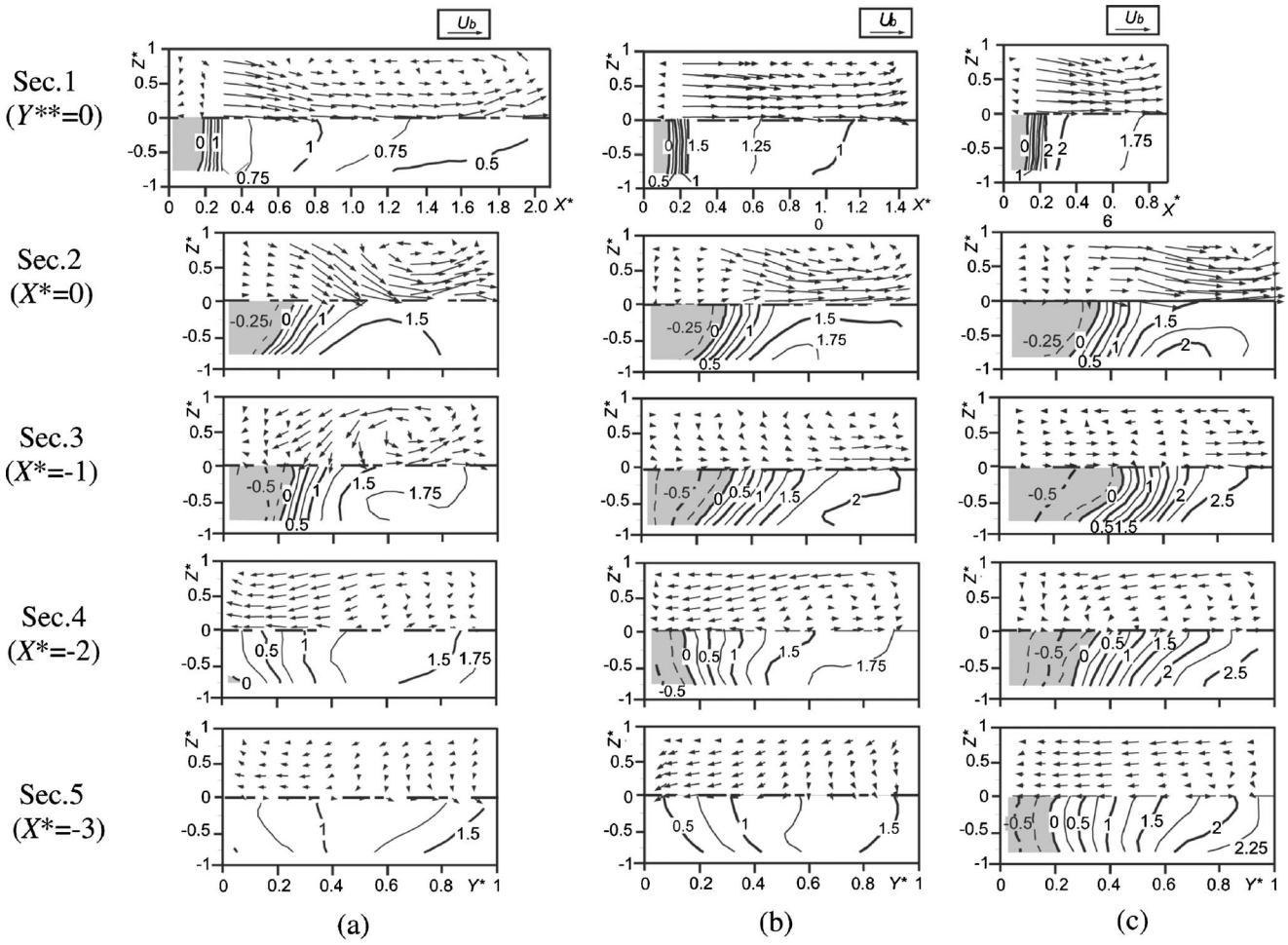


**Fig. 11 Secondary flow vectors (upper half) and primary flow velocity $U/U_b$ ($V/U_b$ in section 1) (lower half). (*a*) $C^*=1.4$; (*b*) $C^*=1.0$; (*c*) $C^*=0.6$.**

In the channel with a larger turn clearance of $C^*=1.4$, the characteristics of the primary and secondary flow velocity distributions are qualitatively similar to those for $C^*=1.0$ described above. In section 3, however, the longitudinal vortex is observed quite clearly in comparison with the channel of $C^*=1.0$. This is explained as follows. In the channel of $C^*=1.4$, the streamwise length of the separation bubble is smaller than that of $C^*=1.0$ (reattachment points in the $Z^*=0$ plane are at $X^*=-1.9$ for $C^*=1.4$ and $X^*=-2.4$ for $C^*=1.0$). Thus, in section 3 located at $X^*=-1$, the region near the divider wall of $C^*=1.4$ is dominated by the reattaching flow. As a result, the centrifugal-force-induced secondary flow proceeding outwards along the $Y$ axis and the flow returning inwards along the long-side wall that is intensified by the flow reattachment can coexist. This causes such a clear longitudinal vortex in section 3: as shown in Fig. 12(*b*), the secondary flow velocity near the upper wall attains about $0.6U_b$ and it is the largest among three turn clearances. In sections 4 and 5, which are located downstream of the separation bubble, similar to the case of $C^*=1.0$, the secondary flow directing outwards becomes very weak, as low as about $0.2U_b$, and thus the longitudinal vortex disappears.

In the channel of $C^*=0.6$, the secondary flow directing outwards in sections 1 and 2 is much intensified due to the acceleration of flow in passing through the narrow turn clearance. As shown in Fig. 12(*a*), the maximum cross-stream velocity in section 2 ($X^*=0$) is as high as $1.6U_b$ near the outer wall. It is noted that such high secondary flow velocity is maintained to the vicinity of the upper wall as observed in Fig. 12(*b*).

The reverse flow region near the divider wall occupies large part of the cross-sectional area, and it exists to the end of the present test section. Accordingly, the deflection of the high primary flow velocity region to the outer-wall side is enhanced compared to the other channels. As a whole, however, the mean velocity distributions for $C^*=0.6$ are qualitatively similar to those for larger turn clearances.

*3.2.2 Turbulence Intensities and Turbulent Kinetic Energy*. In Fig. 13, the contour maps of the turbulent kinetic energy $k/U_b^2$ and the streamwise velocity fluctuation $u'/U_b$ ($v'/U_b$ in section 1) are shown in the upper and the lower halves of the figures, respectively. As an overall trend, the distribution of $k$ is qualitatively similar to that of $u'$ (or $v'$), because the streamwise velocity fluctuation is the largest among three fluctuating velocity components. In section 1, the midplane of the turn section, $v'$ attains the local maximums in the vicinity of the long-side wall as well as in the separation shear layer near the divider wall. Considering the production of $\overline{v^2}$ expressed by the following equation:

$$\text{Production of } \overline{v^2} = -2\left(\overline{uv}\frac{\partial V}{\partial X} + \overline{v^2}\frac{\partial V}{\partial Y} + \overline{vw}\frac{\partial V}{\partial Z}\right) \qquad (2)$$

it follows that large $v'$ near the long-side wall is brought about by the increase of $\partial V/\partial Z$, and the $v'$ near the divider wall is caused by large $\partial V/\partial X$ that is inherent in the separation shear layer. Since $\partial V/\partial X$ in the shear layer becomes larger as $C^*$ is decreased, $v'$ there shows largest values in $C^*=0.6$. On the other hand, the increase of $\partial V/\partial Z$ near the long-side wall and the resulting in-

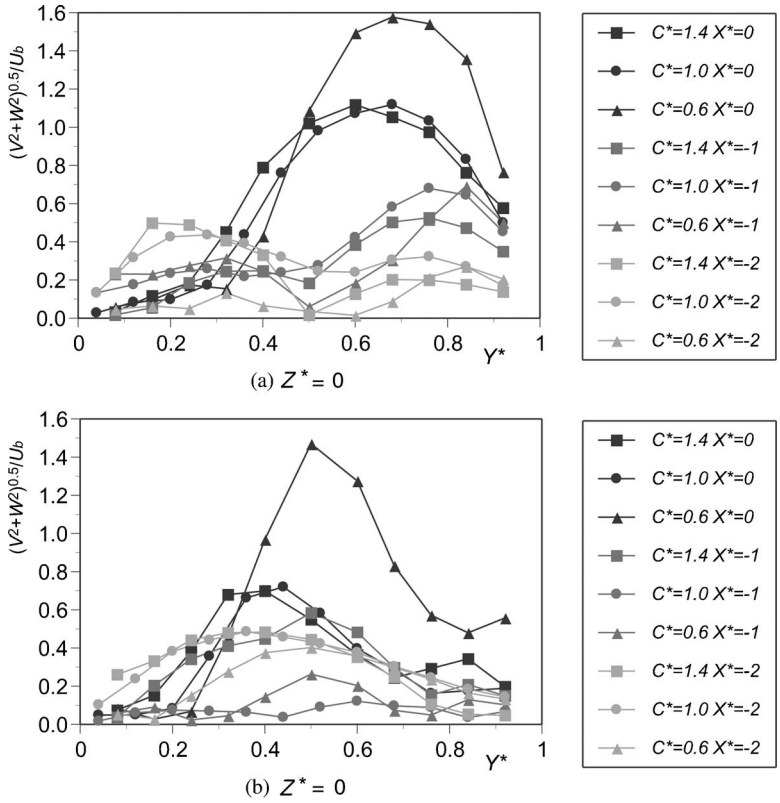


**Fig. 12 Magnitude of secondary flow velocity at various $X^*$ position of second flow pass**

crease of $v'$ are most pronounced in the channel of $C^*=1.4$.

In sections 2 and 3, similar to section 1, $k$ and $u'$ show considerably large values in the separation shear layer near the divider wall. In all $C^*$, the maximums of $k$ and $u'$ in this shear layer lie not on the $Y$ axis but at a location deviated toward the long-side wall. Such a tendency is observed in the results of Son et al. [16] as well. This is because both $-\partial U/\partial Y$ and $-\partial U/\partial Z$ become large at that location and the production of $\overline{u^2}$, expressed by the following equation, is most promoted there:

$$\text{Production of } \overline{u^2} = -2\left(\overline{u^2}\frac{\partial U}{\partial X} + \overline{uv}\frac{\partial U}{\partial Y} + \overline{uw}\frac{\partial U}{\partial Z}\right) \tag{3}$$

In section 4 ($X^*=-2$), located in the downstream part of the separation bubble for all $C^*$, the substantial flow passage is increased in comparison with the upstream cross sections, as recognized from Figs. 9 and 11. As a result, the primary flow in the outer-wall side is decelerated slightly. Since this streamwise decrease of $U$ makes a positive contribution to $\overline{u^2}$ production, the values of $u'/U_b$ in the outer-wall side in section 4 become somewhat larger than that in section 3.

In section 5, $k$ and $u'$ near the divider wall show smaller values than those in section 4 for $C^*=1.0$ and 1.4, because this cross section is behind the reattachment point. In the case of $C^*=0.6$, the reattachment point is at $X^*=-3.6$, and thus this cross section ($X^*=-3$) cuts across the separation bubble as observed in Fig. 11. Therefore, $k$ and $u'$ are as large as those in the other cross sections located upstream.

Next, the distributions of the spanwise (parallel to the long-side wall) velocity fluctuation $v'/U_b$ ($u'/U_b$ in section 1) are shown in the upper halves of Fig. 14. In sections 1 and 2, the maximum value of this velocity fluctuation appears not in the separation shear layer but in the vicinity of the long-side wall; this tendency is significantly different from the streamwise velocity fluctuation described above. Such large $v'$ near the long-side wall is caused by the additive effects of the large velocity gradient $\partial V/\partial Z$ that is ascribed to the formation of the longitudinal vortex, and of large $\partial V/\partial Y$ caused by the impingement between the secondary currents directing inward along the long-side wall and those flowing in the opposite direction. As found in Fig. 12, $\partial V/\partial Y$ in these cross sections becomes larger as $C^*$ is increased. Accordingly, the increase of $v'$ near the long-side wall appears more sharply in the channel with larger $C^*$. In spite of such an increase of $v'$, it is again found from a comparison of $k$ and three normal components of the Reynolds stresses that the high $u'$ is responsible for the large turbulence kinetic energy in the region near the long-side wall.

After section 3, such high $v'$ region near the long-side wall diminishes gradually with the change of the secondary flow distribution, and $v'$ attains the maximum in the separation shear layer like $u'$. Since $v$ in this region mainly arises through the redistribution from $u$, the distribution of $v'/U_b$ is qualitatively similar to that of $u'/U_b$, and shows somewhat smaller values than $u'/U_b$ for all $C^*$.

The contour maps of $w'/U_b$ are presented in the lower halves of Fig. 14, where $w$ is parallel to the outer and divider walls. As a whole, the distribution of $w'$ is qualitatively similar to that of $u'$ shown in Fig. 13. In sections 1 and 2 with large $C^*$, however, $w'/U_b$ near the outer wall becomes as large as that in the separation shear layer. It is thought that this increase of $w'$ in the outer-wall side is caused by the impingement of the secondary flow on this wall. This flow impingement originally produces the wall-normal fluctuating component $v$ (or $u$ in section 1) and then $w$ is increased by the blocking effect of the wall [33]. After section 2, similar to $u'/U_b$, $w'/U_b$ shows the maximum in the separation shear layer and it gradually diminishes in the streamwise direction in all the channels. In section 4 for $C^*=1.0$ and 1.4, which is located behind the reattachment point, three normal components of Reynolds stresses are quantitatively in the same level and thus

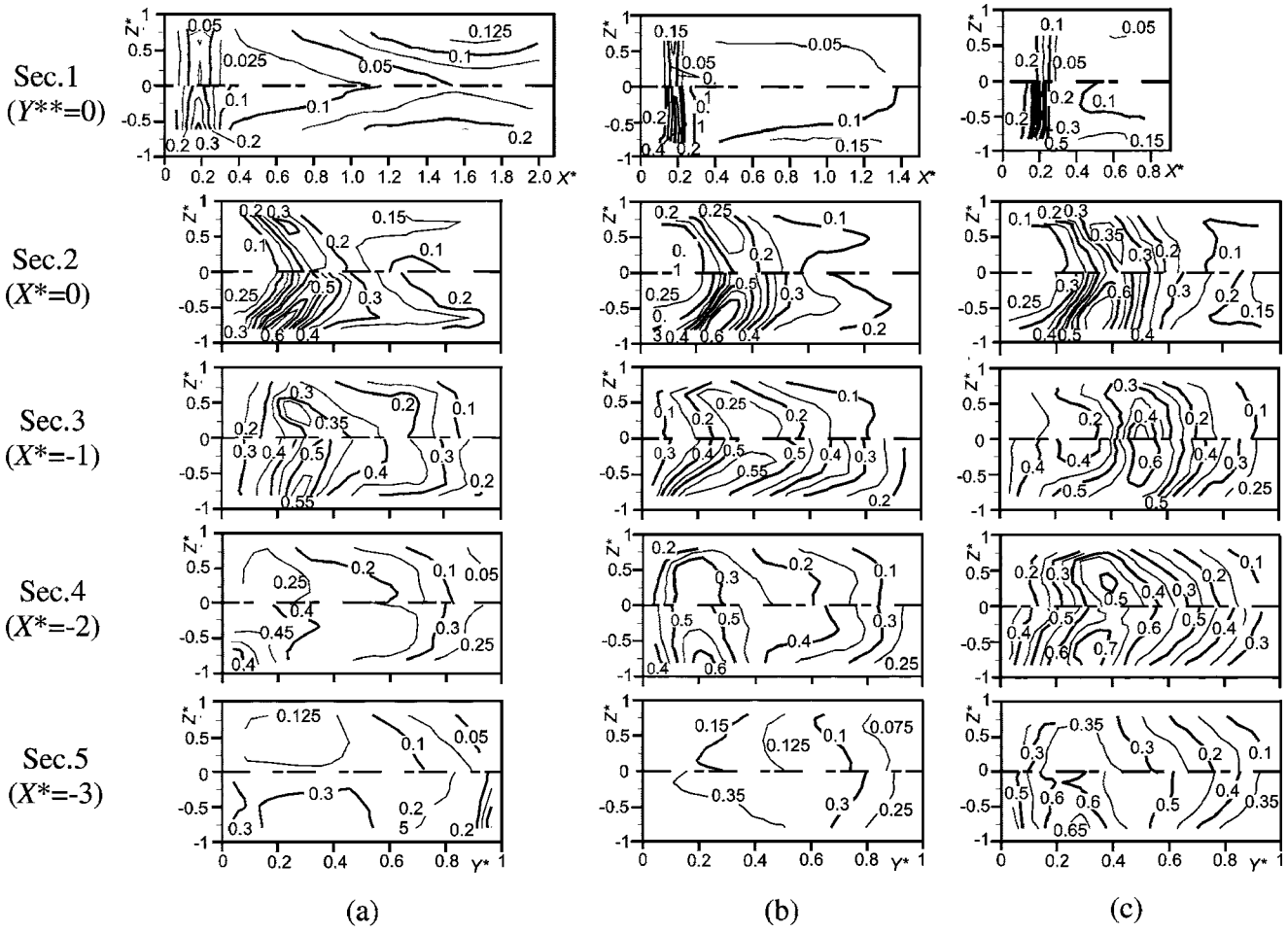


**Fig. 13 Contour maps of turbulent kinetic energy $k/U_b^2$ (upper half) and streamwise velocity fluctuation $u'/U_b$ ($v'/U_b$ in section 1) (lower half). (*a*) $C^*=1.4$; (*b*) $C^*=1.0$; (*c*) $C^*=0.6$.**

they equally contribute to $k$. From a comparison of the secondary flow vectors shown in Fig. 12 and $w'$ distributions, it is found that the maximum value of $w'/U_b$ appears on the $Y$ axis, albeit $W$ is very small on it. This suggests that a large-scale unsteady motion in the $Z$ direction is dominant in this region.

**3.3 Relation Between Local Heat Transfer and Near-Wall Flow Parameters.** From the past research on heat (mass) transfer and pressure loss in the two-pass channels with the same geometry as the present study [21], it was found that the highest heat transfer enhancement is provided at $C^*=0.6$, and the smallest friction loss is given at $C^*=1.4$. However, the detailed mechanism of heat transfer in this complex flow was not well understood in the past study. Hence, in this study, the heat (mass) transfer mechanism is examined after Liou et al. [15,34] by comparing closely the local Sherwood number (Sh) distribution on a channel wall measured in the earlier experiment [21] with the velocity distributions near the corresponding wall. We take the end wall, the divider wall, and the outer wall after the turn as an object of this study, over which Sh changes steeply in the streamwise direction.

*3.3.1 End Wall*. In Fig. 15, the distributions of normalized local Sherwood number $\mathrm{Sh}/\mathrm{Sh}_0$ on the spanwise centerline of the end wall, the streamwise (wall-parallel) mean velocity $V/U_b$ and fluctuating velocity $v'/U_b$, and the wall-normal mean and fluctuating velocities $U/U_b$ and $u'/U_b$ measured in a plane 3 mm apart from the end wall are presented, taking $C^*$ as a parameter.

In $-1<Y^{**}<-0.5$ near the first corner, Sh shows larger values as $C^*$ is decreased, and its local maximum moves downstream with the increase of $C^*$. After this local maximum, Sh shows almost the same values irrespective of $C^*$ up to $Y^{**}=0.2$. Such Sh characteristics in this region are most correlated with $u'/U_b$ distribution shown in Fig. 15(*e*), suggesting that the heat transfer in the upstream half of the end wall is dominated by the fluctuating velocity component normal to the wall. This velocity perturbs the thermal boundary layer and even impinges upon the end wall, and thus heat transfer is enhanced on it.

In the downstream region of $Y^{**}>0.2$, Sh distribution shows remarkably different characteristics depending on $C^*$. In the channels of $C^*=0.6$ and 1.0, Sh shows two local maximums in $Y^{**}=0.5-0.7$ and $Y^{**}=0.95$; Sh values for $C^*=0.6$ are much larger than those for $C^*=1.0$. On the other hand, in $C^*=1.4$, there exists only one local maximum at $Y^{**}=0.95$. A comparison of these Sh distributions and the velocity distributions reveals that the local maximum Sh at $Y^{**}=0.95$ corresponds well to the steep increase of the wall-normal velocity component $U/U_b$ and $u'/U_b$. Therefore, similar to the first corner, the high Sh near the second corner is also caused by the flow impinging upon the end wall. From Fig. 6, it is found that this velocity is yielded by the reversal of the flow that impinges on the outer wall. As for the local maximum Sh observed in $Y^{**}=0.5-0.7$ for $C^*=0.6$ and 1.0, the wall-normal velocities are not so large; meanwhile, the wall-parallel velocity component $V/U_b$ shows considerable magnitude. This suggests that the large Sh in this region is ascribed to the acceleration of the flow proceeding along the end wall, but the correlation between Sh and velocity distributions is not so clear as the local maximums near both corners.

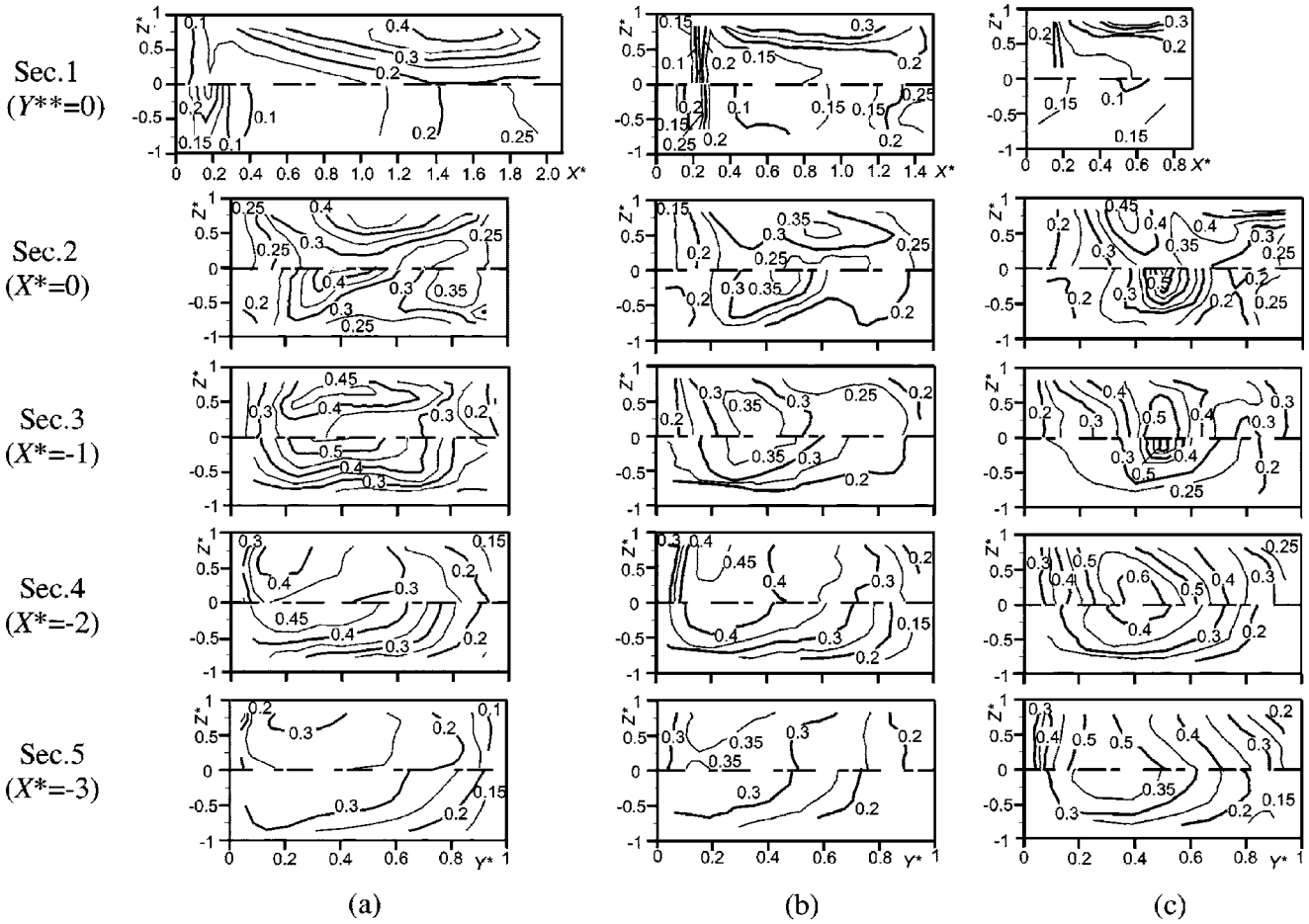


**Fig. 14 Contour maps of spanwise velocity fluctuation $v'/U_b$ ($u'/U_b$ in section 1) (upper half) and transverse velocity fluctuation $w'/U_b$ (lower half). (*a*) $C^*=1.4$; (*b*) $C^*=1.0$; (*c*) $C^*=0.6$.**

*3.3.2 Divider Wall After Turn*. Figure 16 shows the Sh and velocity distributions along the spanwise centerline of the divider wall after the turn. In this figure, the positive value of $U$ corresponds to the reverse flow, while negative $V$ presents the wall-normal velocity impinging upon the divider wall.

Sh on this wall attains the maximum at $X^*=-1.8$, $-2.5$, and $-3.4$ for $C^*=1.4$, 1.0, and 0.6, respectively, and it shows higher value as $C^*$ is increased. These locations of the maximum Sh almost agree with the flow reattachment points as previously noted. From a comparison of the Sh distributions and the flow characteristics, it is again ascertained that the local heat transfer on the divider wall is generally dominated by the wall-normal velocity components $V$ and $v$, which are caused by the flow reattachment on this wall. $V$ becomes larger as the turn clearance is increased, and this brings about the higher heat transfer rate for larger $C^*$.

*3.3.3 Outer Wall After Turn*. The results on the outer wall after the turn are shown in Fig. 17, in which the end wall is located at $X^*=0.9$, 1.5, and 2.1 for $C^*=0.6$, 1.0, and 1.4, respectively. In all the channels, Sh shows the first local maximum near the end wall and the second one at $X^*=-2--3$. The Sh distributions for $C^*=1.0$ and 1.4 agree quantitatively with each other, whereas the local maxima of Sh for $C^*=0.6$ attain considerably larger values.

The Sh distributions near the end wall are qualitatively similar to those of the wall-normal velocity $V/U_b$ shown in Fig. 17(*d*). This clearly shows that the first local maximum Sh is caused by the impingement of the flow that passes through the turn clearance. Since the flow passing through the narrower turn clearance is accelerated more steeply, $V$ and resulting Sh for $C^*=0.6$ become much larger than those for larger $C^*$.

On the other hand, around the second local maximum of Sh at $X^*=-2--3$, $V/U_b$ is rather small for all $C^*$ and it does not contribute much to heat transfer. It is found that in this region the distributions of $U/U_b$ and Sh are correlated, suggesting that the second local maximum Sh is attributed to the relatively high primary flow velocity near the outer wall. As previously described, this deflection of high velocity flow toward the outer wall originates from the large separation bubble formed along the divider wall. Since the separation bubble for smaller $C^*$ occupies a larger part of the channel cross section, as observed in Figs. 9 and 11, the acceleration of $U$ and resulting increase of Sh on the outer wall after the separation bubble are most pronounced in the channel of $C^*=0.6$.

In this paper, as described so far, we have discussed the relation between the velocity distributions near the wall and the local Sherwood number distributions on three representative walls in and after the turn. The overall conclusion of this aero-thermal comparison is that both the wall-normal and wall-parallel velocity components are important parameters, and that the dominant velocity component changes depending on the wall. Considering that there exists a close correlation between the Reynolds stress $\overline{uv}$ and the heat/mass transfer from the walls in a simple turbulence such as 2D channel flow, it is possible that $\overline{uv}$ has a considerable effect on the local heat/mass transfer in the present channel with a complex flow structure. As noted before, however, the correlation between two velocity components was not measured in this experiment. The measurement of this flow parameter is the problem that will confront us in a future study.

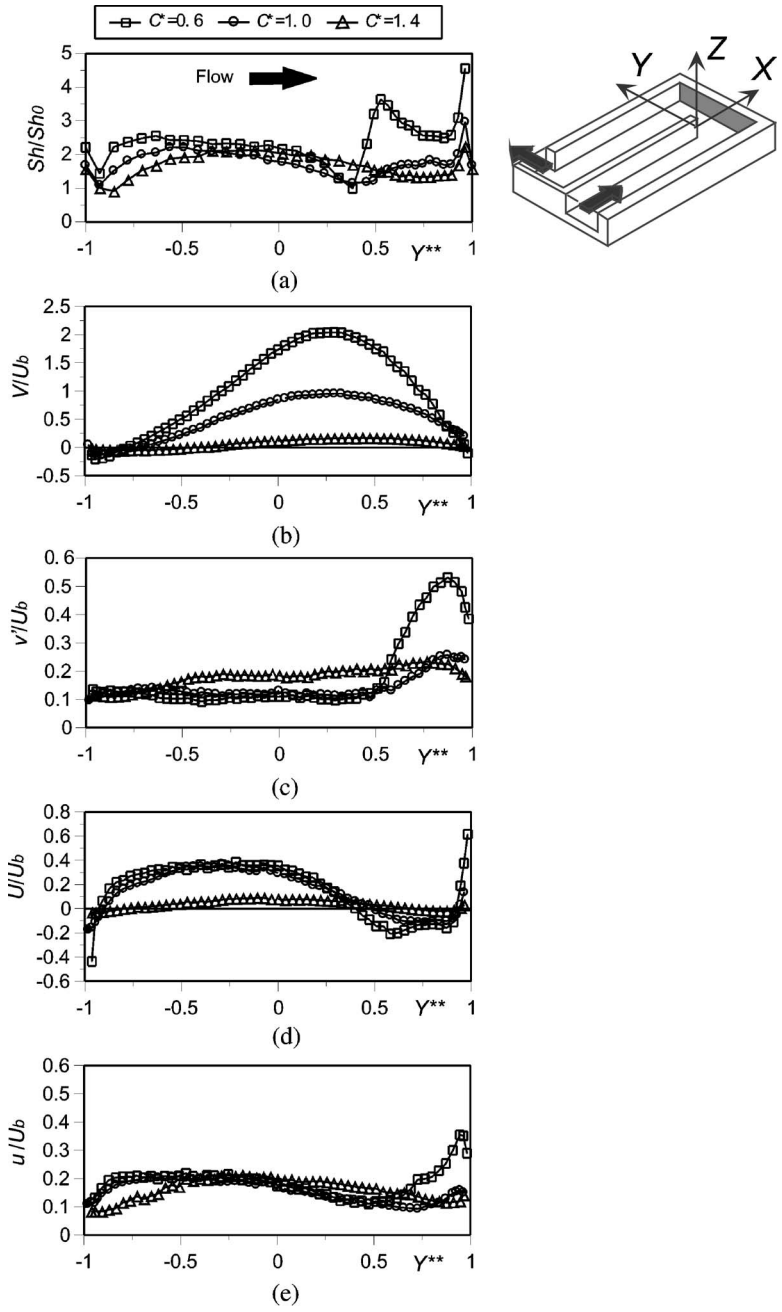


**Fig. 15 Distributions of Sh and near-wall flow parameters on the end wall ($Z^*=0$). (*a*) $Sh/Sh_0$; (*b*) streamwise mean velocity $V/U_b$; (*c*) streamwise velocity fluctuation $v'/U_b$; (*d*) wall-normal mean velocity $U/U_b$; (*e*) wall-normal velocity fluctuation $u'/U_b$.**

## 4 Conclusions

LDV measurements have been carried out in order to make clear the influence of the turn clearance on turbulent flow characteristics in stationary two-pass rectangular channels with a sharp 180-deg turn. Based on the data obtained, the flow parameter that dominates the heat transfer in and after the turn has been examined. Primary conclusions drawn from the present results are as follows.

(1) In all the test channels, there appear flow recirculation zones in the first (upstream) corner in the turn section as well as along the divider wall after the turn. The recirculation zone in the first corner enlarges as $C^*$ is increased, while the separation bubble after the turn shrinks with the increase of $C^*$. This separation bubble has a three-dimensional shape for all $C^*$, which bulges outwards in the upstream part and is curved inward in the downstream part.
(2) In the midplane of the turn section the secondary flow dominates, which proceeds from the center toward the outer wall along the symmetric plane of the channel. This secondary flow becomes stronger as $C^*$ is decreased. In the cross section at the turn exit, a clear longitudinal vortex is formed near the outer wall. In further downstream region, the secondary currents directing outwards diminish and those directing inwards along the long-side wall become more predominant for all $C^*$.
(3) After the turn section, the streamwise velocity fluctuation $u'$ and the transverse velocity fluctuation $w'$ attain the

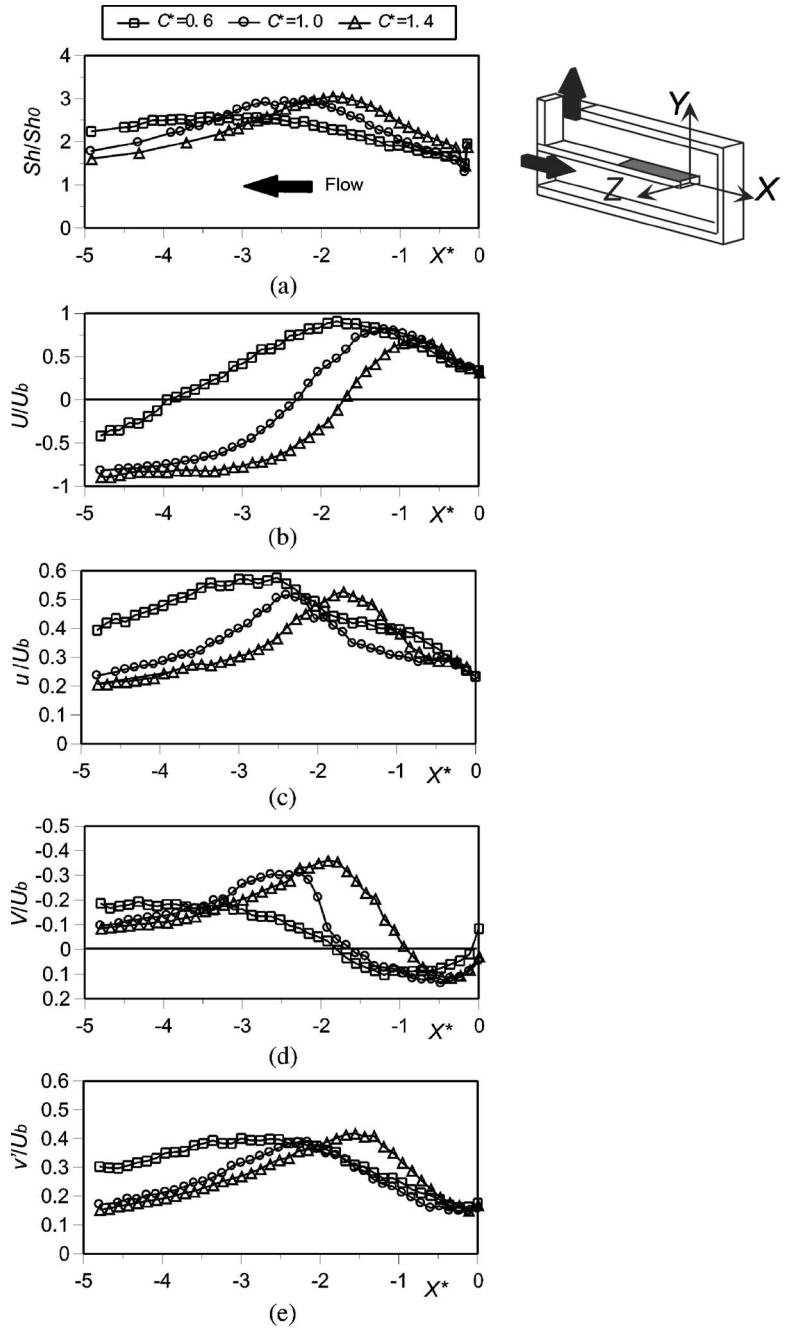


**Fig. 16 Distributions of Sh and near-wall flow parameters on the divider wall after the turn ($Z^*=0$). (*a*) $Sh/Sh_0$; (*b*) streamwise mean velocity $U/U_b$; (*c*) streamwise velocity fluctuation $u'/U_b$; (*d*) wall-normal mean velocity $V/U_b$; (*e*) wall-normal velocity fluctuation $v'/U_b$.**

maximums in the shear layer around the separation bubble, and they show larger values as $C^*$ is decreased. The spanwise velocity fluctuation $v'$ shows the maximum not in the separation shear layer but in the vicinity of the long-side wall inside and just after the turn section. This high-$v'$ region appears more sharply in larger $C^*$. In further downstream region, $v'$ attains the maximum in the separation shear layer like $u'$ and $w'$.

(4) The local maxima of the local Sherwood number that appear on the short-side walls inside and after the turn are mainly caused by the velocity component that is normal to each wall, i.e., by the impingement of the flow on the walls. On the outer wall downstream of the separation bubble, however, the contribution of the wall-normal velocity to heat transfer is quite small, and the deflection of the primary flow with higher velocity to the outer-wall side brings about large heat transfer rates.

## Nomenclature

$A$ = spanwise width ($Y$-way length) of the channel cross section, 50 mm
$C$ = turn clearance of the channel, mm
$C^*$ = dimensionless turn clearance$=C/A$
$D$ = naphthalene-air molecular diffusion coefficient, $m^2/s$

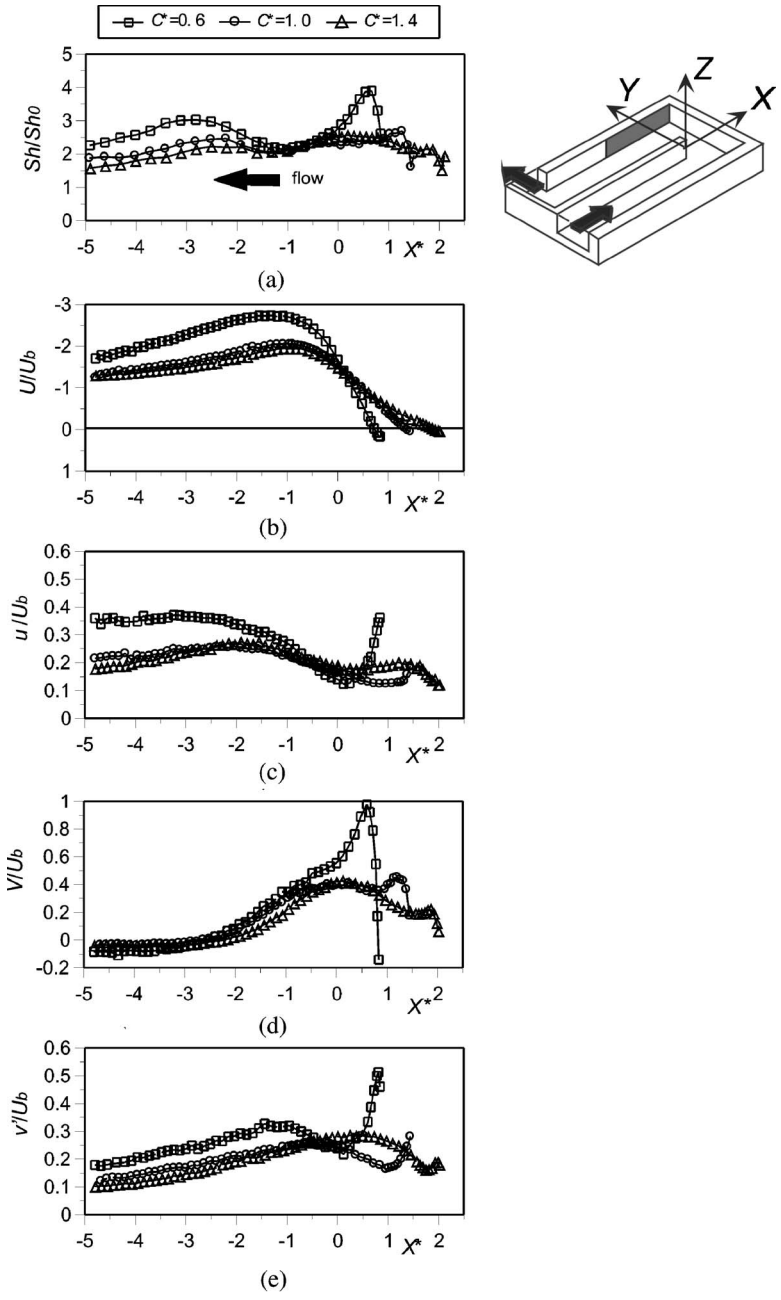


**Fig. 17 Distributions of Sh and near-wall flow parameters on the outer wall after the turn ($Z^*=0$). (*a*) $Sh/Sh_0$; (*b*) streamwise mean velocity $U/U_b$; (*c*) streamwise velocity fluctuation $u'/U_b$; (*d*) wall-normal mean velocity $V/U_b$; (*e*) wall-normal velocity fluctuation $v'/U_b$.**

$d_h$ = hydraulic diameter of the channel, 33.3 mm
$h_m$ = local mass transfer coefficient, m/s
$k$ = turbulent kinetic energy=$(\overline{u^2}+\overline{v^2}+\overline{w^2})/2$, $m^2/s^2$
Re = Reynolds number=$U_b d_h/v$
Sh = local Sherwood number=$h_m d_h/D$
$Sh_0$ = mean Sherwood number for fully developed turbulent flow in a straight pipe
$T$ = thickness of the divider wall, 10 mm
$U$, $V$, $W$ = mean velocity components in the $X$, $Y$, and $Z$ directions, m/s
$U_b$ = bulk velocity at the channel entrance, m/s
$u$, $v$, $w$ = fluctuating velocity components in the $X$, $Y$, and $Z$ directions, m/s
$u'$, $v'$, $w'$ = root mean square of $u$, $v$, and $w$ (for example, $u'=\sqrt{\overline{u^2}}$), m/s
$X$ = streamwise coordinate, m, Fig. 2
$X^*$ = normalized streamwise coordinate=$X/d_h$
$Y$ = spanwise coordinate, m, Fig. 2
$Y^*$, $Y^{**}$ = normalized spanwise coordinate; (i) straight section before the turn $Y^*=(Y+T/2)/A$; (ii) straight section after the turn $Y^*=(Y-T/2)/A$; (iii) inside the turn $Y^{**}=Y/(A+T/2)$
$Z$ = transverse coordinate, m, Fig. 2
$Z^*$ = normalized transverse coordinate=$Z/(A/4)$
$\psi$ = stream function=$\psi=1/U_b\int_0^{Y^*} U\,dY^*$
$v$ = kinematic viscosity of air, $m^2/s$

## References


[1] Iacovides, H., and Raisee, M., 1999, "Recent Progress in the Computation of Flow and Heat Transfer in Internal Cooling Passages of Turbine Blades," Int. J. Heat Fluid Flow, **20**, 320–328.

[2] Metzger, D. E., and Sahm, M. K., 1986, "Heat Transfer Around Sharp 180-deg Turns in Smooth Rectangular Channels," ASME J. Heat Transfer, **108**, pp. 500–506.

[3] Chyu, M. K., 1991, "Regional Heat Transfer in Two-Pass and Three-Pass Passages With 180-deg Sharp Turn," ASME J. Heat Transfer, **113**, pp. 63–70.

[4] Han, J. C., Chandra, P. R., and Lau, S. C., 1988, "Local Heat/Mass Transfer Distributions Around Sharp 180 deg Turns in Two-Pass Smooth and Rib-Roughened Channels," ASME J. Heat Transfer, **110**, pp. 91–98.

[5] Ekkad, S. V., and Han, J. C., 1995, "Local Heat Transfer Distributions Near a Sharp 180° Turn of a Two-Pass Smooth Square Channel Using a Transient Liquid Crystal Image Technique," J. Flow Visualization Image Process., **2**, pp. 285–297.

[6] Ekkad, S. V., and Han, J. C., 1997, "Detailed Heat Transfer Distributions in Two-Pass Square Channels With Rib Turbulators," Int. J. Heat Mass Transfer, **40**, pp. 2525–2537.

[7] Ekkad, S. V., Pamula, G., and Shantiniketanam, M., 2001, "Detailed Heat Transfer Measurements Inside Straight and Tapered Two-Pass Channels With Rib Turbulators," Exp. Therm. Fluid Sci., **22**, pp. 155–163.

[8] Wang, Z., Ireland, P. T., Kohler, S. T., and Chew, J., 1998, "Heat Transfer Measurements to a Gas Turbine Cooling Passage With Inclined Ribs," ASME J. Turbomach., **120** No. 1, pp. 63–69.

[9] Mochizuki, S., Murata, A., Shibata, R., and Yang, W.-J., 1998, "Detailed Measurements of Local Heat Transfer Coefficients in Turbulent Flow Through Smooth and Rib-Roughened Serpentine Passages With a 180° Sharp Bend," Int. J. Heat Mass Transfer, **42**, pp. 1925–1934.

[10] Astarita, T., and Cardone, G., 2000, "Thermodynamic Analysis of the Flow in a Sharp 180° Turn Channel," Exp. Therm. Fluid Sci., **20**, pp. 188–200.

[11] Schabacker, J., Boelcs, A., and Johnson, B. V., 1998, "PIV Investigation of the Flow Characteristics in an Internal Coolant Passage With Two Ducts Connected by a Sharp 180 Deg Bend," ASME Paper No. 98-GT-544.

[12] Schabacker, J., Boelcs, A., and Johnson, B. V., 1999, "PIV Investigation of the Flow Characteristics in an Internal Coolant Passage With 45 Deg Rib Arrangement," ASME Paper No. 99-GT-120.

[13] Liou, T.-M., and Chen, C.-C., 1999, "LDV Study of Developing Flows Through a Smooth Duct With a 180 Deg Straight-Corner Turn," ASME J. Turbomach., **121**, pp. 167–174.

[14] Liou, T.-M., Tzeng, Y.-Y., and Chen, C.-C., 1999, "Fluid Flow in a 180-deg Sharp Turning Duct With Different Divider Thickness," ASME J. Turbomach., **121**, pp. 569–576.

[15] Liou, T.-M., Chen, C.-C., Tzeng, Y.-Y., and Tsai, T.-W., 2000, "Non-Intrusive Measurements of Near-Wall Fluid Flow and Surface Heat Transfer in a Serpentine Passage," Int. J. Heat Mass Transfer, **43**, pp. 3233–3244.

[16] Son, S. Y., Kihm, K. D., and Han, J. C., 2002, "PIV Flow Measurements for Heat Transfer Characterization in Two-Pass Square Channels With Smooth and 90° Ribbed Walls," Int. J. Heat Mass Transfer, **45**, pp. 4809–4822.

[17] Besserman, D. L., and Tanrikut, S., 1992, "Comparison of Heat Transfer Measurements With Computations for Turbulent Flow Around a 180 Deg Bend," ASME J. Turbomach., **114**, pp. 865–871.

[18] Wang, T. S., and Chyu, M. K., 1994, "Heat Convection in a 180-Deg Turning Duct With Different Turn Configurations," Int. J. Heat Mass Transfer, **8**, pp. 595–601.

[19] Murata, A., and Mochizuki, S., 2004, "Large Eddy Simulation of Turbulent Heat Transfer in a Rotating Two-Pass Smooth Square Channel With Sharp 180° Turns," Int. J. Heat Mass Transfer, **47**, pp. 683–698.

[20] Hirota, M., Fujita, H., Tanaka, A., Araki, S., and Tanaka, T., 1997, "Local Heat (Mass) Transfer Characteristics in Rectangular Ducts With a Sharp 180-Degree Turn," Energy Convers. Manage., **38**, pp. 1155–1168.

[21] Hirota, M., Fujita, H., Syuhada, A., Araki, S., Yoshida, T., and Tanaka, T., 1999, "Heat/Mass Transfer Characteristics in Two-Pass Smooth Channels With a Sharp 180-Deg Turn," Int. J. Heat Mass Transfer, **42**, pp. 3757–3770.

[22] Syuhada, A., Hirota, M., Fujita, H., Araki, S., Yanagida, M., and Tanaka, T., 2001, "Heat (Mass) Transfer in Serpentine Flow Passage With Rectangular Cross-Section," Energy Convers. Manage., **42**, pp. 1867–1885.

[23] Hirota, M., Fujita, H., Cai, L., Nakayama, H., Yanagida, M., and Syafa'at, A., 2002, "Heat (Mass) Transfer in Rectangular Cross-Sectioned Two-Pass Channels With an Inclined Divider Wall," Int. J. Heat Mass Transfer, **45**, pp. 1093–1107.

[24] Hjelmfelt, A. T., and Mockros, L. F., 1966, "Motion of Discrete Particles in a Turbulent Fluid," Appl. Sci. Res., **16**, pp. 149–161.

[25] Visualization Society of Japan, 1986, *Handbook of Flow Visualization*, Asakura Pub., Tokyo, pp. 158–164 (in Japanese).

[26] JSME, 1987, Measurement Uncertainties (translated from ASME performance test codes, supplement on instruments and apparatus, Part 1), Maruzen, Tokyo (in Japanese).

[27] Burggraf, F., 1970, "Experimental Heat Transfer and Pressure Drop With Two-Dimensional Discrete Turbulence Promoters Applied to Two Opposite Walls of a Square Tube," *Augmentation of Convective Heat and Mass Transfer*, E. E. Bergles and R. L. Webb, eds., ASME, New York, pp. 70–79.

[28] Fujita, H., Hirota, M., Yokosawa, H., Hasegawa, M., and Gotoh, I., 1990, "Fully Developed Turbulent Flows Through Rectangular Ducts With One Roughened Wall," JSME Int. J., Ser. II, **33**, pp. 692–701.

[29] Taylor, A. M. K. P., Whitelaw, J. H., and Yianneskis, M., 1982, "Curved Ducts With Strong Secondary Motion: Velocity Measurements of Developing Laminar and Turbulent Flow," ASME J. Fluids Eng., **104**, pp. 350–359.

[30] Nakayama, H., Hirota, M., Ono, Y., and Fujita, H., 2003, "Aerodynamic Analysis of the Sharp Turn Channel Flow Using PIV," *Proceedings of Turbulence, Heat and Mass Transfer*, **4**, pp. 293–300.

[31] Hsieh, S.-S., Chen, P.-J., and Chin, H.-J., 1999, "Turbulent Flow in a Rotating Two-Pass Smooth Channel," ASME J. Fluids Eng., **121**, pp. 725–734.

[32] Kostas, J., Soria, J., and Chong, M. S., 2002, "Particle Image Velocimetry Measurements of a Backward-Facing Step Flow," Exp. Fluids, **33**, pp. 838–853.

[33] Nishino, K., Samada, M., Kasuya, K., and Torii, K., 1996, "Turbulence Statistics in the Stagnation Region of an Axisymmetric Impinging Jet Flow," Int. J. Heat Fluid Flow, **17**, pp. 193–201.

[34] Liou, T.-M., Chen, C.-C., and Chen, M.-Y., 2003, "Rotating Effect on Fluid Flow in Two Smooth Ducts Connected by a 180-Degree Bend," ASME J. Turbomach., **125**, pp. 138–148.

# Analysis and Optimization of Transonic Centrifugal Compressor Impellers Using the Design of Experiments Technique

**Duccio Bonaiuti**
**Andrea Arnone**
**Mirco Ermini**

"Sergio Stecco" Department of Energy Engineering,
University of Florence,
50139 Florence, Italy

**Leonardo Baldassarre**
GE Nuovo Pignone,
50127 Florence, Italy

*The turbomachine industry is increasingly interested in developing automated design procedures that are able to summarize current design experience, to take into account manufacturing limitations and to define new rules for improving machine performance. In this paper, a strategy for the parametric analysis and optimization of transonic centrifugal impellers was developed, using the technique of the design of experiments coupled with a three dimensional fluid-dynamic solver. The geometrical parameterization was conducted using Bezier curves and a few geometrical parameters, which were chosen after a screening analysis in order to determine the most significant ones. The range of variation of the parameters was defined taking into account the manufacturing requirements. The analysis of the influence of such parameters on the main impeller performance was subdivided into two steps: first, the effect of the parameters acting on the blade shape was investigated and an optimum configuration was chosen, then the influence of three functional parameters was analyzed, fixing the already optimized variables. The whole strategy aimed at an industrial design approach, and attention was focused on the time required in the design process. From the present analysis it was possible not only to define an optimum geometry, but also to understand the influence of the input parameters on the main machine performance.* [DOI: 10.1115/1.1579507]

## Introduction

Numerical optimization techniques seem to be a promising tool for the aerodynamic design of new generation turbomachine components. The development of the flow inside turbomachines has a complex three-dimensional nature and depends on the interaction between the various parameters that define the machine geometry.

Numerical optimization methods provide an efficient tool for exploiting the great amount of information provided by computational fluid dynamics (CFD) calculations, for analyzing the complex correlations between the geometrical parameters and the machine performance, and for finding their optimal combination. Another interesting feature of such techniques is that they are based on the parameterization of the machine geometry and can be easily linked to CAD systems.

Optimization methods can be grouped into three categories: gradient based optimizers, exploratory techniques and methods based on the concept of function approximation. The choice of the best technique depends on the nature of the problem under investigation and on the kind of analysis to be performed.

The first methods calculate the gradient of an objective function and move the solution toward the closest local optimum. They are very efficient if the parameter space is unimodal, convex and continuous.

Exploratory techniques, as Genetic Algorithm and Simulating Annealing, are based on statistical hypotheses such as the evolutionary theory (Goldberg [1]), and are able to seek the optimum solution in the whole design space. Their use is then necessary when dealing with a multi-peak problem. On the other hand, the number of calculations required to reach an optimal configuration increases.

The last techniques, such as design of experiments and neural networks, are based on the definition of approximated functions which correlate the input parameters with the objective functions, using statistical considerations. The drawback of looking for approximated functions is counterbalanced by the reduced number of calculations required.

All these techniques have been successfully applied for the optimization of axial machine blade profiles (Burgreen and Baysal [2], Trigg [3], Obayashi [4], Pierret and Van den Braembussche [5], Shahpar [6], Manna and Tucillo [7], Glas and Jaberg [8]).

In the last few years, these techniques have been used also for the design of centrifugal machine components.

Wahba and Tourlidakis [9] used a single-objective and a multi-objective Genetic Algorithm coupled with a two dimensional fluid-dynamic solver for the optimization of the blade shape of a centrifugal pump impeller.

Ashimara and Goto [10] used an inverse method together with both gradient-based techniques and exploratory techniques to optimize the performance of a pump impeller, and showed how only the latter are able to find the optimum value of a multi-peak problem.

Van den Braembussche et al. [11] combined a genetic algorithm with an artificial neural network to improve the efficiency of a centrifugal compressor impeller.

Bonaiuti and Pediroda [12] performed a constrained optimization of a radial centrifugal compressor, analyzing the influence on impeller peak efficiency of the parameters that are usually investigated through CFD in an industrial design process.

Benini and Tourlidakis [13] conducted the optimization of a diffuser using a multi-objective Genetic Algorithm and a CFD code. As a result, they found the Pareto optimal set regarding the pressure recovery and the efficiency of the component.

In the present paper the parametric analysis and optimization of transonic centrifugal impellers was conducted using the design of experiments technique (DOE). The DOE strategy is part of a quality production system, the 6 *Sigma*, and the designers of companies that adopt such system are encouraged to use tools belonging

Contributed by the International Gas Turbine Institute of ASME for publication in the JOURNAL OF TURBOMACHINERY. Manuscript received February 13, 2002; final manuscript received May 1, 2003. Paper No. 2002-GT-30619. Review Chair: E. Benvenuti.

  

to the DFSS (design for 6 *Sigma*). With this in mind, the University of Florence and GE Nuovo Pignone started a long-term project to develop a design procedure able to couple the DOE technique with a CFD solver for the aerodynamic optimization of centrifugal compressors.

The optimization of the impeller is a crucial point in the design of a centrifugal compressor, as the flow development inside that component not only determines the aerodynamic efficiency of the impeller itself, but also strongly affects the efficiency of the downstream diffuser. This aspect is particularly important when dealing with high flow rate and high Mach number impellers where the aerodynamic losses cause the greatest reduction in efficiency. This kind of impeller is usually employed in large centrifugal compressors for natural gas liquefaction or ethylene synthesis. Such applications are characterized by high molecular weight gases working at very low temperatures, which determine transonic conditions at the impeller inlet. The extreme values of flow coefficients (from 0.04 to 0.16) and peripheral Mach numbers (from 1.0 to 1.3) make these impellers critical both in terms of aerodynamic efficiency and in terms of achievable operating envelope.

The goal of the present paper is to develop a design strategy that, beginning with the analysis of the transonic impellers produced, will be able to summarize the industrial design experience, to determine the most critical parameters and to analyze their impact on machine performance. The aim is not only to define an optimal configuration, but also to understand the correlations between the input geometrical parameters and the main impeller performance in order to define new design rules. Parameters with an immediate physical meaning were selected to make the analysis easily understood.

The whole strategy was aimed at an industrial application, and attention was focused on both the accuracy of the result and the time required for the design.

**Table 1 List of geometrical parameters**

| | |
|---|---|
| NB | Number of blades |
| $D_{1H}$ | Inlet hub diameter |
| $D_{1S}$ | Inlet shroud diameter |
| $B_2$ | Outlet blade height |
| $\Delta x$ | Impeller axial length |
| $\alpha_{\mathrm{LEAN}}$ | Blade inlet leaning angle |

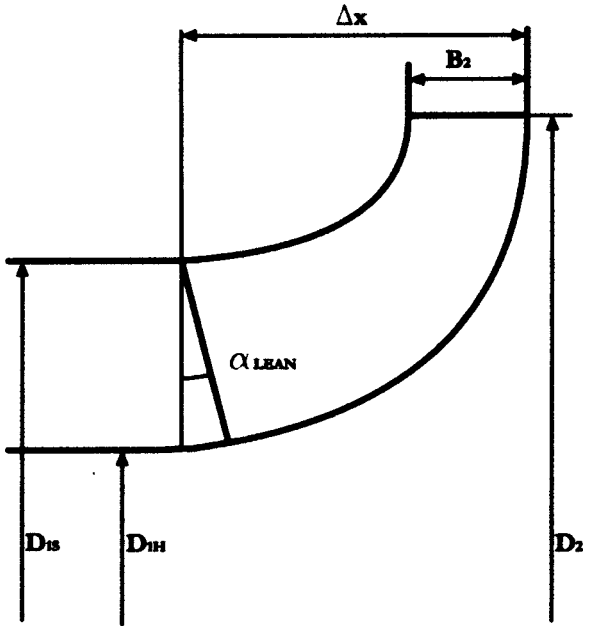


**Fig. 1 Geometrical parameterization of the impeller**

## The Design Strategy

**The DOE Approach.** A design process can be considered as the optimization of the functions that correlate the machine performance $U_j$ (responses) to the design parameters $X_i$ (factors):

$$U_j = F_j(X_i) \quad j = 1,M \quad i = 1,N. \tag{1}$$

The exact value of these functions is given by an analysis code.

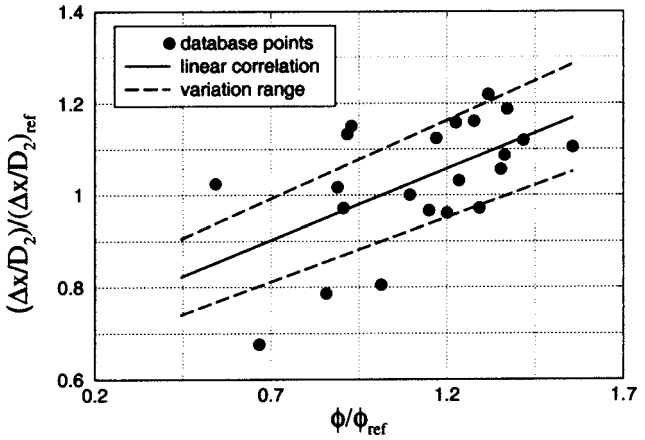


**Fig. 2 Correlation between the axial length and the flow coefficient**

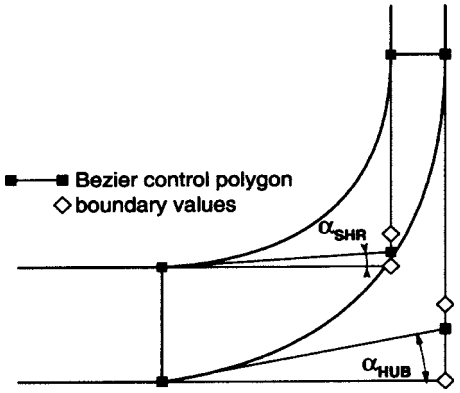


**Fig. 3 Meridional channel parameterization**

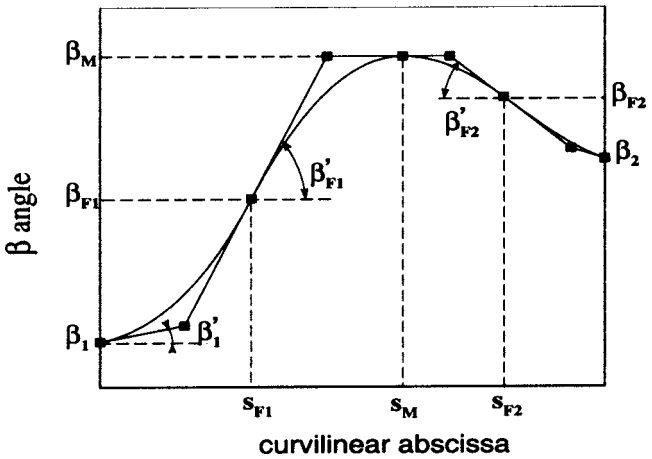


**Fig. 4 Blade turning angle parameterization**

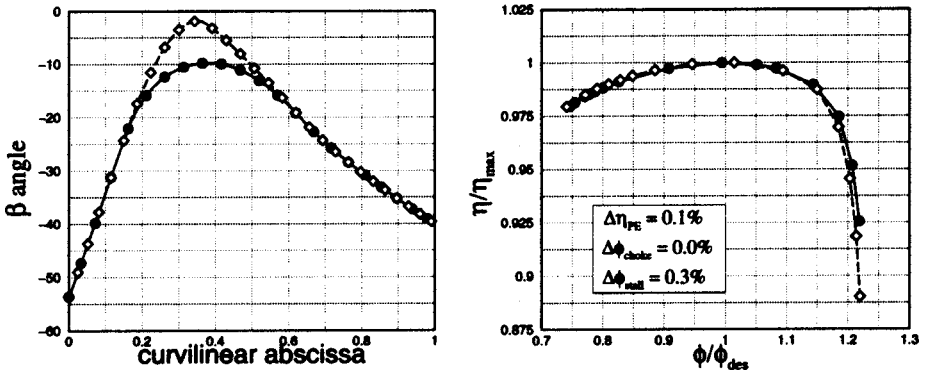


Fig. 5 Effect of the maximum value of the hub $\beta$ distribution

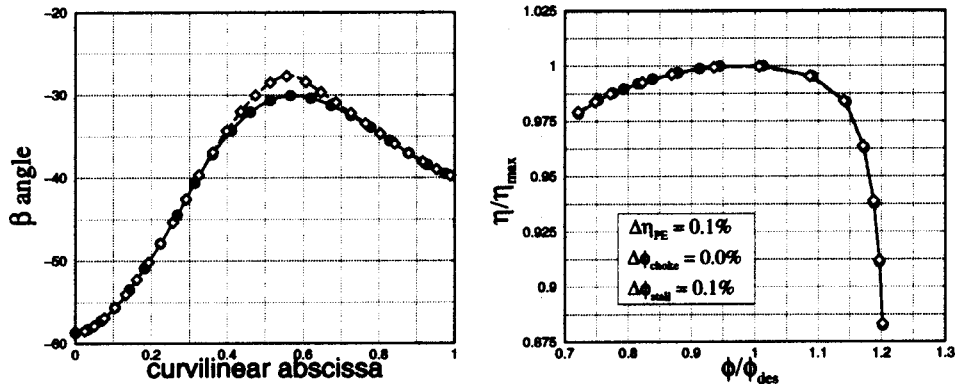


Fig. 6 Effect of the maximum value of the shroud $\beta$ distribution

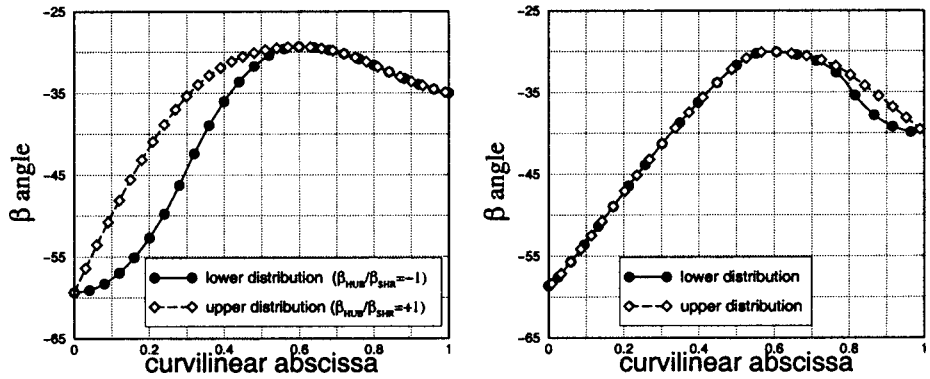


Fig. 7 Limit distributions of the inlet and outlet $\beta$ shape

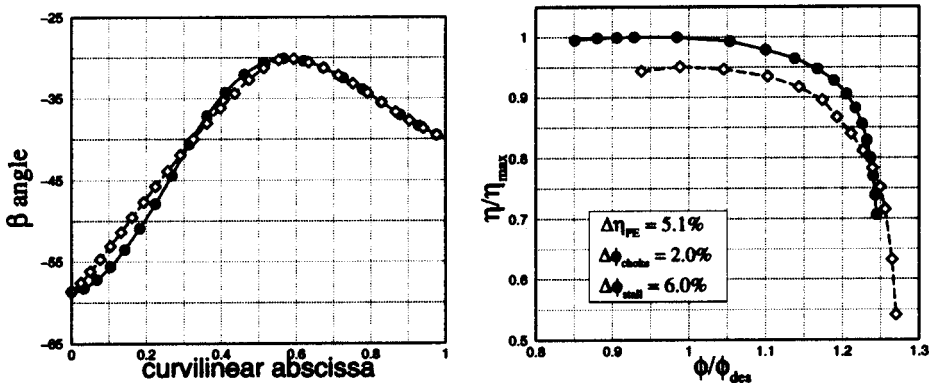


Fig. 8 Effect of the inlet shape of the shroud $\beta$ distribution

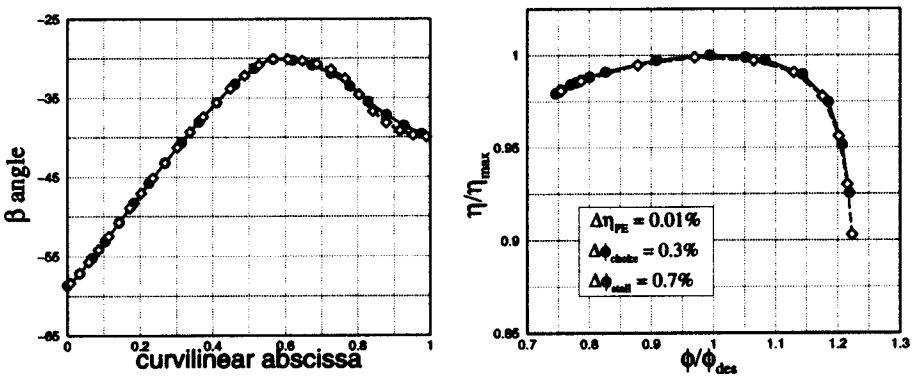


**Fig. 9 Effect of the outlet shape of the shroud $\beta$ distribution**

Statistical techniques are widely used in engineering design to build *approximations* of these functions, using data from a set of analyses:

$$\tilde{U}_j = \tilde{F}_j(X_i) \quad j = 1,M \quad i = 1,N. \tag{2}$$

A common method for building approximations of computer analyses consists of the design of experiments technique (DOE) with the response surface methodology (RSM). RSM approximates the initial function with a polynomial, whose order must be defined a priori. In the case of a second-order polynomial:

$$\tilde{U}_j = \beta_0^j + \sum_{i=0}^{n} \beta_i^j X_i + \sum_{i=0}^{n} \beta_{ii}^j X_i^2 + \sum_{i<k}^{n} \beta_{ik}^j X_i X_k . \tag{3}$$

The coefficients $\beta_0$, $\beta_i$, $\beta_{ii}$, and $\beta_{ij}$ of the polynomials are determined through the least squares regression which minimizes the sum of the squares of the deviations of the predicted values $\tilde{U}_j$ from the actual values $U_j$, for a set of points.

The DOE theory gives the sampling points (experimental design) at which the tests have to be performed, in order to maximize the amount of information generated with the minimum number of simulations.

The main advantages of such a technique are the immediate intelligibility and robustness of the approach, the better understanding of the relationship between the input variables $X_i$ and the responses $U_j$, and the possibility of an easy and fast sensitivity analysis and optimization. Optimization techniques like genetic algorithms can be quickly applied to the approximation function.

The main drawback is that the exact function is replaced by an approximated model and only afterwards it is possible to understand if the approximation is acceptable. It is possible to avoid this problem by using a limited number of parameters with a direct impact on the responses. It is well known that this technique is much less reliable when dealing with more than ten variables.

The strategy can be divided into four steps: definition of the problem, parameterization and screening analysis, characterization and experimental setup, analysis of the results and optimization.

**Definition of the Problem.** The input data of the problem are the design specifications for centrifugal impellers: the outlet diameter, the design mass flow, the rotational Mach number and the minimum value of the work input at design point. Given those specifications, the aim is to highlight the most critical design parameters and analyze their influence on the main machine performance.

In industrial practice, the performance parameters used to

**Table 2 DOE factors**

| | |
|---|---|
| Shape parameters | |
| $\alpha_{HUB}$ | Inlet slope of the hub meridional contour |
| $\alpha_{SHR}$ | Inlet slope of the shroud meridional contour |
| $\beta_{HUB}$ | Inlet shape of the hub $\beta$ angle distribution |
| $\beta_{SHR}$ | Inlet shape of the shroud $\beta$ angle distribution |
| $\Delta x$ | Impeller axial length |
| $\alpha_{LEAN}$ | Blade inlet leaning angle |
| Functional parameters | |
| NB | Number of blades |
| $\beta_2$ | Outlet blade angle |
| DR | Deceleration ratio |

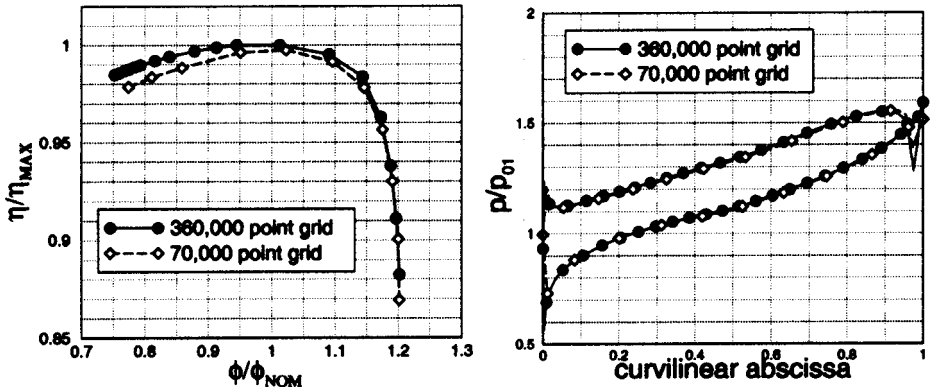


**Fig. 10 Effect of the grid dimension on the efficiency curve and on the midspan blade pressure distribution at design point, for a reference impeller**

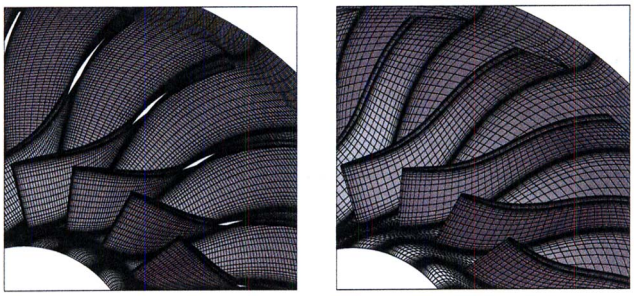

**Fig. 11 Computational grids: 360,000 point grid (left) and 70,000 point grid (right)**

**Table 3 Impeller specifications**

| | $\phi_{des}$ | $M_U$ | $D_2$ (mm) | $\tau_{des}$ |
|---|---|---|---|---|
| Impeller 1 | 0.1217 | 1.049 | 1280 | 0.60 |
| Impeller 2 | 0.0488 | 1.275 | 1220 | 0.70 |
| Impeller 3 | 0.1600 | 1.050 | 1100 | 0.57 |

**Table 4 Validation analysis**

| | First analysis | | Second analysis | |
|---|---|---|---|---|
| Variable | $R^2$ | $R^2_{adj}$ | $R^2$ | $R^2_{adj}$ |
| Impeller 1 | | | | |
| SL | 98.2% | 97.5% | 95.7% | 93.9% |
| CL | 99.9% | 99.2% | 99.5% | 99.0% |
| PE | 97.2% | 96.3% | 99.0% | 98.8% |
| TAU | 87.2% | 83.3% | 99.9% | 99.7% |
| Impeller 2 | | | | |
| SL | 98.1% | 96.9% | 98.9% | 97.8% |
| CL | 99.9% | 99.7% | 99.9% | 99.9% |
| PE | 96.2% | 94.3% | 99.9% | 99.9% |
| TAU | 85.2% | 82.7% | 99.9% | 99.9% |
| Impeller 3 | | | | |
| SL | 98.4% | 97.2% | 98.7% | 96.6% |
| CL | 99.8% | 99.7% | 99.8% | 99.7% |
| PE | 97.3% | 95.2% | 99.8% | 99.7% |
| TAU | 90.4% | 89.3% | 99.9% | 99.9% |

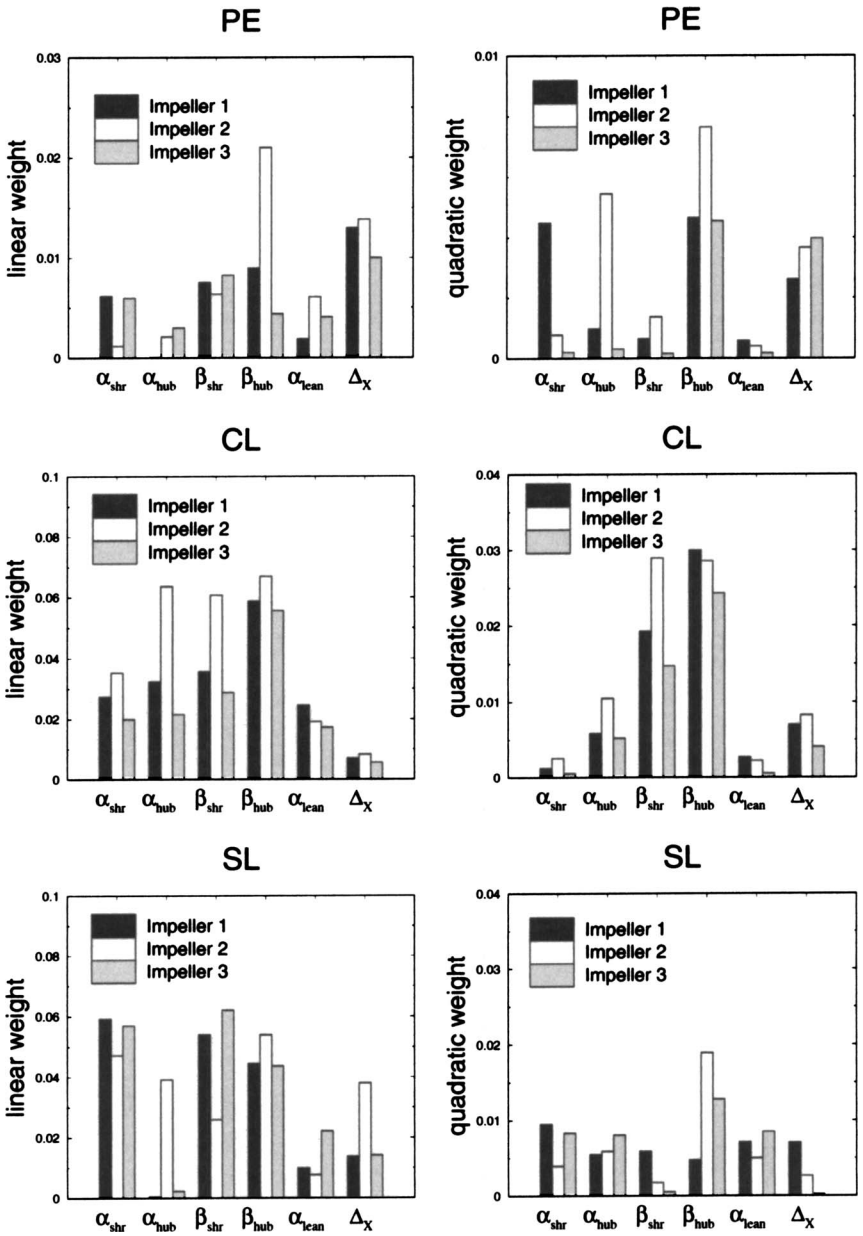


**Fig. 12 First analysis: linear and quadratic weights of the single factors in the response functions**

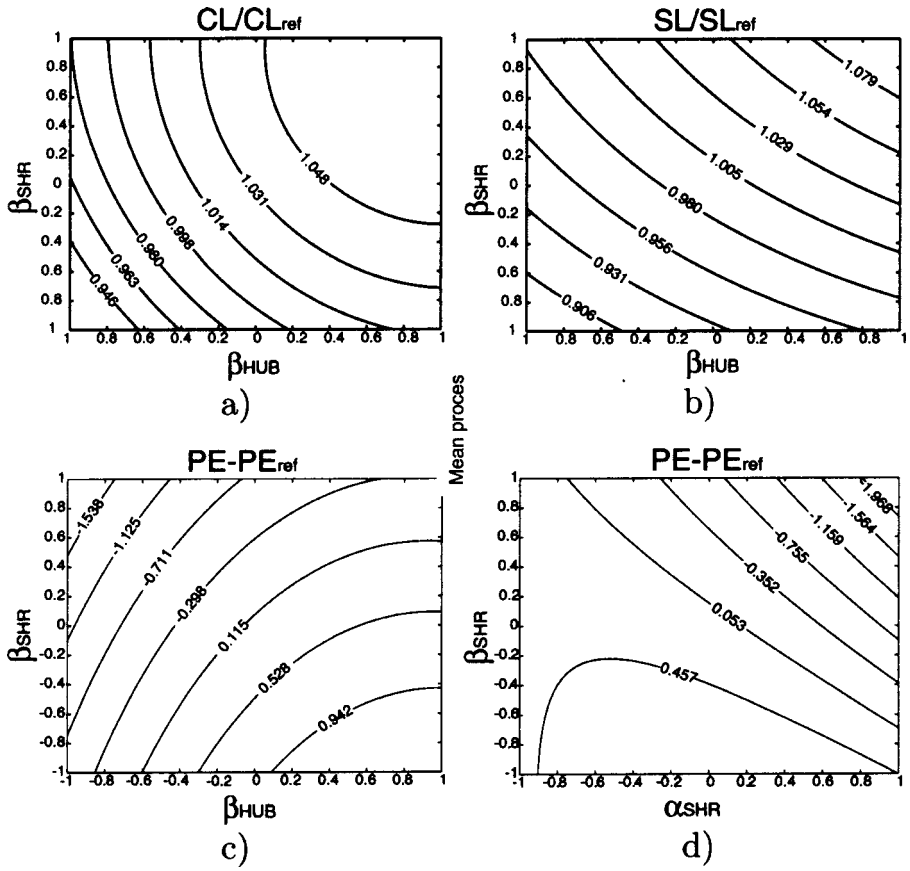


**Fig. 13 First analysis: examples of interaction plots**

qualify impellers are the peak efficiency, the stall and the choke limits. The following objective functions were considered:

$$PE = \eta_{pe} \tag{4}$$

$$CL = \frac{\phi_{\text{choke}}}{\phi_{\text{des}}} \tag{5}$$

$$SL = \frac{\phi_{\text{stall}}}{\phi_{\text{des}}}. \tag{6}$$

The *peak efficiency* was chosen instead of the efficiency at design point as it is more directly correlated to the design parameters.

As it is impossible to define beforehand if a specific configuration is able to guarantee the minimum work input required, the approximated function of the nondimensional work input coefficient at design point was also investigated:

$$TAU = \tau_{\text{des}}. \tag{7}$$

In the optimization process this function was considered a constraint and not an objective function.

In an industrial design process, the designer has to deal with two kinds of parameters: the *functional parameters* which are usually chosen through correlations or one-dimensional analyses, and the *shape parameters* which define the impeller blade shape and that are usually optimized using CFD calculations.

The present analysis was divided into two steps. First, the standard design tools were used to determine the *functional parameters*, and the effect of the *shape parameters* was investigated. After that, an optimal configuration was fixed and the influence of three *functional parameters* was studied.

The two analyses were conducted separately as their aim is different. The goal of the first one is to define an optimal blade shape, which will be kept constant for all the impeller applications. The aim of the second investigation is to define the effect of the *functional parameters* on the impeller performance, in order to give designers the rules to adjust the impeller geometry to the specific application performance requirements.

**Geometric Parameterization and Screening Analysis.** The geometrical parameterization was conducted using the GEPAC code, developed at the University of Florence. This code is able to handle axial-radial turbomachine geometries using few design parameters and Bezier curves or patches of Bezier curves.

The impeller geometry is defined when the parameters, shown in Table 1 and explained in Fig. 1, are set and the blade shape is prescribed.

Centrifugal impellers are commonly built using ruled surfaces. The use of ruled surfaces simplifies the design process and reduces manufacturing costs as the blades can be simply generated in only one continuous sweep of a 5-axis flank milling machine. The shape of this kind of blades is completely set when the coordinates of the hub and of the shroud airfoils are fixed. In order to do this, the following three curves are employed:

- The camberline meridional contour in the plane $x$-$r$.
- The distribution of the blade turning angle $\beta$. This angle is correlated to the azimuthal coordinate of the camberline $\theta$:

$$\tan\beta = r\frac{d\theta}{ds} \tag{8}$$

  where $s$ is the curvilinear abscissa and $r$ is the local radius. This angle is given as a function of the meridional curvilinear abscissa.

- The normal thickness distribution, usually given as a function of the meridional curvilinear abscissa.

A crucial point in the DOE strategy is to perform a screening analysis aimed at identifying the most critical parameters (*vital few*) and reducing the number of design factors to investigate in order to simplify the analysis and shorten the design time. This analysis was conducted trying to exploit the industrial design experience, and using standardized tools and correlations. First, a parameterization of the existing transonic impellers was performed to create a database of the already optimized and produced impellers, then each parameter was analyzed separately.

- The number of blades was considered a *functional parameter* and the standard value was imposed in the first analysis and investigated in the second one.
- The inlet hub diameter $D_{1H}$ is standardized through a correlation with the external diameter while the value of $D_{1S}$ was optimized using one-dimensional correlations, in order to minimize the inlet relative Mach number at the shroud.
- The outlet blade height $B_2$ was correlated to a one-dimensional definition of the deceleration ratio:

$$\mathrm{DR} = \frac{w_2}{w_{1S}} \tag{9}$$

  which was considered a *functional parameter*.
- The axial length $\Delta x$ was treated as a *shape parameter*. Analyzing the database, a linear correlation was set between $\Delta X$, adimensionalized with $D_2$, and the flow coefficient, as shown in Fig. 2. As most of the impeller axial lengths fall within $\pm 10\%$ of that value, that range of variation was imposed in the analysis.
- The hub and shroud meridional contours were parameterized using Bezier curves. From the analysis of the database, most of the impellers were well described by a simple second-order Bezier polynomial with a radial slope at the blade exit. Therefore, the curve slope at the inlet section was considered the only parameter acting on these distributions. With similar considerations as for $\Delta x$, the range of variation of the slopes was set for the hub and for the shroud curves, as shown in Fig. 3.
- Analyzing the database, the shape of the $\beta$ angle distributions was always characterized by a curve with a maximum and two flex points. This kind of distribution can be described by four patches of second-order Bezier curves constrained to have the same slope at the conjunction points. This type of parameterization allows for the use of parameters with an immediate physical meaning, as shown in Fig. 4. The inlet blade angle $\beta_1$ was imposed optimizing the incidence angle for the hub and shroud sections by means of a through-flow analysis, while the outlet blade angle $\beta_2$, which is the same for the hub and shroud distributions, was considered a *functional parameter*. The position of the flex points $S_{F1}$ and $S_{F2}$ and of the maximum $S_M$ were optimized after analyzing their effect on several characteristic impellers. The maximum value of the blade angle $\beta_M$ was also investigated. Once an optimum value is defined, variations of less than 10% from the standard value may change the shape of the performance curves but do not have a relevant impact on the performance parameters. Figure 5 and Fig. 6 show the effect of changing the maximum of the hub and of the shroud distributions for a reference impeller. The other parameters were grouped into two functions in order to vary the inlet and outlet curve shapes, using only two variables. The limit distributions obtained varying such variables are shown in Fig. 7.

The curve shape in the inducer region has a much greater influence on the performance than the one in the rear part of the impeller, and only that parameter was introduced in the variable set. As an example, Figs. 8 and 9 show the effect of similar variations in the two shapes of the shroud distribution on the performance of a reference impeller.

- The blade normal thickness is imposed by structural limita-

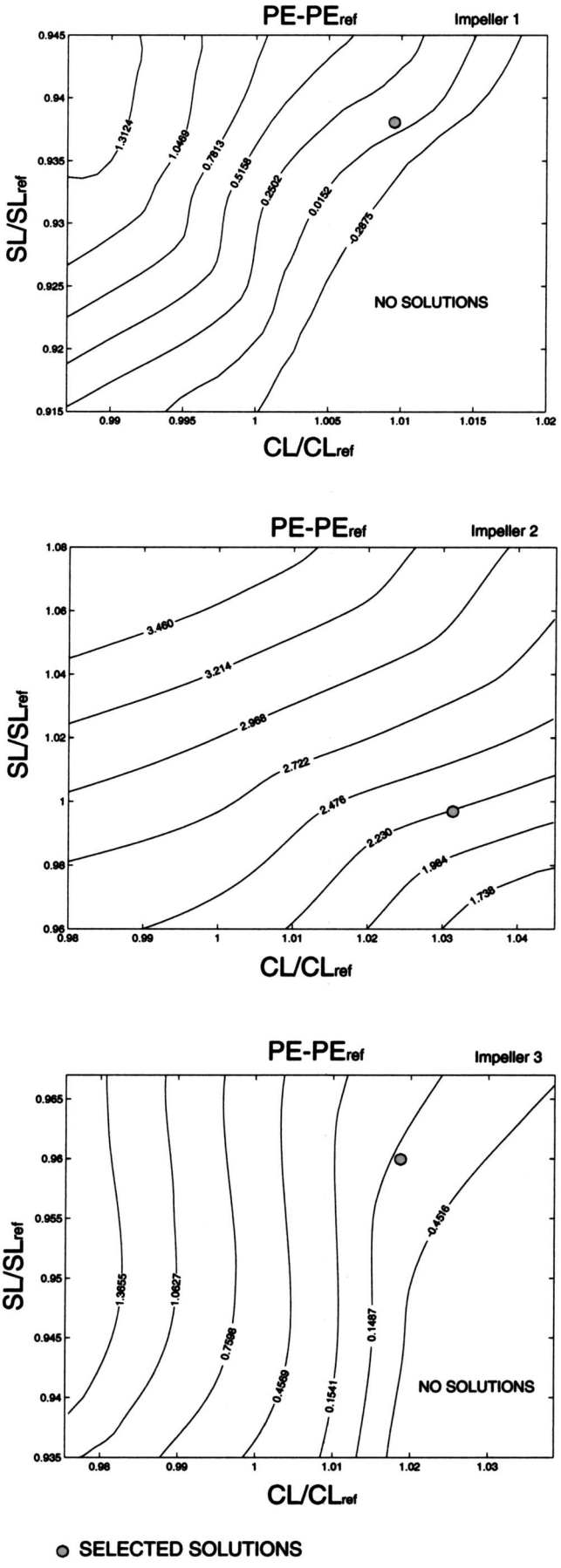


**Fig. 14 First analysis: Pareto front**

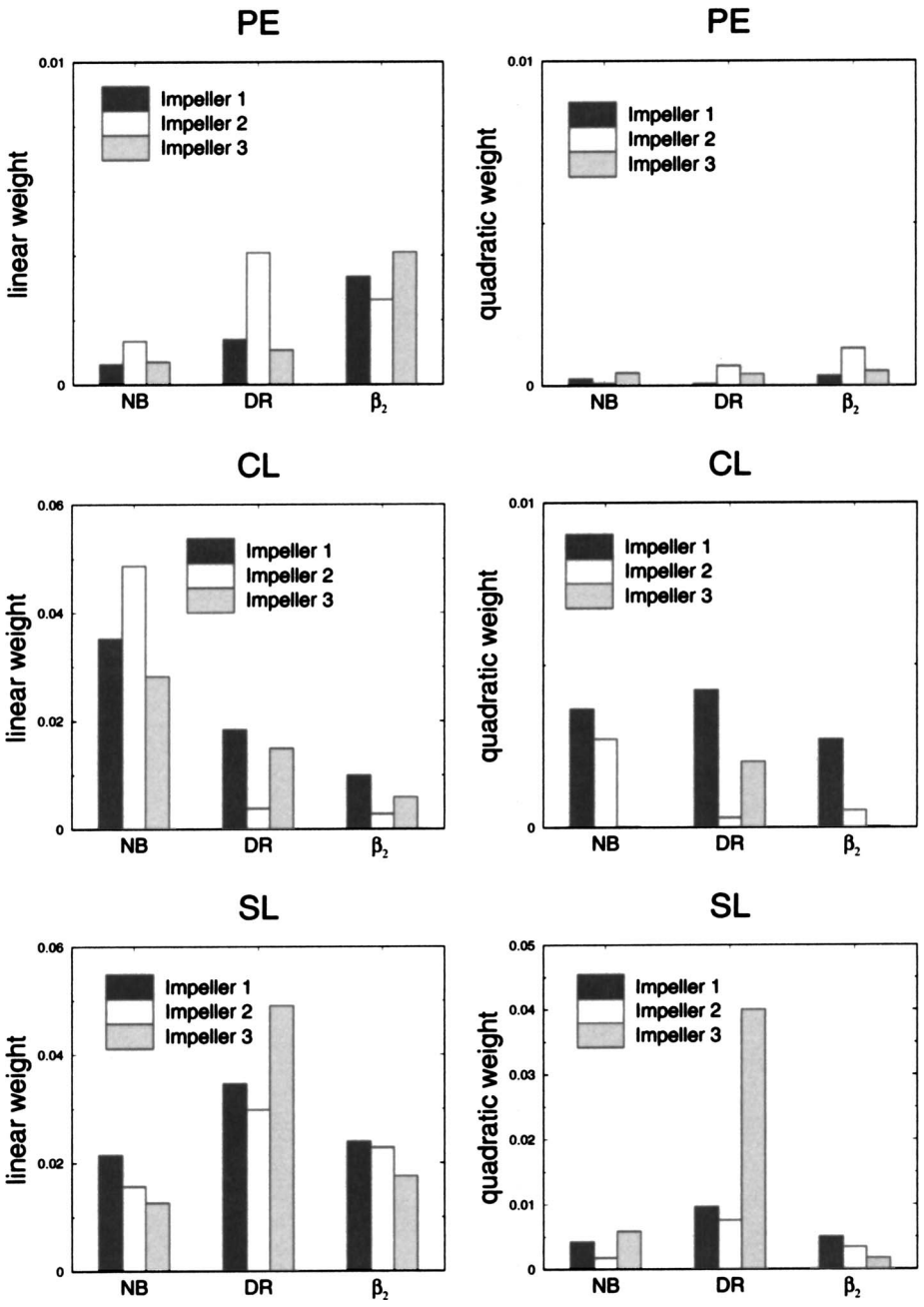


**Fig. 15 Second analysis: linear and quadratic weights of the single factors in the response functions**

tions. The effect of varying the thickness distribution near the leading edge (L.E.) was not considered and a circular rounded L.E. was imposed.

- The leaning angle $\alpha_{LEAN}$ was considered a *shape parameter*.

The parameters, selected after the screening analysis, are summarized in Table 2. The ranges of variation of all the variables were fixed, taking into account the manufacturing limitations.

**Characterization and Experimental Setup.** A second-order response surface was selected and coupled with the *face centered central composite* DOE model (FCCD) to set the test plane. This model varies the factors on three levels to estimate the quadratic effects, and leads to an experimental table with 45 tests for the first analysis and 15 tests for the second one.

All the tests were performed coupling the impellers with a straight inlet duct and with a short diffuser with 10% area reduction in order to avoid diffuser stall.

Computation results were obtained using the TRAF code (Arnone et al. [14]), a fully viscous, multigrid code, developed at the University of Florence.

In order to estimate the value of the four performance parameters, it was necessary to calculate the whole operating range of the impeller. To do this, the points on the functional curve were sequentially obtained, from the choke to the stall, imposing a low back pressure and gradually increasing its value. Fifteen to 20 points were calculated to describe the whole curve.

The peak efficiency and the nondimensional work input coeffi-

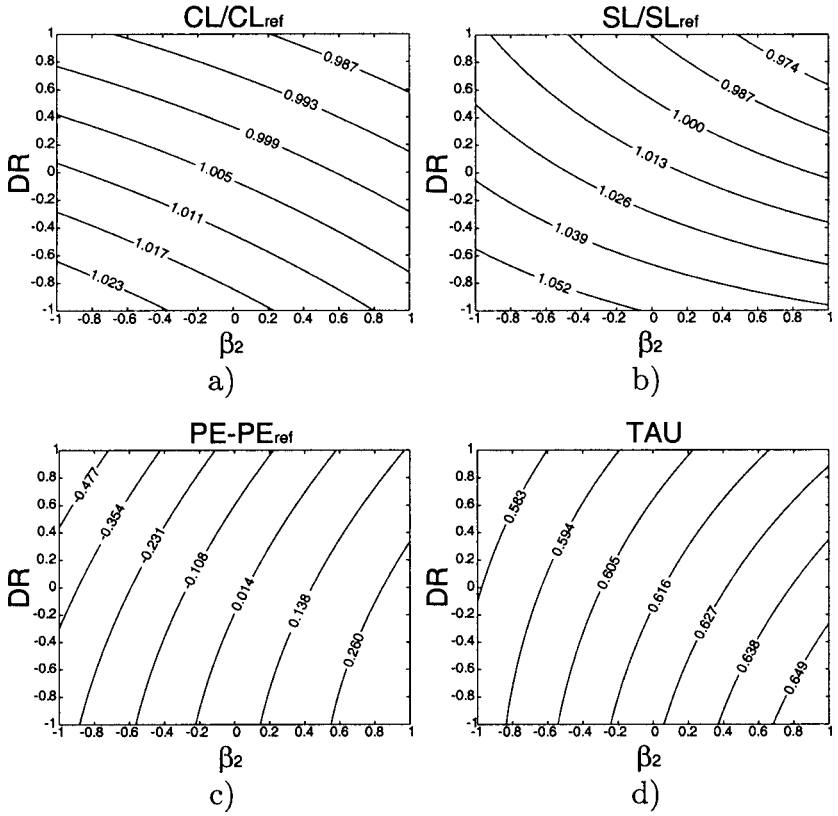


**Fig. 16 Second analysis: example of interaction plots between $\beta_2$ and *DR* for a fixed number of blades**

cient at design point were calculated using a cubic interpolation on the dataset. Such values were evaluated considering the impeller inlet section and a section at a diameter $D=1.08D_2$, where $D_2$ is the impeller exit diameter. Therefore, this evaluation allowed one to take into account the mixing losses, which occur in the first part of a vaneless diffuser in the estimate of the efficiency. Configurations with a smooth total pressure profile at the impeller exit were therefore favored.

As it is impossible to find the stall limit with a steady calculation, a conventional definition was used. The stall was defined as the last point for which the code reached convergence, when increasing the back pressure by a fixed step. Using such an approach, the stall identification may depend on the CFD code used and on its turbulence model, but the aim of this investigation was to compare different design configurations and not to give an exact estimate of the stall point. The assumption was made that the bias error in defining the stall point was the same for all the tested configurations. Furthermore, after analyzing the existing database, the numerical stall was correlated to the one found in the experimental tests.

All the calculations were performed on an nonperiodic H-type grid, with the same grid parameters. A sensitivity analysis of the grid dimension on the results was conducted. A good grid independence was obtained with a 360,000 point grid.

In order to reduce the design time, the effect of using a coarser grid was investigated. Calculations on coarser grids lead to a change in the performance curve shape, and in an underestimation of the peak efficiency and of the stall limit, but the main flow physics seems to be well described, as shown in Fig. 10. The effect of the grid reduction is the same for all the geometries tested, and it is still possible to make a comparison between different configurations. In terms of RSM, there is a shift of the response surface, but the surface shape is the same.

As the aim of the first analysis is to find the best blade shape and not to give quantitative information about the effect of the changes, a 70,000 point grid was chosen. A sensitivity analysis of the result is still possible, which does not consider the absolute value of the responses, but the difference from the performance of a reference geometry.

A 360,000 point grid was used for the second analysis. A three-dimensional view of the two computational grids is shown in Fig. 11.

**Analysis of the Results.** The data fitting was performed using a least squares regression. For numerical stability, the range of each variable was scaled to span $[-1,1]$.

The validation of the model was checked through the analysis of $R^2$ (the ratio of the model sum of squares to the total sum of squares), of the $R^2_{\text{adj}}$ ($R^2$ adjusted to the number of parameters in the model) and other statistical tests.

A sensitivity analysis was conducted on the model to investigate the influence of the single parameters on the responses and the effect of their interaction.

A genetic algorithm optimization was performed using the approximation functions in order to define the Pareto front of the solutions.

## Optimization of Three Impellers

The strategy was applied for the redesign of three impellers, whose specifications are shown in Table 3.

The two analyses were performed sequentially, as mentioned above, and their model validation is reported in Table 4.

The high value of $R^2$ indicates that the choice of the a quadratic response model was correct and that the terms of an order greater than the quadratic one can be neglected in the correlation functions. The only exception seems to be the $\tau_{\text{des}}$ function in the first

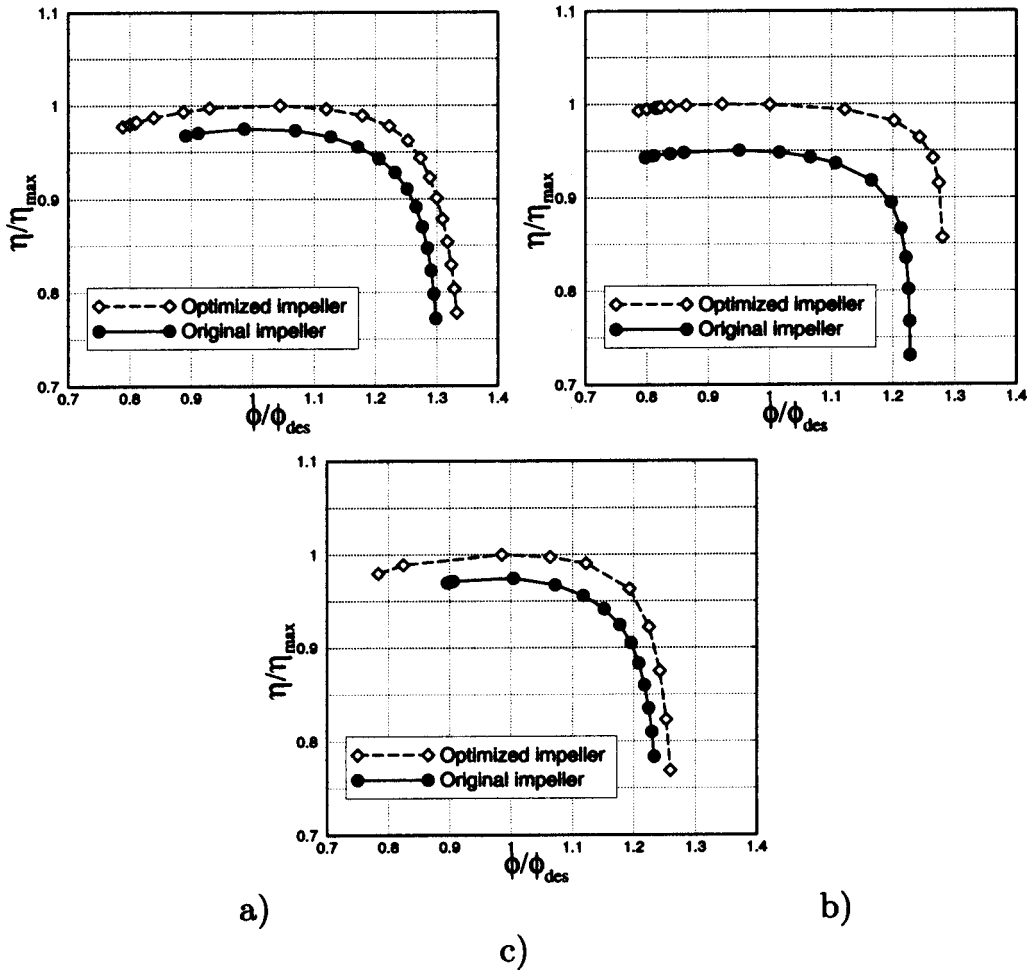


**Fig. 17 Comparison of the efficiency curve between the original and optimized configuration, for the first (*a*), the second (*b*), and the third (*c*) impeller**

analysis. For this reason, an increased value of the minimum $\tau_{\text{des}}$ was imposed as constraint in the optimization process.

The high value of $R^2_{\text{adj}}$ indicates that parameters with relevant impact on the impeller performance were selected.

From the analysis of the model, it is possible to extract information about the influence of each parameter on the performance and the effect of their interactions. This analysis is very important for determining physical correlations and defining new design rules.

The coefficients $\beta_i$ and $\beta_{ii}$ of Eq. (3) are representative of the linear and quadratic weights of the single factors in the response function, while the coefficients $\beta_{ij}$ are representative of their interactions. The values of the first two coefficients from the first analysis of the three impellers are plotted in Fig. 12.

In order to understand the effect of the interactions between two parameters, it is a common practice to set the value of all the other factors at a predetermined value and to plot the response surface only as a function of the two parameters under investigation. Figure 13 reports significant examples from the analysis of the first impeller. All the variables are scaled to span $[-1,1]$, while the performance parameters are adimensionalized with respect to the reference values. Figure 13(*a*) shows that hub and shroud $\beta$ distributions close to the $+1$ one (Fig. 7) broaden the throat area and then extend the choke limit. Blade angle distributions close to the $-1$ one minimize the inducer curvature which determines the detrimental flow acceleration at low mass flow rates, and then improve the stall limit, as shown in Fig. 13(*b*). The combination of $\beta_{SHR}$ close to the $-1$ distribution, and $\beta_{HUB}$ close to the $+1$ one, leads to a configuration with high peak efficiency, as shown in Fig. 13(*c*). This is also the best compromise in order to have a large operating range: the hub distribution guarantees an acceptable throat area while the shroud one reduces the local flow acceleration which is more harmful going toward the shroud, because of the higher tangential velocity component. Figure 13(*d*) indicates that an axial inducer ($\alpha_{\text{SHR}} \simeq -1$) has to be coupled with such a $\beta$ distribution at the shroud in order to keep a high value of the efficiency.

Similar results were obtained in the analysis of the other two impellers.

A genetic algorithm solver was applied to the approximation functions to find the Pareto front of the solutions. Then, a configuration belonging to the Pareto front was chosen for each impeller, as shown in Fig. 14.

The optimized *shape parameters* were fixed and kept constant in the following analysis.

The linear and quadratic weights of the three *functional parameters* investigated in the second analysis are reported in Fig. 15.

For all the impellers, the interaction plots between the diffusion ratio DR and the discharge angle $\beta_2$ were drawn for each number

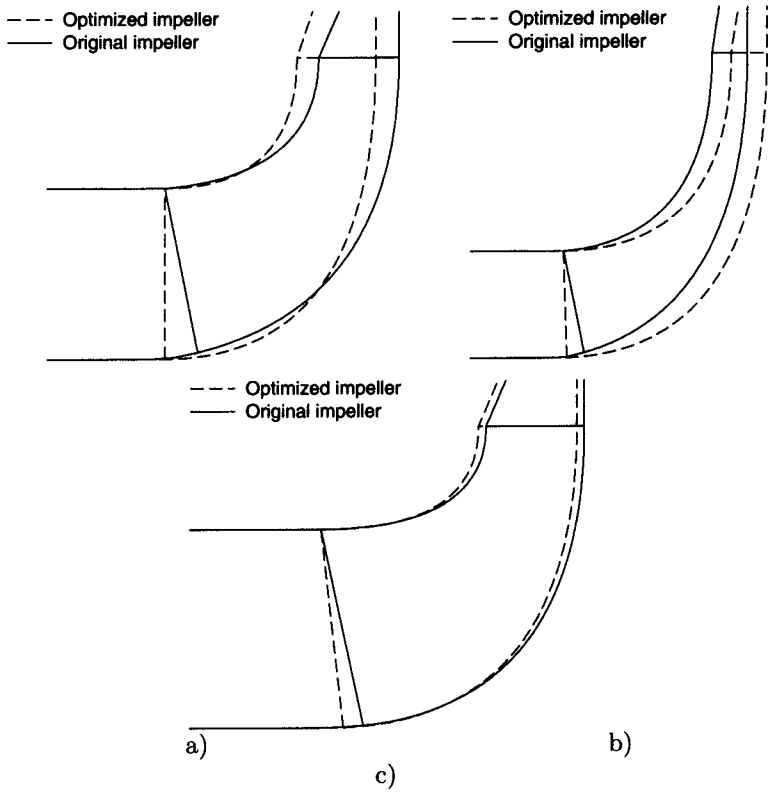


**Fig. 18 Comparison of the meridional contour curve between the original and optimized configuration, for the first (*a*), the second (*b*), and the third (*c*) impeller**

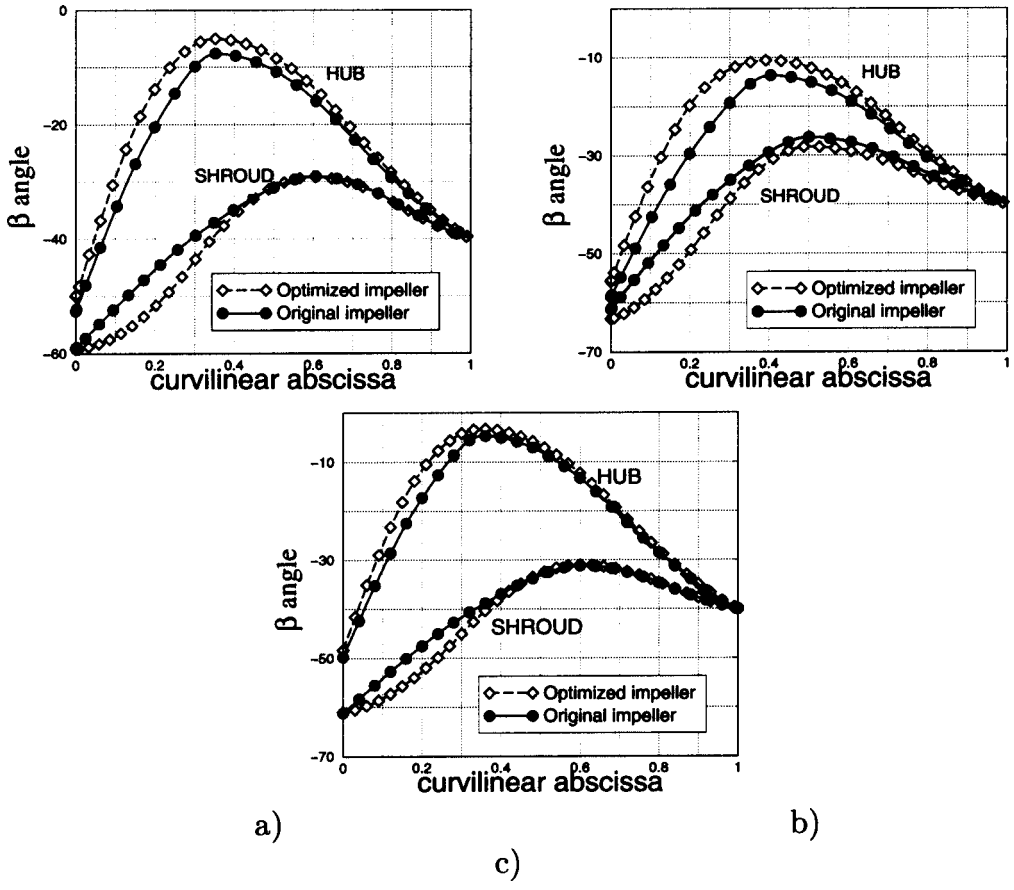


**Fig. 19 Comparison of the $\beta$ distribution curve between the original and optimized configuration, for the first (*a*), the second (*b*), and the third (*c*) impeller**

of blades. An example is shown in Fig. 16. These graphs constitute a tool for the designer for choosing the best parameter combination when approaching to a new impeller design. In the present case, the new configurations were chosen in order to reach a balanced improvement of the three performance parameters with respect to the original impellers.

The efficiency curves relative to the original and to the optimized configurations are shown in Fig. 17, while Figs. 18 and 19 report the differences in the meridional channel and in the blade angle distributions.

## Conclusions

In this paper, the design of experiments (DOE) technique was coupled with a fluid-dynamic solver for the analysis and optimization of centrifugal compressor impellers.

Starting from the analysis of the existing industrial impellers, and after conducting a screening analysis, the most influential geometrical parameters were isolated and their effect on machine performance was investigated.

The reasonable validation of the obtained model allowed us to use this tool for the design of new transonic impellers.

The strategy was applied for the redesign of three impellers. As a result, it was not only possible to define an optimized configuration but also to determine the correlations between the input geometrical parameters and the impeller performance in order to introduce new design rules.

Computer cost is consistent with industrial standards, as the optimization of each impeller required 900 CFD runs, corresponding to 600 h using a Personal Computer Pentium III 750 MHz.


## Acknowledgment

The authors would like to thank Prof. Ennio Carnevale of the University of Florence for encouraging this work and Dr. Alberto Milani for his cooperation.


## Nomenclature

$D_2$ = impeller exit diameter

$h_0$ = total enthalpy

$M_u \equiv \frac{U_2}{\sqrt{\gamma R T_{01}}}$ = impeller rotational Mach number

$p_0$ = total pressure

$Q_1$ = inlet volume flow

$R$ = perfect gas constant

$s$ = curvilinear abscissa

$T_0$ = total temperature

$U_2$ = impeller exit peripheral velocity

$x,r,\theta$ = cylindrical coordinates

$\beta$ = blade turning angle

$\gamma$ = gas specific heat ratio

$\eta \equiv \frac{\gamma-1}{\gamma}\left[\frac{\ln\left(\frac{p_{02}}{p_{01}}\right)}{\ln\left(\frac{T_{02}}{T_{01}}\right)}\right]$ = impeller polytropic efficiency

$\phi \equiv \frac{4Q_1}{\pi D_2^2 U_2}$ = mass flow coefficient

$\tau \equiv \frac{h_{02}-h_{01}}{U_2^2}$ = work input coefficient

### Subscripts

1 = impeller inlet

2 = impeller exit

des = design point

$H$ = hub

$S$ = shroud

pe = peak efficiency

## References


[1] Goldberg, D. E., 1989, *Genetic Algorithms in Search, Optimization and Machine Learning*, Addison-Wesley, Reading, MA.

[2] Burgreen, G. W., and Baysal, O., 1996, "Three-Dimensional Aerodynamic Shape Optimization Using Discrete Sensitivity Analysis," AIAA J., **34**, pp. 1761–1770.

[3] Trigg, M. A., Tubby, G. R., and Sheard, A. G., 1999, "Automatic Genetic Optimization Approach to Two-Dimensional Blade Profile Design for Steam Turbines," ASME J. Turbomach., **121**, pp. 11–17.

[4] Obayashi, S., 1998, "Pareto Genetic Algorithm for Aerodynamic Design Using the Navier-Stokes Equations," *Genetic Algorithms in Engineering and Computer Science*, John Wiley and Sons, New York, pp. 245–266.

[5] Pierret, S., and Van den Braembussche, R. A., 1999, "Turbomachinery Blade Design Using a Navier-Stokes Solver and Artificial Neural Network," ASME J. Turbomach., **121**, pp. 326–332.

[6] Shahpar, S., 2000, "A Comparative Study of Optimization Methods for Aerodynamic Design of Turbomachinery Blades," ASME Paper No. 2000-GT-0523.

[7] Manna, M., and Tuccillo, R., 2000, "The Combined Use of Navier-Stokes Solvers and Optimization Methods for Decelerating Cascade Design," ASME Paper 2000-GT-0524.

[8] Glas, W., and Jaberg, H., 2001, "Multi-Objective Evolutionary Algorithm for the Optimization of Swept Pump Impellers," *Proc., Fourth European Conference on Turbomachinery*, Paper No. ATI-CST-038/01.

[9] Wahba, W. A., and Tourlidakis, A., 2001, "A Genetic Algorithm to the Design of Blade Profiles for Centrifugal Pump Impellers," AIAA Paper No. 2001–2582.

[10] Ashimara, K., and Goto, A., 2001, "Turbomachinery Blade Design Using 3-D Inverse Design Method, CFD and Optimization Algorithm," ASME Paper 2001-GT-0358.

[11] Cosentino, R., Alsalihi, Z., and Van den Braembussche, R. A., 2001, "Expert System for Radial Impeller Optimization," *Proc., Fourth European Conference on Turbomachinery*, Paper No. ATI-CST-039/01.

[12] Bonaiuti, D., and Pediroda, V., 2001, "Aerodynamic Optimization of an Industrial Centrifugal Compressor Impeller Using Genetic Algorithms," Proc., Eurogen 2001.

[13] Benini, E., and Tourlidakis, A., 2001, "Design Optimization of Vaned Diffusers of Centrifugal Compressors Using Genetic Algorithms," AIAA Paper No. 2001–2583.

[14] Arnone, A., Liou, M. S., and Povinelli, L. A., 1992, "Navier-Stokes Solution of Transonic Cascade Flow Using Non-Periodic C-Type Grids," J. Propul. Power, **8**, pp. 410–417.

# Influence of Blade Leading Edge Geometry on Turbine Endwall Heat (Mass) Transfer

**S. Han**

**R. J. Goldstein**[1]
e-mail: rjg@me.umn.edu

Heat Transfer Laboratory,
Department of Mechanical Engineering,
University of Minnesota,
Minneapolis, MN 55455

*The secondary flows, including passage and other vortices in a turbine cascade, cause significant aerodynamic losses and thermal gradients. Leading edge modification of the blade has drawn considerable attention as it has been shown to reduce the secondary flows. However, the heat transfer performance of a leading edge modified blade has not been investigated thoroughly. Since a fillet at the leading edge blade is reported to reduce the aerodynamic loss significantly, the naphthalene sublimation technique with a fillet geometry is used to study local heat (mass) transfer performance in a simulated turbine cascade. The present paper compares Sherwood number distributions on an endwall with a simple blade and a similar blade having a modified leading edge by adding a fillet. With the modified blades, a horseshoe vortex is not observed and the passage vortex is delayed or not observed for different turbulence intensities. However, near the blade trailing edge the passage vortex has gained as much strength as with the simple blade for low turbulence intensity. Near the leading edge on the pressure and the suction surface, higher mass transfer regions are observed with the fillets. Apparently the corner vortices are intensified with the leading edge modified blade.* [DOI: 10.1115/1.2221326]

## Introduction

The secondary flows in a turbine cascade result in significant aerodynamic loss and a high thermal load. Endwall contouring and blade leading edge modification have been investigated to reduce the secondary flows. Endwall contouring, applicable in the first-stage stator section, accelerates the main flow before and through the turbine cascade and can suppress the secondary flow development, as indicated by Burd and Simon [1]. Leading edge modifications considered include a sharp edge fillet, round fillet, and bulb at the junction between the blade leading edge and the endwall. Unlike endwall contouring, leading edge modification is applicable to both stator vanes and rotating blades in the turbine. Sauer et al. [2] used a different "bulb" design. They reported a 50% of reduction of aerodynamic loss. The authors suggest that this remarkable reduction came from the increased strength of the counter vortex on the suction side, which interacts with the passage vortex reducing the aerodynamic loss. However, others suggest the interaction can increase the loss. Becz et al. [3] used three different leading edge modifications: fillet, small bulb, and large bulb. They found that both the small bulb and fillet reduced total area-averaged loss by 8%, but the large bulb increased the total area-averaged loss. Becz et al. [4] reported that only the fillet reduced the total mass-averaged loss by 7%. Zess and Thole [5] investigated the effect of different fillet geometries computationally and experimentally. They recommend an asymmetric fillet with $1\delta$ height and $2\delta$ length. Shih et al.'s [6] numerical study of aerodynamic loss and surface heat transfer for two fillets with and without swirl indicated that surface heat transfer was reduced by more than 10% on the airfoil and 30% on the endwall. Using a commercial CFD software, Lethander et al. [7] found that a large fillet provides better thermal performance which is most affected by the height of the fillet. Many of the previous studies on leading edge modification have focused on aerodynamic loss reduction. This was a computational work and no experiments were reported on the effect of leading edge modification on heat transfer performance. The present study investigates the local heat (mass) transfer performance on an endwall with a fillet on the blades.

## Experimental Method and Setup

**Naphthalene Sublimation Method.** The naphthalene sublimation technique for mass transfer measurement is employed to investigate the thermal performance of leading edge modification. A detailed description of this technique is provided by Goldstein and Cho [8]. This method can measure local mass transfer coefficients with a constant concentration wall condition. The method consists of preparing a naphthalene test section, making a first scan of the surface profile, conducting a wind tunnel experiment, and making a final surface scan. There are several methods to make a naphthalene sublimation section including machining, dipping, spraying, and casting. The casting technique has been developed to make a smooth naphthalene surface with good repeatability. Casting is used in the present study.

A surface coated with uniform temperature (surface vapor pressure) naphthalene is equivalent to an isothermal boundary condition in heat transfer, and a "noncoated" surface corresponds to the adiabatic wall condition. Concentration gradients and mass flux are analogous to temperature gradients and heat flux.

To determine the saturated vapor density, the temperature of the naphthalene surface and the saturated vapor pressure are needed in Eq. (1)

$$\rho_{v,w} = \frac{p_{v,w}}{RT_{n,w}} = \frac{M_{\text{naph}} p_{v,w}}{\bar{R} T_{n,w}} \tag{1}$$

The saturated vapor pressure is obtained from a correlation given

[1]Corresponding author.

Contributed by the International Gas Turbine Institute (IGTI) of ASME for publication in the JOURNAL OF TURBOMACHINERY. Manuscript received October 1, 2004; final manuscript received February 1, 2005. IGTI Review Chair: K. C. Hall. Paper presented at the ASME Turbo Expo 2005: Land, Sea and Air, Reno, NV, June 6–9, 2005, Paper No. GT2005-68590.

  

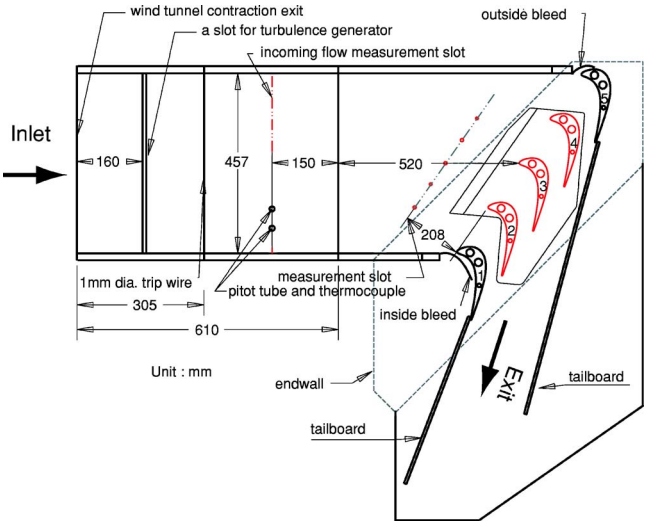


**Fig. 1 Test section for the heat transfer experiment**

by Ambrose et al. [9]. The saturated vapor pressure is very sensitive to temperature. A 1°C variation in the surface temperature causes about a 10% variation in the vapor pressure. To guarantee the appropriate boundary condition, the temperature of the naphthalene surface should be controlled very carefully. The mass transfer coefficient is determined from

$$h_m = \frac{\dot{m}}{\rho_{v,w} - \rho_{w,\infty}} = \frac{\rho_s \delta t / \delta \tau}{\rho_{v,w}} \tag{2}$$

where $\rho_{v,w}$ is the vapor concentration at an impermeable wall and $\rho_{v,\infty}=0$ for the mainstream.

The mass diffusion coefficient of naphthalene in air is evaluated

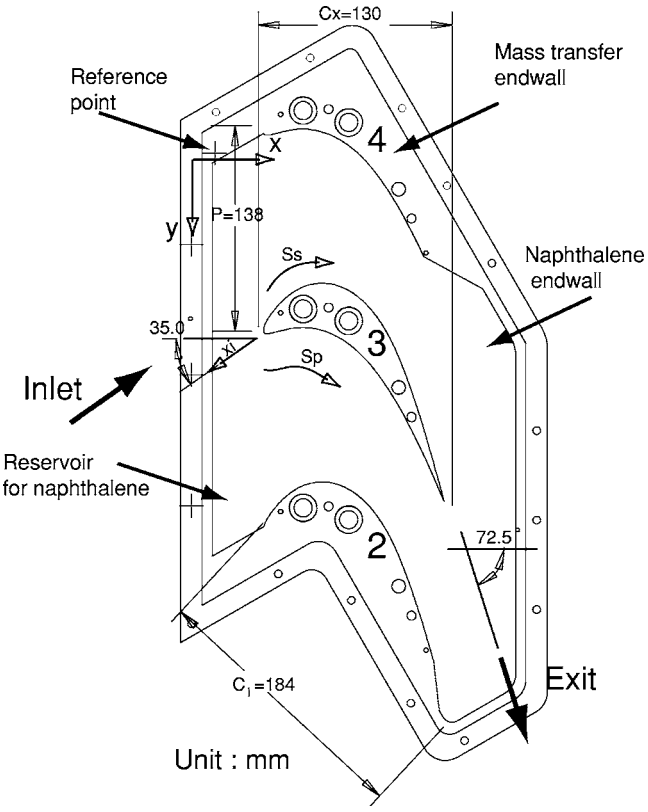


**Fig. 2 Blades configuration on the mass transfer endwall**

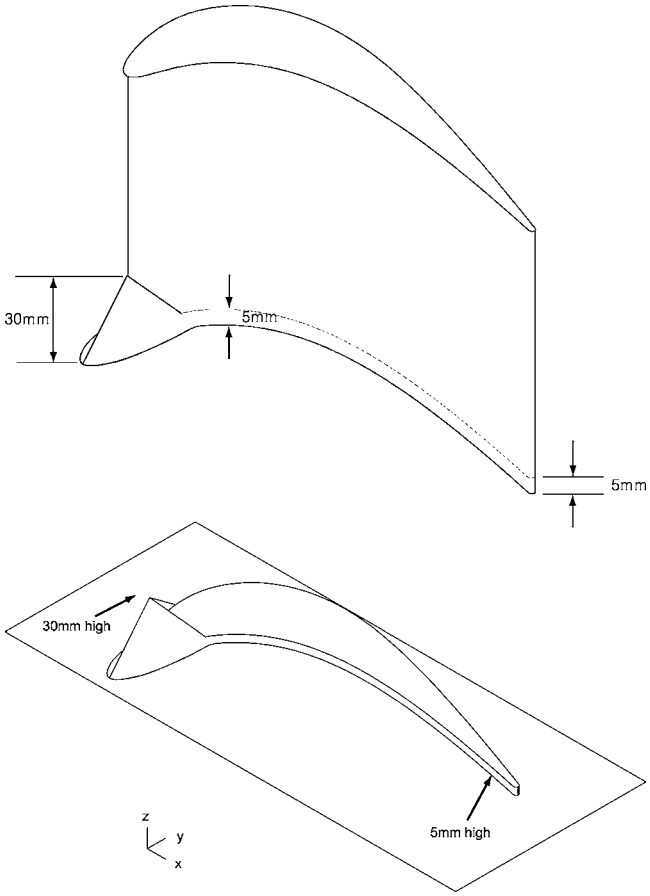


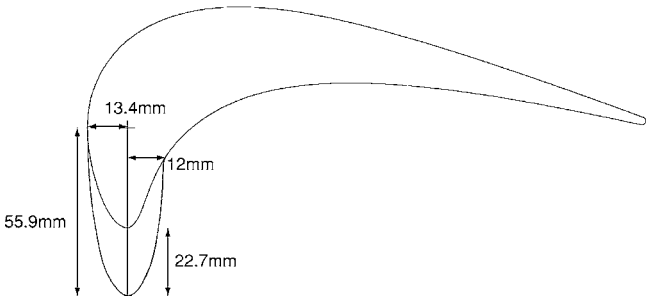


**Fig. 3 The geometry of the blade with the fillet**

by averaging two different values from the literature. The average value, 0.0681, is obtained from 0.066 from Cho [10] and 0.0702 from Chen and Wung [11] at 298.16 K. Cho [10] states that humidity of air does not change the naphthalene diffusion coefficient in air. The Sherwood number can be expressed as

$$\mathrm{Sh} = \frac{h_m C_l}{D_{\mathrm{naph}}} \tag{3}$$

Using the methodology described in Coleman and Steele [12], the uncertainty in the Sherwood number is estimated to be approximately 7% at the 95% confidence level ($\pm 2\sigma$). However, the uncertainty is mainly due to the uncertainty of the naphthalene properties primarily the diffusion coefficient. The measurement uncertainty not including the uncertainty of the naphthalene properties is 5.2%.

**Test Section.** The test section, shown in Fig. 1, is connected to the exit of the contraction of a blow-type wind tunnel. The bottom endwall has a large opening to hold the mass transfer plate. The straight section, with a cross section of 457 mm × 457 mm and a

**Table 1 Mass transfer experimental conditions on the endwall without fillets**

| Run | Trip wire (mm) | $Re_{ex}$ | $U_{ex}$ (m/s) | $\delta_1$ (mm) | Tu (%) |
|---|---|---|---|---|---|
| Run-1 | 0.5 | $4.50\times10^5$ | 39.2 | 2.7 | 0.2 |
| Run-2 | 0.5 | $5.82\times10^5$ | 50.6 | 3.2 | 0.2 |
| Run-3 | 1.0 | $4.38\times10^5$ | 38.5 | 3.9 | 0.2 |
| Run-4 | 1.0 | $5.77\times10^5$ | 50.6 | 4.0 | 0.2 |
| Run-5 | 1.0 | $4.27\times10^5$ | 37.4 | 3.9 | 8.5 |
| Run-6 | 1.0 | $5.67\times10^5$ | 49.9 | 4.0 | 8.5 |

length of 610 mm, has slots reserved for generation of mainstream turbulence by inserting various grid turbulence generators, cf. Ref. [13] and is followed by the linear cascade section.

The linear turbine cascade consists of five 457 mm long simulated high-performance turbine rotor blades made of aluminum which were used in Wang et al. [14]. Blades 1 and 5 are fixed by screws from the bottom to the top wall and connected to two downstream tailboards. The tailboards as well as the space between the bleeds and the outside blades can be adjusted to obtain periodic flow in the blade passages. The three central blades are fixed by screws at the bottom wall. Higher turbulence intensity is generated by inserting a bar grid 970 mm ahead of the blade 3 leading edge.

To ensure a fully developed turbulent boundary layer on the endwall at the inlet to the cascade, a 0.5 or 1 mm diameter trip wire is placed near the exit of the contraction section on the bottom endwall, which is 820 mm ahead of the stagnation point of the central blade. There are two incoming flow measurement slots normal to the flow direction, one incoming flow measurement slot parallel to the flow direction, and five measurement holes. The incoming flow velocity and turbulence intensity are measured using a hot wire anemometer and a traversing system at the incoming flow measurement slot, which is 670 mm ahead of the leading edge of the center blade in the direction of the incoming flow. The incoming flow dynamic pressure (velocity), static pressure, and temperature are also measured at this position, using a pitot tube and a E-type thermocouple. Five measurement holes are 208 mm ahead and parallel to the leading edges of the blades, where the boundary layer on the endwall is measured at three different locations at half pitch distance. Outgoing flow velocity is calculated using incoming flow velocity and the area aspect ratio (2.72).

**Table 2 Mass transfer experimental conditions on the endwall with fillets**

| Run | Trip wire (mm) | $Re_{ex}$ | $U_{ex}$ (m/s) | Tu (%) |
|---|---|---|---|---|
| Run-f1 | 1.0 | $4.31\times10^5$ | 38.4 | 0.2 |
| Run-f2 | 1.0 | $5.65\times10^5$ | 49.9 | 0.2 |
| Run-f3 | 1.0 | $3.57\times10^5$ | 31.8 | 8.5 |
| Run-f4 | 1.0 | $4.97\times10^5$ | 44.0 | 8.5 |

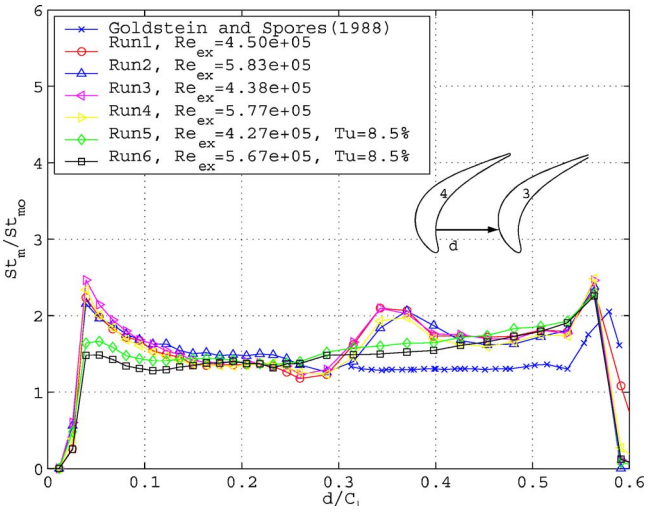


**Fig. 4 St number comparison at $x/C_l$=0.15**

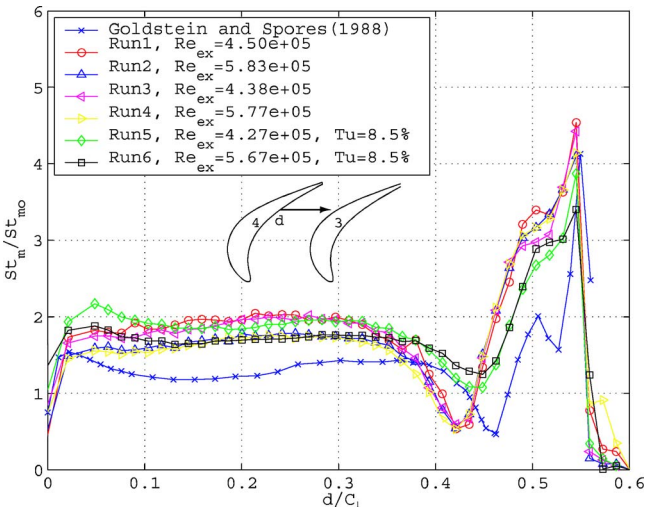


**Fig. 5 St number comparison at $x/C_l$=0.51**

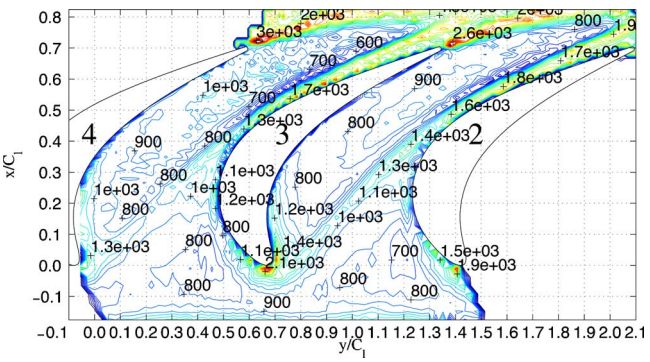


**Fig. 6 Sh contour plot (Run-1) with $Re_{ex}=4.50\times10^5$ and Tu =0.2%**

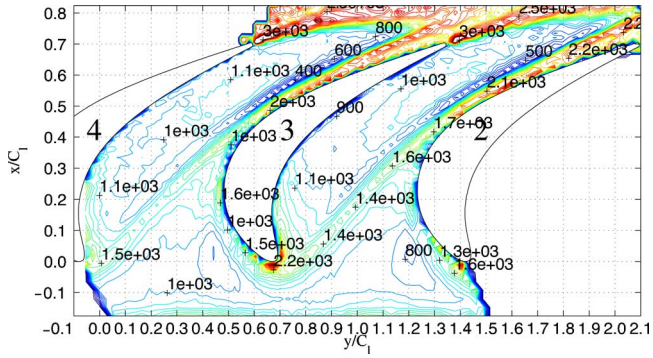

**Fig. 7 Sh contour plot (Run-2) with $Re_{ex}=5.82\times10^5$ and Tu =0.2%**

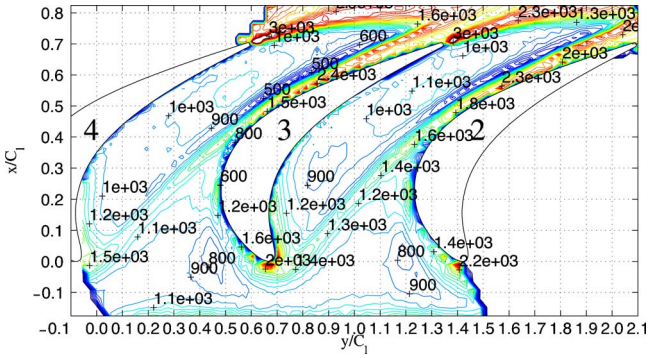

**Fig. 10 Sh contour plot (Run-4) with $Re_{ex}=5.77\times10^5$ and Tu =0.2%**

**Mass Transfer Endwall.** One mass transfer endwall is designed by Pro/Engineer and machined from aluminum. It has a reservoir 2.54 mm deep to hold naphthalene. The side rims have a 5 mm width for reference points. The rims of the test endwall are highly polished to enhance the repeatability of the measurements. To align two separate measurement points before and after wind tunnel experiments, a small reference point is drilled into the reference rim surface. Before each surface scanning, the reference point is found and set to zero by the linear voltage displacement transformer (LVDT) and NF-90 motion controller. Three holes for three E-type thermocouples are drilled into the reservoir so that the surface temperature of the naphthalene can be monitored during each experiment. General Electric RTV-108, a high temperature silicon, is used to protect the thermocouples when the naphthalene endwall is prepared. To generate reliable mass transfer results, the naphthalene surface should be smooth. This is accomplished in the casting method by using a highly polished cover plate. For casting purposes, two holes are drilled inside the reservoir. One is a vent hole, and the other is the injection (pouring) hole for melted naphthalene liquid. Bolts and nuts prevent the cover plate from lifting in the center of the endwall, otherwise molten naphthalene would leak through the gap between the reservoir endwall and the cover plate, leading the LVDT to go out of range during the surface scanning. The mass transfer endwall without the cover plate is shown in Fig. 2.

**Fillet.** The design of the fillet is based on the suggestion by Zess and Thole [5]. They tested nine fillets computationally and experimentally to find an optimal shape. They found that a 1/4 and a 1/7 power law profile does not significantly eliminate the horseshoe vortex, but a linear fillet profile does. An asymmetric fillet is found to be effective in reducing separation on the suction side. Considering their suggestion, the elliptical, asymmetric, and sharp slope fillet in Fig. 3 is manufactured in aluminum by a CNC machine. The fillet is $7.5\delta_1$ high and $6\delta_1$ long from the stagnation point. Even though Sung and Lin [15] recommend that the length of the fillet should be larger than the height, six displacement thickness is chosen for the length of the fillet from the stagnation point since the typical extended length of the endwall disk part ahead of the stagnation point is about 15% of the chord length (184 mm) from the leading edge.

Near the stagnation point the displacement thickness ($\delta_1$) is 4 mm in the test so that the height of the fillet is chosen to be approximately 30 mm. The other part of the fillet is 5 mm high and fixed on the blade with a mounting pin. As can be seen, the fillet has a design like a shoe for easy assembly. It is fixed by

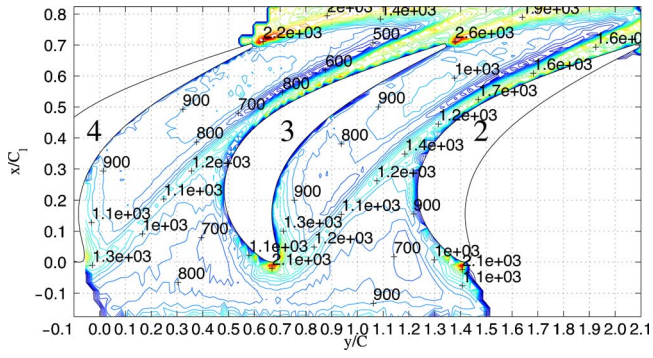

**Fig. 8 Sh contour plot (Run-3) with $Re_{ex}=4.38\times10^5$ and Tu =0.2%**

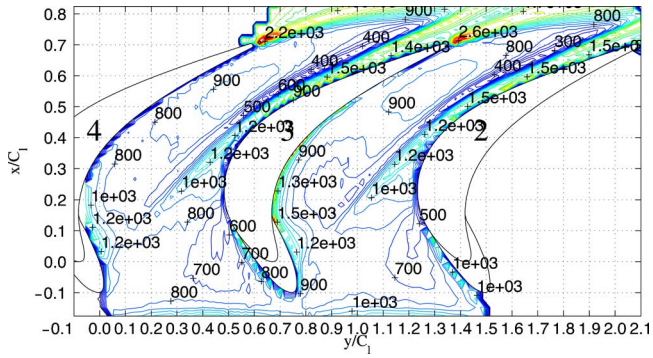

**Fig. 9 Sh contour plot (Run-f1) with fillets, $Re_{ex}=4.31\times10^5$ and Tu=0.2%**

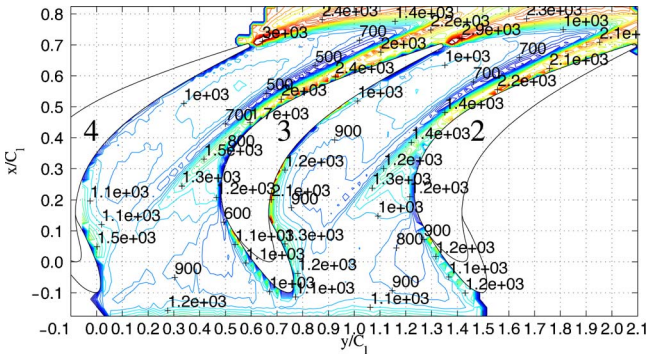

**Fig. 11 Sh contour plot (Run-f2) with fillets, $Re_{ex}=5.65\times10^5$ and Tu=0.2%**

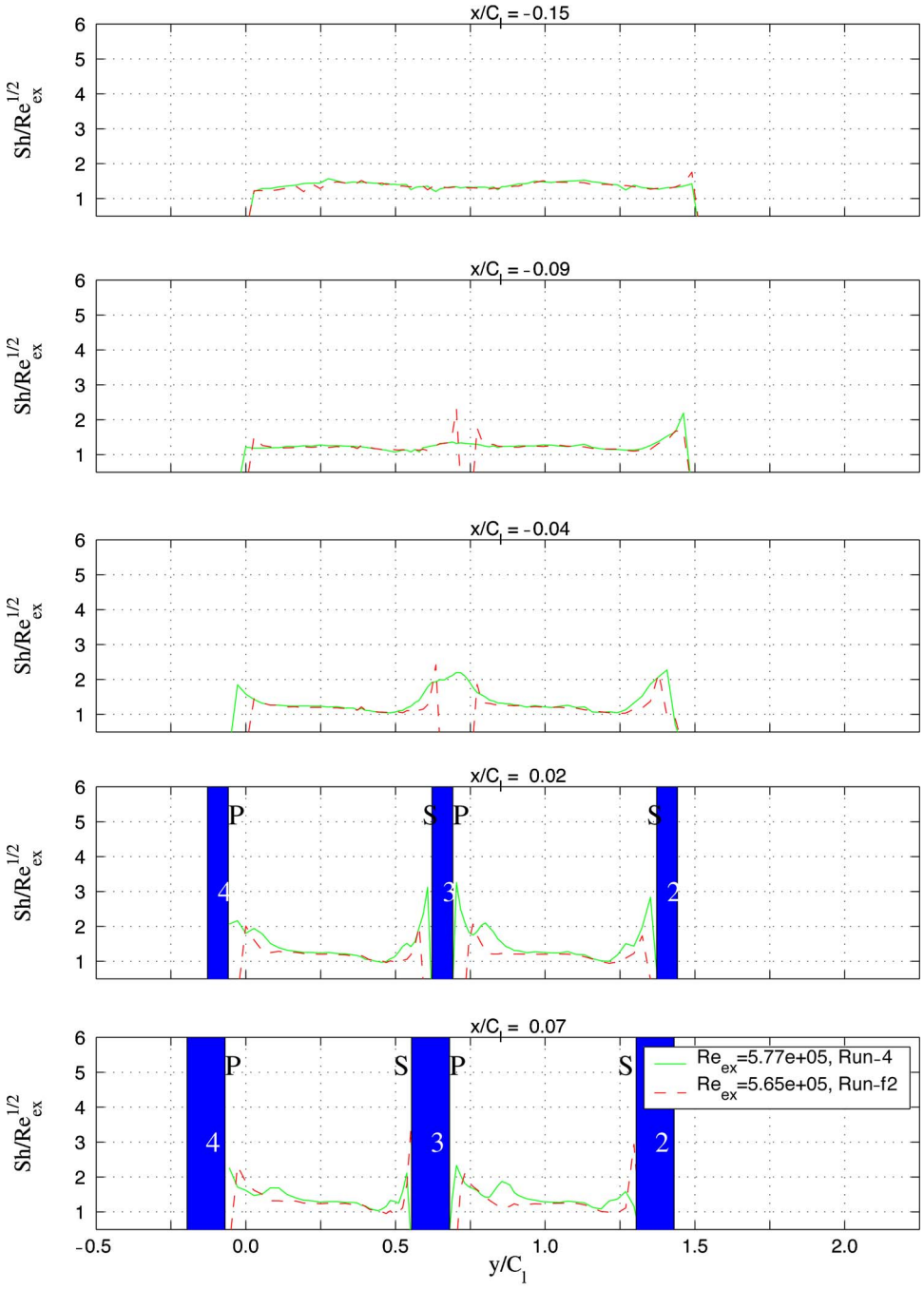


**Fig. 12 Sh number comparison at different streamwise position I**

mount pins and bolts on the blade and the endwall. The fillets sit on the endwall and cover the blades like shoes. Fillets are located on blades 2, 3, 4 to provide periodic flow in the blade passage.

## Results and Discussion

Mass transfer measurements with different Reynolds numbers, boundary layer thicknesses, and turbulence intensities are conducted to evaluate the effect of a fillet on endwall mass (heat) transfer. For comparison purposes, six different mass transfer experiments are conducted without a fillet: two $Re_{ex}$ ($4.5\times10^5$ and $5.8\times10^5$) with two trip wire diameters (0.5 and 1.0 mm) and low turbulence intensities (0.2%), and two $Re_{ex}$ ($4.5\times10^5$ and $5.8\times10^5$) with 1.0 mm trip wire diameters and high turbulence intensity (8.5%) as shown in Table 1.

Two Reynolds numbers are employed to investigate the effect of velocity and two turbulence intensities (Tu=0.2% and 8.5%) are applied to determine the effect of turbulence. Since different boundary layer thicknesses created by the different trip wire diameters do not significantly affect the mass transfer coefficients for the same Reynolds number, only a 1 mm diameter trip wire is used to conduct the experiments with a fillet. Detailed experimental conditions are tabled in Table 2.

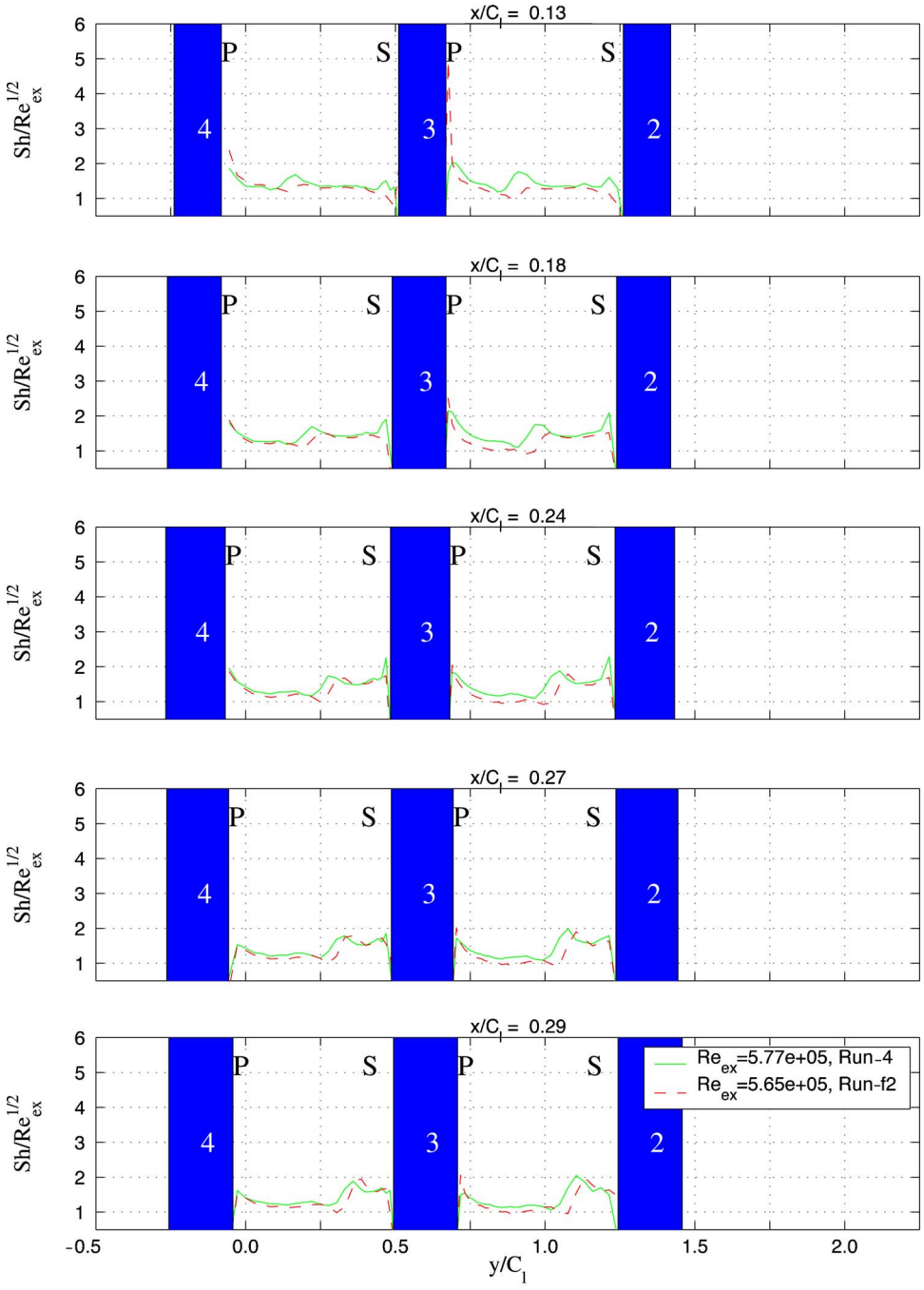


**Fig. 13 Sh number comparison at different streamwise position II**

For local measurements, about 5000 positions are selected to cover two flow passages on the mass transfer endwall.

To quantify the mass transfer results in the current setup, Stanton numbers on the endwall are compared with those from Goldstein and Spores [16]. They used active endwall and nonactive blades as in the current experiment but for a different blade geometry. Normalized Stanton numbers from the experiments with plain blades are compared at two different streamwise positions in Figs. 4 and 5. Even though Goldstein and Spores [16] used a blade which has a blunt leading edge, normalized Stanton numbers shows similar features at the different streamwise positions. $St_{mo}$ represents the Stanton number which is measured without blades, which is obtained from Goldstein and Spores [16].

**Low Turbulence Intensity.** The contour plots of the Sherwood number on the endwall are presented for a simple blade and a similar blade with fillets from Figs. 6–11. With no turbulence generator, the test flow has 0.2% turbulence intensity. With low turbulence intensity, the effect of the Reynolds number and the boundary layer thickness are plotted and compared. The boundary layer development is measured at four different streamwise positions, located from 400 to 600 mm ahead of the blade 3 leading edge. These hot-wire measurements confirm that there is a fully developed turbulent boundary layer in the cascade. Values of $\delta_1$ given in Table 1 are determined at the start of the naphthalene (mass-transfer) surface.

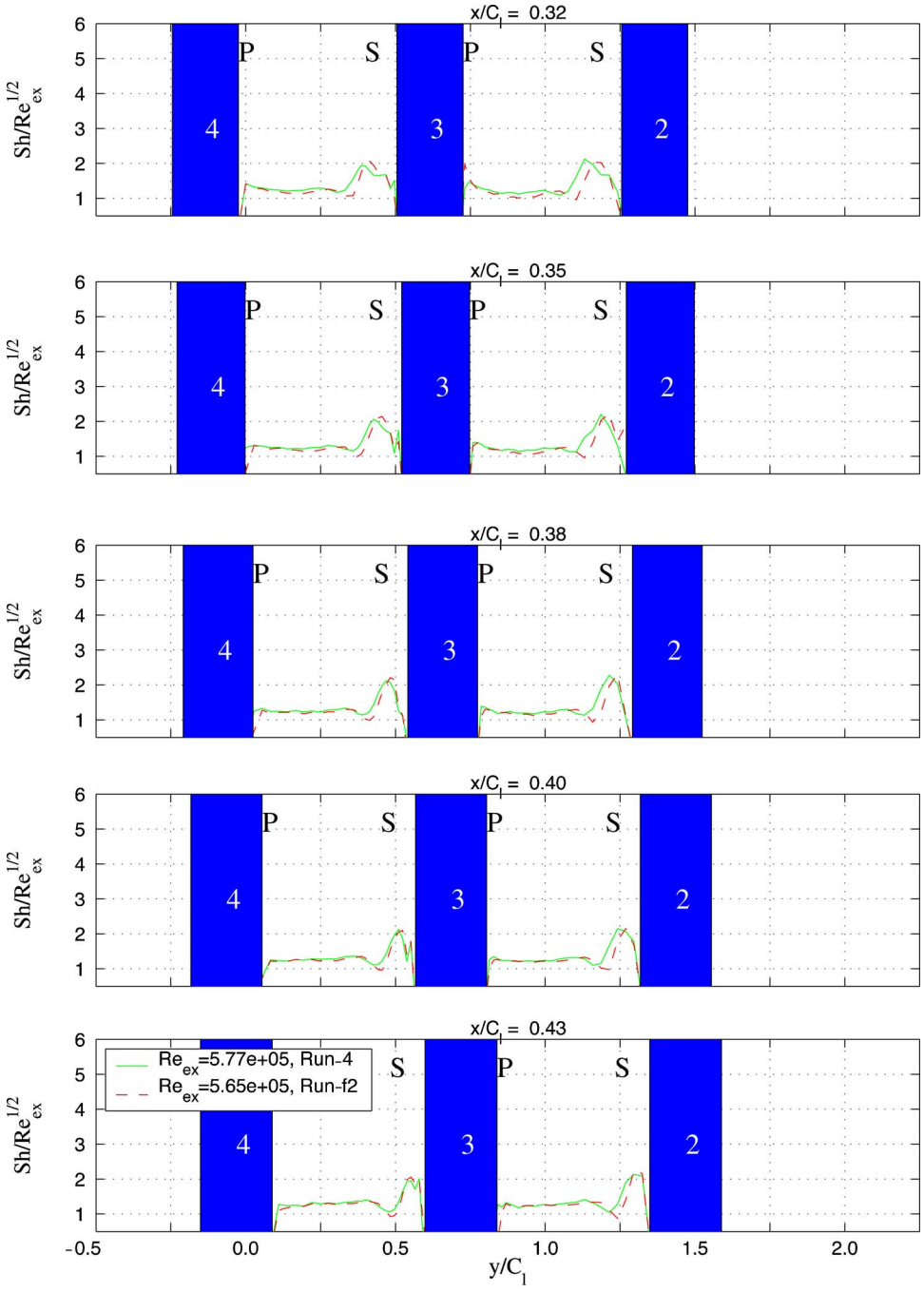


**Fig. 14 Sh number comparison at different streamwise position III**

Two experiments are conducted with 0.5 mm trip wire, which are Run-1 and Run-2 in Table 1. The 0.5 mm trip wire is used to check the effect of different boundary layer thickness and compare with additional heat transfer experiments which are not presented in this paper. The Sherwood number distribution of Run-1 is shown in Fig. 6 and that of Run-2 is presented in Fig. 7. They have a different Reynolds number and boundary layer thickness which cause a higher Sherwood number near the trailing edge in Fig. 7. Except for the higher Sherwood number near the trailing edge, any significant differences are not observed for a different Reynolds number. For easy comparisons, all contour plots have the same scale to show Sherwood number distribution. Note the blade numbers (cf. Fig. 1) are shown in the blades. With 5000 measurement points, a detailed local mass transfer and flow pattern are clearly observed on the endwall. The upgraded current measurement system in the Heat Transfer Laboratory, University of Minnesota, can measure 5000 points in an hour. Shorter measurement time reduces natural sublimation errors and enhances the reliability of the results.

For these tests with simple blades, the horseshoe vortex near the leading edge is clearly observed and leads to the development of the passage vortex near the pressure side of the blade. It should be noted here that the horseshoe vortex is caused by the roll-up of the inlet endwall boundary layer and is thus strongly influenced by the blade/endwall junction geometry (fillet). Conversely, the passage vortex forms because of the flow turning in the passage, and not because of the inlet endwall boundary layer. The high mass transfer regions caused by the passage vortex and the suction side

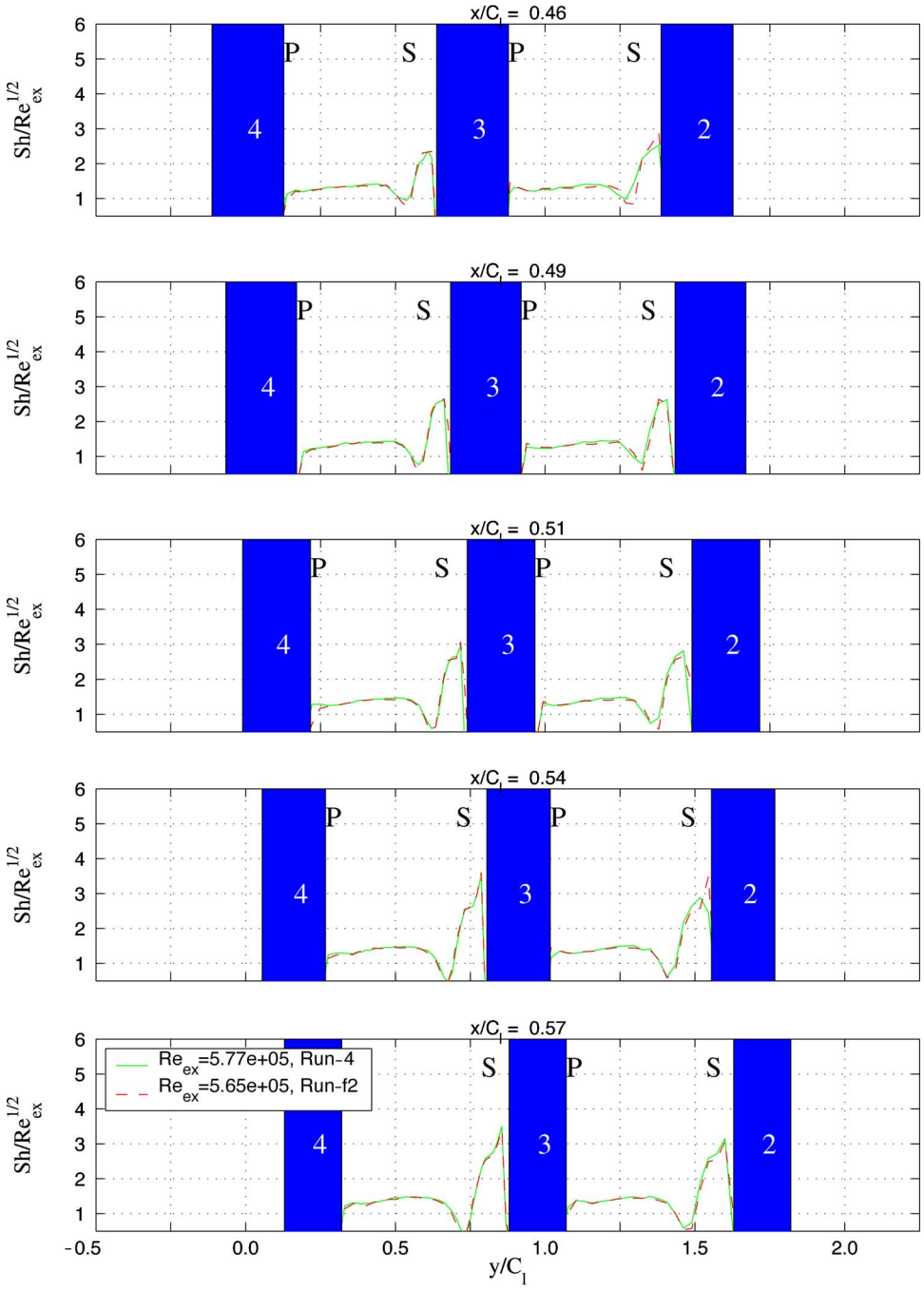


**Fig. 15 Sh number comparison at different streamwise position IV**

corner vortex continue down to the trailing edge and get higher close to the suction side near the trailing edge. A very low mass transfer region accompanies a high mass transfer region caused by the passage vortex and the suction side corner vortex. Beyond the trailing edge, vortex shedding from the blade generates high masstransfer regions. Near the leading edge, a high mass transfer is found in the region of the leading edge corner vortex. While a high mass transfer region by the suction side corner vortex is clear due to the strong passage vortex, the press side corner vortex is not clear. These vortices are visualized by Wang et al. [14] and agree with the location found from their mass transfer measurement. Normalized mass transfer results from two different Reynolds numbers agree well as shown in Figs. 4 and 5.

Figures 8 and 10 are plotted from Run-3 and Run-4 in Table 1. The main difference between Run-1 and Run-3 and between Run-2 and Run-4 is the boundary layer thickness due to the different trip wire. It does not make a noticeable difference in the Sherwood number distribution. Since a smaller trip wire did not change the Sherwood number distribution significantly, mass transfer experiments with fillets are conducted only with the 1 mm trip wire.

Mass transfer experiments with fillets at the different $Re_{ex}$ are presented in Figs. 9 and 11. The extended part in front of the blade indicates the fillet in the contour plots. With fillets, a high mass transfer region caused by the horseshoe vortex is not observed around the modified leading edge in Figs. 9 and 11. The passage vortex is weakened and delayed downstream. Along the suction side near the trailing edge, the passage vortex and the suction side corner vortex appear as strong with fillets as without fillets.

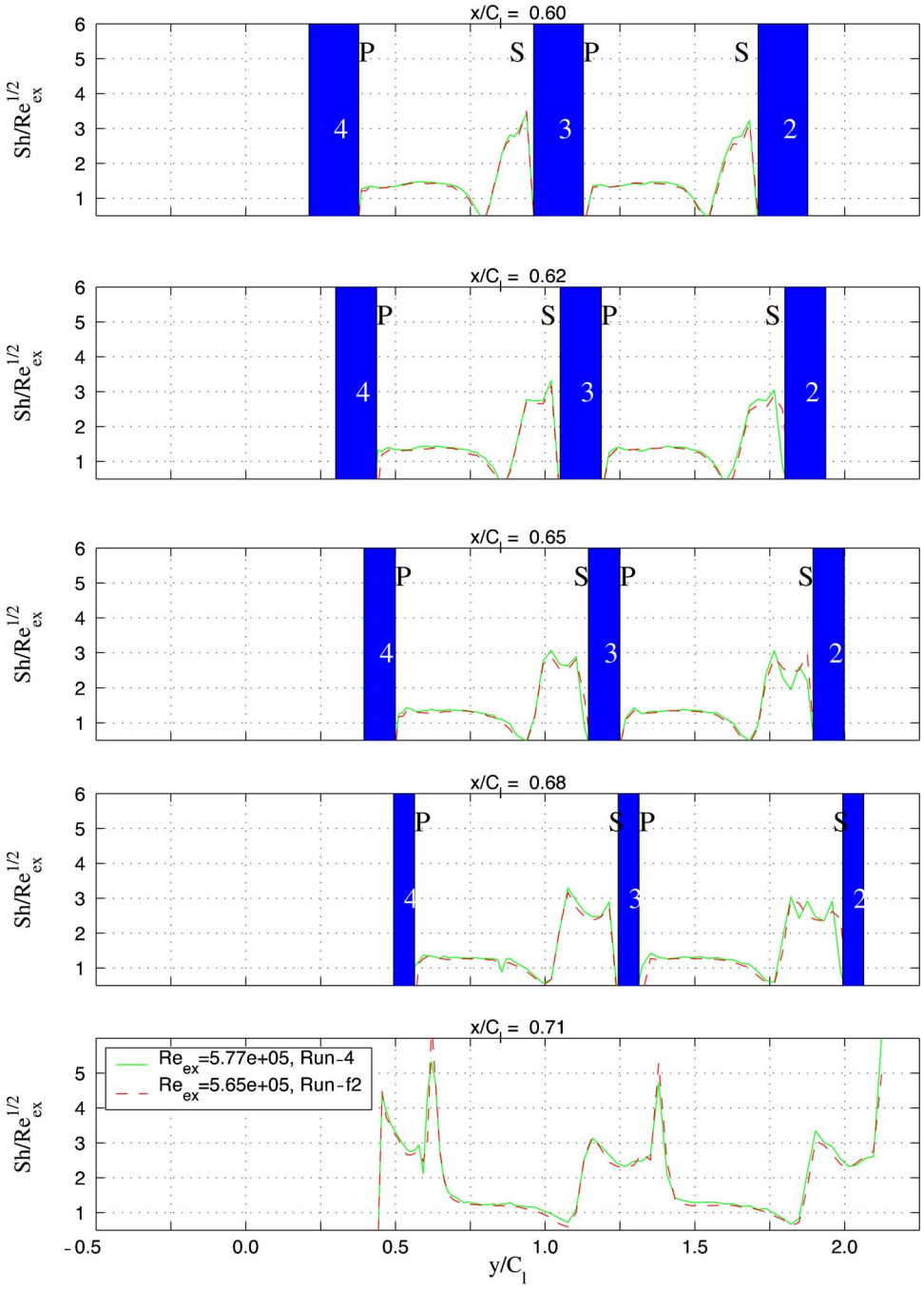


**Fig. 16 Sh number comparison at different streamwise position V**

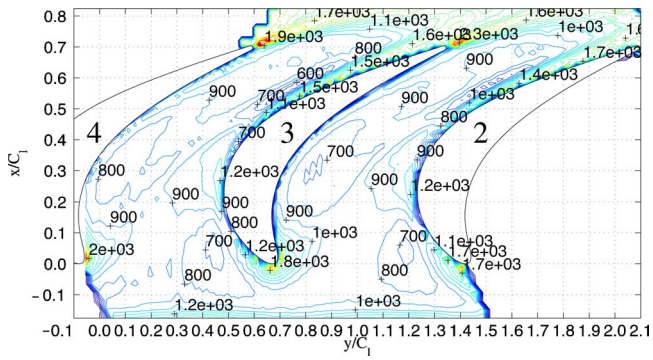


**Fig. 17 Sh contour plot (Run-5) with $Re_{ex}=4.27\times10^5$ and Tu =8.5%**

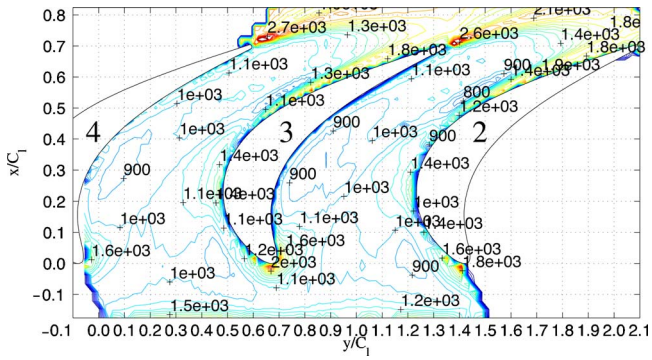


**Fig. 18 Sh contour plot (Run-6) with $Re_{ex}=5.67\times10^5$ and Tu =8.5%**

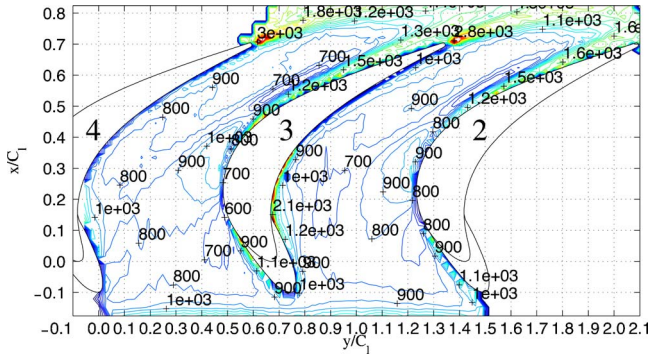


Fig. 19 Sh contour plot (Run-f3) with fillets, $Re_{ex}=3.57\times10^5$ and Tu=8.5%

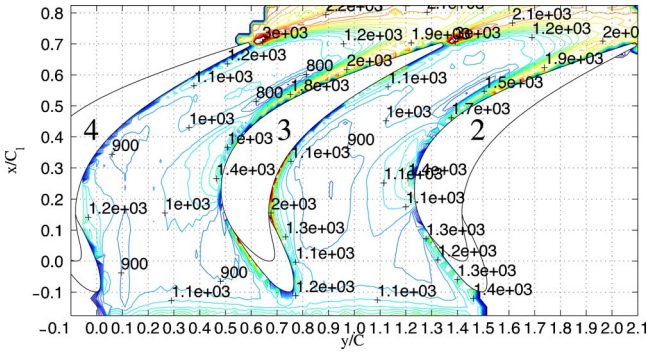


Fig. 20 Sh contour plot (Run-f4) with fillets, $Re_{ex}=4.97\times10^5$ and Tu=8.5%

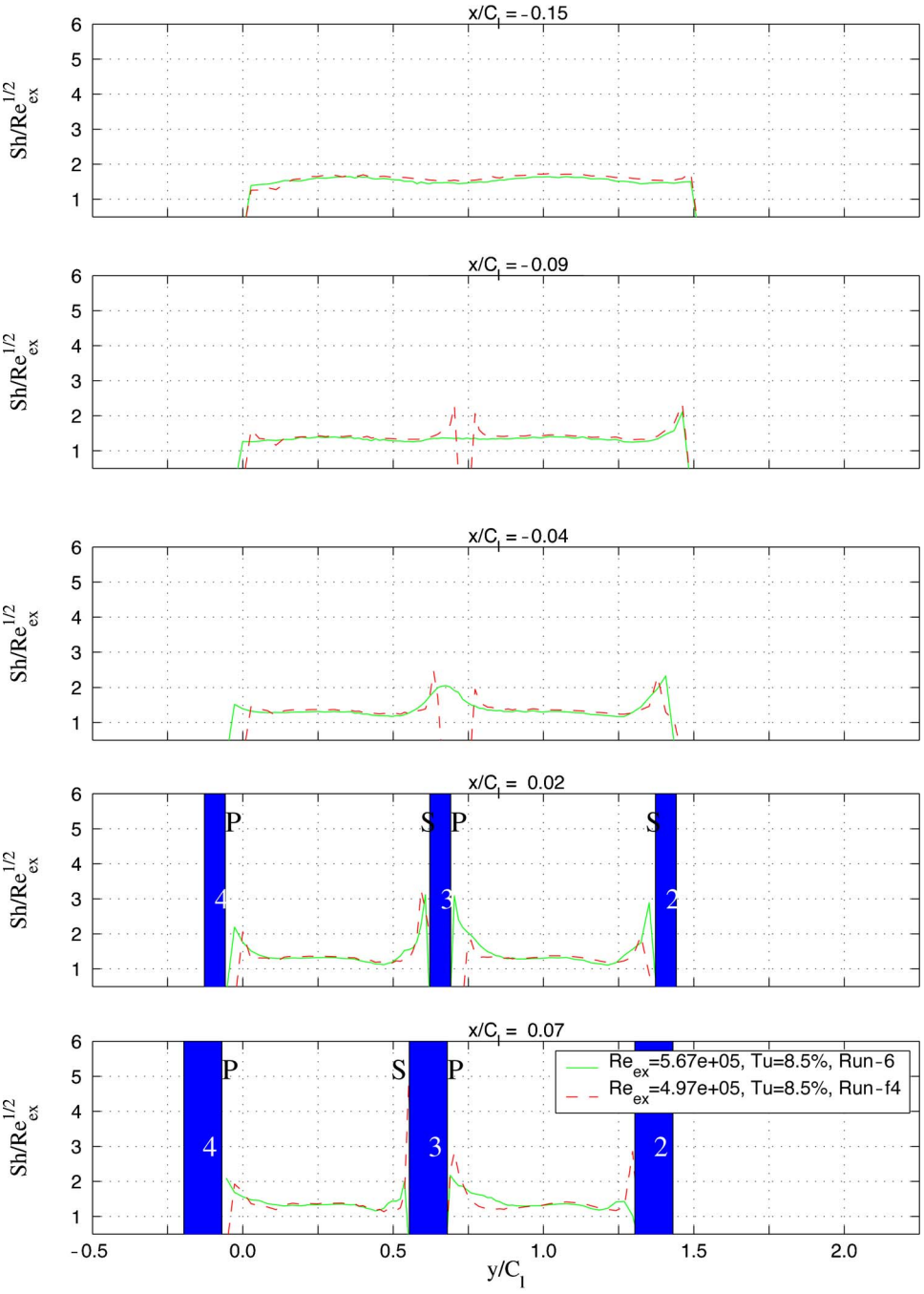


Fig. 21 Sh number comparison at different streamwise position I

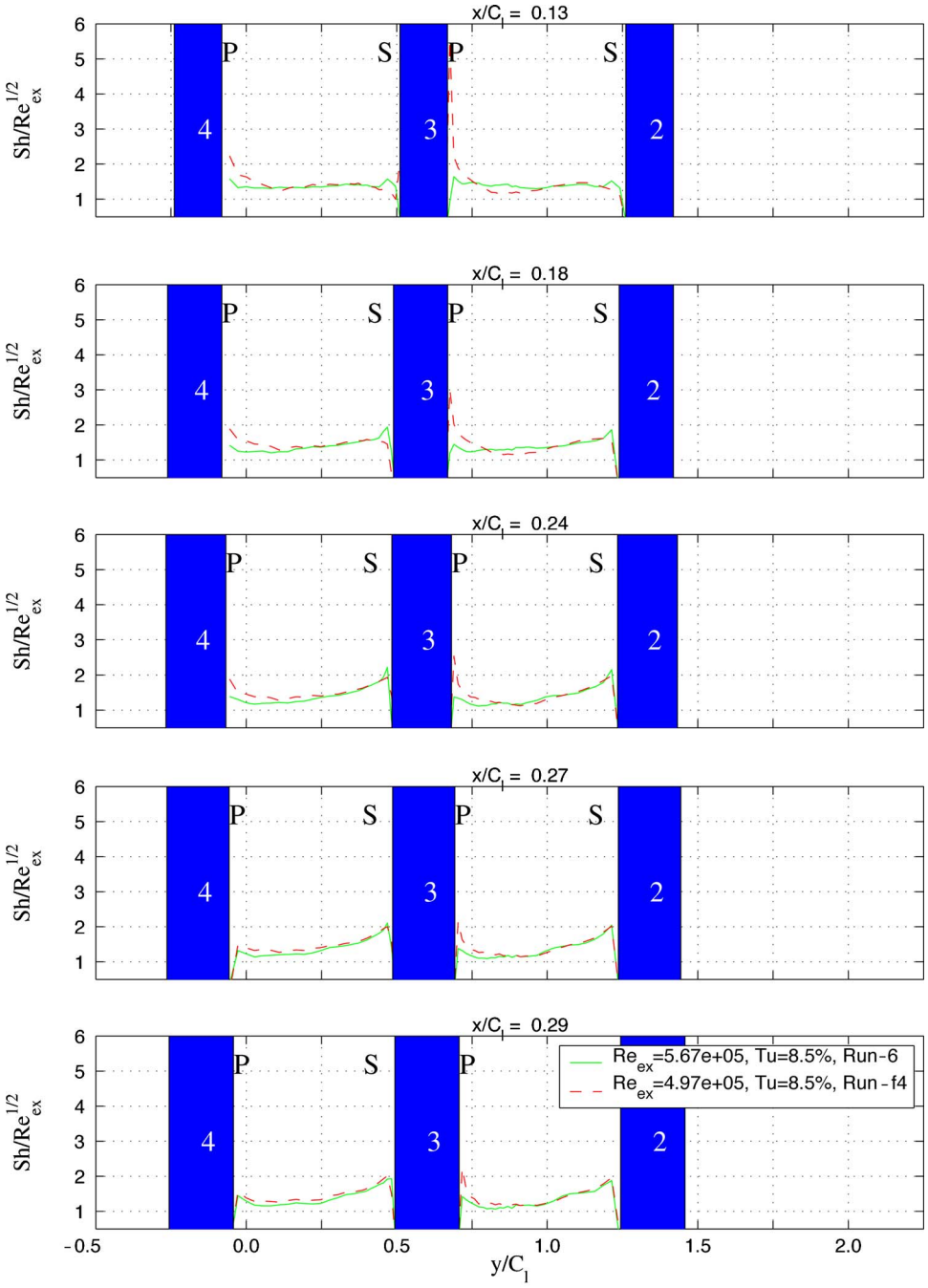


**Fig. 22 Sh number comparison at different streamwise position II**

Higher mass transfer regions are observed near the junction between the fillet and blade on the pressure and suction sides. High mass transfer regions by the leading edge corner vortices are extended beyond the middle of the blade on the pressure and suction sides with fillets.

Contour plots are not convenient to compare the Sherwood number quantitatively so that the Sherwood numbers for simple blades and similar blades with the fillets are plotted at different streamwise locations from Figs. 12–16. In these plots, the rectangular bars represent the turbine blades and change their widths at each streamwise position. The numbers inside of the rectangular bars represent the blade number. The letter "*P*" means the pressure side and the letter "*S*" means the suction side. Run-4 and Run-f2 are compared here at different streamwise positions between blades. At $x/C_1=-0.09$ (Fig. 12), a horseshoe vortex was observed for only fillet geometry. At $x/C_1=-0.04$, a horseshoe vortex was observed for both geometries. Figures 12 and 13 show that the passage vortex is delayed and weakened from $x/C_l=0.02$ to 0.18. Both near the pressure and suction side of the blade, somewhat higher mass transfer regions with the fillet are shown at $x/C_l=0.07$ and 0.13. These regions correspond to the leading edge corner vortices which are enhanced by the current fillets. After $x/C_l=0.32$ in Figs. 14–16, no significant difference is observed to the trailing edge.

**High Turbulence Intensity.** High turbulence intensity is generated by inserting a bar grid in the straight section. The turbulence intensity, measured one chord length upstream of the lead-

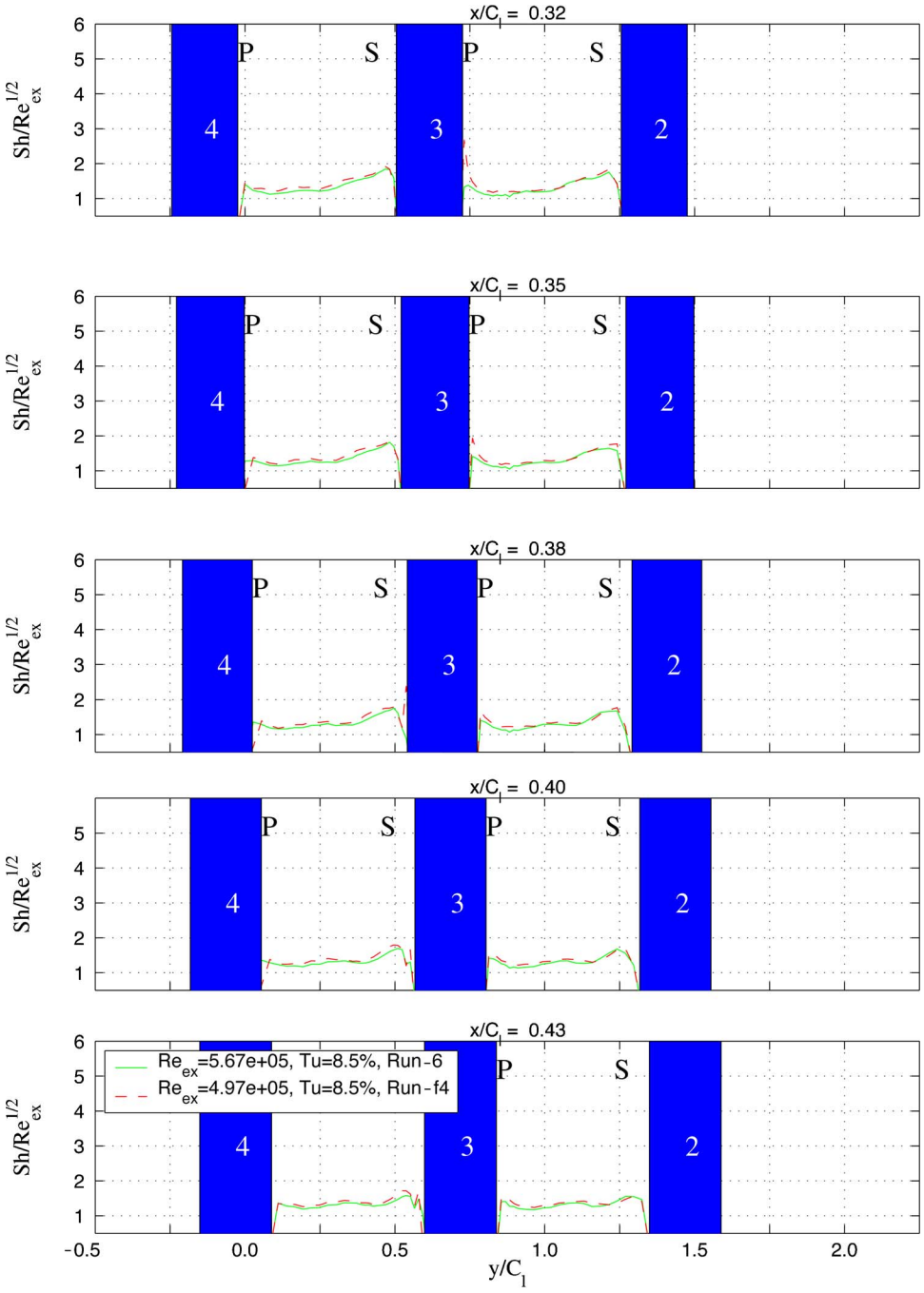


**Fig. 23 Sh number comparison at different streamwise position III**

ing edge of blade 3, is 8.5%. Since a smaller trip wire did not change the Sherwood number distribution significantly for the earlier tests, high turbulence experiments are conducted only with the 1 mm trip wire. Two different Reynolds number are selected.

Figures 17 and 18 are plotted from Run-5 and Run-6. High mass transfer regions near the leading edge are observed without fillets in Figs. 17 and 18. Compared with low turbulence intensity, the high mass transfer regions by the horseshoe vortex and the leading edge corner vortices are smaller. The high mass transfer region generated by the passage vortex is not clearly observed near the middle of blade unlike the experiments at low turbulence intensity. Near the trailing edge, high mass transfer regions are generated by the passage vortex and the suction side corner vortex, and are still present along the suction side. Due to high turbulence intensity, the starting position of the passage vortex is delayed and the strength of the passage vortex is weaker.

Sherwood number distributions in Figs. 19 and 20 show the effect of the fillets at high Tu. Figures 19 and 20 are plotted from Run-f3 and Run-f4 in Table 2, respectively. The high mass transfer region in front of the stagnation region is not observed, but the high mass transfer regions by the leading edge corner vortices are larger and stronger at the junction of the end of the fillet and blade. The high mass transfer region in the passage vortex region is not observed near the middle of the blade passage as in the experiments without fillets. However, high mass transfer regions along the suction side near the trailing edge still exist. With high

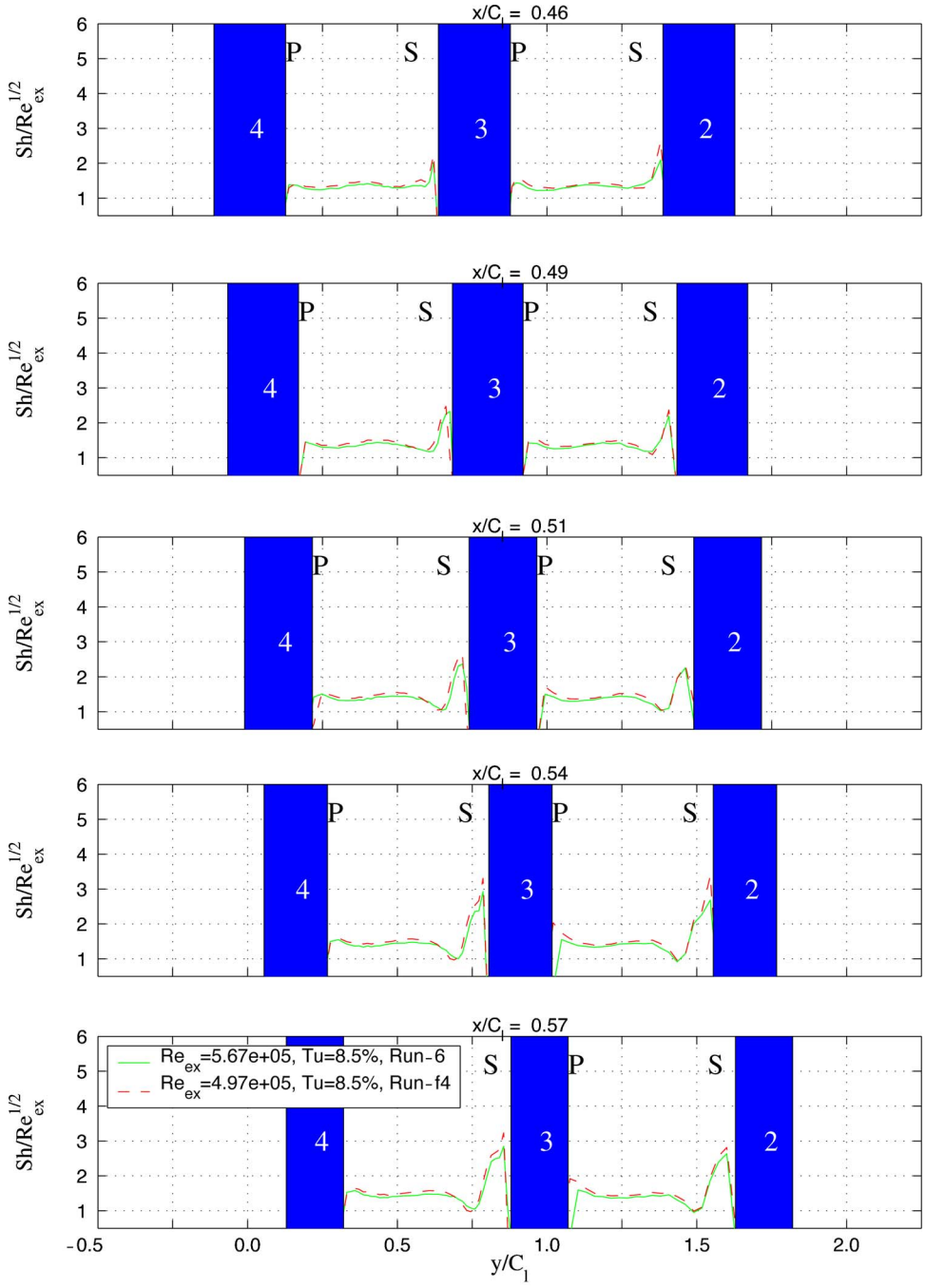


**Fig. 24 Sh number comparison at different streamwise position IV**

turbulence intensity, the Sherwood numbers are smaller than those in the experiments with low turbulence intensity near the trailing edge. The effect of the fillets which are used for the measurement is limited to the reduction of the horseshoe vortex, not to the reduction of the passage vortex with high turbulence intensity.

The Sherwood numbers for high turbulence flow are plotted between blades at different streamwise locations from Figs. 21–25. Run-6 and Run-f4 are compared at different streamwise positions between blades. At $x/C_1=-0.09$, a horseshoe vortex was observed for only fillet geometry (Fig. 21). At $x/C_1=-0.04$, a horseshoe vortex was observed for both geometries. The high mass transfer regions near the leading edge, generated by the horseshoe vortex, and leading edge corner vortices are clearly observed with a simple blade. At $x/C_l=0.07$ and 0.13 the development of the passage vortex is observed with a simple blade, but it disappears downstream at $x/C_l=0.18$ with a high turbulence intensity and with no fillets. Both near the pressure and suction side of the blade, somewhat higher mass transfer regions with the fillet are shown at $x/C_l=0.07$, 0.13, and 0.24. These regions correspond to the leading edge corner vortices which are enhanced by the current fillets. After $x/C_l=0.29$, the comparison of the Sherwood numbers does not show any significant difference with the high turbulence intensity.

Integrated $\mathrm{Sh}_{\mathrm{avg}}/\mathrm{Re}_{\mathrm{ex}}^{0.5}$ plots of the total mass transfer (averaged along radial direction ($y$-direction in Fig. 2)) without and with fillets at various streamwise positions are shown in Figs. 26 and 27, respectively. It is observed that blades with the fillets generate

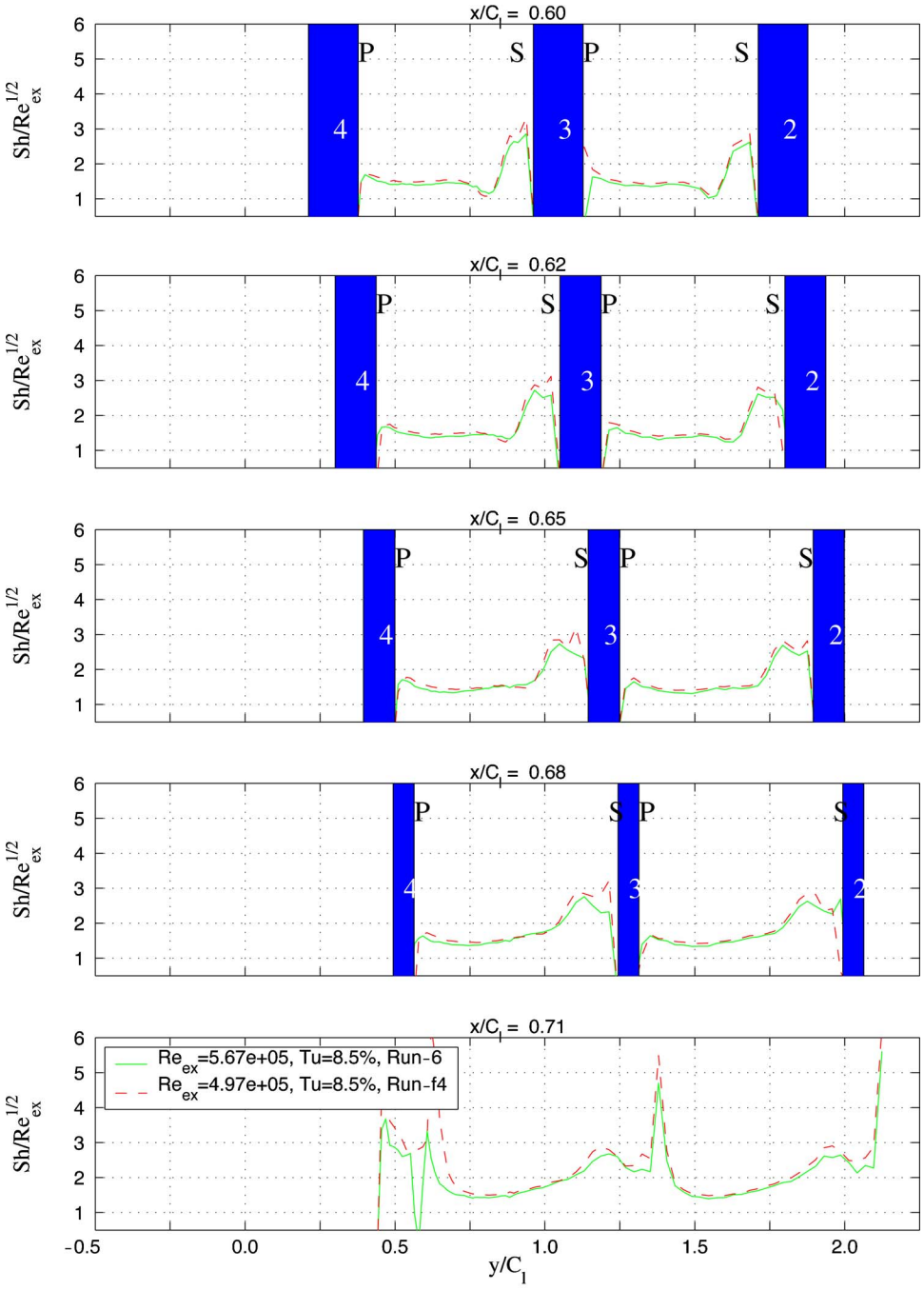


**Fig. 25 Sh number comparison at different streamwise position V**

a lower normalized Sherwood number until $x/C_l=0.1$ regardless of the turbulence intensity than the blades without the fillets. Compared with the pick value near $x/C_l=0.0$ without the fillet, the normalized Sherwood number in blades with the fillet show lowest values at $x/C_l=0.0$.

Sherwood numbers can be converted into Nusselt numbers with heat/mass transfer analogy. The analogy factor $(\mathrm{Nu}/\mathrm{Sh}=(\mathrm{Pr}/\mathrm{Sc})^n)$, 0.55 can be used to get a Nusselt number with Pr $=0.707$, Sc $=2.28$, and $n=0.5$. Even though Nusselt numbers are not presented in this paper, Nusselt numbers are measured in a heat transfer experiment with the same experimental conditions and agree with the Sherwood numbers with heat/mass transfer analogy.

## Summary

The heat (mass) transfer on a turbine endwall is evaluated with a simple blade and a similar blade with fillets. With low turbulence intensity, the fillet appears to significantly reduce the horseshoe vortex and delays formation of the passage vortex. The delayed passage vortex acquires strength near the trailing edge. With high turbulence intensity, the passage vortex is not clearly observed with a simple blade nor with a similar blade with fillets. The fillet significantly reduces the horseshoe vortex with a high turbulence intensity. With both lower and high turbulence intensity, the leading edge corner vortices on the pressure and suction side are enhanced by the fillet and generate a high mass transfer region.

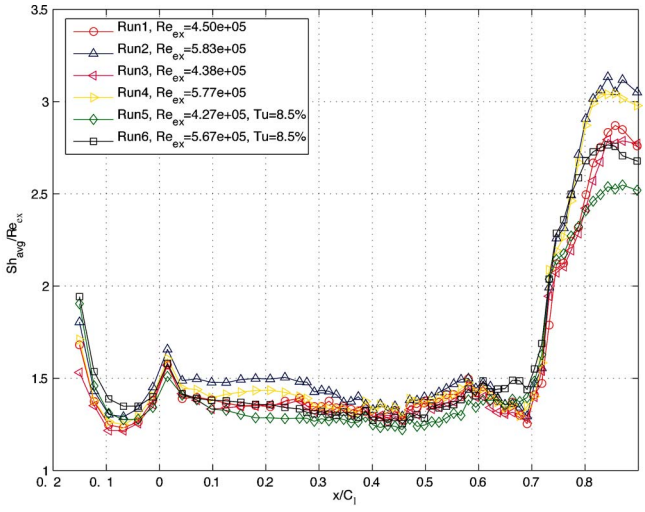


**Fig. 26 Integrated (averaged along radial direction) $Sh_{avg}/Re_{ex}^{0.5}$ at different streamwise positions (no fillet)**

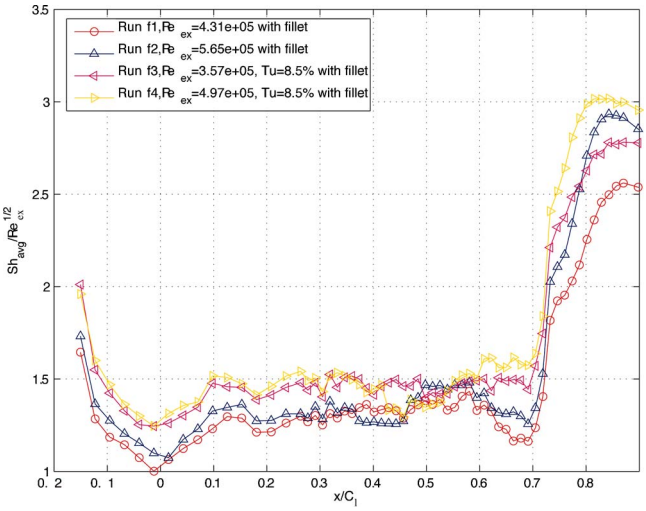


**Fig. 27 Integrated (averaged along radial direction) $Sh_{avg}/Re_{ex}^{0.5}$ at different streamwise positions (fillet)**


## Acknowledgment

This research was performed with financial support (02-01-SR096) from University Turbine System Research Program, Department of Energy.


## Nomenclature

AR = inlet/exit area ratio of the cascade, =2.72
$C_l$ = chord length of blade and characteristic length, =184 mm
$c_w$ = local wall concentration
$C_x$ = axial chord length of blade, =130 mm
$d$ = distance from a blade surface
$D_{naph}$ = mass diffusion coefficient
$h_m$ = convective mass transfer coefficient
$\dot{m}$ = mass flux per unit area
$M_{naph}$ = molecular mass for naphthalene, =129.17 kg/kmol
$P$ = pitch of blade, =138 mm
$p_{v,w}$ = naphthalene vapor pressure at the wall
$R$ = gas constant for naphthalene ($C_{10}H_8$) 0.06487 J/gK
$\bar{R}$ = Universal Gas Constant, =8.315 kJ/kmol K
$Re_{ex}$ = exit Reynolds number, $=\rho U_{ex} C_l/\mu$
Sc = Schmidt number, $Sc=\nu/D_{naph}\approx 2.28$ in the current study
Sh = Sherwood number, $Sh=h_m C_l/D_{naph}$
$Sh_{avg}$ = Sherwood number averaged along $y$ at a given $x$
$St_m$ = mass transfer Stanton number, $=Sh/(Re\cdot Sc)$ $=h_m/U_\infty$
$St_{mo}$ = mass transfer Stanton number without blades
$T_w$ = local wall temperature
$T_\infty$ = mainstream flow temperature
$T_{aw}$ = adiabatic wall temperature
$T_{n,w}$ = surface temperature of naphthalene
$U_\infty$ = mainstream velocity which is approaching blades
$U_{ex}$ = mainstream velocity at the exit of the cascade, $=AR U_\infty$

### Greek Symbols

$\delta$ = boundary layer thickness
$\delta_1$ = boundary layer displacement thickness
$\delta_2$ = boundary layer momentum thickness
$\delta\tau$ = time duration of data run
$\delta t$ = sublimation depth of naphthalene
$\nu$ = kinematic viscosity
$\rho$ = mainstream air density in wind tunnel
$\rho_s$ = density of solid naphthalene
$\rho_{v,\infty}$ = naphthalene vapor density in freestream flow, zero in present study
$\rho_{v,w}$ = naphthalene vapor density on the surface
$\tau_0$ = shear stress at the wall

### Subscripts

atm = atmosphere property
st = static property
$w$ = wall property

## References


[1] Burd, S. W., and Simon, T., 2000, "Flow Measurements in a Nozzle Guide Vane Passage With a Low Aspect Ratio and Endwall Contouring," ASME Paper No. 2000-GE-0213.
[2] Sauer, H., Müller, R., and Vogeler, K., 2000, "Reduction of Secondary Flow Losses in Turbine Cascades by Leading Edge Modifications at the Endwall," ASME Paper No. 2000-GT-0473.
[3] Becz, S., Majewski, M. S., and Langston, L. S., 2003, "Leading Edge Modification Effects on Turbine Cascade Endwall Loss," ASME Paper No. GT2003-38898.
[4] Becz, S., Majewski, M. S., and Langston, L. S., 2004, "An Experimental Investigation of Contoured Leading Edges for Secondary Flow Loss Reduction," ASME Paper No. GT2004-53964.
[5] Zess, G. A., and Thole, K. A., 2002, "Computational Design and Experimental Evaluation of Using a Leading Edge Fillet on a Gas Turbine Vane," ASME J. Turbomach., **124**, pp. 167–175.
[6] Shih, T.I.-P., and Lin, Y.-L., 2002, "Controlling Secondary-Flow Structure by Leading-Edge Airfoil Fillet and Inlet Swirl to Reduce Aerodynamic Loss and Surface Heat Transfer," ASME Paper No. GT-2002-30529.
[7] Lethander, A. T., Thole, K. A., Zess, G., and Wagner, J., 2003, "Optimizing the Vane-Endwall Junction to Reduce Adiabatic Wall Temperatures in a Turbine Vane Passage," ASME Paper No. GT2003-38939.
[8] Goldstein, R. J., and Cho, H. H., 1995, "A Review of Mass Transfer Measurements Using Naphthalene Sublimation," Exp. Therm. Fluid Sci., **10**, pp. 416–434.
[9] Ambrose, D., Lawrenson, I., and Sparke, C., 1975, "The Vapor Pressure of

Naphthalene," J. Chem. Thermodyn., **7**, pp. 1173–1176.
[10] Cho, K., 1989, "Measurement of the Diffusion Coefficient of Naphthalene Into Air," Ph.D. thesis, State University New York at Stony Brook, Stony Brook, NY.
[11] Chen, P. H., and Wung, P. H., 1990, "Diffusion Coefficient of Naphthalene in Air at Room Temperature," personal communication.
[12] Coleman, H. W., and Steele, W. G., 1999, *Experimentation and Uncertainty Analysis for Engineers*, 2nd ed., Wiley-Interscience, New York.
[13] Wang, H., 1997, "Local Mass Transfer Measurement From a Turbine Blade: Influence of High Turbulence With Large Length Scale on Heat/Mass Transfer," Ph.D. thesis, University of Minnesota, Minneapolis, MN.
[14] Wang, H. P., Olson, S. J., Goldstein, R. J., and Eckert, E. R. G., 1997, "Flow Visualization in a Linear Turbine Cascade of High Performance Turbine Blades," ASME J. Turbomach., **119**, pp. 1–8.
[15] Sung, C.-H., and Lin, C.-W., 1988, "Numerical Investigation on the Effect of Fairing on the Vortex Flows Around Airfoil/Flat-Plate Juctures," AIAA Paper AIAA-88–0615.
[16] Goldstein, R. J., and Spores, R. A., 1988, "Turbulent Transport on the Endwall in the Region Between Adjacent Turbine Blades," ASME J. Heat Transfer, **110**, pp. 862–869.

Journal of Turbomachinery

Technology Review

# Overview of Creep Strength and Oxidation of Heat-Resistant Alloy Sheets and Foils for Compact Heat Exchangers

**Philip J. Maziasz**
e-mail: maziaszpj@ornl.gov

**John P. Shingledecker**

**Bruce A. Pint**

**Neal D. Evans**

**Yukinori Yamamoto**

**Karren More**

**Edgar Lara-Curzio**

Oak Ridge National Laboratory,
Metals and Ceramics Division,
Oak Ridge, TN 37831-6115

*The Oak Ridge National Laboratory (ORNL) has been involved in research and development related to improved performance of recuperators for industrial gas turbines since about 1996, and in improving recuperators for advanced microturbines since 2000. Recuperators are compact, high efficiency heat-exchangers that improve the efficiency of smaller gas turbines and microturbines. Recuperators were traditionally made from 347 stainless steel and operated below or close to* 650°C*, but today are being designed for reliable operation above* 700°C. *The Department of Energy (DOE) sponsored programs at ORNL have helped defined the failure mechanisms in stainless steel foils, including creep due to fine grain size, accelerated oxidation due to moisture in the hot exhaust gas, and loss of ductility due to aging. ORNL has also been involved in selecting and characterizing commercial heat-resistant stainless alloys, like HR120 or the new* AL20-25+Nb*, that should offer dramatically improved recuperator capability and performance at a reasonable cost. This paper summarizes research on sheets and foils of such alloys over the last few years, and suggests the next likely stages for manufacturing recuperators with upgraded performance for the next generation of larger* 200–250 kW *advanced microturbines.*
[DOI: 10.1115/1.2187525]

## Introduction

Microturbines are ultraclean, relatively quiet, and fuel flexible, and are attractive for distributed generation (DG), combined heat and power (CHP), and possibly combined cycle (microturbine-fuel cell) applications. DG can immediately remedy some of the power transmission grid problems and deficiencies that were magnified by the Blackout of 2003 in the Midwestern and the Northeastern U.S. [1]. Microturbines can also play an important role in various homeland security strategies in the U.S. by removing critical facilities, like hospitals and water treatment plants and infrastructure, from dependence on the electric grid [1,2]. Recuperators are the compact heat exchangers necessary for high-efficiency, advanced microturbines; however, recuperators are also a costly and challenging component of such systems that limit maximum operating temperature and lifetime [3–5]. Recuperators for industrial turbines and microturbines have traditionally been made from 347 stainless steel, but problems with performance and durability are becoming evident for such steels as temperatures approach or exceed 675–700°C, particularly in moist air. Economic and efficiency advantages have pushed microturbine engine sizes up from 30–70 to 200–250 kW, for both stand-alone power generation and CHP applications. If microturbines are used to generate power during peak demand, then cycling will further challenge the recuperator with thermal shock during rapid heat-up. Durable, reliable recuperators (and packaging or ducting) are critical components for any attractive microturbine systems.

## Recuperator Development Over the Last Decade

Today, there are two main types of recuperator used on commercial microturbines in the U.S. Both are compact, counterflow recuperators with high effectiveness, and both are designed for high quality mass manufacturing at a reasonable cost [4]. One type is the primary surface recuperator (PSR), designed by Solar Turbines and Caterpillar; it consists of welded air cells made from folded foils, and is used in several different kinds of final geometries [3–6]. Rectangular PSR air cell stacks positioned horizontally above the engine have been employed in various Solar Turbines industrial gas turbines, in Honeywell 75 kW microturbines, and most recently, in the new Mercury 50 4.6 MW gas turbine engine [7]. The Capstone Turbines microturbine systems (30, 60, and new 200 kW units) all have used specially-designed annular essemblies of the PSR air cells, which surround the turbine [8]. The other type is the brazed plate and fin recuperator (BPFR), which includes (a) the completely-brazed, vertical stack developed by Toyo [5], and (b) the uniquely-designed air cells of folded foils brazed to sheet-plates which are also stacked vertically and were developed by Ingersoll Rand for their PowerWorks 70 kW, and new 250 kW, microturbines [9]. The Ingersoll Rand BPFR made from foils and sheets of alloy 625 is also employed on the

Contributed by the International Gas Turbine Institute (IGTI) of ASME for publication in the JOURNAL OF TURBOMACHINERY. Manuscript received October 1, 2004; final manuscript received February 1, 2005. IGTI Review Chair: K. C. Hall. Paper presented at the ASME Turbo Expo 2005: Land, Sea and Air, Reno, NV, June 6–9, 2005, Paper No. GT2005-68927.

  

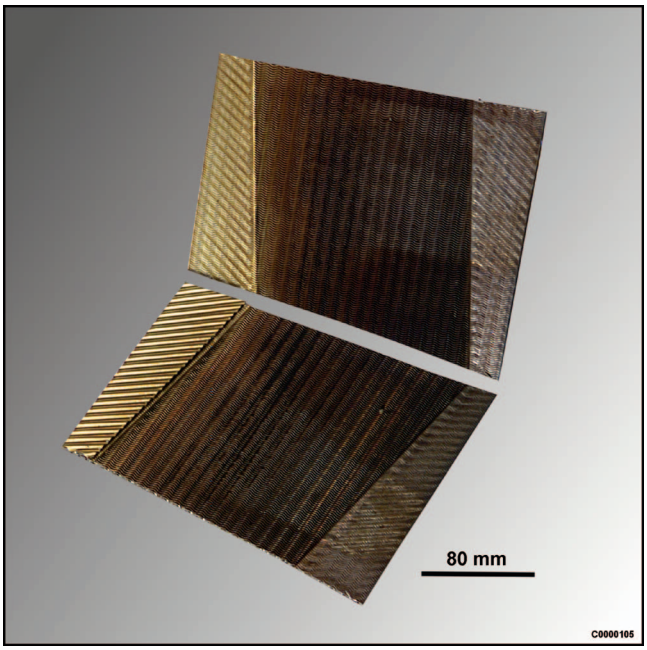


**Fig. 1 Photograph of two PSR aircells from a Honeywell recuperator made from 347 stainless steel foil, after relatively short term microturbine exposure. The darker right-hand portion of the air cell has seen the maximum temperature and oxidation, whereas the lighter golden left-hand side has seen a lower temperature and has developed a slight heat tint; this indicates the temperature gradient across the air cell that such components typically have due to the counterflows of cool air and hot exhaust. This component showed no evident of AA yet.**

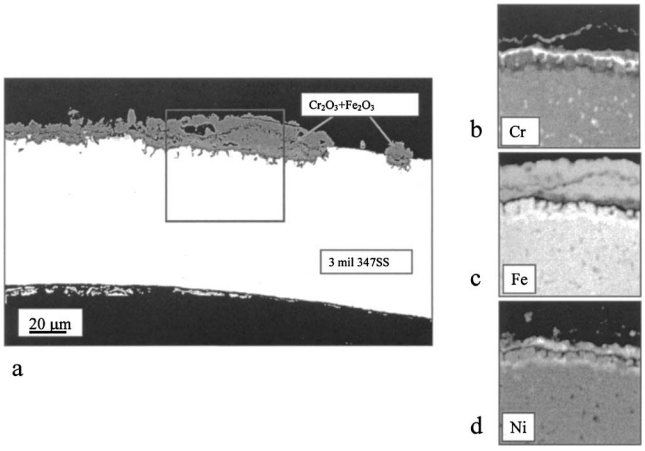


**Fig. 2 (a) Scanning electron microscope (SEM) backscattered electron (BSE) imaging of 347 stainless steel air-cell foil cross section from a recuperator with significant service in a microturbine. It shows (*a*) the formation of heavy, Fe-rich oxide nodules at the exhaust-side surface (higher % of $H_2O$) that are characteristic of the onset of AA due to oxidation in the presence of water vapor. Higher magnification SEM x-ray mapping images using $K\alpha$ peaks of the elements indicated show the complex nature of the surface oxides for the elements (*b*) Cr, (*c*) Fe, and (*d*) Ni. The thick outer oxide scale is Fe-rich (*c*), with a thin Cr-rich oxide (*b*) and a Ni-depleted region in the sub-surface metal beneath (*d*).**

Rolls Royce WR21 advanced cycle gas turbine designed for naval marine applications [10]. Another type of primary surface recuperator is the spirally-wrapped recuperator, manufactured by continuously spooling foils or sheets [5], with different designs and sizes being developed by Rolls Royce [11] and by Acte, S.A. [12].

Development of durable and reliable recuperator technology has paralleled and been pushed by the introduction of commercial microturbines in 1996-1997, in conjunction with the initial and continuing phases of a collaboration by Southern California Edison, U.S. Department of Energy (DOE), and others to study the installation, operation, and maintenance of microturbines to promote distributed power generation [13,14]. Another driver for the development of higher temperature recuperators came from the DOE Advanced Microturbine Program in 2000 [15], which included the ambitious goal to design and build microturbines with efficiencies of 40% or more. Prior to 2000, recuperators were made almost exclusively from 347 stainless steel (Fig. 1) [5,16], and generally performed well at temperatures below 650°C (1200°F). More recent research has highlighted the problems that can limit the performance of 347 stainless steel at 675–700°C (about 1250–1300°F) and above, particularly the accelerated attack (AA) caused by moisture enhanced oxidation at these conditions (Fig. 2) [17,18]. Larger microturbines with higher efficiencies will also operate with higher temperatures and pressures in the recuperator. Focused research on the DOE Advanced Microturbines Program over the last several years has defined and addressed the needs for better metal foils and sheets that can withstand prolonged use at higher temperatures, but which also still remain affordable for recuperator applications.

## Summary of Challenges to Metal Sheet/Foil Recuperators

The first challenge is, of course, manufacturing the desired components, but by far the greatest challenge is long-term operation at elevated temperatures without failure. While the minimum need for recuperators is to survive until scheduled maintenance intervals (5000 to 10,000 h), the desired lifetime is the same as that of the overall microturbine system, which can range from 40,000 to 80,000 h [13,15]. Both PSR and BPFR air cells are made using high-quality, automated and/or continuous manufacturing processes that produce consistent results, and each air cell is pressure checked at room temperature to ensure no leakage [8,9].

In service, several metallurgical effects of high-temperature exposure can degrade recuperator performance prior to the cracking that causes leakage of pressurized air into the exhaust, or the severe deformation that reduces effectiveness. These effects include oxidation, creep, fatigue, and aging-induced precipitation in the matrix and along grain boundaries of the alloy. For 347 stainless steel, such effects are not significant at 1100–1200°F, become concerns at 1200–1250°F, and can be severe at 1300°F and above. Creep can close the exhaust gas passages of a PSR to restrict gas flow, and the heavy ferrous oxide growth on the surfaces of foils associated with severe AA can reduce thermal conductivity and heat transfer. Oxidation resistance is mainly a function of alloy composition (Cr and Ni contents [19]), but oxidation, creep and aging behavior can all also be affected by metallurgical processing parameters (i.e., grain size, solution annealing (SA) temperature, dispersion and abundance of various precipitate phases).

The significant differences in manufacturing processes between PSR and BPFR air cells may also affect how they behave, particularly for service above 1300°F. The PSR air cells are made from folded foils of 347 stainless steel that are 0.003 to 0.005 in. thick, and are welded to similar steel wire or bar (321 or 347 steel) to form the seal at the end. Folding produces from 5 to 15% cold strain in the foil, depending on the location along the fold. However, the ends of the foil near the weld are crushed flat prior to welding, so they may be cold-worked 30% or more. Relative to SA material (which is usually tested to produce properties data), 20–25% cold-working can enhance the formation of deleterious intermetallic phases ($\sigma$, Laves) during aging, and would certainly cause recrystallization of the original grain structure into a new

fine-grained microstructure, with details that are very sensitive to minor or impurity alloying elements in austenitic stainless steels [20–22]. Moreover, 5–15% cold work can cause either accelerated or retarded creep-rates [20–22]. By contrast, BPFR air cells are welded to seal the ends and then brazed, which removes all prior cold deformation and restores all the materials in the air cell to a SA condition. However, the braze joint and its effects on the bonded stainless steel sheets and foils are an additional and unique factor that needs to be considered for this kind of recuperator. To date, there are no systematic studies or data to address all of these concerns, but data should be accumulated as ongoing studies of turbine-exposed or failed air cells continue, particularly the studies from the ORNL Recuperator Test Facility [23].

## Selection and Evaluation of Advanced Alloys for Recuperators With Higher-Temperature Capability

**Creep-Rupture Testing of Advanced Alloys.** Advanced alloy sheets and foils with higher-temperature capability and more reliability than type 347 stainless steel (Fe-18Cr-10Ni) above 700°C are heat- and corrosion-resistant alloys with more Cr and more Ni, plus various other alloying elements added for more strength. However, these elements, particularly Ni, make better alloys more expensive, so that higher cost must also be balanced with improved performance. Relative to the same alloys made as coarse-grained plate or tubing, fine-grained foils tend to be much weaker in creep; therefore, there is no guarantee that alloy rankings from strongest to weakest will be the same for both foil and plate products. ORNL worked with Solar Turbines and Allegheny-Ludlum in 1996–1999 to define creep properties of foils of type 347 stainless steel, and lab-scale experiments led to modified processing parameters for improved creep-rupture resistance [22,24]. In 2002–2003, ORNL and Allegheny Ludlum engaged in a follow-up commercial-scale 347 steel foil and sheet processing effort [25–27], and produced AL347HP™ with more creep-resistance, which is now commercially available [27]. However, improved creep strength and rupture resistance for foils and sheets of 347 steel still does not solve the inherent oxidation and AA problem; oxidation data in air with 10% $H_2O$ shows severe AA after only about 1000 h at 650°C [25,26,28].

Since about 2000, there have been several broader studies considering the properties of foils made from a range of heat-resistant and corrosion resistant alloys for microturbine applications [16,23,25,26,28–32]. These alloys can be divided into two groups, one for alloys that can be used from 650 to up to 800°C, and the other for use at 800°C and above. Many of these alloys are also considered and used for many other high-temperature applications of thicker, larger components, including power boiler and turbine applications [33–36]. For temperatures above 800°C, Ni-based alloys with aluminum, for example HR214, or the Fe-based oxide dispersion-strengthened (ODS) Plansee alloy, PM2000, have both the strength and oxidation resistance as sheets and foils to be used for recuperators. However, fabricating and manufacturing recuperator air cells or components from such alloys may be more difficult, and their cost is at least ten times that of 347 stainless steel. There are several commercial or near-commercial alloys that show good strength and oxidation resistance at 650–750°C, including alloy 625 (Ni-22Cr-9Mo-3.5Nb), HR120 (Fe-25Cr-35Ni–Mo,Nb,N) and the new AL20-25+Nb (Fe-20Cr-25Ni–Mo,Nb,N), which are 2–4 times more expensive that 347 steel. ORNL efforts in the last few years have focused on testing and evaluating commercial sheets and foils of these particular alloys, because of their interest to recuperator manufacturers.

Results of creep testing of recent commercial sheets and foils obtained from commercial materials producers or from recuperator manufacturers, creep-rupture tested at 750°C and 100 MPa, are shown in Fig. 3. PM2000 sheet showed virtually no creep (even at 120 MPa), and alloy 625 showed very little after 7000–8000 h (both tests are ongoing). Previous results for alloy 625 foil

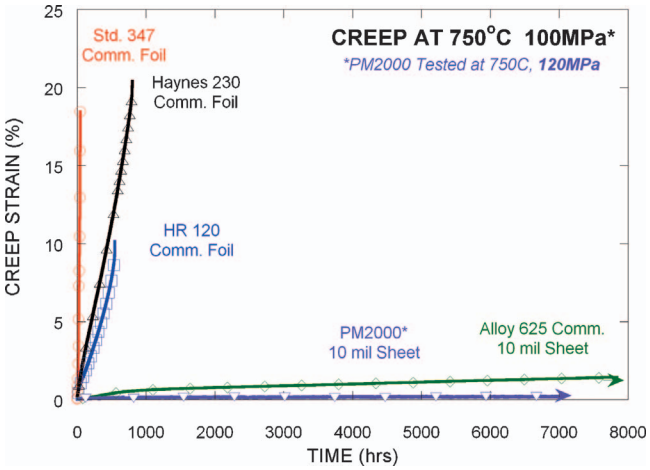


**Fig. 3 Creep data for commercial sheets and foils tested at 750°C and 100 MPa (except for the PM2000 ODS alloy, tested at 120 MPa) in air. The 3–4 mil (0.003–0.004 in. thick) foils crept at a high rate with little secondary creep regime, but both the HR120 and HR230 alloy foils exhibited almost 10 times longer rupture life than typical 347 steel foil. By contrast, both alloy 625 and the PM2000 (ODS ferritic alloy) exhibited a prolonged secondary creep regime, with a very low creep rate, and lasted more than 100 times longer than 347 steel (still in test).**

with lab-scale processing at ORNL indicated rupture after only about 4500 h at the same creep conditions, so that the commercial sheet is much stronger. Both alloy 625 and PM2000 would have advantages for recuperators in which strain limits, rather than rupture, define lifetime. Alloy 625 is being used for the PSR for the Solar Turbines Mercury 50 industrial turbine engine [7], and for the Ingersoll-Rand BPFR used with the Rolls-Royce WR-21 marine turbine engine [10]. Given the combination of cost and creep resistance, alloy 625 is clearly the most cost effective at about 3.5–4 times the cost of 347 steel [9,16]. Foils of HR120 and HR230 (0.003–0.004 in. thick) show much less creep resistance than alloy 625, but are still about ten times better than 347 steel.

The effects of grain size/processing on creep resistance at these conditions are shown for HR230 in Fig. 4 and HR120 in Fig. 5. Thicker products (boiler-tubing, plate) of HR230 showed much

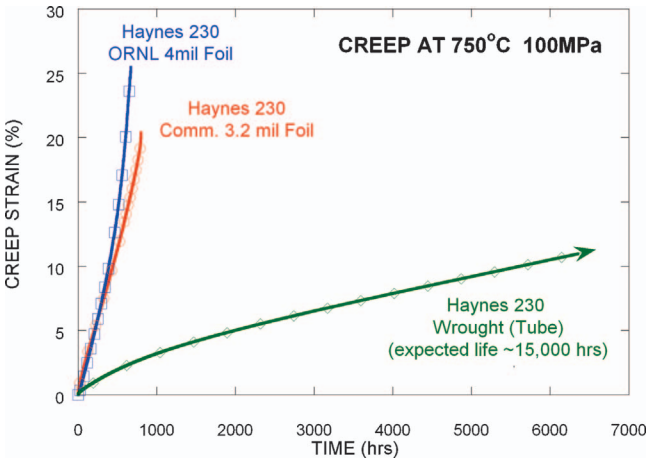


**Fig. 4 Creep tests of fine-grained foils and coarser-grained tubing of HR230, illustrating the fine-grain size effect, which dramatically reduced or eliminated the secondary creep regime, when that grain size was below the critical grain size for creep resistance. Such data are the basis for the premise that foil behavior cannot be predicted from creep data on tube or plate of the same alloy.**

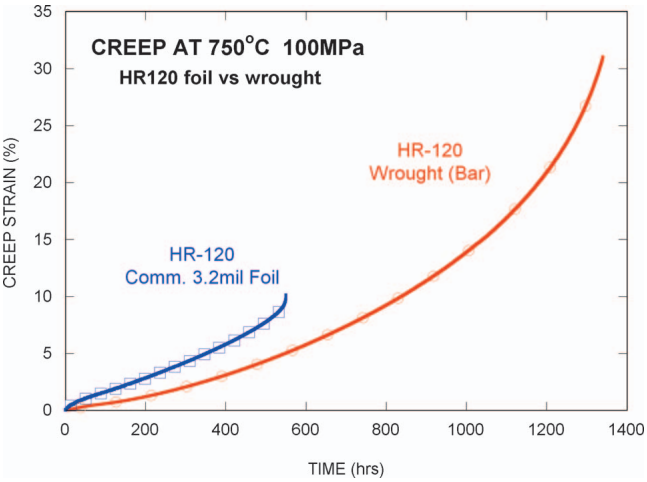


**Fig. 5 Creep testing of foil and bar of alloy HR 120 shows roughly parallel creep curves, despite significant differences in processing and grain size between these specimens**

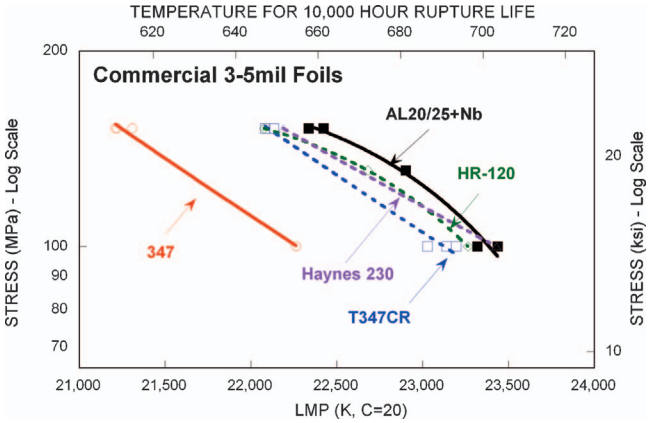


**Fig. 6 Larson-Miller Parameter (LMP) plot of creep data for commercial foils of several different alloys, tested at 704–750°C and 100–150 MPa in air. Creep-rupture stress is plotted against the LMP, calculated from both the test temperature and rupture-time to unify the data from different test conditions. The foils include 347 and T347CR (AL347HP) austenitic stainless steels, the new AL20-25+Nb and HR120 austenitic stainless alloys, and HR230 Ni-based superalloy. Clearly the AL20-25+Nb has creep strength as good as or better than HR120 and HR230, and much better than standard 347 stainless steel.**

more creep resistance than foils [36], indicating that these foils have a grain size below the critical grain size for creep resistance in this alloy (typically 10–20 $\mu$m grain size). Processing and microstructural behavior during aging determine such creep behavior, with foils usually being exposed to somewhat lower processing temperatures, and much shorter processing times than plate or tubing products. Given the tubing behavior, it is unlikely that sheet of HR230 would perform as well as alloy 625, and at 8–9 times the cost of 347 steel, HR230 is not a cost-effective choice.

By contrast, the creep-rupture resistance of HR120 is similar for foil and bar products (Fig. 5), indicating much less sensitivity to grain size/processing than HR230. However, previous ORNL data on a similar foil showed 2–3 times better creep resistance for the same test conditions [25,32], so that there is clearly a need for more data to better define the typical creep resistance of such foils and their microstructural characteristics. It is likely that HR120 sheet would have similar creep resistance as foil, and at about 3.5 times the cost of 347 steel, this also represents a cost-effective performance upgrade, particularly considering its excellent oxidation resistance.

Creep-rupture testing on this group of alloys was also performed at 704°C (1300°F) and 150 MPa, because most near-term microturbine recuperators would benefit from reliable materials that can be used at or slightly above this temperature; data are shown in Fig. 6. Alloy 625 sheet was very creep-resistant (test is ongoing), while 347 steel foil was very weak. The two foils of HR120 alloy behaved differently, with one being only slightly weaker at 704°C, and the other being several times weaker than the same foils tested at 750°C [25,26].

In 2003–2004, Allegheny Ludlum introduced a new high temperature alloy, AL20-25+Nb, which was developed together with Solar Turbines for foil recuperator applications [6]. This alloy is another in a group of improved alloys based on the austenitic stainless alloy composition of Fe-20Cr-25Ni developed during the 1980s, which includes British work on that alloy for high-temperature gas-cooled fission reactors, Nippon Steel Corp.'s NF709 and Sandvik's 12R72HV, for fossil energy boiler tubing with more corrosion resistance and creep strength than 17-14CuMo and 347H stainless steels [34,37–39]. ORNL made some lab-scale foils, rolled from slit and flattened NF709 boiler tubing, for creep and oxidation testing in 2001–2003 [25,26,28]. Based on these preliminary results, interest from the microturbine recuperator manufacturers, and potential for pricing in between the cost of 347 steel and alloy 625, ORNL and Allegheny defined a joint project in 2004 to expand commercial foil development for microturbine recuperator manufactures. In 2005, Phase I of this project produced 10 and 15 mil sheets and 4, 5, and 8 mil foils in commercial quantities, suitable for manufacturing trials of both the PSR and the BPFR recuperator aircells. ORNL has completed the initial creep-testing and some microstructural analyses of the Phase I trials of AL20-25+Nb alloy foils (0.003 to 0.005 in. thick). Creep rupture data for such foils of the AL20-25+Nb alloy creep-rupture tested at 704–750°C and 100–150 MPa are shown in Fig. 6, with rupture stress plotted against Larson-Miller Parameter (LMP). Data from similar creep-rupture testing of foils of standard 347 austenitic stainless steel, AL347HP(T347CR) with modified processing for enhanced creep resistance [25–27], HR120 austenitic stainless alloy, and HR230 Ni-based superalloy are also included in Fig. 6. The AL20-25+Nb (Phase I) is somewhat stronger than HR120 and HR230 alloys, stronger than AL347HP, and much stronger than standard 347 stainless steel. Generally the AL20-25+Nb alloy shows very good creep-rupture ductility as well. Based on these initial data, ORNL and Allegheny-Ludlum later in 2005 defined processing changes for improved creep-resistance (similar to the approach on the previous joint project on 347 steel [25–27]), and then produced limited quantities of selected sheets and foils in a Phase II effort of commercial processing. Creep-testing of Phase II AL20-25+Nb alloy materials is in-progress, and microstructural analysis will be done after that testing is complete.

These advanced heat-resistant austenitic stainless alloys, particularly HR120 and AL20-25+Nb, are both expected to provide microturbine recuperator manufacturers with all of the fabrication benefits of 347 steel (easy folding, welding and brazing), while also providing substantial performance and durability improvements, including higher temperature capability, cyclic operation, and good oxidation/corrosion resistance, even with alternative, more corrosive opportunity fuels (flare gas, land-fill gas, biofuels, etc.).

**Microstructural Analysis of Creep-Tested Foils.** Microstructural analysis of the gage portions of creep-ruptured foil specimens tested at 704 or 750°C has included scanning and analytical electron microscopy (SEM and AEM) to characterize the microstructural changes and identify precipitate phases forming during creep. Creep data on these alloys, including 347 steel, and alloys HR120, NF709 and 625, have been published previously [25,26].

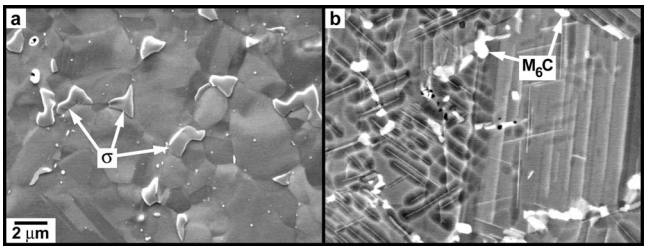


**Fig. 7 SEM micrographs showed (*a*) formation of Fe-Cr $\sigma$-phase at grain boundaries in 347 steel during creep at 704°C and 152 MPa (rupture after only 51.4 h), whereas (*b*) a relatively stable dispersion of Si-Mo-Cr-Ni $M_6C$ phase developed and remained stable along grain boundaries of alloy 625 during creep at 750°C and 100 MPa (rupture after 4510 h)**

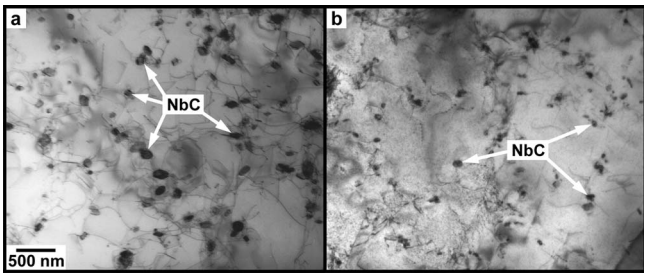


**Fig. 9 TEM micrographs show the fine NbC precipitation within the grains in foils of (*a*) alloy NF709 (rupture after 5015 h), and (*b*) alloy HR120 (rupture after 3319 h), both creep tested at 750°C and 100 MPa**

Figure 7(*a*) shows the formation of Fe-Cr $\sigma$-phase at grain boundary triple points in standard 347 steel (having a very fine, 2–5 $\mu$m grain size) after only 51.4 h creep at 704°C. Coarser-grained (>20 $\mu$m) alloy 625 creep-tested at 750°C for 4510 h exhibited a stable dispersion of Si-Mo-Cr-Ni $M_6C$ particles along the grain boundaries, and dense lath/subgrain boundary structure within each grain (Fig. 7(*b*)). The grains in alloy 625 showed no dislocation networks and no fine $\gamma'$ precipitation. Apparently the fine laths and intergranular precipitation helped to provide the creep-strength observed in alloy 625.

The NF709 and HR120 austenitic stainless alloys developed similar grain boundary structures during creep, but exhibited somewhat different intragranular precipitate structures, as shown in Fig. 8. The NF709 showed a finer grain structure (10–15 $\mu$m), a uniform dispersion of mainly Si-Mo-Cr-Ni $M_6C$ and some Cr-rich $M_{23}C_6$ particles along the grain boundaries, and little or no coarse intragranular precipitation after 5015 h of creep. By comparison, the HR120 had a coarser grain structure (30–40 $\mu$m), and copious precipitation of $M_{23}C_6$ along the grain boundaries and inside the grains. Higher magnification AEM showed that both NF709 and HR120 contain fine dispersions of NbC precipitates within the grains that formed during creep and pinned the dislocation networks. The stable carbide strengthening of grain boundaries and matrix provides the creep resistance for both of these alloys (Fig. 9).

**Screening in the ORNL Recuperator Test Facility.** Commercial foils and sheets of advanced alloys evaluated by laboratory creep and oxidation tests at ORNL are also being evaluated in an actual microturbine exhaust environment in the ORNL Recuperator Test Facility, based on a modified Capstone 60 kW microturbine [23,40]. More comprehensive test data on many different alloys have been presented elsewhere [23], and data directly comparing standard 347 steel and HR120 alloy foils, as well as other alloys, are presented in another paper at this conference [41]. Actual recuperator applications involve much lower stresses than the high-stress creep-rupture tests described above, but do include the dynamic interplay of stress, creep and oxidation with water vapor in a flowing, high gas velocity environment. Initial screening tests for 500 h clearly show that 347 steel foils degrade rapidly due to moisture-induced AA during oxidation and creep at 700°C and above. Consistent with the relative alloy comparisons in this work, the HR120 alloy has dramatically better performance at 700°C and above. Currently, similar testing of the ORNL modified 347 steels developed earlier [25,26] is complete, and testing of foils of the new AL20-25+Nb alloy, and alloy 625 are in progress.

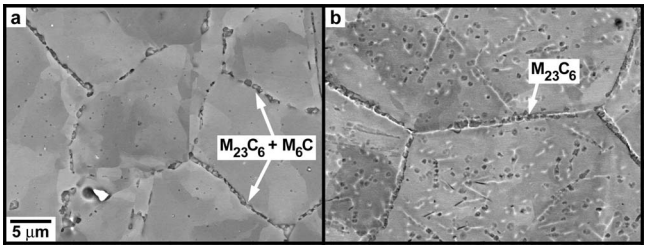


**Fig. 8 SEM micrographs show the precipitation that occured along grain boundaries in foils of (*a*) alloy NF709 (rupture after 5015 h), and (*b*) alloy HR120 (rupture after 3319 h), both creep tested at 750°C and 100 MPa. The NF709 alloy has mainly the Si-Mo-Cr-Ni $M_6C$ particles with some Cr-rich $M_{23}C_6$ particles, while the HR120 alloy has only $M_{23}C_6$ particles dispersed along the grain boundaries and in the matrix.**

## Summary and Future Work

Alloys 625 and HR120 are commercially available in sheet and foil forms that have significantly better oxidation- and creep-resistance compared to standard commercial 347 steel at 650–750°C. Such property differences should enable enhanced performance and temperature capability of recuperators at about 3.5–4 times the cost of 347 steel. The new AL20-25+Nb alloy has the potential to offer similar improvements in performance at a lower cost.

## Acknowledgment

Cooperation of Capstone Turbines, Inc., and Ingersoll-Rand Energy Systems, with the materials research efforts at ORNL is greatly appreciated. Research was sponsored by the U.S. Department of Energy, Assistant Secretary for Energy Efficiency and Renewable Energy, Office of Distributed Energy and Electrical Reliability, under Contract No. DE-AC05-00R22725 with UT-Battelle, LLC.

## References

[1] Monitor, D. G., 2003, Resource Dynamics Corp., Vienna, VA, Vol. III(5), September/October.
[2] "Microturbines are Generating Interest," *Materials and Components in Fossil Energy Applications*, Newsletter No. 143 (Dec. 1, 1999), U.S. DOE and EPRI, published by Oak Ridge National Laboratory, Oak Ridge, TN.
[3] Ward, M. E., 1995, "Primary Surface Recuperator Durability and Applications," Report No. TTS006/395, Solar Turbines, Inc., San Diego, CA.
[4] McDonald, C. F., 1996, "Heat Recovery Exchanger Technology for Very Small Gas Turbines," Int. J. Turbo Jet Engines, **13**, pp. 239–261.
[5] McDonald, C. F., 2003, "Recuperator Considerations for Future Higher Efficiency Microturbines," Appl. Therm. Eng., **23**, pp. 1463–1487.
[6] Rakowski, J. M., Stinner, C. P., Lipschutz, M., and Montague, J. P., 2004, "The Use and Performance of Oxidation and Creep-Resistant Stainless Steels in an Exhaust Gas Primary Surface Recuperator Application," ASME Paper No. GT2004-53917.
[7] Stambler, I., 2004, "Mercury 50 Rated at 4600 kW and 38.5% Efficiency With 5 ppm NOx," Gas Turbine World (Feb.-Mar.), pp. 12–16.
[8] Treece, B., Vessa, P., and McKeirnan, R., 2002, "Microturbine Recuperator Manufacturing and Operating Experience," ASME Paper No. GT-2002-30404.
[9] Kesseli, J., Wolf, T., Nash, J., and Freedman, S., 2003, "Micro, Industrial, and

Advanced Gas Turbines Employing Recuperators," ASME Paper No. GT2003-38938.
[10] Branch, D., 2003, "The WR-21 – From Concept to Reality," *Parsons 2003: Engineering Issues in Turbine Machinery, Power Plants and Renewables*, The Institute of Materials, Minerals and Mining, Maney Publishing, London, UK, pp. 1039–1055.
[11] Oswald, J. I., Dawson, D. A., and Clawley, L. A., 1999, "A New Durable Gas Turbine Recuperator," ASME Paper No. 99-GT-369.
[12] Antoine, H., and Prieels, L., 2002, "The ACTE Spiral Recuperator for Gas Turbine Engines," ASME Paper No. GT2002-30405.
[13] Hamilton, S. L., 2003, *The Handbook of Microturbine Generators*, PennWell Corp., Tulsa, OK.
[14] Agular, V. D., and Hamilton, S. L., 2004, "The Best Applications for Microturbines," Cogeneration and On-Site Power Production, **5**(4), pp. 101–106.
[15] *Advanced Microturbine Systems – Program Plan for Fiscal Years 2000 – 2006*, Office of Power Technologies, Office of Energy Efficiency and Renewable Energy, U.S. Department of Energy, Washington, DC, March.
[16] Maziasz, P. J., and Swindeman, R. W., 2003, "Selecting and Developing Advanced Alloys for Creep-Resistance for Microturbine Recuperator Applications," ASME J. Eng. Gas Turbines Power, **125**, pp. 310–315.
[17] Pint, B. A., and Rakowski, J. M., 2000, "Effects of Water Vapor on the Oxidation Resistance of Stainless Steels," Paper 00259 from Corrosion 2000, NACE-International, Houston, TX.
[18] Pint, B. A., More, K. L., and Tortorelli, P. F., 2002, "The Effect of Water Vapor on Oxidation Performance of Alloys Used in Recuperators," ASME Paper No. GT-2002-30543.
[19] Pint, B. A., and Peraldi, R., 2003, "Factors Affecting Corrosion Resistance of Recuperator Alloys," ASME Paper No. GT2003-38692.
[20] Maziasz, P. J., 1986, "Microstructural Stability and Control for Improved Irradiation Resistance and for High-Temperature Strength of Austenitic Stainless Steels," *MiCon 86: Optimization of Processing, Properties and Service Performance Through Microstructural Control*, ASTM-STP-979, ASTM, Philadelphia, PA, pp. 116–161.
[21] Maziasz, P. J., and Swindeman, R. W., 1987, "Modified 14Cr-16Ni Stainless Steels With Improved Creep Resistance at 700°C Due to Tailored Precipitate Microstructure," *Advances in Materials Technology for Fossil Power Plants*, ASM-International, Materials Park, OH, pp. 283–290.
[22] Maziasz, P. J., et al., 1999, "Improved Creep-Resistance of Austenitic Stainless Steel for Compact Gas Turbine Recuperators," Mater. High. Temp., **16**(4), pp. 207–212.
[23] Lara-Curzio, E., Trejo, R., More, K. L., Maziasz, P. J., and Pint, B. A., 2004,"Screening and Evaluation of Materials for Microturbine Recuperators," ASME Paper No. GT2004-54254.
[24] Swindeman, R. W., Maziasz, P. J., Pint, B. A., Montague, J. P., and Fitzpatrick, M, 1996, "Evaluation of Stainless Steels for Primary Surface Recuperator Applications," Oak Ridge National Laboratory Report C/ORNL96-0453, Oak Ridge, TN.
[25] Maziasz, P. J., Swindeman, R. W., Shingledecker, J. P., More, K. L., Pint, B. A., Lara-Curzio, E., and Evans, N. D., 2003, "Improving High Temperature Performance of Austenitic Stainless Steels for Advanced Microturbine Recuperators," *Parsons 2003: Engineering Issues in Turbine Machinery, Power Plants and Renewables*, The Institute of Materials, Minerals and Mining, Maney Publishing, London, UK, pp. 1057–1073.
[26] Maziasz, P. J., Pint, B. A., Shingledecker, J. P., More, K. L., Evans, D. E., and Lara-Curzio, E., 2004, "Austenitic Stainless Steels and Alloys With Improved High-Temperature Performance for Advanced Microturbine Applications," ASME Paper No. GT2004-54239.
[27] Stinner, C., 2003, "Processing to Improve Creep and Stress Rupture Properties of Alloy T347 Foil," Allegheny Ludlum Technical Center internal report, Brackenridge, PA, available upon request.
[28] Pint, B. A., and More, K. L., 2004, "Stainless Steels With Improved Oxidation Resistance for Recuperators," ASME Paper No. GT2004-53627.
[29] Pint, B. A., Swindeman, R. W., More, K. L., and Tortorelli, P. F., 2001, "Materials Selection for High Temperature (750–1000°C) Metallic Recuperators for Improved Efficiency Microturbines," ASME Paper No. 2001-GT-0445.
[30] Harper, M. A., Smith, G. D., Maziasz, P. J., and Swindeman, R. W., 2001, "Materials Selection for High Temperature Metal Recuperators," ASME Paper No. 2001-GT-0540.
[31] Pint, B. A., More, K. L., and Tortorelli, P. F., 2002, "The Effect of Water Vapor on Oxidation Performance in Alloys Used In Recuperators," ASME Paper No. GT-2002-30543.
[32] Maziasz, P. J., Pint, B. A., Swindeman, R. W., More, K. L., and Lara-Curzio, E., 2003, "Selection, Development and Testing of Stainless Steels and Alloys for High-Temperature Recuperator Applications," ASME Paper No. GT-2003-38762.
[33] Swindeman, R. W., 1998, "Stainless Steels With Improved Strength for Service at 760°C and Above," *Fatigue, Environmental Factors and New Materials*, Book No. H01155, PVP-Vol. 374, ASME, New York, pp. 291–298.
[34] Staubli, M., et al., "Materials for Advanced Steam Power Plants: The European COST522 Action," *Parsons 2003: Engineering Issues in Turbine Machinery, Power Plants and Renewables*, The Institute of Materials, Minerals and Mining, Maney Publishing, London, UK, pp. 305–324.
[35] Blum, R., and Vanstone, R. W., "Materials Development for Boilers and Steam Turbines Operating at 700°C," *Parsons 2003: Engineering Issues in Turbine Machinery, Power Plants and Renewables*, The Institute of Materials, Minerals and Mining, Maney Publishing, London, UK, pp. 489–510.
[36] Shingledecker, J. P., Swindeman, R. W., Klueh, R. L., and Maziasz, P. J., 2004, "Mechanical Properties and Analysis of Ultra-Supercritical Steam Boiler Materials," *Proceedings of the 29th International Technical Conference on Coal Utilization & Fuel Systems*, National Energy Technology Laboratory, Morgantown, WV.
[37] Kikuchi, M., Sakakibara, M., Otoguro, Y., Mimura, H., Araki, S., and Fujita, T., 1987, "An Austenitic Heat Resisting Steel Tube Developed For Advanced Fossil-Fired Steam Plants," *High Temperature Alloys, Their Exploitable Potential*, Elsevier Science, New York, pp. 267–276.
[38] Takahashi, T., 1988, "Development of High-Strength 20Cr-25Ni (NF709) Steel for USC Boiler Tubes," Nippon Steel Technical Report No. 38, July, Nippon Steel Corp., Tokyo, Japan.
[39] *Quality and Properties of NF709 Austenitic Stainless Steel for Boiler Turbing Applications*, 1996, Nippon Steel Corp., Revision 1.1, Tokyo, Japan.
[40] Lara-Curzio, E., Maziasz, P. J., Pint, B. A., Stewart, M., Hamrin, D., Lipovich, N., and DeMore, D., 2002, "Test Facility for Screening and Evaluating Candidate Materials for Advanced Microturbine Recuperators," ASME Paper No. GT-2002-30581.
[41] Lara-Curzio, E., Trejo, R., More, K. L., Maziasz, P. J., and Pint, B. A., 2005, "Evaluation and Characterization of Iron- and Nickel-Based Alloys for Microturbine Recuperators," ASME Paper No. GT2005-68630.